

AD-A284 124



LEOS 1993

0

# Summer Topical Meeting Digest on

## Optical Microwave Interactions

July 19-21, 1993



Sponsored by  
the IEEE Lasers and Electro-Optics Society in  
cooperation with the IEEE Microwave Theory  
and Techniques Society

## Visible Semiconductor Lasers

July 21-22, 1993

Sponsored by  
the IEEE Lasers and Electro-Optics Society

## Impact of Fiber Nonlinearities on Lightwave Systems

July 26-27, 1993

Sponsored by  
the IEEE Lasers and Electro-Optics Society

## Hybrid Optoelectronic Integration and Packaging

July 26-28, 1993



Sponsored by  
the IEEE Lasers and Electro-Optics Society  
and the IEEE Components, Hybrids, and  
Manufacturing Technology Society

N00014-93-1-1081  
Gigabit Networks

July 28-30, 1993



Sponsored by  
the IEEE Lasers and Electro-Optics Society  
and the IEEE Communications Society

94 9 02

099

Document has been approved  
for release and sale; its  
distribution is unlimited.



Red Lion Inn  
Santa Barbara, California

320P

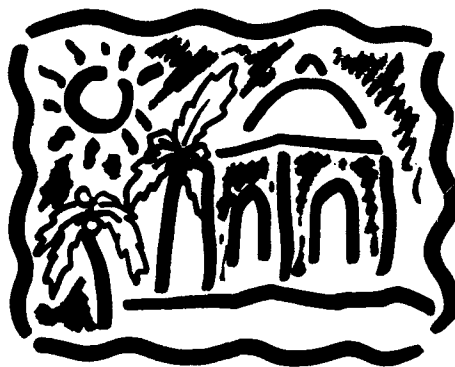


94-28656

# **Optical Microwave Interactions**

**July 19-21, 1993**

**Fess Parker's Red Lion Inn Resort  
Santa Barbara, California**



**Sponsored by  
the IEEE Lasers and Electro-Optics Society  
in cooperation with the IEEE Microwave Theory  
and Techniques Society**

**Support has been provided by the National Science Foundation**

**IEEE Catalog Number: 93TH0549-6  
Library of Congress Number: 93-77778**

**DTIC QUALITY INSPECTED 8**

The papers in this book comprise the digest of the meeting mentioned on the cover and title page. They reflect the authors' opinions and are published as presented and without change, in the interest of timely dissemination. Their inclusion in this publication does not necessarily constitute the endorsement by the editors, the Institute of Electrical and Electronics Engineers, Inc.

Copyright and reprint permissions: Abstracting is permitted with credit to the source. Libraries are permitted to photocopy beyond the limits of the U.S. copyright law for private use of patrons those articles in this volume. Instructors are permitted to photocopy isolated articles for noncommercial classroom use without fee. For other copying reprint or republication permission, write to Director, Publishing Services, IEEE, 345 E. 47th St., New York, NY 10017. All rights reserved. Copyright ©1993 by the Institute of Electrical and Electronics Engineers, Inc.

IEEE Catalog Number:	93TH0549-6
ISBN Number: Softbound	0-7803-1284-8
Microfiche Edition:	0-7803-1285-6
Library of Congress Number:	93-77778

# Optical Microwave Interactions Technical Committee

## Co-Chairs

G. Arjavalingam  
IBM T.J. Watson  
Research Center

C.H. Lee  
University of Maryland

## Program Committee

H. Fetterman  
UCLA

T. Kamiya  
University of Tokyo

D. Hornbuckle  
Hewlett Packard

A. Seeds  
University College, London

T. Itoh  
UCLA

J. Wiesenfeld  
AT&T Bell Labs

X.C. Zhang  
RPI

Accession For	
NTIS	CRA&I
DTIC	IAB
Unannounced	
Justification	
By	
Distribution	
Availability	
Dist	Availability Special
A-1	

# T A B L E O F C O N T E N T S

**MONDAY, JULY 19, 1993**

## **M1: MICROWAVE GENERATION AND DETECTORS**

<b>M1.1</b>	<b>New Concepts in 100 GHz High-Efficiency Photodetectors .....</b>	<b>3</b>
<b>M1.2</b>	<b>A 3-18 GHz Microwave Signal Generator Based on Optical Phase Locked Semiconductor DFB Lasers .....</b>	<b>5</b>
<b>M1.3</b>	<b>Microwave Generation Using Laser Activated High <math>T_c</math> Superconductors .....</b>	<b>7</b>
<b>M1.4</b>	<b>An Optically Controlled Microwave Attenuator .....</b>	<b>9</b>

## **M2: SYSTEMS I**

<b>M2.1</b>	<b>Analog Lightwave Links for CATV Applications .....</b>	<b>11</b>
<b>M2.2</b>	<b>Experimental Investigation of a Linewidth-Insensitive Coherent AM Optical Link .....</b>	<b>13</b>
<b>M2.3</b>	<b>Microwave Signal Generation Using a Standing-Wave Surface-Acoustic-Wave Bragg Device .....</b>	<b>15</b>
<b>M2.4</b>	<b>On the Behaviour of Microwave Signals in Optical Networks .....</b>	<b>17</b>

## **M3: CHARACTERIZATION TECHNIQUES**

<b>M3.1</b>	<b>Picosecond Optical Techniques for MMIC Characterization and Control .....</b>	<b>19</b>
<b>M3.2</b>	<b>Optimization of Optical-Microwave Phase-Locked Loop for Fast Real-Time Circuit Characterization .....</b>	<b>21</b>
<b>M3.3</b>	<b>Novel Technique for Optoelectronic Phase Locking of Microwave Signals Using a Laser-Diode-Based Electro-Optic Harmonic Mixer .....</b>	<b>23</b>
<b>M3.4</b>	<b>Variations in the Gain and Bandwidth of the MESFET Photoresponse with Bias and Optical Intensity .....</b>	<b>25</b>

## **M4: MODULATORS**

<b>M4.1</b>	<b>Lithium Niobate Traveling-Wave Optical Modulators to 50 GHz .....</b>	<b>27</b>
<b>M4.2</b>	<b>A Rigorous Analytic Model for Traveling Wave Optical Modulators with Conventional and Resonant Electrodes .....</b>	<b>29</b>
<b>M4.3</b>	<b>Polarization-Independent Fiber-Optic Microwave Modulator .....</b>	<b>31</b>
<b>M4.4</b>	<b>Modulation of Millimeter Waves by Optically Illuminating n-i-p-i Structures .....</b>	<b>33</b>

**TUESDAY, JULY 20, 1993**

## **T1: SPECTROSCOPY**

<b>T1.1</b>	<b>Generation of Terahertz Radiation From Semiconductor Optoelectronic Devices .....</b>	<b>37</b>
<b>T1.2</b>	<b>Optoelectronic Surface Field Spectroscopy .....</b>	<b>39</b>
<b>T1.3</b>	<b>Optically Steered MM-Wave Grating Surface Emitter .....</b>	<b>42</b>
<b>T1.4</b>	<b>Tunneling of Electromagnetic Waves in Two-Dimensional Photonic Crystals .....</b>	<b>44</b>

# T A B L E O F C O N T E N T S

## **T2: SYSTEMS II**

<b>T2.1 High Optical Power Effects in Fiber-Optic Links.....</b>	<b>46</b>
<b>T2.2 Fiber-Optic PSK Subcarrier Transmission at 35 GHz Over 6.3 km Using a Grating External Cavity Semiconductor Laser.....</b>	<b>48</b>
<b>T2.3 A Novel Optical Carrier Distribution for Millimeter Wave Personal Communication Systems.....</b>	<b>50</b>

## **T3: TRANSMISSION AND PROPAGATION**

<b>T3.1 Transmission-Line Characterization with Ultrafast Optoelectronics.....</b>	<b>52</b>
<b>T3.2 Picosecond Pulse Propagation on Coplanar Striplines with Lossy Semiconductor Substrates .....</b>	<b>53</b>
<b>T3.3 Transmission of Ultra-High-Bandwidth Pulses on a Low-Distortion Coplanar Stripline .....</b>	<b>55</b>
<b>T3.4 Ultrafast Scanning Probe Microscopy .....</b>	<b>57</b>

**WEDNESDAY, JULY 21, 1993**

## **W1: ULTRAFAST TECHNIQUES**

<b>W1.1 Measurement of New Millimeterwave Devices and Components Using Picosecond Techniques.....</b>	<b>61</b>
<b>W1.2 Ultrafast Photonic-to-Microwave Transformer (PMT) .....</b>	<b>63</b>
<b>W1.3 Characterization of Planar Antennas Fabricated on GaAs Epilayers Containing As Clusters For Picosecond Short-Pulse Applications .....</b>	<b>65</b>
<b>W1.4 Photoconductive Monolithic Wideband Transmitter Characterization.....</b>	<b>67</b>

## **W2: SYSTEMS III**

<b>W2.1 Transparent Optical Links Using Optical FM .....</b>	<b>69</b>
<b>W2.2 Fiber-Optic Prism True Time-Delay Antenna Feed .....</b>	<b>71</b>
<b>W2.3 Intensity Noise Reduction of Semiconductor Lasers Using External Optical Feedback .....</b>	<b>73</b>

<b>Author Index.....</b>	<b>75</b>
--------------------------	-----------

# Monday, July 19, 1993

## **Sessions:**

**M1: Microwave Generation and Detectors**

**M2: Systems I**

**M3: Characterization Techniques**

**M4: Modulators**



## New Concepts in 100 GHz High-Efficiency Photodetectors

John Bowers, Kirk Giboney, Yih-Guei Wey, and Mark Rodwell

*Department of Electrical and Computer Engineering*

*University of California, Santa Barbara, CA 93106, USA*

*(805)893-8447, (805)893-8714 (FAX)*

(Invited)

**ABSTRACT-** Passive components have been integrated with high-speed (>100 GHz), high-efficiency (>30%) photodiodes to enhance their usable frequency response. Travelling-wave photodetectors capable of >100 GHz bandwidth with nearly 100% internal quantum efficiency have been proposed and analyzed using a distributed model.

Demands for higher performance at lower cost are driving increased levels of integration in optoelectronics. Optical transmitters and receivers are now commonly based on optoelectronic integrated circuits (OEIC's) to enhance overall system performance while reducing cost. Photonic integrated circuits (PIC's) promise a means to increased capacity and flexibility by facilitating techniques such as wavelength division multiplexing. Rapid advances in materials and processing technologies have enabled impressive progress in these areas.

High-speed surface-normal-illuminated photodiodes have been fabricated using GaInAs/InP p-i-n graded double-heterostructures [1]. Bandgap grading at each hetero-interface has minimized carrier trapping and series resistance, allowing bandwidths as high as 110 GHz. However, the usable frequency response is generally degraded by connections to bulk bias tees and various mismatched loads.

These devices have been integrated with bias tees and matched resistors to extend their usable performance (Fig. 1) [2]. The integrated bias tees eliminate bandwidth limitations imposed by external, connectorized bias tees. The matched source resistors reduce frequency response variations resulting from load mismatches, extend the bandwidth, but reduce efficiency.

The response of the circuit shown in Fig. 1 is

$$v_{meas} = i_{photo} Z_0 \cdot \frac{R_s}{R_s + Z_0} \cdot \frac{1}{1 - \Gamma_s \Gamma_L e^{-j2\beta\ell}} \quad (1)$$

where  $\Gamma_s$  and  $\Gamma_L$  are the source and load reflection coefficients,  $\beta$  is the (frequency dependent) propagation constant, and  $\ell$  is the length of the transmission line connecting the source and load.

The matched source resistor greatly reduces  $\Gamma_s$ , so the frequency dependence from the third term is minimized. It also shunts photocurrent as expressed by the second term, doubling the ideal RC bandwidth while cutting the quantum efficiency in half. The bias tee and matched resistor are both implemented without additional process steps by using large area photodiodes instead of dielectric bypass capacitors, and by forming the resistors in the n-InP layer.

The actual improvement in reflection coefficient was better than 13 dB from 45 MHz to 40 GHz. Time domain optical responses of various size photodiodes with and without bias tees and matched resistors were measured by pump-probe electro-optic sampling, and the derived bandwidths are plotted in Fig. 2. The largest bandwidths were 109-110 GHz for the 2 and 3  $\mu\text{m}$  square devices without bias tees or matched resistors, and 108 GHz for the 7  $\mu\text{m}$  square device with bias tee and matched resistor. The external quantum efficiency was 32% from measurements at the anti-reflection coating center wavelength of 1.3  $\mu\text{m}$  on large area devices.

Consideration of the microwave waveguide nature of an edge-coupled photodetector has led to a distributed model that can be used to exploit the optical/electrical travelling-wave interaction through the travelling-wave photodetector (TWPD) [3]. TWPD's are capable of large bandwidths with quantum efficiencies approaching unity by designing the electrical waveguide to control propagation of the electrical wave in parallel with the optical wave and to eliminate reflections. These devices retain moderate optical bandwidth, temperature insensitivity, and high saturation intensity, qualities compromised in devices based on resonant cavity enhancement or quantum confinement. In addition, the in-plane optical waveguide configuration of this type of device is conducive to direct integration with other active and passive optical components, such as lasers, amplifiers, couplers, filters, wavelength demultiplexers, etc.

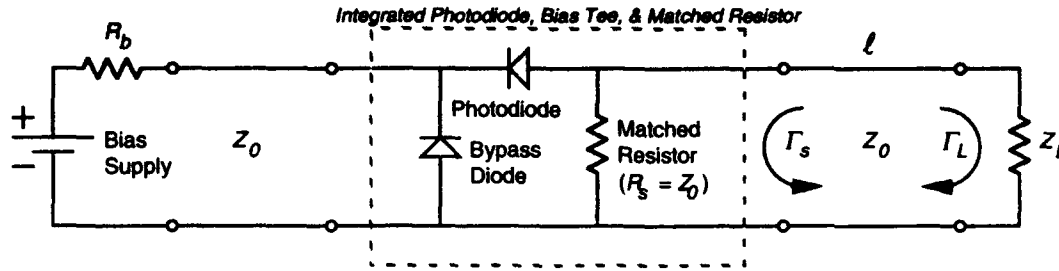


Figure 1. Integrated photodiode, bias tee, & matched resistor in external circuit.

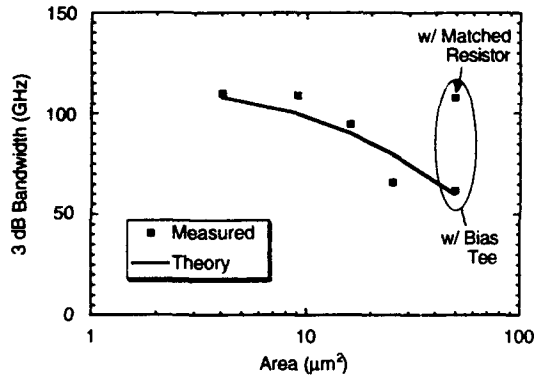


Figure 2. 3-dB electrical bandwidth vs. photodiode area.

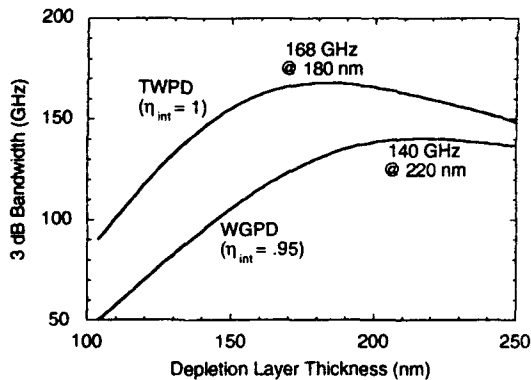


Figure 3. 1  $\mu\text{m}$  wide, GaAs/AlGaAs TWPD & WGPD calculated net bandwidths vs. depletion layer thickness.

The p-i-n waveguide of a TWPD supports slow-wave mode propagation of microwaves, and a circuit model can be used to derive the transmission line properties as well as the RC bandwidth limitations. The primary bandwidth limitations result from carrier drift time, parasitic RC time, and velocity mismatch time. The velocity mismatch bandwidth limitation is effectively an intrinsic RC limitation, given by

$$B'_{vm} \approx \frac{\Gamma \alpha}{2\pi} \frac{\sqrt{2} v_o v_e}{\sqrt{5v_o^2 - v_e^2}} \quad (2)$$

where  $\Gamma \alpha$  is the modal absorption coefficient,  $v_o$  is the optical group velocity, and  $v_e$  is the electrical phase velocity.

The net bandwidths for TWPD's, including effects of carrier transit, parasitic RC, and velocity mismatch, are plotted vs. depletion layer thickness in Fig. 3 along with those for similar WGPD's for comparison. The values can be considered close to the bandwidth-internal efficiency product, since they are calculated for optically long devices. The external efficiency is dominantly limited by input coupling. Various tapered waveguide schemes could be used to maximize free-space or fiber coupling.

In conclusion, simple methods for including passive components to enhance the performance of high-speed photoreceivers have been demonstrated. Such methods could be more generally applied to integrate filters, matching networks, coupling structures, or other functions in OEICs. TWPD structures have been modelled and analyzed, and they promise large bandwidth and very high efficiency. This type of device can be simply included in high-speed OEIC or PIC photoreceivers.

This work was sponsored by the ONT Block Program on Electro-Optics Technology, DARPA, and Rome Labs.

Yih-Guei Wey is now with A T & T Bell Laboratories, Holmdel, NJ 07733.

- [1] Y. G. Wey, K. S. Giboney, J. E. Bowers, M. J. W. Rodwell, P. Silvestre, P. Thiagarajan, and G. Y. Robinson, "110 GHz Double Heterostructure GaInAs/InP p-i-n Photodiode," presented at Ultrafast Electronics and Optoelectronics, San Francisco, Jan., 1993, PD1-1.
- [2] K. S. Giboney, Y. G. Wey, J. E. Bowers, M. J. W. Rodwell, P. Silvestre, P. Thiagarajan, and G. Y. Robinson, "High-Speed GaInAs/InP p-i-n Photodiodes with Integrated Bias Tees," presented at Fifth International Conference on Indium Phosphide and Related Materials, Paris, Apr., 1993, TuE5.
- [3] K. S. Giboney, J. E. Bowers, and M. J. W. Rodwell, "Traveling-Wave Photodetectors," *IEEE Photon. Technol. Lett.*, vol. 4, pp. 1363-1365, Dec., 1992.

## A 3-18 GHz Microwave Signal Generator based on Optical Phase Locked Semiconductor DFB Lasers

U. Gliese, T.N. Nielsen, M. Bruun, E. Lintz Christensen and K.E. Stubkjaer  
Center for Broadband Telecommunications, Electromagnetics Institute  
Technical University of Denmark, Building 348, DK-2800 Lyngby, Denmark

Recently, there has been great interest in optical phase locked loops (OPLLs) with semiconductor lasers for optical generation of microwave signals with high spectral purity [1]-[4]. The use of semiconductor lasers as opposed to solid state lasers, such as the Nd:YAG, is attractive due to their compactness and potential for monolithic opto-electronic integration. A major drawback of semiconductor lasers is, however, phase noise which must be reduced significantly for most practical applications. For this purpose, a wideband OPLL can be very efficient if properly designed [2]. We present the experimental results of a 3 to 18 GHz microwave signal generator based on a heterodyne OPLL with offset phase locked 1.5  $\mu\text{m}$  DFB lasers without external cavities or electrical feedback for linewidth narrowing.

As shown in Fig. 1, the microwave signal generator consists of an OPLL carrier generator and an optical modulator [6]. The OPLL carrier generator consists of a free running transmitter laser (Tx-laser) with a 2 MHz linewidth, an optical frontend, a microwave mixer, a loop filter (lowpass with phase lead correction) and a Current Controlled Oscillator laser (CCO-laser) with a 6 MHz linewidth [5]. The microwave signal generated by the beat of the two semiconductor lasers is compared to the signal from a microwave reference oscillator. The resulting phase error signal is then fed back to the CCO-laser which is forced to track the Tx-laser. This causes a significant reduction of the phase noise of the beat signal. The OPLL is a second order loop with a loop bandwidth,  $f_z$ , as defined in [2], of 180 MHz, a loop gain of 181 dBHz and a loop propagation delay,  $\tau_d$ , of only 400 ps. To our knowledge, these loop data are the best ever reported.

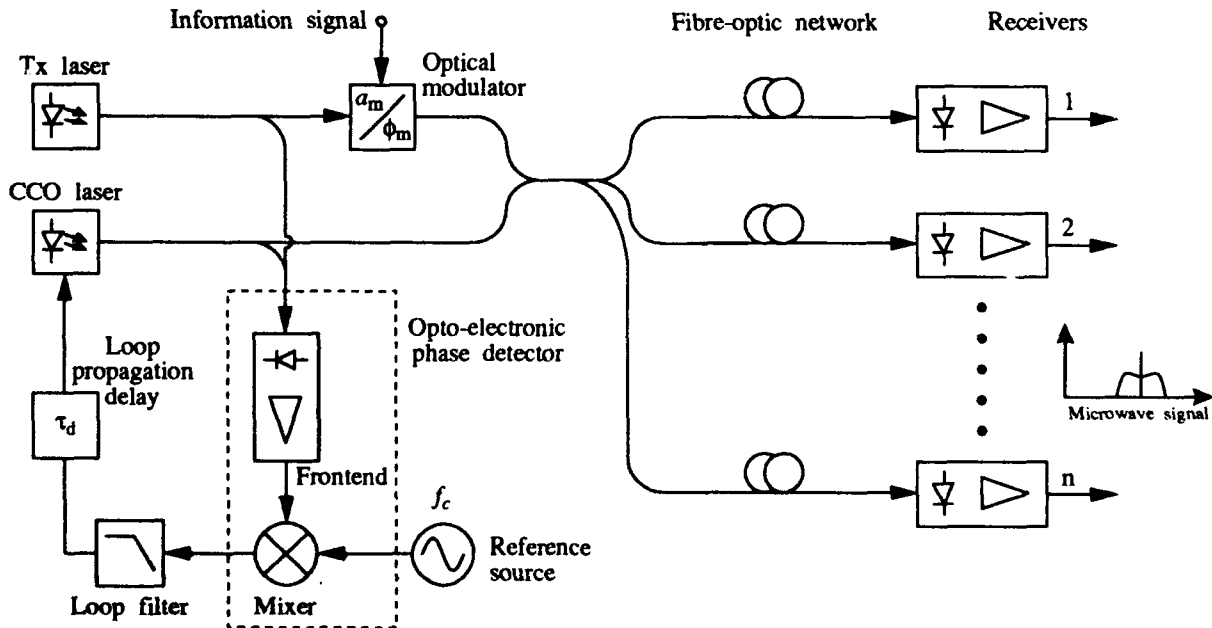


Figure 1: Configuration of the optical microwave signal generator.

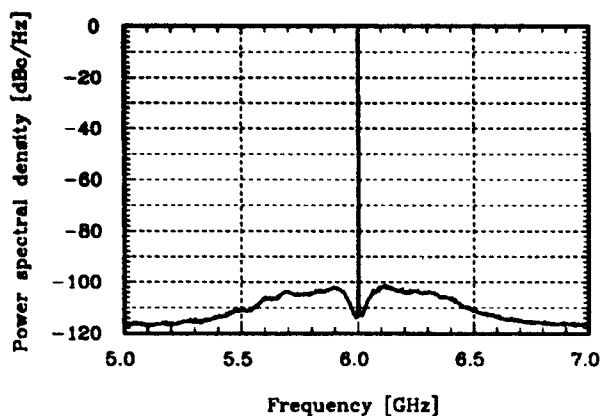


Figure 2: Measured power spectral density of the phase locked beat signal at 6 GHz.

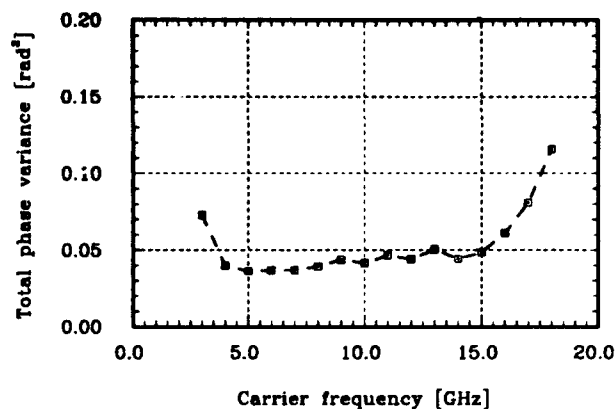


Figure 3: Total phase variance of the generated microwave carrier versus carrier frequency.

At present, the carrier generator operates a continuous frequency range of 3 to 18 GHz determined by the frontend and mixer bandwidths. With MMIC technology it is expected that this range can be extended to 100 GHz. In Fig. 2 the power spectral density of the carrier generated by the phase locked lasers is shown for a frequency of 6 GHz. Close to carrier the spectral shape corresponds exactly to that of the microwave reference oscillator, i.e.,  $\sim 1/f$  Hertz linewidth. The noise level is as low as -110 dBc/Hz @ 100 kHz, -115 dBc/Hz @ 200 kHz to 20 MHz and less than -102 dBc/Hz at all offsets. Of the total signal power 97.7 % is phase locked in the carrier and the total phase variance is only 0.04 rad<sup>2</sup>. This is the lowest value reported for phase locked semiconductor lasers to date. From Fig. 3 it is seen that the phase variance is below 0.05 rad<sup>2</sup> for carriers from 4 to 15 GHz. The carriers in this range fulfill the phase noise requirements of existing QPSK/DQPSK microwave telecommunication systems. Furthermore, the locked loop operation is very reliable. An acquisition range of 640 MHz has been measured, and the average time to cycle slip,  $T_{av}$ , is estimated to  $10^{11}$  seconds. This yields a probability of less than 0.3 % for one cycle slip within 10 years.

In conclusion, the results clearly demonstrate the feasibility of optical generation of microwave signals with high spectral purity by the use of moderate linewidth semiconductor lasers. As opposed to solid state lasers they are compact and has potential for monolithic opto-electronic integration, which is a very important issue for practical applications.

### Acknowledgement

Part of this work was carried out under ESA, ESTEC contract 110938, and the lasers were made by the Swedish Institute of Microelectronics.

### References

- [1] M. Kourogi et. al.: Photonics Technology Letters, Vol. 3, No. 3, 1991, pp. 270-272.
- [2] U. Gliese et. al.: Journal of Lightwave Technology, Vol. 9, No. 6, 1991, pp. 779-790.
- [3] R.T. Ramos et. al.: Electronics Letters, Vol. 28, No. 1, 1992, pp. 82-83.
- [4] U. Gliese et. al.: Photonics Technology Letters, Vol. 4, No. 8, 1992, pp. 936-938.
- [5] R.J.S. Pedersen et. al.: In Proceedings of ECOC, 1990, pp. 279-282
- [6] T.N. Nielsen et. al.: Electronics Letters, Vol. 28, No. 3, 1992, pp. 235-236.

### **M1.3 9:20am - 9:40am**

#### **Microwave Generation Using Laser Activated High $T_c$ Superconductors**

**Wei-Lou Cao, Yuan-Qun Liu, Yi-Sern Lai, Sheng-Lung L. Huang, Vutthi Bhanthumnavin  
and Chi H. Lee**

**Department of Electrical Engineering  
University of Maryland, College Park, MD 20742  
Phone: (301) 405-3739, FAX: (301) 314-9281**

**Zhi-Yuan Shen, Philip Pang, Dennis J. Kountz and William L. Holstein  
Central Research and Development, Du Pont  
P.O.Box 80304, Wilmington, Delaware 19880-0304**

#### **Summary**

The generation of microwaves by illuminating a high temperature superconducting switch with a 50 ps pulse train from a mode-locked laser is reported. Microwave power as a function of frequency was measured.

##### **1. The HTS switches and the experimental setup**

$Tl_{0.5}Pb_{0.5}Sr_2CaCu_2O_7$  and  $Tl_2Ba_2CaCu_2O_8$  films of thickness  $0.8 \mu m$  were fabricated on (100)  $LaAlO_3$  substrates by two-step post-deposition anneal processes. The thallium thin films were epitaxially oriented, with their c-axes normal to the surface and their a-axes aligned with the  $\langle 100 \rangle$  directions of the underlying substrate. The critical temperature  $T_c$  of the  $Tl_2Ba_2CaCu_2O_8$  films used in this experiment were measured inductively and resistively to be 105 K. Critical current density was measured and found to be  $1.5 \times 10^6 A/cm^2$  at 80 K,  $2.6 \times 10^6 A/cm^2$  at 70 K and  $5.0 \times 10^6 A/cm^2$  at 50 K respectively. The HTS switches were fabricated as 50 Ohm coplanar lines.

The HTS switch was mounted on a cold finger located in a vacuum cryogenic chamber and provided with a dc or microwave bias (Fig.1). The devices were illuminated with 50 ps pulses from a Coherent ANTARES 76-YLF CW mode-locked laser with a repetition rate of 75.70 MHz.

##### **2. CW microwave generation**

An opening switch is made for generating electrical pulses with a laser pulse train. The frequency content of this electrical pulse train includes harmonics of its repetition rate extending up to very high frequency. The power of the microwave signal generated by laser interaction with the HTS devices was investigated as a function of frequency. The microwave attenuation varies with microwave frequency as  $f^{2.34}$  at temperature of 78.6 K (Fig. 2). Microwave signals up to 10 GHz were generated. An average laser power of 280 mW and a charging current of 10 mA were used for H-type HTS switches, and 730 mW and 20 mA for coplanar type switches. The relative attenuation was introduced from the decay time of the switched signal caused by the thermal effect of the laser-HTS interactions which is strongly depended on the thickness of the devices, the average laser power and the operating temperature.

##### **3. Discussion**

The efficiency of the laser-microwave generation using HTS devices is very low. It can be greatly improved by selecting optically thin HTS films ( $0.1 \mu m$ ) and lower operating temperatures (half  $T_c$ ) as thermal effects from the laser-HTS interactions can be ignored under such condition.

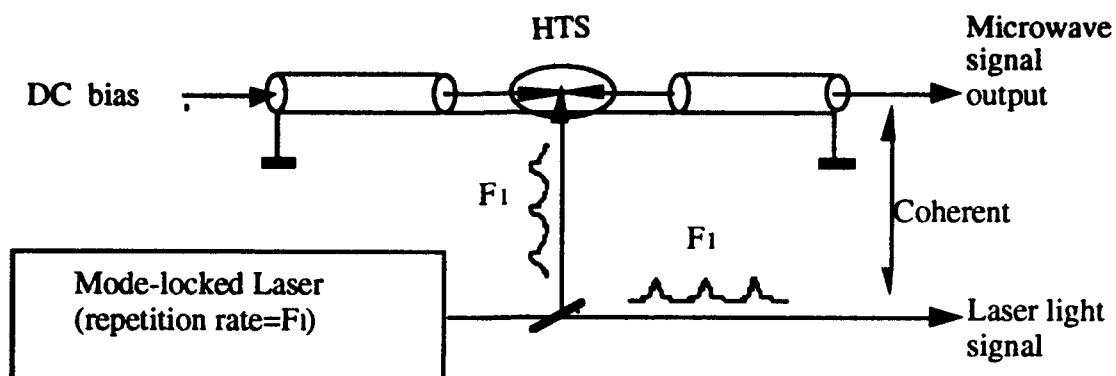


Fig.1 Experimental Setup for Microwave Genetation

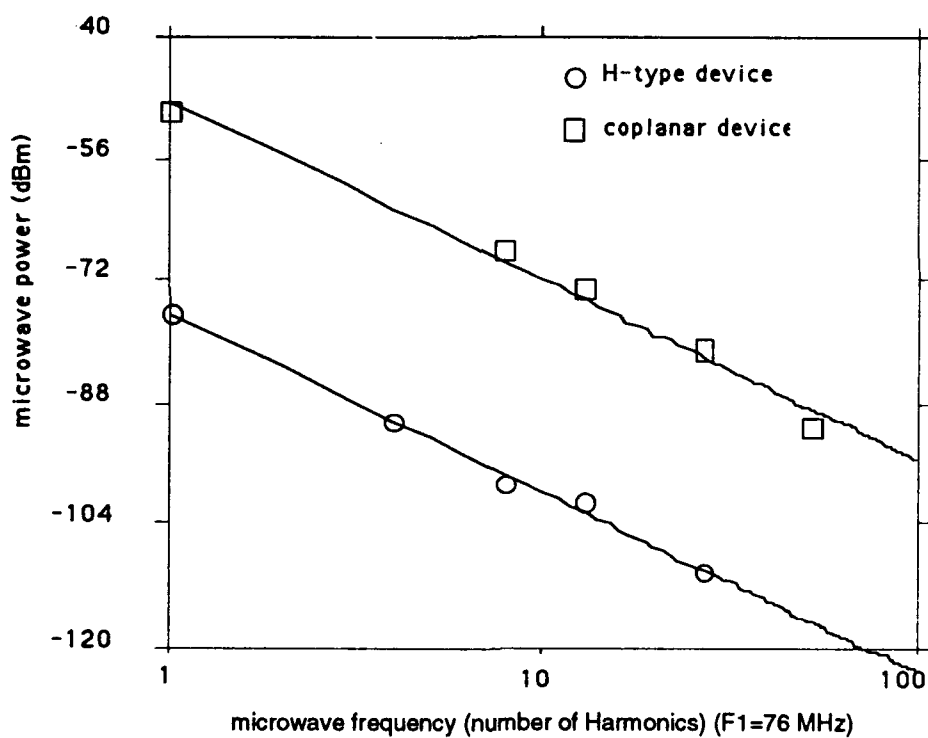


Fig.2 The Power of the Microwaves Generated by Laser Interaction with HTS Switch as The Function of the Frequency

**An Optically Controlled Microwave Attenuator**

Stephen E. Saddow, Bruno J. Thedrez,<sup>†</sup> Armand Balekdjian,<sup>‡</sup> and Chi H. Lee<sup>†</sup>

Army Research Laboratory  
2800 Powder Mill Road  
Adelphi, MD 20783

<sup>†</sup>University of Maryland  
Department of Electrical Engineering  
College Park, MD 20782

<sup>‡</sup>Army Research Laboratory  
Fort Monmouth, NJ 07703

***Summary***

A hybrid optoelectronic scheme, suitable for controlling microwave integrated circuits, has been demonstrated. By employing optoelectronic techniques, we have demonstrated up to 26 dB of rf attenuation using a linear one-dimensional (1-D) AlGaAs laser diode array and a silicon photoconductive switch. Calculations indicate that this attenuation scheme can provide up to 40 dB of broad-bandwidth isolation, once optimized.

The optically controlled attenuator scheme is as follows. A planar microwave transmission line is fabricated on either a silicon (Si) or gallium-arsenide (GaAs) substrate. Silicon and GaAs are both excellent photoconducting materials; therefore, fabrication of high-speed transmission lines on these materials yields imbedded photoconductive switches (PCSs) resident in the high-speed lines. Illumination of these switches by the appropriate light source creates a conductive plasma in the switch gap, and since this switch is between the transmission lines conductors, the plasma changes the transmission line's characteristic impedance.

Thus the creation of a plasma within the transmission line causes the propagating wave to be attenuated, with the degree of attenuation being a function of the induced plasma density. For example, calculations indicate that this attenuation scheme yields 30 dB of rf attenuation for a shunt rf impedance of  $1\ \Omega$ . In addition, the attenuation value is roughly an exponential function of the shunt rf impedance (i.e., the induced plasma density), which can be accurately controlled by varying the incident laser pulse intensity.

The planar transmission line geometry that was chosen was coplanar waveguide, since broad-area laser diodes can be easily focused onto the gaps between the transmission line's conductors. Both Si and GaAs were used as the substrate material. GaAs has a photo-carrier lifetime of  $\approx 5$  ns. Si was used for applications where a long attenuation time is desired, since the photo-carrier lifetime in Si is on the order of microseconds. 50- $\Omega$  coplanar waveguide-photoconductive switches (CPW-PCSs) were fabricated with multiple gap spacings between the coplanar conductors of 10, 20, 30 and 50  $\mu\text{m}$ . The switch resistance is proportional to the square of the gap length, which permits the switch resistance to be characterized as a function of laser

intensity and applied electric field (i.e., drift-assisted carrier conduction). The GaAs CPW-PCSs were characterized in this fashion using both single-stripe broad-area laser diodes and a tunable titanium sapphire laser [1]. The results of these measurements show that the optimum laser photon energy is just above the switching materials band gap energy, with the optimum electric field equal to 500 V/cm or less.

Using a linear 1-D AlGaAs laser diode array operating at  $\lambda \approx 800$  nm with a peak power of 5 W, a dynamic resistance of  $4.5\ \Omega$  was achieved with a silicon CPW-PCS (10- $\mu\text{m}$  gap) that was placed in a high-speed 50- $\Omega$  circuit. When a 500-MHz cw rf waveform is sent through the CPW-PCS, we achieved 26 dB of rf attenuation during a time equal to the 4 $\mu\text{s}$  FWHM of the LD array pulse (see Fig. 1). The attenuation as a function of both optical and rf power were also measured. The attenuation is a slight function of rf power, with the attenuation increasing with increasing rf power. The dependence on optical power, as shown in Fig. 2, follows theoretical predictions for the CPW-PCS.

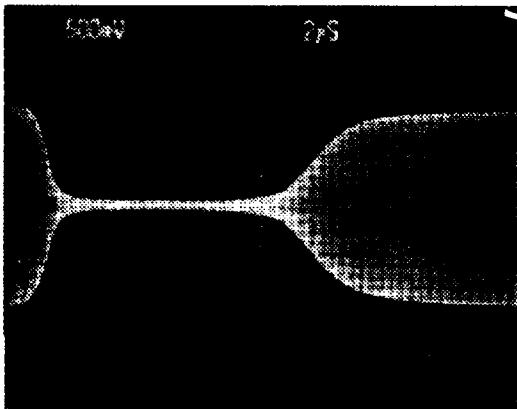


**Fig. 1** CPW-PCS output waveform showing attenuation of 500 MHz envelope of 26 dB.

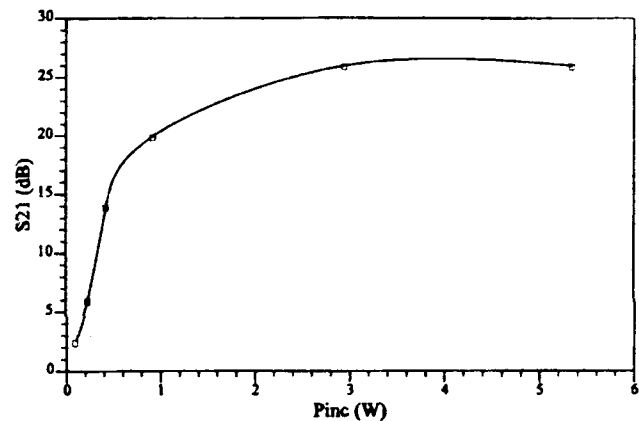


**Fig. 2** Si CPW-PCS attenuation,  $S_{21}$ , versus incident laser diode peak power.

In this paper, details covering the CPW-PCS design, fabrication and characterization will be presented, along with attenuation results using a 10 $\mu\text{m}$  gap CPW-PCS. Discussion as to the implementation of this attenuation scheme using single stripe laser diodes will also be given.

### References

- [1] S. E. Saddow, B. J. Thedrez, S. L. Huang, T. J. Mermagen, and C. H. Lee, "An Investigation of the Temperature and Electric Field Dependence of a GaAs Microwave Photoconductive Switch," *SPIE-OE/LASE 93: Optically Activated Switching III*, conference proceedings, No. 1873-31, Los Angeles, CA, Jan. 21, 1993.

**M2.1 10:30am - 11:00am  
(Invited)**

### **Analog Lightwave Links for CATV Applications**

**M. R. Phillips and T. E. Darcie**

**AT&T Bell Laboratories — Crawford Hill Laboratory  
791 Holmdel-Keyport Road, Holmdel, NJ 07733-0400**

Analog lightwave links for CATV application continue to penetrate the CATV industry, especially as cable operators position themselves in the race to provide broadband information services to the mass market. The analog lightwave systems are remarkably simple. The RF spectrum of the CATV signal, without format change, modulates the transmitted light intensity, and an optical receiver reverts the light intensity back to RF. This simplicity comes at the price of very demanding requirements on the noise and distortion performance of the transmitter and receiver. The AM-VSB formatted signal currently used for television requires a signal-to-noise ratio (SNR) of about 50 dB. With an additional distortion requirement of -60 dB with respect to the signal, and the CATV spectrum of 40-60 subcarriers spread over a multi-octave spectrum (55 - 500 MHz), the source must be extremely linear [1]. A workhorse of the CATV lightwave industry is the directly modulated 1.3  $\mu\text{m}$  distributed feedback (DFB) laser. Recently introduced to the market is an externally modulated YAG laser at 1.3  $\mu\text{m}$ . Erbium-doped fiber amplifiers (EDFAs) have not found wide application because the amplifier noise impairs the system noise performance [2], and suitable source lasers are not widely available. We present the system design issues for the various transmitter types.

Directly modulated distributed feedback (DFB) lasers at 1.3  $\mu\text{m}$  with extremely linear light-current (L-I) characteristics have been developed and are very attractive to use because the CATV spectrum is simply imparted onto the drive current of the laser. Transmission at 1.3  $\mu\text{m}$  is necessary for transmission over standard fiber in order to avoid distortion that is generated by the interplay between chirp and dispersion [3]. The broad modulated linewidth of directly modulated DFBs ( $\approx 3$  GHz) is sometimes an advantage, however. Multipath interference, which is unavoidable in fiber transmission because of Rayleigh backscatter, converts phase noise into intensity noise [4]. The broad linewidth of the directly modulated bulk lasers results in most of that intensity noise falling outside of the modulation bandwidth.

Dispersion problems associated with a wide linewidth source can be avoided by modulating a CW source with an external interferometric modulator. For zero-chirp modulation, the bandwidth of the modulated signal is essentially the linewidth of the CW source. In this case, the intensity noise falling into the CATV band from multipath interference is minimized as the linewidth is reduced. Typically the linewidth must be less than about 1 MHz. Interferometric modulators have an inherent nonlinear (cosine) transmission-voltage characteristic. Second-order distortion is suppressed by keeping the modulator biased at the exact 50% transmission point, and third-order is suppressed by predistorting the RF signal. The channel capacity of such systems is determined largely by the performance of the predistorter. Another consideration for a narrow linewidth source is that the power launched into the fiber must be kept below the stimulated Brillouin scattering threshold [5]. These and other constraints for the two transmitter types are listed in Table 1.

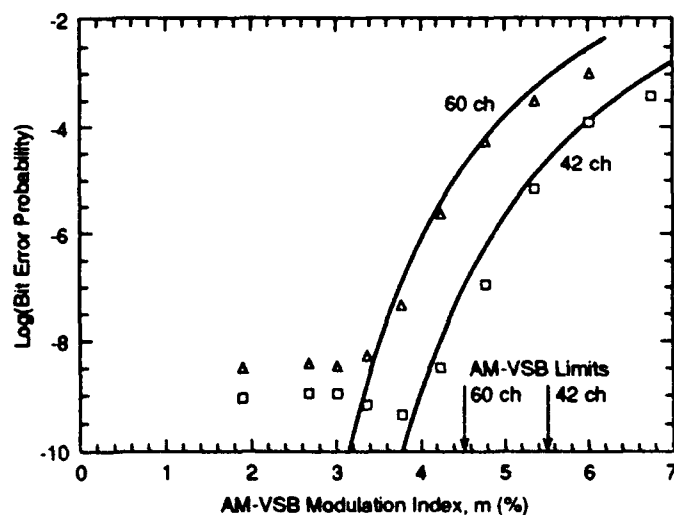
On the horizon for CATV systems is the broadcast of digital channels in addition to or replacing the AM-VSB channels. Even for multi-level or quadrature amplitude modulated (QAM) formats, the signal-to-noise ratio required for error-free ( $\text{BER} = 10^{-9}$ ) transmission is 29 dB, 20 dB less than that necessary for AM-VSB signals. It is proposed that a band of QAM channels be added at the high end of the CATV spectrum ( $>500$  MHz). In the case of a directly modulated DFB laser, the additional

harmonic distortion is not a significant impairment [6]. Actual measurements of hybrid (AM and QAM) systems have shown, however, that another type of distortion is significant. A measurement of the bit-error rate (BER) of a 64-QAM signal in the presence of AM channels is shown in Figure 2. The error rate is severely degraded by clipping of the laser. A calculation which models the clipping noise as impulse noise predicts the error rates shown as a solid line [7]. Surprisingly, the QAM signal can impose a more stringent limit on the modulation depth than the AM signal. We present additional considerations for QAM analog modulated signals.

- [1] T.E. Darcie et al, *IEEE Trans. Micro. Theory Techniq.*, Vol. 38, 1990, pp.524-33
- [2] M.R. Phillips et al, *Phot. Tech. Lett.*, Vol. 4, 1992, pp. 790-2
- [3] M.R. Phillips et al, *Phot. Tech. Lett.*, Vol. 3, 1991, pp. 481-3
- [4] A.F. Judy, *Proceedings ECOC*, 1989, Paper TuP-11, p.486
- [5] X.P. Mao et al, *Phot. Technol. Lett.*, Vol. 4, 1992, pp. 287-9
- [6] R.H. Wentworth, *Tech. Digest OFC '93*, Vol.4, pp.223-4
- [7] I.M.I. Habbab, G.E. Bodeep, and X. Lu, *to be published*.

Table 1. CATV transmitter constraints due to fiber transmission		
15 km FIBER LINK	DIRECTLY MODULATED DFB	EXTERNALLY MODULATED CW SOURCE
CHROMATIC DISPERSION	OK at 1.3 $\mu\text{m}$ → Distortion at 1.5 $\mu\text{m}$ , Compensate	OK
POLARIZATION MODE DISPERSION	→ Distortion Need low chirp	OK
STIMULATED BRILLOUIN SCATTERING	OK	→ Noise $P < 9.5 \text{ mW}$ , or phase dither
EDFA	→ Distortion Tune to flat of gain spectrum or compensate	OK (1.5 $\mu\text{m}$ source?)
MULTIPATH INTERFERENCE	→ 1-2 dB Noise penalty for typical DFB Higher chirp better	OK for $\Delta\nu < 0.7 \text{ MHz}$

Figure 2. Bit-error rate performance of a 64-QAM signal, 0.56% modulation depth, vs. modulation depth per channel of 42 and 60 AM channels. The solid lines are the predicted BER due to clipping noise.



## Experimental Investigation of a Linewidth-Insensitive Coherent AM Optical Link

Masafumi Tabara<sup>2</sup>, Delfin Jay M. Sabido IX, Thomas K. Fong, Chung-Li Lu and Leonid G. Kazovsky  
 Stanford University, Department of Electrical Engineering  
 202 Durand Bldg., Stanford, CA 94305-4055  
 Phone (415) 725-4542, Fax (415) 723-9251  
 E-mail: tabara@cher.stanford.edu

Video delivery and antenna remoting are two important applications of analog optical links [1]. High dynamic range is needed for both applications. At low signal power, the dynamic range of coherent systems is larger than that of direct detection systems [2]. In many applications, semiconductor lasers have to be used as light sources to make the system compact. However, laser diodes have relatively large linewidth (due to phase noise) that may cause signal degradation. To reduce the impact of phase noise, some kind of phase noise cancellation is required. Theoretical investigation of one cancellation technique - AM-WIRNA (WIRNA stands for the receiver structure: Wide bandpass filter - Rectifier - NARrow lowpass filter) heterodyne system - has been reported in [2]. That theory predicts that, with WIRNA detection, distortion is quite small.

In this paper we investigate the AM-WIRNA system experimentally. We use the Spurious Free Dynamic Range -- SFDR -- as the measure of system performance. The SFDR is defined as the ratio of the maximum RF power as limited by the third order intermodulation product (IMP) to the minimum power as limited by the receiver noise; i.e.,

$$SFDR = \frac{RFpower \big|_{IMP = noise}}{RFpower \big|_{signal = noise}} = \frac{m^2 \big|_{IMP = noise}}{m^2 \big|_{signal = noise}}$$

where  $m$  is the modulation index. We measured the dependency of the SFDR on the linewidth and the optical signal power.

Fig. 1 shows the block diagram of the AM-WIRNA system and Table 1 lists the system parameters used in the experimental investigations. The power of the two-tone IMP is measured to evaluate the SFDR experimentally. The 1.4 GHz and 1.5 GHz sinusoidal signals are sent to the LiNbO<sub>3</sub> Mach-Zehnder intensity modulator. The intermediate frequency (IF) at the receiver is 10 GHz. The bandwidth of the bandpass filter is 4 GHz, while the lowpass filter bandwidth is 2 GHz. A frequency doubler is used as the square law detector. The signal laser is a 1.5  $\mu$ m distributed feedback laser; its linewidth is varied by changing its temperature and driving current. To obtain linewidths greater than 30 MHz, the effect of spectral broadening due to laser chirp is used. To stabilize the IF frequency, an AFC loop is used.

Fig. 2 shows the dependency of the SFDR on the linewidth of the transmitter laser. No degradation is observed up to 1.0 GHz. The reason is that the frequency separation between the test signal and the edge of the bandpass filter is 500 MHz (since the RF input signal frequency is about 1.5 GHz, the IF spectral components are observed at 10 GHz and 10 $\pm$ 1.5 GHz). Even if the linewidth is 1 GHz, most of the signal power is within the bandpass filter bandwidth.

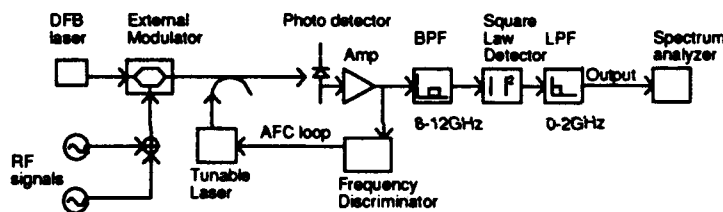
<sup>1</sup> This work is supported by Department of the Air Force under Contract Number F30602-91-C-0141 and ONR under Contract Number N00014-91-J-1857.

<sup>2</sup> Permanent address : the Furukawa Electric Co., Ltd. 5-1-9, Higashi-Yawata, Hiratsuka 254 JAPAN.

Fig. 3 shows the dependency of the SFDR on the received optical signal power for (a) the coherent detection system and (b) the direct detection system. Solid lines represent the theoretical results for the same system parameters. The SFDR of the coherent system is larger than that of the direct detection system as long as the received signal power is less than 100  $\mu\text{W}$ . Even if the received signal power is greater than 100  $\mu\text{W}$ , it is possible to make the SFDR of the coherent system better than that of the direct detection system by increasing the local oscillator power. There is some discrepancy between theoretical and experimental results. The causes of the discrepancy are the nonlinearity of amplifiers, the nonidealities of components and the polarization mismatch. The distortions produced by the squarer are the dominant source of the discrepancy.

In summary, we have proved experimentally that the AM-WIRNA coherent system is insensitive to laser phase noise and has a better SFDR than a similar direct detection system for the input powers lower than 100  $\mu\text{W}$ . Since this system has good dynamic range, a passive star network can be used for transmission; that is, there is no need to use active devices and amplifiers between the distribution center and the subscribers.

- [1] H. Sobol, "The application of microwave techniques in lightwave systems", *J. Lightwave Technol.*, vol. LT-3, no 3, March 1987.
- [2] T. K. Fong, D. J. M. Sabido IX and L. G. Kazovsky, "Linewidth-insensitive Coherent AM Analog Optical Links Using Semiconductor Lasers", *IEEE/OSA Photonics Technology Letters*, vol. 4, April 1993, accepted for publication.



Local oscillator power	228uW
Local oscillator linewidth	147kHz
Transmitter linewidth	7.9MHz
BPF bandwidth	4GHz
LPF linewidth	2GHz
RF input frequency	1.4GHz, 1.5GHz
Noise figure of amplifier	1.22dB
Relative intensity noise	-148dB/Hz

Fig. 1 : Block diagram of the AM-WIRNA heterodyne link (BPF: bandpass filter; LPF: lowpass filter)

Table 1 : System parameters

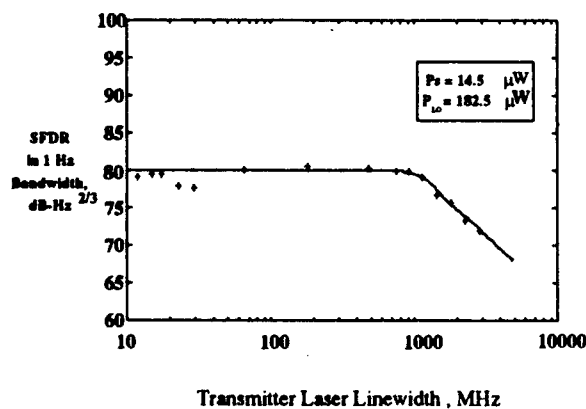


Fig. 2 : Impact of transmitter laser linewidth on the spurious-free dynamic range

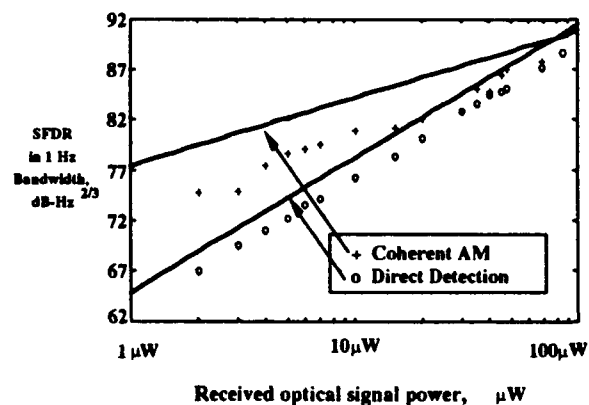


Fig. 3 : Spurious-free dynamic range versus the received optical signal power: theoretical and experimental results

## Microwave signal generation using a standing-wave surface-acoustic-wave Bragg device

R. D. Martin\*, R. G. Hunsperger and C. S. Ih  
Department of Electrical Engineering  
University of Delaware  
140 Evans Hall, Newark, DE 19716

Guided-wave acousto-optic (AO) devices using surface-acoustic-waves (SAWs) and optical waveguides have many applications. One possible employment is in a Bragg standing-wave surface-acoustic-wave (SW-SAW) device. The SW-SAW Doppler shifts the optical beam both up and down by the acoustic frequency. Thus, upon detection, the beat frequency of the two coherent Doppler shifted beams effectively generates a carrier for the optical signal at twice the acoustic frequency. The generation of carriers by heterodyning two copropagating optical beams has been dubbed Double Beam Modulation (DBM). Previously carriers in the hundreds of MHz have been demonstrated with this technique using both bulk and guided-wave acousto-optic devices.[1] The use of a guided-wave acousto-optic device has been extended into the GHz range.

The SW-SAW acousto-optic device is shown in figure 1. A single mode titanium indiffused optical waveguide was formed in the lithium niobate substrate ( $\text{LiNbO}_3$ ) to confine the light near the surface. The standing-wave surface-acoustic-waves were created using a pair of interdigital transducers (IDTs). Since lithium niobate is a highly piezo-electric material the IDTs could be placed directly on the surface. The geometry of the device insured that the acousto-optic interaction was in the Bragg regime. Rutile prisms were used to couple the light into and out of the device. Devices with acoustic frequencies of approximately 300 MHz, 400 MHz, 600 MHz and 875 MHz, generating carriers of 600 MHz, 800 MHz, 1.2 GHz, and 1.75 GHz respectively, were fabricated.

A 600 MHz device was implemented in a Double Beam Modulation configuration. An 830 nm laser diode was intensity modulated with VHF television channels 2, 4, and 6. Figure 2 shows the spectrum of the diffracted/shifted beam captured by an avalanche photodetector. A 1.2 GHz carrier is generated from the heterodyning of the up and down Doppler shifted beams. A 700 MHz local oscillator was used to down convert the video signal to UHF channels 28, 30, and 32 where a TV or VCR was used to demodulate the signals. Three different video signals were transmitted and demodulated simultaneously with no obvious crosstalk and minimal signal degradation.

\* current address :

MicroDevices Laboratory, Jet Propulsion Laboratory, 4800 Oak Grove Drive, Pasadena , CA 91109

[1] C. S. Ih, R. G. Hunsperger, X. L. Wang, J. J. Kramer, K. Kissa, R. S. Tian, J. Butler, X. C. Du, W. Y. Gu, and D. Kopchick, "Double-Beam-Modulation Technologies for Free-Space Laser Communications." SPIE OE-LASE '90, *Proceedings of Free-Space Laser Communication Technologies II*, Vol. 1218, p. 53, Los Angeles, January 1990.

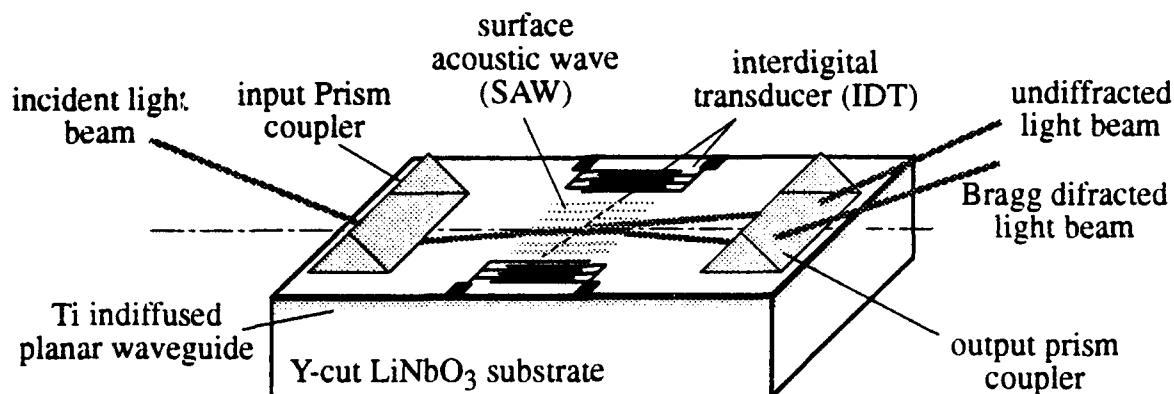


Figure 1 Guided-wave AO setup with optical waveguide and surface acoustic waves.

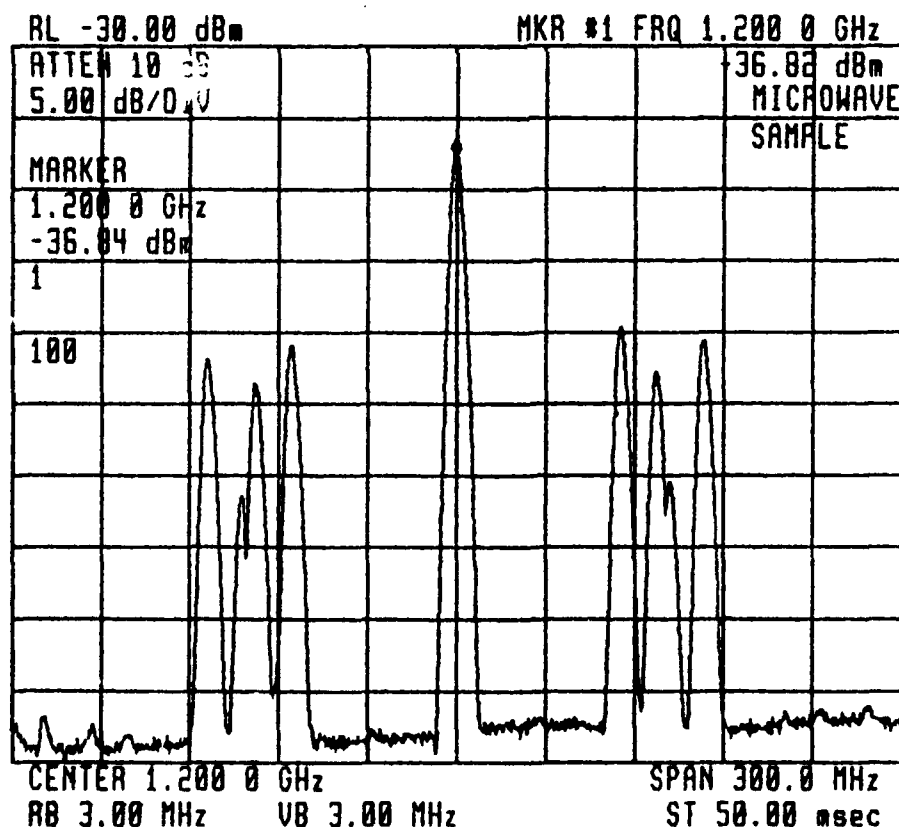


Figure 2 Detected signal showing 1.2 GHz carrier with three video signals.

## On The Behaviour of Microwave Signals in Optical Networks

Smail TEDJINI senior member, Diaa KHALIL and Anh HO QUOC  
LEMO-CNRS 833, 23 Avenue des Martyrs BP 257, 38016 Grenoble, FRANCE.

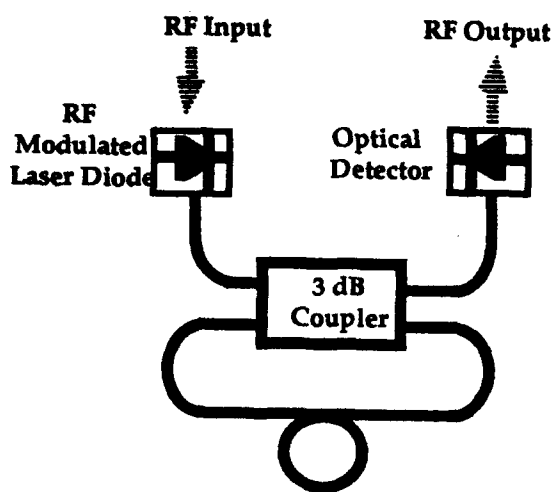
### SUMMARY

In the last years, significant progress have been accomplished in the domain of optical communications such that the microwave transmission by optical carriers is now an existing system currently used. The technological advances in optical-to-electrical and electrical-to-optical conversion allows today to consider not only the simple optical transmission of microwave signals but also the processing of these signals using optical networks. For this purpose the propagation of the optical signal in a network with dimensions comparable to the wavelength of the modulating microwave signal should be studied. This requires to overcome some problems like the polarisation dependence, the dimensional effects on the modulating signals, the multimode properties of some optical components, etc., which makes the optical network fed by a microwave modulated laser beam a subject of great interest. The object of this work is to study the behaviour of the microwave modulating signal in two optical elements : the Fabry-Perot interferometer and the unbalanced Mach-Zehnder one. The two interferometers are constructed using single mode optical fibers and 3 dB directional couplers as shown in Fig. 1 a and b. The system is excited by an optical signal of wavelength  $\lambda=1.3 \mu\text{m}$  modulated by an electrical (microwave) signal of frequency between 0.3 MHz and 3 GHz. A suitable photodetector is used to extract the electrical output signal. The overall system (source, network and detector) may be considered as a microwave "device" for which we can define a microwave transfer function or, in general, microwave scattering parameters. Using the HP8702 lightwave component analyser with the HP83400A light source and the HP83410A lightwave receiver, we have measured the characteristics of this system.

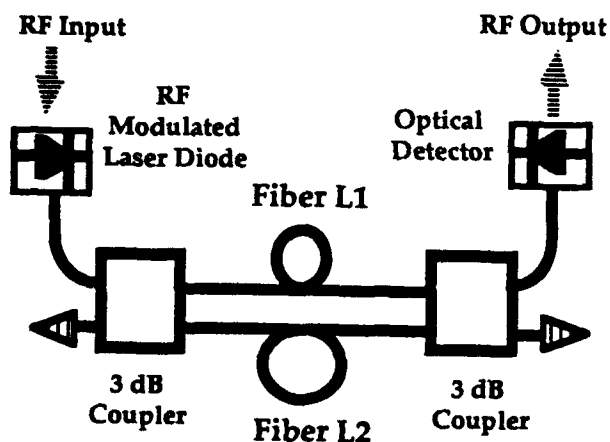
For the Fabry Perot interferometer with a delay length  $L=10 \text{ m}$ , the  $S_{12}$  parameter, measured in the frequency range from 1 to 1.1 GHz, is shown in Fig. 2. Oscillations with multiple periodicities can be seen in the amplitude variations of  $S_{12}$ . Similar oscillations are also obtained in the phase variations. These oscillations are due to the existence of two propagating optical modes : the TE and the TM modes. Using an optical polarizer, one mode can be filtered and we obtain the amplitude variations shown in Fig. 3-a where a harmonic oscillation with good purity is obtained. For the phase variations shown in Fig. 3-b, the harmonic oscillations are superposed on the linear phase variation of the transmission line. This results in frequency zones with constant phase shift (about 10 MHz for each zone). This frequency range is a function of the delay length  $L$  of the interferometer. Such a constant phase shift may be interesting for certain microwave applications in which a phase shift independent of the frequency (for a certain range) is required. On the other hand, the amplitude variations show a filtering effect with about 3 dB amplitude of oscillation (corresponding to the coupler division ratio). This effect may perturb the functional behaviour of the network and then it should be taken into account.

For the Mach-Zehnder interferometer, the microwave frequency response  $S_{21}(f)$  is shown in Fig. 4. As a "microwave device", we can notice that this response corresponds to a band rejection filter with a very interesting rejection ratio exceeding 40 dB. The device has also shown a very good phase linearity and a delay time which is frequency independent, except for the rejected frequencies. Measuring the performances in the band 0.3MHz-3GHz we have obtained a quasi zero dispersion device and all the rejected frequencies are given by  $n.f_0$  where  $n$  is an integer and  $f_0$  is a characteristic frequency determined by the optical path difference  $L_1-L_2$ . In our experiment we have  $L_1-L_2 = 5 \text{ m}$  which corresponds to  $f_0 = 43.456 \text{ MHz}$ . The rejected frequencies can thus be controlled by changing the path difference. This gives a large domain of application as the length difference can be easily varied from some centimetres to some ten's of meters. Moreover, for millimeterwaves, an integrated optical device with a path difference less than 1cm can be used. Finally, these results open the door for a new family of optical-based microwave devices with exciting characteristics. These "devices" are interesting as they enables to perform functions on the microwave modulating signals in the optical domain and then it enables to avoid all the problems of coupling and radiation when treating the microwave signals at high frequencies. The final paper will include more experimental results as well as their theoretical analysis.

# **Figures:**



**a-) Fabry-Perot interferometer**



**b-) Unbalanced Mach-Zehnder Interferometer**

**Fig. 1. Schematic diagram of the measured networks.**

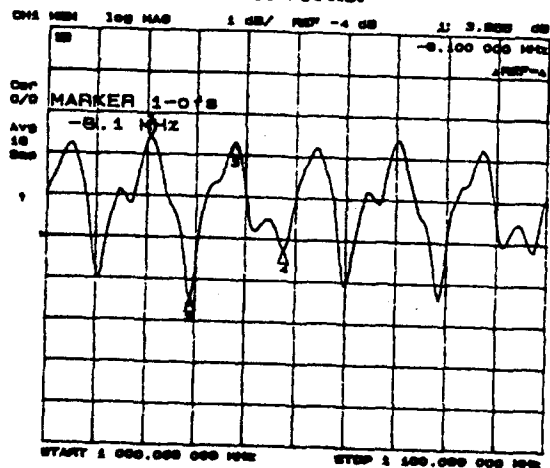
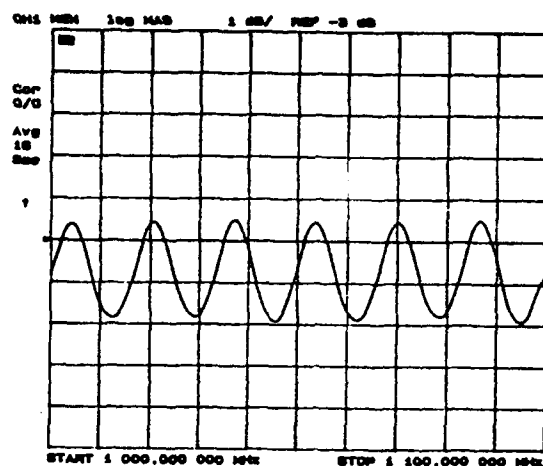
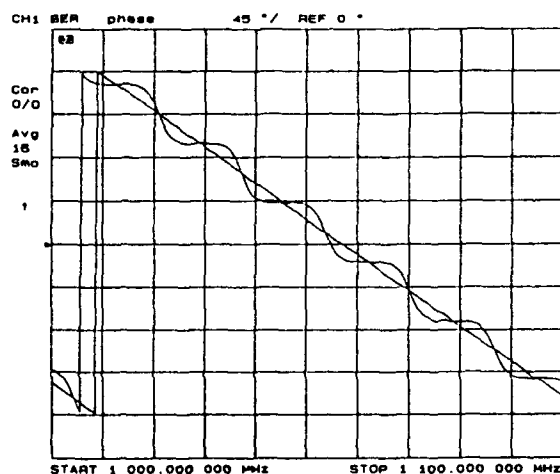


**Fig 2. Measured microwave transmission coefficient  $S_{12}$  (in dB) of the Fabry-Perot interferometer (without polarizer) in the frequency range 1 to 1.1 GHz.**



**a-) Amplitude in dB**



**b-) Phase**

**Fig 3. Measured transmission coefficient  $S_{21}$  of the Fabry-Perot interferometer in the frequency range 1 to 1.1 GHz when a polarizer is used between the laser diode and the interferometer.**

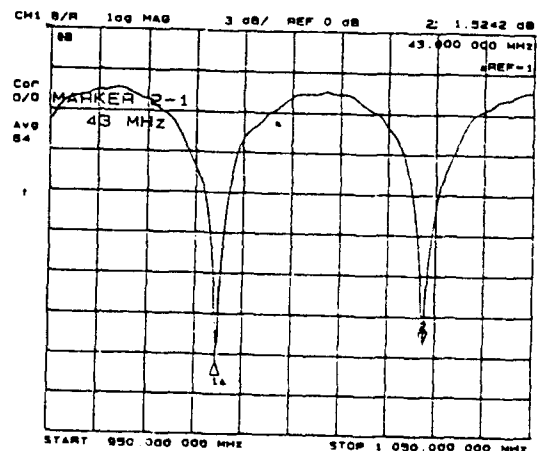


**Fig 4. Measured microwave transmission coefficient  $S_{12}$  (in dB) of the Mach-Zehnder interferometer in the frequency range 0.95 to 1.05 GHz.**

## **Picosecond Optical Techniques for MMIC Characterization and Control**

Hing-Loi A. Hung <sup>1</sup>

COMSAT Laboratories, Clarksburg, Maryland 20871

Chi. H. Lee and Sheng-Lung L. Huang

University of Maryland, Department of Electrical Engineering  
College Park, Maryland 20742

Ultrafast optical techniques using photoconductive (PC) switches have demonstrated microwave/millimeter-wave monolithic integrated circuit (MMIC) characterization, millimeter-wave (MMW) signal generation, and true-time phase-shift delay. Using microwave/optical intermixing techniques, phase-lock of voltage controlled oscillators (VCOs), waveform display of microwave signal, and device characterization have also been achieved. This paper presents some of the recent accomplishments in these areas, and their potential applications MMIC manufacturing, real-time network analyzer measurements, and signal generation and controls in microwave systems.

### **1. MMIC CHARACTERIZATION**

The successful progress of MMIC development has resulted in the insertion of these components into various microwave and MMW systems. The conventional coaxial/waveguide frequency-domain approach for testing GaAs MMIC, especially in MMW frequencies is one of the major cost drivers in MMIC production. In addition, oscillations may occur during the characterization of these active devices that are not properly terminated with matching circuits over a wide bandwidth.

Optical techniques using picosecond pulse excitation and photoconductive (PC) sampling or electrooptic (EO) sampling offer several advantages over conventional network analyzer method using contacting CPW (coplanar waveguide) probes for on-wafer device and MMIC characterizations. Broadband frequency response results (over 100 GHz bandwidth) can be achieved with one single measurement setup. In one of these optical/microwave techniques, a narrow picosecond electrical pulse which contains very broadband signal is generated on-wafer using a fast photoconductive (PC) switch. Measurements performed in the time domain are then converted to conventional microwave S-parameter results by applying Fourier transformation to the measured data. The real time display of the frequency response can be accomplished by the same computer controlling the optical system.

An example of recent accomplishment includes the successful characterization of a 60 GHz P-HEMT MMIC amplifier using MMIC-process compatible optical test structures, with a measurement bandwidth of 160 GHz, and a sensitivity of  $5 \text{ mV}/(\text{Hz})^{1/2}$ . A six-port calibration method has been employed to allow the use of reduced-size test structure, and to increase measurement accuracy. It has been found that the PC sampling technique provides better sensitivity compared to that offered by EO sampling on microstrip MMICs. Other achieved characterization results, and measurement requirements such as fabrication-compatible PC test structures, signal strength, and dynamic range will be addressed.

---

<sup>1</sup> Currently with Raytheon Company, M/S E21, 430 Boston Post Road, Wayland, MA 01778.

## 2. OPTICAL/MICROWAVE INTERMIXING SYSTEMS FOR PHASE-LOCK, WAVEFORM DISPLAY, AND DEVICE CHARACTERIZATION

The theory behind this technique is the intermixing of picosecond optical pulses and microwave signals in an ultrafast GaAs PC switch, or in a GaAs microstrip circuit via the EO effect. With this technique, optically phase-locked MMIC VCO has been demonstrated at 10 GHz with reduced phase noise. Other applications include the on-wafer frequency and phase characterization of VCOs, measurements of output power and spectral noise of a microwave oscillation signal.

The technique has also been extended to obtain the display of the waveform of a microwave/MMW signal on a conventional oscilloscope via a low frequency replica, and to produce a two-dimensional electrical field distribution of a GaAs microstrip circuit. The phase locked scheme can also be used to characterize other non-linear devices and circuits by displaying the waveforms of the signal passing through them.

Recently, the intermixing technique combined with a step recovery diode has been used to achieve real-time, time-domain S-parameter characterization of MMICs using PC switches. The PC switch was used as an optical-microwave mixer to establish the synchronization between a laser pulse train and a free running microwave oscillator. By employing the equivalent-time sampling principle, one can map out the time domain waveform of the signal propagating along the microwave circuit, with high sensitivity. This technique enables the characterization of the linear frequency response of a MMIC via time-domain measurement. In contrast to the all-electronic technique such as the one mentioned in Section 1, this optical approach requires the detection of low frequency signal from the MMIC chip. As a result, S-parameter characterization can be achieved without relying on the accurate positioning of the short electrical pulses.

## 3. MMW GENERATION AND CONTROL

Synchronization between ultrafast laser pulse trains and MMW signal can be readily established when the MMW signal is generated directly by laser pulses on a PC switch and passing them through an MMIC amplifier. The technique can also provide optical control of amplitude and/or phase of the generated MMW signal. Signal in the 60 GHz range has been obtained using this technique, and true-time delay phase-shift of broadband MMW signal has also been demonstrated through control of the optical path. Phase-shift of 360 degrees has been demonstrated at the center frequency of 60 GHz. Potential applications include phased-array radar systems.

## 4. CONCLUSIONS

The incorporation of picosecond optics into microwave/MMW technologies has created a new class of techniques and devices that can provide various functions not readily attainably by conventional electronic means. In this paper, a number of applications using these techniques have been presented. Recently, the phase-locked technique using a laser-diode source has been demonstrated by other researchers; the compact source makes the optical techniques discussed here even more suitable for the realization of commercial on-wafer characterization system, as well as optically controlled communications and radar systems.

## Optimization of Optical-Microwave Phase-Locked Loop for Fast Real-Time Circuit Characterization

Sheng-lung L. Huang\*, Chi H. Lee\*, and Hing-Loi A. Hung†

\* Electrical Engineering Department,

University of Maryland, College Park, MD 20742

† COMSAT Laboratories, Clarksburg, MD 20871

For a real-time sampling system, time coherence between the test signal and sampling signal is crucial [1]. In this paper, we used photoconductive (PC) switches as optical-microwave mixer for phase-locking between a mode-locked laser pulse train and a free running microwave oscillator. The optical microwave phase-locked loop (OM-PLL) is used in a real-time sampling system with 100 GHz bandwidth and a sensitivity of  $5 \mu V/\sqrt{Hz}$ . Optimization of the OMPLL is important to have fast measurement time and less noise in the sampling system.

The schematic diagram of the optical-microwave phase-locked loop is shown in Figure 1.  $f_{mw}$ ,  $f_l$ ,  $f_{if}$ , and  $f_{ref}$  are the microwave frequency, laser repetition rate, intermediate frequency (IF), and reference signal frequency, respectively. The frequency of the reference signal, 4.75 MHz, is frequency divided from the laser mode-locker frequency. The transfer function of the phase-locked loop,  $H(s)$ , is

$$H(s) = \frac{(2\xi - \frac{MN \pm 1}{k_0 k_d A_0} \omega_n) \omega_n s + \omega_n^2}{s^2 + 2\xi \omega_n s + \omega_n^2}$$

where  $\omega_n = \sqrt{\frac{k_0 k_d A_0}{(MN \pm 1)(\tau_1 + \tau_2)}}$  and  $\xi = \frac{(MN \pm 1) + k_0 k_d A_0 \tau_2}{2} \sqrt{\frac{1}{k_0 k_d A_0 (MN \pm 1)(\tau_1 + \tau_2)}}$   
 $\tau_1$  and  $\tau_2$  are the time constants of the loop filter.

$H(s)$  has an optimized 2.5-dB resonance peak at  $\omega_n$ . 50-dB improvement in signal-to-noise ratio is observed in the phase-locked microwave oscillator, as shown in Figure 2. Its S/N is close to the S/N of the optical-microwave intermixed signal.

The phase-locked microwave oscillator was then used to drive a step recovery diode (SRD), which generates 40-ps electrical pulses. The output waveform of the SRD was measured by its low frequency replica, as shown in Figure 3. The IF frequency was reduced to 300 kHz to increase time resolution. The PC sampler has a 10 ps response time and  $5 \mu V/\sqrt{Hz}$  sensitivity. Due to the high sensitivity, PC sampler is suitable for real-time linear time-domain network analysis. Signals with 200 mV magnitude can clearly be sampled in a few microsecond.

### References

- [1] See references in R. B. Marcus, ed., "Measurement of High-Speed Signals in Solid State Devices," Chap. 3 - 7, Academic Press Inc., 1990.

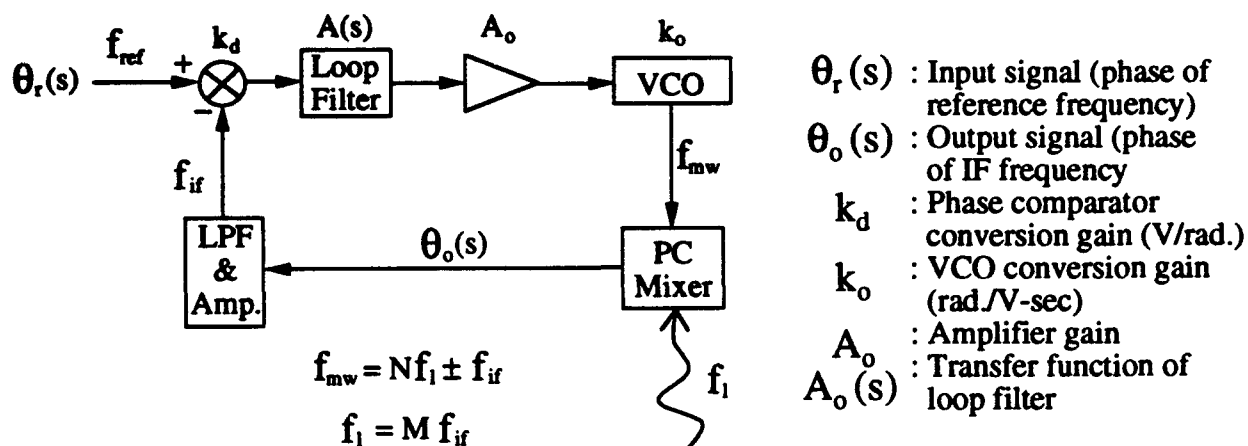


Figure 1 : Schematic diagram of the OMPLL.

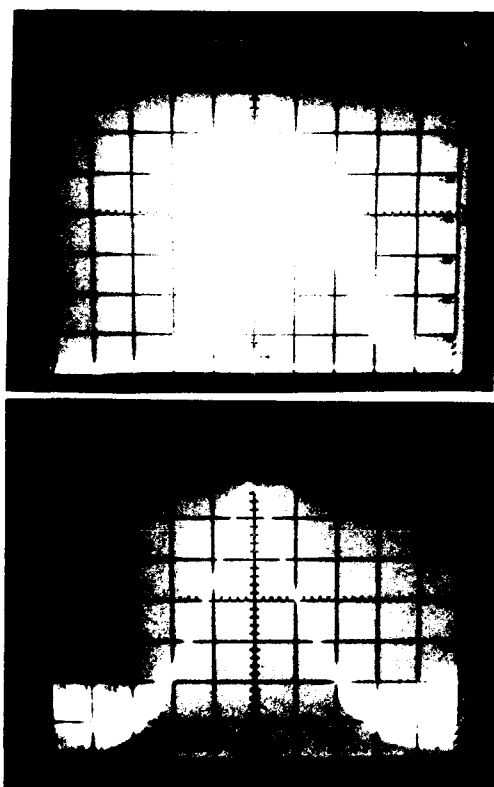


Figure 2 : Free running microwave oscillator spectrum (top), phase-locked microwave oscillator spectrum (bottom). Center frequency : 979 MHz, resolution bandwidth : 10 kHz, scan bandwidth : 200 kHz.

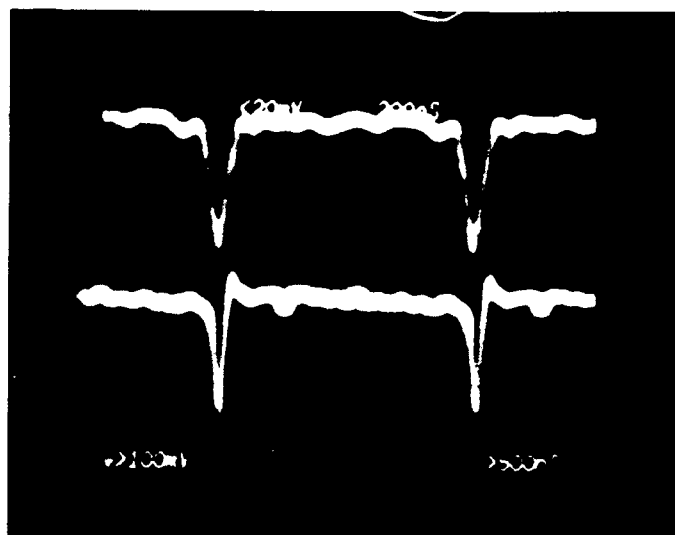


Figure 3 : Real-time display of the SRD output waveform using a sampling scope (top trace) and with the OMPLL technique (bottom trace).

## NOVEL TECHNIQUE FOR OPTOELECTRONIC PHASE LOCKING OF MICROWAVE SIGNALS USING A LASER-DIODE-BASED ELECTRO-OPTIC HARMONIC MIXER

Ci-Ling Pan, C.-S. Chang, Chi-Luen Wang, Gong-Ru Lin, and Hsiao-Hwa Wu<sup>†</sup>  
National Chiao Tung University and Tunghai University<sup>†</sup>, Taiwan, R.O.C.

### SUMMARY

For measurement of cw microwave signals in discrete devices or MMIC's by either photoconductive or electro-optic sampling techniques, it is important to maintain phase coherence or time synchronization between the microwave signal and optical pulse train. To accomplish this, we have recently demonstrated compact laser-diode-based optoelectronic phase lock loops (OEPLL). [1,2] The key element of the OEPLL's is a laser-diode-activated GaAs:Cr photoconductive switch or a reflection-mode electro-optic sampler which functions as an optoelectronic harmonic mixer (OEHM) for intermixing microwave signal from the target VCO and the optical pulse train. In practice, the microwave or millimeter wave signal to be probed on the MMIC might not be from a VCO. To solve this problem, we show in this paper that synchronization can also be achieved by using the microwave signal to be probed as the clock to phase lock the optical pulse train.

Our experimental apparatus (Fig.1) consists of an OEPLL with a laser-diode-based electro-optic sampler (LD1,  $\lambda=1.3\mu\text{m}$ ) as the OEHM; and a laser-diode-based photoconductive sampler (LD2,  $\lambda=0.8\mu\text{m}$ ) to display the synchronization results via a low-frequency replica [3]. The target oscillator (VCO1,  $f \approx 500\text{MHz}$ ) drives both LD1 and LD2. Microwave signals from a synthesizer (VCO2,  $f_0 \approx 1\text{GHz}$ ), simulating the monolithic device, intermixed electro-optically with the optical pulse train from LD1. The down-converted signal at the intermediate frequency,  $\Delta f = nf - f_0$  (shown in Fig.2(b)), is then mixed with the countdown signal from VCO1,  $f/N$  ( $N=6400$ , as shown in Fig.2(a)), for phase locking. Figure 2(c) shows the waveform of the photoconductively replicated 1.0GHz signal from VCO2, which is indeed synchronized with the countdown signal,  $f/N$ , from VCO1.

**Acknowledgments:** This work was supported in part by the National Science Council of the Republic of China under grant, NSC81-0417-E-009-629 and 630.

### REFERENCES

- [1] H.-H.Wu, C.-S.Chang, and C.-L.Pan, "Optoelectronic phase-locking of microwave signals up to 18GHz by a laser-diode-based GaAs:Cr photoconductive harmonic mixer," *IEEE Microwave Guided Wave Lett.*, vol.2, pp.11-13, Jan. 1992.
- [2] C.-L.Pan, K.-Y.Tang, and H.-H.Wu, "Optoelectronic phase-locking of microwave signals up to 4GHz using a laser-diode-based electrooptic harmonic mixer," *ibid.*, vol.3, No.4, 1993, to be published.
- [3] H.-H.Wu, C.-S.Chang, and C.-L.Pan, "A laser-diode-based photoconductive harmonic mixer for microwave waveform and spectrum measurements," *ibid.*, vol.2, pp.273-275, July 1992.

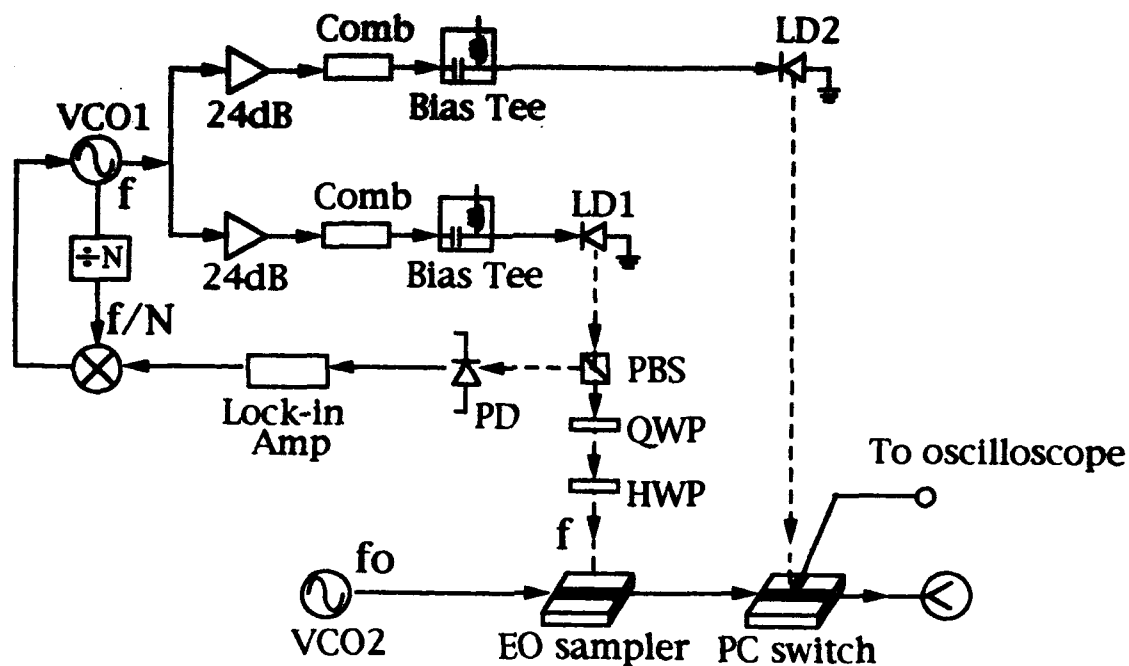


Fig.1 Experimental setup : PBS : polarizing beam splitter, QWP : quarter-wave plate, HWP : halfplate, PD : photodiode , PC : photoconductive

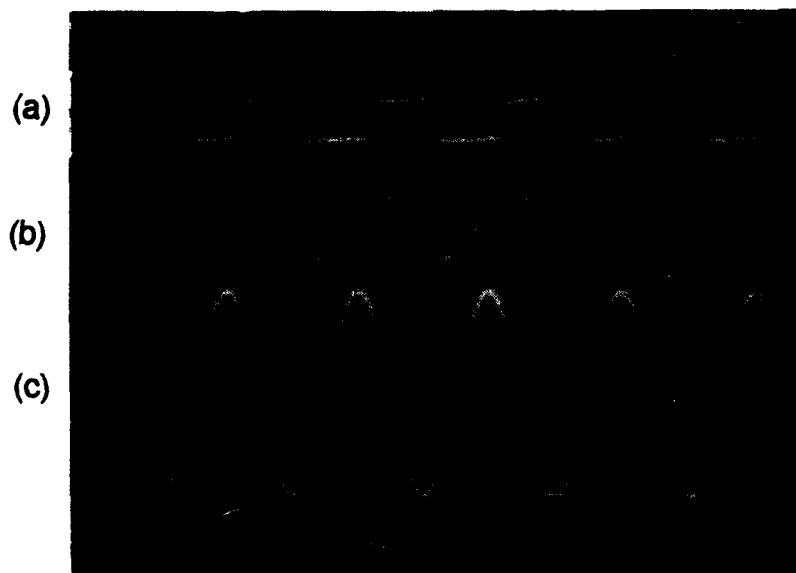


Fig.2 VCO1 optoelectronically phase-locked with a 1 GHz (VCO2) signal as monitored on the oscilloscope. ( trace (a):  $N/f$  reference signal from VCO1. trace (b): electro-optic mixing signal after lock-in amplifier. trace (c): output waveform of VCO2 by photoconductive sampling technique.)

### M3.4 2:40pm - 3:00pm

## Variations in the Gain and Bandwidth of the MESFET Photoresponse with Bias and Optical Intensity

Arthur Paoella

Army Research Laboratory, Electronic & Power Sources Directorate,  
Ft. Monmouth, NJ 07703, Phone: 908-544-2825

### Introduction

Exploring the photoresponse of the MESFET is important, particularly if the emphasis is on monolithic integration of optical and microwave components. An Experimental investigation and theoretical study [1] reveal that the bandwidth, gain and gain-bandwidth product [2] of the MESFET's photoresponse are dependent on the optical power density incident on the device and gate bias. These two parameters can be optimized for high gain operation or for high speed applications in microwave FO links.

### Experimental Results

The two modes of operation for the MESFET as an optical detector, *active* and *cut-off*, are bounded by the gate-to-source ( $V_{gs}$ ) pinch-off voltage. In the *cut-off* region, the photoresponse is the result of photoconductivity in the substrate and photocurrent developed at the gate junction, both which are small but have good speed characteristics. In the *active* region, the photoresponse is dependent on the device transconductance ( $g_m$ ) and the photovoltaic effect at the channel-substrate interface. The photoresponse of the MESFET, under various operating conditions, was measured as a function of optical power and  $V_{gs}$  for frequencies between 300 KHz to 3 GHz.

With the device biased at pinch-off (-1.5 volts), the gain and bandwidth were measured as a function of optical power as shown in Figure 1. The gain was referenced to 0 dB at the maximum optical power from the laser (2.3 mW). As the optical power decreased the relative low frequency gain increased from 0 to 10.5 dB and the bandwidth was reduced from 50 MHz to 5 MHz. It was observed that increasing the optical power beyond 0.5 mW had no effect on the bandwidth. These results are indicative of the non-linear photovoltaic that has high gain characteristics at low optical intensities and saturates at higher optical powers compressing the gain [3,1].

The gain and bandwidth were measured as a function of bias for a constant optical intensity of 2.3 mW. The results, shown in Figure 2, indicate that the photoresponse and the bandwidth are both dependent on the bias. In this experiment, the gain was referenced to 0 dB at  $V_{gs}=0.0$  volts (the bias where the photoresponse is maximum). At  $V_{gs}=-3.0$ ,

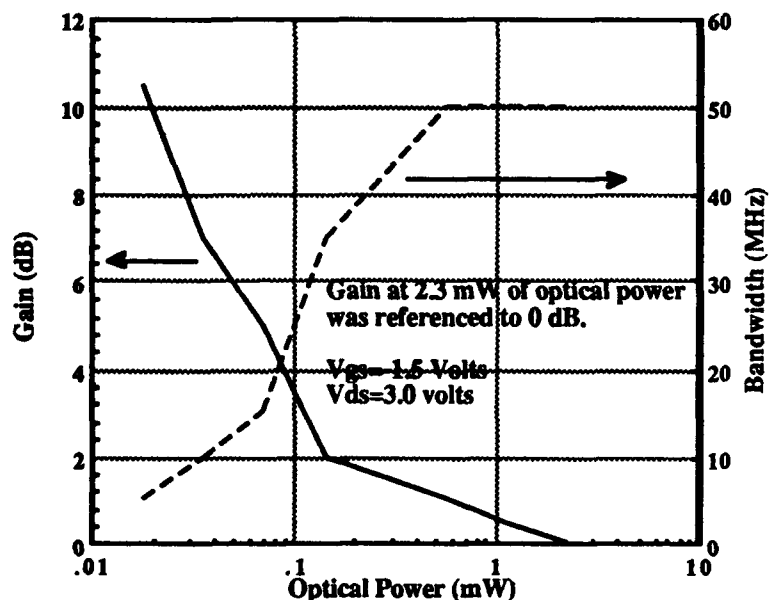


Figure 1. Gain and bandwidth as a function of optical intensity.

the device was well *cut-off* thus the gain is low at -8 dB due to  $g_m$  approaching zero. As  $V_{gs}$  increased, the device operation moved from *cut-off* into the *active* region, and the photoresponse increases as  $g_m$  increases until the maximum gain is obtained at 0.0 volts. The bandwidth changes from 110 MHz to 45 MHz as the bias goes to 0.0 volts. The reduction in bandwidth can be accounted for by the photovoltaic effect that has a lower bandwidth than the photocurrent developed at the gate junction.

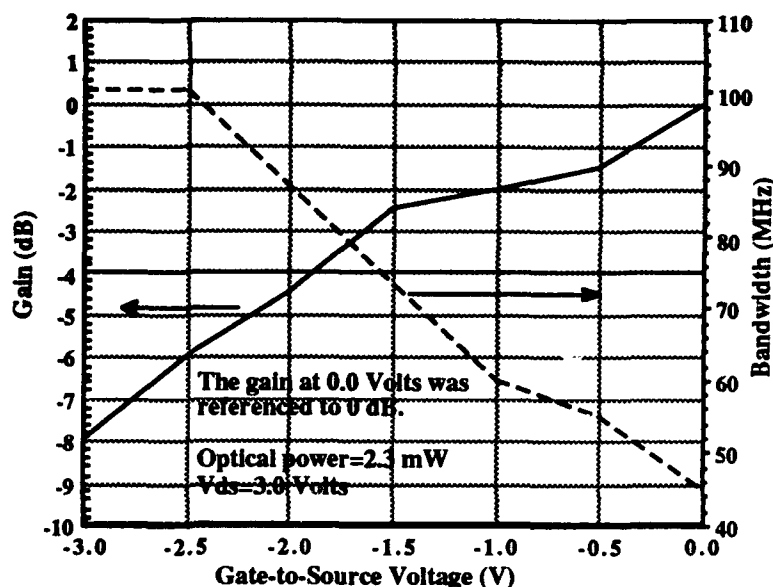


Figure 2. Gain and bandwidth as a function of gate-to-source voltage.

### Conclusion

The results presented, indicate that the MESFET can be used as an optical detector in GaAs based MMICs. This device offers these advantages: compatibility with standard GaAs processing techniques, and versatility in that the photoresponse can be adjusted by either electrical or optical means. The results indicate that the gain is a decreasing function and the bandwidth is an increasing function of optical intensity. The gain decreased by 10 dB and the bandwidth increased from 5 MHz to 50 MHz. The results also indicate that the gain is an increasing function and the bandwidth is a decreasing function of the reduction in the magnitude of  $V_{gs}$ . The bias change results in an 8 dB variation in gain, as the bandwidth went from 100 MHz to 45 MHz. To summarize, for large gain application low optical power or small gate biasing is best. High speed applications require high optical power or large reverse bias.

### References

1. "The Photoresponse Response of the GaAs MESFET," Paoletta, A., Ph.D. Thesis, Drexel University, Phila., PA.
2. "The Effect of Optical Intensity on the Photoresponse of the GaAs MESFET", Paoletta, A., Herczfeld P. R., and Madjar, A., *Microwave and Optical Technology Letters*, Vol. 6, No.1, Jan. 1993.
3. "The Compressive Nature of the Optical Detection in GaAs MESFETs and Possible Applications as an RF Logarithmic Amplifier," Madjar, A., Paoletta, A., and Herczfeld P. R., Accepted for publication in the *IEEE Transactions on Microwave Theory and Techniques*.

**M4.1 3:30pm - 4:00pm**  
**(Invited)**

## **Lithium Niobate Traveling-Wave Optical Modulators to 50 GHz**

**Roger L. Jungerman**  
**Hewlett-Packard Lightwave Operation**  
**1412 Fountaingrove Parkway**  
**Santa Rosa, CA 95403**

**David W. Dolfi**  
**Hewlett-Packard Laboratories**  
**3500 Deer Creek Road**  
**Palo Alto, CA 94303**

Modulation of optical signals is necessary for both high-speed digital and analog fiber-optic systems. Direct modulation of laser diodes is possible in some of these systems, but linewidth broadening due to chirp can lead to dispersion penalties. In addition, the highest modulation rates have been achieved with external modulators, with performance up into the millimeter-wave frequency range. The most mature external modulator technology is based on waveguide devices in lithium niobate.<sup>1</sup> Earlier problems of high optical insertion loss in the devices have largely been overcome. Much of the recent work has concentrated on increasing the bandwidth and reducing the drive power requirements in the external modulators.

Optical waveguides can be formed in lithium niobate by either titanium in-diffusion or proton exchange. Lithium niobate is strongly electrooptic, so that electric fields produced by electrodes on the surface of the crystal can modulate the phase of an optical signal in a waveguide beneath it. A typical modulator structure consists of an input y-branch to generate two arms of an interferometer, followed by a second y-branch to recombine the output and launch it into an optical fiber. Electric fields produced by electrodes over the waveguides in the two arms operate in a push-pull fashion to give a net differential phase shift which modulates the output of the interferometer. To reduce the drive voltage for a given optical modulation depth, the electrodes are designed to be as long as possible along the direction of optical propagation. For low frequencies, these electrodes can be treated as lumped elements. However, for efficient modulation at microwave frequencies the electrode must be considered as a coplanar waveguide structure. Typical effects which limit the bandwidth of the device are electrode loss, mismatch in propagation velocity between the optical and microwave signals in their respective waveguides, and bonding and packaging parasitics.

Lithium niobate is an anisotropic crystal. To maximize the electrooptic phase modulation, both the electric field of the microwave and optical signals must be along the z-axis of the crystal. Thus, the modulator is sensitive to the optical polarization of the input signal. Also, the design of the coplanar electrodes depends on the crystal orientation of the lithium niobate substrate used. Figure 1 shows the electrode design for x-cut and z-cut substrates, the most commonly used for

---

<sup>1</sup> R. C. Alfiness: "Waveguide Electrooptic Modulators". *IEEE Trans. Microwave Theory Tech.*, vol. MTT-30, pp. 1121-1137, 1982.

waveguide devices. In z-cut crystals the waveguides are positioned near the edge of the electrodes to take advantage of the strong vertical fringing fields. In x-cut devices, the waveguide is placed between the electrodes to make use of the maximum horizontal electric field.

The high dielectric constant of lithium niobate ( $\epsilon \sim 40$ ) makes the typical impedance of the coplanar line low ( $\sim 25 \Omega$ ) for typical geometries. One approach to using a low impedance device is to design a custom driver or impedance matching circuit.<sup>2</sup> Another method is to modify the electrode geometry to achieve  $50 \Omega$  impedance while maintaining velocity matching. Narrow ground planes and thicker electrodes and buffer layer give an impedance nearly matching the driving source.<sup>3</sup> The thicker buffer layer also increases the microwave velocity to match that of the optical signal. The electric fields in the vicinity of the waveguides are reduced, but this can be overcome by increasing the electrode length without sacrificing bandwidth in the velocity-matched structure. The frequency response of the narrowed ground-plane modulator extending to 50 GHz is shown in Fig. 2. The device has a 3 dB optical bandwidth in excess of 50 GHz, fiber-fiber insertion loss of  $< 4$  dB and a full-off to full-on switching voltage of 10.4 V at 1300 nm. The device operates at both 1300 nm and 1550 nm with greater than 20 dB extinction ratio.

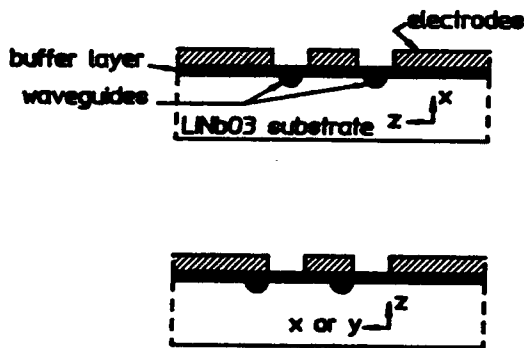


**Fig. 1:** Coplanar electrode structure on x-cut (top) and z-cut (bottom) lithium niobate.

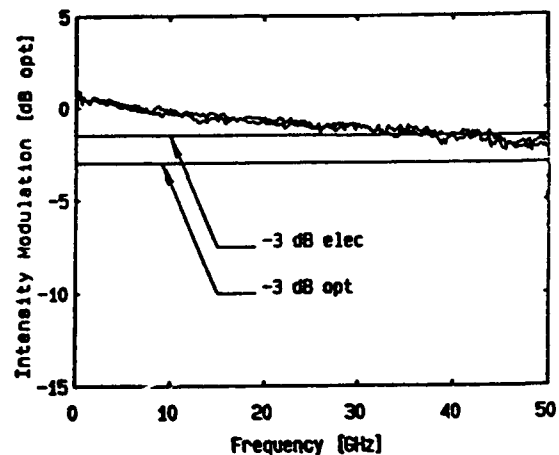


**Fig. 2:** Frequency response of two finite ground plane modulators.

<sup>2</sup> R. L. Jungerman, C. A. Johnsen, D. J. McQuate, K. Salomaa, M. P. Zurakowski, R. C. Bray, G. Conrad, D. Cropper, and P. Hernday, "High-Speed Optical Modulator for Application in Instrumentation", *J. Lightwave Tech.*, vol. 8, pp. 1363-1369, 1990.

<sup>3</sup> D. W. Dolfi and T. R. Ranganath, "50 GHz Velocity-Matched Broad Wavelength Lithium Niobate Modulator with Multimode Active Section", *Electronics Lett.*, vol. 28, pp. 1197-1198, 1992.

## A Rigorous Analytic Model for Traveling Wave Optical Modulators with Conventional and Resonant Electrodes

G.K. Gopalakrishnan\* and W.K. Burns†

\*Maryland Advanced Development Laboratory, Greenbelt, MD 20770

†Naval Research Laboratory, Code 5671, Washington D.C. 20375-5338

Recently, traveling wave (TW) LiNbO<sub>3</sub> optical modulators, in the coplanar waveguide (CPW) configuration, with performance extending well into the millimeter-wave frequency spectrum have been fabricated by engineering a near velocity match between microwave and optical signals [1,2]. In these devices, the characteristic impedance ( $Z_D$ ) of the active section of the CPW electrode is designed to be between 35 and 40  $\Omega$ , as it is difficult to design a CPW line on LiNbO<sub>3</sub> to simultaneously achieve microwave-optical velocity match with 50  $\Omega$  characteristic impedance [1]. Further, to obtain a low drive voltage ( $V_\pi$ ) with good overlap between microwave and optical fields, the active section of the CPW electrode must be very narrow; for the device reported in ref. 1, the center strip width ( $w$ ) = 8  $\mu\text{m}$  and gap width ( $g$ ) = 15  $\mu\text{m}$ . Therefore, to facilitate external microwave and optical access to the modulator, CPW tapers and bends are designed in conjunction with the active section. This is illustrated in the inset of fig. 2 where the layout of the complete device [1] is shown. Previously, high frequency operation of TW modulators, in the velocity matched condition, has been believed to be limited by only the conductor loss of the electrode. However, reflections due to impedance mismatches and other losses such as dielectric loss that stems from the loss tangent of the material and radiative loss that stems from radiation from discontinuities such as tapers and bends may also become significant. Since these losses and reflections are factors intrinsic to the device, they affect the overall device response and hence should be taken into consideration. In this paper, we first investigate losses that occur in different sections of a TW modulator [1]. Then, by using the loss coefficients obtained and by allowing for reflections due to impedance mismatches, we develop an accurate model that is applicable to modulators with both conventional and resonant electrodes.

To evaluate losses in each section of our device [1], we fabricated a set of test structures whose layouts are shown in fig 1. The dimensions of each structure correspond to dimensions of different sections of our modulator, and loss coefficients of each section as a function of frequency, were sequentially de-embedded from response of each of these test structures. The loss coefficients thus obtained were used to model device performance. Owing to space limitations, we only briefly outline here our approach to modeling: we treat the CPW electrode of the modulator as a microwave cavity with reflections at each end of the cavity being proportional to the degree of impedance mismatch between the CPW electrode and a 50  $\Omega$  line. We then compute the fields inside the cavity and solve for the optical response thus allowing for the co-existence of co and counter-propagating microwave and optical waves. Propagation constants for non-active sections of the device were obtained from finite-element calculations and for the active section it was obtained from a fit to the actual optical response. We applied the model to one of our devices ( $V_\pi = 4.2$  V, microwave-optical index mismatch = 0.101), and as shown in fig. 2, the modeled co-propagating response is in good agreement with data; also shown is the modeled response neglecting reflections due to impedance mismatches. In fig. 3 we show the counter-propagating response of the same device. As shown, reflections and phase changes in non-active sections of the device significantly alter the position of nulls in the response compared to the case without reflections, and hence cannot be neglected. In this case, the discrepancy between model and measurements will be explained at the meeting.

In conclusion, we have developed an accurate model for real-world TW modulators. The generality of the model also makes it applicable to resonant devices. Other results and experimental comparisons will be presented at the meeting.

### REFERENCES

- [1] G.K. Gopalakrishnan et al., Electron. Lett., 1992, 28, pp. 826-827.
- [2] D.W. Dolfi and T.R. Ranganath, Electron. Lett., 1992, 28, pp. 1197-1198.

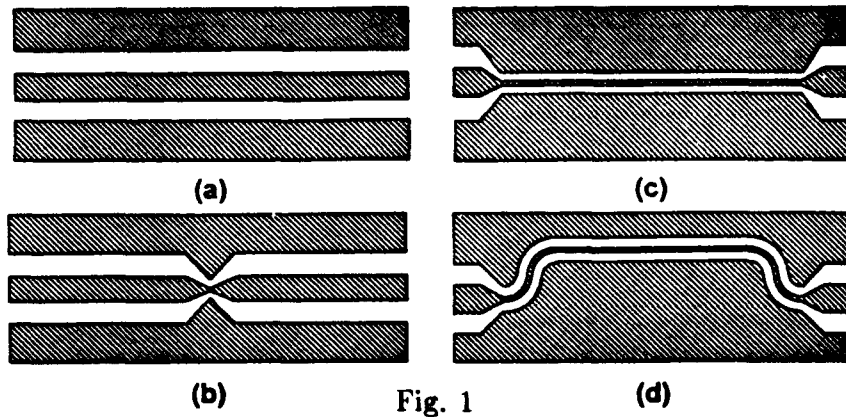


Fig. 1

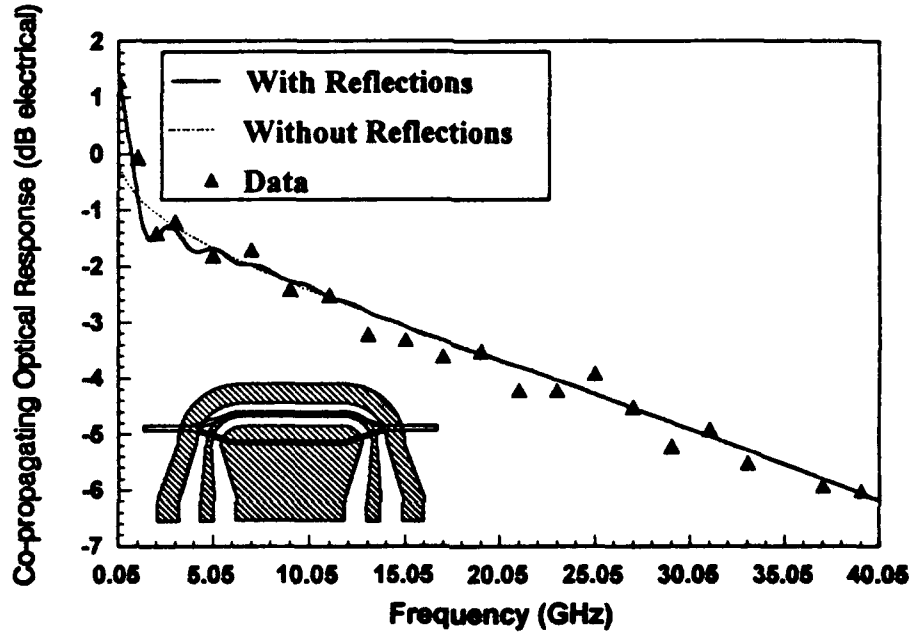


Fig. 2

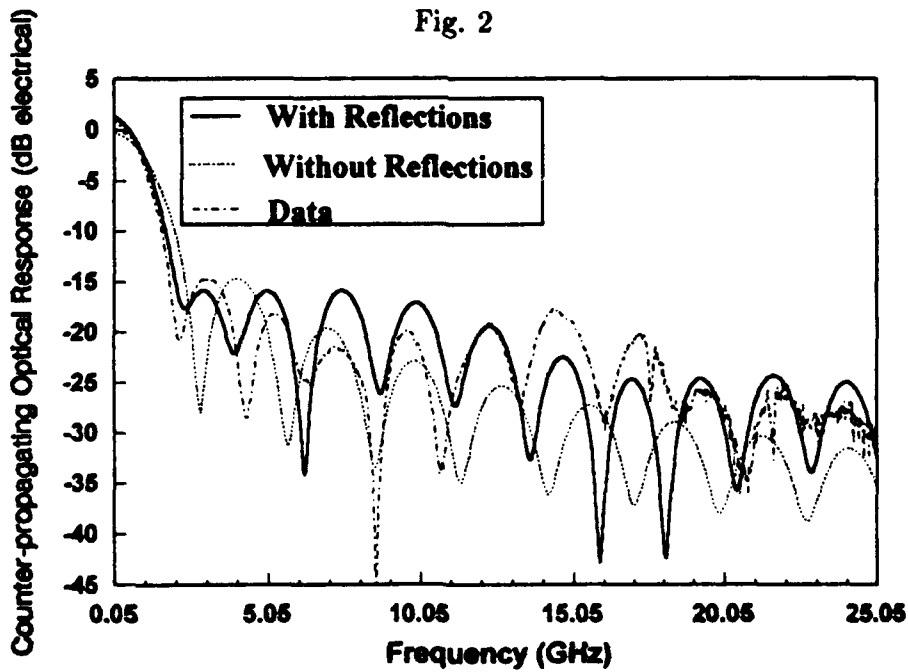


Fig. 3

### Polarization-Independent Fiber-Optic Microwave Modulator

R.D. Esman and M.J. Marrone, Naval Research Laboratory, Code 5670, Washington, DC 20375

**Introduction:** Many types of modulators suitable for fiber-optic systems exhibit a strong dependence of the modulation on the input state of polarization (SOP). Several schemes have been devised to overcome the effects of polarization changes including feedback input polarization control,<sup>1</sup> source depolarization,<sup>2</sup> and use of polarization maintaining fiber (PMF). Recently, we reported a passive scheme to address low-frequency modulators over conventional fiber links.<sup>3</sup> The configuration, termed an orthoconjugating loop mirror (OCLM), uses a polarization beam splitter (PBS) with the fibers from the output ports connected in a loop that contains a 90° Faraday rotator. Here we expand the technique to include wideband dual-feed traveling-wave devices.

**OCLM:** The operation of the OCLM (Fig. 1) is described as follows. A linear input SOP (assumed normal to the diagram) enters PBS1 and is transmitted via a conventional singlemode fiber (SMF) to PBS2. The evolution of the SOP along the SMF results in an arbitrary and time

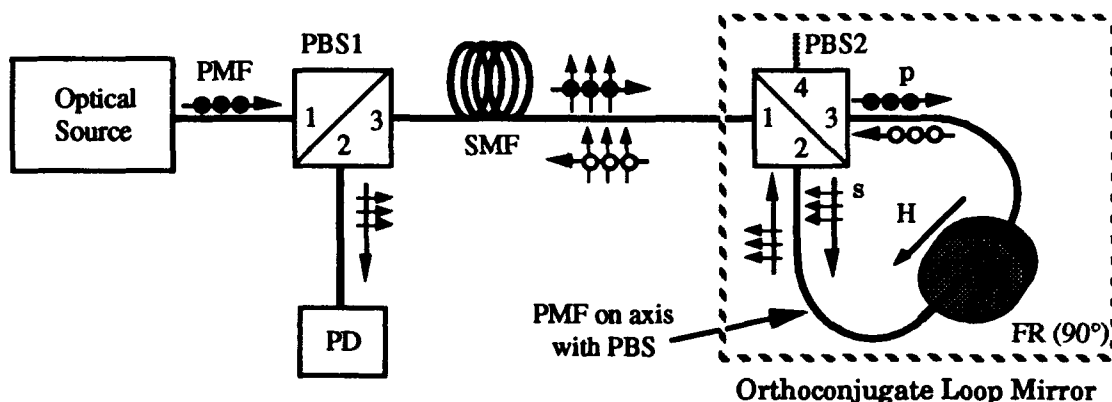


Figure 1. Fiber optic setup utilizing the orthoconjugate loop mirror.

varying SOP at the input (port 1) to PBS2. The PBS2 divides the input SOP into s and p components which are directed to ports 2 and 3, respectively. The output ports of PBS2 are coupled to PMFs joined to form a loop in which the fast and slow axes of the fibers are aligned. Each component reenters PBS2 with a SOP that exits the 4th port. However, by inserting a passive 90° Faraday rotator (FR) within the loop, the counter-propagating beams reenter the respective fibers on the opposite birefringence axis. Each circulating component now exits PBS2 at the original input port 1. Furthermore, analysis of this configuration shows that the return SOP is orthogonal to the input SOP. In this respect the OCLM is equivalent to a 45° Faraday rotator and mirror.<sup>4</sup> We note here that a simple cross-alignment of the birefringence axes in the loop would not produce an orthoconjugate SOP. Because of the reciprocal birefringence property of fibers,<sup>5</sup> the SOP reentering PBS1 at port 3 is orthogonal to the SOP which exited this port and consequently the light beam is diverted to port 2 with a constant intensity diminished only by normal losses in the system. We note that an alternate configuration delivers a constant optical output at port 4 for a return on a separate SMF.

**OCLM with Microwave Modulator:** With the FR attached to one loop port (Fig. 2), each circulating component of light in the OCLM travels on the same birefringence axis of the PMF. Therefore, any bidirectional modulator can be inserted in the OCLM and its operation will be independent of the input SOP.<sup>3</sup> Unfortunately, microwave modulators often exhibit directional dependence above some characteristic frequency,  $f_c$ , due to traveling wave effects. However, the directional dependence can be removed with a symmetric device by synchronously driving the mod-

ulator in both directions. To maintain wideband operation the modulator is located at the appropriate midpoint of the OCLM and a line stretcher is used for microwave path matching. At all microwave frequencies the OCLM light in either direction will interact with the corresponding co-propagating microwaves. At frequencies less than  $f_c$  the light will interact with both the co- and counter-propagating microwaves. The response of the modulator will then be doubled at low frequencies but, when included in the OCLM, complete polarization independence is obtained.

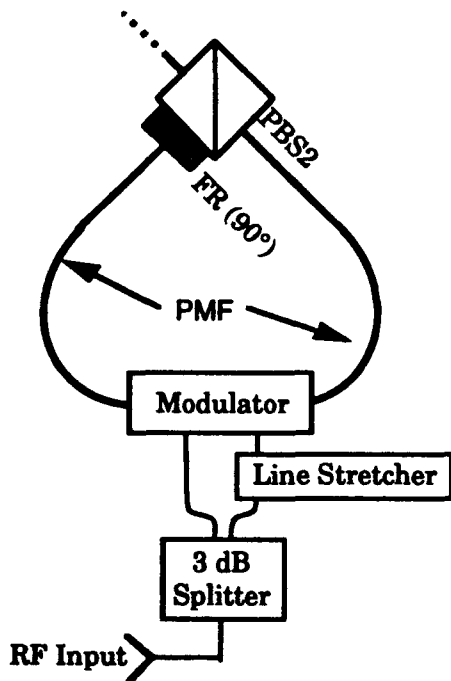


Figure 2. Polarization-Independent Microwave Modulator Setup

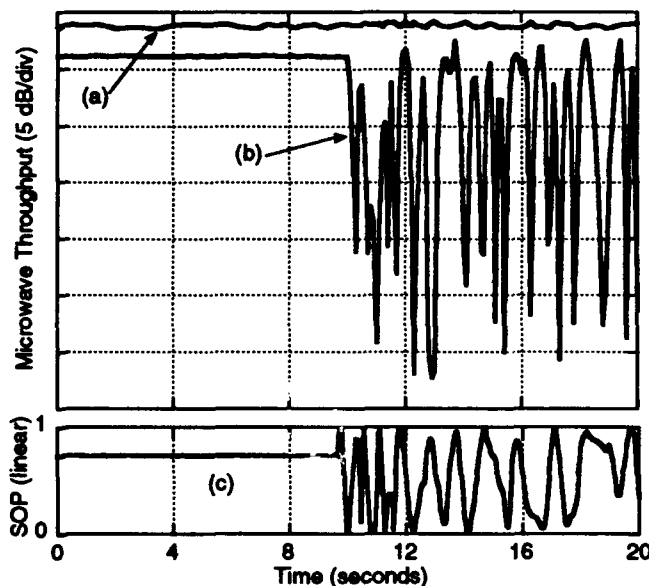


Figure 3. Variation in 12 GHz Signal During Input Polarization Fluctuations

**Experiment:** In an experimental implementation of this technique, the polarization-sensitive modulator was a 31 GHz GaAs-AlGaAs traveling-wave intensity modulator.<sup>6</sup> The input SOP in SMF was varied with a fiber loop controller and monitored by a pick-off splitter inserted between PBS1 and PBS2. In Fig. 3 trace (a) and (b) show the demodulated RF at 12 GHz from the PD with and without the FR(90°) in place, respectively. Trace (c) is the input SOP variation in SMF. The variation in the RF power is found to be  $< \pm 0.3$  dB with an OCLM.

**Conclusion:** A technique has been presented to utilize bidirectional traveling wave polarization-sensitive modulators with standard SMF while not requiring the use of PMF, input polarization control, or depolarization. The technique can be implemented in either an orthoconjugate or transmissive configuration.

#### References:

1. N.G. Walker and G.R. Walker, *IEEE J. Lightwave Techn.*, LT-8, p. 438, 1990.
2. A.D. Kersey and A. Dandridge, *Electron. Letters*, 23, pp. 634- , 1987.
3. R.D. Esman, *et al.*, presented at CLEO'93, Baltimore, MD, paper CMA2, May 2-7, 1993.
4. M. Martinelli, *Optics Communications*, 72, pp. 341-5, 1989.
5. C. Edge and W.J. Stewart, *IEE Colloq. on Optical Fiber Measurements*, No. 1987/55, 1987.
6. R.G. Walker, *IEEE J. Quantum Electronics*, JQE-27, pp. 654-667, 1991.

## Modulation of millimeter waves by optically illuminating n-i-p-i structures

Linda West, T.C. Hasenberg, Alan Kost, Mehran Matloubian,  
George C. Valley, and Jeffrey O. White  
Hughes Research Laboratories  
3011 Malibu Canyon Road, Malibu, CA 90265

Semiconductor n-i-p-i structures have been used as all-optical spatial light modulators in devices where one optical beam controls another.<sup>1</sup> Here we demonstrate that a n-i-p-i can also be used as an optically controlled microwave modulator. The basis for the device is the change in free carrier density of several orders of magnitude caused by illumination with low intensity light.<sup>2</sup> In our measurements, light from an argon ion laser with an intensity of about 800 mW/cm<sup>2</sup> illuminates the n-i-p-i to produce free carriers that attenuate the transmitted signal through a combination of reflection and absorption.

In our semiconductor n-i-p-i, grown by molecular beam epitaxy (MBE) on a semi-insulating GaAs substrate, we use 32 periods, each of which consists of a 400-Å GaAs n-type layer (Si -  $2 \times 10^{18}$  cm<sup>-3</sup>) and a 400-Å p-type layer (Be -  $2 \times 10^{18}$  cm<sup>-3</sup>) with no intrinsic layer. The layer thicknesses and doping levels are chosen to make the n-i-p-i completely depleted of free charge in the dark. The sample is about 50 mm in diameter.

The microwave transmission of the n-i-p-i sample is measured using picosecond transient radiation generated and detected by focusing picosecond optical pulses (575nm) onto broadband coplanar antennas<sup>3</sup> as shown in Fig.1. The antennas are exponentially flared transmission lines fabricated on resistive substrates. The transmitting antenna was fabricated on a 1-micron thick MBE-grown GaAs layer. To enhance the recombination rate in the layer, it was grown at low temperature (200 °C) and subsequently annealed for 10 minutes at 600 °C under arsenic over-pressure.<sup>4</sup> The receiving antenna was fabricated on a silicon-on-sapphire substrate.

To create free charge carriers in the n-i-p-i, it is excited with above-band-gap light from a cw argon ion laser operating in the multi-line mode. The laser spot is expanded to a  $1/e^2$  diameter of about 3.7 mm at the sample. On the sample, the laser spot is centered on a line between the centers of the 25.4 mm lenses used to collimate and focus the millimeter wave signal.

Fig. 2 shows the microwave signal transmitted by the n-i-p-i with and without cw laser excitation. Laser excitation results in a decrease of the transmission by 50%. When the sample is rotated 180° so that the substrate is illuminated, then light is absorbed before it reaches the n-i-p-i layers. For this geometry, the transmitted microwave signal is not attenuated showing that no substrate effect, such as heating, causes the attenuation.

The insertion loss of the sample, 5 dB (transmission ~ 30%), is somewhat larger than expected. Taking surface reflections into account but assuming the substrate and un-illuminated n-i-p-i do not absorb, one expects a transmission of about 50%. The additional loss may come from residual conductivity in the substrate or may be due to a n-i-p-i epilayer which is not fully depleted of charge when the argon-ion laser control beam is off.

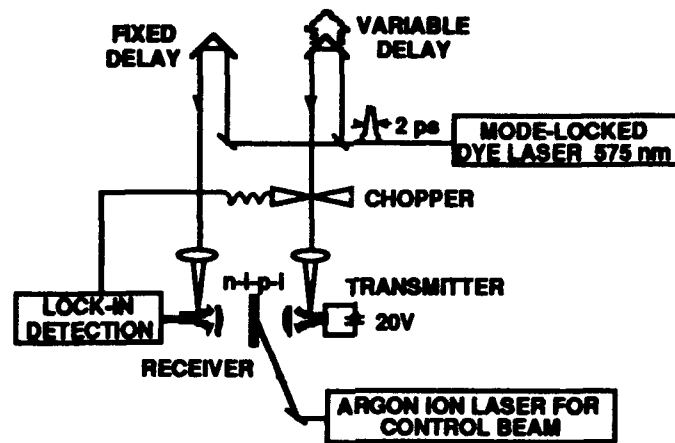


Figure 1. Experimental set-up to measure the photo-induced change in the transmission of free space microwaves by a semiconductor n-i-p-i structure.

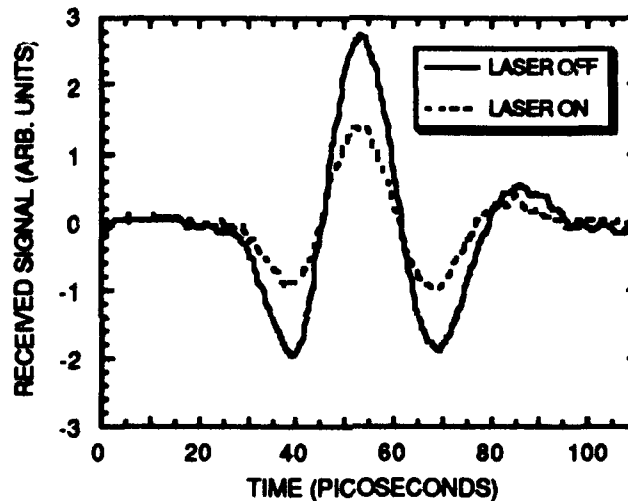


Figure 2. A microwave signal, transmitted through a n-i-p-i and sampled photo-conductively at the receiving antenna, exhibiting additional loss due to photoexcitation.

#### REFERENCES:

1. G. H. Döhler: 'Nonlinear optical properties of n-i-p-i and hetero n-i-p-i structures and their potential for application in photonics', *Optical and Quantum Electronics*, 1990, 22, p. S121; Alan Kost: 'Performance Characteristics of Hetero n-i-p-i Structures', Alan Kost, *Optical and Quantum Electronics*, 1990, 22, p. S187.
2. Gottfried H. Döhler: 'Electro-optical and opto-optical devices based on n-i-p-i doping superlattices', *Superlattices and Microstructures*, 1990, 8, p. 49.
3. G. Arjavalingam, Yvon Pastol, Jean-Marc Halbout and Gerard V. Kopcsay, 'Broad-Band Microwave Measurements with Transient Radiation from Optoelectronically Pulsed Antennas', *IEEE Trans. Microwave Theory and Tech.*, 1990, 38, p. 615.
4. S. Gupta, M. Y. Frankel, J. A. Valdmanis, J. F. Whitaker, and G. A. Mourou, 'Subpicosecond Carrier Lifetime in GaAs Grown by Molecular Beam Epitaxy at Low Temperatures', *Appl. Phys. Lett.* 1991, 59, p. 3276.

**Tuesday, July 20, 1993**

**Sessions:**

**T1: Spectroscopy**

**T2: Systems II**

**T3: Transmission and Propagation**



## Generation of Terahertz Radiation From Semiconductor Optoelectronic Devices

B.B. Hu, L. Xu, and D. H. Auston

Department of Electrical Engineering, Columbia University, NY, NY 10027

Recently, we observed terahertz radiation induced by femtosecond optical excitation of semiconductor optoelectronic devices [1]. In the first part of this talk, we present a systematic experimental study of the physical origin of this THz radiation. In the second part, we study electron velocity overshoot in bulk GaAs under high bias field using THz radiation as a probe.

### *1. Physical mechanisms of THz radiation induced by femtosecond optical excitation :*

Two physical models have been proposed to explain the origin of this radiation. One of them attributes the THz radiation to the time-dependent transport current [1]. The other proposes that the displacement current generated by instantaneous creation of polarized electron hole pairs causes radiation [2]. In a MQW structure, since carrier transport is prohibited by quantum confinement, THz radiation induced should be caused only by the displacement current [3]. In bulk material, both the transport and the displacement current exist and contribute to THz radiation. In this paper, we present a systematic experimental study of the THz radiation from bulk GaAs samples in which we vary the dc bias field and the laser wavelength.

The sample we use consists of a 1.2  $\mu\text{m}$  intrinsic GaAs layer sandwiched between undoped 3500  $\text{\AA}$  thick  $\text{Al}_{0.4}\text{Ga}_{0.6}\text{As}$  layers. DC field can be applied between a semi-transparent Cr contact on the sample surface and an  $n^+$  GaAs substrate. A self modelocked femtosecond Ti: Sapphire laser is used in the measurement. The photocarrier density is held below  $10^{13}/\text{cm}^3$  to avoid space charge effects in the GaAs layer. The induced THz radiation is collected by a photoconducting

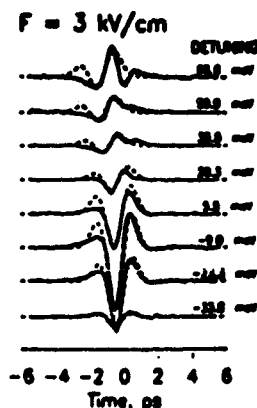


Fig 1

dipole antenna which is placed in the direction of specular reflection, 4 cm away from the sample.

First, we fixed the optical wavelength and measured the THz radiation at different biases. The amplitude of the THz signal is found to increase linearly at low fields and saturate when the field reaches 10 kV/cm.

Secondly, we fixed the bias field at different values, and scanned the laser

wavelength around the bandedge of the GaAs. In Fig.1, the solid curves are THz signals measured under a small dc field (3 kV/cm). The waveform drastically changes with the detuning energy, suggesting a competition between the displacement and the transport currents for inducing

radiation, and can be qualitatively explained by a fully quantum mechanical treatment of the transient photoconductive response of GaAs [4]. The dashed line is a theoretical fit.

When we increase the dc field to 10 kV/cm, no change in the THz waveform is observed. This is again in agreement with the prediction by the theory that the transport current dominates at high dc field and detuning energy.

## 2. Hot electron dynamics- Velocity overshoot in GaAs:

The transient behavior of electrons photogenerated by short optical pulses in GaAs under electric fields has been studied by experiments [5] and Monte-Carlo simulations [6]. An important feature predicted is the velocity overshoot, i.e. the transient velocity of the electrons overshoots its steady state value under high dc bias fields and low photon energies. However, the experimental observation of velocity overshoot is difficult. The previous experimental results [5] of overshoot response on picosecond time scales have been interpreted as space charge effects due to the high photocarrier density used in these experiments [6].

Since the THz radiation can be attributed to the first time derivative of the transient photocurrent, hence, a quantitative picture of velocity overshoot can be obtained by a proper deconvolution of the THz radiation waveform. Here, we report an observation of velocity overshoot by studying the THz radiation induced by femtosecond optical excitation of bulk GaAs.

The experimental setup is the same as described before. Large aperture GaAs p-i-n diodes are used as THz emitters. By reverse biasing, a large ( $\sim 100$  kV/cm) and uniform field can be achieved in the intrinsic region. The photocarrier density is kept below  $10^{13}/\text{cm}^3$  to avoid the space charge effects. We also measured the THz signal from a Si p-i-n diode under the same conditions.

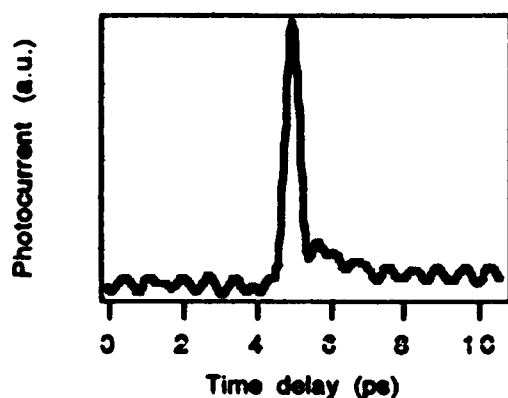


Fig 2

Since no overshoot response should be expected from a Si sample under our condition, we can use Si signal as reference for deconvolution.

Fig2. shows the deconvolved transient photocurrent of GaAs under a femtosecond pulse excitation with a photon energy of 1.50 eV, and a dc field of 100 kV/cm. A strong overshoot feature is present.

## References:

- [1] X.-C. Zhang, B.B. Hu, J. T. Darrow and D. H. Auston, APL, **56**, 1011, 1990.
- [2] S.L. Chuang, S. Schmitt-Rink, B.I. Greene, P.N. Saeta, A.F.J. Levi, PRL. **68**, 1992.
- [3] P. Planken, M. Nuss, W. Knox, D. A. Miller and K. Goossen, APL. **17**, 2009, 199.
- [4] A.V. Kuznetsov, C.J. Stanton, submitted to Phys. Rev B.
- [5] K. Meyer, M. Pessot, G. Mourou, R. Grondin, and S. Chamoun, APL. **53**, 2254 (1988).
- [6] A. E. Iverson, G. M. Wysin, D. L. Smith, and A. Redondo, APL, **52**, 2148 (1988).

**Optoelectronic Surface Field Spectroscopy**X. Zhang, Y. Jin, *Rensselaer Polytechnic Institute, Troy, NY*L. Kingsley, M. Weiner, *US Army Research Laboratory, Pulse Power Center, Fort Monmouth, NJ*

We present experimental results of using a recently developed THz spectroscopic technique to measure the static field of semiconductor surfaces and interfaces and their related carrier dynamics. This technique provides alternative measurement of the amplitude and the direction of the static field with a non-contact approach.

Figure 1 schematically illustrates the experimental configuration (side view) of optoelectronic spectroscopy. A femtosecond laser beam illuminates the sample at normal incidence. The focused spot diameter of the optical beam on the sample is about one millimeter. An external magnetic field is applied orthogonal to both the surface static field and the optical beam propagation direction, as shown in Figure 2. The backward radiated THz beam, reflected by a beam splitter (BS in Figure 1) which is coated with an ITO film, is detected by a photoconducting antenna. If the semiconductor is semi-insulating the inward radiated THz signal can be detected in the forward direction.

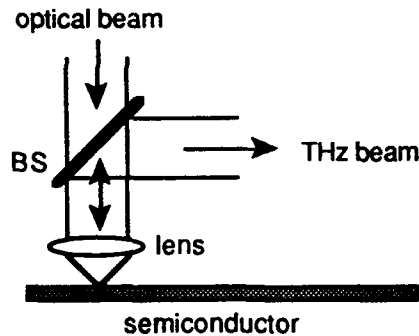


Figure 1

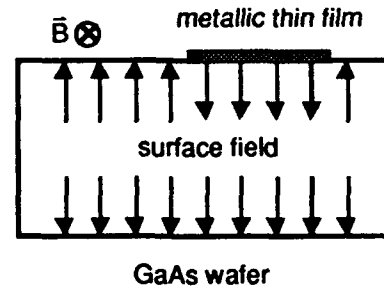


Figure 2

We can estimate the dependence of the THz radiation on the strength of the electric and magnetic fields applied on the semiconductor. It is well known that the projection trace of a moving charge will be bent by a magnetic field if the magnetic field direction is not parallel to the initial charge velocity direction. Since the driving forces on the carriers are the Coulomb force and the Lorentz force, the equation of the acceleration of an electron in a semiconductor is:

$$\vec{a} = \frac{d\vec{v}}{dt} = -\frac{e}{m_e^*}(\vec{E} + \vec{v} \times \vec{B}) \quad (1)$$

where  $m_e^*$  is the effective mass of the electron. Because of the heavier mass of the hole, we have ignored the contribution from hole motion. If we assume an uniform electric field in x-direction, and an uniform magnetic field in the z-direction, the

solution for the y component of the carrier acceleration, with the proper initial conditions, has the simple form:

$$a_y = -\frac{eE_x}{m_e^*} \sin\left(\frac{eB_z}{m_e^*} t\right) \quad (2)$$

This classical treatment of a moving charge does not take into consideration the saturated velocity in semiconductors. For a magnetic field strength of 0.1 Tesla, the cyclotron frequency  $eB_z / m_e^*$  of an electron in GaAs is about 0.25 THz. For a very short measurement time (for example, less than 2 ps), we can take the lowest order term in the Taylor expansion, and rewrite the equation (2) as:

$$a_y = -\left(\frac{e}{m_e^*}\right)^2 E_x B_z t \quad (3)$$

Since the radiated electric field  $E_r$  is proportional to the charge acceleration y-component at far field (dipole detector is polarized in y direction), the THz radiation should be described by the charge acceleration  $a_y$ . Equations (2) and (3) clearly show that the polarity of the forward radiation depends on the direction of  $E_x$  and  $B_z$  (again we ignore the contribution from holes due to their larger effective mass). The effect of electric and magnetic fields on THz radiation has been demonstrated in n-i-p and p-i-n GaAs diodes [2].

Figure 3(a) to 3(d) are plots of temporal waveforms of terahertz optical rectification from a GaAs wafer, InGaAs/GaAs superlattice, GaAs eptaxially grown at low temperature, and ion-implanted GaAs. Different samples show very different temporal waveforms which reflect different carrier transport dynamics.

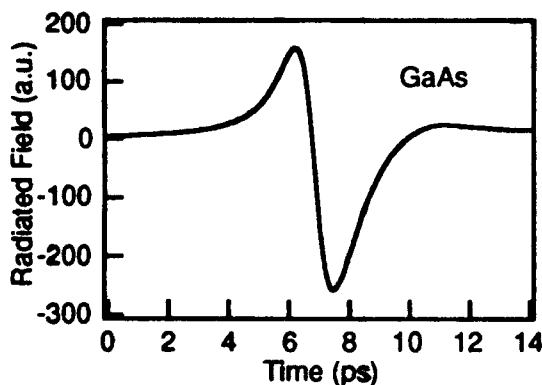


Figure 3(a)

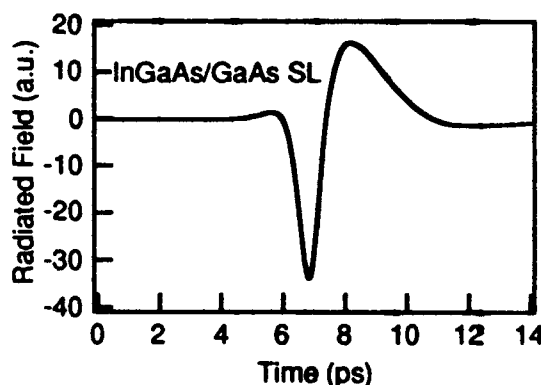


Figure 3(b)

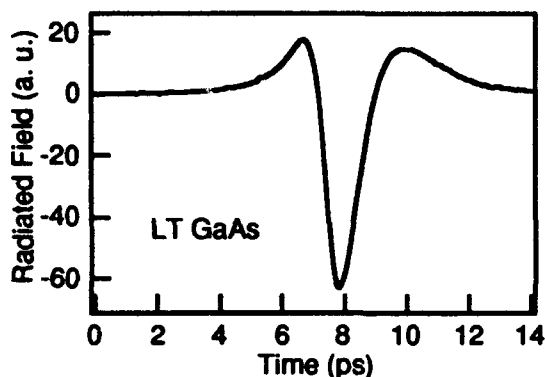


Figure 3(c)

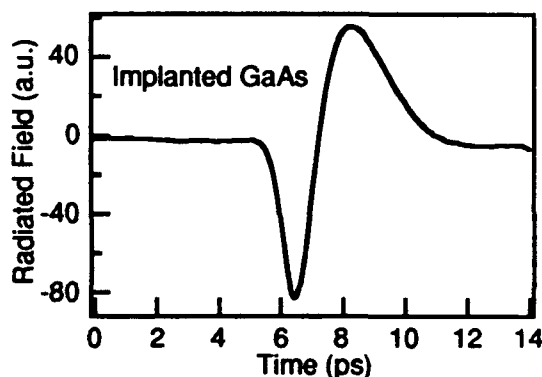


Figure 3(d)

We have measured THz radiation from a GaAs wafer with and without the thin metallic Au/Pt film (about 80 Angstroms), as shown in Figure 2. The results are plotted in Figure 4 and Figure 5. Figure 4 shows temporal THz signals and Figure 5 plots the peak value of the radiation signal vs laser scanning distance across the Pt/Au film edge. Opposite polarity of the surface field in Figure 4 is reflected by the opposite THz waveform, as indicated in the equation (2) and (3).

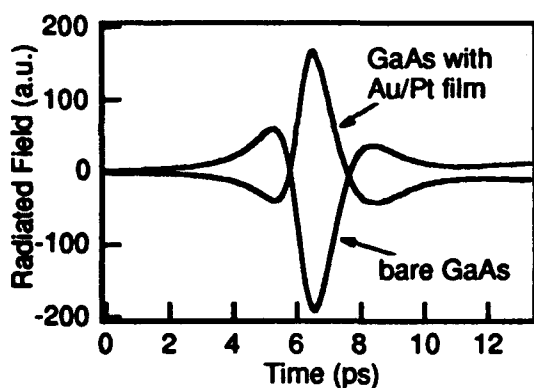


Figure 4

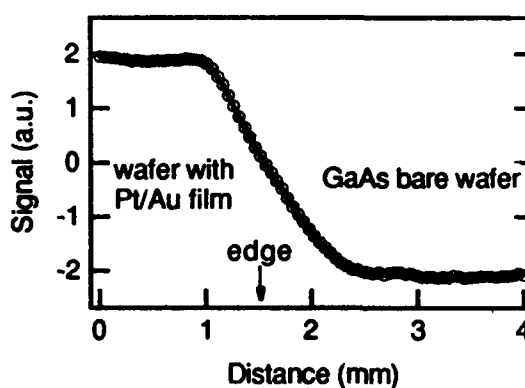


Figure 5

In conclusion, we present the use of optoelectronic THz spectroscopy to measure semiconductor surface and interface electronic properties. The surface static field and carrier dynamics can be characterized by this alternative non-contact technique.

#### References:

- [1] X.-C. Zhang, B.B. Hu, J.T. Darrow, and D.H. Auston, *Appl. Phys. Lett.* **56**, 1011 (1990); X.-C. Zhang and D.H. Auston, *J. Appl. Phys.* **71**, 326 (1992)
- [2] X.-C. Zhang, Y. Jin, L. Kingsley, and M. Weiner, "Influence of Electric and Magnetic Fields on THz Beams," submitted to *Appl. Phys. Lett.* (1993)

## Optically Steered MM-Wave Grating Surface Emitter

Robert Amantea, Arye Rosen, Paul J. Stabile, Walter M. Janton, and Dean B. Gilbert  
David Sarnoff Research Center, Princeton, New Jersey 08543-5300  
Jerome K. Butler

Southern Methodist University, Dallas TX 75275

### INTRODUCTION

A wafer form high power steerable source at millimeter wave integrating an IMPATT and an antenna is envisioned. In this paper, a unit cell configuration which consists of the IMPATT source coupled to a top-metallized-image (TMI) guide was first modeled and then constructed and measured. Approximately 60% of the power obtainable in a high  $Q$  cavity was coupled to the TMI guide. Grating calculations and measurements were performed on an optically induced periodic structure in a dielectric guide with base metal (an image guide) showing that it is emulated by the TMI guide with slots cut in the top metal forming a grating. The measured results on the fabricated unit cell and the optical calculations combine to prove the concept of the optically steered MMW integrated source.

### OPTICALLY INDUCED GRATINGS IN SILICON

The task of millimeter-wave system design is hampered by the lack of available high-power, compact, broad band millimeter-wave emitters. In 1989, the concept of millimeter-wave surface emitters with optically induced gratings was introduced<sup>1</sup>. Recently, a key aspect of this concept was demonstrated: gratings were optically induced in a dielectric wave guide made from semiconductors.<sup>2</sup>

The first optically induced grating experiment was performed using a 1.4 by 1.4 mm dielectric guide. A separate optical mask placed upon the top of the guide has a 0.2mm opening and a 1.85mm period. This emulsion mask served to create a periodic pattern of plasma on the dielectric guide when illuminated with a high power laser diode array, thereby forming a second-order grating that can surface emit power from the guide. A two-dimensional edge-emitting laser diode array with a power conversion efficiency of 40% was used as the optical source. Figure 1 shows this configuration.

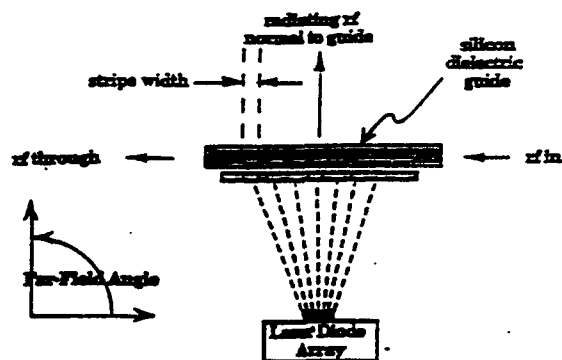


Figure 1. The experimental setup for a millimeter-wave emitter with optically induced gratings.

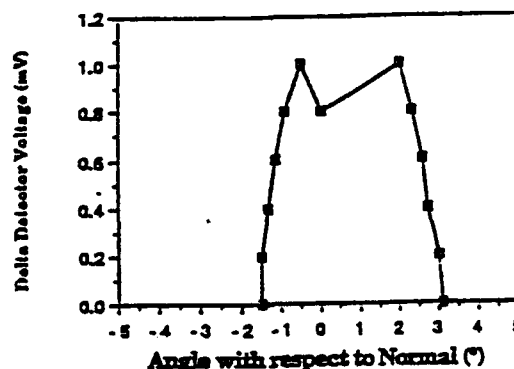


Figure 2. The main lobe far-field pattern of the detected 60 GHz power with the optically induced 1.85 mm grating. The delta detector voltage ( $\Delta V$ ) is the detector voltage with the "laser on" minus the voltage with the "laser off".

A 60 GHz mmw signal was coupled into the end of the dielectric guide through a tapered transition from the metal wave guide into the dielectric. Figure 2 shows far field measurements of the emitted radiation. Note that the center of the lobe is within 1° of the normal to the guide.

### IMPATT-WAVEGUIDE SOURCE

The source consists of an IMPATT device centered in a rectangular dielectric bar of width  $2a$  as depicted in Figure 3.



Figure 3. Cross-section of waveguide, cavity, and post.

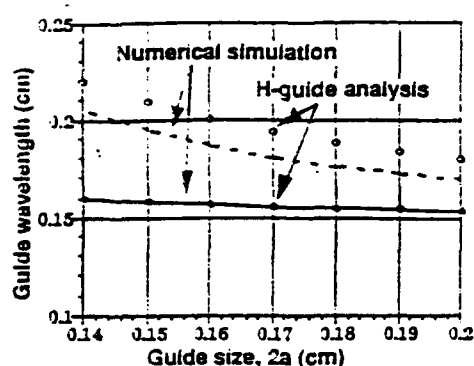


Figure 4. Comparison of numerical solution for modes in the TMI-guide and analytic solutions for modes in an H-guide

The TMI guide can be shown to be similar to an H-guide by comparing numerically calculated modes of the TMI guide to analytically calculated modes of an H-guide<sup>3,4</sup>. Figure 4 shows that the fundamental mode of both guides have the same guide wavelength as a function of width. Furthermore, the wavelengths of the next order mode are within 5% of each other.

Theoretical solutions for the coupling of RF power using a probe in a rectangular metal wave guide have been obtained<sup>5</sup>. Since the TMI-guide is an open guide with both continuous and discrete spectrum, we simplify by approximating the TMI-guide by an H-guide and then close the ends to form a rectangular wave guide of width  $2c$ .

Several modes of this wave guide are shown in Figure 5. The fundamental mode is bound to the dielectric and the higher-order modes belong to the rectangular wave guide. These higher order modes approximate the leaky modes of the H-guide (TMI-guide). As  $c$  is increased, the bound mode remains unchanged but the higher-order modes increase in number thereby approximating the continuous part of the spectrum. Figure 6 shows the final results of these calculations for several values of post diameter and rectangular wave guide width. We found that the power coupling coefficient varied linearly with respect to  $\sqrt{a/c}$ . When the calculations are extrapolated to  $c \rightarrow \infty$ , the power coupling coefficient for the H-guide (TMI-guide) is found.

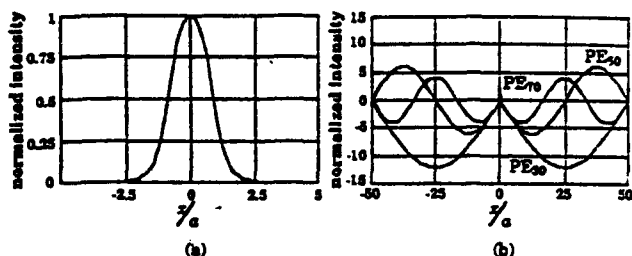


Figure 5. Modes of the dielectrically loaded rectangular waveguide ( $c=50a$ ,  $a=0.07$  cm,  $f=60$  GHz) normalized to unity at  $x=0$  (a)  $PE_{10}$  mode (b)  $PE_{50}$ , and  $PE_{70}$  modes.

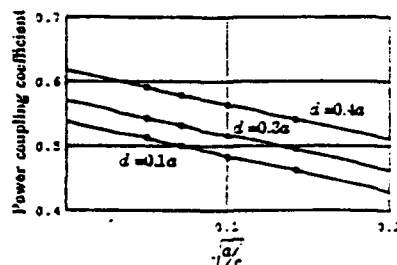


Fig. 6. The power coupling coefficient versus  $\sqrt{a/c}$ .

## REFERENCES

1. A. Rosen, P.J. Stabile, P. Herczfeld, A. Daryoush, and J.K. Butler, "Optically Controlled IMPATT Diodes and Subsystems," *1989 SBMO International Microwave Symposium Proceedings*, Vol. II, pp. 589-594, July 1989.
2. Paul J. Stabile, Richard E. Marx, Gary Evans, Arye Rosen, Robert Amantea, Edgar J. Denlinger, and Jerome K. Butler, "Millimeter-Wave Surface Emitters with Optically Induced Gratings," *IEEE LEOS '90 Conference Proceedings*, p. 279, November 1990.
3. K. Bierwirth, N. Schulz, and F. Arndt, "Finite-Difference of Analysis of Rectangular Dielectric Waveguide Structures," *IEEE Trans. Microwave Theory Tech.*, Vol. MTT-34, No. 11, p 1104, Nov. 1986.
4. Bhartia and I.J. Bahl, "Millimeter Wave Engineering and Applications," John Wiley & Sons, New York, 1984.
5. Williamson, A.G., "Analysis and Modeling of a Coaxial Line-Rectangular Waveguide Junction," *Proc. IEEE*, Vol. 129, Part H, No. 5, Oct. 1982, pp 271-277.

# Tunneling of electromagnetic waves in two-dimensional photonic crystals

S.Y. Lin and G. Arjavalingam

IBM Research Division, Thomas J. Watson Research Center,  
P.O. Box 218, Yorktown Heights, New York 10598

By analogy to electron wave propagation in crystals, electromagnetic (EM) waves in periodic dielectric structures also encounter allowed bands of perfect transmission and forbidden regions of strong attenuation (band gaps). The propagation of electron waves in resonant tunneling structures has been well investigated, and gave rise to one of the first observations of quantized states in a semiconductor heterostructure [1]. So far, electromagnetic tunneling in the band gap region of photonic crystals has not been systematically studied, nor have quantized states in the photonic analog of a double barrier resonant tunneling structure (DBRT) been observed.

In this paper, we investigate evanescent propagation of EM waves in a series of thin periodic dielectric arrays using the coherent microwave transient spectroscopy (COMITS) technique. The tunneling probability through the fundamental band gap of the photonic crystal is found to depend exponentially on layer thickness, from which the imaginary wavevector,  $\kappa$ , is directly deduced. Moreover, a photonic DBRT was constructed with  $n$ -rows of empty lattice (well) sandwiched on both sides by  $m$ -rows of periodic dielectric rods (barrier), i.e.  $m$ - $n$ - $m$  DBRT structure. We observed sharp transmission peaks in the band gap region, providing the first evidence of photonic quantized states.

COMITS is based on the transmission and detection of picosecond duration electromagnetic transients by optoelectronically pulsed antennas [2]. The transmitting and receiving elements are exponentially tapered coplanar strip lines photolithographically fabricated on silicon-on-sapphire. The radiated transient contains frequency components in the range of 15-140 GHz, and is strongly polarized with its E-field parallel to the plane of the antennas. In the transmission configuration, samples are placed in the beam path such that the transient radiation propagates in the 2D plane. The voltage signal at the receiver is measured as a function of time by photoconductive sampling, and subsequently Fourier transformed to yield its amplitude spectrum.

In Figure 1(a), transmission amplitude is plotted as a function of frequency,  $f$ , for a series of photonic crystals with different layer thicknesses. When the layer thickness is less than 6 lattice constants ( $a_0$ ), there is finite transmission of electromagnetic energy in the band gap region. The transmission amplitude is found to depend exponentially on layer thickness, and is plotted in figure 1(b) for  $f = 55$  GHz. In figure 2, we show the transmission spectrum taken with a 2-2-2 DBRT sample, having a well thickness of  $2 a_0$ . The sharp peak observed in the gap region at  $f=59$  GHz is a manifestation of resonant tunneling of EM waves into and out of the quantized state in the well. Consistent with tunneling picture, the peak amplitude becomes weaker as barrier width is increased. By varying the quantum well thickness, the effect of size quantization is also studied. We observed two resonant peaks in the gap region when the well width was increased to  $3 a_0$ .

## References

- [1] L.L. Chang, L. Esaki, and R. Tsu, Appl. Phys. Lett. 24, 593 (1974).
- [2] G. Arjavalingam et. al., IEEE Trans. Microwave Theory Tech. 38, 615 (1990).

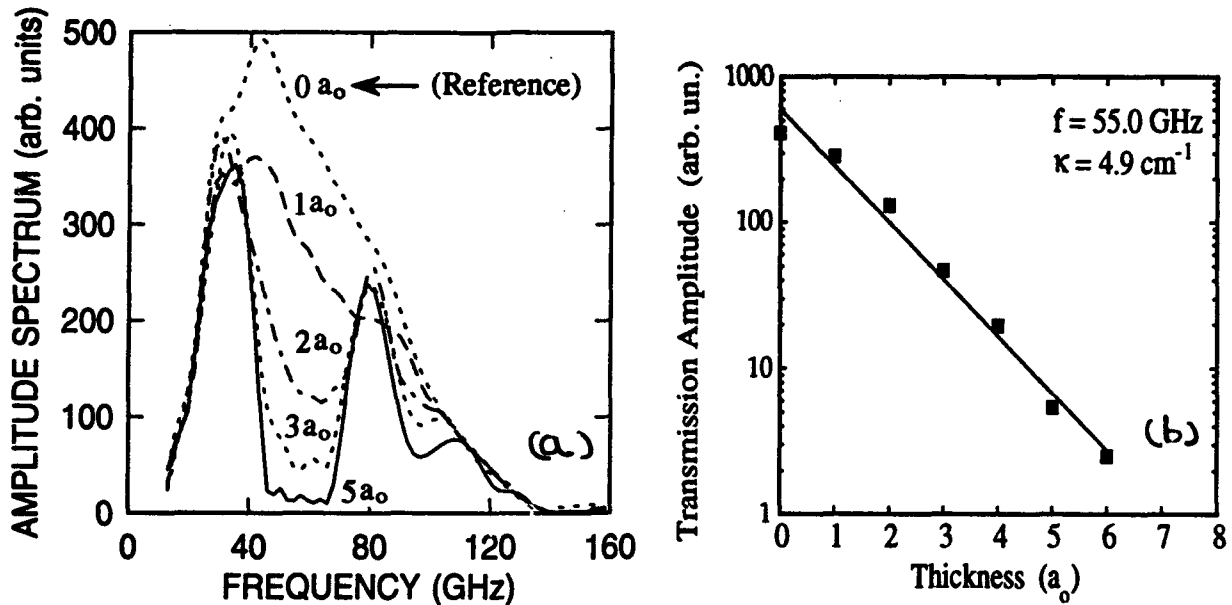


Figure 1 : (a) Transmission spectra corresponding to arrays of 0.74mm diameter alumina - ceramic cylinders of different thickness, i.e. different number of rows; (b) Amplitude transmission at 55GHz as a function of thickness.

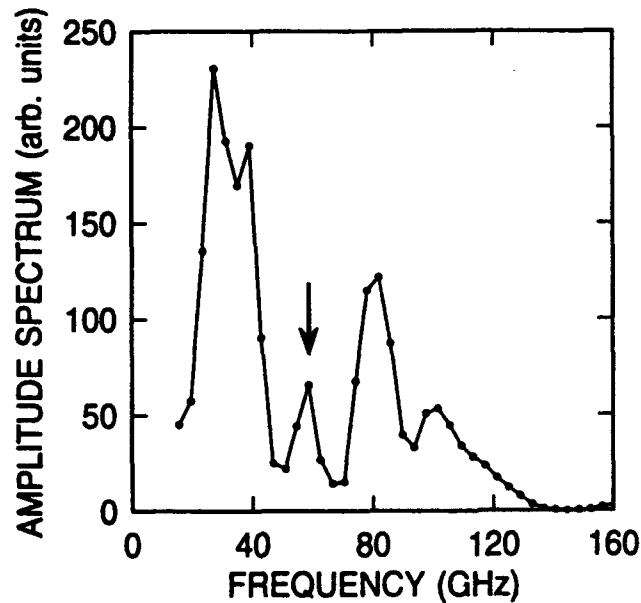


Figure 2 : Transmission spectrum corresponding to a 2-2-2 double-barrier resonant tunneling structure, i.e. 2 rows of empty lattice sandwiched on both sides by 2 rows of dielectric array. Note the extra peak in the band gap region.

## **High Optical Power Effects in Fiber-Optic Links\***

**C. H. Cox III**

**Lincoln Laboratory, Massachusetts Institute of Technology  
Lexington, MA 02173-9108**

It has been demonstrated that there are significant performance advantages to operating externally modulated fiber-optic links with high average optical power [1]. For example the link gain, noise figure and dynamic range all improve, to varying degrees, with increasing average optical power. In principal these improvements continue without limit as the optical power is increased. In practice the improvements are limited by a variety of deleterious effects which become increasingly more severe as the optical power increases. In this talk we will examine the limiting effects in presently available modulators, fibers and photodetectors under high optical power as well as the prospects for increasing these limits in the future.

The primary optical power limiting effect in modulators is optical damage. In the most common integrated-optic-modulator material lithium niobate, a small fraction of the light ionizes iron impurities and the resulting electric field modifies the waveguide parameters. The first measurable effect of optical damage is a shift in the optical phase which causes a shift in the operating point of an interferometric modulator such as a Mach-Zehnder. Higher optical powers increase the optical attenuation in the waveguide. Early LiNbO<sub>3</sub> devices operated around 0.8 micrometers where optical damage effects limited the optical power to less than 100 microwatts. By changing to a wavelength longer than the absorption edge of iron, LiNbO<sub>3</sub> devices have been operated at powers up to 100 mW and higher powers appear possible [2]. We will discuss the status of alternative approaches to reducing optical damage: using a different material such as LiTaO<sub>3</sub>, adopting a different waveguide formation process such as proton exchange and co-doping LiNbO<sub>3</sub> with Zn to increase its conductivity.

The first optical power limiting effect encountered in fibers is stimulated Brillouin scattering SBS. This effect arises because as the optical power increases acoustic phonons are created which frequency shift and reflect an ever increasing fraction of the incident optical power. The net effect of SBS is to limit the optical power that can be transmitted over a given length of the fiber - the shorter the length the higher the optical power which can be transmitted. The SBS limit is also a function of the spectral width of the source; a narrow-linewidth source, such as a solid state laser, has a lower

---

\* This work was sponsored by the Department of the Air Force

SBS limit than a spectrally wider source such as a diode laser . For example, the maximum power from a single-frequency, solid-state laser which can be transmitted over 1 km of common, polarization-maintaining fiber is 20 mW. Using a typical multimode diode laser, the SBS-limited power could be as high as 100 mW, also over a 1 km length. However the high RIN of these lasers usually precludes using them as the CW source in externally modulated links. We will present alternatives for raising the SBS limit which include using a multi-spectral-mode solid state laser, broadening the laser linewidth and using a larger core fiber.

The primary photodetector optical power limitations are thermal and non-linear optical-to-RF response, which generate spurious signals in the photodetected output. The thermal limit can be mitigated by using a low-thermal resistance mount for the photodetector. Non-linear photoresponse effects have been reported at optical power levels as low as 1 mW, when all the power was focused into a diffraction-limited spot [3]. These effects can be reduced by reducing the power density on the photodetector, e.g. by increasing the photodetector area over which the power is detected. This technique has been used to increase the maximum photodetector power to 20 mW [2]. While this technique is effective, it is limited to applications where the reduced bandwidth - due to the increase in junction capacitance with photodetector area - is not a problem.

Pre-production diode-pumped solid state lasers have been built with output powers of 700 mW and fiber coupled powers of 550 mW. Thus the available powers exceed the present limitations of other optical link components. At present the solid state laser power is limited primarily by the optical power from the pump diodes. Higher power diodes are in development, as well as new configurations for arranging the pump diodes. Thus it appears that laser power will not be the limitation for the foreseeable future.

This work was sponsored by the Department of the Air Force.

## References

1. C.H. Cox III, "Gain and Noise Figure in Analog Fiber-Optic Links," *IEE Proceedings-J. Microwave Opto-electronics* , Vol. 139, No. 4, pp. 238-242, August 1992.
2. C.H. Cox III, G.E. Betts and A.C. Yee, "Incrementally-Lossless, Broad-Bandwidth, Analog Fiber Optic Link," *Broadband Analog Optoelectronics--Devices and Systems*, Monterey, CA, 23-25 July 1990.
3. R. D. Esman and K. J. Williams, "Measurement of Harmonic Distortion in Microwave Photodetectors", *IEEE Photon. Technol. Lett.* **2**, 502 (1990).

## Fiber-Optic PSK Subcarrier Transmission at 35 GHz over 6.3 km using a Grating External Cavity Semiconductor Laser

Radhakrishnan Nagarajan, Shmuel Levy <sup>a)</sup>, Roger Helkey, Paul Humphrey, and John Bowers  
Dept. of Electrical & Computer Engineering, Univ. of California, Santa Barbara, CA 93106.

<sup>a)</sup> Was on leave from RAFAEL, Dept. 87, P.O. Box 2250, Haifa, Israel 31021.

Millimeter wave modulation of semiconductor lasers is of great interest for radar, communications, satellite links and electronic warfare systems. Applications include phased array radars, antenna remoting, and delay lines. Optical fiber technology offers many advantages such as high bandwidth, low loss, low weight, low dispersion, flexibility and immunity to EMI and lightning, and is an excellent replacement for a mmwave waveguide.<sup>1,2,3</sup>

Many mmwave systems require only narrow bandwidth at center frequencies much higher than the presently attainable direct modulation bandwidth of a laser diode. These systems will benefit from efficient narrow-band optical modulation techniques at frequencies above the intrinsic laser modulation bandwidth. In an earlier paper,<sup>4</sup> we presented the results of a transmission system experiment using a mmwave subcarrier at 35 GHz modulating a 1280 nm laser diode whose mm-wave response had been resonantly enhanced in an external cavity configuration. The setup used a mirror in the external cavity for feedback, and output was longitudinally multi-moded. The dispersion in the optical fiber limited our transmission distance to only about 200 m. In this paper, we present the results of an external grating tuned semiconductor laser whose single longitudinal mode operation has enabled us to achieve bit error rates (BER) of  $10^{-9}$  over transmission distances of 6.3 km for a narrowband 40 Mbit/s binary phase shift keyed (BPSK) digital data.

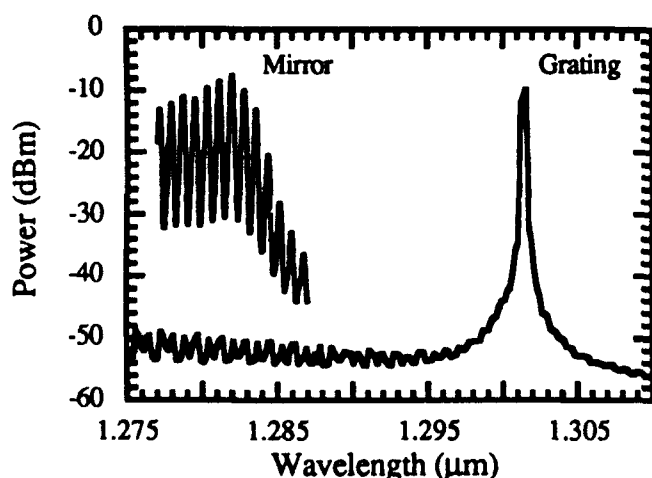


Fig. 1 Comparison of the longitudinal mode optical spectrum for the mirror reflector and grating tuned external cavity.

The transmitter and receiver systems are essentially the same as the ones we had previously used,<sup>4</sup> except that instead of a gold mirror we use a 800 lines/mm blazed grating reflector in the external cavity. The light from the anti-reflection coated rear facet of the buried crescent laser is focused onto this grating to form the external cavity, and the front facet is coupled to a single mode silica fiber for transmission. The external cavity length is tuned to give the third external cavity harmonic at 35

GHz. Fig. 1 compares the optical spectrum with a mirror to that with a grating in the external

cavity. The side mode suppression in the grating tuned case is about 40 dB without any appreciable loss in the output power. Also with the grating the lasing wavelength was able to be detuned nearer the zero dispersion point of the optical fiber at around 1.3  $\mu\text{m}$ .

In the analysis of the external cavity configuration, we have shown<sup>5</sup> that the modulation response as well as the relative intensity noise is enhanced as a result of optical feedback. Although this enhancement in noise is undesirable, the transmission system in that case was dispersion limited. The noise spectrum for the grating tuned case is much narrower, as predicted by our single mode rate equation analysis,<sup>5</sup> and also higher in intensity. Using grating feedback, the laser noise proved to be the limiting factor. The laser modulation bandwidth around 35 GHz is 0.86 GHz, as compared to the 0.7 GHz bandwidth obtained with the mirror in the cavity.

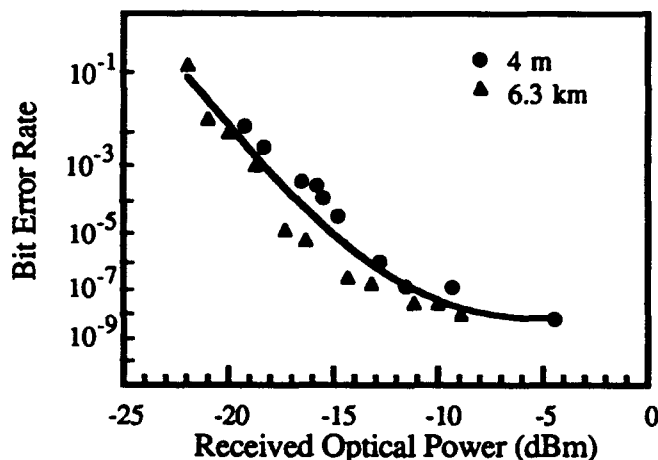


Fig. 2 Comparison of bit error rate as a function of received optical power for 40 Mbit/s BPSK data transmitted over a distance of 4 m and 6.3 km.

The BER performance of the system for a 40 Mbit/s BPSK digital data recovered from the 35 GHz subcarrier is shown in Fig. 2. The BER for the back to back case (4m) was always slightly worse than the transmission over 6.3 km. This shows that the system is not dispersion limited, and receiver sensitivity has improved by about 10 dB over the mirror reflector case.<sup>4</sup> There is a error floor at  $10^{-9}$  BER that we believe is the result of the enhancement in the transmitter noise. The error floor can

be lowered by increasing the signal power to the laser diode, but the mmwave subcarrier power level of 20 dBm at the input to the laser diode was close to its damage threshold.

In summary, we have demonstrated a system capable of transmitting narrow-band digital data modulated on a mmwave subcarrier at 35 GHz using a grating tuned external cavity semiconductor laser. We have achieved a bit error rate of  $10^{-9}$  for transmission over a distance of 6.3 km.

We would like to thank Tom Reynolds and Alan Mar for technical assistance. This work was sponsored by the Office of Naval Technology block program in Electro-Optics Technology.

1. See papers in the special issue on 'Applications of RF and Microwave Subcarriers to optical Fiber Transmission in Present and Future Broad-Band Networks', *J. Selected Areas in Communications* (1990).
2. H. Blauvelt, D.B. Huff, G.J. Stern, and I.L. Newberg, *Trans. Microwave Th. Tech.* **38**, 662 (1990).
3. I.L. Newberg, C.M. Gee, G.D. Thurmond, and H.W. Yen, *Trans. Microwave Th. Tech.*, **38**, 664 (1990).
4. S. Levy, R. Nagarajan, A. Mar, P. Humphrey, and J.E. Bowers *Electron. Lett.* **28**, 2103 (1992).
5. R. Nagarajan, S. Levy, A. Mar, and J.E. Bowers, *Photon. Tech. Lett.* **5**, 4 (1993).

# A NOVEL OPTICAL CARRIER DISTRIBUTION FOR MILLIMETER WAVE PERSONAL COMMUNICATION SYSTEMS

Tibor Bercei\* and Peter R. Herczfeld<sup>o</sup>

\*Technical University of Budapest, Research Institute for Telecom., Hungary

<sup>o</sup>Drexel University, Philadelphia, US

## Introduction

Millimeter wave personal communications, which utilizes a microcellular radio network, is a very promising new service which has many attractive features. The microcellular architecture requires the generation of a stabilized millimeter wave carrier signal at each remotely located radio base station. Furthermore, since the number of the radio base stations in a typical system is high, cost is a major concern, which precludes the generation of the carrier frequency at the individual radio base station. Instead, it is desirable that the carrier signals for the radio base stations be provided by the center, and optical methods are suitable for the distribution of high frequency carrier signals. In this paper a new optical-millimeter wave distribution network, with emphasis on MMIC components, will be presented.

## The optical generation of the millimeter wave carrier

The transmission of microwave carrier signals via optical fibers is a well established technique. However, at millimeter waves, at frequencies above the relaxation oscillation frequency of the semiconductor diode laser, new approaches are needed. One common approach, shown in Fig. 1, utilizes frequency multipliers, which however exhibit excessive losses and thus amplifiers are also needed. This arrangement is complex and not suitable for monolithic integration because of the poor efficiency of the monolithic frequency multipliers.

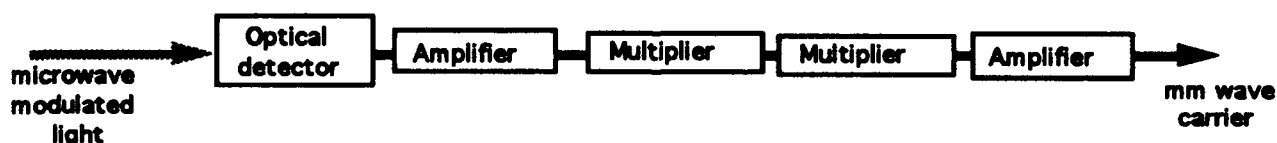


Fig. 1 Conventional approach to generate a millimeter wave carrier.

An alternate approach, using frequency dividers, is depicted in Fig. 2. Here a millimeter wave oscillator is phased locked using a microwave frequency reference signal transmitted by a fiber. Instead of multipliers, in this configuration, dividers are used in the control arm where losses do not present a significant problem.

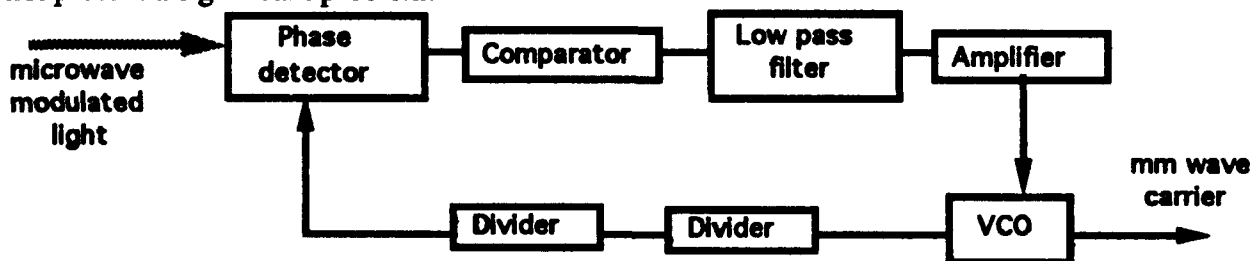


Fig. 2 An alternate way of generating a millimeter wave carrier.

This proposed new arrangement has numerous advantages. The entire circuitry can be constructed in a single MMIC chip because every element is MMIC compatible. The crucial block is the combined optical-microwave phase detector which has been developed utilizing illuminated FETs [3]. Applying a phase locked loop enables most of the circuits to operate at low power levels (except the VCO) and thus the overall efficiency of the chip becomes very good.

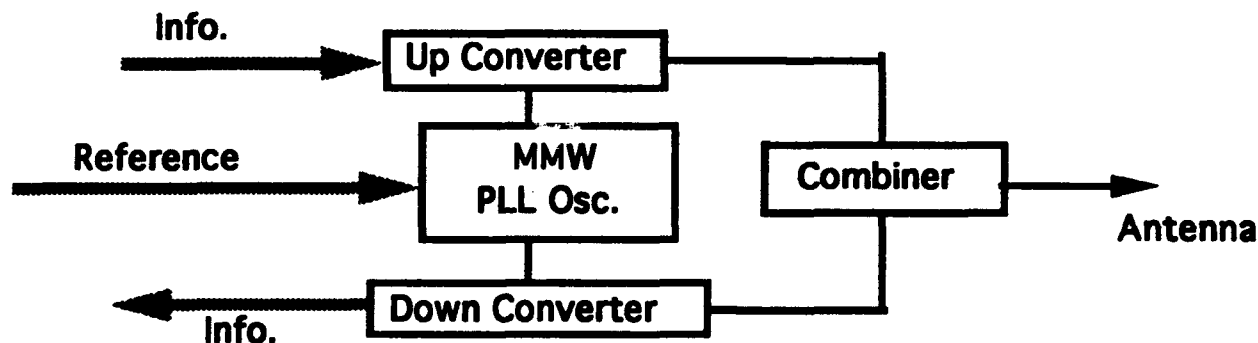


Fig. 3 The optically fed radio base station.

The new arrangement is very flexible as well. Changing the division numbers of the dividers a wide range of millimeter wave region can be covered applying a microwave frequency reference signal.

### The new radio base station

The application of the new carrier distribution method is shown in Fig. 3 where the block diagram of a radio base station is depicted. The transmit and receive information signals are also carried by fibers. All of the blocks can be included into a single MMIC chip utilizing combined optical-microwave mixers for up- and down-conversion [4]. Thus the same chip is applicable at any radio base station, only the carrier frequency has to be selected properly.

The further details of the new method will be presented at the Workshop.

### Conclusion

The optical methods are very suitable for the distribution of carriers in mobile communications systems because the center should supply the carriers for the radio base stations.

### References

1. T. Berceli, P. R. Herczfeld, A. S. Daryoush, and A. Rosen, "Performance Optimization of Optically Controlled Phased Array Antenna T/R Modules", 10th European Microwave Conference, London, U.K., Sept. 1989.
2. H. R. Fetterman, "Optical Technology Applied to SubMM/MMW", Conf. Digest of Thirteenth International Conference on Infrared and Millimeter Waves, Dec. 1988, Honolulu, Hawaii, p. T2.1.
3. T. Berceli, "A MMIC based new lightwave-microwave phase detector", Proc. of the 21st European Microwave Conference, Stuttgart, Germany, pp. 1311-1316, September 1991.
4. S. Malone, A. Paoella, P. R. Herczfeld, and T. Berceli, "MMIC Compatible Lightwave Microwave Mixing Techniques", IEEE MTT International Microwave Symposium, Albuquerque, USA, June 1992.

## **Transmission-Line Characterization with Ultrafast Optoelectronics**

G. Arjavalingam, A. Deutsch, and M. R. Scheuermann  
IBM Research Division, Thomas J. Watson Research Center  
P.O.Box 218, Yorktown Heights, NY 10598.  
(914) 945 1359 (ph); (914) 945 2141 (fax).

Recent advances in the characterization of resistive transmission lines by optoelectronically - generated ultrashort electrical pulses will be discussed. Resistive transmission lines are those in which dielectric losses are negligible, and where attenuation is dominated by losses in the metallic interconnections. Circuit-to-circuit wiring on large integrated circuits and in most modern electronic inter-chip interconnection structures are examples of resistive transmission lines. So are the coplanar waveguides and microstrip lines, fabricated on insulating substrates, commonly used in microwave hybrids. In the technique developed by us, the propagation of short electrical pulses and low-frequency capacitance are used to extract the frequency-dependent complex propagation constant and complex impedance. The basic idea was first demonstrated up to 25 GHz with inexpensive off-the-shelf instrumentation and some custom fixturing [1]. Subsequently, a custom software package was developed to automate data acquisition and analysis. In this configuration, the short-pulse propagation technique is routinely employed to characterize various chip-to-chip interconnection hardware [2]. Recently, optoelectronically generated and sampled pulses have been used to extend the technique to 70 GHz [3]. Details of the short-pulse propagation technique for transmission-line characterization, its mathematical basis, and its extension to high frequencies will be presented, together with representative results.

### **REFERENCES**

1. A. Deutsch, G. Arjavalingam, and G.V. Kopcsay, IEEE Microwave and Guided-Wave Letters, Vol. 2, pp. 25 - 27, (1992).
2. A. Deutsch et al., IBM Journal of Res. and Develop, Vol. 37, pp. 22 - 38, (1993).
3. A. Deutsch, M. R. Scheuermann, G. Arjavalingam et al, IEEE Microwave and Guided-Wave Letters, Vol. 3, pp. 75 - 78, (1993).

## Picosecond Pulse Propagation on Coplanar Striplines with Lossy Semiconductor Substrates

J. Son, H. H. Wang, and J. F. Whitaker

*Center for Ultrafast Optical Science, University of Michigan  
2200 Bonisteel Blvd., Ann Arbor, MI 48109-2099*

The widely used microstrip, as well as the higher-bandwidth coplanar transmission lines, may both be fabricated on semiconductor substrates that could become lossy due to unintentional doping during the growth of thin-film layer. The effect of these substrate losses, particularly on the ultra-short-duration signal propagation which will be required in future high-speed circuits, has not been thoroughly considered. This is the case even though the distortion of ultrawide-bandwidth signals would severely degrade the performance of microwave and digital circuits. We demonstrate the attenuation and dispersion characteristics of coplanar striplines (CPS) fabricated on poorly insulating semiconductor substrates both experimentally and computationally by observing the evolution of picosecond electrical pulses guided by these structures.

In our computations, a time-domain waveform propagating on a transmission line has been represented as a signal  $V(t, z)$ . Considering  $V(t, 0)$  as the waveform at a spatial origin,  $V(t, z)$ , was thus given by

$$V(t, z) = F^{-1} [F \{V(t, 0)\} \exp\{-\gamma(f) z\}] \quad (1)$$

where  $F$  is the Fourier transform,  $F^{-1}$  the inverse transform, and  $\gamma(f)$  the complex propagation factor. We have used a distributed-circuit analysis to calculate  $\gamma(f)$ . Although the analysis was based on the quasi-static behavior of the transmission line, a good deal of success has been realized by modifying and applying it to high-frequency propagation [1]. The transmission-line circuit parameters were related to the attenuation and phase factor through

$$\gamma(f) = \alpha(f) + j\beta(f) = \sqrt{Z(f)Y(f)} \quad (2)$$

where  $Z(f)$  and  $Y(f)$  represented the series impedance and the shunt admittance of the transmission line, respectively [1]. These quantities provided for the effects of radiation, metal (ohmic) and substrate losses, and hybrid-mode dispersion.

Coplanar stripline was chosen for this study because it is believed planar structures such as CPS will be used with the fastest devices, since they can support wider bandwidths with less distortion. The CPS series impedance depends most critically on the surface impedance of the electrodes, while the admittance is related to both the frequency-dependent effective permittivity and the loss tangent,  $\tan\delta(f)$ . This quantity relates the substrate loss with the propagation

factor in our investigation. For a semiconductor substrate having free carriers due to doping, this loss tangent can be expressed by

$$\tan\delta(f) = \frac{2\pi f \epsilon''(f) + \sigma'(f)}{2\pi f \epsilon''(f) + \sigma''(f)} \quad (3)$$

where  $\epsilon'$  and  $\epsilon''$  are the real and imaginary parts of the complex dielectric permittivity and  $\sigma'$  and  $\sigma''$  are the real and imaginary components of the complex conductivity as drawn from the Drude model [2]. To our knowledge, this is the first time this approach has been taken to model picosecond electrical pulse propagation.

As an example, a Gaussian pulse of 1-ps full-width-at-half-maximum (FWHM) duration was used as the input pulse at a spatial origin,  $V(t, 0)$ , on a CPS fabricated on GaAs. To illustrate the effect of the lossy substrate, three different shunt conductivities, 0, 0.1, and 1.0 mho/cm, were used for the substrate material in the computations. The zero conductivity case had a purely dielectric loss only (see Eq.(3)), and without a dielectric resonance, the loss tangent was negligible compared with the loss from the conductor and the radiation from the CPS [3]. This case, serving as a reference to the lossy ones, is illustrated in Fig. 1(a). Modal dispersion due to the dielectric inhomogeneity of the structure can be clearly seen by the broadening of the rising edge and the negative dip in the tail as the pulse propagates longer than 1 mm. Also, some attenuation was observed due to the ohmic loss of the metal lines and the radiation loss.

The overall attenuation became much stronger when the substrate had a conductance of 0.1 mho/cm, corresponding to a GaAs free-carrier doping of around  $10^{14} \text{ cm}^{-3}$  (Fig. 1(b)). The modal dispersion effect was less visible because of the strong substrate absorption, especially of the higher frequencies associated with ringing in the tail of the transient. If the conductance of the substrate was further increased to 1.0 mho/cm, the shunt conductive factor totally dominated in the pulse propagation in terms of not only the attenuation, but also the dispersion as shown in Fig. 1(c). The peak, less than 5 % of the input after 1-mm propagation, arrived later in time compared to the lower conductance case because the conductance loss now played a more significant role in the dispersion of the signal.

Experimentally, a self-mode-locked Ti:sapphire laser was used for the photoconductive generation of picosecond electrical pulses and the subsequent detection

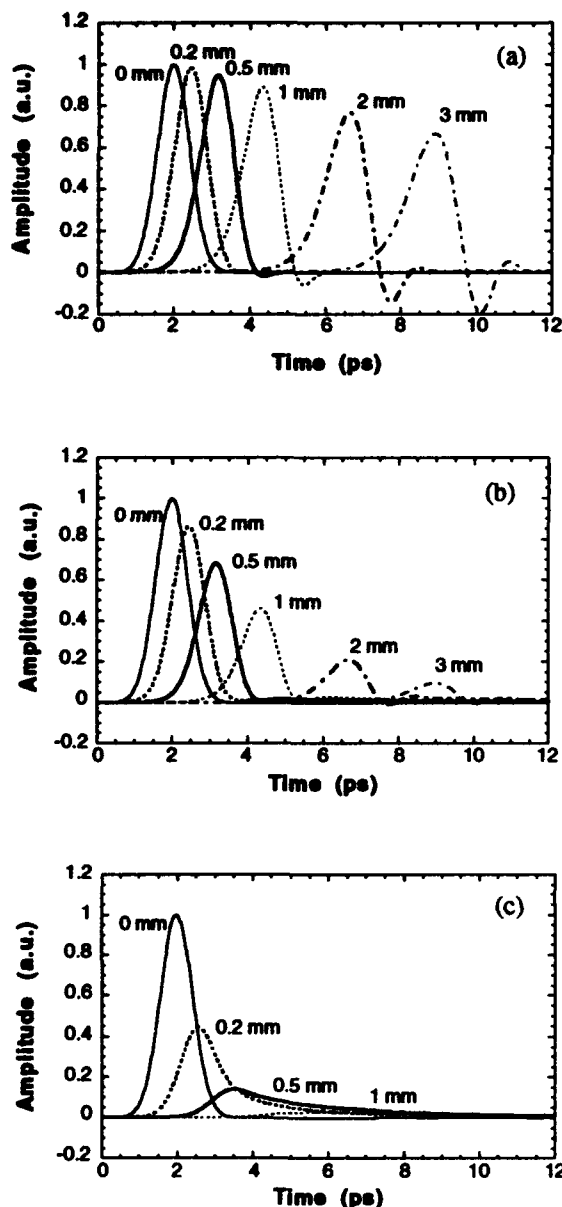


Fig. 1. Temporal evolution of a 1-ps-FWHM electrical pulse propagating on a coplanar stripline (width = 20 mm, spacing = 10 mm), showing distortion due to the attenuation and dispersion for three different substrate conductivities. (a) 0 (lossless substrate), (b) 0.1, and (c) 1.0 mho/cm.

of the propagating transients via the electro-optic (EO) sampling technique. The time-domain waveforms measured at successively longer propagation distances along the transmission-line are presented in Fig. 2(a). This first waveform measured on the n-doped region (0 mm) displayed some effect of dispersion because it was generated at a photoconductive switching gap 500  $\mu\text{m}$  from the n-doped interface. The successive waveforms at four different points demonstrated the very strong absorption due to the high conductance of the substrate.

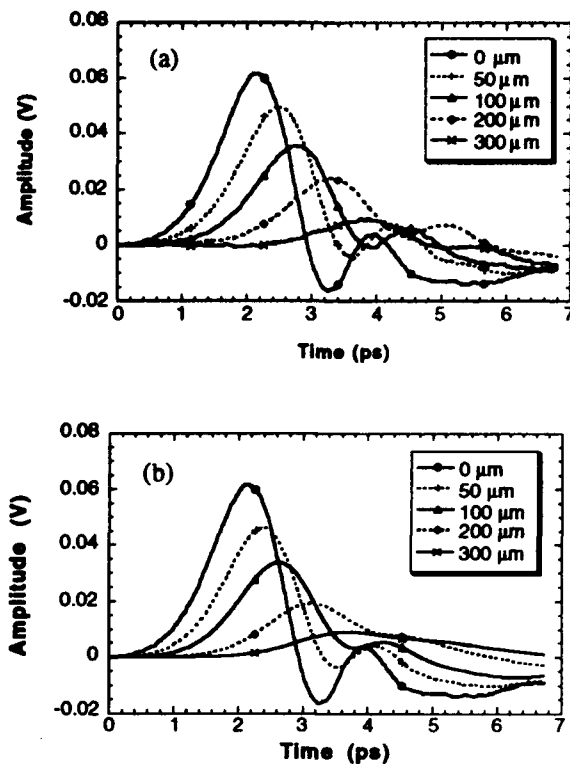


Fig. 2. Pulse propagation on coplanar stripline fabricated on 5-mho/cm GaAs substrate. (a) Experimental results probed by electro-optic sampling technique and (b) simulation results obtained after using the experimental input to the modeling code.

Also, the dispersion due to the substrate conductance became apparent as the pulse propagated.

The experimental input at the spatial origin was input to the simulation code described in the previous section and compared with the experimental results to verify the validity of our modeling. The result is shown in Fig. 2(b). Fast Fourier transforms were also performed and compared on both sets of time-domain signals. Good agreement between the calculation and the experiment was found in both the time-domain and the spectral-domain. This leads us to believe that the simple model put forward can be used to quickly predict, to "first-order," the degree of distortion to be expected from broad-bandwidth propagation on CPS fabricated on lossy substrates.

## REFERENCES

- [1] J. F. Whitaker, R. Sobolewski, D. R. Dykaar, T. Y. Hsiang, and G. A. Mourou, *IEEE Trans. Microwave Theory Tech.*, vol. MTT-36, pp. 277-285, Feb. 1988.
- [2] N. W. Ashcroft and N. D. Mermin, *Solid State Physics*. Philadelphia, PA: Saunders College, 1976, ch. 1.
- [3] S. Gupta, J. F. Whitaker, and G. A. Mourou, *IEEE Microwave and Guided Wave Lett.*, vol. 1, pp. 161-163, Jul. 1991.

### **T3.3 2:20pm - 2:40pm**

#### ***Transmission of Ultra-High-Bandwidth Pulses on a Low-Distortion Coplanar Stripline***

***H.J. Cheng and J.F. Whitaker***

University of Michigan, Center for Ultrafast Optical Science, Ann Arbor, MI 48109

***T.M. Weller and L.P. Katehi***

University of Michigan, NASA Center for Space Terahertz Technology, Ann Arbor, MI 48109

In recent years the desire to increase the bandwidth of guided propagation along planar transmission lines [1] and to create submillimeter-wave integrated circuits with low-radiation and dispersion characteristics [2] has led to the development of a structure using a thin membrane as a substrate. This so-called "microshield" technology uses a 1.5- $\mu\text{m}$ -thick membrane comprised of silicon dioxide and silicon nitride to support metal lines and other patterned circuit structures. The use of the membrane, which is rugged enough to withstand standard processing techniques, eliminates the frequency-dependent radiation into the substrate material and the frequency-dependent phase velocity caused by modal dispersion, both of which increase with the relative permittivity of the substrate. These improvements are realized because the electric fields from the conductors essentially do not experience any dielectric inhomogeneity, *i.e.*, they are completely surrounded by air. To demonstrate the benefits provided by such a guiding geometry for millimeter- and submillimeter-wave propagation, we have experimentally launched a single-picosecond-duration electrical pulse on a coplanar stripline (CPS) fabricated on a membrane substrate and measured the transmitted waveform at several distances from the source. Results indicate nearly negligible distortion of the signals even after 5 mm of propagation, with only a small attenuation attributed to the ohmic losses of the conductors.

The membrane was prepared using a silicon wafer with a composite material,  $\text{SiO}_2/\text{Si}_3\text{N}_4/\text{SiO}_2$ , grown on the surface using a combination thermal oxidation/chemical vapor deposition process. An etched rectangular region in another composite layer on the back of the wafer is used as a mask to define an area which is subsequently etched away until a window is formed in the silicon wafer with the top oxide/nitride composite as the pane. The transmission lines were fabricated from Ti/Au and had a strip separation and width of 20  $\mu\text{m}$ .

In order to generate and measure electrical pulses having subpicosecond duration, the optoelectronic technique of photoconductive switching, along with a subpicosecond-temporal-resolution electro-optic sampling characterization system, have been employed. These techniques are both based on the use of laser pulses of extremely short duration ( $\leq 100$  fs), in this instance from a solid-state Ti:sapphire laser. The photoconductive source utilizes the ultra-short laser pulse to convert a dc bias to a subpicosecond electrical transient which is launched onto the guiding structure. Electro-optic sampling uses the optical pulse along with an electro-optic crystal, dipped into the electric field above the transmission line under test, to produce a sampling gate having a duration of only several tenths of a picosecond.

For the measurement of transients in the time domain, reflections from any source near the probing point cause a loss of accuracy in the acquisition of clean, easily analyzed signals. Therefore, it was necessary to integrate a 200- $\mu\text{m}$ -wide photoconductive-generator patch with the CPS fabricated on the membrane. This was a convenient alternative compared with transporting a short electrical transient onto the CPS via inductive wirebonds or through the use of an unwieldy flip-chip geometry. The subpicosecond-lifetime photoconductor employed was a 1- $\mu\text{m}$  layer of GaAs grown by molecular beam epitaxy at the low substrate temperature of  $\sim 200^\circ\text{C}$  (known as LT-GaAs). This photoconductor was lifted off its substrate through etching techniques to form a free-standing film, and then grafted to the membrane substrate using a van der Waals bonding technique [3]. The CPS was then defined on the LT-GaAs and the

membrane using standard photolithographic techniques.

The pulse output after optical excitation of the photoswitch was measured at distances of 1, 3, and 5 mm from the generator, with no discernable distortion except for a small decrease in peak amplitude at the 5 mm propagation distance. The measured pulse rise time in each instance was  $\sim 0.75$  ps, and the FWHM was  $\leq 1.2$  ps. When the Fourier transforms of the time-domain signals were compared, the phase velocity between 50 and 500 GHz was found to be flat, indicating the absence of dispersion, while the attenuation was found to increase only slightly, to about 0.09 Np/mm (0.8 dB/mm) at 500 GHz (Fig. 1). This loss is directly compared to that found for propagation of subpicosecond pulses along CPS of the same dimensions on GaAs and quartz [4]. For the CPS on the GaAs substrate, the attenuation at 50 GHz is only about 0.09 Np/mm, while at 500 GHz it is in excess of 1.1 Np/mm. This is mainly due to the extreme radiation loss present even in uniform lines that are fabricated on high-permittivity substrates. A much larger degree of phase-velocity dispersion also results from propagation on the GaAs-substrate line (and to a lesser extent for the CPS on quartz), leading to pulses with rise times and durations that rapidly expand with increasing propagation distance. This is dramatically observed in Fig. 2, where the degradation of the rise time versus propagation distance is plotted for all three CPS plus another low-distortion line demonstrated by Dykaar *et al.* [5].

We have demonstrated low-loss and virtually dispersionless propagation of pulses with frequencies in the millimeter- and submillimeter-wave regimes using a novel microshield technology being developed for use in a new family of integrated circuits.

**Acknowledgment:** The authors wish to thank F.W. Smith of Lincoln Laboratory for providing the low-temperature-grown GaAs material. This work has been supported by AFOSR under contract No. AFOSR-90-0214 (University Research Initiative), the National Science Foundation through the Center for Ultrafast Optical Science under STC PHY 8920108, the Office of Naval Research under contract No. N00014-92-J-1070, and the NASA Center for Space Terahertz Technology.

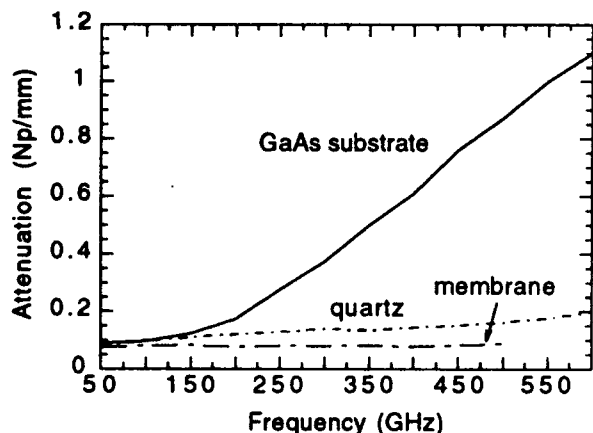


Figure 1

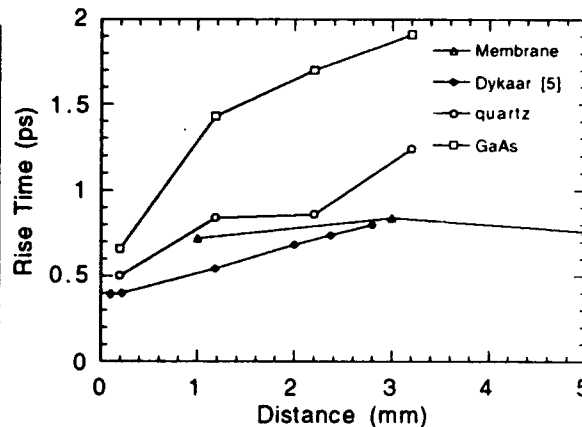


Figure 2

## References

- [1] N. Dib *et al.* 1991 *IEEE MTT-S International Microwave Symposium Digest*, New York: IEEE, pp. 623-626, 1991.
- [2] T.M. Weller *et al.*, *Proceedings of the 4th International Symposium on Space Terahertz Technology*, Los Angeles, CA, Mar. 1993.
- [3] E. Yablonovitch *et al.*, *Appl. Phys. Lett.*, vol. 56, p.2419 (1990).
- [4] H.J. Cheng *et al.*, to appear in the *OSA Proceedings on Ultrafast Electronics and Optoelectronics*, 1993.
- [5] D.R. Dykaar, *et al.*, *Appl. Phys. Lett.*, vol. 57, p. 1123, (Sept. 1990).

## Ultrafast Scanning Probe Microscopy

*S. Weiss, D. Botkin, D.F. Ogletree, M. Salmeron and D.S. Chemla*

*Department of Physics  
University of California at Berkeley  
and  
Materials Sciences Division, MS 2-300  
Lawrence Berkeley Laboratory  
Berkeley, CA 94720*

### **Summary**

We have combined the time resolution of short pulse laser techniques with the spatial resolution of the scanning tunneling microscope to image surfaces with 2 ps time resolution and 50 Å spatial resolution. Conventional short-pulse laser experiments have spatial resolution of a few  $\mu\text{m}$  due to the diffraction limit of optical beams. Scanned probe microscopes (SPM) have demonstrated spatial resolution better than 1 Å, sufficient to resolve individual atoms, but time resolution is on the order of 1 ms for point measurements and 1 s for imaging, limited by the mechanical constraints of SPM scanners.

Our ultrafast STM is a powerful tool to study the physics of mesoscopic systems. It opens a window to observe processes and excitations which propagate at velocities of a few Å per fs. We can now spatially resolve in real time phenomena such as carrier transport in semiconductor structures, electric field and voltage wavefront propagation at metal semiconductor interfaces, or charge transfer in molecular electronic devices. The operation of sub-micron optoelectronic devices can be directly characterized with this technique.

We have proposed to exploit the nonlinear nature of the different tip-sample interactions in scanning probe microscopy (STM, AFM, NSOM) to obtain ultrafast time-resolution [1]. This nonlinearity can be intrinsic to the nature of tip-sample coupling or can be artificially produced by fabrication of custom designed tips. Time resolution is achieved by modulating both the sample and the tip response with two short optical pulses. By scanning the time delay between the two pulses and integrating the signal, a cross-correlation of the tip-sample response is obtained. This basic principle is very general, and can be implemented in a wide variety of applications.

In the experiment presented here, we have integrated an ultrafast silicon on sapphire (SOS) photoconductive switch with an STM tip assembly to provide time resolution. Short (0.6 ps) voltage pulses were generated by shorting a transmission line with a second SOS switch. The switches were operated with pulses from a 100 fs Ti:sapphire laser. The transmission line consisted of a pair of 20  $\mu\text{m}$  wide gold strips deposited on a sapphire substrate (Fig. 1). The STM tip was positioned over one strip of the transmission line, and cross-correlation measurements were performed by varying the delay between the two optical pulses.

Fig 2 shows a 2 ps wide cross-correlation pulse detected by the STM while tunneling at 5 nA with a +80 mV bias on the strip. The average tunnel current is increased by  $\sim 0.5$  nA when the transmission line pulse passes beneath the tip, for a signal/background ratio of 10%. Fig 3 shows a series of pulses recorded at tunneling gap resistances between 16 M $\Omega$  and 256 M $\Omega$  at +80 mV bias. The size of the correlation pulse is approximately proportional to the tunnel current.

Additional structure can be observed following the correlation peak in figure 2. We attribute this to ringing of the tip structure, which decays with a time proportional to the tunnel gap resistance.

When the tip is withdrawn from the surface by 50 Å, both the DC tunneling and the cross-correlation signal drop to zero. Contributions to the time resolved signal from capacitive coupling or radiative effects were not detected.

Fig 4 shows a 0.7 μm square image of one of the transmission line conductors acquired as the fast pulse passed under the tip. A similar image was acquired 2.5 ps before the arrival of the pulse. We do not attribute features in the image to propagation of the voltage pulse since the transmission line propagation velocity is ~ 100 μm/ps, too fast to be resolved with this instrument.

Ultrafast scanned probe microscopy is not limited to the STM. As we discussed before [1], the non-linear nature of the probe-sample interactions in STM, atomic force microscopy (AFM) and near-field optical microscopy (NSOM) offer many opportunities for resolving ultrafast phenomena.

This work was supported by ONR and DARPA under contract #N000-14.93.105.36

### References:

- [1] S. Weiss, D. Botkin and D.S. Chemla, Ultrafast electronics & optoelectronics, January 25 1993, San Francisco, Technical Digest, paper #WA4-1

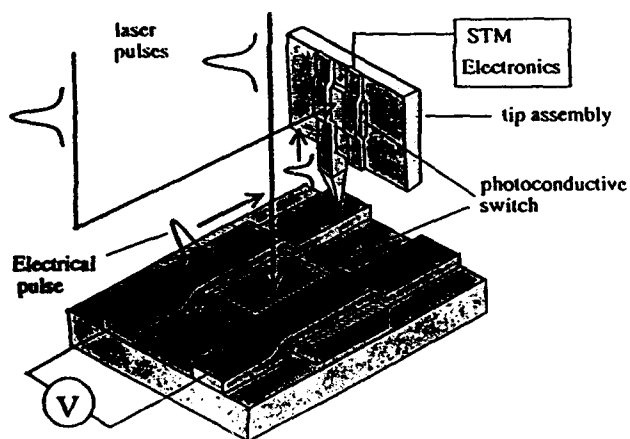


Fig.1: Ultrafast STM. One laser pulse excites a voltage pulse on a transmission line. The second pulse photoconductively samples the tunneling current on the tip assembly

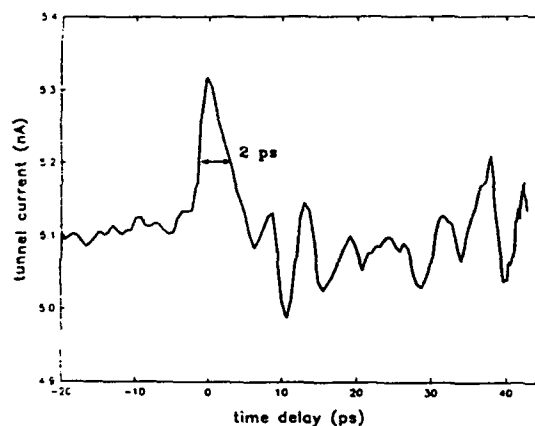


Fig. 2: Tunnel-current cross-correlation detected on the tip assembly, at 5nA and 80mV settings

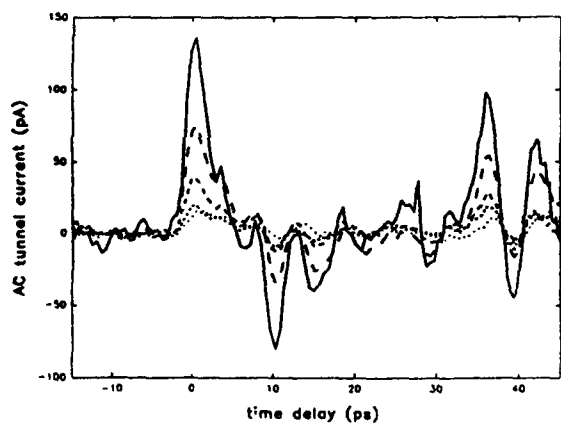


Fig. 3: The AC part of the tunnel-current for different gap resistances (16, 32, 64, 128 and 256MΩ from top to bottom)

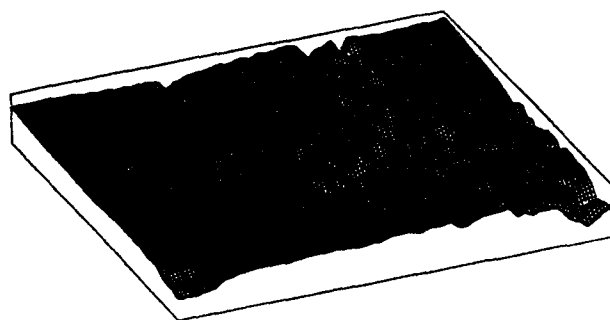


Fig. 4: A topographic image (0.7 x 0.7 μm<sup>2</sup>) of the transmission line, taken with the exact same conditions as in Fig. 2, and at time delay ΔT=0.

**Wednesday, July 21, 1993**

**Sessions:**

**W1: Ultrafast Techniques**

**W2: Systems III**



## MEASUREMENT OF NEW MILLIMETERWAVE DEVICES AND COMPONENTS USING PICOSECOND TECHNIQUES

H.R. Fetterman, M. Martin, F. Oshita, D.V. Plant, A.Z. Kain  
Department of Electrical Engineering  
University of California, Los Angeles  
Los Angeles, California 90024

The use of picosecond testing for semiconductor devices has been demonstrated to be extremely useful to measure semiconductor devices at high frequencies. We report here the extension of this technology to low temperatures and new devices and systems. In each example we find that the use of picosecond techniques permits a wide frequency spectra to be obtained using relatively simple, convenient configurations. Although the approach we use is primarily based upon the use of electro-optic switches, we also employ direct optical injection and in some cases autocorrelators.

Looking at HBTs and HEMTs we have extended our earlier measurements to faster devices, new wavelengths and lower temperatures. The results of some of these measurements are shown in figures 1 and 2. In some of our measurements, using direct optical probing, we introduced a second laser to generate the infrared probe beam while the visible system was still used to operate the switches. Results of this type of measurement is shown in figure 3. Other devices such as Theta transistors were also examined and typical measurements shown in fig. 4.

Another set of measurements were made on-wafer optical guides that we are using to generate photonic integrated systems. In this set of experiments we sent picosecond light through both grating and step index guide and measured the pulse width on our autocorrelators. Preliminary results of these measurements are shown in figure 5. These are particularly important since we are using related structures to form our delays in an optical controlled millimeter wave phased array radar system.

Finally, we are also making delay line measurements on high temperature superconducting coplanar systems. These measurements are to determine directly the phase velocity associated with an effect known as kinetic inductance in these systems. The essence of this internal inductance effect is seen in the penetration depth close to the transition temperature (figure 6). This is usually observed indirectly via measurements of the Q of a microwave resonator but we are now using the picosecond techniques developed for our semiconductor S parameter measurements.

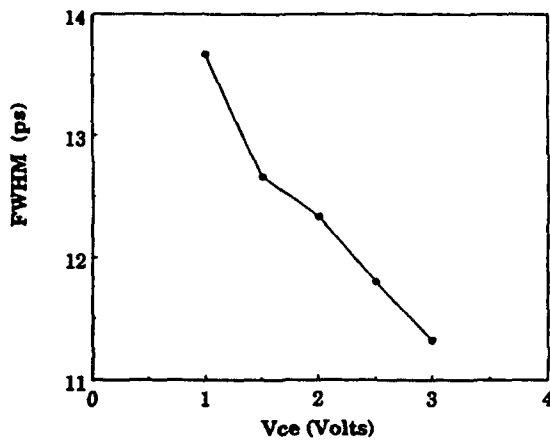


Fig.1 FWHM of HBT optical response as a function of  $V_{ce}$

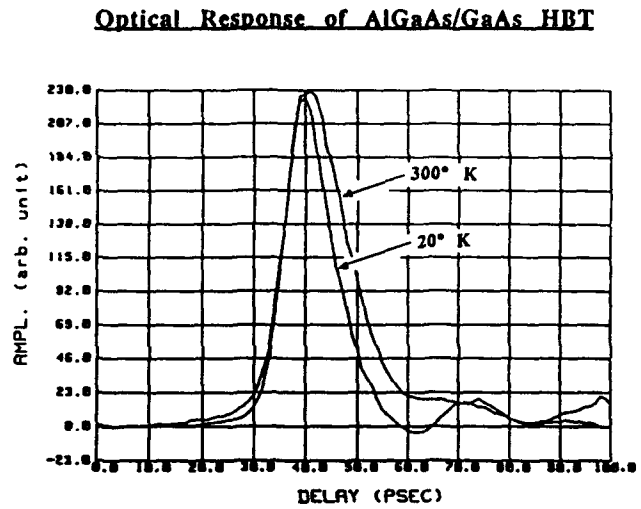


Fig.2 Time domain HBT optical response at different temperatures.

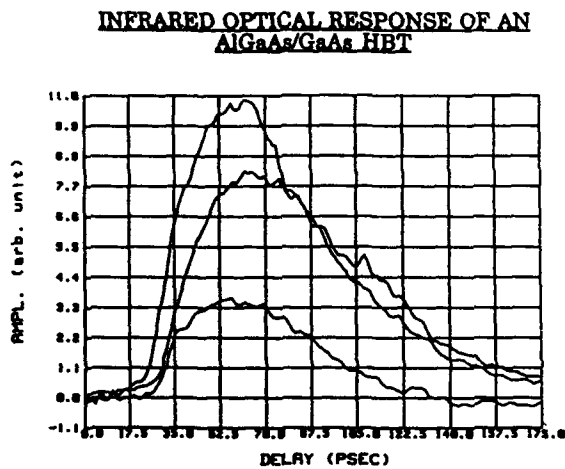


Fig.3 Optical response at 850nm for AlGaAs/GaAs HBT

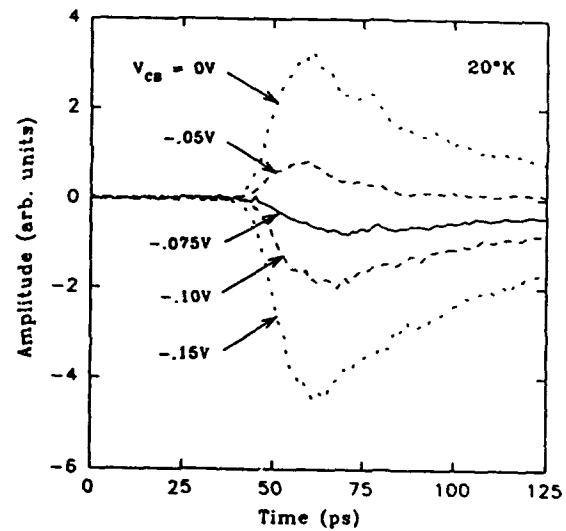


Fig.4 Visible Optical Response for common-base planar doped GaAs/AlGaAs THETA vs CB voltages

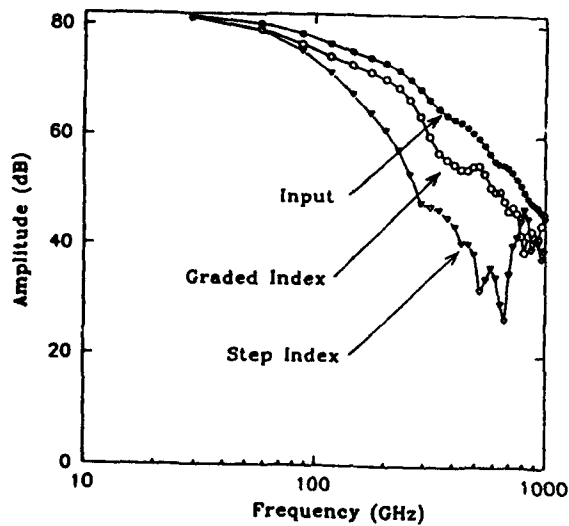


Fig.5 Dispersion in the frequency domain for 10cm optical on-wafer polymer guide.

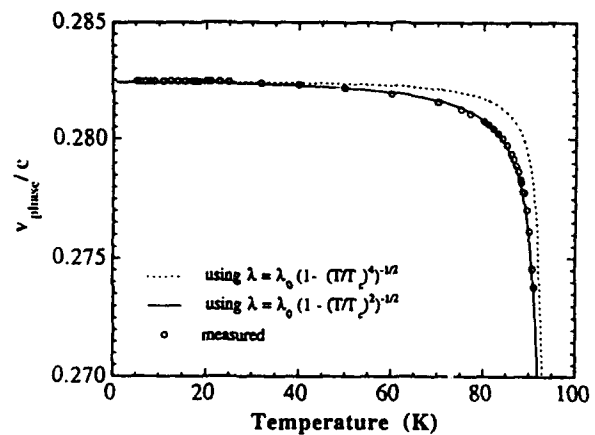


Fig.6 Normalized velocity vs. Temp. for 200nm thick superconducting CPW YBCO YBCO film

**Ultrafast Photonic-to-Microwave Transformer (PMT)**

**Ming C. Wu and Tatsuo Itoh**

**UCLA, Electrical Engineering Department, Los Angeles, CA 90024-1594**

Ultrafast photodetectors with high quantum efficiency are required for optoelectronic generation of microwaves and millimeter-waves, ultra-high speed optical communication systems. Optical signals with subcarrier modulation at several hundred GHz can be achieved by using optical heterodyning techniques [1] or monolithic mode-locked diode lasers [2]. For example, sub-picosecond optical pulse generation at 350 GHz were demonstrated using a monolithic colliding pulse mode-locked quantum well laser [3][4]. These ultrafast optical pulses can be efficiently converted into millimeter-waves by broadband photonic-to-microwave transformers (PMT). This paper describes a broadband ultrafast PMT with nearly 100% efficiency at 100 GHz.

The response of conventional pin photodiodes is limited by the fixed bandwidth-efficiency product due to carrier transit time. Though bandwidth above 100 GHz is possible, the efficiency becomes very low at high frequencies. For example, a 100 GHz detector has a efficiency less than 31% [5]. The bandwidth-efficiency product was improved by using waveguide detectors. However, the bandwidth is limited by the velocity mismatch between the microwave transmission line and the optical waveguide [5]. An alternative approach using nanometer metal-semiconductor-metal (MSM) photoconductive detectors has reported a bandwidth of 500 GHz. However, reasonable conversion efficiency is yet to be demonstrated [6].

The schematic structure of the ultrafast PMT is shown in Fig. 1. It consists of an input optical waveguide and an output microwave waveguide. Discrete photodiodes are placed at the periodical intersections of the passive optical waveguide and the output microstrip lines. The microstrip line winds around the optical waveguide to contact the photodiodes as well as to match the effective path lengths of the optical and microwave transmission lines [7]. Because the overall efficiency of the PMT is summed over many photodiodes, the efficiency of each individual photodetector need not be very high, therefore, it can be optimized to have bandwidth of several hundred GHz. This design of PMT is different from the conventional waveguide detectors in several aspects: (1) the separation of the optical waveguide and the microwave transmission line allows simultaneous optimization for both waveguides; (2) velocities of the lightwaves and the microwaves are better matched, which extends the bandwidth to higher frequency; and (3) higher efficiency can be obtained because all photocurrents add up in phase.

We have developed a theoretical model to investigate the performance and the fundamental limits of the PMT. The model takes into considerations the velocity mismatch, waveguide attenuation, and the parasitics of the photodetector. Photodiodes with intrinsic bandwidths of 200 GHz are used here. With a single photodiode, the quantum efficiency is only around 16%. By adding 4 more photodetectors into the PMT, the quantum efficiency is improved to 58%. With 15 photodetectors, efficiency as high as 92% can be achieved while the bandwidth is over 100 GHz. The bandwidth is mainly limited by the loss of microwave transmission lines, in contrast to the conventional waveguide detectors which are limited by velocity mismatch. Hence the degradation of the PMT at high frequency tends to be more gradual. More detailed design considerations and the ultimate performance of the PMT will be presented in the conference.

[1] D. C. Scott, D. V. Plant, and H. R. Fetterman, *Appl. Phys. Lett.*, Vol. 61, pp. 1-3, 1992.

[2] K. Lau, *IEEE J. Quantum Electron.*, Vol. 25, pp. 250-261, 1990.

- [3] M. C. Wu, Y. K. Chen, T. Tanbun-Ek, R. A. Logan, M. A. Chin, and G. Raybon, *Appl. Phys. Lett.*, Vol. 57, No. 8, pp. 759-761, August 1990.
- [4] Y. K. Chen and M. C. Wu, *IEEE J. Quantum Electron.*, Vol. 28, pp. 2176-2185, 1992.
- [5] J. E. Bowers and C. A. Burrus, Jr., *IEEE J. Lightwave Technology*, Vol. LT-5, No. 10, pp. 1339-1350, October 1987.
- [6] S. Y. Chou and M. Y. Liu, *IEEE J. Quantum Electron.*, Vol. 28, No. 10, pp. 2358-2368, Oct. 1992.
- [7] H.-Y. Lee and T. Itoh, *Int. J. Infrared and Millimeter Waves*, Vol. 10, No. 3, pp. 321-335, March 1989.

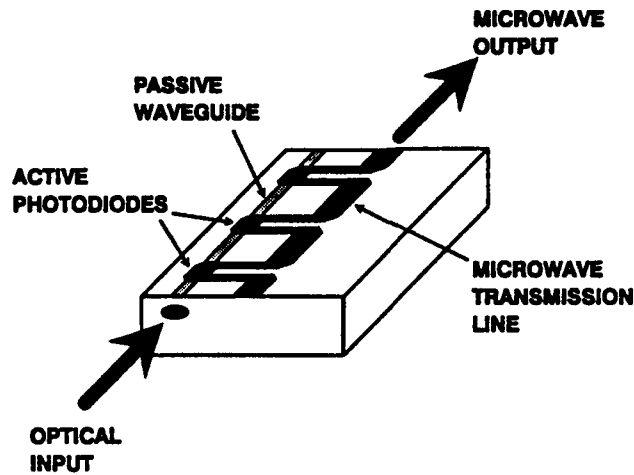


Fig. 1. The schematic diagram of the ultrafast photonic-to-microwave transformer (PMT).

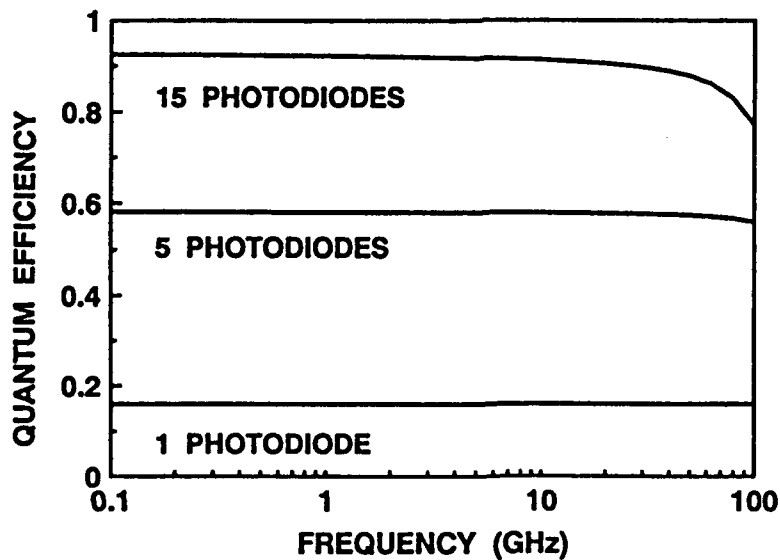


Fig. 2. The simulated frequency response of the PMT with 1 photodiode, 5 photodiodes, and 15 photodiodes, respectively.

**W1.3 9:20am - 9:40am**

**Characterization of Planar Antennas Fabricated on GaAs Epilayers  
Containing As Clusters For Picosecond Short-Pulse Applications**

**Lawrence Carin and David R. Kralj  
Department of Electrical Engineering/ Weber Research Institute  
Polytechnic University  
Brooklyn, NY 11201**

**Michael R. Melloch and Jerry M. Woodall  
School of Electrical Engineering  
Purdue University  
West Lafayette, IN 47907**

When one grows GaAs using normal molecular beam epitaxy (MBE) conditions except at low substrate temperatures, excess As can be incorporated into the epilayer. The amount of excess As is strongly dependent on the substrate temperature during MBE. Upon annealing these epilayers at temperatures of 600°C or higher, the excess As precipitates. The final As cluster density and average diameter is a function of the time and duration of this anneal<sup>1</sup>. We will designate this composite material consisting of As clusters in a GaAs matrix as GaAs:As. In this paper we present experimental results which assess the performance of antennas that are fabricated on GaAs:As and are switched photoconductively with a picosecond pulsed laser system.

Our measurements are performed with a mode-locked Nd-YLF laser and the infrared pulses it generates are pulse compressed and frequency doubled to produce green (527 nm) pulses of approximately 4 ps duration and 200 mW average power at a 76 MHz repetition rate. These pulses are used to switch coplanar-strip horn antennas photoconductively<sup>2</sup>. The antenna and feed were fabricated using AuGeNi lines in an oil diffusion pumped system. We considered several different GaAs:As epilayers. The epilayers were grown in a Varian GEN II MBE system on two-inch diameter semi-insulating GaAs substrates using an As<sub>2</sub> to Ga beam equivalent pressure ratio of 20. Each GaAs:As epilayer began with a GaAs buffer layer grown at 600°C, then while continuing to grow GaAs, the substrate temperature was lowered to the growth temperature for the epilayer with excess As. Below we present results for substrate growth temperatures of 220, 250 and 270°C, with respective epilayer thickness of 0.4  $\mu\text{m}$ , 0.5  $\mu\text{m}$  and 0.9  $\mu\text{m}$ , and respective post-growth anneals at 600°C under the As<sub>2</sub> flux of 20, 45 and 50 minutes.

The antenna measurements were performed as follows. The transmitting antenna was dc biased with a 40 V battery and the receiving antenna was connected to a current preamplifier and then to a lockin amplifier. The pump (used to switch the transmitter) and probe (used to switch the receiver) optical pulses were split equally such that approximately 100 mW average-power pulses switched each antenna and the pump pulse was chopped at 1 KHz. The antennas were arranged in transmission and separated by 10 cm; fused silica hemispherical lenses were placed in front of each antenna to significantly increase the detected signal amplitude. In all measurements, GaAs:As grown at 250° C with a 45 minute

post-growth anneal at 600° C was used as the substrate for the receiving antenna. In Fig. 1(a)-(b) we show results for transmitting antennas which were fabricated on GaAs:As epilayers grown at 220 and 270° C, respectively.

The results in Fig. 1(a)-(b), which represent a small subset of the results which will be presented at the meeting, show that the detected pulse duration for our picosecond applications is not very susceptible to the substrate growth temperature. Although the pulse shapes are different for the transmitting antennas grown at different temperatures, the pulse duration of each waveform is essentially the same. Moreover, a numerical Fourier transform of each waveform shows that each contains significant frequency components over approximately the same bandwidth (10-80 GHz). The most noticeable difference between the waveforms received from the two different epilayers is found in the peak radiated amplitude.

In the presentation we will also compare the performance of antennas fabricated on GaAs:As epilayers with results obtained using silicon-on-sapphire (SOS) substrates with typical ion-implantation levels. We will show that properly designed GaAs:As epilayers produce radiated waveforms of much higher signal levels than on similar antennas fabricated on conventional ion-bombarded SOS.

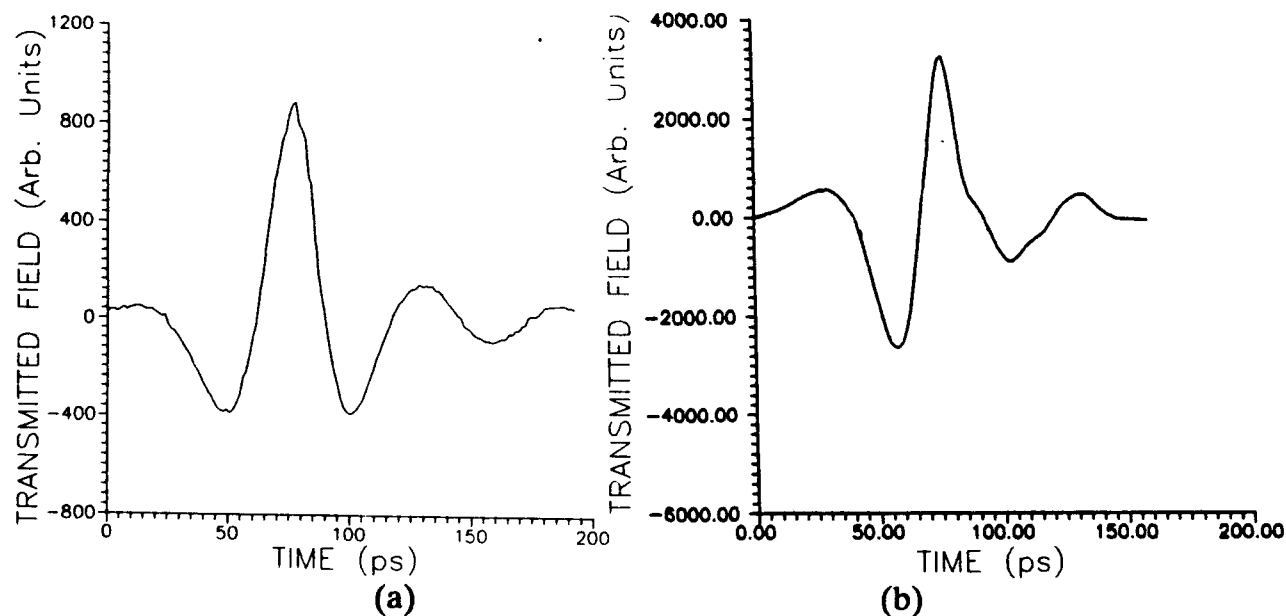


**Fig. 1.** Received signals generated by coplanar-strip horn antennas fabricated on GaAs:As epilayers MBE-grown at (a) 220°C and (b) 270°C. Each waveform was measured with a coplanar-strip antenna fabricated on GaAs:As grown at 250°C.

### References

1. M. R. Melloch, D. D. Nolte, N. Otsuka, C. L. Chang, and J. M. Woodall, *J. of Vac. Sci. and Tech.*, **B10**, (May/June 1993).
2. G. Arjavalingam, Y. Pastol, J.-M. Halbout, G. V. Kopcsay, *IEEE Trans. Microwave Theory Tech.*, **38**, 615 (1990)

**Photoconductive Monolithic Wideband Transmitter Characterization**

**A. Kim,<sup>1</sup> S. E. Saddow,<sup>2</sup> R. Youmans,<sup>1</sup> L. Jasper,<sup>2</sup> M. Weiner,<sup>1</sup> and C. H. Lee<sup>3</sup>**

**<sup>1</sup>Army Research Laboratory - EPSD  
Fort Monmouth, NJ 07703**

**<sup>2</sup>Army Research Laboratory - WTD  
Adelphi, MD 20783**

**<sup>3</sup>University of Maryland - Dept. of Elect. Engr.  
College Park, MD 20742**

***Summary***

A compact, monolithic, photoconductive wideband transmitter has been fabricated and evaluated, which is suitable for wireless communication and advanced impulse radar applications, such as automobile collision avoidance. Activation of this device with 30-ps optical pulses of 500-Hz repetition rate, delivered through a fiber-optic bundle from a mode-locked Nd:glass laser, produced an wideband rf signal with an instantaneous bandwidth of more than 500 MHz, with a center frequency of 1.2 GHz.

The monolithic, photoconductive wideband transmitter combines the functions of the energy storage medium, the dc-to-rf conversion element (i.e., photoconductive switch), and the radiating element (i.e., spiral antenna), all integrated on a single semi-insulating GaAs (SI-GaAs) wafer substrate. The device was fabricated on a 3-inch, 3-mm thick, SI-GaAs wafer substrate. The metallized electrode patterns on both sides of the SI-GaAs wafer (antenna on front side, ground plane on back) provide the necessary capacitive energy storage medium at the outer edge of the spiral arms. The photoconductive switching is performed at the ends of the spiral arm antenna.

Soon after the energy storage mediums were pulse biased with opposite polarity pulses of + 1- and - 1-kV, the switches (i.e., gaps between the spiral arms) were illuminated with optical pulses from an Nd:glass mode-locked laser. The pulse energy required to create a conductive plasma in the switch gaps was less than a fraction of a nanojoule. The instantaneous creation of a conductive path between the energy storage medium and the spiral arm antenna results in the conversion of the pulse-biased energy into an rf pulse. The radiated rf signal is picked up by a D-dot sensor and measured with a sampling scope. The measured voltage versus time waveform is shown in Figure 1(a), with its corresponding frequency spectrum given in Figure 1 (b).

To determine the rf waveform sensitivity with optical energy, an OD 10 neutral density filter was placed in front of the fiber bundle. The only change in the rf signal was a decrease in signal amplitude - there was no shift in the frequency content. In addition, we measured the dependence as a function of switch activation. Figure 2 (a) shows the radiated spectrum when the one switch was activated, and Figure 2 (b) shows the other. Note that there is a shift in the frequency spectrum which shows that the device response was not completely symmetrical. This may be due to either processing variations or, more likely, a difference in the optical trigger level between the two fibers.

***Acknowledgment***

The authors gratefully acknowledge the assistance of Sheng-Lung Huang and Yuan-Qun Liu, both of the University of Maryland, for their assistance in performing the Nd:glass measurements.

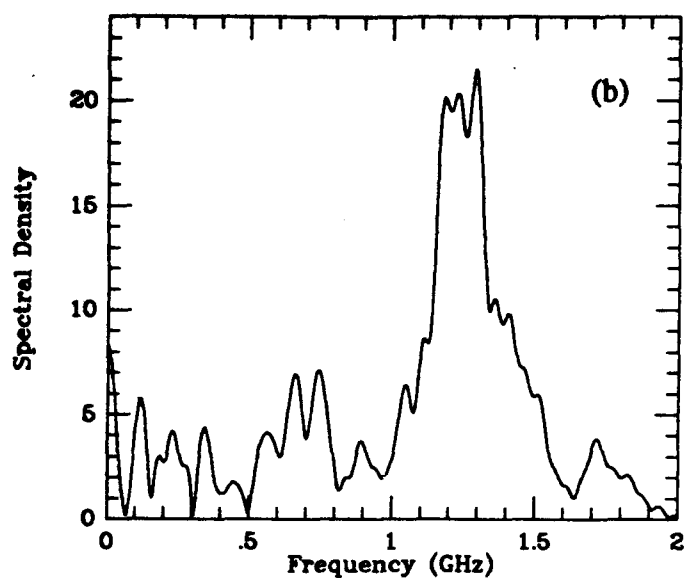
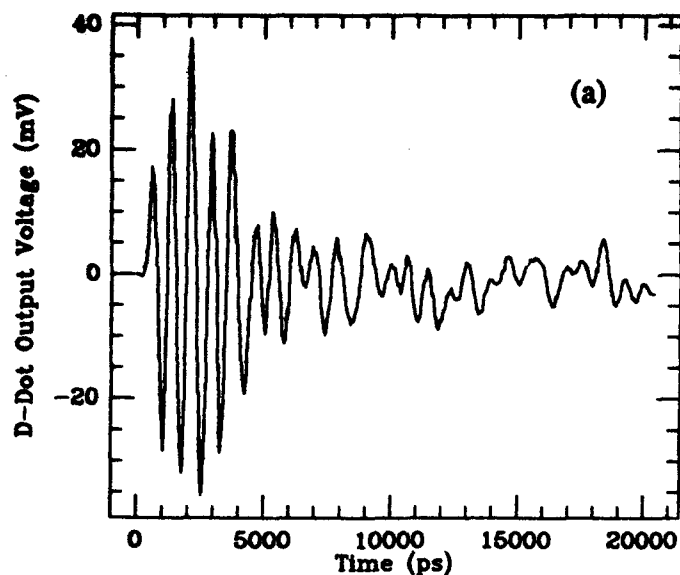


**Figure 1.** Transmitter output with charging voltage of 600 V. (a) D-dot sensor output and (b) the corresponding fourier transform.

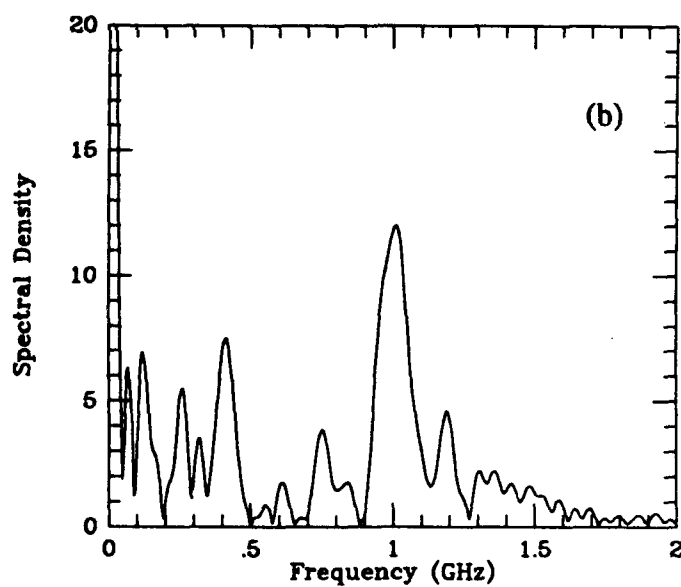
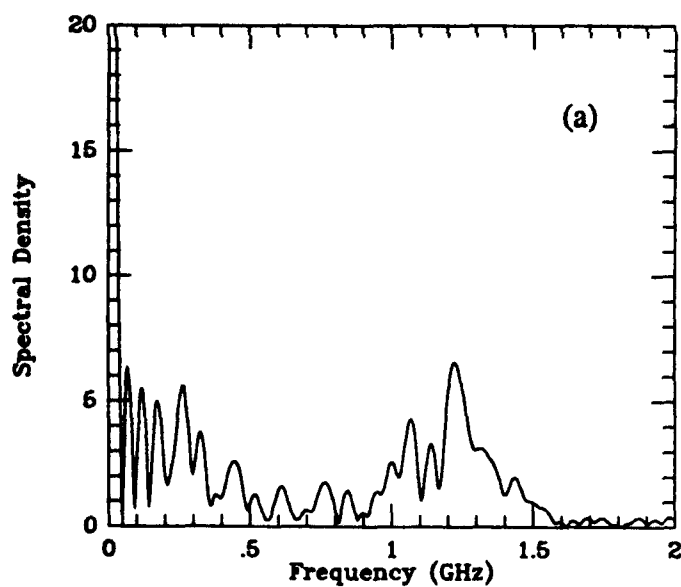


**Figure 2.** Transmitter output with a charging voltage of 1 kV. Fourier transform with (a) activation of positively charged switch gap and (b) with negatively charged gap.

## TRANSPARENT OPTICAL LINKS USING OPTICAL FM

A. J. Seeds and B. Cai

Department of Electronic and Electrical Engineering,  
University College London,  
Torrington Place, London, WC1E 7JE, England.

### Abstract

Optical fibre links for microwave applications usually employ intensity modulation and direct detection (IMDD). The dynamic range is limited by non-linear distortion at high signal levels and by noise at low signal levels. For large received optical powers the main noise source is often source relative intensity noise (RIN) which, for semiconductor lasers, usually peaks at microwave frequencies. This paper considers an alternative systems approach; optical frequency modulation (OFM), in which it is possible to make a trade-off between system bandwidth and signal to noise ratio (SNR).

### OFM Links

Fig. 1 shows an OFM link. The optical source is frequency modulated with the base-band signal.

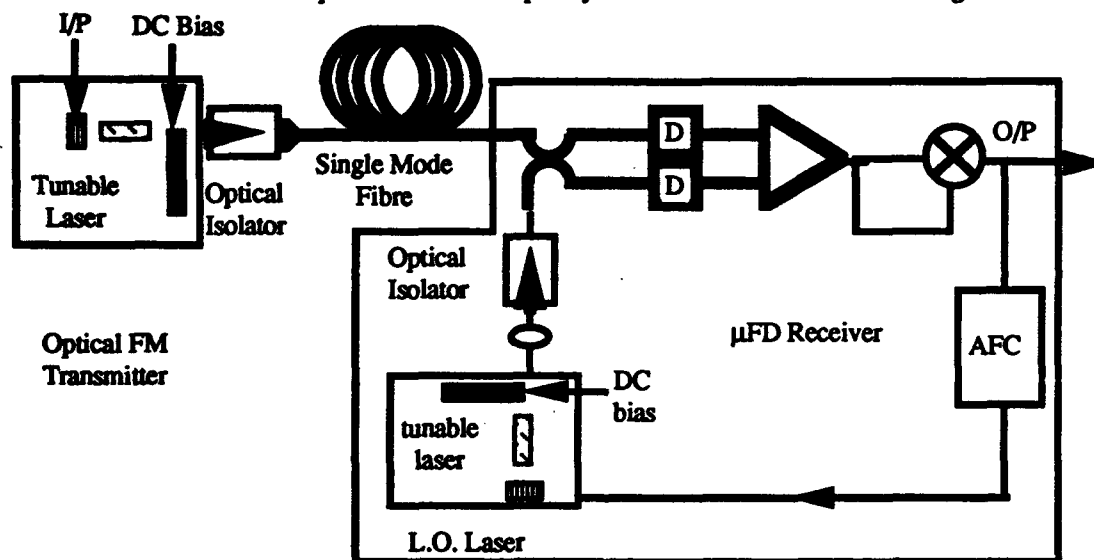


Fig. 1 Optical frequency modulation link.

The resulting OFM signal passes through the transmission fibre to the receiver. In order to permit base-bandwidth/SNR trade-off a coherent receiver is required. The intermediate frequency (IF) of the receiver is set to be substantially greater than the peak frequency deviation to allow good discriminator linearity to be obtained. In Fig. 1 the baseband signal is recovered using a conventional microwave delay line discriminator, which also provides automatic frequency control (AFC) for the local oscillator (LO) laser. If the LO laser power is sufficient to give shot noise limited reception and the discriminator input SNR is much greater than unity the output SNR is given by

$$SNR_o = \frac{3\Delta f^3 P_r R}{2eB^4} \quad (1)$$

where  $\Delta f$  is the peak frequency deviation,  $P_r$  is the received optical power,  $R$  is the photo-detector responsivity,  $B$  is the base-bandwidth and  $e$  is the electronic charge. For a system having  $B = 1$  GHz,  $\Delta f = 10$  GHz,  $P_r = -20$  dBm and  $R = 0.9$  A W<sup>-1</sup>  $SNR_o$  would be 169 dB.Hz. Thus high SNR is possible for modest received powers. Eqn. 1 does not include the effect of finite source and LO laser linewidth. For Lorentzian lineshapes with white frequency noise

broadening the output SNR is limited to

$$SNR_0 = \frac{\pi \Delta f^2}{2 B \delta f_1} \quad \text{---(2)}$$

where  $\delta f_1$  is the summed FWHM linewidths of the source and LO lasers. For  $\Delta f = 10$  GHz and  $\delta f_1 = 50$  kHz the output SNR would be limited to 155 dB.Hz, so that this is likely to be the dominant limitation in practical systems.

### Experimental Work

We have constructed an OFM demonstrator using a novel, reverse biased, MQW tuned, external cavity semiconductor laser [1] as the optical source. This offers a modulation response uniform to within  $\pm 1$  dB at frequencies up to 1.2 GHz. The local oscillator for the coherent receiver is a grating tuned external cavity laser, adjusted to give an IF of 8 GHz, and baseband signal recovery is by electrical delay line discriminator. Fig. 2 shows the overall OFM link frequency response obtained.

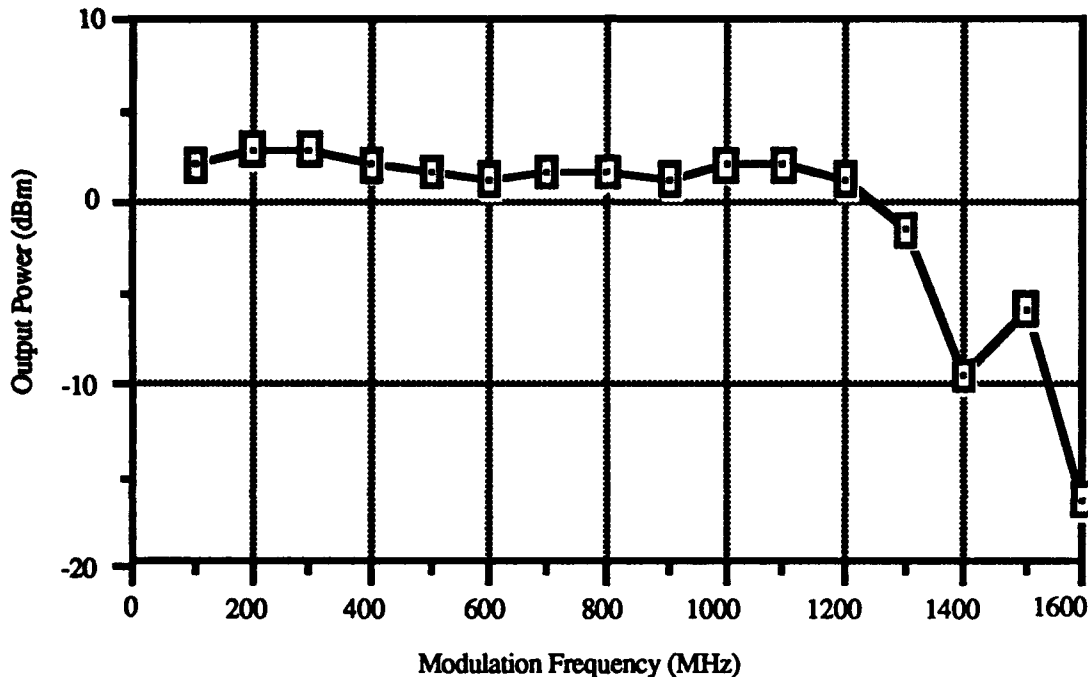


Fig. 2 OFM link frequency response.

The roll-off above 1.3 GHz was due to the IF port frequency response of the double balanced mixer used in the frequency discriminator. Initial measurements of  $SNR_0$  at a modulation frequency of 500 MHz gave a value of 111 dB.Hz, limited by low LO laser power (-7 dBm) and the limited peak deviation of the source laser (1.5 GHz). Increasing the LO laser power would enable the SNR to approach the linewidth limited value.

### Discussion

OFM allows high SNR to be achieved with modest source powers. It is also attractive for multi-channel architectures, since the selective receiver allows dense wavelength division multiplexed systems to be assembled without optical pre-filtering. Against these advantages must be weighed the increase in system complexity relative to IMDD systems. Recent developments in very narrow linewidth semiconductor lasers [2] may tilt the advantage in favour of OFM for wide dynamic range systems of limited base-bandwidth.

This work was supported by the SERC through the LINK WORFNET programme (GR/F 93999).

### References

- [1] B. Cai, A. J. Seeds, A. Rivers, and J. S. Roberts, *Electron. Lett.*, **25**, 145, 1989.
- [2] M. Okai and T. Tsuchiya, *Electron. Lett.*, **29**, 349, 1993.

## Fiber-Optic Prism True Time-Delay Antenna Feed

R.D. Esman, M.Y. Frankel, J.L. Dexter, D.G. Cooper,\* and L. Goldberg

Naval Research Laboratory, Code 5672, 4555 Overlook Ave. SW, Washington, DC 20375

\*Jaycor, 1608 Springhill Road, Vienna, Virginia 22180-2270

**Introduction:** Next-generation RF and microwave antenna arrays are expected to possess many advancements beyond existing antenna designs. In particular, improved range and cross-range resolution and new beam capabilities would be available with a wideband true time-delay antenna feed. Fiber-optic feeds offers well-known advantages of size, weight, bandwidth, propagation loss, immunity to EMI, and channel isolation. To take full advantage of a fiber feed and to provide new optical signal processing techniques, especially true time delay, many new optical schemes have been proposed, including 1) heterodyne techniques,<sup>1,2</sup> which require tight-tolerance bulk optics and rely on RF-frequency dependent optical beamsteering to emulate time delay; 2) fiber length switching techniques,<sup>3-5</sup> which require large number of phase-matched lasers or optical switches and only offer discrete values of incremental delay; 3) fiber stretching,<sup>6</sup> which is limited by speed, size, and power supply requirements; and 4) fiber chromatic<sup>7</sup> and modal<sup>6</sup> dispersion, which also require large number of critical components. Here we present a new fiber-optic approach that is not optically coherent, is continuously tuned by a low voltage signal, and requires few components.

**True Time-Delay Modulation:** The basic true time-delay technique<sup>8</sup> utilized here is similar to that proposed by Soref<sup>9</sup> and is based on a modification of a standard externally modulated link: a dispersive optical fiber and a widely tunable laser are now used (Figure 1). Modulation of the source wavelength modulates the velocity and, hence, the delay of the optical signal. Wide continuous tuning is achieved with the  $\sigma$  laser.<sup>8</sup> In initial single-element experiments the relative tuning delay of 520 ps is obtained from 108 m of high-dispersion ( $\sim 100$  ps/km-nm) fiber<sup>9</sup> and a 50 nm tuning range;

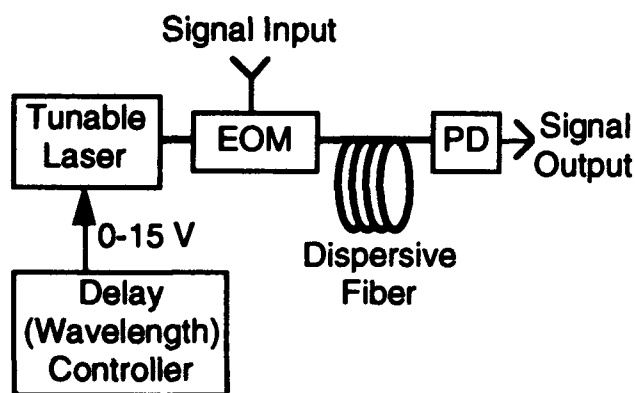


**Figure 1. True Time-Delay Fiber-Optic Modulator**

EOM: Electro-optic modulator (e.g., LiNbO<sub>3</sub> Mach-Zehnder Modulator); PD: Photodetector.

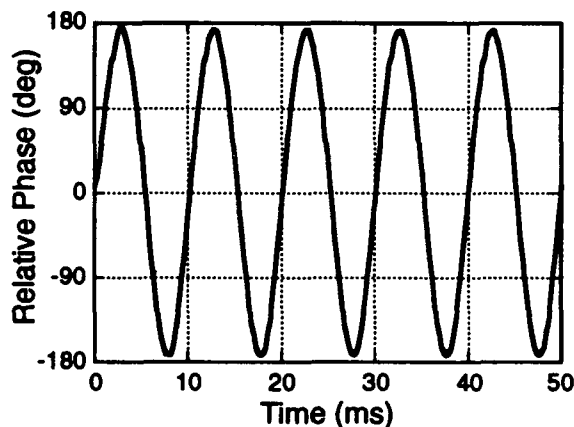


**Figure 2. Continuous Delay Modulation at 6 GHz.**

the tuning sensitivity is 730 ps/km·V ( $\sim 150$  ps/ $\mu$ s·V). Full-wave modulation, at 6 GHz, of the time delay is demonstrated by applying a sinusoidal tuning voltage. Continuous phase modulation as a function of time is observed (Figure 2). The non-ideal sinusoid is suspected to be due to nonlinearities in the laser tuning element (PZT) or due to local fluctuation in the chromatic dispersion characteristic. We note that either of these effects can be compensated for without loss of functionality.

**Fiber-Optic Dispersive Prism:** This dispersion-based, continuously variable, true-time delay technique is well-suited for controlling wideband phased arrays. To feed numerous array elements or subarrays, a parallel bank of variable-delay fiber-optic links could be formed.<sup>7</sup> However, here we

propose use of a fiber-optic prism (Figure 3). Namely, a true time-delay array feed is easily formed by splitting the optical carrier onto numerous optical fibers each having the same nominal group delay but with slightly different net dispersion—easily made by connecting varying amounts of dispersive and non-dispersive fiber. Hence, a change in the optical wavelength will result in differing

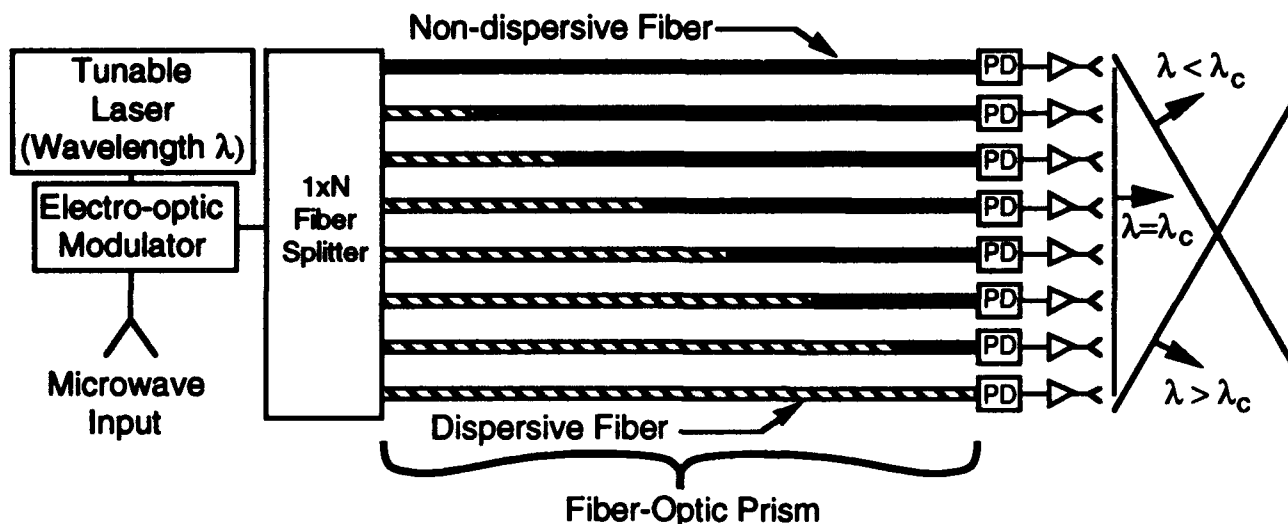


Figure 3. Fiber-Optic Prism True Time Delay Antenna Feed

amounts of delay in each fiber. At a center wavelength  $\lambda_c$ , all the time delays are matched by cutting and stretching (non-dispersive post-detection matching is possible). Thus, at  $\lambda_c$  the beam will be directed broadside. At wavelengths less (more) than  $\lambda_c$ , each of the prism fibers will add (subtract) a time delay its signal proportional to its dispersion to thus resulting in element phasing such that the beam will be steered toward (away from) the non-dispersive fiber side. Since the relative phasing is due to true dispersive time delay, all frequencies will be directed at the same angle. Beam patterns for a two- to seven-element array will be presented at the conference. We note that multiple optical signals are used to incorporate multiple beams, beamshaping, etc. Similar to Koepf<sup>1</sup> this technique can be used in a receive mode. Lastly, this method can be used twice in series to form feeds for two-dimensional antenna beamforming and steering.

**Conclusions:** We have presented a new technique for a fiber-optic true time-delay antenna feed. The technique requires only a single laser and modulator while offering continuous low-voltage steering and fiber-inherent advantages (easy to remote, small size, lightweight, EMI immune, etc.).

**Acknowledgments:** This work was supported by the Electro-optics Technology 6.2 Block and DARPA.

\*Jaycor, 1608 Springhill Road, Vienna, Virginia 22180-2270

#### References :

1. G.A. Koepf, SPIE 477, pp. 75-81, 1984.
2. E.N. Toughlian and H. Zmuda, *IEEE J. of Lightwave Technology*, LT-8, pp. 1824-1828, 1990.
3. E. Ackerman, et al., *IEEE MTT-S'92*, paper R-6, pp. 681-684, 1992.
4. W. Ng, et al., *IEEE J. of Lightwave Technology*, 9, pp. 1124-1131, 1991.
5. D. Dolfi, et al., *Optics Letters*, 16, pp. 2552-2557, 1991.
6. P.R. Herczfeld, et al., *IEEE MTT-S'87*, paper Q-15, pp. 603-606, 1987.
7. R.A. Soref, *Applied Optics*, 31, pp. 7395-7397, 1992.
8. R.D. Esman, et al., *Electronics Letters*, 28, pp. 1905-6, 1992.
9. J.M. Dugan, et al., *OFC'92*, pp. 367-370, 1992.

## Intensity Noise Reduction of Semiconductor Lasers Using External Optical Feedback

Tsang-Der Ni, Xiangdong Zhang, and Afshin S. Daryoush  
Center for Microwave/Lightwave Engineering  
ECE Department, Drexel University  
Philadelphia, PA 19104

### SUMMARY

A clear choice in design of an optically fed phased array antenna is T/R level data mixing architecture [1]. The advantage of this architecture, however, lies in the use of optically distributed frequency reference and data links. The performance of directly modulated fiberoptic links at microwave frequencies is very poor in terms of gain and dynamic range. We have been able to devise methods to extend the effective bandwidth of directly modulated fiberoptic links to high microwave frequencies, resulting in synchronization of millimeter wave oscillators [2]. However, the measured dynamic range of the receivers in the T/R level data mixing is limited by the data signal fiber optic link performance [1]. Furthermore, the dynamic range of the directly modulated fiber optic links is dictated by the linearity and relative intensity noise (RIN) of semiconductor laser diode [3]. A method based on the coherent feedback to the laser diode, which achieved an efficient frequency response over a narrow band corresponding to the frequency reference signals was demonstrated [4]. In this paper we demonstrate the potential of this technique to significantly reduce the RIN of laser at data signal frequencies.

Optical feedback from an external cavity may have profound impact on the dynamic and the spectral behavior of laser diodes. The noise increases caused by optical feedback is a serious problem for long-haul optical communication system [5]. In fact, it can be significantly stronger than the intrinsic noise of the laser itself [6]. Simple models, based on the phase variation between the feedback laser output light, have been proposed to justify the RIN noise variation under strong optical feedback [7]. However, the intensity noise can be suppressed by a slight change in the feedback condition without any change in the feedback power [7]. Therefore, we present a new theoretical model based on Maxwell-Bloch equations to predict the RIN of the laser diode with coherent optical feedback.

Relative intensity noise (RIN) is related to the spectral power density of amplitude fluctuations of lasers. These laser fluctuations are expressed analytically as  $RIN = \langle \Delta p^2 \rangle / \langle P \rangle^2$ , where  $\langle P \rangle$  is the average laser light output intensity,  $\langle \Delta p^2 \rangle$  is the mean-square intensity fluctuation spectral density of light output. By use of the Maxwell-Bloch equations [8], the rate equation for the specially averaged photon densities is modified as:

$$dP/dt = \Gamma\alpha(1-\epsilon P)(N-N_{om})P - P/\tau_p (1 + \mathcal{C}) + \beta\Gamma N/\tau_s$$

where  $N_{om}$  is the steady state spatially averaged carrier density,  $\Gamma$  is the optical confinement factor,  $\alpha$  is the optical gain coefficient,  $\tau_p$  is the photon lifetime in the cavity without feedback,  $\tau_s$  is the carrier lifetime,  $\epsilon$  is the gain compression factor,  $\beta$  is the spontaneous emission factor, and  $\mathcal{C}$  is the coupling coefficient due to the optical feedback which is a function of delay time, reflectivities of external mirror, and the laser facets [8]. If the Langevin noise sources  $F_p(t)$  and  $F_N(t)$  are adding [9], the small-signal analysis leads to a second-order, low-pass filter-type response for the fluctuated photon density. Therefore, the RIN can be expressed as

$$RIN = \frac{\langle F_p^2(f) \rangle a^2 + \langle F_N^2(f) \rangle b^2 + \langle F_p(f) F_N(f) \rangle (ab^* + ba^*)}{P_o^2 (s^2 + s\omega_d^2 + \omega_f^2)^2}$$

where  $a = 1/\tau_s + \alpha P_o + j\omega$ ,  $b = \Gamma\alpha P_o$ ,  $s = j\omega$ , and,

$$\omega_d^2 = \frac{1}{\tau_s} + \alpha P_o - \Gamma\alpha(N_o - N_{om}) + [1 + \mathcal{C}(\phi)]/\tau_p$$

The corner frequency of this response is given by

$$\omega_r = \sqrt{\left(\frac{1}{\tau_s} + \alpha P_o\right) \left[ -\Gamma \alpha (N_o - N_{om}) + \frac{1 + \mathcal{C}(\phi)}{\tau_p} \right] + \Gamma \alpha^2 P_o (N_o - N_{om})}$$

This theoretical model was verified by a multimode InGaAsP laser diode. The measured and simulation results of the RIN are shown in Fig. 1, where it is increased at the frequency corresponds to the round trip time delay. However, the RIN is suppressed about 40dB at the relaxation frequency peak and at other frequency beside this frequency by 20dB to 30dB. The mismatch at low frequency (<500MHz) is explained by the lack of inclusion for multimodes in our model. The theoretical model matches well with the measured data in most of the frequency range.

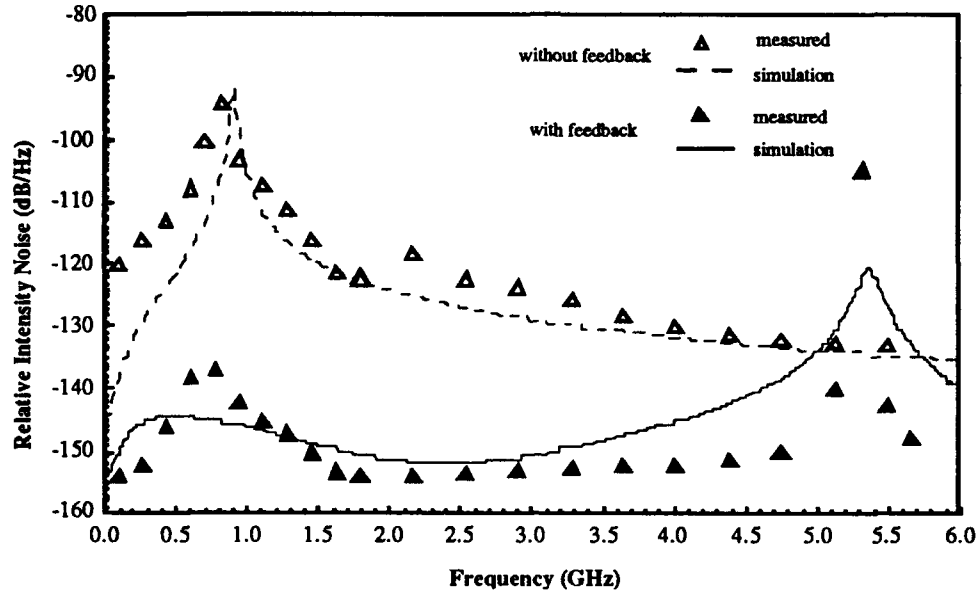


Fig.1 Measured and simulation results of a laser diode with and without external optical feedback.

Since the data frequency is usually within a bandwidth of a few GHz, the dynamic range of fiber optic links of data signal will be much improved as the RIN is reduced. Although, the modulation response is also enhanced at the same frequency that the RIN is increased [4], but this frequency is used to transmit the frequency reference signal by the laser diode and the high AM noise would not influence the fidelity of the frequency reference.

#### REFERENCES

- [1] A.S. Daryoush, *et al.* "Fiber Optic Fed Active Phased Array Antennas," *IEEE International Microwave Symp. Dig.*, pp.437-450, Albuquerque, New Mexico, 1992.
- [2] A.S. Daryoush, "Optical Synchronization of Millimeter-Wave Oscillator for Distributed Architecture," *IEEE Trans. Microwave Theory and Tech.*, MTT-38, no.5, pp.467-476, 1990.
- [3] A.S. Daryoush, *et al.*, "Interfaces for High-Speed Fiber-Optic Links: Analysis and Experiment," *IEEE Trans. Microwave Theory and Tech.*, vol.39, no.12, pp.2031-2044, 1991.
- [4] T.D. Ni, X. Zhang, A.S. Daryoush, "Harmonic Enhancement of Modulated Semiconductor Laser with Optical Feedback," *IEEE Microwave and Guided Wave Letters*, to be published in May, 1993.
- [5] K. Petermann, G. Arnold, "Noise and Distortion Characteristics of Semiconductor Lasers in Optical Fiber Communication Systems," *IEEE J. of Quantum Electronics*, vol.18, no.4, pp.543-555, 1982.
- [6] O. Hirota, Y. Suematsu, "Noise Properties of Injection Lasers Due to Reflected Waves," *IEEE J. of Quantum Electronics*, vol.15, no.3, pp.142-149, 1979.
- [7] T. Fujita, S. Ishizuka, K. Fujito, H. Serizawa, H. Sato, "Intensity Noise Suppression and Modulation Characteristics of a Laser Diode Coupled to An External Cavity," *IEEE J. of Quantum Electronics*, vol.20, no.5, pp.492-499, 1984.
- [8] T.D. Ni, X. Zhang, and A.S. Daryoush, "Mode Locked Subharmonic Laser Diodes," *International Symposium on Signals, Systems and Electrons Proc.*, Paris, France, pp.185-188, 1992.
- [9] C. Harder, J. Katz, S. Margalit, J. Shacham, and A. Yariv, "Noise Equivalent Circuit of a Semiconductor Laser Diode," *IEEE J. of Quantum Electronics*, vol.18, no.3, pp.333-337, 1984.

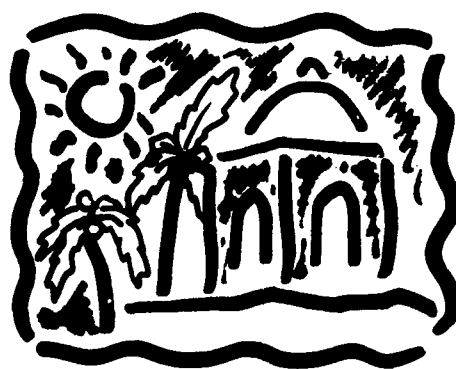
# A U T H O R I N D E X

R. Amantea.....42	K. Giboney.....3	D. Kralj.....65	A. Seeds.....69
G. Arjavelingam.....44, 52	D. Gilbert.....42	Y. Lai.....7	Z. Shen.....7
D. Auston.....37	U. Giese.....5	C. Lee.....7, 9, 19, 21, 67	J. Son.....53
A. Balekdjian.....9	L. Goldberg.....71	S. Levy.....48	P. Stabile.....42
T. Berceci.....50	G. Gopalakrishnan.....29	G. Lin.....23	K. Stubkjaer.....5
V. Bhanthumnavin.....7	T. Hasenberg.....33	S. Lin.....44	M. Tabara.....13
D. Botkin.....57	R. Helkey.....48	Y. Liu.....7	S. Tedjini.....17
J. Bowers.....3, 48	P. Herczfeld.....50	C. Lu.....13	B. Thedrez.....9
W. Burns.....29	W. Holstein.....7	M. Martin.....61	G. Valley.....33
M. Bruun.....5	A. Ho Quoc.....17	R. Martin.....15	C. Wang.....23
J. Butler.....42	B. Hu.....37	M. Marrone.....31	H. Wang.....53
B. Cai.....69	S. Huang.....7, 19, 21	M. Matloubian.....33	M. Weiner.....39, 67
W. Cao.....7	P. Humphrey.....48	M. Melloch.....65	S. Weiss.....57
L. Carin.....65	H. Hung.....19, 21	R. Nagarajan.....48	T. Weller.....55
C. Chang.....23	R. Hunsperger.....15	T. Ni.....73	L. West.....33
D. Chemla.....57	C. Ih.....15	T. Nielsen.....5	Y. Wey.....3
H. Cheng.....55	T. Itoh.....63	C. Pan.....23	J. Whitaker.....53, 55
E. Christensen.....5	W. Janton.....42	P. Pang.....7	J. White.....33
D. Cooper.....71	L. Jasper.....67	A. Paolella.....25	J. Woodall.....65
C. Cox.....46	Y. Jin.....39	M. Phillips.....11	M. Wu.....63
T. Darcie.....11	R. Jungeman.....27	D. Plant.....61	H. Wu.....23
A. Daryoush.....73	A. Kain.....61	D. Ogletree.....57	L. Xu.....37
A. Deutsch.....52	L. Kazovsky.....13	F. Oshita.....61	R. Youmans.....67
J. Dexter.....71	L. Katahi.....55	M. Rodwell.....3	X. Zhang.....39, 73
D. Dolfi.....27	D. Khalil.....17	A. Rosen.....42	
R. Esman.....31, 71	A. Kim.....67	D. Sabido.....13	
H. Fetterman.....61	L. Kingsley.....39	S. Sadow.....9, 67	
T. Fong.....13	A. Kost.....33	M. Salmeron.....57	
M. Frankel.....71	D. Kountz.....7	M. Scheuermann.....52	

# **Visible Semiconductor Lasers**

**July 21-22, 1993**

**Fess Parker's Red Lion Inn Resort  
Santa Barbara, California**



**Sponsored by  
the IEEE Lasers and Electro-Optics Society**

**IEEE Catalog Number: 93TH0549-6  
Library of Congress Number: 93-77778**

The papers in this book comprise the digest of the meeting mentioned on the cover and title page. They reflect the authors' opinions and are published as presented and without change, in the interest of timely dissemination. Their inclusion in this publication does not necessarily constitute the endorsement by the editors, the Institute of Electrical and Electronics Engineers, Inc.

Copyright and reprint permissions: Abstracting is permitted with credit to the source. Libraries are permitted to photocopy beyond the limits of the U.S. copyright law for private use of patrons those articles in this volume. Instructors are permitted to photocopy isolated articles for noncommercial classroom use without fee. For other copying reprint or republication permission, write to Director, Publishing Services, IEEE, 345 E. 47th St., New York, NY 10017. All rights reserved. Copyright ©1993 by the Institute of Electrical and Electronics Engineers, Inc.

IEEE Catalog Number:	93TH0549-6
ISBN Number: Softbound	0-7803-1284-8
Microfiche Edition:	0-7803-1285-6
Library of Congress Number:	93-77778

**Visible Semiconductor Lasers  
Technical Committee**

**Chairman**

**T.L. Paoli**  
*Xerox Palo Alto Research Center*

**Program Committee**

**Chairman**

**D. Welch**  
*Spectra Diode Laboratories*

**D. Bour**  
*Xerox PARC*

**C.P. Kuo**  
*Hewlett Packard  
Optoelectronics Div.*

**R.D. Dupuis**  
*The University of  
Texas at Austin*

**Keichi Yodoshi**  
*Sanyo Electric Co., Ltd.*

**Peter Zory**  
*University of Florida*

# T A B L E O F C O N T E N T S

**WEDNESDAY, JULY 21, 1993**

## **W1: MATERIALS GROWTH**

<b>W1.1 Growth and Characterization of AlGaInP Diode Lasers .....</b>	<b>3</b>
<b>W1.2 Pseudomorphic SCH Blue-Green Diode Lasers .....</b>	<b>5</b>
<b>W1.3 P-Type Doping of Wide-Bandgap II-VI Semiconductors: Reference to ZnSe:N .....</b>	<b>6</b>

## **W2: II-VI LAYER STRUCTURES**

<b>W2.1 Blue/Green Lasers Based on II-VI Semiconductor Heterostructures.....</b>	<b>8</b>
<b>W2.2 Improved Blue-Green Injection Lasers with Pseudomorphic Quaternary Cladding Layers.....</b>	<b>9</b>
<b>W2.3 Proposal of Novel Blue-Green Diode Laser Based on MgZnSeTe Alloys.....</b>	<b>11</b>

## **W3: LIGHT EMITTING DIODES**

<b>W3.1 High Performance AlGaInP Light-Emitting Diodes.....</b>	<b>13</b>
<b>W3.2 UV/Blue Light Emitting AlGaIn/GaN Heterostructures.....</b>	<b>14</b>
<b>W3.3 Blue/UV Emitters from SiC and Its Alloys .....</b>	<b>16</b>

## **W4: PHYSICS OF MATERIALS AND DEVICES**

<b>W4.1 The New Blue Horizon: Quantum Well Lasers from II-VI Semiconductors: Quantum Well Physics.....</b>	<b>18</b>
<b>W4.2 Optoelectronic Properties of GaN, AlGaIn and AlGaIn-GaN Quantum Well Heterostructures .....</b>	<b>19</b>
<b>W4.3 Wide Bandgap Al<sub>x</sub>Ga<sub>1-x</sub>N Material System for Visible and Ultraviolet Optoelectronic Devices .....</b>	<b>21</b>

**THURSDAY, JULY 22, 1993**

## **T1: AlGaInP LASERS I**

<b>T1.1 Short Wavelength Oscillation of InGaAlP Visible Light Laser Diodes .....</b>	<b>25</b>
<b>T1.2 High-Performance 630-nm Band AlGaInP Strained Multiple Quantum Well Laser Diodes with a Multiquantum Barrier.....</b>	<b>27</b>
<b>T1.3 Strained AlGaInP Multiple Quantum Wire Lasers Grown by Gas Source Molecular Beam Epitaxy .....</b>	<b>29</b>

## **T2: AlGaInP LASERS II**

<b>T2.1 Application of a Window Structure, MQB and Strained MQW to High Power Visible Lasers.....</b>	<b>31</b>
<b>T2.2 High Power, Low Threshold 630nm Lasers .....</b>	<b>33</b>
<b>T2.3 Design and Growth of Short-Wavelength InAlGaP Visible Vertical-Cavity Surface-Emitting Laser Diodes .....</b>	<b>35</b>
<b>T2.4 1 W CW, 645 nm GaInP/GaAlInP Broad Stripe Laser Diodes.....</b>	<b>37</b>
<b>T2.5 High-Power Operation of Self-Aligned Stepped Substrate (S<sup>3</sup>) AlGaInP Visible Laser Diode .....</b>	<b>39</b>

<b>Author Index.....</b>	<b>41</b>
--------------------------	-----------

# Wednesday, July 21, 1993

## **Sessions:**

**W1: Materials Growth**

**W2: II-VI Layer Structures**

**W3: Light Emitting Diodes**

**W4: Physics of Materials and Devices**



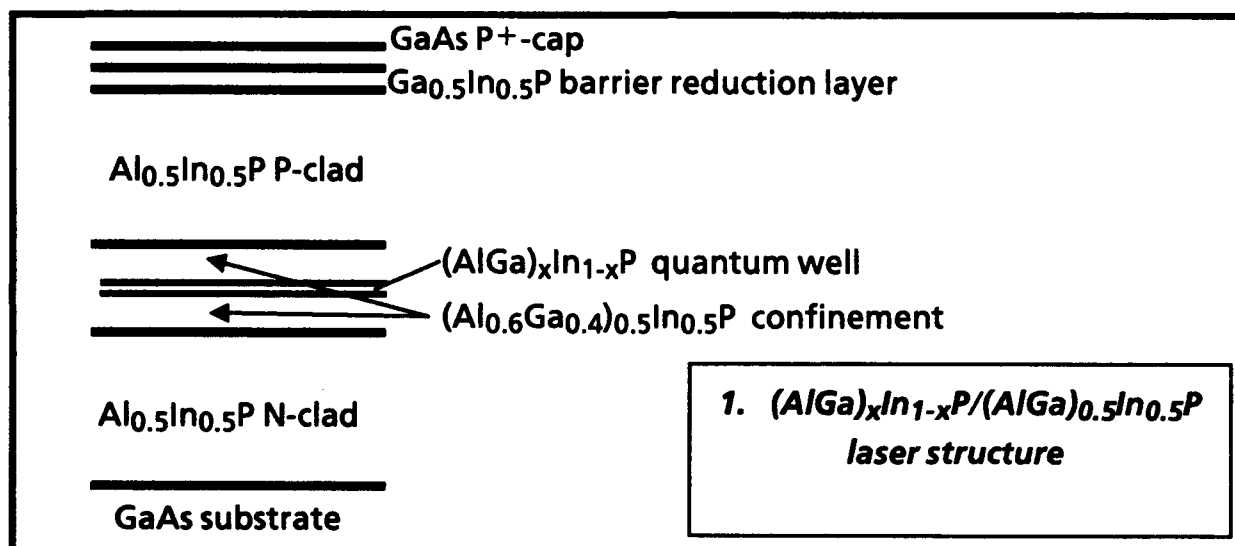
**W1.1 8:30am - 9:00am  
(Invited)**

### **Growth and characterization of AlGaInP diode lasers**

**D. P. Bour, D. W. Treat, and R. D. Bringans  
Xerox Palo Alto Research Center  
3333 Coyote Hill Road, Palo Alto, CA 94304**

**R. S. Geels and D. F. Welch  
Spectra-Diode Laboratories  
80 Rose Orchard Way, San Jose, CA 95134**

High-power, broad-area AlGaInP visible lasers are under development for pumping Cr-doped, tunable solid state lasers and for photodynamic therapy, while high-power index-guided lasers are applied in laser printing, optical recording and scanning, and as He-Ne laser substitutes. We have fabricated  $(\text{AlGa})_{0.5}\text{In}_{0.5}\text{P}$  visible lasers by low pressure organometallic vapor phase epitaxy (OMVPE), using the single quantum well (QW) laser structure shown below (Figure 1). Typical

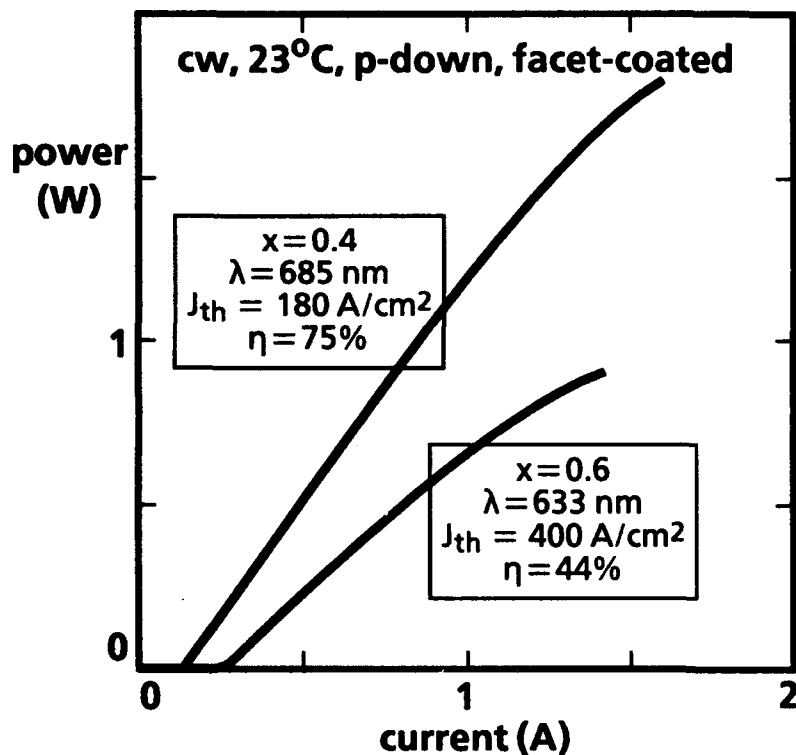


$(\text{AlGa})_x\text{In}_{1-x}\text{P}$  QW thicknesses are 40-80 Å, and the composition is adjusted between tension ( $x > 0.5$ ) and compression ( $x < 0.5$ ), in which case aluminum is sometimes included for shortest wavelengths. For maximum optical confinement and electron leakage heterobarrier, especially important at short wavelengths,  $\text{Al}_{0.5}\text{In}_{0.5}\text{P}$  cladding layers and  $(\text{Al}_{0.6}\text{Ga}_{0.4})_{0.5}\text{In}_{0.5}\text{P}$  confining layers are used.

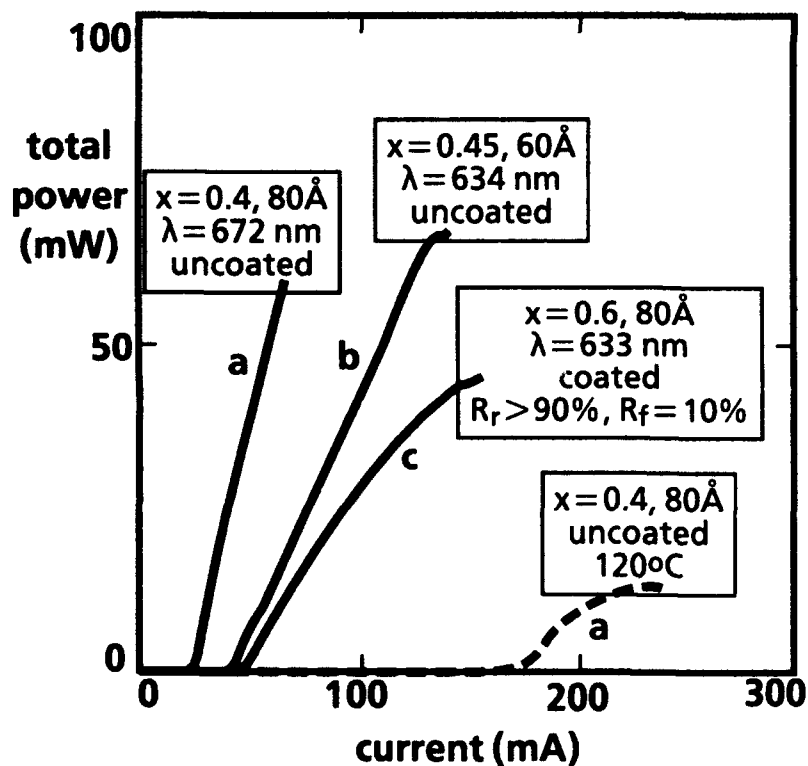
For room temperature, cw operation of 100 μm x 750 μm, facet coated ( $R_{\text{rear}} > 90\%$ ,  $R_{\text{front}} = 10\%$ ) broad-area lasers with 80 Å  $\text{Ga}_x\text{In}_{1-x}\text{P}$  QWs, power outputs of 900 mW have been obtained at 633 nm ( $x = 0.6$ , tension) and 1.8 W at 685 nm ( $x = 0.4$ , compression), as shown in Figure 2. As a result of weaker electron confinement, the shorter wavelength lasers have a lower characteristic temperature, and so their high-power and high-temperature operation are more limited.

Power-current characteristics of index-guided lasers (~ 5 μm wide, selectively buried ridge waveguide) with different QW parameters and wavelengths are shown in Figure 3. The long-wavelength, single QW structure is capable of cw operation at 120°C (dashed curve). For facet-coated lasers, cw, single-mode powers as high as 70 mW at 680, and 50 mW at 633 nm have been demonstrated. These high powers are achieved with QW devices only, indicating the higher catastrophic damage threshold of QW devices, compared to double heterostructures. Using a 60 Å quaternary

$(\text{Al}_{0.2}\text{Ga}_{0.8})_{0.45}\text{In}_{0.55}\text{P}$  QW, cw, room temperature operation at a wavelength as short as 623 nm has been obtained, from this structure with AlInP cladding layers and no multiquantum barrier for enhanced electron confinement.



2.  
room temperature, cw  
power-current  
characteristics  
of 80Å  $\text{Ga}_x\text{In}_{1-x}\text{P}/\text{AlGaInP}$   
quantum well lasers, with  
 $x=0.4$  (685 nm) and  
 $x=0.6$  (633 nm). Devices  
are facet-coated, 100  $\mu\text{m}$  x  
750  $\mu\text{m}$  broad-area lasers  
soldered p-side down  
onto copper heat sinks



3.  
room temperature, cw  
power-current  
characteristics of  
 $\text{Ga}_x\text{In}_{1-x}\text{P}/\text{AlGaInP}$   
selectively buried ridge  
waveguide quantum well  
lasers, with (a),  $x=0.4$ ,  
 $L_z=80\text{Å}$  (672 nm; dashed  
curve for 120°C  
operation); (b)  $x=0.45$ ,  
 $L_z=60\text{Å}$  (634 nm); and (c)  
 $x=0.6$ ,  $L_z=80\text{Å}$  (633 nm).  
Devices are soldered p-  
side down onto copper  
heat sinks

**W1.2 9:00am - 9:30am**  
**(Invited)**

### **Pseudomorphic SCH Blue-Green Diode Lasers**

**R.L. Gunshor**

*School of Electrical Engineering; Purdue University, W. Lafayette, IN 47907-1285*

**A.V. Nurmikko,**

*Divison of Engineering, Brown University, Providence, RI 02912*

**N. Otsuka**

*School of Materials Engineering; Purdue University, West Lafayette, IN 47907-1285*

Since the first blue-green diode lasers were reported by 3M and the Brown/Purdue group in the summer of 1991, a number of layered arrangements have been used for laser diodes emitting from green to blue. In the earliest devices, and the configuration adapted by several other groups, one to three quantum wells of (Zn,Cd)Se were used; the optical confinement was provided by an intrinsically non-pseudomorphic structure having dislocation arrays between the Zn(S,Se) outer cladding layers and the ZnSe waveguiding/barrier regions. A second type of structure, primarily employed by the Brown/Purdue group, was pseudomorphic and contained (usually) six quantum wells of (Zn,Cd)Se imbedded in Zn(S,Se); the configuration served as a compromise between optimum electrical and optical confinement. These MQW structures relied on the lower optical refractive index of the (Zn,Cd)Se wells to provide the optical waveguiding.

In August of 1992 Sony reported the use of the quaternary (Zn,Mg)(S,Se) in a six quantum well diode laser, similar in design to the Brown/Purdue structures but for the materials, and operating pulsed at 77K. Of significance was the reduced wavelength resulting from the increased bandgap energy of the quaternary. The Sony results suggested that such a quaternary compound presented the opportunity for maintaining lattice compatibility to GaAs while providing an increased bandgap for the implementation of separate confinement heterostructure (SCH) QW lasers. In this talk we describe our efforts to employ the quaternary to realize pseudomorphic SCH diode configurations. These preliminary devices have been operated at room temperature under pulsed conditions ( $\sim 1\mu\text{sec}$ ,  $10^{-3}$  duty cycle) for periods exceeding 1/2 hour before failure, and have reached a 20% duty cycle at room temperature before thermal failure. A group at Phillips laboratories has recently obtained nearly 400K operation with 10 to 50 nsec pulses in a similar structure.

Achieving pseudomorphism requires specific choice and control of Mg and S fractions necessitating precise flux measurement. A combination of PL, x-ray diffraction, and electron microprobe analysis was employed to determine alloy fractions. Using appropriate alloy fractions, and nucleating the II-VI lower cladding layer on a GaAs homoepitaxial layer, FWHM values of as low as 44 arcsec, consistent with TEM images showing few dislocations or stacking faults, were obtained for laser structures employing quaternary cladding layers (Mg=9%, S=12%). The diode laser devices had a single (75-100Å) (Zn,Cd)Se quantum well, 1100-2000Å Zn(S,Se) confinement layers, and 0.75-1.5  $\mu\text{m}$  quaternary cladding layers. The Zn(Se,Te) graded contact scheme, first reported last summer as a means for forming low-resistivity ohmic contact to p-ZnSe, was adapted to make ohmic contact to the quaternary p-type cladding layers. LED action was observed below three volts of bias, and lasing was obtained at 15 volts with a gain-guided structure at room temperature. Room temperature LED devices were operated CW at up to 300 A/cm<sup>2</sup> indicating a possibility for obtaining room temperature CW laser operation.

This work was supported by DARPA/ONR URI grant 286-25043, AFOSR grant F49620-92-J-0440 and NSF/MRG grant 8913706-DMR, and a gift from Hewlett Packard.

## P-Type Doping of Wide-bandgap II-VI Semiconductors: Reference to ZnSe:N

Robert M. Park  
Department of Materials Science and Engineering  
University of Florida  
Gainesville, FL

The recently announced successful demonstration of ZnSe-based blue-green diode lasers<sup>[1,2]</sup> is due, to a significant extent, on our ability to dope ZnSe and related alloys p-type during MBE growth using an Oxford Applied Research rf plasma discharge, nitrogen free-radical source.<sup>[3,4]</sup> It was shown early on, in fact, that resistivities as low as  $0.75 \Omega\text{cm}$  could be achieved in p-type ZnSe grown with the OAR radical source, such resistivity measurements being made employing a non-contact inductively-coupled rf bridge apparatus.[5]

Subsequently, more recent Hall-effect measurements performed on p-type ZnSe:N grown using an OAR radical source have revealed free-hole concentrations in the  $10^{17}\text{cm}^{-3}$  range in this material.<sup>[6-8]</sup> Such Hall-effect measurements were made possible by the development of low-resistance contacting schemes to p-type ZnSe:N involving in one case the growth of ZnSe capping layers at low-temperature ( $\sim 150^\circ\text{C}$ ),<sup>[6]</sup> in a second case epitaxial HgSe electrodes<sup>[7]</sup> and in a third case a Zn (Se,Te) pseudograded bandgap region grown epitaxially between p-ZnSe:N and  $p^+\text{-ZnTe:N}$ .<sup>[8]</sup> Heavily-doped p-type ZnTe:N having free-hole concentrations around  $10^{19}\text{cm}^{-3}$  was achieved by employing the OAR rf plasma source during MBE growth.<sup>[9]</sup>

We currently employ the OAR rf plasma source at the University of Florida to produce either a flux of atomic nitrogen for p-type doping of wide-bandgap II-VI compounds or a flux of atomic hydrogen for low-temperature in-situ cleaning (oxide reduction) of GaAs wafers prior to II-VI epitaxy.<sup>[10]</sup> In this case the OAR rf plasma source is configured with independent  $\text{H}_2$  and  $\text{N}_2$  gas lines. As will be discussed in the presentation, our assumption that the OAR rf plasma source generates a significant concentration of either N atoms when used with  $\text{N}_2$  gas or H atoms when  $\text{H}_2$  gas is bled into the discharge chamber is based on an interpretation of the optical emission spectra recorded in each case from the plasma region, emission spectra having been recorded for the nitrogen and hydrogen plasmas during operation using a wavelength spectrometer/OMA apparatus.

Our efforts to detect and quantify the cathodoluminescence emission which is observed during the MBE growth of doped (either n- or p-type) ZnSe epilayers as a consequence of the impinging electron beam normally employed for RHEED analysis will also be discussed in this presentation in the context of p-type doping. We have previously reported on real-time in-situ CL intensity measurements during the growth of n-type ZnSe.<sup>[11]</sup> As will be discussed, the CL intensity recorded in-situ during the growth of p-type ZnSe is a function of the OAR rf plasma source operating conditions as well as a function of the growth parameters. A correlation will be made in this presentation between the CL intensity data recorded in-situ during growth and the electrical characteristics of the p-type ZnSe material.

- [1] M.A. Haase, J. Qui, J.M. DePuydt, and H. Cheng, Appl. Phys. Lett. **59**, 1272 (1991).
- [2] H. Jeon, J. Ding, W. Patterson, A.V. Nurmikko, W. Xie, D.C. Grillo, M. Kobayashi, and R.L. Gunshor, Appl. Phys. Lett. **59**, 3619 (1991).
- [3] R.M. Park, M.B. Troffer, C.M. Rouleau, J.M. DePuydt, and M.A. Haase, Appl. Phys. Lett. **57**, 2127 (1990).
- [4] K. Ohkawa, T. Karasawa, and T. Mitsuyu, Jpn. J. Appl. Phys. **30**, L152 (1991).
- [5] R.M. Park, M.B. Troffer, E. Yablonovitch, and T.J. Gmitter, Appl. Phys. Lett. **59**, 1896 (1991).
- [6] C.T. Walker, J.M. DePuydt, M.A. Haase, J. Qiu, and H. Cheng, 7th Trieste Semiconductor Symposium on Wide-Bandgap Semiconductors, June 8-12, 1992, Trieste, Italy (paper published in Physica B, **185**, 27 (1993)).
- [7] Z. Yang, K.A. Bowers, J. Ren, Y. Lansari, J.W. Cook, Jr., and J.F. Schetzina, Appl. Phys. Lett., **61**, 2671 (1992).
- [8] Y. Fan, J. Han, L. He, J. Saraie, R.L. Gunshor, M. Hagerott, H. Jeon, A.V. Nurmikko, G.C. Hua and N. Otsuka, Appl. Phys. Lett., **61**, 3161 (1992).
- [9] J. Han, T.S. Stavrinides, M. Kobayashi, R.L. Gunshor, M.M. Hagerott, and A.V. Nurmikko, Appl. Phys. Lett., **62**, 804 (1993).
- [10] C.M. Rouleau and R.M. Park, Appl. Phys. Lett., **73**, 4610 (1993).
- [11] C.M. Rouleau and R.M. Park, Appl. Phys. Lett., **60**, 2723 (1992).

The research at the University of Florida has been supported by the National Science Foundation (Grant No. DMR-9116880) and by the Advanced Research Projects Agency (University Research Initiative Grant No. N-00014-92-J-1895).

**W2.1 10:45am - 11:15am**  
**(Invited)**

**Blue/Green Lasers Based on II-VI Semiconductor Heterostructures**

*J.F. Schetzina, North Carolina State University, Raleigh, NC*

In June, 1991, scientists at 3M Company announced a blue/green laser diode based on wide-band-gap II-VI semiconductor materials. Blue/green lasers have now been reported by at least nine research groups throughout the world, including NCSU. Work in this exciting new field will be reviewed, and recent NCSU results will be presented. Issues that must be addressed before these new short-wavelength light emitters can be commercialized will be described and possible solutions to these issues will be discussed. The potential market for blue/green/red/light emitters is expected to exceed \$5B per year within five years.

## Improved Blue-Green Injection Lasers with Pseudomorphic Quaternary Cladding Layers

*D. J. Olego*

Philips Laboratories,  
Briarcliff Manor, NY 10510

The improvement of the performance of II-VI wide band gap blue-green injection lasers is receiving considerable attention. To this end, the reduction of the structural defects and increase in band offsets are of primary importance together with the realization of ohmic contacts to p-type layers. This paper deals with the properties of injection lasers containing  $\text{Zn}_{1-x}\text{Mg}_x\text{S}_y\text{Se}_{1-y}$  quaternary cladding layers. Larger band gaps can be obtained by incorporating Mg in  $\text{ZnS}_y\text{Se}_{1-y}$ , thus improving carrier and light confinement, while maintaining in principle the ability to lattice match to the substrates for reduced structural defects. Separate confinement heterostructure lasers implemented for the first time with  $\text{Zn}_{1-x}\text{Mg}_x\text{S}_y\text{Se}_{1-y}$  cladding layers [1] yielded dramatic improvements in threshold current densities, peak output powers, maximum operating temperatures and dislocation densities over previous results [2,3].

The performance and optical and structural properties of the single quantum well lasers shown in Fig.1 were compared. These lasers were grown by molecular beam epitaxy on (100) GaAs substrates. The n- and p-type dopings are provided by Cl donors and N acceptors, respectively. The strained active regions contain a single well of  $\text{Zn}_{0.8}\text{Cd}_{0.2}\text{Se}$ . The compositions of the ternary and quaternary alloys were chosen to lattice match the substrate. The low temperature band gap of  $\text{ZnS}_{0.06}\text{Se}_{0.94}$  lies at 2.84 eV and of  $\text{Zn}_{0.9}\text{Mg}_{0.1}\text{S}_{0.1}\text{Se}_{0.9}$  at 2.98 eV. High resolution x-ray diffraction and transmission electron microscopy were applied to determine the lattice mismatch and dislocation densities.

In the laser structures 1-a and 1-b the 0.27 % lattice mismatch between the ZnSe guiding layer and the cladding layers gives rise to a large density of threading dislocations throughout the devices and misfit dislocations at the heterointerfaces. Typical values of  $10^7$  threading dislocations  $\text{cm}^{-2}$  are detected in laser 1-b and even larger densities in the structure 1-a. However, by combining quaternary and ternary layers in structure 1-c a dramatic reduction in dislocation density is realized. Values smaller than  $10^6$  threading dislocations  $\text{cm}^{-2}$  are established with no indication of misfit dislocations at the heterointerfaces. The measured lattice mismatch between the cladding and guiding layers and the substrate is less than 0.1 and 0.03 %, respectively.

The reduced dislocation density and increased carrier confinement are reflected in the performance of laser 1-c. This device operates at room temperature with a record low threshold current density (without facet coating) of  $500 \text{ A cm}^{-2}$  as compared for example to  $1300 \text{ A cm}^{-2}$  for the structure 1-b. Figure 2 displays the light output as a function of input current under pulsed conditions. Laser emission is achieved up to 394 K, which surpasses by

far the operation reported with structures of the type 1-a [2,3]. Continuous wave output was achieved up to 170 K which is the highest temperature reported so far [2,3]. Peak powers of about 0.5 Watts were recorded at room temperature.

This work is in collaboration with J. Gaines, R. Drenten, K. Haberern, T. Marshall, P. Mensz, J. Petruzzello and P. v. Sluis.

[1] J. Gaines, R. Drenten, K. Haberern, T. Marshall, P. Mensz, J. Petruzzello, Appl. Phys. Lett. (in press).

[2] C. Walker, J. DePuydt, M. Haase, J. Qiu, H. Cheng, Physica B (in press).

[3] R. Gunshor, N. Otsuka, A. Nurmikko, IEEE Spectrum Vol 30(5), 28 (1993).

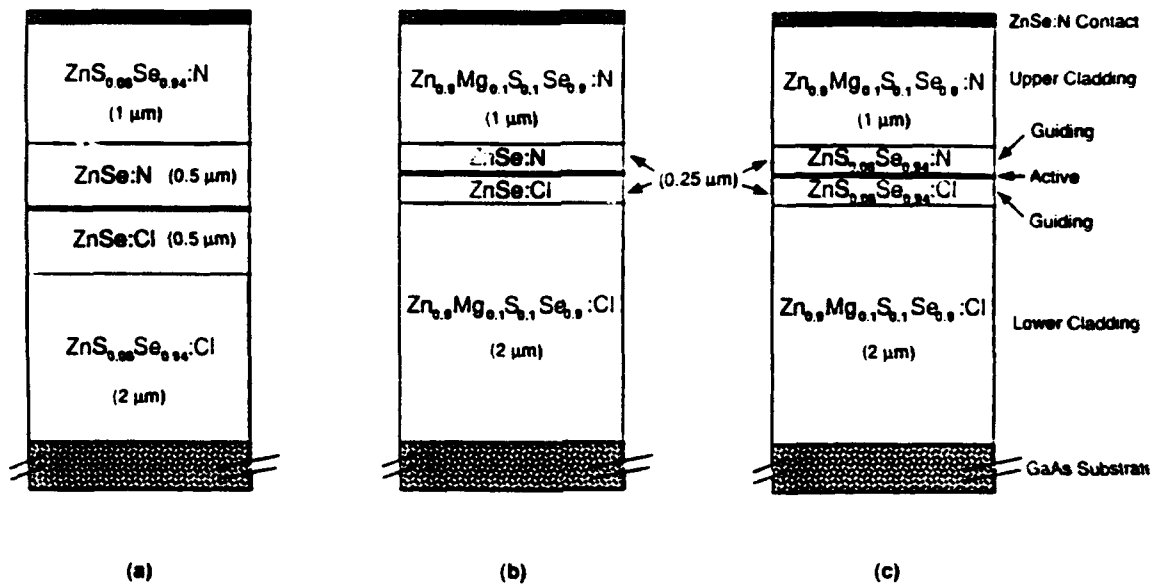


Fig. 1 - Diagram of the separate confinement laser structures investigated

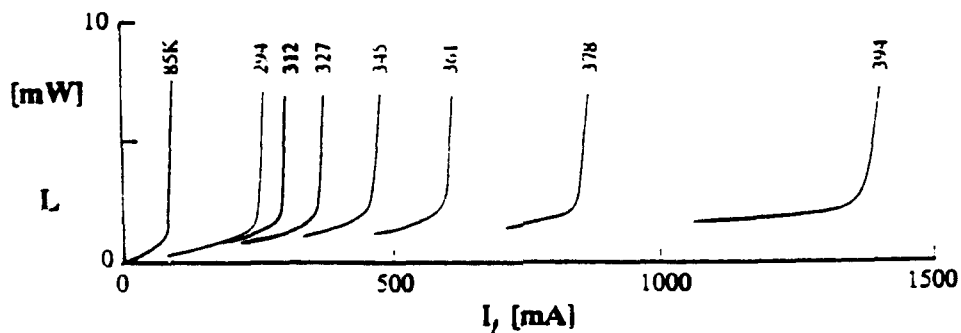


Fig. 2 - Light output versus input current for laser 1-c (50 μm stipe width , 1000 μm long) at selected temperatures.

## Proposal of Novel Blue-Green Diode Laser Based on MgZnSeTe Alloys\*

Yijun Cai and Reinhart Engelmann

Department of Electrical Engineering and Applied Physics  
Oregon Graduate Institute of Science & Technology, Beaverton, OR 97006.

There are many obstacles in developing a CW room temperature blue-green diode laser with the high band gap II-VI compounds. The most significant ones are inability to readily dope these materials both p-type and n-type (amphoteric doping), the lack of a lattice matched heterostructure with good carrier confinement, and poor ohmic contacts. ZnSe is known to have residual n-type conductivity, and its doping has been extensively studied. A breakthrough in p-type doping has been demonstrated only 3 years ago by applying the nitrogen radical doping technique in molecular beam epitaxy (MBE)<sup>1</sup>. This lead Haase *et al.*<sup>2</sup> to successfully fabricate the first blue-green laser diode operating at 77 K, based on a ZnCdSe/ZnSe strained-layer SQW structure.

An alternate way to overcome this doping problem is to mix the selenides with the tellurides. It is well known that ZnTe is the only binary of the wide bandgap II-VI semiconductors with a p-type residual conductivity, and it was found that the  $\text{ZnSe}_y\text{Te}_{1-y}$  alloy could be doped both p and n type in the composition range of  $0.4 < y < 0.5$ <sup>3</sup>. Good quality ZnSeTe material has been grown by MBE<sup>4</sup> and MOCVD<sup>5</sup> on various substrates (GaAs, InP, InAs, and ZnTe). Mg introduction opens up the band gap energy range of the standard II-VI compounds for diode laser design<sup>6</sup>. Recently Okuyama *et al.* have proposed using MgZnSSe as cladding layer material, and achieved CW operation of a ZnSe/MgZnSSe blue laser diode at 77K<sup>7</sup>. Compared with MgSe and MgS, MgTe has less ionicity in the bonding and can be more easily formed in zinc-blende structure. Adding Mg does not change the doping property very much<sup>6</sup>, so by engineering the new material MgZnSeTe, a novel diode laser with improvements in carrier confinement, amphoteric doping (particularly high p-type doping) and ohmic contacts are very likely to be achieved.

A separate-confinement-heterostructure (SCH) single quantum well (SQW) laser structure provides significant superiority in performance over conventional DH laser structures. Such a SCH SQW diode laser can be obtained by choosing the appropriate quaternary composition of the MgZnSeTe alloy for each of the active, barrier and cladding layers at a chosen lattice constant. The band gap energy and lattice constant of quaternary  $\text{Mg}_x\text{Zn}_{1-x}\text{Se}_y\text{Te}_{1-y}$  varies from 2.2 to 3.5 eV and from 5.66 to 6.28 Å, respectively (Fig.1). Notice that  $\text{MgSe}_y\text{Te}_{1-y}$  has a similar bowing characteristic as  $\text{ZnSe}_y\text{Te}_{1-y}$ . Also, the doping property of  $\text{Mg}_x\text{Zn}_{1-x}\text{Te}$  is very similar to that of ZnTe for x as high as 0.8<sup>6</sup>. Hence, we expect that the engineered Zinc blende  $\text{Mg}_x\text{Zn}_{1-x}\text{Se}_y\text{Te}_{1-y}$  quaternaries ( $0.4 < y < 0.5$ ) between the dotted tielines in Fig. 1, have a similar amphoteric doping property as the ternary  $\text{ZnSe}_y\text{Te}_{1-y}$  ( $0.4 < y < 0.5$ ). For blue light emission, the band gap of the cladding should be close to 3 eV. A high Mg mole fraction x (about 0.6-0.8 from Fig.1) is needed in this case. Hence,  $\text{Mg}_{0.8}\text{Zn}_{0.2}\text{Se}_{0.4}\text{Te}_{0.6}$  is chosen as cladding layer material (C in Fig.1), which is lattice matched to GaSb (ZnTe). For the barrier and active layers, the band offset is the most important issue. Based on the common anion rule, it is the advantage of the MgZnSeTe system that the Se/Te ratio can be adjusted to provide a reduced valence band offset thus overcoming the type II alignment problem of the ZnSe/ZnTe system, as shown in Fig. 2. The barrier can be easily chosen to be lattice matched with the cladding, as B ( $\text{Mg}_{0.6}\text{Zn}_{0.4}\text{Se}_{0.3}\text{Te}_{0.7}$ ) in Fig.1. A1 (ZnTe) could be the choice for an unstrained QW. For shorter wavelength light emission, preferably a strained QW such as A2 ( $\text{Mg}_x\text{Zn}_{1-x}\text{Te}$ ) could be incorporated.

In conclusions, we have proposed a novel diode laser structure based on the MgZnSeTe

## **High Performance AlGaInP Light-Emitting Diodes**

**C. P. Kuo, R. M. Fletcher, J. G. Yu, T. D. Osentowski,  
D. A. Steigerwald, D. C. DeFevere, M. J. Peanasky and F. A. Kish**

**Hewlett-Packard Optoelectronics Division  
370 W. Trimble Road, San Jose, California 95131**

Significant progress in AlGaInP material quality has been made in the last decade using organometallic vapor phase epitaxy. Double heterostructure AlGaInP/GaInP/AlGaInP lasers emitting in the 650-680 nm wavelength range have been commercially available for the last five years. However, the development of high-brightness AlGaInP LEDs has been slower due to slightly different requirements in material properties and device structures. One of the problems experienced by the researchers in developing AlGaInP LEDs was the issue of poor current spreading. This is because the upper confining layer employed in the DH structure, usually high aluminum containing alloys, is highly resistive. The current flows virtually straight down from the top contact toward p-n junction without much current spreading to the edge of the chip, and light is generated only beneath the contact and is blocked by the contact. This greatly reduces the external quantum efficiency of the AlGaInP LEDs despite high internal efficiency. Conceptually, any transparent and conductive epitaxial layer grown on top of the DH structure should solve this problem. From an epitaxial growth point of view, however, AlGaAs and GaP are two of the best materials, among other potential candidates. AlGaAs is lattice-matched to the substrate and has reasonable conductivity. However, it is only transparent enough in the red and orange spectral range. GaP is highly conductive and transparent to the wavelength range from red to green but is lattice-mismatched by 4%, as compared to the GaAs substrate. Currently, both types of window layers are found in commercially available AlGaInP LEDs. The device performance of orange and yellow AlGaInP LEDs grown using GaP as the window layer exhibits higher external quantum efficiency and luminous performance than those grown using an AlGaAs window layer. AlGaInP LEDs with the GaP window represent the brightest visible LEDs that have ever been made and are expected to accelerate several new applications requiring high flux and/or low power consumption.

## UV/Blue Light Emitting AlGaIn/GaN Heterostructures

Isamu Akasaki and Hiroshi Amano

Department of Electrical and Electronic Engineering,  
Meijo University,  
1-501 Shiogamaguchi, Tempaku-ku, Nagoya 468 Japan

Blue-LED has been eagerly demanded not only for use as small indicators but also for the realization of a new all solid state full color flat panel display systems. Besides, the practical short wavelength LD enables us to develop compact and high density optical storage systems and small medical equipments. Column-III nitrides, InN, GaN, AlN and their alloys  $(\text{Al}_x\text{Ga}_{1-x})_{1-y}\text{In}_y\text{N}$  ( $x \geq 0, y \geq 0$ ), especially AlGaIn alloys are promising candidates as the materials for fabrication of such short wavelength light emitters, because AlGaIn alloy system has the direct transition type band structure with the band gap energies at room temperature (RT) from 3.39eV to 6.2eV which correspond to the wavelengths from 375nm to 200nm.

In contrast with other III-V compounds such as GaAs or InP, however, it had been fairly difficult to grow high crystalline quality nitride films with a specular surface free from cracks because of the lack of substrate materials of which lattice constant and thermal expansion coefficient are close to those of nitrides. Recently, we succeeded in overcoming these problems and in growing high quality GaN film and AlGaIn film with a specular surface free from cracks on the sapphire substrate by the prior deposition of a thin AlN buffer layer in MOVPE growth. The electrical and optical properties as well as the crystalline quality can be remarkably improved at the same time. Intrinsic nature of the nitrides is being clarified more and more by characterizing such high quality thin films. Moreover, these films enable us to develop high-performance short wavelength light emitting devices.

This paper provides a preliminary results of UV/blue p-n homojunction LEDs and AlGaIn/GaN heterostructure diodes.

A horizontal type MOVPE reactor operated at an atmospheric pressure was used for the growth of GaN and AlGaIn films. TMGa, TMAI and  $\text{NH}_3$  were used as source gases and  $\text{H}_2$  as a carrier gas. Polished (0001) sapphire was used as a substrate. In our process, before the nitride growth, a thin AlN buffer layer about 50nm thick was deposited at 600°C by feeding TMAI and  $\text{NH}_3$  diluted with  $\text{H}_2$ . The electron concentrations and resistivities of n-type GaN and n-type AlGaIn can be easily controlled by changing silane flow rate from the undoped level of less than  $10^{15}\text{cm}^{-3}$  up to near by  $10^{19}\text{cm}^{-3}$ . Doping of Mg was carried out during the growth of GaN and AlGaIn by supplying  $\text{Cp}_2\text{Mg}$  as a Mg source gas. We can obtain the desired Mg concentration and its profile in nitrides by controlling the flow rate of  $\text{Cp}_2\text{Mg}$ . Mg-doped nitrides tend to become low resistivity with p-type conduction by the low energy electron beam irradiation treatment. Hole concentration at RT up to about  $1.4 \times 10^{17}\text{cm}^{-3}$  has been achieved. The newly developed p-n homojunction LED showed broad blue emission peaking at 423 nm, which is due to transition related with the Mg-associated centers in the p-type GaN layer. Sharp UV emission peaking at 375 nm was also observed, which is thought to originate from band-to-band transition in n-type GaN layer. The output power at room temperature under DC biased condi-

tion of more than 1.5mW with a forward current of 30mA and the bias voltage of 5.0V has been achieved. The power efficiency is more than 1% at RT, which is the highest efficiency ever reported in LED mode operation of the blue LEDs.

$\text{Al}_{0.1}\text{Ga}_{0.9}\text{N}/\text{GaN}$  heterostructures have been constructed by modulating flow rates of TMGa and TMAI during the growth. The P- $\text{Al}_{0.1}\text{Ga}_{0.9}\text{N}/\text{n-GaN}/\text{N-Al}_{0.1}\text{Ga}_{0.9}\text{N}$  doubleheterostructure (DH) diode with the output power of a few mW at RT have also been fabricated.

Spectroscopic ellipsometry revealed that the difference of the refractive index at  $\lambda=368\text{nm}$  between  $\text{Al}_{0.1}\text{Ga}_{0.9}\text{N}$  and GaN is about 0.09, which is sufficient to confine optical field in the GaN active layer. By using AlGaIn/GaN DH, the threshold powers for UV stimulated emission by optical pumping can be markedly decreased to about  $0.1\text{MW}/\text{cm}^2$  at RT for both longitudinal and transverse mode operations compared with those of the single GaN layer. Therefore it can be concluded that AlGaIn/GaN DH is useful for optical confinement of the UV laser.

Further characterization of the optical properties of the nitrides must be necessary for the design of the future heterojunction optical devices based on nitrides.

### Acknowledgments

The authors are indebted to N.Okazaki, K.Manabe and N.Koide of Toyoda Gosei Co.Ltd. for assistance with this work. This work was partly supported by "The Mitsubishi Foundation" and the Grant-in-Aid from the Ministry of Education, Science and Culture of Japan for Scientific Research on Priority Areas "Crystal Growth Mechanism in Atomic Scale".

**Blue/UV Emitters from SiC and its Alloys**

John A. Edmond, Hua-Shuang Kong, Vladimir Dmitriev and Calvin H. Carter, Jr.  
Cree Research, Inc.  
2810 Meridian Parkway  
Durham, N.C. 27713

A strong need exists in many commercial and military applications for solid state blue emitters, but until recently a suitable material or material system from which to fabricate these devices had not been commercially developed. Some of the applications for blue emitters include rugged solid-state full color indicators and flat panel displays. The material system used for such emitters will also provide the basis for the development of blue/UV laser diodes. This paper reports on the most recent advancements in increasing the performance of blue light emitting diodes fabricated in 6H-SiC and the potential for SiC-nitride based alloys.

Silicon carbide has been known for many years to have physical and electronic properties which allows production of electronic devices that exhibit blue electroluminescence. The 6H polytype has an indirect band-gap of  $\sim 3.0$  eV. Light is generated via radiative recombination in a compensated layer doped with nitrogen donors and aluminum acceptors. This doping scheme results in a device which emits light with a peak wavelength of  $\sim 470$  nm with a spectral halfwidth ( $\Delta\lambda_p$ ) of  $\sim 70$  nm. The present authors previously reported<sup>1</sup> a typical output power of between 12 and 18  $\mu$ W for a forward current of 20 mA at 3 V or external power efficiency of  $\sim 0.02$ - $0.03\%$ . The optical power output of the LED has been substantially increased over the past year. Figure 1a shows the relative spectral emission versus wavelength for a Cree blue LED operating at a forward current of 20 mA measured in an integrating sphere. As shown, the peak emission is  $\sim 470$  nm with  $\Delta\lambda_p \sim 70$  nm and a dominant wavelength of 480.8 nm. The resultant spectral purity is 82.5 %. The radiant flux or optical power output of this device is 30  $\mu$ W. The typical output power of the new LEDs is between 20 and 30  $\mu$ W for a forward current of 20 mA at 3.4 V or external power efficiency of  $\sim 0.030$ - $0.043\%$ . With respect to photometric units, the die luminous intensity is 0.41 millicandela for a radiant flux output of 30  $\mu$ W.

The effect of increasing forward current to 50 mA on the radiant flux and corresponding value of the external power efficiency is shown in Fig. 1b. As shown, the radiant flux increases in a sublinear fashion with increasing current. This translates into a decreasing external power efficiency also shown in this figure. This sublinear behavior is most probably due to the onset of decreasing D-A pair recombination or pair saturation and an increase in lower efficiency recombination events at higher energy. Included in this graph is the radiant flux output versus forward current for devices produced during 1992. Comparing these two plots, a 67% increase in the LED output has been realized this past year.

Another important aspect of any light emitting source is its stability in light output over time. Other potential blue emitting semiconductor materials like ZnSe and its alloys have shown very limited lifetime ( $< 24$  hours) under normal ambient operation conditions. On the other hand, blue LEDs from SiC are extremely stable. Using a stress current of 50 mA at room temperature, the typical

24 hour degradation is ~1%. After 10,000 hours the degradation is typically ~10-15%; better than most commercial green and red LEDs produced today.

In addition to increasing the output of 6H-SiC blue LEDs, research is ongoing to develop the SiC-AlN and SiC-GaN alloy systems. Much like the Ga, Al, In, As, P system, SiC has been shown to have a large range of solid solubility with both AlN and GaN with nitride-rich alloys having direct bandgaps. These materials also have similar lattice constants and coefficients of thermal expansion which should make it possible to produce heterojunctions from single crystal thin films of these alloys. Since the bandgaps of these materials cover the range of 3.3 to 6.3 eV, a very wide spectrum of high efficiency emitters in the blue to deep UV regions is possible.

Growth of AlN and SiC-AlN have been initiated on 6H-SiC and Si wafers via epitaxial techniques. Aluminum nitride layers with smooth and mirror-like surfaces have been achieved. Auger analysis results indicate that only Al and N exist in these films. Alloy layers of AlN with SiC also exhibit a smooth surface finish. Auger of these layers shows the presence of Al, N, Si, and C indicating the alloy composition. The maximum percentage of AlN in SiC achieved to date is 63%, nearing the theoretical level required to become a direct-gap alloy (~70%AlN). Optical and structural characterization of these layers is presently underway.

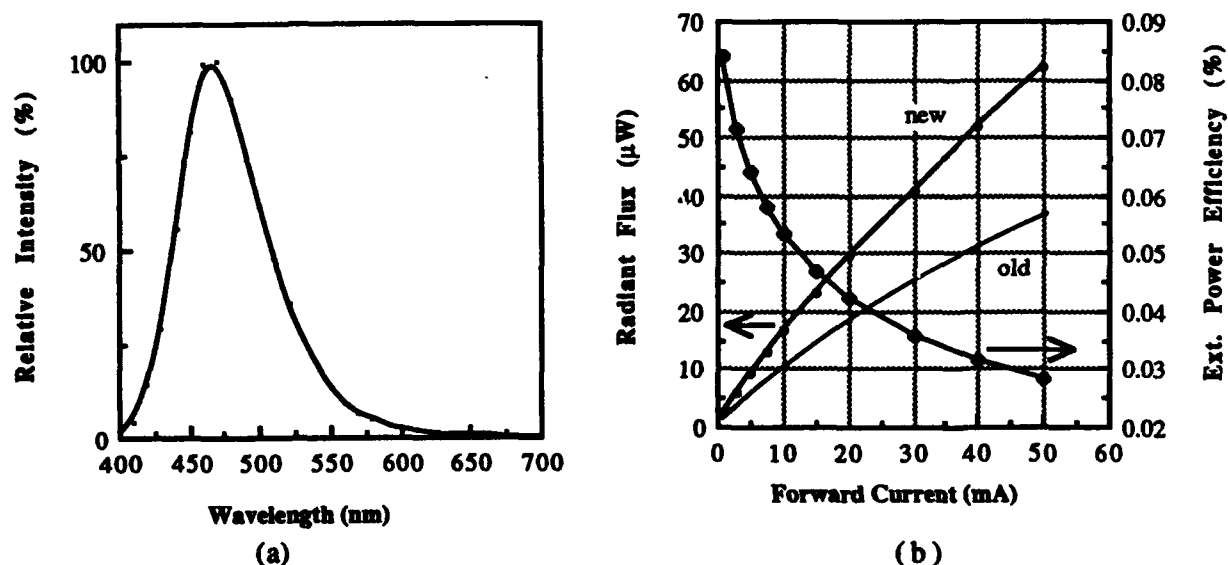


Fig. 1. Typical (a) emission spectra and (b) current-dependent output of 6H-SiC blue LEDs produced at Cree Research, Inc. The old and new current dependence on the radiant flux is shown for comparison.

## References

1. J.A. Edmond, H.S. Kong and C.H. Carter, Jr., *Physica B* 185, 453 (1993).

## Acknowledgement

Cree Research wishes to acknowledge the Advanced Research Projects Agency and the Office of Naval Research for the support of this work.

**W4.1 4:00pm - 4:30pm**  
**(Invited)**

**The New Blue Horizon: Quantum Well Lasers from II-VI Semiconductors:  
Quantum Well Physics**

*A.V. Nurmikko, Brown University, Providence, RI*

The ongoing developments in II-VI blue/green diode lasers call for detailed attention to the designs and modeling of gain in the active quantum well region in the ZnSE-based heterostructures. These include issues of many electron-hole Coulomb interaction, including 2-dimensional excitonic effects.

W4.2 4:30pm - 5:00pm  
(Invited)

# Optoelectronic Properties of GaN, AlGa<sub>x</sub>N and AlGa<sub>x</sub>N-GaN

Quantum Well Heterostructures  
R. M. Kolbas and S. Krishnakutty  
North Carolina State University, Raleigh, NC  
27695-7911

The dramatic advances in wide bandgap semiconductors since the mid 1980s have been driven by new developments in growth processes, new requirements for high power and high temperature operation and radiation hardness, and the desire for blue and ultraviolet optoelectronic devices. Al<sub>x</sub>Ga<sub>1-x</sub>N has a direct bandgap (3.4-6.2 eV), a large and sharp optical absorption edge, a large radiative recombination coefficient, and is quite hard and stable in chemical environments and at elevated temperatures. Challenges in the continued development of the AlGa<sub>x</sub>N material system are the lack of a native substrate, high n-type carrier concentrations in epitaxial films and controlled p-doping. In this paper we describe the optical properties that have been achieved with MOCVD grown AlGa<sub>x</sub>N on sapphire substrates and the diffusion of zinc into these GaN epitaxial layers.

For GaN samples with carrier concentrations less than  $1 \times 10^{18}/\text{cm}^3$  a low intensity peak approximately 70 meV down from the main peak (attributed to a TO phonon replica) can be observed as shown in Fig. 1. For GaN samples with a background doping less than  $1 \times 10^{17}/\text{cm}^3$  features identified as excitonic in nature (A and C in Fig. 1) by Gershenson and co-workers can be observed at 77K. Typical linewidths are 25 meV at 77K for Al<sub>x</sub>Ga<sub>1-x</sub>N ( $x < 0.15$ ).

The photoluminescence spectra from Al<sub>x</sub>Ga<sub>1-x</sub>N-GaN-Al<sub>x</sub>Ga<sub>1-x</sub>N quantum wells of different thicknesses and  $x$  values are shown in Fig. 2. Note that the emission from the quantum wells is shifted to higher energies characteristic of a type I heterojunction. However the shifts are more than the calculated quantum effects by an amount (40 meV at  $x=0.13$ ) that is linearly dependent on the alloy composition. The added shift can be accounted for by including strain induced bandgap shifts for the hexagonally symmetric AlGa<sub>x</sub>N-GaN crystal. Also note that the thicknesses and compositions of these samples are below the Matthews and Blakeslee critical thickness.

During the 1976-1981 time frame researchers tried to diffuse a number of elements into GaN (Mg, Cd, Zn, Li, Be, Si, Ge,

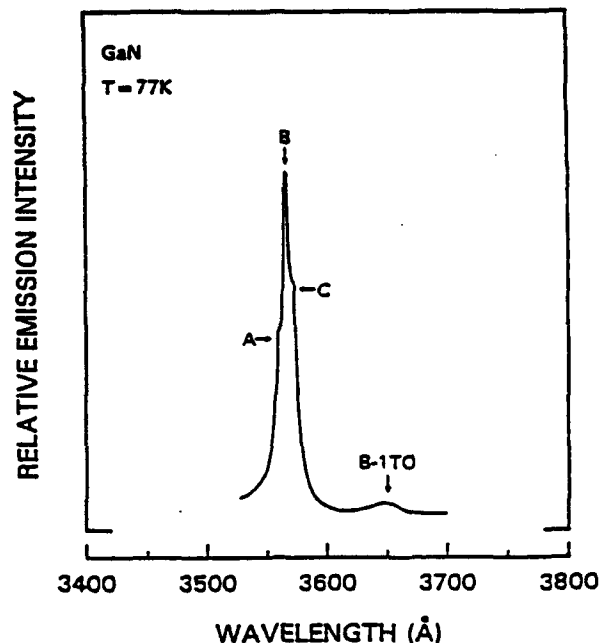


Figure 1

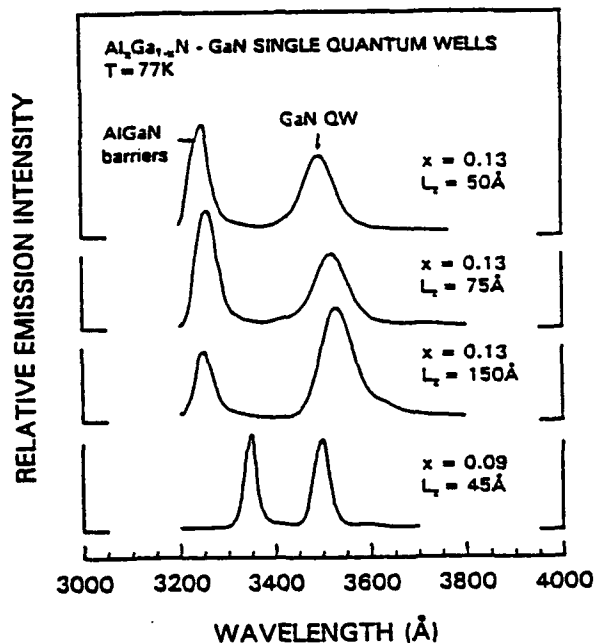


Figure 2

and S) to obtain p-type doping but were successful only with Li. Subsequently the post-growth doping of GaN focused on ion implantation. Most recently we have successfully diffused Zn into epitaxial layers of GaN with as grown n-type carrier concentrations of approximately

$5 \times 10^{17}/\text{cm}^3$ . The successful diffusions were measured by photoluminescence and secondary ion mass spectroscopy. The photoluminescence spectra of GaN before diffusion (a), and after diffusion for various times at  $925^\circ\text{C}$  are shown in Fig. 3. The emission peaks are: 1- near band edge transition, 2- TO phonon replica of main peak, 3- a  $3775\text{\AA}$  peak attributed to a transition from the conduction band to a substitutional zinc level, and 4- a  $4250\text{\AA}$  peak attributed to a transition from the conduction band to a level introduced by a complex associated with substitutional zinc impurities.

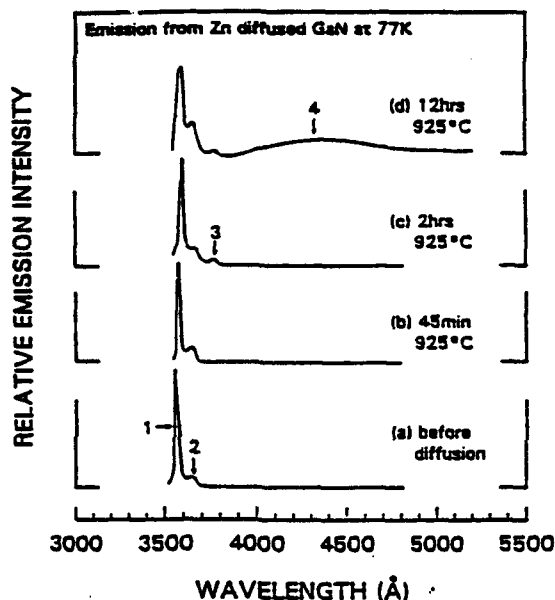


Figure 3

The photoluminescence spectra of GaN after 12 hour Zn diffusions at various temperatures are shown in Fig. 4 where the same peak assignments are applicable. The peak at  $3775\text{\AA}$  (labeled 3) is  $220\text{ meV}$  below the band edge which corresponds closely to the calculated hydrogenic acceptor level in GaN. At higher temperatures or longer diffusion times the Zn concentration increases and the broad peak, labeled 4, appears. The SIMS depth profiles for these samples are shown in Fig. 5. The Zn concentration is based on an ion implanted GaN:Zn calibration sample. The diffusion appears to be an interstitial-substitutional process where the interstitial Zn acts as a donor and the substitutional Zn acts as an acceptor. The interstitial diffusion coefficient and activation energy were calculated to be  $5.7 \times 10^3\text{ cm}^2/\text{s}$  and  $3.8\text{ eV}$ , respectively. The presentation will include details of the diffusion and SIMS

data and a brief discussion of the movement of hydrogen in the film during diffusion.

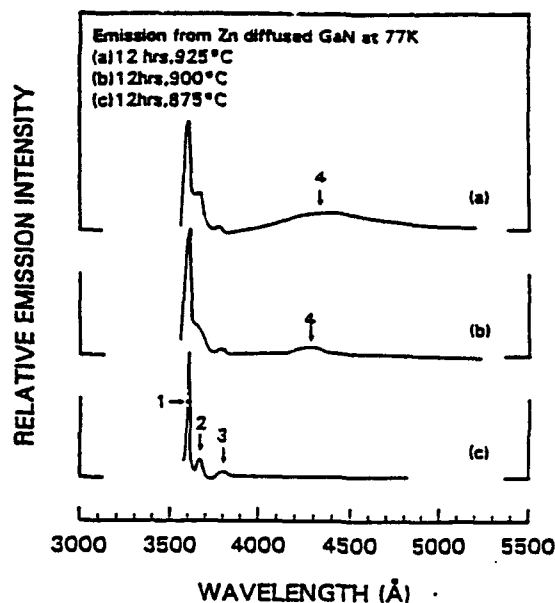


Figure 4

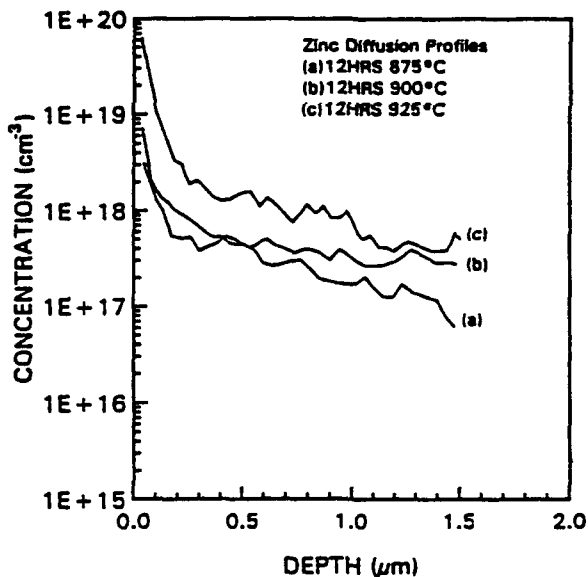


Figure 5

In summary, significant progress is being made to meet the challenges of understanding and controlling the AlGaIn material system for optoelectronic devices.

We thank APA Optics for AlGaIn samples the SDIO/IST through the Army Research Office DAAL03-90-G-0018 for support.

## **Wide Bandgap $\text{Al}_x\text{Ga}_{1-x}\text{N}$ Material System for Visible and Ultraviolet Optoelectronic Devices**

**M. Asif Khan, Jon Kuznia, D. Olson and A. Bhattarai**  
**APA Optics Inc.**  
**2950 N. E. 84 th. Lane**  
**Blaine, MN 55449**

$\text{Al}_x\text{Ga}_{1-x}\text{N}$  with its tunable and direct bandgap is an important semiconductor system for visible and ultraviolet devices. The bandgap tunability from 200 nm at  $x=1$  to 365 nm at  $x=0$  combined with the tunable refractive index makes possible the fabrication of waveguide structures. Recently high quality single crystal films of AlN, GaN and AlGaIn have been deposited over sapphire substrates by several research groups using metalorganic chemical vapor deposition<sup>1,2,3,4</sup>. N- and p- type doping<sup>4,5</sup> and high quality heterojunctions have also been reported<sup>6</sup>. These material quality improvements and control has resulted in several optoelectronic devices such as high responsivity UV detectors, Bragg reflectors, waveguides, transistors and visible LED's. We will briefly describe these recent advances and some current research directions.

All the material described in our research is deposited using low pressure metalorganic chemical vapor deposition. Sapphire substrates are used due to their transparency in the ultraviolet. The growth systems are capable of conventional or atomic layer depositions. In the conventional mode all the reactants namely triethylgallium (TEG), triethylaluminum (TEA) and ammonia are introduced in the growth chamber simultaneously. In the atomic layer growths the TEG, TEA and  $\text{NH}_3$  are introduced one at a time with some sweepout interval between the individual pulses. For majority of the growths described in here a growth temperature of 1000° C and a pressure of 76 torr is used.

As grown GaN samples are typically n-type with carrier densities around  $1 \times 10^{17} \text{ cm}^{-3}$  and an electron mobility of  $600 \text{ cm}^2 \text{ V}^{-1} \text{ sec}^{-1}$  at room temperature. From such high quality single crystal layers we were able to observe room temperature stimulated emission at 365 nm. In Figure 1 we plot the photoemission intensity (in a surface emission mode) as a function of input power. A threshold is clearly observable.

We also fabricated several pn-junctions using low pressure MOCVD depositions. The p-type GaN layers were formed using 'Mg' as a dopant followed by an insitu anneal of the grown film at 650° C in a nitrogen ambient. In Figure 2 we plot the current voltage and the light output characteristics of these pn-junction light emitting diodes. As seen the emission is in the purple around 410 nm. Results of detailed junction characterization will be discussed.

Using atomic layer epitaxy we have succeeded in depositing high quality insulating and conducting GaN,  $\text{Al}_x\text{Ga}_{1-x}\text{N}$  and AlN layers over sapphire substrates. The ALE process offers an excellent thickness and compositional control. Using this we were able to deposit quarter wave GaN- $\text{Al}_x\text{Ga}_{1-x}\text{N}$  reflector stacks over sapphire substrates. The structure and reflectivity spectra of a stack with peak reflectivity in the blue wavelength region is shown in Figure 3. The  $\text{Al}_x\text{Ga}_{1-x}\text{N}$  material system is an excellent choice for reflective filters in the blue and ultraviolet parts of the spectrum.

### **References:**

1. S. Nakamura, Y. Harada and M. Seno, Appl. Phys. Lett. 58, 2021 (1991).
2. M. Asif Khan, J.N. Kuznia, R.A. Skogman, D.T. Olson, M. Mac Millian and W.J. Choyke, Appl. Phys. Lett. 61, 2539 (1992).
3. H. Amano, T. Asahi and I. Akasaki, Jpn. J. Appl. Phys. 29, L205 (1990).
4. H. Amano, M. Kito, K. Hiramatsu and I. Akasaki, Jpn. J. Appl. Phys. 28, L2112 (1989).

5. S. Nakamura, M. Senoh and T. Mukai, Jpn. J. Appl. Phys. 30, L1708 (1991).
6. M. Asif Khan, J.N. Kuznia, J.M. Van Hove, N. Pan and J. Carter, Appl. Phys. Lett. 60, 3027 (1992).
7. M. Asif Khan, J.N. Kuznia, A.R. Bhattarai and D.T. Olson, Appl. Phys. Lett. 62, 1786 (1993).

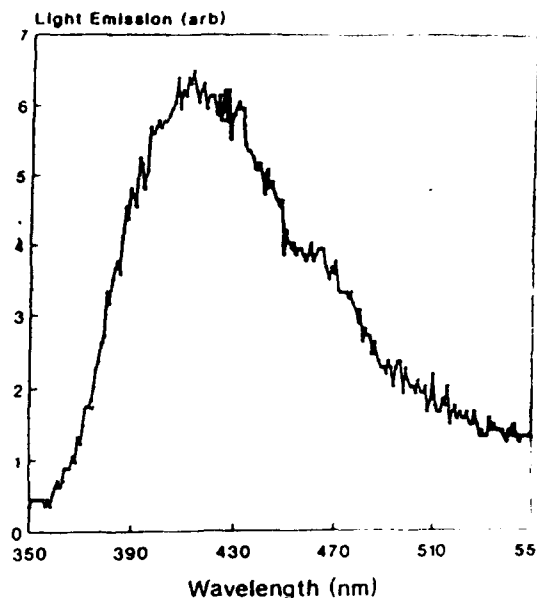
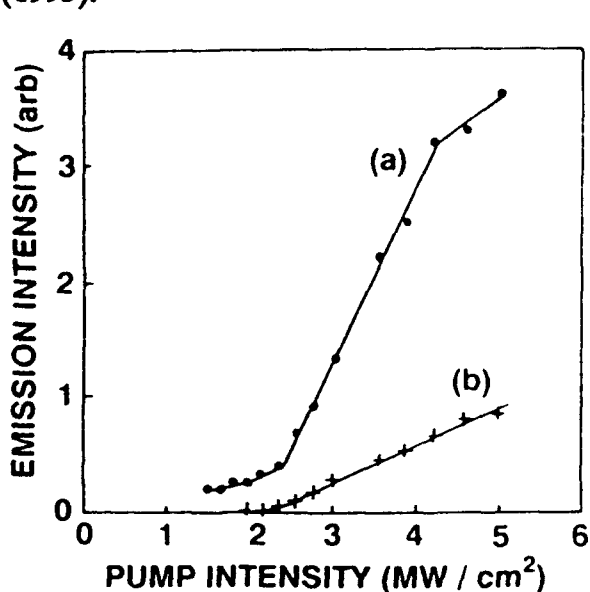


Figure 1. Dependence of stimulated UV signal on the pump power intensity. (a) surface emission (b) edge emission.

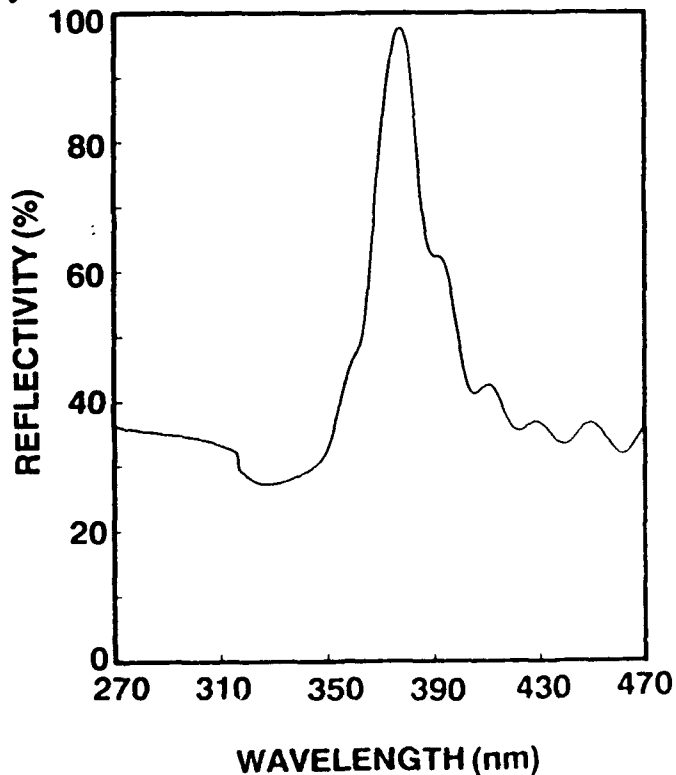
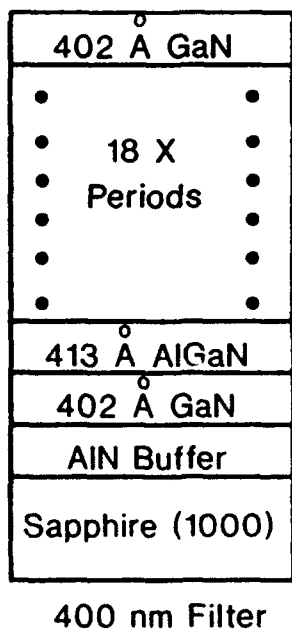


Figure 3. AlGaIn based Bragg reflector structure and the measured reflectivity vs wavelength.

**Thursday, July 22, 1993**

**Sessions:**

**T1: AlGaInP Lasers I**

**T2: AlGaInP Lasers II**



## Short Wavelength Oscillation of InGaAlP Visible Light Laser Diodes

K. Itaya, J. Pennie, and G. Hatakoshi

Toshiba Research & Development Center  
1 Komukai Toshiba-cho, Saiwai-ku, Kawasaki, Japan

InGaAlP laser diodes have become practical light sources in various applications in data storage, bar-code reader systems, and solid state laser pumping. Strong requirements remain for further shortening of lasing wavelength and improvement of temperature characteristics of InGaAlP lasers. In this paper, we review and discuss the results of our work and critical problems in realizing InGaAlP laser diodes with shorter wavelength oscillation.

Figure 1 shows the relation between maximum CW operation temperature ( $T_{max}$ ) and wavelength for the InGaAlP laser diodes previously reported. As shown in this figure, there is a strong correlation between  $T_{max}$  and the wavelength. The shorter the wavelength is, the lower the possible operation temperature becomes. This correlation is considered to originate in the electron overflow from the active layer into the cladding layer. Highly p-doped cladding layer increases an effective heterobarrier height.(1) The off-angle substrate also increases a band-gap of cladding layer by disordering.(2) Figure 1 shows a significant increase of  $T_{max}$  by these techniques.

Figure 2 shows a schematic band diagram of the InGaAlP laser diode with multi-quantum barrier (MQB).(3) An interwell interference of the electron levels can be obtained by incorporating a series of wells and barriers in the p-doped cladding layer, which raises the effective conduction level. Figure 3 shows a dependence of I-L characteristic on temperature of the laser shown in Fig.2. A room temperature threshold current was 49 mA with 633 nm lasing,  $T_{max}$  of 74 °C was obtained. Threshold current is reduced by employment of strained MQW active layer, which is also effective for the increase of  $T_{max}$  of InGaAlP lasers. Thus,  $T_{max}$  has been greatly improved by using quantum effects such as MQB, and strained MQW active layer, as shown in Fig. 1.

The strained MQW structure and the MQB structure have a lot of design parameters. Optimization of these quantum structures would make it possible to further shorten the wavelength of InGaAlP lasers.

- (1)G. Hatakoshi, et al. IEEE J. Quantum Electron. 27, 147, (1991).
- (2)Valster, et al. in Tech. Dig., 12th IEEE Int. Semiconductor Laser Conf., Davos, 1990, C1.
- (3)J. Rennie, et al. to be published in IEEE J. Quantum Electron. 29,NO.6,(1993).

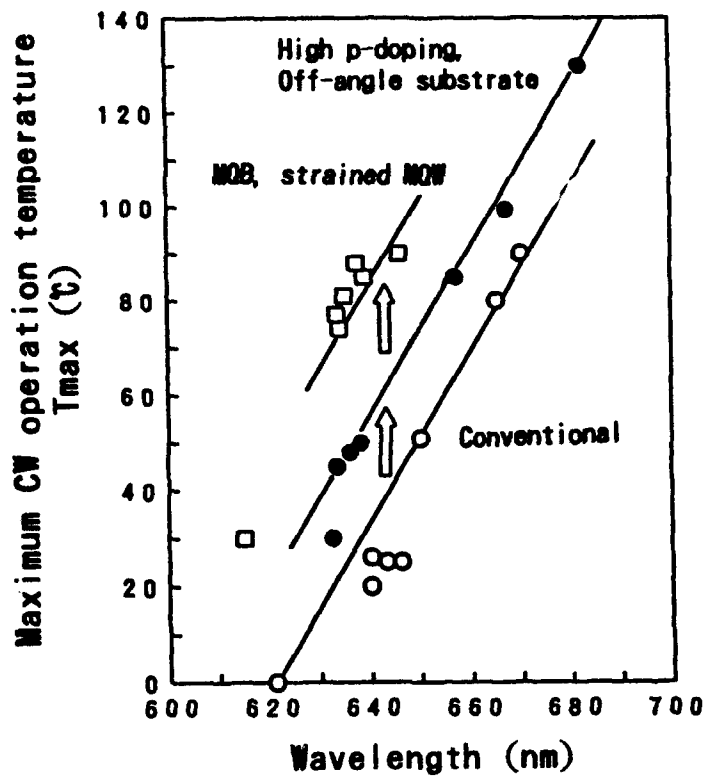


Fig.1 Relation between maximum CW operation temperature ( $T_{max}$ ) and wavelength

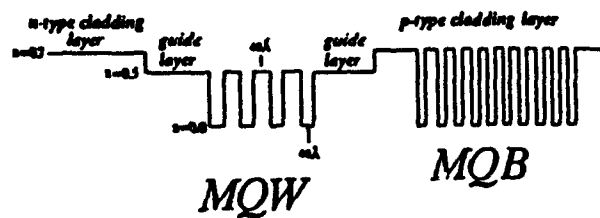


Fig.2 Schematic band diagram of the InGaAlP laser diode with MQB

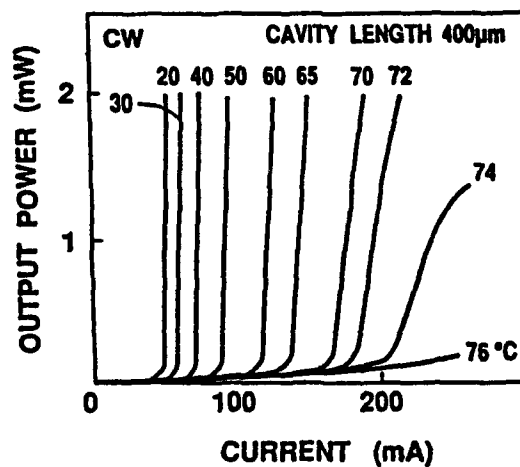


Fig.3 Dependence of I-L characteristic on temperature of the laser shown in Fig.2

**High-Performance 630-nm Band AlGaInP Strained Multiple Quantum Well Laser Diodes with a Multiquantum Barrier**

H. Hamada, M. Shono, S. Honda, K. Yodoshi, T. Yamaguchi, and T. Niina.

Semiconductor Research Center, SANYO Electric Co., Ltd.  
1-18-13 Hashiridani, Hirakata, Osaka, 573, Japan

**Summary**

630-nm band AlGaInP laser diodes are important as light sources for optical information systems such as high-density optical discs, bar-code readers, laser printers, and so on, and as a replacement for the He-Ne gas laser. Recently, highly reliable 630-nm band laser diodes have been developed by introducing a single quantum well (SQW) active layer [1], a strained multiple quantum well (S-MQW) active layer [2-3], and an S-MQW active layer with a multiquantum barrier (MQB) [4]. However, 630-nm band laser diodes with high-power, high-temperature operating characteristics and high reliability have not yet been reported. This paper reports on transverse-mode stabilized 630-nm band tensile S-MQW laser diodes incorporating an MQB. The lasers have been operating stably for more than 500 h under 20 mW at 50°C.

Epitaxial growth was carried out by a three-step low-pressure MOCVD method using n-GaAs (100) substrates with a misorientation of 9° towards the [011] direction (9° misoriented substrates).

Fig. 1 shows the schematic structure of the buried ridge stripe lasers with misoriented substrates (BRMS). The S-MQW active layer consists of a tensile strained well [ $\text{Ga}_{0.58}\text{In}_{0.42}\text{P}$ , 75 Å×5] with barriers [ $(\text{Al}_{0.5}\text{Ga}_{0.5})_{0.5}\text{In}_{0.5}\text{P}$ , 40 Å×4]. This layer was sandwiched between an optical guide layer [ $(\text{Al}_{0.5}\text{Ga}_{0.5})_{0.5}\text{In}_{0.5}\text{P}$ , 300 Å] and a cladding layer [ $(\text{Al}_{0.7}\text{Ga}_{0.3})_{0.5}\text{In}_{0.5}\text{P}$ , 1.0 μm]. The MQB structure is composed of a p- $(\text{Al}_{0.7}\text{Ga}_{0.3})_{0.5}\text{In}_{0.5}\text{P}$  first barrier (d~350 Å) and a 10-pair multi-layer with a p- $\text{Ga}_{0.5}\text{In}_{0.5}\text{P}$  well (d~11 Å) and p- $(\text{Al}_{0.7}\text{Ga}_{0.3})_{0.5}\text{In}_{0.5}\text{P}$  barrier (d~17 Å). The stripe width and cavity length of the BRMS are 4-5 μm and 700 μm, respectively. The front and rear facets were coated with a 10%  $\text{Al}_2\text{O}_3$  layer and an 80%  $\text{Al}_2\text{O}_3/\text{a-Si}$  multi-layer, respectively. The chips were mounted on a diamond heat-sink with Sn solder in a p-side down configuration.

Fig. 2 shows the current-light output power characteristics, and far-field patterns of the BRMS at room temperature (RT). A maximum light output power of 40 mW is obtained, and this is limited by catastrophic optical damage. Stable fundamental transverse-mode operation is obtained up to 20 mW (shown in the inset of Fig. 2). The threshold current is 83 mA.

Fig. 3 shows the temperature dependence of the current-light output power characteristics. The  $T_0$  value (10-45°C) is as high as 90 K. 20 mW CW operation is obtained up to 80°C, and the maximum CW operation temperature is 95°C. These values are the highest ever reported for 630-nm band laser diodes. The lasing wavelength is 636 nm under 20 mW at RT.

Fig. 4 shows the life-test results for the BRMSs under 20 mW at both 50°C and 40°C. Five devices have been operating for more than 1,500 h at 40°C, and four devices have been operating for more than 500 h at 50°C. Their reliability is the highest ever reported for 630-nm band laser diodes.

In conclusion, high-performance 630-nm band AlGaInP tensile-strained MQW laser diodes with an MQB have been successfully fabricated by low-pressure MOCVD using 9° misoriented substrates. 20 mW CW operation was obtained up to 80°C, and the maximum CW operation temperature was as high as 95°C, for laser diodes oscillating in

the 630-nm band. These laser diodes have been operating reliably for more than 500 h under 20 mW at 50°C. These results show that reliable high-power 630-nm band AlGaInP laser diodes are promising candidates for practical application to erasable high-density optical discs, optical measurement systems, and so on.

## References

- [1] S. S. Ou et al, Electron. Lett., 1993, 29, pp233-234.
- [2] A. Valster et al, Electron. Lett., 1992, 28, pp144-145.
- [3] M. Manno et al, in Tech. Dig. Int. Electron Devices Meeting, San Francisco, CA, December 1992, pp867-870.
- [4] R. Hiroyama et al, in Conf. Dig. 13th IEEE Int. Semiconductor Laser Conf., Takamatsu, Kagawa, Japan, September 1992, pp154-155.

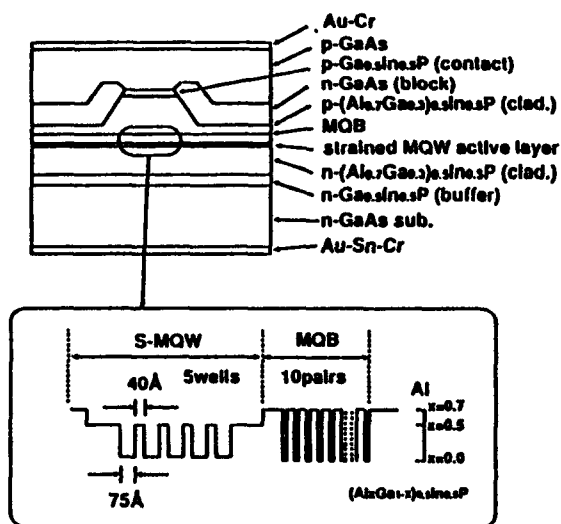


Fig. 1 Schematic structure for BRMS

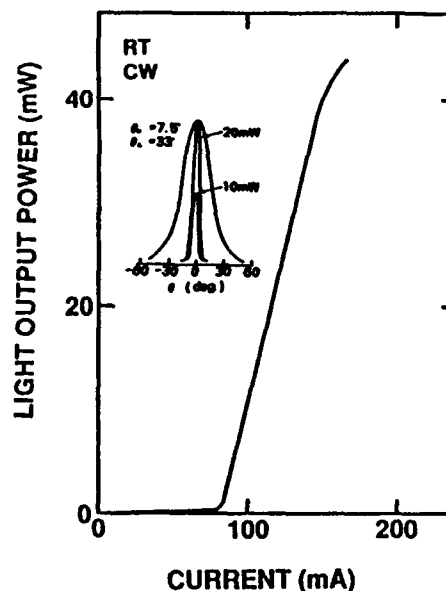


Fig. 2 Current vs. light output power, and far-field patterns

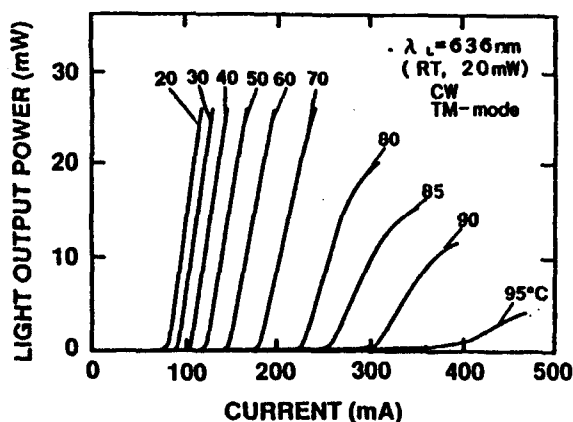


Fig. 3 Temperature dependence of current vs. light output power

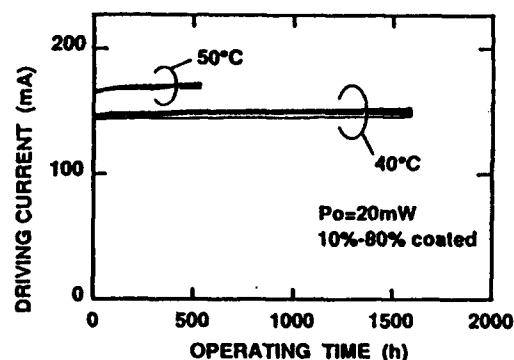


Fig. 4 Life test

## Strained AlGaInP Multiple Quantum Wire Lasers Grown by Gas Source Molecular Beam Epitaxy

P.J. Pearah, A.C. Chen, A.M. Moy, E.M. Stellini, K.C. Hsieh, and K.Y. Cheng  
Department of Electrical and Computer Engineering and Microelectronics Laboratory  
University of Illinois at Urbana-Champaign, Urbana, IL 61801

### SUMMARY

Experimental research into quantum wire (QWR) semiconductor heterostructures has been motivated primarily by theoretical predictions of performance enhancements in laser applications. The practical advantages of QWR lasers are associated with physical manifestations of the two-dimensional confinement, notably the modification to the density of electronic states. These are expected to lead to lower threshold current densities, narrower spectral linewidths, increased modulation bandwidths, and increased stability. Experimental progress, however, has been hampered by the profound technological difficulties inherent in the realization of manmade structures with such small dimensions (on the order of  $100 \text{ \AA} \times 100 \text{ \AA}$ ). Several methods involving either vicinal (slightly off-axis) or patterned substrates, or the processing of quantum well heterostructures into QWR structures have been investigated [1], but success has thus far been limited by processing defects and geometrical constraints.

We report the creation of strained AlGaInP visible laser diode heterostructures incorporating a multiple QWR (MQWR) array as the active region. The MQWR array is formed *in situ* during growth by gas source molecular epitaxy (GSMBE) on GaAs substrates. The formation of strained QWR arrays occurs spontaneously via the strain-induced lateral layer ordering (SILO) process, which produces columns of the ternary alloy  $\text{Ga}_x\text{In}_{1-x}\text{P}$  with the composition quasiperiodically modulated in the  $[110]$  direction with a periodicity of less than  $200 \text{ \AA}$ , small enough to produce the quantum size effect. By limiting the thickness of these SILO regions in the growth direction, quantization is attained in the  $[100]$  direction as well, and a MQWR array is formed. The SILO growth technique does not require any pregrowth substrate patterning or postgrowth processing, and performs optimally using standard, on-axis  $(100)$ -oriented substrates.

A strained AlGaInP/GaInP MQWR laser diode structure is shown in Figure 1. The active region is comprised of five  $120 \text{ \AA}$  thick SILO MQWR structures separated by  $\text{Ga}_{0.51}\text{In}_{0.49}\text{P}$  barriers. A lattice-matched GaInP/AlInP superlattice forms the waveguide region. The entire structure is clad by doped  $\text{Al}_{0.5}\text{In}_{0.5}\text{P}$ . Transmission electron microscopy and photoluminescence polarization spectroscopy were used to confirm the existence of the MQWR arrays [2]. Laser diode contact stripes  $60 \text{ }\mu\text{m}$  in width were defined both parallel and perpendicular to the wires. When tested under pulsed conditions at  $77\text{K}$ , the threshold current of diodes emitting in the  $[110]$  direction is  $240 \text{ A/cm}^2$ , more than a factor of 8 lower than in the  $[\bar{1}10]$  (wire) direction. The polarization of the electroluminescence is TE and TM in the  $[110]$  and  $[\bar{1}10]$  directions, respectively, depending on the direction of dominant strain. Furthermore, as can be seen in Figure 2, the emission wavelength in the wire direction is  $715 \text{ nm}$ , which is blue shifted by approximately  $14 \text{ nm}$  with respect to that in the orthogonal direction.

In conclusion, strained AlGaInP MQWR heterostructure lasers have been prepared *in situ* using GSMBE. Laser diodes fabricated from these materials exhibit emission at energies corresponding to the ground state of the strained quantum wire system. Anisotropies in the gain and emission polarization and energy are observed and explained in terms of the reduced symmetry, quantization, and strain present in the QWR system.

1. E. Kapon, Proc. of the IEEE 80, 398 (1992).
2. P.J. Pearah, E.M. Stellini, A.C. Chen, A.M. Moy, K.C. Hsieh, and K.Y. Cheng, Appl. Phys. Lett. 62, 729 (1993).

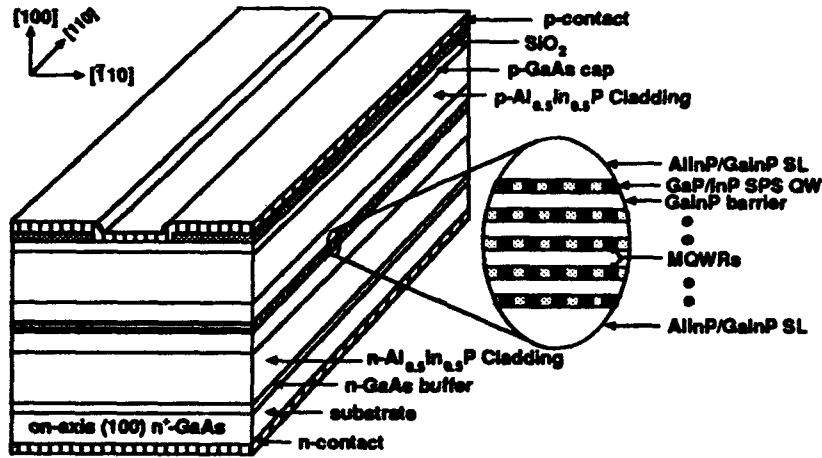


Fig. 1. Schematic illustration of the stripe geometry strained AlGaInP separate-confinement heterostructure multiple quantum wire laser on GaAs substrate. Note that the Quantum Wires run in the  $[\bar{1}10]$  direction.

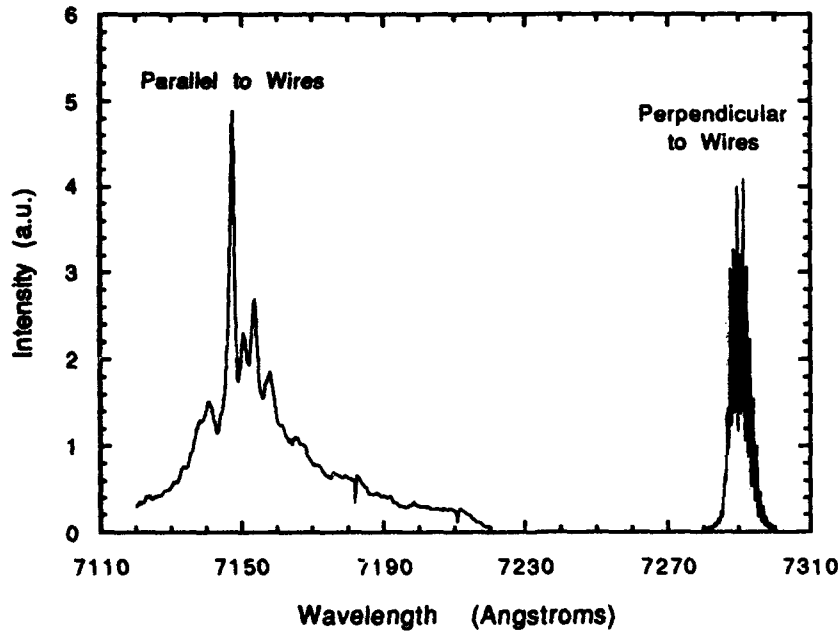


Fig. 2. The lasing mode spectra measured from edge-emitting diodes with stripes defined in the  $[110]$  and  $[\bar{1}10]$  (wire) directions at 77 K under pulsed conditions. The threshold current is 8 times lower in the  $[110]$  direction, and the emission is red-shifted by 14 nm with respect to that in the  $[\bar{1}10]$  direction.

**T2.1 10:30am - 11:00am**  
**(Invited)**

**Application of a Window Structure, MQB and Strained MQW  
to High Power Visible Lasers**

Satoshi Arimoto, Mikako Yasuda, Kaoru Kadoiwa, Akihiro Shima,  
Hitoshi Watanabe, Takeshi Kamizato, Etsuji Omura, Masao Aiga and Kenji Ikeda

Optoelectronic and Microwave Devices Laboratory,  
Mitsubishi Electric Corporation  
4-1, Mizuhara, Itami, Hyogo 664, Japan  
Tel:+81-727-84-7394, Fax:+81-727-80-2696

AlGaInP/GaInP 670nm laser diodes are developed eagerly for the next generation writing light source of high density optical disk memories. In our previous study[1], multi-quantum barrier (MQB)[2] and strained active layer were successfully incorporated to the visible laser in which the temperature characteristic was improved and high power operation over 60mW at 90°C was realized[1]. In this paper, further improvements in the life time by incorporating strained multi-quantum well (MQW) and a window structure will be presented.

We have carried out the aging test for the laser diodes prepared in our previous study, and have analyzed the data by plotting the time that has elapsed before the operating current increases by 10% as a function of initial operating current,  $I_{op}$ , for various operating conditions, as shown in Fig. 1. One can see that to realize the life time  $\sim 10^4$  hrs,  $I_{op}$  must be reduced to 70-80mA.

In order to reduce the  $I_{op}$ , the strained DQW( $n=2$  in MQW) active layer has been adopted as well as the MQB, as shown in Fig. 2. The basic structure of the rest of the laser is the same as that previously reported[1]. As a result,  $I_{op}$  has been lowered to 70-80mA at 60°C, 30mW CW.

The long term aging test at 60°C, 30mW CW has been carried out, as shown in Fig.3. No discernible degradation is found over 5,000 hours. Thus the MTTF of more than 20,000hrs has been achieved.

For higher power levels, the catastrophic optical damage becomes a serious failure mode. To prevent it, the window structure has been incorporated. For the window material, disordered GaInP[3][4][5] has been used. In order to induce disordering, solid phase Zn-diffusion from a sputtered ZnO film[6] formed at the end regions of the ridge wave guide, as shown in Fig. 4.

As a result, an excellent high power performance is realized as shown in Fig. 5. The kink level of 160mW has been obtained in contrast to the maximum power of 120mW (COD limited) for the non-window structure. In the aging test shown in Fig. 6, a stable performance at 50°C, 50mW CW operation for more than 2,500hrs has been proved.

In conclusion, by using the window structure, strained DQW and MQB, the stable 50°C, 50mW CW operation for more than 2,500hrs has been realized in AlGaInP/GaInP 670nm laser.

The authors wish to acknowledge Dr.Y.Kokubo for the helpful discussion on MQB design.

**References:**

- [1] S.Arimoto, H.Watanabe, T.Kamizato, T.Nishimura, T.Motoda, K.Kadoiwa, E.Omura, M.Aiga, K.Ikeda, and S.Mitsui; CLEO (Anaheim, 1992) Technical Digest, 12, 2-5, 1992.
- [2] K.Iga, H.Uenohara, and F.Koyama; Electron. Lett., 22, pp.1008-1010, 1986.

- [3] A.Gomyo and T.Suzuki; Phys. Rev. Lett., **60**, pp.2645-2648, 1988.  
 [4] Y.Ueno, H.Fujii, K.Kobayashi, K.Endo, A.Gomyo, K.Hara, S.Kawata, T.Yuasa, and T.Suzuki; Japan. J. Appl. Phys., **29**, pp.L1666-L1668, 1990.  
 [5] K.Itaya, M.Ishikawa, G.Hatakoshi, and U.Uematsu; IEEE J. Quantum Electron., QE-27, pp.1496-1500, 1991.  
 [6] K.Isshiki, T.Kamizato, A.Takami, A.Shima, S.Karakida, H.Matsubara, and W.Susaki; IEEE J. Quantum Electron., **26**, pp.837-842, 1990.

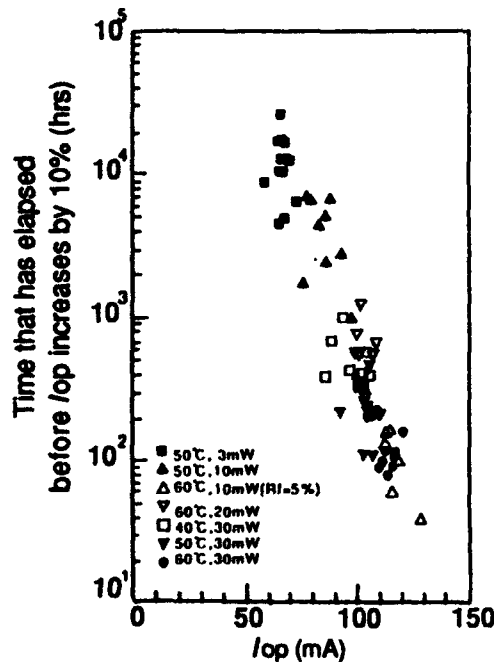


Fig. 1 Time that has elapsed before  $I_{op}$  increases by 10% v.s. initial  $I_{op}$ .  $Rf=13\%$  otherwise specified.

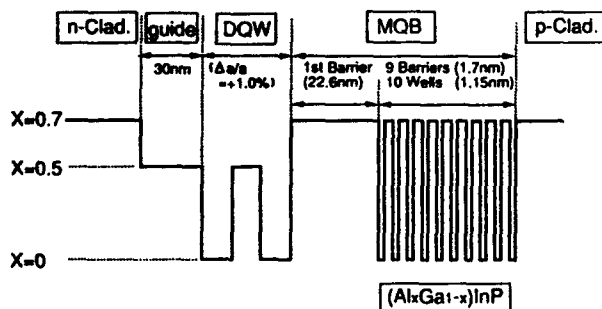


Fig. 2 Schematic diagram of epitaxially grown layers  
Width of the well in DQW is 8nm.

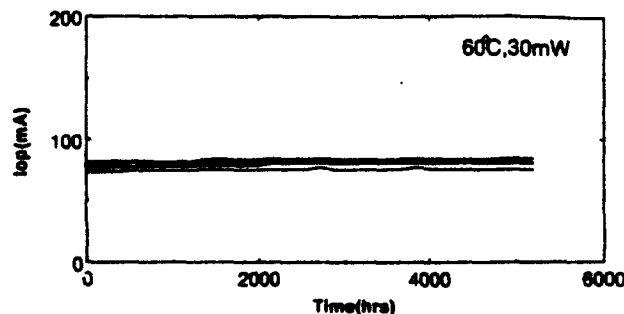


Fig. 3 Aging test of the DQW laser at 60°C, 30mW

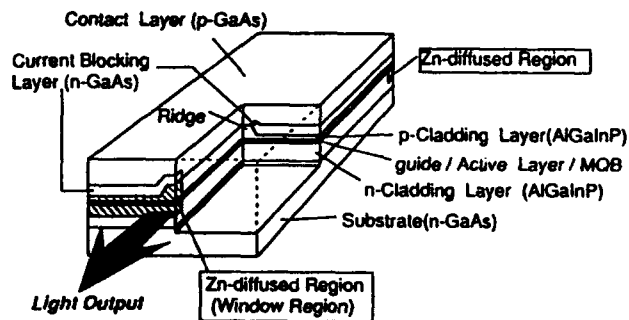


Fig. 4 Schematic drawing of the window laser structure  
Width of the well in DQW is 5nm.

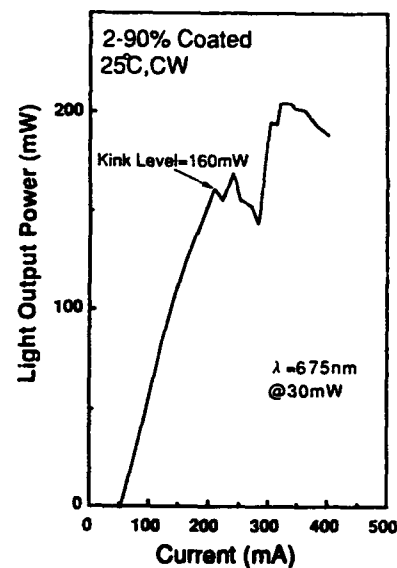


Fig. 5 P-I characteristic of the window laser  
( $Rf=2\%$ ,  $Rr=90\%$ )

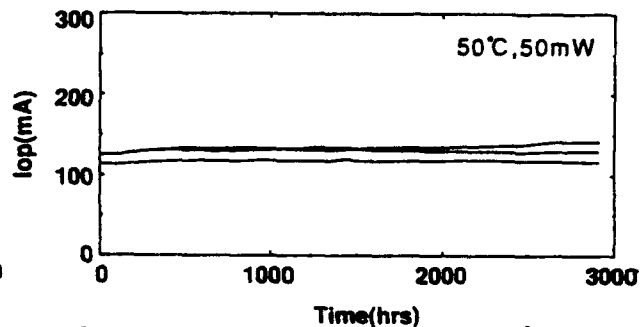


Fig. 6 Aging test of the window laser at 50°C, 50mW

## High Power, Low Threshold 630 nm Lasers

Randall S. Geels and David F. Welch  
SDL, Inc., 80 Rose Orchard Way, San Jose, CA, 95134  
Ph.: (408) 943-9411, Fax: (408) 943-9411  
David P. Bour, David W. Treat, and Ross D. Bringans  
Xerox PARC, 3333 Coyote Hill Road, Palo Alto, CA, 94304

Visible semiconductor laser diodes are receiving increasing attention for various uses. Important applications of visible semiconductor lasers include laser pointers, solid state laser pumping, printing, medicine, bar code scanning, and optical data storage. While devices emitting near 680 nm are relatively mature, there is interest in obtaining emission wavelengths in the 630 nm band. Benefits of shorter wavelength emission include increased visibility to the human eye and reduced spot size. The apparent brightness to the human eye is increased by a factor of 15 by moving from 680 nm to 630 nm. Additionally, since emission at a shorter wavelength leads to a smaller diffraction limited spot size, short wavelength semiconductor lasers will yield higher storage densities in optical data storage.

A number of groups have reported laser operation at wavelengths less than 640 nm.<sup>1,2</sup> We have previously reported threshold current densities in lasers emitting in the 630 nm band with values as low as 400 A/cm<sup>2</sup> and continuous wave (CW) output powers greater than 3 W.<sup>3</sup> We have also previously reported low threshold lasers emitting in the 630 nm band using tensile strained quantum wells.<sup>4</sup> In this paper we report low threshold, high power 630 nm band laser diodes fabricated using thin compressively strained quantum wells.

The lasers described in this work utilize epitaxial layers of AlGaInP grown by metal organic chemical vapor deposition (MOCVD). The epitaxial layers are grown lattice matched to n-type GaAs substrates. A single quantum well (QW) embedded in a separate confinement heterostructure (SCH) is used to form the active region. The QW is compressively strained In<sub>0.55</sub>Ga<sub>0.45</sub>P. Compressive strain modifies the valence band structure resulting in a reduced effective mass for holes in the quantum well. The reduced effective mass results in a lower carrier density at transparency and an increased differential gain thereby leading to a reduced threshold current. Waveguiding layers of (Al<sub>0.6</sub>Ga<sub>0.4</sub>)<sub>0.5</sub>In<sub>0.5</sub>P surround the quantum well. Cladding layers of AlInP are used to maximize the band gap and thereby maximize the band offsets at the active region and the carrier confinement.

To characterize the material broad area lasers were fabricated and tested. 100  $\mu$ m wide stripes were defined by proton implantation. Broad area lasers were tested under pulsed operation using 500 ns pulses with a repetition rate of 5 kHz. Threshold current densities as low as 390 A/cm<sup>2</sup> were measured with an emission wavelength of 639 nm. This is comparable to our results of 400 A/cm<sup>2</sup> using tensile strained quantum wells.

After verifying low threshold current densities via broad area lasers, single mode ridge lasers were fabricated. Lasers were cleaved, mounted junction side down on heatsinks, and tested uncoated under continuous wave (CW) operation. Fig. 1 shows the light current (LI) characteristics of a device with a 750  $\mu$ m cavity length at various temperatures up to 45 °C. Fig. 2 shows the threshold current and external differential quantum efficiency as a function of temperature. Between 10 and 30 °C the characteristic temperature,  $T_0$ , is 80 K and over the range from 10 to 45 °C  $T_0$ =62 K. Figure 3 shows the LI curve for the device shown in Fig. 2 up to more than 60 mW cw. The emission wavelength is 634 nm. Facet coated devices of various lengths were also fabricated with facet coatings of 12%/95%. Figure 4 shows an LI curve from a 400  $\mu$ m cavity device. A very low threshold current of 21 mA is measured with an emission wavelength of 632 nm and a slope efficiency of 0.6 W/A.

In summary, we report semiconductor laser diodes emitting output powers in excess of 60 mW cw at room temperature using an active region with a single compressively strained QW.

Threshold currents as low as 21 mA have been obtained and characteristic temperatures as high as 80 K have been measured.

## References

- <sup>1</sup>H. Hamada, M. Shono, S. Honda, R. Hiroyama, K. Matsukawa, K. Yodoshi, and T. Yamaguchi, "High-power operation of 630 nm-band transverse-mode stabilised AlGaInP laser diodes with current-blocking region near facets," *Electron. Lett.*, 1991, 27, pp. 661-662.
- <sup>2</sup>A. Valster, A. Brouwer, C.V.J. Chang, C.J. van der Poel, "Strained (Al)GaInP quantum well visible light-emitting laser diodes," CLEO '93, Baltimore, MD, paper CThQ1.
- <sup>3</sup>R.S. Geels, D.P. Bour, D.W. Treat, R.D. Bringans, D.F. Welch, and D.R. Scifres, "3 W CW, Laser Diodes Operating at 633 nm," *Electron. Lett.*, 1992, vol. 28, pp. 1043-1044.
- <sup>4</sup>R.S. Geels, D.F. Welch, D.R. Scifres, D.P. Bour, D.W. Treat, R.D. Bringans, "High power, low threshold, single mode 630 nm laser diodes," *Electron. Lett.*, 1992, vol. 28, pp. 1810-1811.

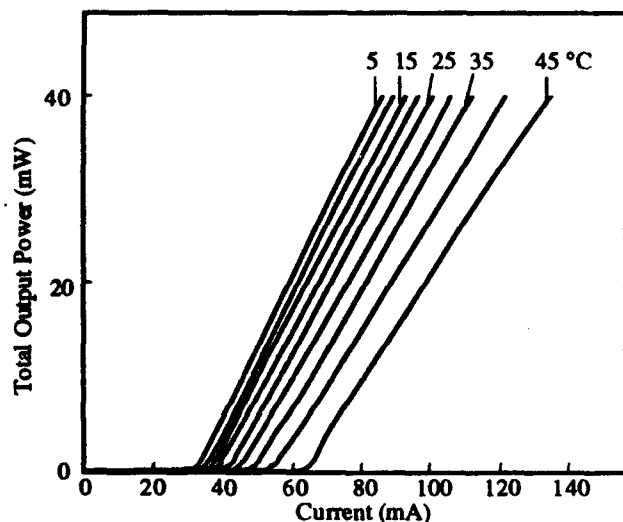


Figure 1 Light-current curves for 634 nm single mode laser vs temperature.

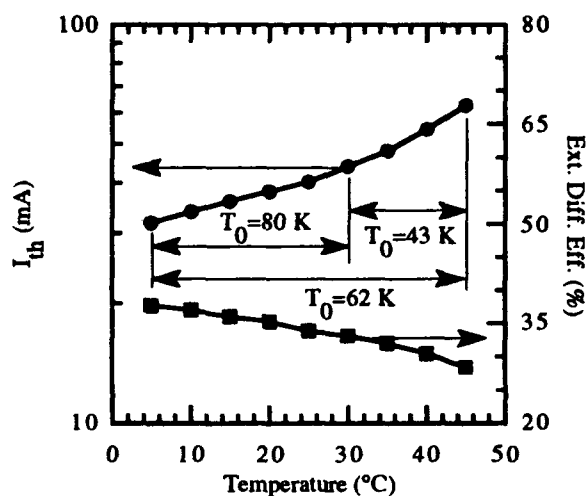


Figure 2  $I_{th}$  and  $\eta_D$  vs temperature for laser shown in Fig. 1.

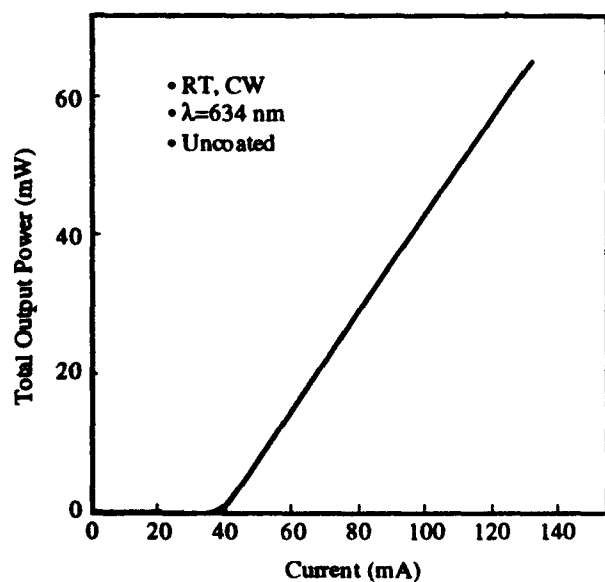


Figure 3 LI curve of 750  $\mu$ m uncoated laser.

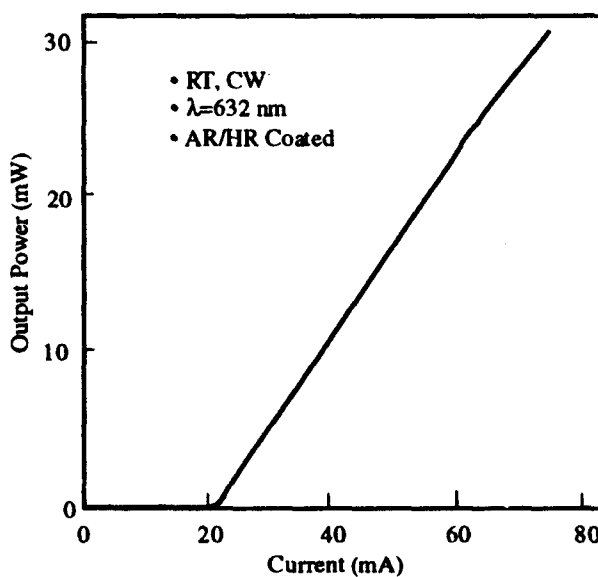


Figure 4 LI curve of 400  $\mu$ m long laser.

### Design and growth of short-wavelength InAlGaP visible vertical-cavity surface-emitting laser diodes

R. P. Schneider, Jr. and J. A. Lott  
Sandia National Laboratories  
Albuquerque, NM 87185-5800

Vertical-cavity surface-emitting laser (VCSEL) diodes offer numerous advantages over edge-emitting lasers including surface-normal output, ease of fabrication into 2-dimensional arrays, low angular divergence ( $6-10^\circ$ ), and the potential for on-wafer testing. Visible VCSEL diodes should be advantageous for applications such as plastic-fiber communications, optical data storage, scanning and 2-dimensional displays. However, while electrically injected VCSEL diodes have been demonstrated at IR wavelengths by many groups, it is only recently that electrically-injected lasing has been achieved in an InAlGaP-based visible VCSEL [1]. In the present work we describe the materials growth and device design issues leading to this demonstration, with emphasis on approaches for short-wavelength ( $\lambda \leq 650$  nm) operation.

The visible VCSELs are grown using metalorganic vapor phase epitaxy (MOVPE), and consist of an InGaP/ InAlGaP strained quantum well (SQW) active region sandwiched between AlAs/ Al<sub>0.5</sub>Ga<sub>0.5</sub>As distributed Bragg reflectors (DBRs). The optical cavity design was based on the performance of gain-guided broad-area edge-emitting laser diodes with cladding layers composed of either In<sub>0.5</sub>Al<sub>0.5</sub>P single layers or AlAs/ AlGaAs (multilayer) DBRs, the latter to simulate injection conditions present in a VCSEL. Using In<sub>0.5</sub>Al<sub>0.5</sub>P cladding layers with an optimized single SQW active region, we have measured threshold current densities of 250 A/cm<sup>2</sup> with differential quantum efficiencies of  $\sim 33-40\%$ / facet at a wavelength of 670 nm. These are among the best values reported for this wavelength. Furthermore, we have found that the threshold current density measured for structures with cladding layers composed of AlAs/ AlGaAs DBRs can be reduced substantially through incorporation of In<sub>0.5</sub>Al<sub>0.5</sub>P spacer layers. Subsequent incorporation of In<sub>0.5</sub>Al<sub>0.5</sub>P optical phase-matching spacer layers into the visible VCSEL (see Fig. 1) resulted in the first demonstration of room-temperature electrically-injected lasing, over the wavelength range 639-661 nm. Lasing spectra are given in Fig. 2. The devices exhibit a threshold current of 30 mA at a wavelength of 650 nm, with peak pulsed power output of 3.4 mW, and very low threshold voltage (2.7 V) and device resistance (15  $\Omega$ ). A light-current (L-I) characteristic for a 20  $\mu$ m-diameter device is given in Fig. 3, along with a lasing spectrum. Improved performance is expected with more sophisticated planar processing.

An additional feature afforded by this VCSEL design is the ability to tune the lasing wavelength away from the peak of the gain, or to higher-order (i.e.,  $n=2$ ) quantum well transitions, by adjusting the optical thickness of the Fabry-Perot cavity. Indeed, in these device structures lasing has been observed at wavelengths consistent with the  $n=2$  quantum well transition. This represents a novel approach to attaining short-wavelength operation in visible semiconductor lasers. Our continued efforts at shorter-wavelength operation, including the tradeoffs associated with the  $n=2$  QW transition, will be discussed.

- [1] J. A. Lott and R. P. Schneider, presented at the Quantum Optoelectronics Topical Meeting (OSA), Palm Springs, CA, 17 March 1993, paper PD-1.

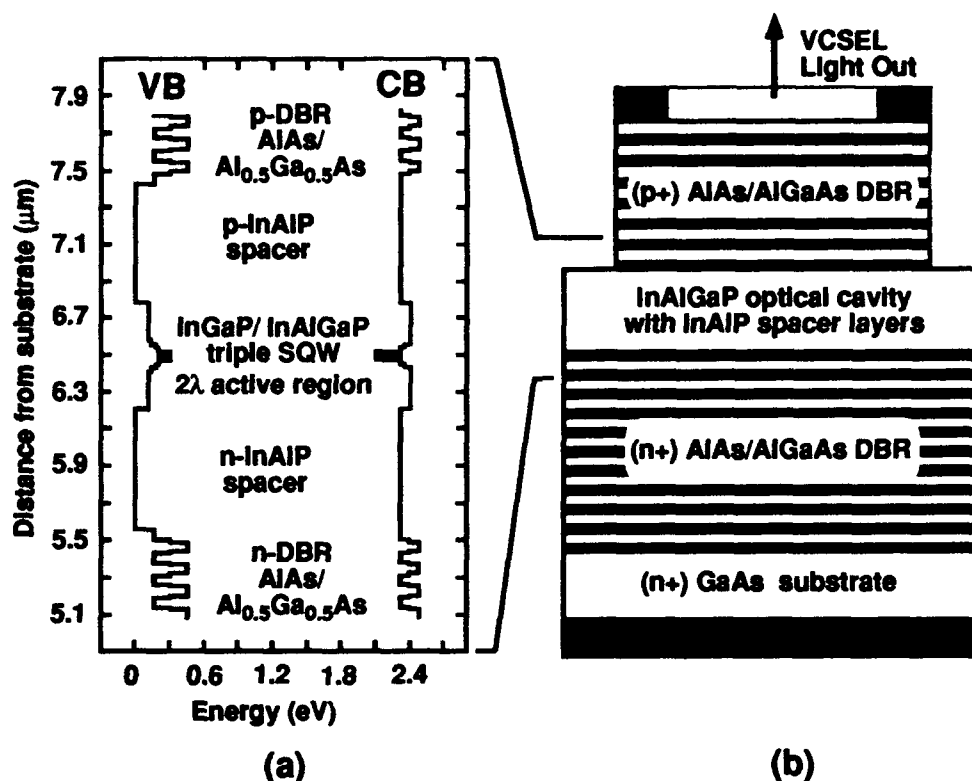


Fig. 1. (a) Real-space, charge-neutral energy band diagram for visible VCSEL optical cavity (b) Device structure schematic.

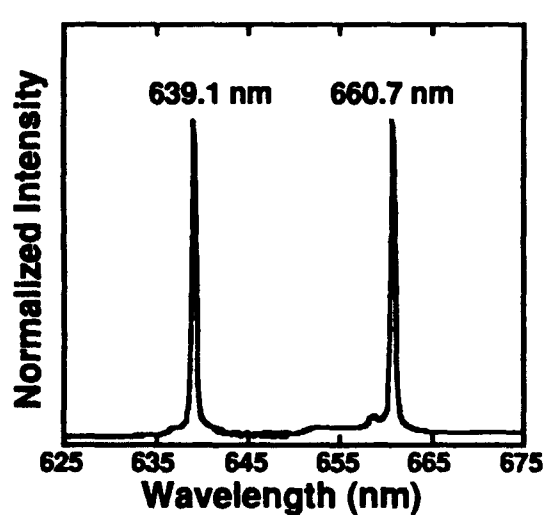


Fig. 2. 300K pulsed (100ns at 1MHz) lasing spectra obtained from visible VCSEL diodes.

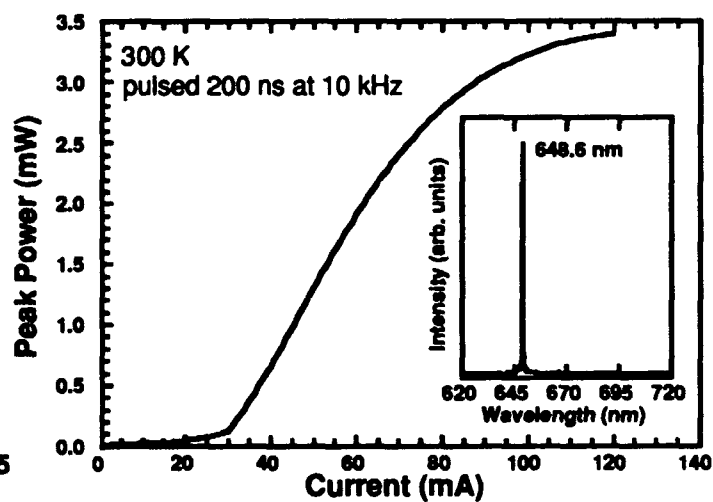


Fig. 3. Light-current (L-I) characteristic for visible VCSEL diode.

**1 W CW, 645 nm GaInP/GaAlInP broad stripe laser diodes**

S. S. Ou, J. J. Yang, and M. Jansen  
TRW, Research Center, Space and Electronics Group  
One Space Park, Redondo Beach, California, 90278

**Abstract**

CW output powers exceeding 1W at room temperature from GaInP/GaAlInP 50- $\mu$ m-wide stripe broad laser diodes with an emission wavelength of 645 nm are reported. An interesting dependence of threshold current density and wavelength on device stripe width is observed.

**Summary**

High-power GaInP/GaAlInP visible laser diodes operating at 630-650 nm band wavelength are promising for various applications such as optical pumping of tunable solid-state lasers, medical radiation sources, high definition displays and high-speed printers. Recently, Geels et al. demonstrated CW power output of 900 mW for 100  $\mu$ m wide stripe laser ( $\lambda=633$  nm) which incorporate a tensile strained single quantum well heterostructure.<sup>1</sup> Serreze et al. demonstrated CW output power of 1W for 60- $\mu$ m-wide compressively strained lasers with emission wavelength of 670 nm at 10°C.<sup>2</sup> However, high power CW operation with emission wavelength < 670nm with compressively strained quantum well laser diodes has not been reported.

The devices used in these experiments consisted of double quantum well graded-index separate confinement (DQW-GRINSCH) structures grown on a n-type (100) 2° off toward (110) GaAs substrate by a low pressure metalorganic chemical vapor deposition (MOCVD). The active region consists of two 40 Å thick  $\text{Ga}_{0.45}\text{In}_{0.55}\text{P}$  wells separated by a 100 Å thick  $(\text{Al}_{0.6}\text{Ga}_{0.4})_{0.5}\text{In}_{0.5}\text{P}$  barrier layer and are sandwiched between 1000 Å lightly doped linearly graded AlGaInP GRINSCH layers. Schottky restricted broad area lasers with different stripe widths were fabricated by using wet chemical etching to define the ridge structures. Lasers were mounted junction-down onto Cu-blocks for CW operation.

Fig. 1 shows the threshold current density versus stripe width for different cavity length. Although the threshold current decreases with stripe width decreases, the threshold current density decreases as width increases from 10  $\mu$ m to 50  $\mu$ m and then increases as width increases from 50  $\mu$ m to 100  $\mu$ m. The threshold current (and thus threshold current density) in conventional GaAs/GaAlAs and GaInAsP/InP quantum well laser diodes can raise rapidly as the width of the stripe narrows down to one micron; usually, as the stripe-width increases, the threshold current density decreases and then levels down. However, in GaInP/GaAlInP laser diodes, the threshold current density increases rapidly as stripe width > 50  $\mu$ m and < 20  $\mu$ m. The threshold current density increase for stripe widths of < 20  $\mu$ m is probably due to leakage current. However, the mechanism behind the threshold current density increases for stripe widths of > 50  $\mu$ m is not clear at this moment. Fig. 2 shows the emission wavelength versus stripe width for different cavity lengths. The wavelength shift corresponds to threshold current density change, except in 100- $\mu$ m-wide devices. It should be noted that this anomalous behavior has also been observed in lattice-matched and tensile-strained devices grown on standard or misoriented (100) GaAs substrate fabricated in our laboratory.

Since the output power of quantum well is a function of threshold current density and differential quantum efficiency, by properly selecting the stripe width and cavity length, we can achieve maximum CW operation. Fig. 3 shows output power versus current characteristics of

50  $\mu\text{m}$  x 1000  $\mu\text{m}$  devices. The threshold current is 400 mA, the differential quantum efficiency is 41% and the output power is > 1W at room temperature with an emission wavelength of ~ 645nm. To the best of our knowledge, this is the highest output power from compressively strained GaInP/GaAlInP laser diodes with wavelength <650 nm. The optical power density of 20 mW per  $\mu\text{m}$  ridge width is the highest reported to date for GaInP/GaAlInP laser diodes with wavelength < 650nm.

This type of devices have operated for > 1000 hrs at room temperature at 250 mW of CW constant power. Because the increase of drive current for 250 mW CW operation is ~  $5 \times 10^{-5} \text{ hr}^{-1}$ , we extrapolate this to lifetimes in excess of 10000 hrs.

In conclusion, we have demonstrated >1W CW operation from DQW-GRINSCH compressively-strained GaInP/GaAlInP laser diodes with emission wavelengths of ~645nm.

This work was partially supported by the US Air Force Phillips Laboratory.

1. R.S. Geels, D. P. Blur, D. W. Treat, R. D. Bringans, D. F. Welch and D. R. Scifres, *Electron. Lett.*, 28, 1043, 1992
2. H. B. W. Serreze, C. M. Harding, and R. G. Water, *Electron. Lett.*, 27, 2245, 1991

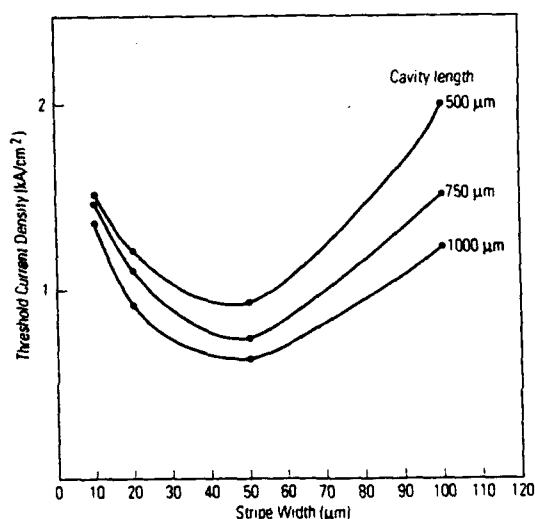


Fig. 1 Threshold current density vs. stripe width

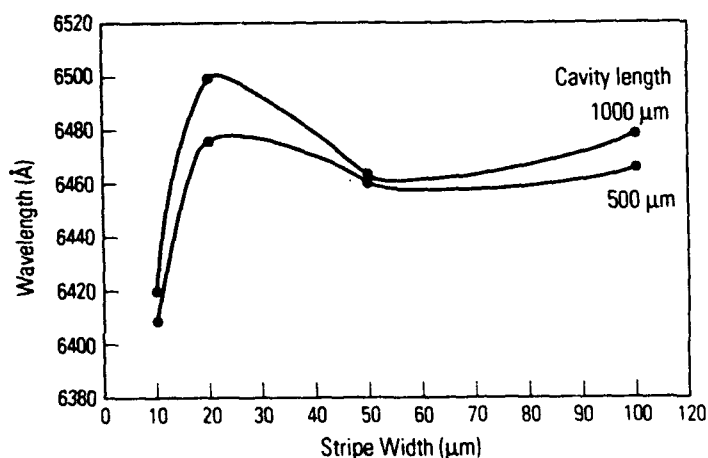


Fig. 2 Emission wavelength vs. stripe width

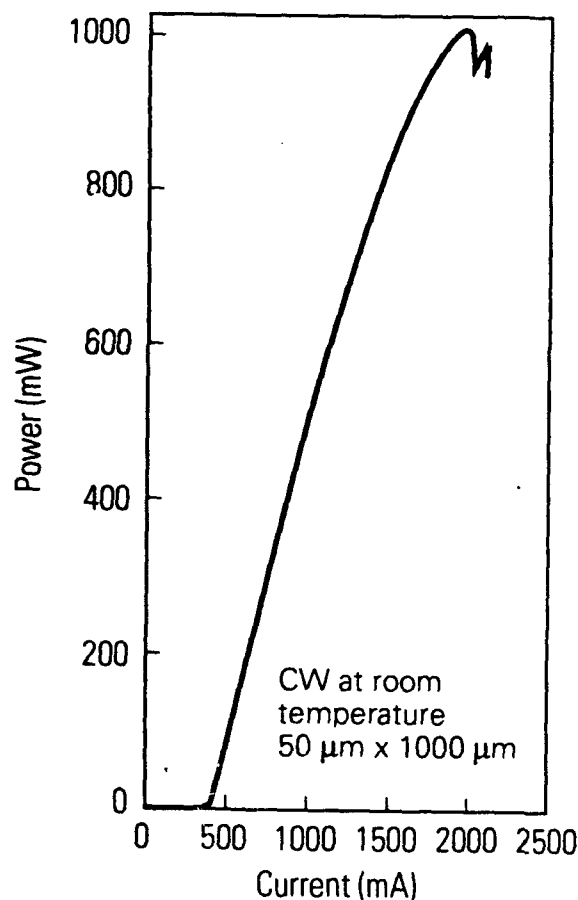


Fig. 3 CW L-I of GaInP/GaAlInP laser diodes

## **High-Power Operation of Self-Aligned Stepped Substrate (S<sup>3</sup>) AlGaInP Visible Laser Diode**

**M. Sugano, Y. Kito, A. Furuya, F. Fukushima, H. Sudo, C. Anayama, M. Kondo, and  
T. Tanahashi**

**Fujitsu Laboratories Ltd.,  
10-1 Morinosato-Wakamiya, Atsugi 243-01, Japan**

Recently, we reported an index-guided GaInP/AlGaInP visible laser grown by one-step MOVPE (Fig. 1)<sup>1)</sup>. This self-aligned stepped substrate (S<sup>3</sup>) laser is easy to fabricate and is expected to have a small astigmatism due to its real-index guided structure. For optical information processing applications, such as rewritable optical disks, lasers must have a high output power and good beam characteristics. In this work, we demonstrate high-power operation and excellent beam characteristics of the S<sup>3</sup> laser.

The S<sup>3</sup> laser structure, including a simultaneously n- and p-type doped lateral p-n junction on a stepped patterned GaAs substrate, can be grown by one-step MOVPE. We used (311)A inclined faces 3.5  $\mu\text{m}$  wide as the stepped substrate. The samples had a cavity 700  $\mu\text{m}$  long and AR (12%) and HR (95%) facet coatings.

Since catastrophic optical damage (COD) limits the AlGaInP laser's output power, we decreased the optical confinement factor to reduce the photon density in the active layer. We changed the optical confinement factor by increasing the guide layer thickness from 5 to 80 nm. We used multiple quantum well (MQW) active layer with a GaInP well layer of 0.75% compressive strain to compensate for the deterioration of the I-L characteristics caused by decreasing the optical confinement factor. The COD power increased as the optical confinement factor decreased (Fig. 2).

We measured the dependence of the MQW S<sup>3</sup> laser's output power on current with an optical confinement factor of 4.2% (Fig. 3). The COD power increased to 70 mW and we obtained kink-free operation up to 55 mW with a threshold current of 50 mA. The lasing wavelength was 670 nm. The beam astigmatism was independent of the output power and less than 1  $\mu\text{m}$  (Fig. 4). This is much smaller than the astigmatism obtained with a conventional loss-guided laser. The fundamental transverse mode was stable up to 40 mW (Fig. 5). The beam divergence parallel to the inclined junction plane was 8° and perpendicular to it was 17°. The aspect ratio was 2.1.

We conducted a preliminary aging test at 50°C and 20 mW APC and did not observe appreciable degradation over 1000 hours.

We obtained a COD power of 70 mW with an AlGaInP S<sup>3</sup> laser diode by decreasing of the optical confinement factor. The beam astigmatism was less than 1  $\mu\text{m}$  and the beam aspect ratio was 2.1.

### **References**

- 1) C. Anayama et.al., Extended Abstracts, SSDM, p. 619 (1992)

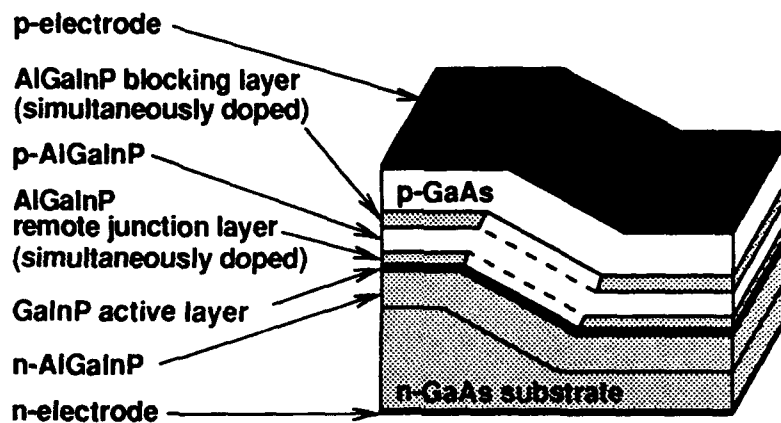


Fig. 1 S<sup>3</sup> laser

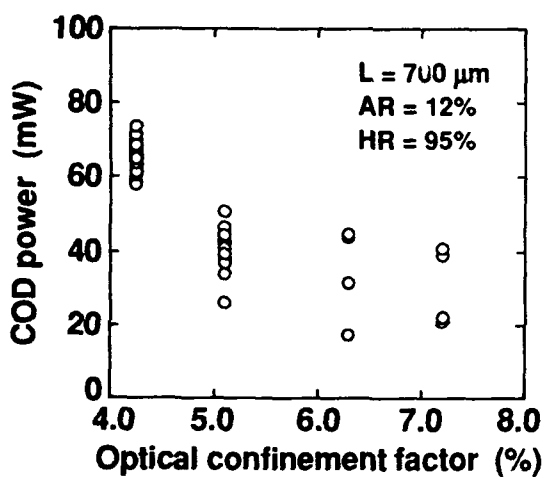


Fig. 2 Dependence of COD power on the optical confinement factor

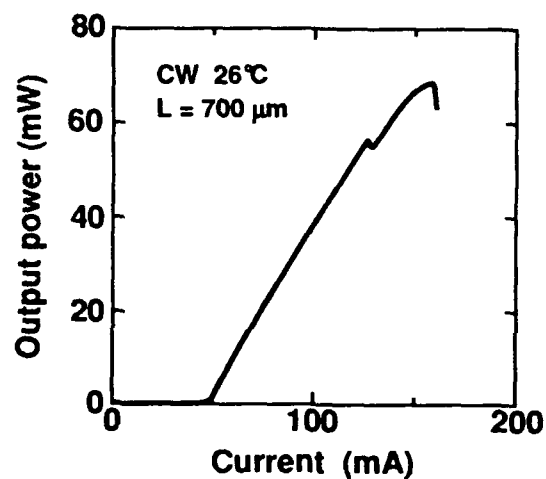


Fig. 3 I-L characteristics

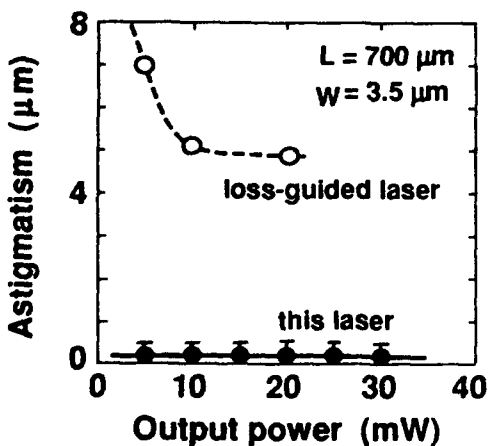


Fig. 4 Dependence of beam astigmatism on the output power

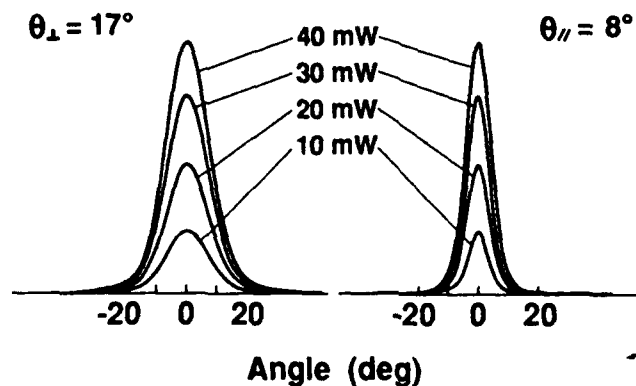


Fig. 5 Far-field pattern

M. Aiga .....	31
I. Akasaki .....	14
H. Amano .....	14
C. Anayama .....	39
S. Arimoto .....	31
A. Bhattarai .....	21
D. Bour .....	3, 33
R. Bringans .....	3, 33
Y. Cai .....	11
C. Carter .....	16
A. Chen .....	29
K. Cheng .....	29
D. DeFevers .....	13
V. Dmitriev .....	16
J. Edmond .....	16
R. Engelmann .....	11
R. Fletcher .....	13
F. Fukushima .....	39

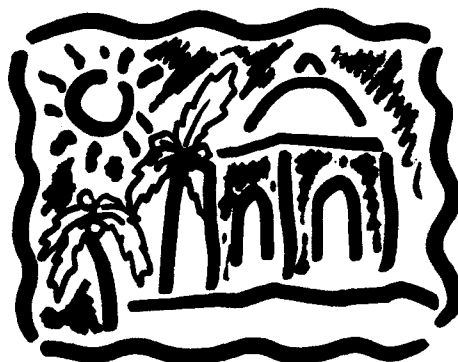
A. Furuya .....	39
R. Geels .....	3, 33
R. Gunshor .....	5
H. Hamada .....	27
G. Hatakoshi .....	25
S. Honda .....	27
K. Hsieh .....	29
K. Ikeda .....	31
K. Itaya .....	25
M. Jansen .....	37
K. Kadohwa .....	31
T. Kamizato .....	31
A. Khan .....	21
F. Kish .....	13
Y. Kito .....	39
R. Kolbas .....	19
M. Kondo .....	39
H. Kong .....	16

S. Krishnankutty .....	19
C. Kuo .....	13
J. Kusnia .....	21
J. Lott .....	35
A. Moy .....	29
T. Niina .....	27
A. Nurmikko .....	5, 18
D. Olego .....	9
D. Olson .....	21
E. Omura .....	31
T. Osentowski .....	13
N. Otsuka .....	5
S. Ou .....	37
R. Park .....	6
M. Peanasky .....	13
P. Pearah .....	29
J. Rennie .....	25
J. Schetzina .....	8

R. Schneider .....	35
A. Shima .....	31
M. Shono .....	27
D. Steigerwald .....	13
E. Stellini .....	29
H. Sudo .....	39
M. Sugano .....	39
T. Tanahashi .....	39
D. Treat .....	3, 33
H. Watanabe .....	31
D. Welch .....	3, 33
T. Yamaguchi .....	27
J. Yang .....	37
M. Yasuda .....	31
K. Yodoshi .....	27
J. Yu .....	13

# **Impact of Fiber Nonlinearities on Lightwave Systems**

**July 26-27, 1993**  
**Fess Parker's Red Lion Inn Resort**  
**Santa Barbara, California**



**Sponsored by**  
**the IEEE Lasers and Electro-Optics Society**

**IEEE Catalog Number: 93TH0549-6**  
**Library of Congress Number: 93-77778**

The papers in this book comprise the digest of the meeting mentioned on the cover and title page. They reflect the authors' opinions and are published as presented and without change, in the interest of timely dissemination. Their inclusion in this publication does not necessarily constitute the endorsement by the editors, the Institute of Electrical and Electronics Engineers, Inc.

Copyright and reprint permissions: Abstracting is permitted with credit to the source. Libraries are permitted to photocopy beyond the limits of the U.S. copyright law for private use of patrons those articles in this volume. Instructors are permitted to photocopy isolated articles for noncommercial classroom use without fee. For other copying reprint or republication permission, write to Director, Publishing Services, IEEE, 345 E. 47th St., New York, NY 10017. All rights reserved. Copyright ©1993 by the Institute of Electrical and Electronics Engineers, Inc.

IEEE Catalog Number:	93TH0549-6
ISBN Number: Softbound	0-7803-1284-8
Microfiche Edition:	0-7803-1285-6
Library of Congress Number:	93-77778

## Impact of Fiber Nonlinearities on Lightwave Systems Technical Committee

### Chairman

A.R. Chraplyvy  
*AT&T Bell Laboratories*

### Co-Chairs

N. Doran  
*EE and Applied Physics  
Aston University*

S. Saito  
*NTT Transmission  
Laboratories*

R.W. Tkach  
*AT&T Bell Laboratories*

### Program Committee

G. Agrawal  
*University of Rochester*

N. Bergano  
*AT&T Bell Laboratories*

K. Emura  
*NEC Corporation*

W. Heinlein  
*Universitat Kaiserslautern*

N. Shibata  
*NTT Transmission  
Laboratories*

S. Wabnitz  
*Fondazione Ugo  
Bordoni*

J.V. Wright  
*BT Laboratories*

S. Yamamoto  
*KDD R&D Laboratories*

## MONDAY, JULY 26, 1993

<b>M1:</b>	<b>ULTRALONG-DISTANCE SYSTEMS I</b>	
M 1.1.	Fiber Nonlinearities in Soliton Transmission .....	3
M 1.2	Soliton Propagation on Standard Monomode Fibers with Lumped Amplifiers: Basic Features and Performance Analysis .....	5
M1.3	A BT View of Nonlinear Effects in Long-Haul Systems .....	7
M1.4	Nonlinear Effects in Transoceanic Transmission Systems .....	9
M1.5	Nonlinearly Induced Chromatic Dispersion Compensation in Long Haul Fiber Links .....	11
<b>M2:</b>	<b>ULTRALONG-DISTANCE SYSTEMS II</b>	
M2.1	Experiments and Numerical Simulations of Nonlinear Effects in Long Distance Transmission .....	13
M2.2	Impact of Self-Phase Modulation on 10-Gb/s Systems using Conventional Single-Mode Fiber .....	15
M2.3	Performance Evaluation of Optical Systems in the Presence of Nonlinear Kerr Effect .....	17
M2.4	Design of Amplified Transoceanic Systems By Numerical Simulation .....	19

## TUESDAY, JULY 27, 1993

<b>T1:</b>	<b>WDM &amp; SBS</b>	
T1.1	Four-Photon Mixing Effects .....	23
T1.2	Statistical Distribution of Four-Wave Mixing Interference in ASK Optical WDM Systems .....	25
T1.3	Impact of Four Wave Mixing on Optical FSK WDM Communication Systems .....	27
T1.4	Power Limitations Due to Four-Wave Mixing Depletion in WDM Systems with Unequally Spaced Channels .....	29
T1.5	What is the Actual Capacity of Single-Mode Fibers in Amplified Lightwave Systems? .....	31
T1.6	Stimulated Brillouin Threshold Dependence on the Mark Density of a Phase Modulated Optical Signal .....	33
<b>LPS:</b>	<b>LATE PAPER SESSION</b>	
LPS1.1	Dispersion Limit Improvement of FM/IM Signals by Self-Phase Modulation .....	35
LPS1.2	2dB Reduction of Transmission Penalty by Self-Phase Modulation in a 5 Gbit/s FM/AM Conversion System Experiment .....	37
LPS1.3	Interplay Between Dispersion and Self-Phase Modulation .....	39
LPS1.4	Transmission Distance of In-Line Amplifier Systems with Group-Velocity-Dispersion Compensation .....	41
LPS1.5	Nonlinear Interaction of Signal and Noise in Lightwave Systems at the Zero-Dispersion Wavelength .....	43
LPS1.6	Nonlinear Effects on Two-Channel Long Distance Optical Fiber Systems .....	44
<b>Author Index .....</b>		<b>46</b>

**Monday, July 26, 1993**

**Sessions:**

**M1: Ultralong-Distance Systems I**

**M2: Ultralong-Distance Systems II**



## **Fiber Nonlinearities in Soliton Transmission**

**L. F. Mollenauer  
AT&T Bell Laboratories  
Holmdel, NJ 07733**

### *Summary*

The soliton owes its very existence to fiber nonlinearity. As a pulse self-trapped in time, it is able to resist a great many effects, such as chromatic dispersion and polarization dispersion, that are highly destructive of ordinary ("linear") pulses. It is extremely robust in this regard. The transmission line picks the soliton out of whatever reasonable pulse is launched into it, and discards the residue as dispersive wave radiation. In a line with amplifiers, the soliton tends to propagate stably over an indefinitely long distance.

For the soliton in a broad-band transmission line, however, one optical frequency is as good as another. This indifference to optical frequency makes it relatively easy for spontaneous emission, by way of the nonlinear term, to change the soliton's frequency, and hence to change its velocity. The resultant random spread in pulse arrival times, known as the Gordon-Haus effect [1], tends to limit the maximum allowable bit-rate for error-free transmission.

In WDM [2], solitons of a higher frequency channel gradually overtake and pass through those of a lower frequency channel. During such soliton-soliton collisions, the pulses interact through the nonlinear term, but the interaction is largely benign. That is, in a lossless fiber, or in one in which the amplifier spacing is short enough with respect to the collision length, solitons emerge from such collisions with shape, spectrum, and velocity unchanged; four-wave mixing components that make a temporary appearance during the collision are reabsorbed. The only net effect of the collision is a small time displacement of each of the two solitons. These time displacements can add significantly to the rate-limiting jitter, however.

The jitter, whether from the Gordon-Haus effect, from WDM collisions, or from any other cause, can be reduced by restricting the bandwidth of the transmission line [3,4]. In practice this means using narrow band filters, typically one per amplifier, and it is furthermore preferred to use etalons, whose multiple orders allow for WDM. Once again, however, the fiber nonlinearity plays a vital and beneficent role. That is, through the action of the non-linear term, the solitons can continuously replenish those spectral components that the filters tend to reduce. [The long chain of narrow-band filters would be highly dispersive to linear pulses.]

The only problem with a scheme using fixed-frequency filters is that extra gain is required from the amplifiers to overcome the loss the solitons experience from passage through the filters. As a result, noise at or near the filter peaks rises exponentially with distance. To keep that rise under control, the filters can be made only so strong, and thus their ability to reduce jitter is limited. An effective way out of that dilemma, however, is

to "slide", i.e. translate, the peak frequency of the filters with distance along the transmission line [5]. As long as the sliding is gradual enough, the solitons will follow, in accord with the same "guiding" principle that dampens the jitter. On the other hand, the noise, being essentially linear stuff, must remain in its original frequency band. Thus, one creates a transmission line that is opaque to noise for all but a small, final fraction of its length, yet remains transparent to solitons. In consequence, the filters can be made many times stronger, and the jitter reduced by a correspondingly large factor, with the final result that the maximum bit rate can be increased at least several fold over that possible without sliding. At the time of this writing, error free transmission of 10 Gbit/s, single channel, and at 20 Gbit/s, in a two-channel WDM, has been demonstrated over much greater than trans-oceanic distances [6]. This result is considered just a beginning, however. Much higher rates and more extensive WDM are expected in the near future.

The sliding-frequency guiding filters provide a number of other benefits as well. They tend to clean up noise fields from all sources, and not just those from spontaneous emission. Thus, for example, dispersive wave radiation from imperfect input pulses and from reaction of the solitons to polarization dispersion becomes much less of a problem. They eliminate the time displacements from soliton-soliton collisions in WDM. They even act to equalize the signal levels among WDM channels, in spite of significant differences in small signal gains. Once again, these benefits would not be possible were it not for the fiber's nonlinearity.

#### REFERENCES

- [1] J. P. Gordon and H. A. Haus, "Random walk of coherently amplified solitons in optical fiber," *Opt. Lett.* **11**, 665 (1986)
- [2] L. F. Mollenauer, S. G. Evangelides, and J. P. Gordon, "Wavelength Division Multiplexing with Solitons in Ultra Long Distance Transmission Using Lumped Amplifiers," *J. Lightwave Technol.* **9**, 362 (1991)
- [3] A. Mecozzi, J. D. Moores, H. A. Haus, and Y. Lai, "Soliton transmission control," *Opt. Lett.* **16**, 1841 (1991)
- [4] Y. Kodama and A. Hasegawa, "Generation of Asymptotically Stable Optical Solitons and Suppression of the Gordon-Haus Effect," *Opt. Lett.* **17**, 31 (1992)
- [5] L. F. Mollenauer, J. P. Gordon, and S. G. Evangelides, "The sliding-frequency guiding filter: an improved form of soliton jitter control," *Opt. Lett.* **17**, 1575 (1992)
- [6] L. F. Mollenauer, E. Lichtman, M. J. Neubelt, and G. T. Harvey, "Demonstration, using sliding-frequency guiding filters, of error-free soliton transmission over more than 20,000 km at 10 Gbit/s, single-channel, and over more than 13,000 km at 20 Gbit/s in a two-channel WDM," *Electron. Lett.* **29**, 910 (1993)

## **SOLITON PROPAGATION ON STANDARD MONOMODE FIBERS WITH LUMPED AMPLIFIERS: BASIC FEATURES AND PERFORMANCE ANALYSIS**

A. Mattheus, Telekom, FTZ, Am Kavalleriesand 3, D-64295 Darmstadt, Germany  
M. Artiglia, F.Sartori, CSELT-TO/FD, Via G. Reiss Romoli, 274, I-10148 Torino, Italy  
P. Crahay, E.Jaunart, Faculte Polytechnique de Mons, Boulevard Dolez, 31, B-7000 MONS, Belgium  
I.Gabitov, Landau-Institute for Theoretical Physics, Kosygina street 2, V 334, Moscow, Russia  
M.Midrio, University of Padova, Via G. Gradenigo 6/A, 35131 Padova, Italy  
M.Romagnoli, S.Wabnitz, Fondazione Ugo Bordoni, Via B. Castiglione 59, 00142, Roma, Italy  
C.Schmidt-Hattenberger, Friedrich-Schiller University, Max-Wien Platz 1, D-07743 Jena, Germany  
S.Turitsyn, University Düsseldorf, Universitätsstr. 1, D-40225 Düsseldorf, Germany

### **I. INTRODUCTION**

In optical soliton transmission systems the group velocity dispersion of a fiber is balanced with its nonlinearity, thus enabling ultra long pulse propagation without significant degradation. However, most of the very successful research work has been carried out on dispersion minimized transmission lines. The question has not been answered if solitons are well-suited for multigigabit-per-second data transmission in existing optical networks based on standard monomode fibers (SMF). This problem is very important for trunk network application in Europe. This paper presents results of research activity in this field done within SG2/WG2 of the COST 241 project.

### **II. SYSTEM ARCHITECTURE AND PRACTICAL CONSTRAINTS**

The system architecture is adapted to practical constraints of the existing network structure in Europe and is roughly indicated on fig.1. The following assumptions are made: The transmission line consists of a chain of SMFs with lumped optical amplifiers. Relative phase shifts between neighboring pulses of the width  $t_h$  can be introduced, as well as optical filters within the repeater amplifiers. In Europe, repeater amplifier spacings  $z_r$  range from 20 km to 60 km. Due to the commercially available EDFAs 1550 nm laser emission is assumed. However, the high chromatic dispersion of SMFs at this wavelength ( $D = 17$  ps/(nm\*km)) results in a small soliton period  $z_{sol}$ . For bit-rates above 5 Gbit/s it is impossible to satisfy two conditions simultaneously, namely  $q := z_r / z_{sol} < 1$  and  $p := t_{bit} / t_h(z=0) > 5/1$ , but according to our investigations, even then use of the solitons as potential carriers of information is still possible.

### **III. RESULTS**

#### **1. Single Pulse Propagation on Standard Monomode Fibers**

If the total distance is less than 300 km, then the single pulse of the width 35 ps is only slightly broadened even for  $q \geq 2$  ( $z_r \geq 56$  km) /2/. However, for longer distances, (say 2800 km) resonances lead to the destruction of a single pulse. In this case we found that the method of sliding filters, that was originally proposed in order to separate solitons from the amplifier spontaneous emission noise in transoceanic transmissions /3,4/, is also very effective in stabilizing soliton pulses against resonance effects, because the resonant radiation is separated in time and in frequency from the soliton. The complex transfer function of the filters reads  $H(\omega - \omega_l) = 1/(1 + 2i(\omega - \omega_l)/B)$ . In the specific example reported here, the separation between amplifiers is two times the soliton period (or 56 km), the fiber loss is 0.24 dB/km, the center frequency of the filters is  $\omega_l = -\beta Z/3 = -0.02Z$ , where  $\beta = 2/(B^2 z_r)$  with the repeater spacing  $z_r$  and the distance  $Z$  in normalized units resp..

#### **2. Pulse Sequence on Standard Monomode Fibers**

Pulse sequences including amplitude and time jitter have been calculated to study the behavior up to 10 GBit/s data transmission on SMFs with given repeater amplifier spacings. A typical example revealing resonance behavior and soliton interaction forces /5,6/ is shown in fig.1. The following set of parameters was chosen:  $B = 10$  GBit/s,  $z_r = 24$  km,  $z_{tot} = 168$  km,  $P_0 = 95$  mW,  $\gamma = 0.2$  dB/km,  $t_h = 32$  ps,  $z_{sol} = 23.9$  km. The bit pattern is "111010011". All initial phases are equal to zero. The regular pulse separation is 100 ps except for the first two pulses (90 ps). Consequently their overlapping and interaction forces are increased. After 6 amplification periods a collision is observed. However, splitting into the initial two pulses appears behind the seventh optical amplifier. We obtained essential reduction of overlapping by introducing a phase shift between neighboring pulses. For a given system architecture with fixed parameters there are optimal values of pulse width and phase shift. As an example, noticeable reduction of soliton pair interaction is observed with alter-

nating phases (180 degree, see fig.2). However, the best choice for that system is  $t_h = 25$ ps and 90 degree phase shift /7/. We have also considered the interaction between adjacent soliton pulses and sliding filters /8/ (see fig. 3). We found that, even in the near-resonance case, these interactions may be effectively suppressed over the whole distance of 2800 km by the filters whenever the pulse width is equal to (or longer than) 49 ps, and the pulse separation  $T_1$  is at least five times the pulse width  $t_h$ .

## ACKNOWLEDGEMENT

The authors are indebted to Prof. E.A.Kuznetsov for valuable advices.

## REFERENCES

- /1/ L.F.Mollenauer, S.Evangelides, and H.A.Haus, J. Lightwave Technol., 9, 194-197(1991)
- /2/ A.Mattheus, report 1300.1 for RACE 2011, June 1992
- /3/ L.F.Mollenauer, J.P.Gordon, and S.G.Evangelides, Opt. Lett. 17, p.1575 (1992)
- /4/ M.Nakazawa, and H.Kubota, Electron. Lett. 28, 958 (1992)
- /5/ K.J.Blow and N.J.Doran, Electron. Lett., 1983, 19, pp. 429-430(1983)
- /6/ J.P.Gordon, Opt. Lett. 11, pp. 596-598(1983)
- /7/ S.Turitsyn, A.Mattheus, to be published
- /8/ Y. Kodama, and S. Wabnitz, Opt. Lett. (in press, 1993)

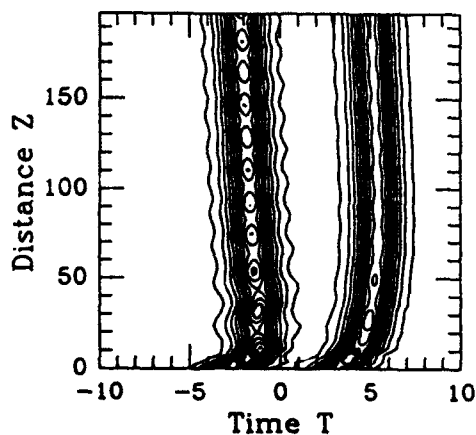


Fig. 3: Suppression of interaction forces with sliding filters and  $T_1/t_h = 3.4$

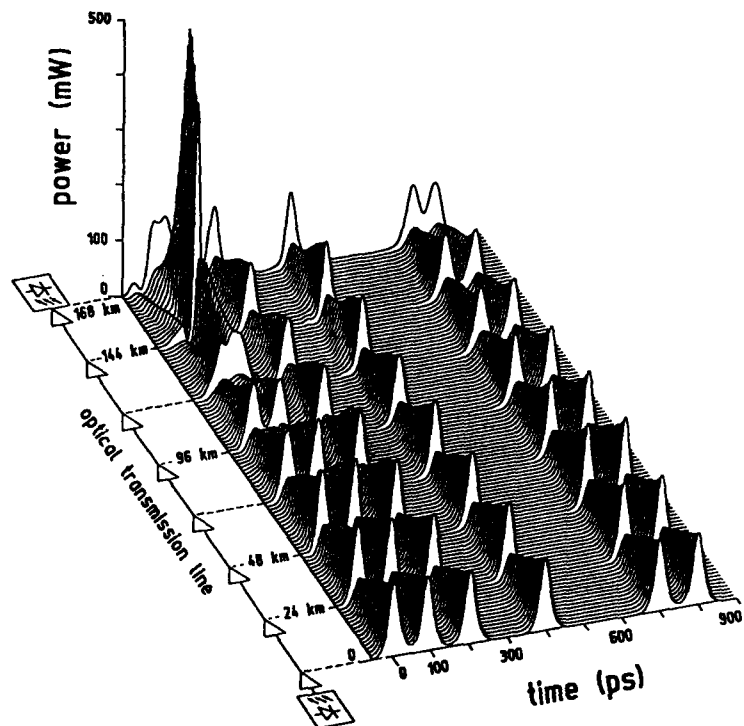


Fig. 1: 10 GBit/s soliton propagation on SMF with equal initial phases. The system parameters (pulse width etc) are written in the text.

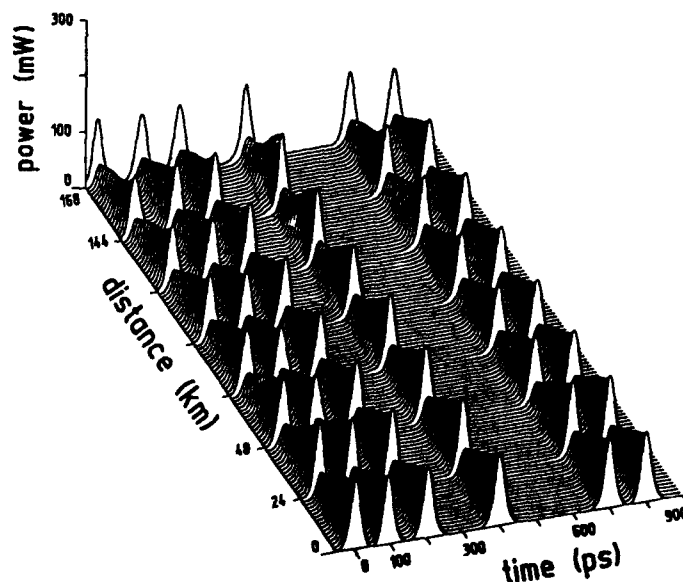


Fig. 2: 10 GBit/s soliton propagation on SMF with alternation of initial phases (same system parameters as in fig. 1)

## A BT View of Nonlinear Effects in Long-Haul Systems

J V Wright

BT Laboratories, Martlesham Heath  
Ipswich, Suffolk, IP5 7RE  
England

### Introduction

The advent of erbium doped fibre amplifiers (EDFAs) has revolutionised the options available for system planners, particularly for high capacity systems, where it was initially hoped that the replacement of electronic regenerators with optical amplifiers would make systems 'optically transparent' allowing future enhancements to be made by changes to just the terminal equipment. In this way, the data rate could be increased, the data format changed or even extra wavelength channels added whenever needed by traffic requirements.

Optically amplified systems may be subdivided into three broad classes:

- i. Long haul systems spanning trans-oceanic or trans-continental distances containing hundreds of optical amplifiers.
- ii. Short to medium haul systems spanning distances of less than  $\approx 2000\text{km}$  containing up to a few tens of amplifiers.
- iii. Unrepeated systems which are 'optically transparent' since they contain no intermediate amplifiers but may employ EDFAs at the terminal or receiver in order to extend the range.

Whilst it is largely true that systems (ii & iii) can be designed to offer significant optical transparency, this need not be true for long haul systems (i) where severe limitations may be imposed by non-linear fibre impairments and invalidate the concept of 'optical transparency'. However, even in the case of (iii) it is now possible to design very long unrepeated systems, in excess of  $300\text{km}$ , by the use of high launch powers and in this case both Brillouin scatter and self phase modulation (SPM) may become limitations [1].

### Accumulation of fibre impairments

Optically amplified systems, unlike electrically regenerated systems where signal re-shaping and re-timing occurs at each regenerator, accumulate any fibre impairments together with the amplified

spontaneous emission (ASE) noise from each amplifier over the entire transmission path. These impairments include: chromatic dispersion, polarisation mode dispersion, polarisation dependent loss and fibre non-linearities. They are responsible for the fundamental limitations of the system. The polarisation issues are very important but will not be addressed here.

### Fibre non-linearity

The origin of the fibre non-linearity lies in the dependence of the fibre's refractive index on the intensity of the optical signal  $I$

$$n = n_1 + n_2 I$$

where  $n_2$  is the non-linear Kerr coefficient of the fibre with a value  $\approx 2.7 \times 10^{-20} \text{m}^2/\text{W}$ . This results in a number of effects including self phase modulation (SPM) and four wave mixing (FWM). These are illustrated in Figure 1 which shows the results of modelling a  $5\text{Gbit/s}$  system over  $6000\text{km}$  using non-return to zero (NRZ) format pulses [2]. It should be noted that in the absence of non-linearity, there would be negligible eye-closure.

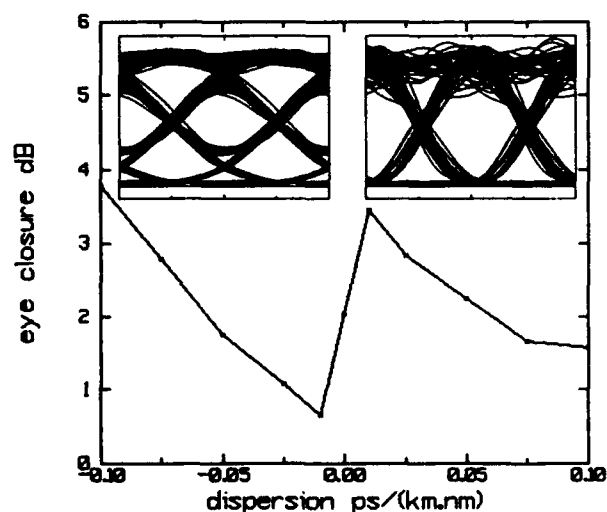


Figure 1. Eye closure as a function of fibre dispersion, insets show eyes for  $D = \pm 0.1 \text{ps}/(\text{km.nm})$

The SPM introduces chirp on the transmitted data which interacts with the fibre dispersion. This results in excessive pulse broadening and eye closure

when the dispersion is negative. When the dispersion is positive, SPM results in pulse compression which causes the data to break up and interact in a complex pattern dependent manner. In the region near zero-dispersion, FWM is enhanced by the phase matching between the signal and ASE noise frequencies. This results in the generation of new optical frequencies and causes severe spectral broadening. By similar means, FWM makes multi-channel operation impossible for the longer systems. It can be seen that the smallest eye closure occurs with fibre of slightly negative dispersion and to limit the eye closure to say  $<2\text{dB}$  requires specification of the signal wavelength to  $\pm 0.3\text{nm}$ . In a practical system, the fibre dispersion will not be uniform and may wander into regions where unacceptable amounts of FWM are generated. To guard against this it may be necessary to employ fibre with stronger negative dispersion and then compensate for the additional eye-closure by using discrete sections of fibre with strong positive dispersion. It may also be necessary to operate at the lowest possible power level consistent with obtaining the required signal to noise ratio (SNR).

#### Soliton transmission

Soliton systems may be used to overcome the non-linear impairments resulting from NRZ transmission formats. Here the fibre non-linearity is used to compensate for the fibre dispersion. This requires the use of positive dispersion fibre. However, a number of other constraints must be considered which are shown in the design diagram, Figure 2.

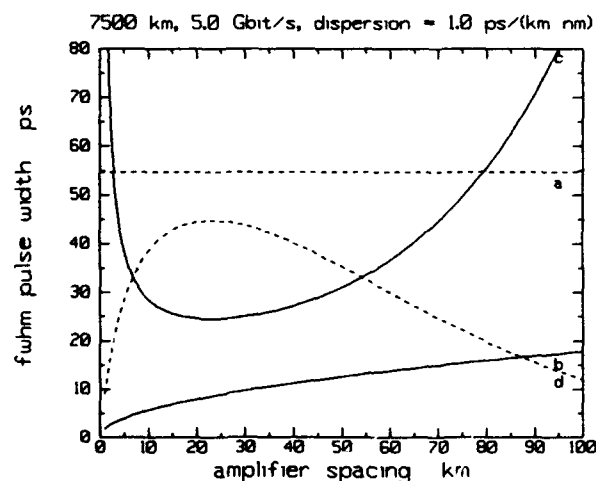


Figure 2. Soliton design diagram for a 7500km system operating at 5Gbit/s,  $D = 1\text{ps}/(\text{km.nm})$

This shows the required soliton pulse width as a function of amplifier spacing for a 5Gbit/s system using fibre of mean dispersion  $1\text{ps}/(\text{km.nm})$  and

with amplifiers whose noise figures are 6dB and whose gains are set to exactly compensate for the fibre attenuation of  $0.2\text{dB}/\text{km}$ . The figure shows four curves labelled (a) - (d) which delimit the borders between safe and unsafe operating regions. The useful operating region lies below the dashed curves and above the solid curves [2].

- prevents the mutual interaction between adjacent solitons by keeping them sufficiently far apart.
- prevents perturbation of the soliton from the fibre attenuation by keeping the amplifier spacing shorter than the soliton period.
- maintains the normalised jitter, arising from the interaction between the soliton and the ASE noise, at less than 0.06 corresponding to an error floor better than  $10^{-16}$ .
- provides an electrical SNR of 23dB.

It can be seen the operating window is limited by jitter and SNR, curves (c) and (d), and consists of the eye which is centred on a pulse width of 35ps and an amplifier spacing of 30km. However this eye closes for operation at 10Gbit/s or even for operation at 5Gbit/s over 9000km unless lower noise figure amplifiers are used or guiding filters are used to restrict the Gordon-Haus jitter [3].

#### Conclusions

Non-linear interactions are not a serious limitation on short to medium haul systems, but longer systems need to be carefully designed in order to achieve operation at 5Gbit/s. Rates higher than this will require novel techniques not only to overcome the non-linear impairments but also to address polarisation issues, particularly polarisation mode dispersion. Soliton transmission is a possible contender here, but guiding filters must be used to reduce the Gordon-Haus jitter.

#### References

- [1] A Hadjifotiou, "The Performance Limits of Unrepeated Systems", Suboptic'93, Versailles, March 93.
- [2] A F Mitchell et al, "The Future of Optically Amplified Submarine Systems", Suboptic'93, Versailles, March 93.
- [3] J Gordon and H Haus, "Random Walk of coherently amplified solitons in optical fibre", Opt. Lett., vol 11, p 665, 1986.

## **Nonlinear Effects in Transoceanic Transmission Systems**

**Neal S. Bergano**

**AT&T Bell Laboratories, Crawfords Corner Road, Holmdel, New Jersey 07733**  
**Tel. (908)-949-3826, Fax. (908)-949-2031, E-mail: bergano@hoggpa.att.com**

Given the advantages of Erbium-doped fiber-amplifiers,<sup>[1]</sup> the next generation of undersea cable transmission systems will use EDFAs in repeaters to boost signals periodically as they travel across the world's oceans.<sup>[2]</sup> The first EDFA-based systems will use the Non-Return-to-Zero modulation format at bit rates up to 5 Gb/s with dispersion-shifted transmission fiber. AT&T, with its partners, plans to install and operate transoceanic cable systems using EDFA repeaters by 1995-96 in the Atlantic and Pacific.

The transmission performance of this type of system is limited by optical noise, chromatic dispersion, and fiber nonlinearities. Unlike regenerator systems, where transmission penalties are reset, these effects accumulate along the amplifier chain and must be managed by the system design. For very long systems the nonlinear refractive index essentially couples the signal and noise which complicates the span engineering. When the system is operated near the dispersion minimum, the data signal and the amplifier noise travel at similar velocities. Thus, the signal and noise waves have long interaction lengths (or are phase matched) in the fiber, and can mix together to form new frequencies. Under these conditions, noise, dispersion, and nonlinearities must be considered together. As an example of how two waves can interact, figure 1 shows four-wave mixing of two CW waves in 1700 km of dispersion-shifted fiber measured in a circulating loop.<sup>[3]</sup> For this experiment the two waves were at the zero dispersion wavelength of the transmission fiber. The optical spectra show the side-band growth for four-wave mixing at different propagation distances. At 600 km the first side-bands are 27% of the transmitted waves, and are equal in intensity at about 1000 km. This characteristic continues until at 1500 km the transmitted waves are at maximum depletion.

The nonlinear interactions in long undersea systems are managed by tailoring the dispersion so that the phase-matching lengths are short, and the end-to-end dispersion is small. The dispersion of the transmission fiber is made slightly negative by using fibers with a mean zero dispersion wavelength 2-3 nm higher than the operating wavelength. The accumulated negative dispersion is reset periodically with short lengths of conventional single-mode fiber. Thus, the nonlinear mixing is minimized by reducing the interaction lengths, and the distortion of the data is minimized by ensuring that the total dispersion returns to zero at the end of the system. Using negative dispersion fiber also avoids the modulation instability regime of the transmission fiber.

These techniques have been used to demonstrate error-free transmission over 9000 km both at 5 Gb/s<sup>[4]</sup> and 10 Gb/s<sup>[5]</sup>. Figure 2 shows the transmitted and received data waveforms at 5 Gb/s for the 9000 km experiment. The characteristic of optical amplifier systems-more noise on the marks rail than the spaces-is easily observed. The shapes of the waveforms before and after transmission are very similar. Thus, the deleterious effects of nonlinearities and dispersion that could distort the waveform have been properly managed.

I thank J. M. Sipress, P. K. Runge, and F. W. Kerfoot for their continued support and encouragement.

## REFERENCES

1. J. L. Zyskind, et al., p. 53, AT&T Technical Journal, Jan/Feb 1992.
2. P. K. Runge and J. M. Sipress, 6th world Telecommunication Forum, Geneva, Oct. 1991.
3. Neal S. Bergano and J. C. Feggler, TuB4, OFC'92, San Jose, Cal. 1992
4. Neal S. Bergano, et al., Topical Meeting on Optical Amplifiers and Their Applications, PD11 Sante Fe, NM, June 1992.
5. H. Taga, et al., OFC'93 PD1, San Jose, Cal. Feb. 1993.

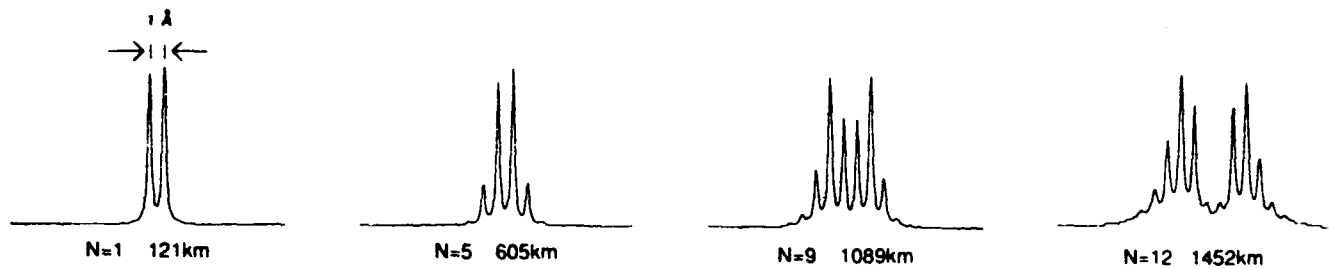


Figure 1 - Optical spectra showing four-wave mixing of two CW waves at different transmission distances.

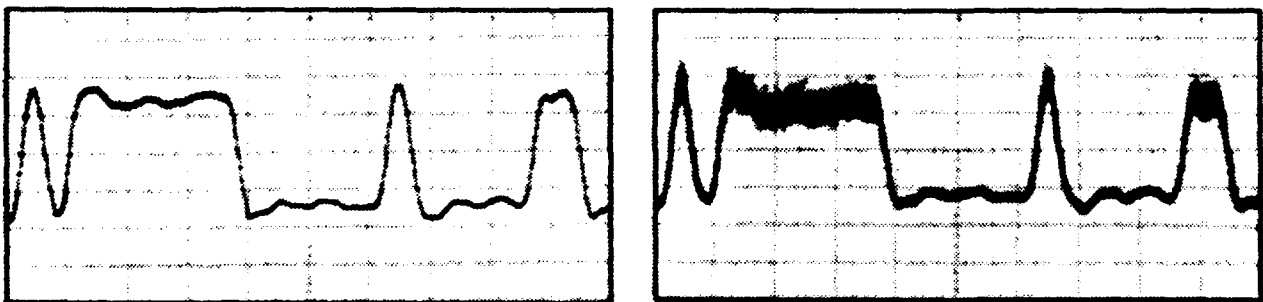


Figure 2 - 5 Gb/s data waveform, back-to-back and after 9000 km.

## NONLINEARLY INDUCED CHROMATIC DISPERSION COMPENSATION IN LONG HAUL FIBER LINKS

*F. Matera, A. Mecozzi, M. Romagnoli, M. Settembre*

Fondazione Ugo Bordoni, via B. Castiglione 59, 00142 Rome, Italy

**SUMMARY.** Recent experimental results have shown the possibility to transmit conventional signals through long haul fiber links at the zero dispersion wavelength. In this paper we show that, even in the case of signals that are not solitons, Kerr effect can limitate the degradation induced by chromatic dispersion in anomalous dispersion region. Such results show the possibility to design, in the anomalous region, systems that do not require a fine adjustment of the GVD. The results have been obtained by solving the nonlinear Schroedinger equation, including the noise (ASE) of the optical amplifiers [1], by means of a split step method. At each amplifier position, the signal is multiplied by the amplifier gain. At the amplifier outputs, optical third-order Butterworth filters are inserted with a bandwidth of 2 nm. The signal performances are studied in terms of penalty evaluated by means of the closure of the eye diagram.

We demonstrate that ASE strongly worsens the signal when the dispersion length,  $L_D$ , is much larger than the length of the link,  $L_{link}$ . In this condition signal degradation can be limited using low level power. When this condition is not met the signal evolution is mainly determined by the mutual interplay between Kerr effect and GVD, and in analogy to links without in line amplifiers, the distortion originating from chromatic dispersion is naturally controlled by the effect of the self-phase modulation [2]. In this paper we show only results regarding the condition  $L_D < L_{link}$ .

Figs.(1) and (2) indicate the penalty, against normalized power  $P_N = P/R^2$  ( $P$  is the input power and  $R$  the signal bit rate) for a PSK coherent systems and a IM-DD system (using the NRZ modulation format respectively). The figures refer to a link 9000 km long with an amplifier spacing  $L=60$  km, a chromatic dispersion  $|\beta_2|=1$  ps<sup>2</sup>/km, a nonlinear coefficient  $\gamma$

$= 2.7 \text{ (W km)}^{-1}$ , a loss  $\alpha=0.057 \text{ km}^{-1}$  (0.25 dB/km) and a third order dispersion  $\beta_3 = 0.1 \text{ ps}^3/\text{km}$  (continuous lines refer to the presence of ASE, while dotted lines without ASE).

For normal dispersion, the system performances worsen as the input power increases, while for anomalous dispersion, on the contrary, there exists an interval of input powers where the fiber dispersion and the Kerr nonlinearity partially compensate each other. The interval of allowed input power narrows when the bit rate increases. Although partial compensation is achieved for both intensity modulated (IM) and phase modulated (PM) signals, good performance is observed only for IM signals.

To compare with soliton systems, a simulation of a soliton transmission system has been carried out and the results are shown in fig. (3). The parameters are the same of fig.(1) and (2), with time width of the solitons  $t_{FWHM}=1/(8R)$  ( $t_s=t_{FWHM}/1.763$ ). The Gordon Haus effect was controlled by placing after each amplifier a Lorentzian optical filter with bandwidth of 1 nm for  $R=5 \text{ Gbit/s}$  and 2 nm for  $R=10 \text{ Gbit/s}$ .

As expected, the penalty of soliton systems is lower than conventional IM systems. In particular, at 5 Gbit/s almost zero penalty was observed, while at 10 Gbit/s, zero penalty is not achieved since the average soliton condition is not fully satisfied.

[1] D. Marcuse Journal of Lightwave Technology , 1991, 9, pp. 356-361.

[2] E. Iannone, et. al. El. Letters, 1992, 28, pp. 1902-1903.

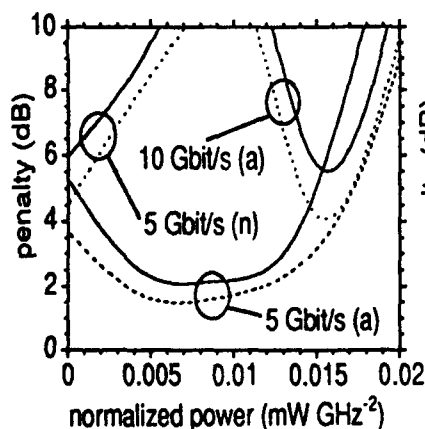


Fig. 1: penalty vs. the input power of a PSK system after propagating in a link 9000 km long, in the presence of ASE (continuous line), and without ASE (dotted line). (a) refers to the anomalous region, (n) to the normal region. Other details in the text.

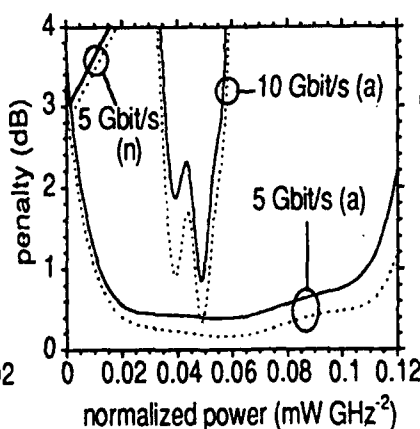


Fig. 2: as fig. 1 but for an IM DD system.

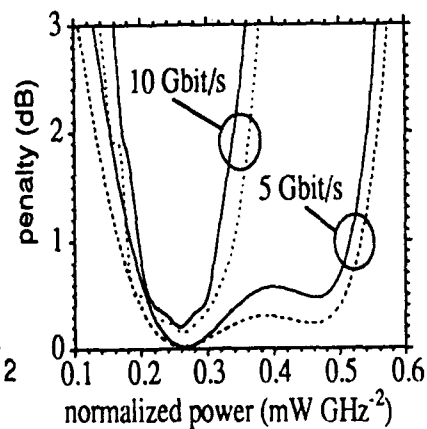


Fig. 3: as fig. 1 but for a soliton system.

**Experiments and Numerical Simulations of Nonlinear Effects  
in Long Distance Transmission**

**Yasuhiro Aoki**

**Submarine Cable Systems Division, NEC Corporation  
1753 Shimonumabe, Nakahara-ku, Kawasaki-city, Kanagawa 211, JAPAN**

**1. Introduction**

With the rapid progress in Er-doped fiber amplifiers(EDFAs), it has become possible to construct long distance transmission systems without conventional 3R regeneration. In practice, transoceanic and transpacific submarine cable systems using EDFAs are being installed in the near future[1]. This optical amplification technology has certainly changed aspect with regard to limiting factors for system performance: We are free essentially from restriction of the fiber loss. Due to high signal power and/or long interaction length, however, optical fiber nonlinearities could impair transmission characteristics together with ASE noise accumulation, and thus care should be taken on the nonlinearities in designing amplifier systems.

Optical communication systems can be categorized in two types; repeaterless and multi-repeater systems. In this paper, we present our recent studies on assessment and management of fiber nonlinearities, including stimulated Brillouin scattering (SBS), self-phase modulation (SPM) and modulational instability (MI), for both kinds of the IM/DD systems.

**2. Repeaterless Transmission Systems**

It is obvious that system lengths for repeaterless transmission can be increased by raising the transmitter signal powers. An Er-doped fiber booster amplifier enabled now to deliver a signal power more than +20 dBm into the fiber. Under such a high power level, however, severe disturbance comes from SBS and SPM.

We have evaluated SBS thresholds of conventional single-mode fibers (SMFs) and dispersion-shifted fibers (DSFs) for the IM/DD systems. The SBS threshold for an externally intensity-modulated signal in a Gb/s range was measured to be approximately +10 dBm, slightly depending on the kind of the fiber, in good agreement with expectation[2]. It was also found that, for transmitter powers above the threshold by a few dB, the SBS process causes unacceptable error rate floor, that is not surprising because the SBS builds up from the spontaneous emission.

In order to solve this problem, we have developed SBS suppression technique which based on spreading the signal spectrum by means of direct frequency modulation of a DFB-LD[3]. This method can easily be implemented in a transmitter that incorporates an external modulator. With proper FM modulation depth and frequency, the generation of SBS could never be seen even for launched powers over +20 dBm.

Other nonlinearity of SPM causes a waveform change as a result of combined effects with chromatic dispersion. This is particularly so under transmission in conventional SMFs with large dispersion. We have quantitatively analyzed ISI power penalty due to such a waveform change by computer simulations of the nonlinear Shroedinger equation[4]. The simulation results have shown that, the SPM could not be detrimental for signal powers by +19 dBm, instead the "soliton effect" sharpens transmitted pulses to reduce ISI power penalty. Above this level, the SPM dominates over dispersion effect, and drastic degradation is predicted to be induced for conventional SMF transmission at 1.55  $\mu\text{m}$ . Thus the upper limit for repeaterless transmission is around +19 dBm, the value of which is close to the maximum output power of the state-of-the-art Er-doped booster amplifiers.

By applying these techniques, transmission experiments were carried out, with conventional single-mode fibers so as to appreciate the low-loss property at 1.55  $\mu\text{m}$ . Eventually repeaterless

transmissions of 2.5Gb/s-279 km and 5Gb/s-204 km have been achieved with little power penalty[3].

### 3. Ultra-Long Multi-Repeater Transmission Systems

In long distance non-regenerative transmission systems with EDFAs, the signal wavelength is usually chosen very close to or at the zero dispersion wavelength of DSFs in order to minimize the waveform distortion. Under this circumstance, however, the phase matching condition is satisfied over the long system length. As a result, four-wave mixing (FWM) or induced MI may cause mutual interaction between the optical signal and ASE noise[5]. In other words, the signal amplifies the ASE noise during the fiber transmission and eventually signal-to-noise ratio degrades with distance in a nonlinear fashion.

In order to address the level of excess noise produced by FWM process, parametric gains for the ASE were measured in terms of the dispersion values and signal powers for several DSFs. The experimental gains in anomalous dispersion (positive dispersion) regime were found to be in very good agreement with the theory[6]. However, gains were also found to be induced even in the normal dispersion (negative dispersion) regime for dispersions up to  $-0.2$  ps/nm/km. This is presumably due to the fact that, in actual fibers, its local dispersion varies along the fiber owing to slight changes in a core diameter, giving some portion exhibits anomalous or zero dispersion.

The findings mentioned above give us an important information that the system may be operated in normal dispersion below  $-0.2$  ps/nm/km. However, computer simulations on pulse shapes show, if all the fibers are arranged in normal dispersion, the pulse broadening due to dispersion in conjunction with SPM severely limits a transmission distance less than a few thousands of km[4]. Obviously the method for its avoidance is to arrange the various sections of fiber in the line in such a way that proper amount of them have positive dispersion at the signal wavelength while the total fiber exhibits zero dispersion on average.

If we consider presently-available fibers, two approaches would be possible in arranging the transmission line. One is to employ DSFs with negative dispersion at most places and to incorporate short pieces of conventional SMFs that have large positive dispersion at  $1.55\text{ }\mu\text{m}$  (type A). The other is to distribute DSFs with negative and positive dispersions equally in each section (type B).

We have experimentally compared long-distance transmission characteristics under these two arrangements, with that under "zero dispersion". In the experiment, a fiber loop that includes several EDFA repeaters is used. Here, the bit rate is either 2.5 Gb/s or 5 Gb/s, and the repeater spacings are set 50 km. In case of "zero dispersion" transmission, the Stokes and anti-Stokes generations were clearly seen in the optical spectrum, and transmission distance for  $\text{BER} < 10^{-9}$  was less than 6,000 km for both bit rates, limited dominantly by FWM nonlinear noise. By contrast, in case of type A, the distances were increased to 21,000 km at 2.5 Gb/s and 8,500 km at 5 Gb/s, respectively. In case of type B, the distances were shorter by approximately -35%, compared with type A. Therefore type A will be a better choice for ultra-long optical amplifier systems.

### 4. Conclusion

In designing the advanced communication systems with optical amplifiers, deep understanding and insight are needed in the effect from optical fiber nonlinearities. Our theoretical and experimental investigations have shown that management of fiber nonlinearities is possible in both repeaterless and ultra-long repeater systems.

### 5. References

- [1] See for example, Tech. Digest, SubOptic'93 (Velsailles France, 1993).
- [2] Y. Aoki, et al., *IEEE J. Lightwave Tech.*, LT-6(1988), p.710.
- [3] T. Ogata, et al., Tech. Digest, 4th Opt. Electron. Conf. (OEC'92, Chiba, Japan, 1992), paper 16A4-3.
- [4] T. Koyama, et al., Tech. Digest, ECOC/IOOC'91 (Paris France, 1991), paper WeC7-2.
- [5] D. Marcuse, *IEEE J. Lightwave Tech.*, LT-9(1991), p.356.
- [6] G. P. Agrawal, "Nonlinear Fiber Optics"(Academic Press), chapter5.

## Impact of Self-phase Modulation on 10-Gb/s Systems using Conventional Single-mode Fiber

A.H. Gnauck and R.W. Tkach  
AT&T Bell Laboratories  
Crawford Hill Laboratory  
Holmdel, NJ 07733-0400

The introduction of erbium-doped-fiber optical amplifiers (EDFA's) has eliminated fiber loss as a fundamental limit to achievable transmission distance. However, the embedded fiber plant throughout the world largely contains "normal-dispersion" fiber with dispersion of  $\sim 16$  ps/km/nm in the erbium-amplifier bandwidth. Chromatic dispersion is therefore a primary limitation in optically-amplified multi-gigabit systems using embedded fiber. Computer modeling shows that an unchirped 10-Gb/s signal will suffer a 1-dB dispersion penalty after  $\sim 70$  km. Dispersion compensation using optical fiber has been achieved by several methods. However, these methods increase system cost and complexity. Therefore, there is great interest in extending the dispersion-limited distance by other means, such as modification of the transmitter chirp [1-3] or exploitation of fiber nonlinearity [4,5]. We now show, using computer simulation and laboratory experimentation, that self phase modulation (SPM) can be used to extend the dispersion-limited distance by roughly 50%.

The computer model contains an ASK transmitter, optical fiber, and a direct-detection receiver. The transmitter consists of a cw laser source and a chirpless, push-pull Mach-Zehnder modulator. The modulator small-signal bandwidth is chosen to be equal to the bit rate. This produces a large-signal risetime (10%-90%) equal to 25% of the bit period. The drive waveform is a pseudorandom NRZ bit sequence of length  $2^7$ . Propagation in the fiber is solved by the split-step Fourier method [6]. The fiber loss is 0.21 dB/km, the dispersion is 16 ps/nm/km, the effective mode area is  $80 \mu\text{m}^2$ , and the nonlinear coefficient is  $2.6 \times 10^{-16} \text{ cm}^2/\text{W}$ . After transmission, the signal is optically filtered, detected, and electrically filtered. Bessel filters are used to minimize group delay dispersion. The optical filter bandwidth is set to 1 nm, and the electrical filter bandwidth is chosen to be 60% of the bitrate (6 GHz at 10 Gb/s). An eye pattern is generated, and the eye opening is automatically found. The penalty due to intersymbol interference is defined as the ratio of the received eye opening to that of a fully-open eye with the same average power. This definition leads to a baseline (negligible fiber length) transmission penalty of  $\sim 0.3$  dB due to electrical filtering at the receiver. Simulation results are shown in Fig. 1 for fiber lengths of 80, 100, and 120 km. The transmission penalty relative to baseline (in decibels) is plotted as a function of launched average power. As the launched power is increased, a reduced transmission penalty is obtained from the interaction of SPM and dispersion. At some point, the power reaches a level where the penalty increases due to the continued spectral broadening caused by SPM. These results are qualitatively similar to the 5-Gb/s results reported in Ref. 5, where an electroabsorption modulator with chirp parameter of +0.6 was used.

An experimental 10-Gb/s system was set up to confirm the simulation results. The transmitter consisted of a commercial external-cavity diode laser and a push-pull  $\text{LiNbO}_3$  Mach-Zehnder modulator with a small-signal bandwidth of 10 GHz. The  $1.54\text{-}\mu\text{m}$  light was ASK modulated at a bit rate of 10 Gb/s with a pseudorandom NRZ sequence of length  $2^{15}-1$ . The fiber exhibited dispersion of 16 ps/nm/km and loss of 0.22 dB/km. A 1-nm-bandpass optical filter was used. The receiver employed a hybrid APD/HEMT front end and hybrid GaAs FET amplifiers. The small-signal bandwidth was 6 GHz. A phase-locked-loop was incorporated to recover timing information. Eye diagrams were taken using a 20-GHz detector followed by a 6-GHz low-pass electrical filter which served to emulate the response of the APD receiver. In Fig. 2, simulated and actual eye patterns for  $\alpha=0.0$  are compared for baseline, 100-km transmission with +2 dBm launched power, and 100-km transmission with +11.5 dBm launched power. Higher transmitted power was not possible in this system due to stimulated Brillouin scattering (SBS). However, a

dithering technique could be used to overcome this limitation [5]. The simulation and experiment produce patterns that are remarkably similar. The baseline receiver sensitivity (bit-error rate= $10^{-9}$ ) in the system is -27.3 dBm at 1.54  $\mu\text{m}$ . At 100 km, the simulation predicts a penalty of 2.2 dB relative to baseline for +2 dBm launched power. We incur a penalty of 2.9 dB for this value. It is not surprising that our penalty is higher than predicted. The intersymbol interference apparent in Fig. 2b causes an extinction-ratio penalty which is exacerbated by the multiplication noise of the APD receiver. When the launched power is raised to +11.5 dBm, the simulation penalty drops to 1.0 dB relative to baseline. The penalty in the transmission experiment is also 1.0 dB. Further reduction of penalty at 100 km should be possible by using an SBS-suppression technique and launching higher power. However, simulation shows that at 120 km, optimum launched power of +14dBm will still produce a penalty of  $\sim 1.6$  dB relative to baseline. Thus, extension of transmission distance using this technique is limited to  $\sim 50\%$ .

#### REFERENCES

1. A.H. Gnauck, *et al.*, IEEE Phot. Tech. Lett. 3, pp. 916-918, 1991.
2. A.D. Ellis, *et al.*, Electron. Lett. 28, pp. 954-955, 1992.
3. B.L. Patel, *et al.*, in *Proc., European Conference on Optical Communication*, postdeadline paper Th PD I.3, Berlin, Germany, 1992.
4. M.J. Potasek and G.P. Agrawal, Electron. Lett. 22, pp. 759-760, 1986.
5. T. Ogata, *et al.*, in *Proc., Fourth Optoelectronics Conference*, paper 16A4-3, Makuhari Messe, Japan, 1992.
6. G.P. Agrawal, "Nonlinear fiber optics," Academic Press, New York, 1989.

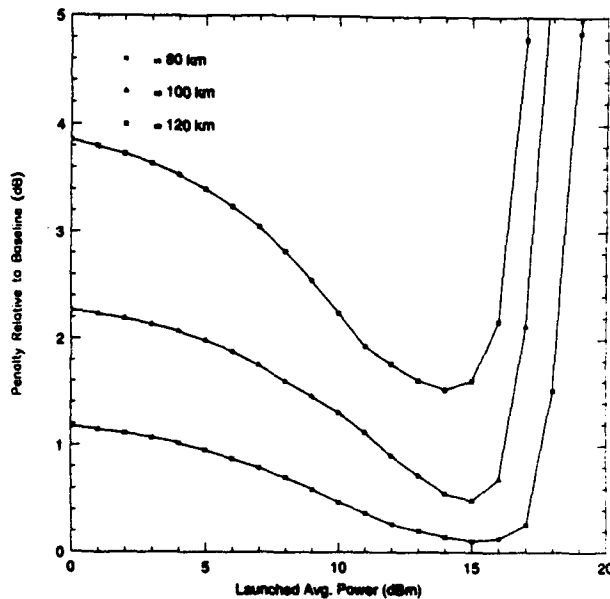


Figure 1: Calculated penalty relative to baseline in a 10-Gb/s system at 80, 100, and 120 km, as a function of launched average power.

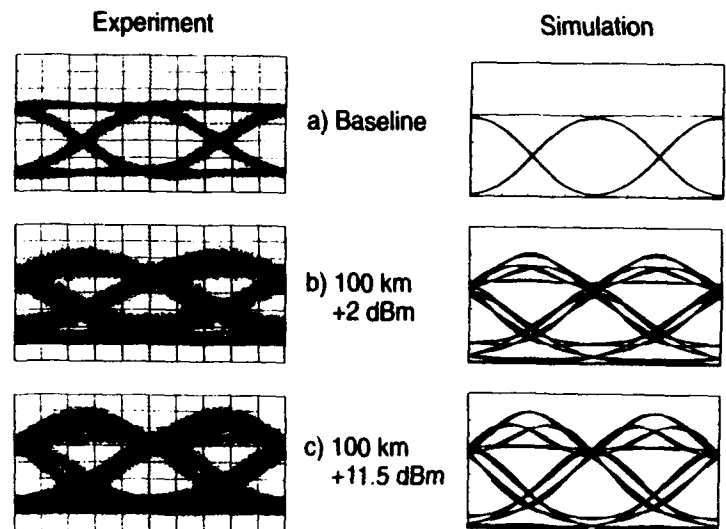


Figure 2: Actual and simulated eye patterns for a) baseline, b) 100 km with launched power of +2 dBm, and c) 100 km with launched power of +11.5 dBm.

## PERFORMANCE EVALUATION OF OPTICAL SYSTEMS IN THE PRESENCE OF NONLINEAR KERR EFFECT.

Francesco Matera

*Fondazione Ugo Bordoni, via B. Castiglione 59, 00142 Roma, ITALY*

In the last years several works have shown the possibility to transmit high bit rate signals over very long distances, using both conventional and soliton systems. Since in such systems the product between the distance and the power results high, fiber nonlinearities are present also in the case of propagation of conventional signals. After the experimental demonstration of transmissions over very long distances, the study of the system performance, in the presence of the fiber nonlinearities, appears very important in order to find the best way to exploit the fiber capacity.

In this work performance evaluations of both coherent and direct detection system will be presented considering the fiber nonlinearity due to the Kerr effect. The Stimulated Brillouin Scattering is considered as a limiting factor for the maximum transmitted power  $P_B$ . The Stimulated Raman Scattering effect can be neglected [1] for systems presenting a bandwidth lower than 100 Gb/s [1].

In the absence of optical amplifiers, and then of amplifier spontaneous emission noise (ASE), the system error probability can be evaluated exactly, since the evolution of a signal in presence of Kerr effect and chromatic dispersion is a deterministic process: noise is generated only at the receiver, in terms of shot noise and thermal noise [2]. In the presence of optical amplifiers the evolution of the signal along the link is a random process and the noise distribution at the fiber output results very complex due to the nonlinear interaction between ASE and signal [3]. Under this condition, the noise statistics is not Gaussian in general [4], and the error probability is not easily evaluated. In this case the system performance is normally studied in terms of eye degradation penalty [5].

In this paper the evolution of the signal has been obtained solving the nonlinear Schroedinger equation, by means of a split step method. In the presence of optical amplifiers, the ASE noise has been included in the frequency domain [3].

In links without optical amplification, the error probability has been obtained from the characteristic function  $G_k(\lambda)$ , where  $\lambda$  is the Laplace variable and  $k$  indicates the transmitted pattern which the characteristic function is conditioned to. In the presence of chromatic dispersion and Kerr effect, the evolution of the bit shape depends on the shape of all the other bits constituting the signal and then the number of the patterns that has to be taken into consideration should be very high. In conditions of weak perturbation, that is the one required in a system with good performance, it can be assumed, with good approximation, that the evolution of a bit shape depends only on the adjacent bits and hence the number of the patterns can be limited to 8-16.

In fig. 1 the error probability is reported, vs. the input average power, for a 20 Gb/s DPSK and an ASK asynchronous system; the link presents a length of 200 km, a chromatic dispersion coefficient of 1.3 ps/(nm km), a nonlinear coefficient equal to  $2.7 \text{ (W km)}^{-1}$  and a loss of 0.25 dB/km. Dotted lines refer to the anomalous chromatic dispersion region (negative group velocity dispersion GVD), while continuous lines to the normal one. The curves for the ASK system are reported for power levels below the Brillouin threshold,  $P_B$ , that it has been assumed equal to 25 mW. Phase modulated signals present a higher  $P_B$  [1].

In the linear regime, as expected, system performance improves increasing the input power. When the Kerr effect shows up, in the anomalous dispersion region the performance is much better with respect to the normal one and this can be explained by the fact that in the anomalous dispersion region the nonlinear Kerr effect can compensate the degradation due to the chromatic dispersion in analogy with the soliton process [6]. This result is confirmed by fig. 2 in which the eye degradation penalty vs input power, corresponding to the systems of fig. 1, is reported. The Kerr nonlinearity reduces the signal degradation due to the chromatic dispersion reaching a minimum penalty in correspondence of the input power  $P_{opt}$ . For power higher than  $P_{opt}$  the modulation instability (MI) effect severely degrades the signal. For ASK systems  $P_{opt} \geq P_B$ .

Figure 3 shows the maximum distance that a DPSK system can reach with an error probability equal to  $10^{-9}$ , without optical regeneration, considering three different bit rates in a link with the same parameters of fig. 1. The main limitation is given by the Kerr effect induced by the high power levels used to compensate the fiber loss. As shown in the figure, in the anomalous region the transmission distance can be longer due to the presence of the nonlinear compensation effect.

In the case of multichannel frequency division multiplexing (FDM) systems the main limitation is given by the FWM. Several works have already analysed the performance considering the channel signal as a quasi monochromatic field [7]. Results show the possibility to transmit several channels (50-100) with an error probability of  $10^{-9}$  over distances as long as 100 km. The main limitation to these results is given by the fact that the actual shape of the signal is not taken into consideration. To accomplish this task the method of the characteristic function can be used even though, in this case,  $G(\lambda)$  should depend on three indices  $k, l, m$ :  $k$  represents the pattern of the

channel in which the error probability is evaluated, while  $m$  indicates the pattern of the  $l$ -th channel.

Whenever ASE is present, the error probability can be calculated only in those particular cases in which the statistics of the noise at the fiber output can be analytically evaluated. This is possible, for instance, in the case of zero chromatic and third order fiber dispersion [4].

Several studies have shown that the degradation due to the ASE can be reduced by means of the use of optical filters located at the amplifier outputs. The ASE degradation could also be limited reducing the bandwidth in which the FWM process results efficient. This can be easily obtained using a nonzero value of chromatic dispersion, even if in this condition the GVD can severely degrade the signal after propagation on very long distances. Furthermore the use of negative GVD induces MI. In any case, it has to be pointed out that in the presence of negative GVD, the ASE does not produce strong modification of the signal evolution if the MI bandwidth results narrower than the signal bandwidth. In this condition, the chirp induced by the chromatic dispersion can be compensated by the nonlinear Kerr effect as shown in fig. 4, where the eye degradation penalty is reported vs input power for a conventional and a soliton IM DD and a coherent PSK 5 Gb/s system transmitting on a link 9000 km long, with an amplifier spacing equal to 60 km. The other parameters are the same of fig. 1. Optical filters with a bandwidth of 1 nm were located at the amplifier outputs [8].

As shown in the figure, in the case of the soliton signals, the nonlinear compensation proves more efficient allowing a minimum penalty close to zero to be reached.

#### REFERENCES

- 1) A. R. Chraplyvy, J. Lightwave Technology vol. 8, 1990, p. 1548.
- 2) E. Iannone, F. S. Locati, F. Matra, M. Romagnoli, M. Settembre, El. Letters Vol. 28 N° 7 1992, p. 645.
- 3) D. Marcuse, J. of Lightwave Technology, vol. 9, 1991, p. 356.
- 4) A. Mecozzi, "The combined effect of Kerr nonlinearities ..." submitted to Optics Letters.
- 5) J. P. Hamaide et, El. Letters, vol. 28, 1992 p. 44.
- 6) E. Iannone, F. S. Locati, F. Matra, M. Romagnoli, M. Settembre, El. Letters Vol. 28 N° 20 1992, p.1902.
- 7) E. Lichtman, J. Opt. Communication, vol. 2, 1991, p. 53.
- 8) F. Matra, A. Mecozzi, M. Romagnoli, M. Settembre, LEOS STM on Impact of Fiber Nonlinearities, M1.5.

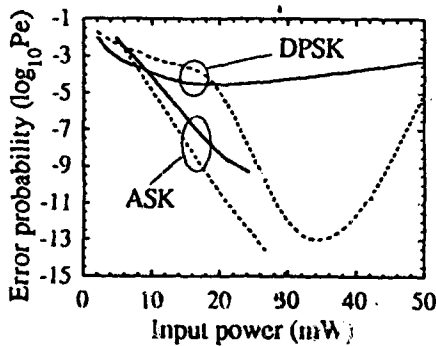


Fig. 1: error probability vs input power for a 20 Gb/s DPSK and ASK system in a link 200 km long with  $D=1.3$  ps/nm/km. Solid lines refer to the normal GVD region, while dotted lines to the anomalous one.

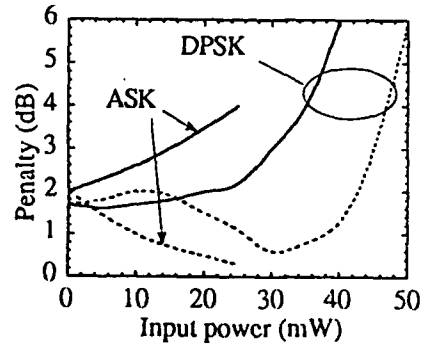


Fig. 2: eye diagram penalty vs input power for the systems of fig. 1.

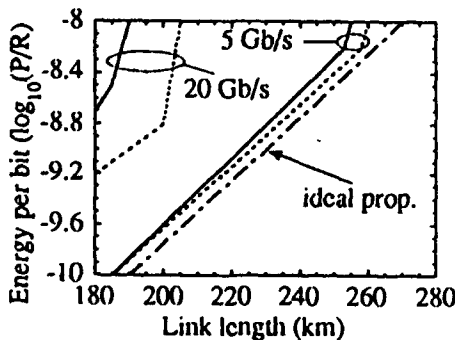


Fig. 3: energy per bit vs input link length in a DPSK system with an error probability of  $10^{-9}$  and  $D=1.3$  ps/nm/km. Solid lines refer to the normal GVD region, while dotted lines to the anomalous one.

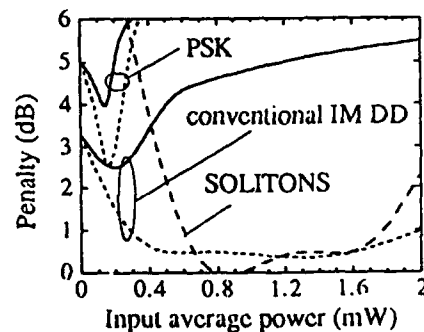


Fig. 4: eye diagram penalty for a 5 Gb/s conventional and soliton IM DD and a coherent PSK system in a link 9000 km long with 150 optical amplifiers and  $D=1.3$  ps/nm/km. Solid lines refer to the normal GVD region, while dotted lines to the anomalous one.

M2.4 3:40pm - 4:20pm  
(Invited)

## DESIGN OF AMPLIFIED TRANSOCEANIC SYSTEMS BY NUMERICAL SIMULATION

O. Audouin, J.-P. Hamaide, L. Prigent, J.-J. Bernard, J. Augé  
ALCATEL ALSTHOM RECHERCHE  
Route de Nozay, 91460 Marcoussis (FRANCE)

### INTRODUCTION

The next generations of transatlantic and transpacific optical links, TAT 12/13 and TPC 5, will use in-line Erbium-doped fiber amplifiers (EDFA) to compensate for the fiber loss. This new transmission technique constitutes a major evolution for the long-haul systems as it allows to build all-optical links, without undersea electronic repeaters. Improvement of the reliability and upgradability are among the advantages of these "light highways". Their capacity to transmit high bit rates (5 to 10 Gb/s) over very long distances (6000 to 9000 km) has been demonstrated by some laboratory experiments [1]. However, new design studies are required to ensure optimum performances during the 25 years life time aimed for a transoceanic system. In absence of regeneration, all the signal distortions are cumulated along the whole link length. A very weak physical effect can then induce dramatic impairments on the transmission quality. The first distortion source is the Amplified Spontaneous Emission generated by the EDFA's. The noise accumulation requires to transmit high signal power to ensure a sufficient signal-to-noise ratio at the end of the link. With this high power propagating along very long distances, the fiber has a nonlinear behaviour : due to Kerr effect, the refractive index depends on the electrical field intensity. A careful study of its consequences on the system performances is necessary in order to choose the optimum component parameters. As the accuracy of an analytical approach of this nonlinear phenomena is limited, numerical simulations are required. Such a numerical tool has been developed at Alcatel Alsthom Recherche [2]. This paper presents its application to the design of high bit rate transoceanic links. The first part concerns transmission of Non-Return-to-Zero (NRZ) streams and a second part is devoted to soliton systems.

### DESIGN OF NRZ SYSTEMS

The Kerr nonlinearity induces a Self Phase Modulation (SPM) of the intensity-modulated signal. This nonlinear chirping is responsible for the creation of new frequencies which broaden the signal spectrum. Interacting with noise and dispersion, SPM influences the choice of the main system features.

#### Chromatic dispersion

Even using an external modulator together with a dispersion-shifted line fiber, chromatic dispersion is a critical parameter because of its interaction with the nonlinear spectrum broadening. The sign of the dispersion  $d$  is determinant for the consequences of Kerr nonlinearity. If  $d$  is positive, the dispersive and nonlinear chirps are opposed, the NRZ pulse are compressed and it appears modulation instabilities which dramatically broaden the signal spectrum. If  $d$  is null, Kerr effect induces a penalizing Four Wave Mixing (FWM) between noise and signal because of their phase matching. If  $d$  is negative an important time broadening is the consequence of the common sign of the dispersive and nonlinear chirps. However, in this last case, a compensation is possible using a span of non-dispersion-shifted fiber in front of the receiver to compress pulses before detection. The length of this compensation span has to be calculated taking into account the nonlinear spectral broadening as it is the product (dispersion  $\times$  spectrum width) that must be compensated for. In spite of this compensation, a dispersion as low as -0.05 ps/nm.km is required for a 5 Gb/s bit rate.

#### Amplifier configuration

The choice of the amplifier spacing  $Z_a$  and output power  $P_{out}$  results from a tradeoff between noise and Kerr nonlinearity. From the noise point of view, the signal to noise ratio must be maximum. This constraint imposes a high output power and a low amplifier spacing as the EDFA noise is approximately proportional to its gain  $G = \exp(\alpha Z_a)$  where  $\alpha$  is the fiber attenuation. On the contrary, to reduce the nonlinearity, it is necessary to decrease the link path-averaged power  $P_{out}(1 - G)/\alpha Z_a$  and thus, to decrease  $P_{out}$  and rise  $Z_a$ . Numerical calculations of the system Bit Error Rate (BER) are used to determine this compromise. The relevant component parameters for this choice are mainly the amplifier noise figure and the fiber attenuation and effective area. For a 9000 km 5 Gb/s system, typical values are  $Z_a = 35$  km and  $P_{out} = 1$  to 3 dBm.

#### Wavelength Division Multiplexing

Wavelength division multiplexed transmission makes it possible to upgrade the bit rate capacity of the systems. In the case of NRZ data, the Kerr nonlinearity limits this possibility for two reasons. The first one is the SPM-induced spectrum broadening which requires to space the channels a few nm apart. The fiber dispersion slope and the amplifier bandwidth become then major issues. The second reason is that Kerr effect induces nonlinear crosstalks between channels by Cross-Phase Modulation (XPM) and FWM processes.

## DESIGN OF SOLITON SYSTEMS

Taking advantage of the Kerr nonlinearity to compensate for the chromatic dispersion, the transmission of soliton pulses is an attractive technique for future ultralong high bit rate links. We consider here its specificity from the system design point of view.

### Chromatic dispersion

The soliton effect resulting from a balance between dispersive and nonlinear chirps, the dispersion  $d$  must be positive and the signal power is proportional to  $d$ . The choice of  $d$  is determined by two opposite constraints concerning the influence of the amplifier noise. The first influence is linear and similar to the NRZ case, the addition of noise induces energy fluctuations of the received pulse level. The specificity of the soliton is the dependence of the signal power, and thus of the signal-to-noise ratio on the dispersion value which must be higher than a minimum value to ensure a given BER. On the other hand, a nonlinear interaction between the noise and the soliton, the so-called Gordon-Haus effect, is responsible for a random fluctuation of the soliton frequency. Because of dispersion, it results a random jitter of the soliton arrival time at the receiver, which is proportional to  $d$ . This effect imposes a maximum value to  $d$ . Simulations have shown that in the case of a 9000 km 5 Gb/s link, the optimum dispersion value is about 0.7 ps/nm.km (Figure 1). The influence of both effects on the BER are then of the same order of magnitude. Some time or frequency control techniques [3], based on in-line filtering or synchronous modulation can be used to reduce the Gordon-Haus jitter.

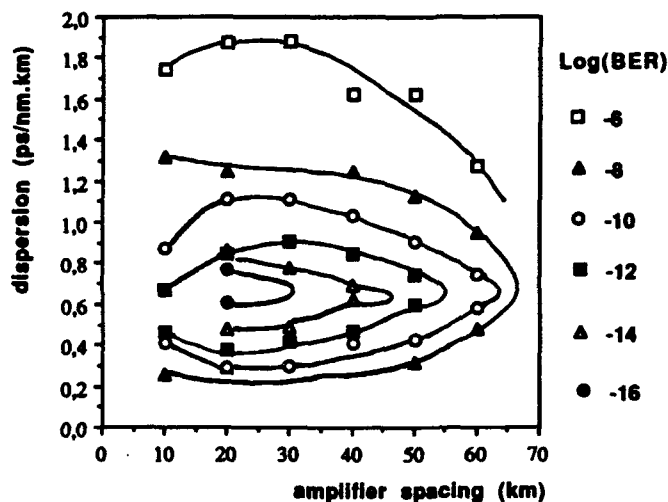


Figure 1  
Simulated bit error rates of a 5 Gb/s  
9000 km soliton system

### Amplifier configuration

The amplifier output power is imposed by the required signal power which is linked to the previous dispersion choice. The influence of the amplifier spacing  $Z_a$  on the noise power amount previously described for NRZ systems is still valid. An additional constraint arises from a condition concerning the influence of the fiber attenuation on the stability of the soliton:  $Z_a$  must be much lower than the soliton period  $Z_0$ . At the 5 Gb/s bit rate, when  $d = 0.7$  ps/nm.km,  $Z_0$  is about 900 km. Considering the two constraints,  $Z_a$  must be chosen around 30 km.

### Wavelength Division Multiplexing

Collisions between solitons of different wavelengths give rise to nonlinear interactions which lead to an increased time jitter. This imposes constraints on the choice of the channel spacing  $\Delta\lambda$ .  $\Delta\lambda$  must be high enough to reduce the intensity of interactions during collisions. However, to avoid an important jitter increase due to a sensitivity of collisions to the presence of an amplifier, the collision length  $Z_c$  must be greater than  $2 Z_a$  [4]. This last condition, as well as the wavelength dependence of the amplifier gain, prevents from choosing a too high channel spacing. Simulations of the transmission of four 5 Gb/s channels over 9000 km have shown that the optimum channel spacing is around 0.35 nm.

## CONCLUSION

We have reviewed the main issues concerning the design of single-channel or wavelength multiplexed ultralong amplified links using NRZ or soliton transmission techniques. Thanks to careful dispersion management methods, NRZ scheme will answer the need of bit rates in the range 5 to 10 Gb/s for the links planned to be laid down in 1995-96. For future bit rate increase (several tens of Gb/s), soliton transmission, associated with frequency control and wavelength division multiplexing, seems to be a promising solution.

## ACKNOWLEDGMENTS

We are grateful to J. Chesnoy for fruitful discussions. This work is supported by Alcatel CIT and France Telecom.

## REFERENCES

- [1] H. Toga et al., OFC'93, PD 1.
- [2] O. Audouin et al., ECOC'91, We.A6.1.
- [3] A. Mecozzi et al., Optics Letters, Vol 16, December 1991, p. 1841.
- [4] L.F. Mollenauer et al., Journal of Lightwave Technology, Vol.9, March 1991, p. 362.

**Tuesday, July 27, 1993**

**Sessions:**

**T1: WDM & SBS**

**LPS: Late Paper Session**



Kyo Inoue

NTT Transmission Systems Laboratories  
1-2356, Take, Yokosuka, Kanagawa, Japan

## I. INTRODUCTION

When three signal lights of frequencies  $f_i$ ,  $f_j$ , and  $f_k$  transmit through fibers, a new frequency light is generated at  $f_i + f_j - f_k$ . This phenomenon is termed four-wave mixing (FWM) or four-photon mixing. In multi-wavelength systems, FWM induces crosstalk and degrades system performance. This paper describes recent studies on fiber FWM in multi-channel systems.

## II. EFFICIENCY

*a. Dependence on the polarization state:* The FWM efficiency depends on the state of polarization (SOP) of signal lights. In an experiment using a 26-km fiber, the efficiency was highest for matched SOPs and zero for orthogonal SOPs for partially degenerate FWM [1]. This result was not expected by a model directly applying the FWM behavior in a bulk media to that in a fiber [2], [3]. To explain it, the expression

$$\hat{P}_{FWM} \propto \|[\hat{E}_j \cdot \hat{E}_k^*]\|^2 \hat{E}_i + \|[\hat{E}_i \cdot \hat{E}_k^*]\|^2 \hat{E}_j \quad (1)$$

was presented [1], where  $\hat{E}_i$ ,  $\hat{E}_j$ , and  $\hat{E}_k$  were the amplitude vectors for  $f_i$ ,  $f_j$ , and  $f_k$  frequency lights, and  $[\cdot]$  denoted the inner product of two vectors. The fact that the SOP randomly changes with propagation through the fiber is taken into account in this model. According to (1), the average efficiency for random SOPs is 3/8 of the maximum value. In designing systems, however, we deal with the worst situation. Thus, the SOPs are usually assumed to be matched, and scalar expressions are used in discussing FWM, as in the following sections.

*b. Multi-amplifier system:* The FWM characteristics in multi-amplifier systems have become important since the advent of fiber amplifiers. The generated FWM light power in these systems is written as [4], [5]

$$P_{FWM} = \kappa P_{in}^3 e^{-\alpha l} \frac{[1 - \exp(-\alpha l)]^2 + 4 \exp(-\alpha l) \sin^2(\Delta\beta l/2)}{\Delta\beta^2 + \alpha^2} \frac{\sin^2(M\Delta\beta l/2)}{\sin^2(\Delta\beta l/2)}, \quad (2)$$

where  $\kappa$  is the constant including the nonlinear coefficient and the degeneracy factor,  $P_{in}$  is signal input power,  $\alpha$  is loss coefficient,  $l$  is the length of one section,  $M$  is the number of sections, and  $\Delta\beta$ , defined as  $\Delta\beta = \beta(f_i) + \beta(f_j) - \beta(f_k) - \beta(f_i + f_j - f_k)$  ( $\beta$  is propagation constant), represents the phase-mismatching. In (2), it is assumed that each channel has an equal input power, the length and the dispersion are equal for each section, and the amplifier gain is set equal to the loss of one section. The phase-mismatch dependence of the efficiency shows sharp peaks at particular conditions due to the last term, which is a unique feature in multi-amplifier systems. At those resonanced conditions, the generated power is  $M^2$  times larger than that in one section.

*c. Frequency dependence:* The FWM efficiency depends on the phase-mismatching  $\Delta\beta$ , as seen in (2), such that the efficiency is large for small  $\Delta\beta$  regarding the envelope of peaks due to the last term.  $\Delta\beta$  is written as [6], [7]

$$\Delta\beta = \frac{2\pi\lambda^2 D}{c} (f_i - f_k)(f_j - f_k) \quad \text{far from the zero - dispersion wavelength,}$$

$$\Delta\beta = -\frac{\lambda^4 \pi}{c^2} \frac{dD}{d\lambda} (f_i - f_0)(f_j - f_0)(f_i - f_k)(f_j - f_k) \quad \text{around the zero - dispersion wavelength.}$$

Here,  $\lambda$  is wavelength,  $c$  is light velocity,  $D$  is the chromatic dispersion, and  $f_0$  is the zero-dispersion frequency of the fiber. In most cases,  $\Delta\beta$  is large and the efficiency is small for large frequency spacing. In particular cases of  $(f_i + f_j)/2 = f_0$ ,  $\Delta\beta = 0$  and the efficiency is highest irrespective of the frequency spacing. However, the above model assumes uniform dispersion, which is not necessarily true in long fibers. In an experiment around the zero-dispersion wavelength, the result for a 10-km fiber was different from the theoretical prediction. This difference was attributed to the deviation of the chromatic dispersion [7]. A detailed study of this issue is now under way.

### III. INFLUENCE ON SYSTEM PERFORMANCE

In multi-wavelength systems, various channel combinations induce the signal deviation at a selected channel through FWM. The signal level at one moment depends on the phase relations among the other channel lights, which are difficult to take into account exactly. A simple approach to evaluating system degradation is to consider that the FWM light at a selected channel consists of FWM lights generated from each channel combination and that those FWM lights independently cause the signal fluctuation like the signal-spontaneous beat noise due to optical amplifiers [8]. This approach is useful in practice, though it is an approximate one since the phases of each FWM light are not completely independent.

Based on the above idea, FWM influence on system performance as well as allowable input power has been evaluated for various modulation schemes [9]-[12]. Allowable input power differs with the modulation scheme even when the other system conditions are the same. Roughly speaking, FWM crosstalk of -16~-20 dB, defined as the power ratio of the signal and FWM lights under the cw condition, causes 1 dB power penalty.

### IV. COUNTER-MEASURES

Several measures have been proposed to reduce the FWM effect. These include (a) modulating signal light frequencies to spread the sig-FWM beat spectrum, a part of which is cut at the demodulation stage [13]; (b) allocating signal wavelength with unequal spacings [14]; (c) inserting multi/demultiplexers and delay lines into multi-amplifier systems to randomize the phase relations of FWM lights generated in each fiber section [15]; and (d) scrambling the polarization states of signal lights [16].

The author wishes to thank Dr. H. Toba and Dr. N. Shibata for their support and Dr. K. Nosu for encouragement during this study.

### REFERENCES

- [1] K. Inoue, IEEE J. Quantum Electron., 28, p. 883, 1992.
- [2] K. O. Hill et al., J. Appl. Phys., 49, p. 5098, 1979.
- [3] J. Botineau and R. H. Stolen, J. Opt. Soc. Am., 72, p. 1592, 1982.
- [4] D. G. Schadt, Electron. Lett., 27, p. 1805, 1991.
- [5] K. Inoue, Opt. Lett., 17, p. 801, 1992.
- [6] N. Shibata et al., IEEE J. Quantum Electron, QE-23, p. 1205, 1987.
- [7] K. Inoue, J. Lightwave Technol., 10, p. 1553, 1992.
- [8] N. A. Olsson, J. Lightwave Technol., 7, p. 1071, 1989.
- [9] E. Lichtman, J. Opt. Commun., 12, p. 53, 1991.
- [10] K. Inoue, H. Toba, and K. Oda, J. Lightwave Technol., 10, p. 350, 1992.
- [11] K. Inoue and H. Toba, J. Lightwave Technol., 10, p. 361, 1992.
- [12] K. Inoue et al., to be published in J. Lightwave Technol..
- [13] K. Inoue, IEEE Photon. Technol. Lett., 4, p. 1301, 1992.
- [14] F. Forghieri et al., OFC93, FC4, 1993.
- [15] K. Inoue, J. Lightwave Technol, 11, March, 1993.
- [16] K. Inoue, to be published in J. Lightwave Technol..

## Statistical Distribution of Four-Wave Mixing Interference in ASK Optical WDM Systems

Ting-Kuang Chiang, Debasish Datta and Leonid G. Kazovsky

Department of Electrical Engineering, STAR LAB, Stanford University, Stanford, CA 94305-4055

Tel. (415) 723-1382, Fax. (415) 723-9251, E-mail: tkchiang@leland.stanford.edu

The four-wave mixing (FWM) effect in optical fiber causes mixing of three optical waves to generate a fourth one. It is caused by the third order nonlinear susceptibility of the fiber. If the frequency of the newly generated wave lies within the desired signal band, the resulting interference leads to crosstalk between channels and degrades system performance [1]. In a wavelength-division-multiplexed (WDM) optical system, the number of interference terms increases rapidly with the number of channels. The power of each FWM interference term is proportional to the cube of the power of the incident waves, and increases with transmission distance. Therefore, the FWM effect is likely to limit the performance of WDM systems by introducing unwanted interferences.

The phase and amplitude of each FWM interference term have well-defined relationship with the phases and amplitudes of the incident waves [2]. The combined effect of a large number of FWM interference terms is treated as a Gaussian random process in some publications [3]. However, the phase relationship between the interference terms makes the interference deviate from a Gaussian process. We performed computer simulations to investigate the statistical properties of the FWM interference. The resulting probability density function (pdf) of FWM interference was further used to calculate the receiver bit error rate (BER). The simulation results are compared with the Gaussian approximation results.

Our simulation program simulates a coherent ASK (amplitude-shifted-keying) optical WDM system. In the program, several independent optical channels are computer-generated with random laser phase noise, uncorrelated random data streams, and independent clocks with random jitter. The program also generates all FWM interference terms that fall within the frequency band of the received channel. Each FWM term is calculated analytically using the expressions given in reference [2]. Next, the program evaluates the pdf of the sum of these FWM terms both at IF and at the envelope detector output. Finally, the receiver BER is evaluated using the simulated pdf's of FWM-impaired signals.

The following numerical results are shown for the 8th channel (the worst case) of a 16-channel WDM system with a link of 100 km dispersion shifted fiber when all the channels except the 8th are transmitting '1'. The rest of system parameters are as follows: incident optical power = 0.1 mW/channel, wavelength = 1.55  $\mu\text{m}$ , attenuation = 0.2 dB/km, channel spacing = 10 GHz, bit rate = 1 Gbit/s, laser linewidth = 10 MHz,  $A_{\text{eff}} = 55 \mu\text{m}^2$ , nonlinear susceptibility  $\chi_{1111} = 6 \times 10^{-15} \text{ cm}^3/\text{erg}$ , responsivity = 0.6 amp/watt, and group velocity dispersion = 0.5 ps/km-nm.

Figure 1 shows the simulated pdf's of the sum of the FWM interference terms at IF when the received channel is transmitting '0'. The in-phase component represents the component of the FWM interference that is in-phase with the desired signal at IF, and the quadrature-phase component represents the one that is 90 degrees out-of-phase with the IF. The main lobe of the simulated pdf is seen to match very well with the Student's t-distribution for both in-phase and quadrature-phase components. The corresponding Gaussian pdf is also shown in Fig. 1 for comparison. In expanded scale, we find that the tails of the simulated pdf's drop off slower than the Gaussian pdf, and tend to decay exponentially.

Figure 2 shows the simulated pdf of the voltage at the envelope detector output for '0' transmission. A Gamma distribution is seen to match the simulated pdf very well. If the interference had a Gaussian-like behavior at the IF, the voltage at the envelope detector output should have a Rayleigh distribution [4]. The corresponding Rayleigh distribution is also shown in Fig. 2 for comparison. It can be found by expanding the scale in Fig. 2 that the simulation results have larger tails than the Rayleigh distribution corresponding to the Gaussian approximation.

Figure 3 shows the simulated pdf's of the sum of the FWM interference terms at IF when the received channel is transmitting '1'. Similar to the '0' transmission case, the main lobe of the in-phase component is seen to match very well with the Student's t-distribution. The quadrature-phase compo-

ment is shifted from the origin and distorted from the t-distribution shape due to cross-phase modulation. The corresponding Gaussian pdf is also shown in Fig. 3 for comparison. The tails of the simulated pdf's still drop off slower than the Gaussian pdf.

Figure 4 shows the simulated pdf of the voltage at the envelope detector output for '1' transmission. The main lobe of the simulated pdf is seen to match the t-distribution in this low power case. If the interference had a Gaussian-like behavior at IF, the voltage at the envelope detector output should have a Rician distribution [4]. The corresponding Rician distribution is also shown in Fig. 4 for comparison. It can be also found by expanding the scale in Fig. 4 that the simulation results have larger tails than the Rician distribution corresponding to the Gaussian approximation. Therefore, the resulting BER is higher in simulation than in Gaussian approximated systems.

In summary, the statistical behavior of FWM interference was investigated by computer simulations. The pdf of the FWM interference was found to be non-Gaussian. The distribution at the IF is well approximated by the Student's t-distribution. The

resulting pdf at the envelope detector output is well approximated by the gamma distribution and Student's t-distribution for '0' and '1' transmission respectively. The slower drop-off of the simulated pdf confirms that the Gaussian approximation under-estimates the system BER.

## References

- [1] A. R. Chraplyvy, "Limitations on lightwave communication imposed by optical-fiber nonlinearities," *J. of Lightwave Tech.*, vol. 8, no. 10, pp. 1548-1557, 1990.
- [2] K. O. Hill, D. C. Johnson, B. S. Kawasaki, R. I. MacDonald, "CW three wave mixing in single-mode optical fiber," *J. of Appl. Phys.*, vol. 49, no. 10, pp. 5098-5106, 1978.
- [3] E. Lichtman, "Performance degradation due to four-wave mixing in multichannel coherent optical communication systems," *J. of Optical Comm.*, vol. 12, no. 2, pp. 53-58, 1991.
- [4] S. Haykin, *Communication Systems*, 2nd Ed., New York: John Wiley & Sons Inc., 1983.

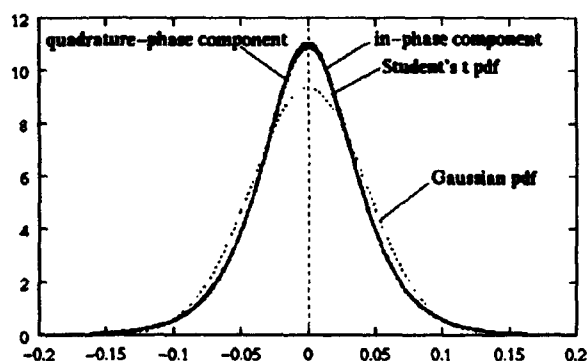


Figure 1. The pdf of FWM interference at IF; '0' transmission.

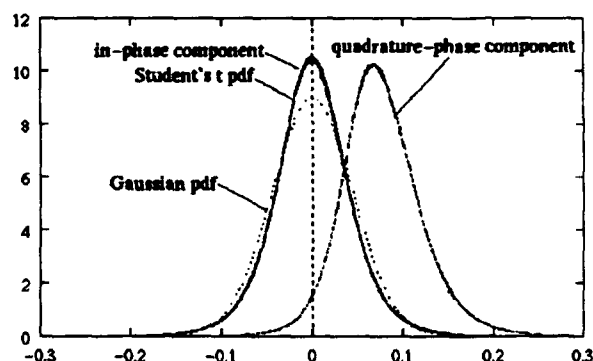


Figure 3. The pdf of FWM interference at IF; '1' transmission.

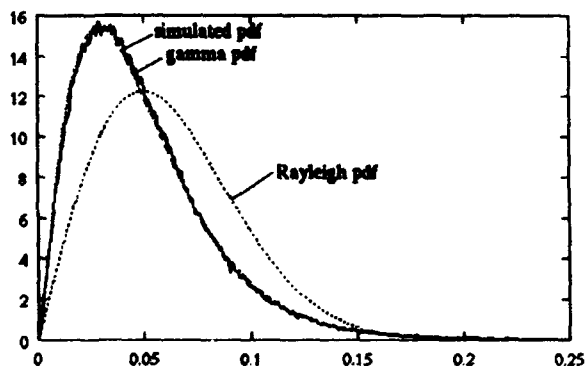


Figure 2. The pdf of FWM interference at the envelope detector output; '0' transmission.

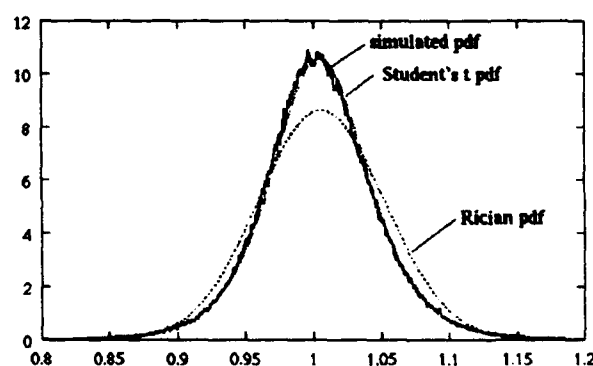


Figure 4. The pdf of FWM interference at the envelope detector output; '1' transmission.

# Impact of Four Wave Mixing on Optical FSK WDM Communication Systems

Debasish Datta, Ting-Kuang Chiang and Leonid G. Kazovsky

Department of Electrical Engineering  
Stanford University  
Durand Building 202  
Stanford, CA 94305-4055

The performance of optical wavelength-division-multiplexed (WDM) systems may be degraded by four wave mixing (FWM) due to the fiber nonlinearities [1]. The impact of FWM on system performance depends on the modulation technique and receiver structure. The frequency-shift-keying (FSK) heterodyne system using nonsynchronous demodulation with single-filter envelope detection (SFED) is relatively easy to implement, and has been used in many experiments [2]. The impact of FWM on heterodyne FSK systems employing dual-filter envelope detection has been analyzed in [3], but the impact of FWM on FSK WDM systems employing SFED receivers is yet to be analyzed.

The FWM-generated interference has a wider spectrum than the signal, and therefore, the receiver bandpass filter (BPF) can help in alleviating the impact of FWM; previous studies do not take this into account.

In this paper we theoretically analyze the impact of FWM on an optical FSK WDM system employing SFED receiver. Our analysis takes into account the spectral mismatch between the signal and FWM interference and the impact of receiver BPF at the intermediate frequency (IF) on both signal and FWM interference. We show that without considering this effect one may underestimate the system performance.

In SFED receiver the IF signal is processed by a BPF at the IF corresponding to the 'mark' transmission, followed by an envelope detector and a decision circuit. The BPF input for a receiver tuned to the  $j$ -th wavelength can be expressed as

$$i(t) = I_j \cos(\omega_{jM}t + \phi_j) + \sum_{m=k+l-j} Z_{klm} g_{klm}(t) \cos(\omega_{jM}t + \phi_{klm}) + n(t) \quad (1)$$

where  $I_j$  and  $\phi_j$  are the amplitude and phase of the signal,  $\omega_{jM}$  is the IF frequency for the mark transmission in the  $j$ -th channel,  $Z_{klm}$  and  $\phi_{klm}$  represent the amplitude and phase of the FWM interference term produced by  $k$ -th,  $l$ -th and  $m$ -th channel signals,  $g_{klm}(t)$  is a unit amplitude random rectangular pulse train representing the normalized envelope of the same FWM term and,  $n(t)$  is the shot noise at BPF input. We assume that the BPF is a matched filter at  $\omega_{jM}$ , with its lowpass equivalent as an integrate-and-dump filter. Hence, at the end of each bit interval in the BPF output, the normalized envelope  $g_{klm}(t)$  (unit amplitude pulse of random width) is

integrated to a value that is uniformly distributed between zero and a maximum value proportional to the bit duration.

Using eq.(1), we first develop a statistical model for the filtered IF envelope resulting from the interference between the desired signal and the FWM components. At the end of a bit interval (say,  $[0, T]$ ), the mark and space envelopes at the BPF output ( $a_M(T)$  and  $a_S(T)$  respectively) due to the signal-FWM interference can be expressed as

$$a_{M,S}^2(T) = [A_{M,S} + \sum_{klm} B_{klm} \cos(\varphi_{klm} - \varphi_j)]^2 + [\sum_{klm} B_{klm} \sin(\varphi_{klm} - \varphi_j)]^2 \quad (2)$$

where  $A_M$  and  $A_S$  are the filtered signal amplitudes for mark and space ( $A_S = 0$ ), and  $B_{klm}$ 's represent the filtered FWM amplitudes at  $t = T$ . The envelopes  $a_{M,S}(T)$  resemble the carrier envelopes encountered in radio communication channels with multipath fading [4]. Following steps similar to [4] and considering the uniformly distributed random contribution of filtered  $g_{klm}(t)$  in  $A_M$  and  $B_{klm}$ , the statistics of  $a_S(T)$  and  $a_M(T)$  can be shown to follow Rayleigh and Rician distributions, respectively. Next we find the receiver bit error rate (BER) in presence of shot noise, conditional on FWM-impaired IF envelope. The overall BER is evaluated by averaging the conditional BER over the IF envelope statistics.

The system performance is evaluated from the plots of receiver BER in the worst-case channel versus input optical power in the fiber for different fiber lengths. For a non-dispersion-shifted fiber the following parameters are assumed: dispersion = 17ps/nm-km, loss = 0.2dB/km, effective core area = 50 $\mu\text{m}^2$ , nonlinear susceptibility = 6 x 10<sup>-15</sup>cm<sup>3</sup>/erg, wavelength = 1.55 $\mu\text{m}$ .

As an example, consider a 16-channel system with the bit rate of 1Gbps/channel and channel spacing of 10GHz. For this system our results show that the bandpass filtering brings the FWM power down by about 4.8dB. Each BER curve has a minimum, which exceeds 10<sup>-9</sup> when the transmission distance exceeds an upper limit. If the impact of BPF on signal and FWM interference is ignored (as in [3]), the theory predicts the maximum transmission distance of about 211km for a  $[\text{BER}]_{\min} = 10^{-9}$ . If this effect is included, the result is 223km. For the transmission distance of 223km, the FWM leads to a receiver power penalty of about 1.8dB with respect to shot noise limited operation.

## REFERENCES

- [1] A. R. Chraplyvy, "Limitations on Lightwave Communications Imposed by Optical-Fiber Nonlinearities," *J. Lightwave Technol.*, vol. LT-8, No. 10, pp. 1548-1557, October 1990.
- [2] G. Nicholson, "Transmission Performance of an Optical FSK Heterodyne System with a Single-Filter Envelope-Detection Receiver," *J. Lightwave Technol.*, vol. LT-5, No. 4, pp. 502-509, April 1987.
- [3] K. Inoue and H. Toba, "Theoretical Evaluation of Error Rate Degradation due to Fiber Four-Wave Mixing in Multichannel FSK Heterodyne Envelope Detection Transmissions," *J. Lightwave Technol.*, vol. LT-10, No. 3, pp. 361-366, March 1992.
- [4] S. Stein and J. J. Jones, *Modern Communication Principles*, McGraw-Hill, New York, 1967, Ch.16.

# POWER LIMITATIONS DUE TO FOUR-WAVE MIXING DEPLETION IN WDM SYSTEMS WITH UNEQUALLY SPACED CHANNELS

**Fabrizio Forghieri**

Università di Parma  
Dip. di Ing. dell'Informazione  
I-43100 Parma, Italy

**Robert W. Tkach**

AT&T Bell Laboratories  
Crawford Hill Laboratory  
Holmdel, NJ 07733

**Andrew R. Chraplyvy**

AT&T Bell Laboratories  
Crawford Hill Laboratory  
Holmdel, NJ 07733

Very high capacity long-haul optical communication systems can be designed by using erbium-doped fiber amplifiers, wavelength division multiplexing (WDM) and dispersion-shifted fiber. The use of dispersion-shifted fiber allows higher bit-rates, but enhances the efficiency of four-wave mixing (FWM) wave generation by reducing the phase-mismatch naturally provided by the fiber dispersion [1], thus causing FWM to become the dominant nonlinear effect [2].

FWM is a nonlinear process in which three waves of frequencies  $f_i, f_j$ , and  $f_k$  ( $k \neq i, j$ ) interact through the third-order electric susceptibility of the optical fiber to generate a wave of frequency  $f_{ijk} = f_i + f_j - f_k$  [3].

In this process power is transferred (in approximately equal amount) from channels  $i$  and  $j$  to channel  $k$  and to the FWM wave at  $f_{ijk}$ , causing depletion of channels  $i$  and  $j$ . The power lost by channel  $i$  can be computed by adding the power that has been transferred at frequency  $f_{ijk}$  at the end of the fiber to the power lost by the FWM wave during propagation.

Denoting with  $P_{ijk}(z)$  the power of the FWM wave at the point  $z$  in the fiber, the power of channel  $i$ ,  $P_i(z)$ , is given by

$$\frac{d}{dz}P_i(z) = -\alpha P_i(z) - \frac{d}{dz}P_{ijk}(z) - \alpha P_{ijk}(z),$$

where  $\alpha$  is the fiber loss coefficient. The first term on the right side is due to fiber loss, the remaining two represent the power loss due to FWM. The differential equation yields

$$P_i(z) = e^{-\alpha z}P_i(0) - P_{ijk}(z) + e^{-\alpha z}P_{ijk}(0).$$

This approach can be extended to the case in which optical amplifiers are employed through the transmission line to compensate fiber loss, by writing a differential equation for each fiber path between amplifiers.

If amplifiers with gain  $G = \exp(-\alpha l)$  are inserted after each of  $N$  fiber segment of length  $l$ , the power of channel  $i$  at the receiver can be found to be

$$P_i(Nl) = P_i(0) - e^{\alpha l}P_{ijk}(Nl),$$

where the initial condition  $P_{ijk}(0) = 0$  has been used. The relative power depletion of channel  $i$  due to the generation of the FWM wave at  $f_{ijk}$  is therefore given by

$$D_i = \frac{e^{\alpha l}P_{ijk}(Nl)}{P_i(0)}.$$

If  $D_i$  is small, as it should be if a large eye opening is desired,  $P_{ijk}(Nl)$  can be computed in the usual undepleted-pump approximation, thus slightly overestimating the power transfer. An expression for  $P_{ijk}(Nl)$  can be found in [4, eq. (11)].

In a WDM system, nine new optical waves are generated through FWM for each choice of three channels [2], therefore, even with only ten channels, hundreds of FWM waves are generated by FWM. If some of them have the same frequency, their build-up is affected by their beating. For example, if two FWM waves with same frequency but opposite phase are generated from different triplets of channels, they cancel each other, so that there is no power transfer at all.

In WDM systems with equally spaced channels, all the waves generated by FWM inside the bandwidth of the system fall precisely at one of the channel frequencies [5], [6]. This effect can be avoided by using unequal channel separations. A design methodology of the channel spacings has been presented in [7], by which no FWM waves are generated at any channel frequency. This result is obtained by choosing the frequency separation of any two channels different from that of any other pair of channels.

With this optimum choice of channel separations the FWM waves are generated at frequencies evenly distributed between channels, only a few of them for each frequency. The few FWM waves that are generated at the same frequency usually have very different phase-mismatch, so that the one with lower phase-mismatch will dominate. For this reason, in the unequal channel spacing case, the power depletion of each channel can be evaluated by considering the FWM waves with higher efficiency that that channel contributes to generate, and just add the depletion relative to each one of them. This is correct if the FWM waves considered are generated at different frequencies and are the dominant ones at their frequency. Also note that to get maximum depletions of a channel, only the signals in that channel and in the channels involved in generating the dominant FWM waves need to be at "1". If the dominant FWM waves are only a few, this is an event with high probability, even if the number of channels is very high.

As an example, the power depletion has been computed with this method for the system reported in [7]. It is a 500 km long, 10 channel WDM system with 10 Gb/s per channel, with amplifiers spaced by 50 km using dispersion-shifted fiber with second order dispersion  $0.08 \text{ ps/nm}^2/\text{km}$ . The channels are unequally spaced, with minimum separation of 1 nm. From the power depletion  $D$ , the eye aperture of each channel has been computed as  $1 - D/2$ .

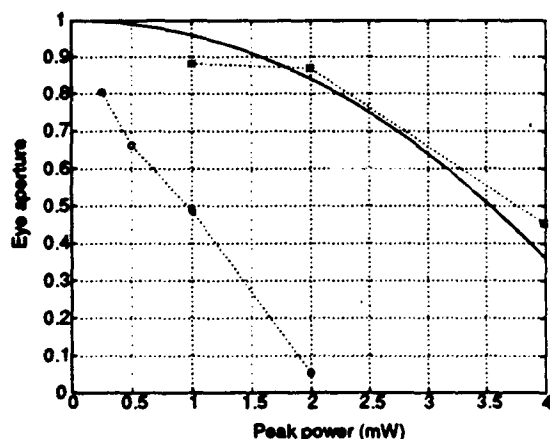


Fig. 1. Eye aperture of the worst channel vs. input peak power per channel. (—) Depletion limit and (•) simulations with unequal spacing. (o) Simulations for equal spacing.

The eye aperture of the worst case channel is shown versus input power in Fig. 1, where simulation results are also given, denoted with stars. Simulation for the equal channel spacing are reported as reference with circles. The lower eye aperture shown by the simulations for low input power might be due to linear distortion of the pulses or to interactions with the FWM waves generated at frequencies near the channel frequencies, that partially overlap with the channels. When the input power increases, depletion due to FWM starts to dominate. At high depletion levels, the variation of the channel power should be considered when computing  $P_{ijk}(z)$ , therefore the theoretical result is less accurate and provides a lower bound of the eye aperture.

## REFERENCES

- [1] N. Shibata, R. P. Braun, and R. G. Waarts, "Phase-mismatch dependence of efficiency of wave generation through four-wave mixing in a single-mode optical fiber," *IEEE J. Quantum Electron.*, vol. 7, pp. 1205-1210, July 1987.
- [2] A. R. Chraplyvy, "Limitations on lightwave communications imposed by optical-fiber nonlinearities," *J. Lightwave Technol.*, vol. 8, pp. 1548-1557, Oct. 1990.
- [3] K. O. Hill, D. C. Johnson, B. S. Kawasaki, and R. I. MacDonald, "CW three-wave mixing in single-mode optical fibers," *J. Appl. Phys.*, vol. 49, pp. 5098-5106, Oct. 1978.
- [4] K. Inoue, "Phase-mismatching characteristic of four-wave mixing in fiber lines with multistage optical amplifiers," *Opt. Lett.*, vol. 17, pp. 801-803, June 1992.
- [5] R. G. Waarts and R.-P. Braun, "System limitations due to four-wave mixing in single-mode optical fibres," *Electron. Lett.*, vol. 22, pp. 873-875, July 1986.
- [6] M. W. Maeda, W. B. Sessa, W. I. Way, A. Yi-Yan, L. Curtis, R. Spicer, and R. I. Laming, "The effect of four-wave mixing in fibers on optical frequency-division multiplexed systems," *J. Lightwave Technol.*, vol. 8, pp. 1402-1408, Sep. 1990.
- [7] F. Forghieri, R. W. Tkach, A. R. Chraplyvy, and D. Marcuse, "Reduction of four-wave mixing crosstalk in WDM systems using unequally spaced channels," in *Proc. OFC '93, San Jose, Ca.*, paper FC4, pp. 252-253, Feb. 1993.

## What Is The Actual Capacity Of Single-Mode Fibers In Amplified Lightwave Systems?

A. R. Chraplyvy, R. W. Tkach

AT&T Bell Laboratories, P. O. Box 400, Holmdel, NJ 07733-0400

In this paper we assume that the degradations caused by SBS, SPM, CPM, and FPM can be minimized by clever system design. The limits on fiber capacity caused by stimulated Raman scattering (SRS) will be discussed. Initially we assume nearly ideal fiber, amplifier, and receiver properties. Subsequently, the additional limitations arising from more realistic assumptions will be discussed.

Unlike conventional lightwave systems, the performance of amplified systems is not measured by received optical power, but by optical signal-to-noise ratio (SNR). A certain SNR is required for a particular bit-error-ratio (BER) [1]. This requires a minimum input power per channel. For longer systems the required input power increases and the systems are more susceptible to SRS degradation. The unpolarized noise,  $N$ , at the end of a system  $L$  km in length is  $2Mh\nu n_{sp} B_O (G-1)$ , where  $M$  is the number of amplifiers,  $h\nu$  is the photon energy,  $n_{sp}$  is the amplifier excess noise factor,  $B_O$  is the optical bandwidth, and  $G$  is the amplifier gain.  $M$  equals  $L/L_A$ , where  $L_A$  is the amplifier spacing.  $G$  equals  $Ee^{\alpha L_A}$ , where  $E$  is the excess input coupling loss factor at each amplifier (e.g.,  $E=2$  for 3 dB coupling loss), and  $\alpha$  is the loss coefficient of the fiber. The minimum average input power,  $P$ , in each channel is  $RN$ , where  $R$  is the required SNR for a particular BER [1]. This power can be expressed as

$$P = 2Rh\nu n_{sp} B_O L (Ee^{\alpha L_A} - 1) / L_A. \quad (1)$$

The SRS degradation in amplified systems is in the form of reduced SNR in the short-wavelength channels. Because the noise is added periodically over the entire length of a system, it experiences less Raman loss than the signal. For small degradations, the fractional depletion of the noise is half the fractional depletion of the signal (e. g. a 1 dB signal depletion corresponds to a 0.5 dB SNR degradation). Therefore, a system that, in the absence of SRS, operated at a particular required BER would no longer meet the required SNR and BER in the presence of SRS degradation.

Following the analysis in [2], to ensure a SNR degradation of less than 0.5 dB in the worst channel the following inequality must be satisfied:

$$n(n-1)P f L_e < 8.7 \times 10^{12} \text{ Hz} \cdot \text{W} \cdot \text{km}, \quad (2)$$

where  $n$  is the number of channels,  $f$  is the frequency separation between channels,  $P$  is given by Equation 1, and  $L_e$  is the effective length of the entire system. Equations 1 and 2 give

$$n(n-1) < \frac{8.7 \times 10^{12}}{2Rh\nu n_{sp} f B_O (L/L_A)^2 \left( \frac{1-e^{-\alpha L_A}}{\alpha} \right) (Ee^{\alpha L_A} - 1)} \quad (3)$$

The total number of channels decreases linearly with total system length, and decreases as the square root of amplifier excess noise factor, channel spacing, and required SNR at the receiver. However, the capacity of WDM systems is most sensitive to the exponential dependence of required amplifier gain on fiber loss and amplifier spacing (last term in the denominator of Equation 4).

We start with the following assumptions. The data rate in each channel is 2.5 Gb/s. The channel separation is 62 GHz (0.5 nm at 1.5  $\mu\text{m}$ ). The amplifiers are ideal, i.e. the gain is flat and infinitely broad, the excess noise factor is unity, and the excess input coupling loss factor is unity. The average fiber loss including splices is 0.2 dB/km. The mode area is  $8 \times 10^{-7} \text{ cm}^2$ . The optical filter width at the receiver is 10 GHz. Receiver margins are assumed to be zero. With these assumptions, the required SNR is  $R = 9$  [1]. The results will be parameterized in terms of amplifier spacing. Four different amplifier spacings are considered, 25 km, 50 km, 100 km, and 150 km.

Figure 1 shows the limits in the number of channels and total capacity using the assumed system parameters. Note that for transcontinental distances, fewer than 100 channels can be accommodated. We now assume more realistic system parameters. The average fiber loss coefficient including all splices is

0.25 dB/km. The excess noise factor of the amplifiers is two, the excess input coupling loss factor of the amplifiers is two, and typically 10 dB of total transmitter/receiver margin ( $R = 90$ ) is required. Figure 2 shows the total number of channels and capacity with these system parameters. Note the dramatic reduction in system capacity. Transcontinental capacity is less than ten channels. In Figure 2 we have assumed that the amplifier gain bandwidth is very large. For erbium-doped fiber amplifiers with 40-nm gain bandwidths the maximum number of channels is 80.

These calculations are for worst-case scenarios, that is, for marks occurring in each channel and absence of chromatic dispersion. Realistically, with chromatic dispersion and balanced bit patterns, on average a mark in any given channel will experience Raman gain or loss due to marks in half the other channels. In addition, a small increase in capacity can be expected by implementing equalization techniques [3].

- [1] D. Marcuse, "Derivation of analytical expressions for the bit-error probability in lightwave systems with optical amplifiers," J. Lightwave Technol. 8, p. 1816, 1990. When using Figure 3 of this reference to determine required signal-to-noise ratios note that the signals are *peak* powers. We, on the other hand, express signals as *average* powers. The reader should be careful to include a factor of two when transferring information between the two papers.
- [2] A. R. Chraplyvy, "Optical power limits in multichannel wavelength-division-multiplexed systems due to stimulated Raman scattering," Electron. Lett. 20, p. 58, 1984.
- [3] A. R. Chraplyvy, J. A. Nagel, and R. W. Tkach, "Equalization in amplified WDM lightwave transmission systems," IEEE Photonics Technol. Lett. 4 R, p. 920, 1992.

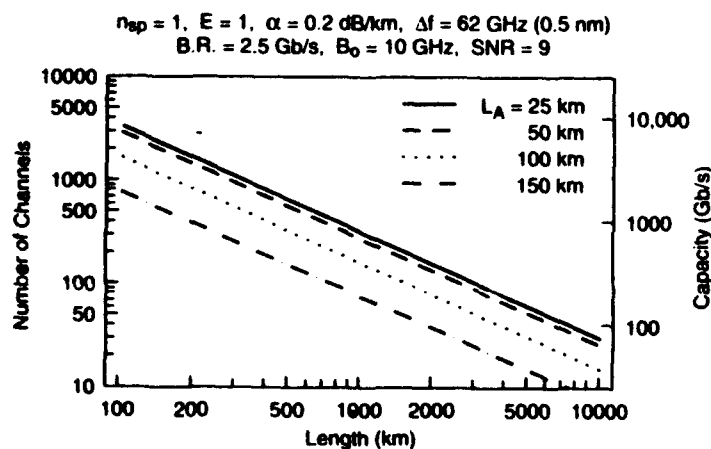


Figure 1

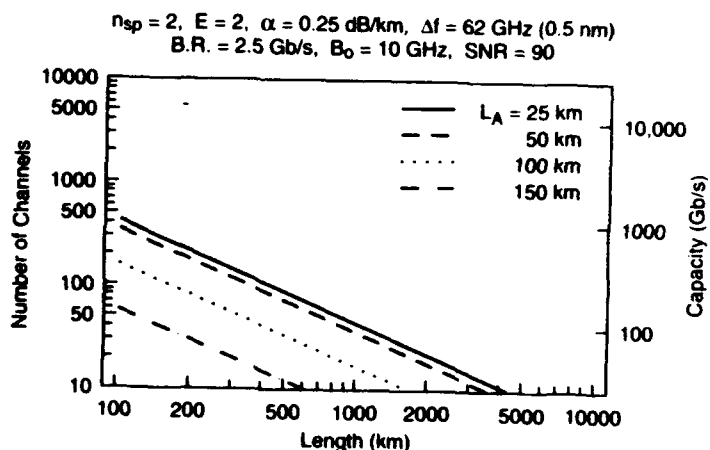


Figure 2

#### FIGURE CAPTIONS

1. The maximum number of 2.5 Gb/s channels and total capacity versus system length for four different amplifier spacings,  $L_A$ , assuming ideal amplifiers.
2. The maximum number of 2.5 Gb/s channels and total capacity versus system length assuming realistic amplifiers ( $n_{sp}=2$  and  $E=2$ ). For erbium-doped fiber amplifiers with 40-nm gain bandwidth the maximum number of channels is 80.

# **Stimulated Brillouin Threshold Dependence on the Mark Density of a Phase Modulated Optical Signal**

X. P. Mao\*, R. W. Tkach, A. R. Chraplyvy and R. M. Derosier

AT&T Bell Laboratories  
Crawford Hill Laboratory  
Holmdel, New Jersey 07733  
(201)888-7242

\* present address: C-Cor Electronics, 60 Decibel Rd., State College, PA 16801

Stimulated Brillouin scattering (SBS) sets a limit on the power injected into the fiber in a lightwave communication system. The threshold power for SBS can be increased, and thus the allowable power increased, by modulation of the signal light. <sup>[1]</sup> The most effective form of modulation is phase-shift-keying (PSK). For example, in a single mode fiber of 50 km and 0.2 dB/km loss, the SBS threshold is about 6 dBm for CW power, while the threshold increases to 26 dBm if 2 Gb/s suppressed-carrier PSK modulation is used. <sup>[2]</sup> Thus this system can operate at a higher level of input optical power, giving a larger system loss budget.

However, this theoretical advantage is obtained only when the optical carrier in the modulated field is fully suppressed. To meet this condition, a balanced modulated signal (mark density=0.5) must be used. While in normal communication systems the binary information signal has a mark density of 0.5 averaged over a large time scale, for SBS suppression the balanced condition must be achieved in a shorter time  $\Delta T_B$ , the characteristic time for the Brillouin scattering process. If the digital signal in  $\Delta T_B$  is not balanced, an instantaneous Brillouin threshold lower than that given by a balanced signal will exist. For example, a sufficiently long string of marks or spaces behaves like a CW wave, and leads to a very low SBS threshold.

In this paper we present measurements and calculations of the SBS threshold for PSK signals as a function of mark density, bit rate, and "averaging time", or the time over which a pattern is balanced. A strong dependence of threshold on mark density was observed, and a characteristic averaging time,  $\Delta T_B$  related to the Brillouin linewidth, is seen.

The experimental setup is diagrammed in Figure 1. To examine the SBS threshold dependence on modulation, digital pseudo-random signals of different pattern combinations are used in the experiments. Our main interest is to see how the SBS threshold behaves with the fluctuation of digital signal streams, in particular the variation of the ratio of marks to spaces. SBS threshold dependence on the bit rate B, mark density p, and the time  $\Delta T$  over which the mark density of the pattern becomes the average mark density.

Figure 2 shows a plot of the SBS threshold as a function of bit rate. The solid line is a theoretical prediction based on calculation of the optical spectrum. The threshold increases with bit rate, in good agreement with the theory. SBS threshold dependence on mark density at a fixed bit rate (151 Mbits/s) is shown in Figure 3. With a low mark density ( $<1/8$ ), the optical carrier is dominant and the measured threshold is almost independent of the bit rate. Again, the solid line is a theoretical prediction.

The marked dependence of threshold on an average quantity such as the mark density, brings into question the time scale over which this averaging should be done. One would expect that a very long stream of consecutive "1"s or "0"s in a completely random pattern would lead to a SBS threshold approaching that of the CW case. To achieve the SBS suppression shown in Figure 2, the modulation should be balanced (mark density = 1/2) in a time less than the characteristic time for the Brillouin process,  $\Delta T_B$ . To verify this point, we use a signal which alternates between high (7/8) and low (1/8) mark density with a dwell time at constant mark density of  $\Delta T$ . We expect that for large  $\Delta T$ , the threshold will be as same as that using signal A with constant mark density of either 1/8 or 7/8, while for small  $\Delta T$ , the thresholds should converge to that given by a mark density of 1/2.

Figure 4 shows a plot of SBS threshold power vs  $\Delta T$ . The experiment was carried out at a bit rate of 900 Mbits/s. The characteristic time obtained from this figure,  $\Delta T_B = -30ns$ , is quite close to the inverse of the measured spontaneous Brillouin linewidth for this fiber of roughly 30 MHz. From this result it becomes

clear that pattern dependence of the SBS threshold can occur only if there is substantial variation of the mark density of the signal when averaged over times longer than  $30 \text{ ns}$ . For a  $2 \text{ Gb/s}$  signal this corresponds to 60 bits. Thus with attention to balanced coding, it is possible to eliminate pattern dependence in PSK systems.

1. A. R. Chraplyvy: "Limitations on lightwave systems due to optical nonlinearities," J. Lightwave Tech. 8, 1548 (1990).
2. E. Lichtman, R. G. Waarts, and A. A. Friesem: "Stimulated Brillouin Scattering Excited by a Modulated Pump Wave in Single-Mode Fibers", Journal of Lightwave Technology, Vol. 7, 1, (1989).

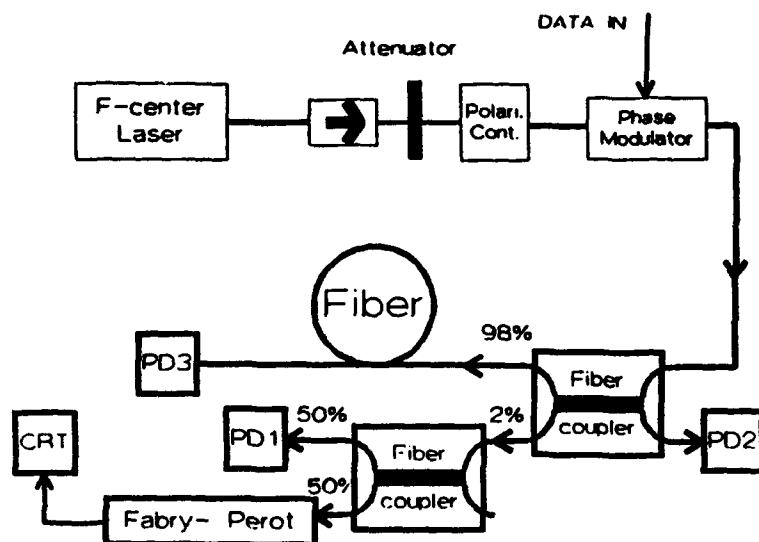


Figure 1. Experimental diagram.

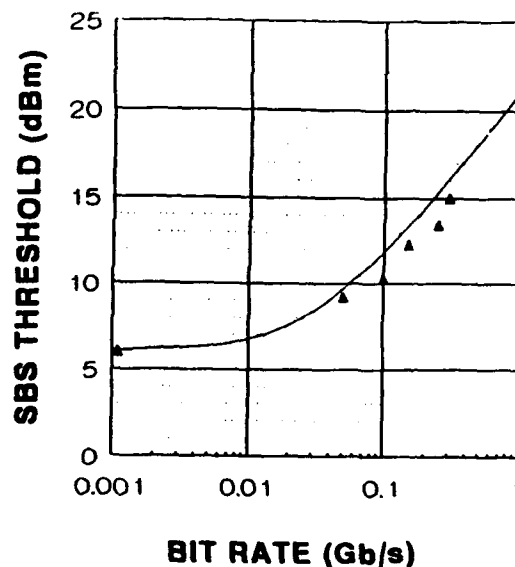


Figure 2. Plot of SBS threshold vs. bit rate.

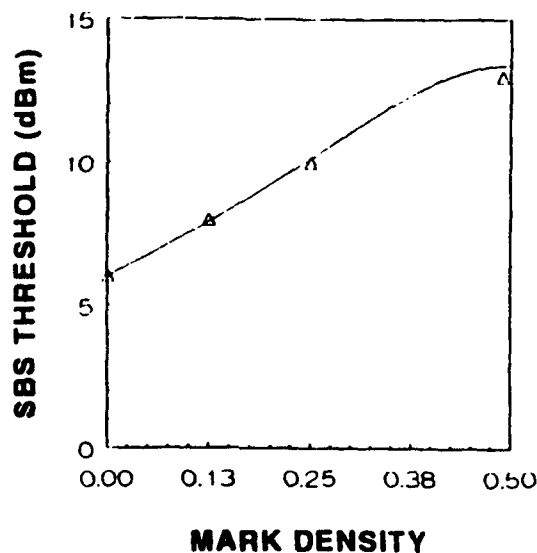


Figure 3. Plot of SBS threshold vs. mark density.

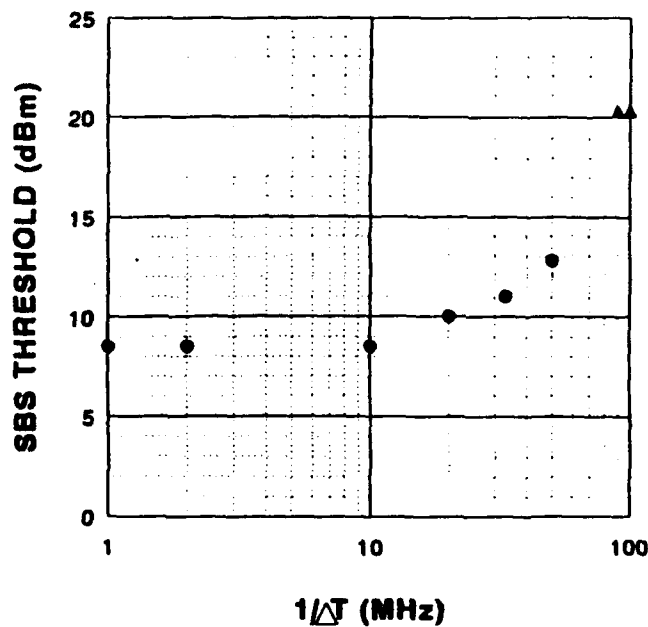


Figure 4. Plot of SBS threshold versus switching rate  $1/\Delta T$  with mark density alternating between  $1/8$  and  $7/8$ .

## Dispersion limit improvement of FM/IM signals by self-phase modulation

C.G. Joergensen, B. Mikkelsen, B.F. Jørgensen, R.J.S. Pedersen and, K.E. Stubkjaer

Center for Broadband Telecommunications  
Electromagnetics Institute, Technical University of Denmark  
Building 348, DK-2800 Lyngby, Denmark  
Phone: +45 42 88 14 44 Fax: +45 45 93 16 34

**Abstract.** *Simulations of unrepeated transmission of 10 Gbit/s signals generated by frequency to intensity modulation conversion show an improvement of the dispersion limit on standard fiber due to self-phase modulation by up to a factor of 2.5. This indicates a 1 dB limit of above 100 km for optimum modulation index of 0.5. For this index, simulations indicate the existence of a maximum allowable input power around +18 dBm, above which the channel breaks down. This also applies for dispersion shifted fiber, even at a lower power of around +14 dBm.*

**Introduction.** The next generation of optical communication systems will operate at 10 Gbit/s. Generation of optical signals modulated at 10 GHz is difficult: direct on/off keying gives excessive chirping even at small extinction ratios. External Mach-Zehnder amplitude modulators on the other hand tend to require very high modulation voltages. Particularly if the power level is very high, since then balanced push-pull operation is prohibited by Stimulated Brillouin Scattering (SBS). An alternative solution is frequency to intensity modulation (FM/IM) conversion [1], which has the advantages of small modulation voltage and high SBS threshold [2]. Typically the drive voltage to the laser is smaller than 2 Vp-p and at 10 GHz modulation the SBS threshold (for suitable modulation index) is higher than 20 dBm. The dispersion limit of FM/IM signals at 10 Gbit/s, however, is quite small [3], dependent on the receiver configuration and the frequency modulation index. This paper gives a theoretical investigation of this limit and the improvement attainable by exploiting non-linear self-phase modulation (SPM). Finally, the maximum allowable input power set by SPM for transmission over both non-dispersion shifted and dispersion shifted fiber is considered.

**Discussion.** The propagation of optical signals on fibers is described by the non-linear Schrödinger equation, which can be numerically investigated using the split-step Fourier transform method [4]. Using this method, we investigate the propagation of a  $2^7$  long bit sequence, obtained from a  $2^7-1$  pseudo random binary sequence (PRBS) and adding a logical zero, using 32 samples per bit. The spectrum of the resulting signal resembles that of the PRBS and simultaneously allows simple mathematical handling in terms of Fast Fourier Transform. The receiver bandwidth is 7 GHz, using a third order Butterworth filter. Figure 1 shows the simulated eye closure versus transmission distance over non-dispersion shifted fiber (17 psec/km/nm dispersion,  $80 \times 10^{-12}$  m<sup>2</sup> effective fiber area and 0.2 dB/km loss) of a 10 Gbit/s FM/IM signal, with the average optical input power as parameter for three different modulation indices (linear loss is compensated). It indicates three things: First, that the distance the signals may be transmitted for a given eye closure is increased by up to a factor of 2.5 by increasing the input power; Secondly, whereas the dispersion limit is increased for increasing modulation index at low input power, the dispersion limit is increased with decreasing modulation index for high input power; Finally, the figure indicates the existence of a maximum allowable input power, above which the channel breaks down.

This breakdown also exists on dispersion shifted fiber (1.6 psec/km/nm,  $40 \times 10^{-12}$  m<sup>2</sup> and 0.2 dB/km). Figure 2 shows the simulated eye closure vs. transmission distance for 10 Gbit/s transmission over dispersion shifted fiber of a FM/IM signal using a modulation index of 0.5. Obviously, with an input power of 10 dBm, a 10 Gbit/s signal can not be received after 300 km since the input power would be around -50 dBm, which is far below the best reported sensitivity of -38.8 dBm [5]. That would require +22 dBm transmitted power, which as mentioned above is possible from an SBS point of view. However, for input powers in that range, the transmission distance is limited by SPM, as seen from figure 2. Hence it seems as if 300 km unrepeated transmission at 10 Gbit/s is not possible. From the simulations, the limit is around 250 km for an input power of +13 dBm, as seen from figure 3.

**Conclusion.** Simulations indicate an increase up to 2.5 times of the dispersion limit of FM/IM signals by self-phase modulation for 10 Gbit/s signals transmitted over standard fiber. They also show, that the modulation index should be low when using high input powers, and finally, that there is a maximum allowable input power, above which

the channel breaks down. For dispersion shifted fiber a breakdown seems to exist at +14 dBm, limiting the maximum unrepeaters transmission distance of 10 Gbit/s signals to around 250 km (for assumed parameter values).

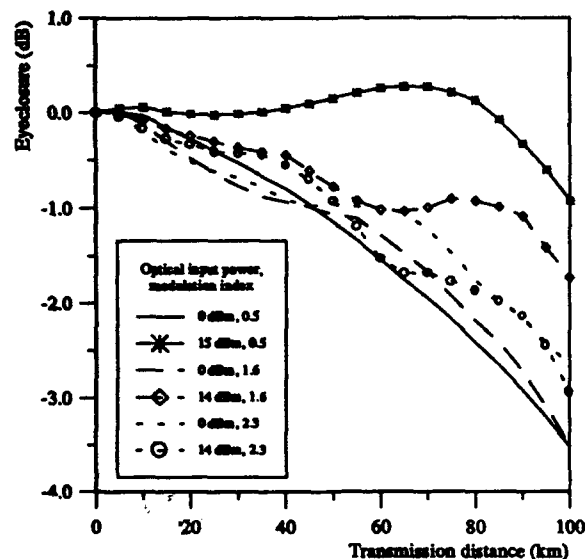


Figure 1a. Eye closure relative to back-to-back signal as function of transmission distance for optimum (within 1 dB) input power for modulation indices of 0.5, 1.6 and 2.3.

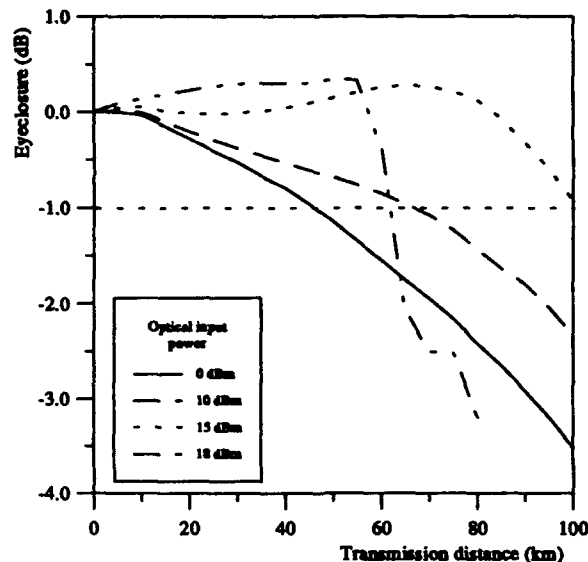


Figure 1b. Eye closure relative to back-to-back signal as function of transmission distance for modulation index of 0.5 with optical input power as parameter.

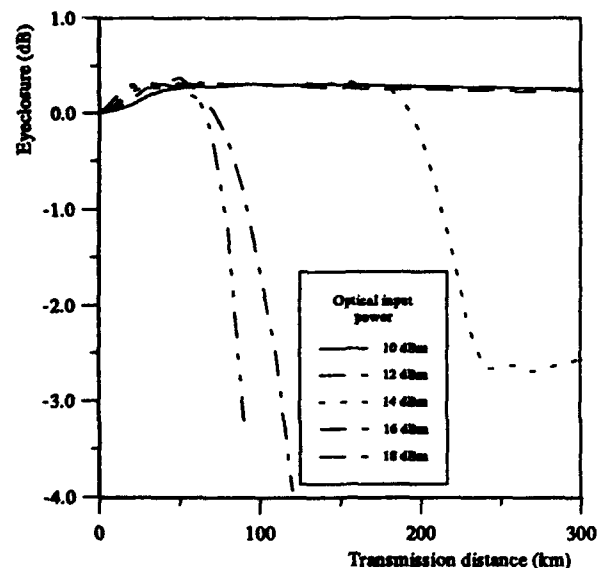


Figure 2. Eye closure relative to back-to-back signal as function of transmission distance for a modulation index of 0.5 with optical input power as parameter for transmission over dispersion shifted fiber.

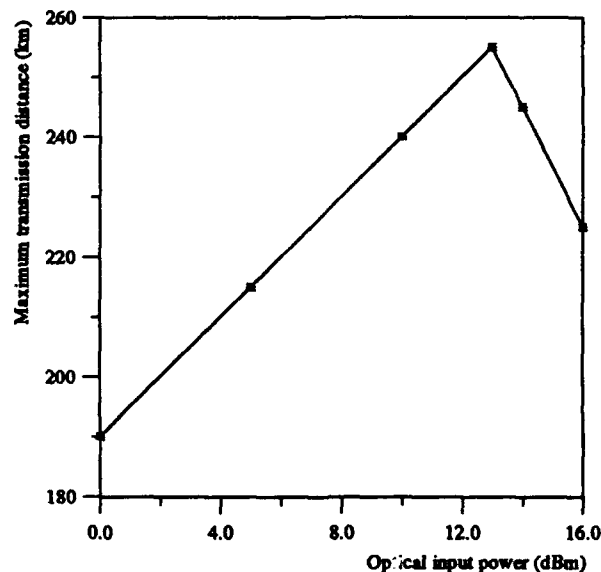


Figure 3. Maximum transmission distance for 10 Gbit/s FM/IM transmission over dispersion shifted fiber assuming receiver sensitivity of -38.8 dBm.

#### References.

- [1] E.G. Bryant et al., *Electron. Lett.*, vol. 26, no. 8, April 1990, pp528-529
- [2] T. Sugie, *J. Lightwave Technol.*, vol. 9, no. 9, September 1991, pp 1145-1155
- [3] A.F. Elrefaie et al *IEEE Photon. Technol. Lett.*, vol. 3, no. 1, January 1991, pp. 71-73.
- [4] G.P. Agrawal, *Nonlinear Fiber optics*, San Diego: Academic Press 1989
- [5] R.I. Laming et al, PD13, *Optical Amplifiers and Their Applications*, Santa Fe 1992

## 2 dB Reduction of Transmission Penalty by Self-Phase Modulation in a 5 Gbit/s FM/AM Conversion System Experiment

Bo Foged Jørgensen, Rune J. S. Pedersen and Carsten Gudmann Joergensen

Center for Broadband Telecommunications, Electromagnetics Institute  
Technical University of Denmark, Bldg. 348  
DK - 2800 Lyngby, Denmark

**Abstract:** The transmission penalty of a standard non-dispersion shifted fiber is experimentally demonstrated to be reduced by Self-Phase Modulation due to the optical Kerr effect. A 2 dB reduction of transmission penalty is achieved in a 5 Gbit/s FM/AM conversion system experiment over 205 km of fiber.

**Introduction:** The group velocity dispersion penalty of an optical communication system depends to some extent on the frequency chirp of the transmitted signal. One way to diminish the dispersion penalty in linear systems is by introducing a suitable chirp in the transmitted signal in order to obtain less dispersive pulse distortion [1]-[4].

In systems with high-power transmitters, the interaction between Self-Phase Modulation (SPM) due to the optical Kerr effect and the group velocity dispersion has to be taken into account. In order to demonstrate the effect of this interaction, we report observation of transmission penalty dependence of Self-Phase Modulation in a 205 km system experiment. The system employs a 5 Gbit/s frequency modulation (FM) to amplitude modulation (AM) conversion transmitter. A 2 dB reduction of transmission penalty with this modulation scheme is experimentally achieved by increasing the transmitter output power from +7 dBm to +14 dBm.

**Experimental Set-up:** The experimental set-up is shown schematically in Fig. 1. A three-electrode  $\lambda/4$ -shifted DFB laser with a 10 GHz FM-response bandwidth is used as transmitter [5]. The laser is operated at a wavelength of 1548 nm and the linewidth is 2 MHz. The laser is modulated directly from the word generator with a 5 Gbit/s Pseudo Random Binary Sequence of length  $2^7-1$ . The Continuous Phase - Frequency Shift Keying (CP-FSK) signal of the

transmitter laser is converted into an AM signal by the Mach-Zehnder interferometer (MZI). The differential delay of the MZI is  $\tau = 42$  ps. An Erbium Doped Fiber (EDF) booster amplifier with a saturated output power of +15 dBm is used in the transmitter. The level of the transmitter output power is adjusted by an optical attenuator.

The receiver is an optically preamplified pin-detector receiver. The two stage EDF preamplifier is pumped at 980 nm. The fiber-to-fiber gain (including input and output connector insertion loss) is 34 dB and the corresponding noise figure is 4 dB. An optical Fabry-Perot filter with a 3 dB bandwidth of 20 GHz ensures that the noise in the receiver is dominated by signal-spontaneous emission beat noise. The filter is locked to the signal by an Automatic Frequency Control (AFC). The periodic frequency response of the Fabry-Perot filter is eliminated by a broadband optical bandpass filter with a bandwidth of 2.5 nm. A fourth-order Bessel filter with 3 dB cut-off frequency of 4 GHz is used as post-detection filter. The Bit Error Rate (BER) is measured with the error counter which is synchronized by a clock signal recovered by the receiver.

205 km of standard non-dispersion shifted optical fiber is inserted in between the transmitter and the receiver. This fiber length is chosen as a compromise between the available dynamic range of input power and the amount

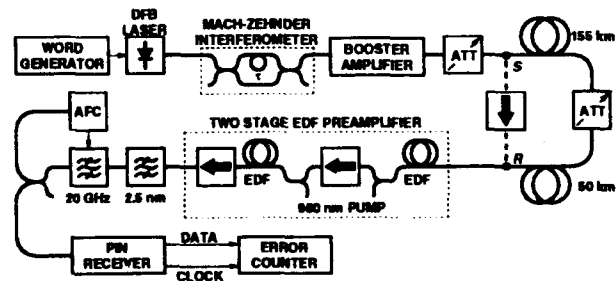


Figure 1. Experimental set-up.

of dispersion penalty. The average dispersion of the fiber is 17 ps/nm/km and the loss is 0.21 dB/km. The transmission fiber is separated in two sections of 155 km and 50 km, respectively. In between the two sections is a second optical attenuator applied in order to vary the level of the received power which is referred to the input connector of the optical preamplifier.

**Experimental Results:** Baseline measurement of the bit error rate is performed with an optical isolator inserted in between point 'S' and 'R' as indicated in Fig. 1. The frequency modulation index,  $\beta$ , is optimized in order to obtain the best receiver sensitivity. At a modulation index of  $\beta = 2.4$ , the extinction ratio at the output of the MZI is approximately 13 dB and the receiver sensitivity is -40.3 dBm @ BER =  $10^{-9}$ .

Transmission experiments are performed with the isolator replaced by the 205 km of fiber. BER measurements are performed at different levels of fiber input power varying from +14 dBm to +7 dBm. The FM index is optimized to  $\beta = 1.6$  at +14 dBm of fiber input power in order to achieve the best receiver sensitivity. The system performance is affected in two counter-acting ways by reduction of the modulation index: a) the frequency chirp of the transmitted signal is reduced proportionally to the reduction of  $\beta$  and b) the extinction ratio is reduced to approximately 10 dB. Consequently, the optimum modulation index is a trade-off between transmission penalty due to frequency chirp and extinction ratio penalty. For transmission over 205 km at +14 dBm of input power, the receiver sensitivity is -38.7 dBm @ BER =  $10^{-9}$  for  $\beta = 1.6$ . The sensitivity corresponds to a transmission penalty of 1.6 dB with reference to the baseline sensitivity.

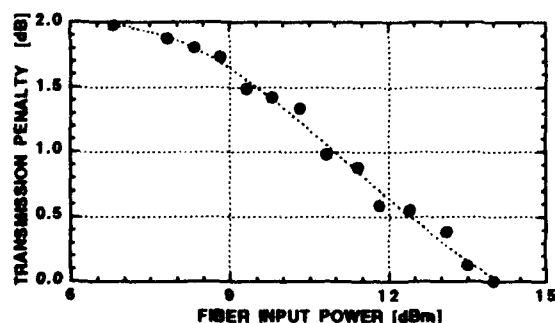


Figure 2. Transmission penalty (@ BER =  $10^{-9}$ ) after 205 km relative to +14 dBm of input power.

The transmission penalty relative to the receiver sensitivity obtained at +14 dBm (@ BER =  $10^{-9}$ ) is shown as a function of fiber input power in Fig. 2. The slope decreases towards low input power which indicates that the linear dispersion regime is encountered for decreasing input power. Reduction of the fiber input power to +7 dBm results in an additional penalty of 2.0 dB. The input power in the experiment can not be reduced below +7 dBm due to fiber losses. The slope also decreases towards high input power which suggests the existence of a minimum transmission penalty limit. However, the saturation output power of the booster amplifier available for this experiment was too low to verify the existence of such a limit.

**Conclusion:** A 2 dB reduction of transmission penalty of 205 km of standard non-dispersion shifted fiber has been achieved in a 5 Gbit/s optical communication system experiment. This reduction has been obtained by non-linear Self-Phase Modulation induced by increasing the input power from +7 dBm to +14 dBm.

**Acknowledgement:** We thank Fujitsu Laboratories Ltd. for supplying the three-electrode laser. We also thank Lycom A/S for supplying the transmission fiber and NKT Elektronik A/S for supplying the booster amplifier and the AFC for the Fabry-Perot filter.

## References

- [1] F. Koyama and K. Iga, "Frequency Chirping In External Modulators", IEEE J. Lightwave Technol., Vol. LT-6, No. 1, pp 87-93, Jan. 1988.
- [2] T. Saito, N. Henmi, S. Fujita, M. Yamaguchi and M. Shikada, "Prechirp Technique for Dispersion Compensation for a High-Speed Long-Span Transmission", IEEE Photon. Technol. Lett., Vol. 3, No. 1, pp 74-76, Jan. 1991.
- [3] A. H. Gnauck, S. K. Korotky, J. J. Veselka, C. T. Kemmerer, W. J. Minford and D. T. Moser, "Dispersion Penalty Reduction Using an Optical Modulator with Adjustable Chirp", IEEE Photon. Technol. Lett., Vol. 3, No. 10, pp 916-918, Oct. 1991.
- [4] A. D. Ellis, S. J. Pycock, D. A. Cleland and C. H. F. Sturrock, "Dispersion Compensation in 450 km Transmission System Employing Standard Fibre", IEE Electron. Lett., Vol. 28, No. 10, pp 954-955, May 1992.
- [5] Y. Kotaki and H. Ishikawa, "Narrow linewidth and wavelength tunable distributed feedback lasers", Proc. 2nd International Conference on Indium Phosphide and Related Materials, Paper TuC.6, pp 185-188, 1990.

## Interplay between Dispersion and Self-Phase Modulation

Christian Kurtzke,  
*Institut fuer Hochfrequenztechnik,  
Technical University of Berlin,  
Einsteinufer 25, 1000 Berlin 10, Germany*

Dietrich Marcuse,  
*AT&T Bell Laboratories, Holmdel, NJ 07733-0400, USA*

The limitations of future optical communication systems will be determined by fiber nonlinearities [1]. Therefore, the challenging problem for physicists and engineers consists in the reduction of nonlinear performance deterioration by developing an appropriate system design. The largest bit rate-distance products reported so far have been achieved with soliton transmission which is per se insensitive to nonlinear degradation. In comparison to nonreturn-to-zero (NRZ) systems, however, solitons involve a rather sophisticated technology. This leads to the question, whether an NRZ-design can be found, that simultaneously meets the requirements of simplicity and effectiveness. As previous studies pointed out, fiber dispersion is a key parameter in this design. In particular, it has recently been shown, that Four-Photon Mixing (FPM) can be successfully suppressed by the use of non-zero dispersion fibers [3].

In this paper, we investigate the impact of chromatic dispersion on another major effect - Self-Phase Modulation (SPM). Although the interplay between dispersion and SPM has been intensively studied in the context of solitons, the actual interaction in NRZ-systems has not yet been fully understood.

To point out the complexity of SPM induced system degradation we investigated the nonlinear behaviour of two different NRZ direct-detection systems, by numerically solving the nonlinear Schroedinger equation. The results in fig. 1 (system 1) suggest that an increase in dispersion leads to a higher nonlinear penalty. In contrast, fig. 2 (system 2) shows that an increase in dispersion reduces the system penalty. (Both systems do not exhibit any dispersion penalty in the linear case). To explain these contradictory results the spectral and temporal interplay between dispersion and self-phase modulation has to be studied.

Due to the strong dependence of SPM on the shape of the pulse propagating in the fiber, an accurate penalty prediction has to account for the changes in pulse shape caused by chromatic dispersion. In fig. 3 we plotted the deformation for a gaussian and a non-gaussian (realistic) pulse as a function of fiber length. As can be seen, the traditional intuitive conception of dispersion resulting only in pulse broadening is limited to gaussian pulses. Whilst the second order temporal moment of realistic input pulses also increases monotonically, the pulse center experiences considerable narrowing. This analytically predictable behaviour [4] occurs in both dispersion regimes and can be understood from the fact that the dispersion builds up a chirp across the pulse, which is significantly different for both pulse shapes. The main difference is that gaussian pulses exhibit a linear chirp, which is red-shifted at one edge and blue-shifted at the other edge, while realistic pulses show nonlinear chirps and blue and red-shifts at both edges of the pulse. This complicates the intuitive understanding of pulse propagation in nonlinear dispersive media, which in the literature has been based primarily on the consideration of gaussian pulses.

The SPM-induced spectral broadening can cause system degradation whenever narrowband optical filters are used. Filters may be necessary in long-haul single channel systems to reduce the accumulated optical amplifier noise and in multichannel systems for channel selection. Therefore, it is important to predict the spectral behaviour. A numerical study of SPM-induced broadening (measured by calculating the second order moment) for single rectangular pulses shows substantially different behaviour depending on the sign and value of chromatic dispersion (see fig. 4). While the spectral width increases monotonically with fiber length in the dispersionless medium, it initially grows and then saturates in the normal dispersion regime. A periodic behaviour can be found in the anomalous dispersion regime, where periods of considerable spectral broadening are followed by periods of spectral narrowing, reducing the spectrum to its initial width. This behaviour can be understood from the fact that a rectangular input pulse develops into a high-order soliton as long as the peak power exceeds a certain minimum power (which is the case in almost all realistic NRZ-systems). In fig. 5 we examined the spectral broadening for

NRZ-modulation (for a sequence of 128 bits). Surprisingly, it turns out, that the soliton-like behaviour observed for single pulses can – to a certain extent – also be observed for NRZ-modulation. This is the first time that soliton behaviour is observed in NRZ-transmission systems.

The results depicted in fig. 3 show that, depending on the specific system parameters, an increase in dispersion may reduce the spectral width. When the system is operated below the dispersion limit, this can improve the performance when a narrowband optical filter is employed. On the other hand an increase in dispersion can also cause enhanced spectral broadening thereby degrading the system performance. Furthermore, a study of temporal signal deformation shows that in the high power regime an increase in dispersion reduces the nonlinear penalty, while the opposite is true for the low power regime.

[1] A.R. Chraplyvy, Journal of Lightwave Technology, Vol. 8, October 1990, pp. 1548-1557

[2] Ch. Kurtzke, Digest on Conf. on Opt. Fiber Communication, 1993, Vol.4, pp. 251-252

[2] Ch. Kurtzke and D. Marcuse, submitted to Journal of Lightwave Technology

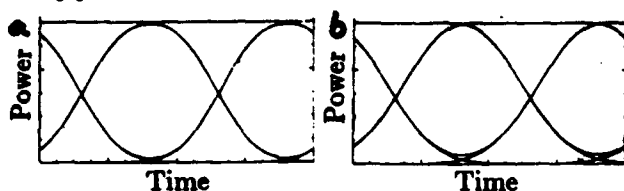


Figure 1: 500 km lossless-fiber transmission, peak power 3 mW, 25 GHz optical filter, a)  $D = -3$  ps/(km-nm) b)  $-6$  ps/(km-nm) 2.5 Gbit/s

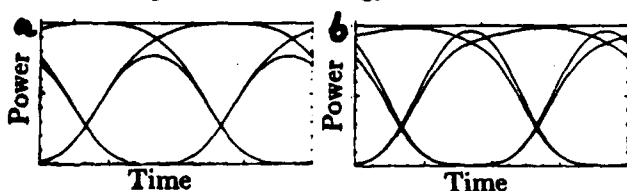


Figure 2: 500 km lossless-fiber transmission, peak power 10 mW, 25 GHz optical filter, a)  $D = 3$  ps/(km-nm) b)  $6$  ps/(km-nm) 2.5 Gbit/s

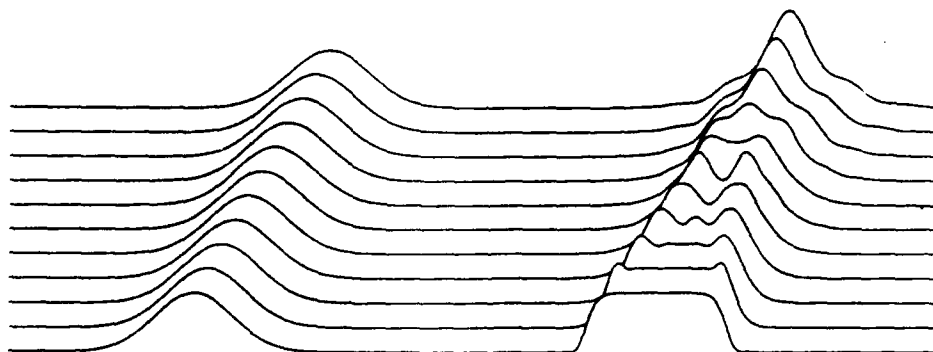


Figure 3: Temporal deformation of a gaussian and rectangular pulse in a purely linear fiber

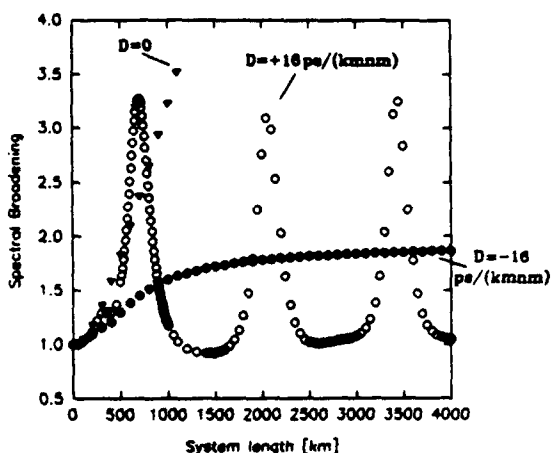


Figure 4: Spectral broadening of single rectangular pulses in different dispersion regimes 2.5 Gbit/s, peak power 3 mW

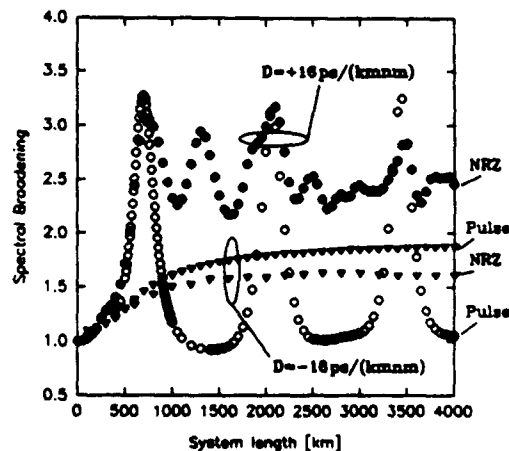


Figure 5: Comparison of spectral broadening for single pulses and 128-bit NRZ-modulation 2.5 Gbit/s, peak power 3 mW

## Transmission Distance of In-Line Amplifier Systems with Group-Velocity-Dispersion Compensation

Akira Naka and Shigeru Saito

NTT Transmission Systems Laboratories  
1-2356 Take, Yokosuka-shi, Kanagawa, 238-03 Japan

**Introduction:** Self-phase modulation (SPM) causes waveform distortion in optical fibers in conjunction with group-velocity dispersion (GVD), and limits the allowable transmission distance of in-line optical amplifier systems [1]. Compensation of GVD was reported to be effective in alleviating this limitation [2],[3], but it has not been quantitatively discussed. This paper evaluates GVD compensation in such systems by numerically solving the nonlinear Schrödinger equation (NLSE). Optimum compensation arrangements and the resulting transmission distances are clarified.

**Calculation Model:** We evaluate three system configurations used to compensate the linear GVD of optical fibers in in-line optical amplifier systems that transmit IM signals with an NRZ format. The first configuration places a GVD compensator ahead of the direct detection receiver. The compensator has a suitable amount of dispersion with a sign opposite to that of the fibers. The second configuration places compensators before every amplifier and the receiver. The third configuration places compensators ahead of several amplifiers and ahead of the receiver. Compensator spacing is determined with reference to system performance. The most simple compensator is a single-mode optical fiber. In our analysis, however, the compensator is assumed to be a lumped element, and neither higher-order GVD nor optical loss is taken into account.

NLSE is solved by means of the split-step Fourier method to simulate signal propagation in optical fibers. It includes the effect of linear and 2nd-order GVD, SPM, and optical attenuation. The carrier wavelength is set in the normal dispersion region (the dispersion parameter  $D < 0$ ), because this region yields benefits with the GVD compensation discussed here. Other parameters are assumed as follows: the carrier wavelength  $\lambda = 1.552 \mu\text{m}$ , the dispersion slope  $dD/d\lambda = 0.07 \text{ ps/nm}^2/\text{km}$ , the Kerr constant  $2.67 \times 10^{-20} \text{ m}^2/\text{W}$ , the effective core area  $5.0 \times 10^{-11} \text{ m}^2$ , and the fiber loss  $0.2 \text{ dB/km}$ .

The transmitter generates an IM signal with a 16-bit sequence, each pulse of which has a super-Gaussian shape of 1.436. The data rate is  $10 \text{ Gbit/s}$ . Besides amplifying the signal, each amplifier adds ASE to the amplified signal. A third-order Butterworth filter with a  $10\text{-nm}$  passband is placed after every amplifier. The receiver consists of a square law detector followed by a low-pass second-order Butterworth filter having a bandwidth of  $0.65$  times the data rate. Optical amplifiers are assumed to be placed at  $50 \text{ km}$  intervals in all configurations. The optical output power of each amplifier, including both the signal and ASE, is adjusted to that of the transmitter.

**Results and Discussion:** Transmission distance under GVD compensation is shown in Fig. 1 as a function of the dispersion parameter. Closed and open circles are the calculated results for the first and second configurations, respectively. Each compensator is assumed to completely counteract the dispersion that the transmitted signal undergoes in the preceding fibers, because 100% GVD compensation yields the longest transmission distances [4]. Here, no ASE is considered. The criterion for the transmission distances is an eye opening penalty of  $1 \text{ dB}$ . The optical output power level of the transmitter and amplifiers is  $P_o = 1 \text{ dBm}$  (time averaged power). For this level of signal power, transmission performance is not determined by beat-noise resulting from linear ASE accumulation but by signal waveform distortion. The three dashed lines indicate the initial distances obtained without GVD compensation [1]. These distances are determined by the GVD effect, the combined effect of GVD and SPM, and the combined effect of 2nd-order GVD and SPM. In the first configuration, the allowable transmission distance is improved by about  $6.5 \text{ dB}$  for the dispersion parameters ranging from  $-0.1$  to  $-10 \text{ ps/nm}^2/\text{km}$ . The second configuration

yields distances that are as long as those limited by the combined effect of 2nd-order GVD and SPM.

Figure 2 shows the transmission distances as a function of the GVD compensation interval normalized by the dispersion length. The transmission distance is inversely proportional to the normalized compensation interval when the interval is larger than 0.3. There exist critical points in the normalized interval. Only the GVD compensation intervals shorter than the critical values achieve transmission distances that are as long as those limited by the combined effect of 2nd-order GVD and SPM. The critical interval is inversely proportional to the cube root of the optical amplifier output power. It is about 400 km for  $D = -1$  ps/nm/km and  $P_0 = 1$  dBm.

ASE deteriorates the eye opening penalty and thus degrades the allowable transmission distances. Resulting distances, under a noise figure of 6 dB, are indicated in Fig.1 with closed and open triangles for the first and second configurations, respectively. Crosses in Fig.1 are the references, which represent system performance without GVD compensation. For dispersion parameters ranging from -0.01 to -10 ps/nm/km, GVD compensation is still effective even when ASE exists. The open square in Fig. 1 is the result for the third configuration with the critical compensation interval. This distance is slightly longer than that of the second configuration because the longer compensation interval makes ASE less effective. At small dispersion parameter values, e.g.,  $|D| \leq 10^{-3}$  ps/nm/km, the system suffers from strong distance degradation caused by four-wave mixing between the signal and ASE [5].

**Conclusion:** GVD compensation was evaluated in in-line amplifier systems. It is effective within the dispersion parameter range of -0.01 to -10 ps/nm/km and the resulting distance approaches the limit determined by the combined effect of 2nd-order GVD and SPM. The optimum amount of compensation is about 100 % of the dispersion which the transmitted signal experiences. There exists a critical compensation interval, which is proportional to the dispersion parameter and inversely proportional to the cube root of the amplifier output power.

**Acknowledgments:** The authors thank Dr. H. Ishio and Dr. T. Ito for their encouragement.

**References:** [1] A. Naka and S. Saito, Electron. Lett., Vol.28, p.2221, 1992. [2] M. Murakami et al., Electron. Lett., Vol.28, p.2254, 1992. [3] S. F. Carter et al., GLOBECOM'92, 42A.04, Orlando, 1992. [4] A. Naka and S. Saito, OAA'93, Yokohama, 1993. [5] D. Marcuse, IEEE J. Lightwave Technol., Vol.9, p.356, 1991.

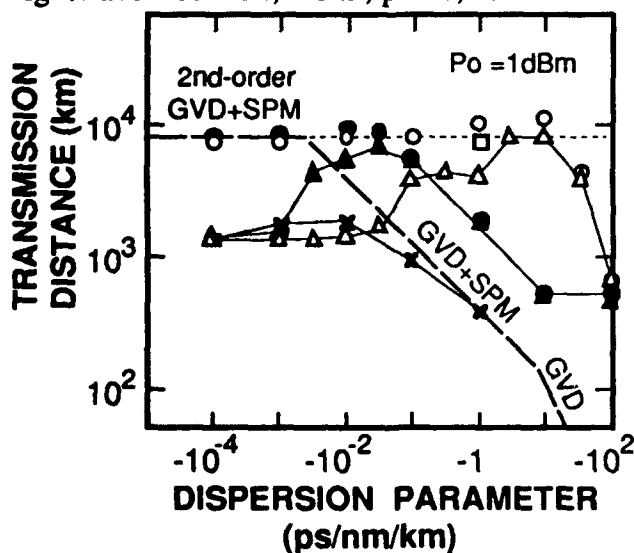


Fig.1 Transmission distance vs. dispersion parameter.

(w.o.noise) (w.noise)  
 ● ▲ : first configuration  
 ○ △ : second configuration  
 □ : third configuration  
 — x : no GVD compensation

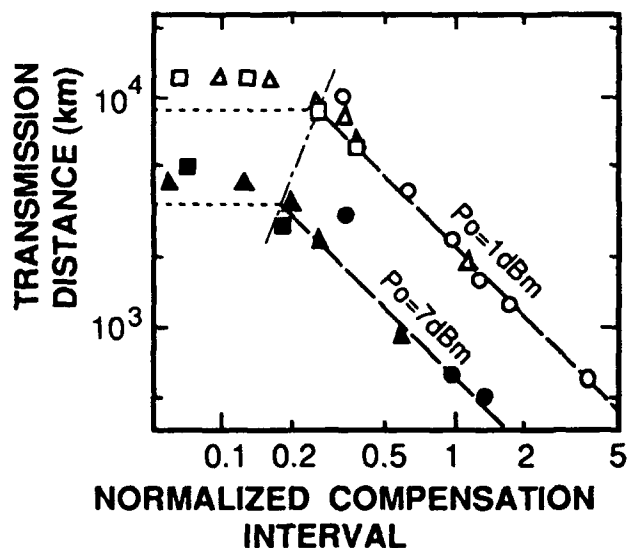


Fig.2 Transmission distance vs. compensation interval normalized by dispersion length.

○ ● : -10.0 ps/nm/km  
 △ ▲ : -1.0 ps/nm/km  
 □ ■ : -0.1 ps/nm/km

**Nonlinear Interaction of Signal and Noise  
in Lightwave Systems at the Zero-Dispersion Wavelength**

E. Lichtman  
AT&T Bell Laboratories  
Holmdel, NJ 07733

*Summary*

Lightwave systems with optical amplifiers are vulnerable to performance degradation due to nonlinearity. In particular, the Kerr effect may lead to strong nonlinear interaction between the transmitted signal and the ASE noise that is generated by the EDFAs. The nonlinear interaction between the signal and the ASE noise was previously investigated by numerical simulations<sup>1</sup>. It was found that the nonlinear interaction is most efficient at the zero-dispersion wavelength, where it can lead to a significant degradation of the system performance.

In this work, we analytically analyzed the nonlinear interaction between the signal and the ASE noise. Assuming operation at the zero-dispersion wavelength, a closed-form expression for the total electric field (signal+noise) at the system output, was derived. The result shows that the performance of a nonlinear system having an infinite bandwidth is almost equivalent to the performance of a similar linear system. This result points out that by itself, nonlinearity at the zero-dispersion wavelength has a negligible effect on the system performance.

Note however that we assumed an infinite bandwidth system. A real system has a bandwidth of  $\approx 4$  nm which is determined by the bandwidth of the EDFAs. Therefore, the broadening of the signal spectrum which is caused by the Kerr effect will lead to signal loss and degradation of the SNR. For that reason, a system that operates at the zero-dispersion wavelength is not feasible.

**REFERENCES**

- [1] D. Marcuse "Single-channel operation in very long nonlinear fibers with optical amplifiers at zero dispersion", *J. Lightwave Tech.* 9, 356 (1991).

# NONLINEAR EFFECTS ON TWO-CHANNEL LONG DISTANCE OPTICAL FIBER SYSTEMS

Xiaobing Ma and Ira Jacobs

Fiber and Electro-Optics Research Center  
Bradley Department of Electrical Engineering  
Virginia Polytechnic Institute and State University  
Blacksburg, VA24061

## §1. Introduction

The interaction between dispersion and nonlinearity is one of the most important distortion factors in very long length in-line optical amplifier systems. Due to cross-phase modulation(XPM), the distortion is more severe in WDM systems. This paper compares the performance of single-channel and two-channel systems.

## §2. Nonlinear Effects

In the case of a single-channel system, the nonlinearity appears in the form of self phase modulation(SPM), which is directly proportional to the average transmitted power in the channel. Both analytical estimation and computer simulation show that the maximum propagation distance is proportional to  $\sqrt{L_d L_n}$  [1][2], where  $L_d$  and  $L_n$  are the characteristic dispersion and nonlinearity lengths, respectively [3].  $L_d$  and  $L_n$  are the distances corresponding to a  $\pi$  phase shift due to dispersion and nonlinearity. The proportionality constant varies between 1 ~ 2, depending on the ratio of  $L_d$  and  $L_n$  and the sign of the dispersion coefficient.

In the case of a two-channel system, nonlinearity creates not only SPM, but also XPM [3], which is proportional to two times the power from the other channel. The magnitude of the phase modulation is three times greater than that of a single channel when there is equal signal power in each channel. Therefore, the maximum propagation distance is reduced as the result of the stronger interaction between nonlinearity and dispersion. Previous simulation [4] indicates the possible distortion effects from XPM but focuses on spurious pulse generation(intermodulation). We consider here the effects on the incident signal, including the transmission of a train of pulses, the effects of optical filtering, and the effects of operating in various dispersion regions.

Results presented here are for the following parameters:  $R_b = 5$  Gbits/s,  $P_0 = 1$  mW,  $D_1 = \pm 0.31$  ps/km-nm,  $D_2 = \pm 0.38$  ps/km-nm,  $\lambda_0 = 1.53$   $\mu$ m,  $\alpha = 0.21$  dB/km, pulse sequence (0 1 0 1 0 0 1 0 1 1 1 0 1 0 1 0), and the optical filter bandwidth is equal to 12GHz. Three different cases, corresponding to different dispersion conditions, are evaluated for a distance of 9000 km ( $= \sqrt{L_d L_n}$ ). Similar to the single-channel system, a pulse in the abnormal( $D > 0$ ) dispersion region tends to split into a number of spikes, while its width is confined much better than in the normal( $D < 0$ ) dispersion region. Therefore pulses can propagate a somewhat longer distance in the abnormal dispersion region if a post optical filter is placed in front of the receiver (see Figure 1 & 2). The third case places the two channels on each side of the zero dispersion wavelength. Due to the interference between the two channels, the channel in the normal dispersion region has more high frequency components, and the pulse width isn't confined as well as the abnormal dispersion case (see Figure 3). Using the same post filter at the receiving end, operating both channels in the abnormal dispersion region gives the best performance.

Considering XPM,  $L_n$  may be redefined as one third of  $L_n$  in the single-channel

case. The maximum propagation distance is then proportional to  $\sqrt{L_d L_n}$  with the proportionality constant again varying between 1 ~ 2.

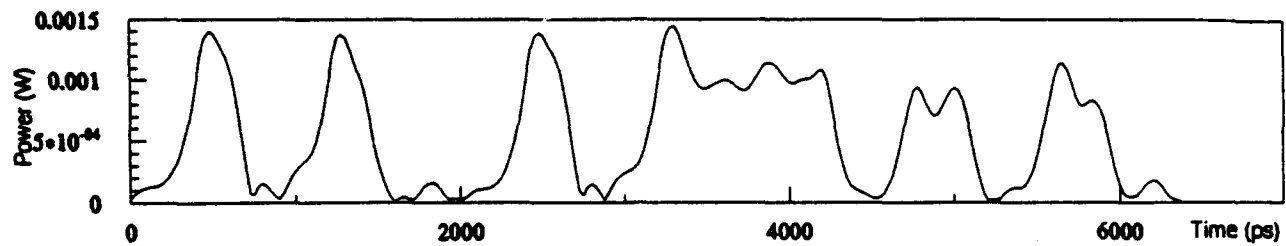


Figure 1. Both Channels Are in Abnormal Dispersion Region

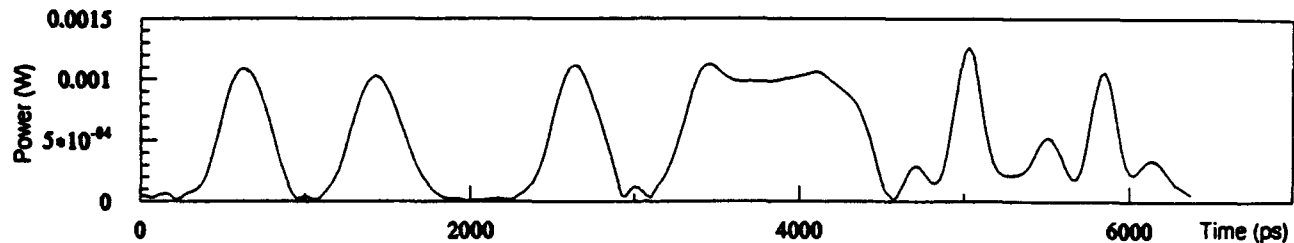


Figure 2. Both Channels Are in Normal Dispersion Region

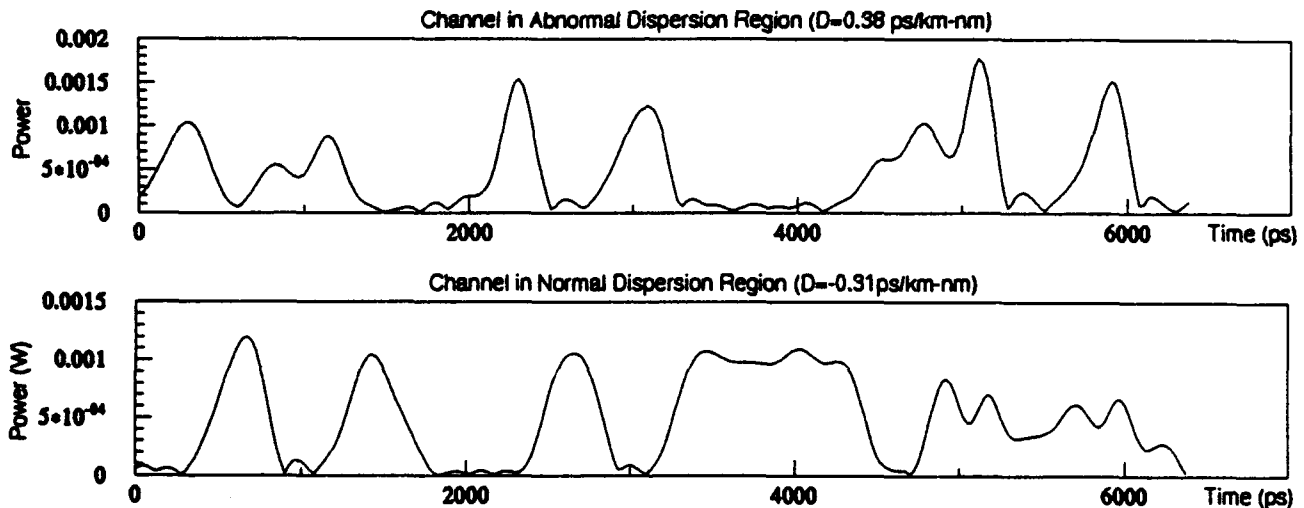


Figure 3. Two Channels Are on Each Side of Zero-Dispersion

### 3. Conclusion

A two-channel system has approximately 1/3 the maximum distance of the corresponding single channel system. Similar to the single-channel system, operating in the proper dispersion region and the use of optical filters can improve performance.

### References

- [1]. S. Saito, A. Naka, and M. Murakami, "Kerr Nonlinearity Limits on Transmission Distance and Data Rate of In-Line Optical Amplifier Systems", Optical Amplifiers and Their Applications Topical Meeting, Paper WC3-1, June 1992.
- [2]. M.J. Potasek, Govind P. Agrawal and S. C. Pinault, "Analytic and Numerical Study of Pulse Broadening in Nonlinear Dispersive Optical Fibers", J. Opt. Soc. Am. B, Vol. 3, No. 2, p205-211, February 1986.
- [3]. G. P. Agrawal, "Nonlinear Fiber Optics", (Academic Press Inc., London, 1989), Ch2 & CH4.
- [4]. D. Marcuse, A. R. Chraplyvy and R. W. Tkach, "Effect of Fiber Nonlinearity on Long-Distance Transmission", J. Lightwave Technology, Vol. 9, No. 1, Jan 1991.

Y. Aoki ..... 13  
M. Artiglia ..... 5  
O. Audouin ..... 19  
J. Auge ..... 19  
N. Bergano ..... 9  
J. Bernard ..... 19  
T. Chiang ..... 25, 27  
A. Chraplyvy ..... 29, 31, 33  
P. Crahay ..... 5  
D. Delta ..... 25, 27  
R. Derosier ..... 33  
F. Forghieri ..... 29

I. Gabitov ..... 5  
A. Gnauck ..... 15  
J. Hamaide ..... 19  
K. Inoue ..... 23  
I. Jacobs ..... 44  
E. Jaunart ..... 5  
B. Jorgensen ..... 35, 37  
C. Jorgensen ..... 35, 37  
L. Kazovsky ..... 25, 27  
C. Kurtzke ..... 39  
E. Lichtman ..... 43

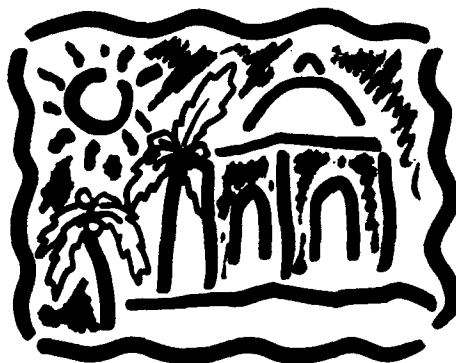
X. Ma ..... 44  
X. Mao ..... 39  
D. Marcuse ..... 39  
F. Matera ..... 11, 17  
A. Mattheus ..... 5  
A. Mecozzi ..... 11  
M. Midrio ..... 5  
B. Mikkelsen ..... 35  
L. Mollenauer ..... 3  
A. Naka ..... 41  
R. Pedersen ..... 35, 37  
L. Prigent ..... 19

M. Romagnoli ..... 5, 11  
S. Saito ..... 41  
F. Sartori ..... 5  
C. Schmit-Hattenberger ..... 5  
M. Settembre ..... 11  
K. Stubkjaer ..... 35  
R. Tkach ..... 15, 29, 31, 33  
S. Turitsyn ..... 5  
S. Wabnitz ..... 5  
J. Wright ..... 7

# **Hybrid Optoelectronic Integration and Packaging**

**July 26-28, 1993**

**Fess Parker's Red Lion Inn Resort  
Santa Barbara, California**



**Sponsored by  
the IEEE Lasers and Electro-Optics Society  
and the IEEE Components, Hybrids, and  
Manufacturing Technology Society**

**IEEE Catalog Number: 93TH0549-6  
Library of Congress Number: 93-77778**

The papers in this book comprise the digest of the meeting mentioned on the cover and title page. They reflect the authors' opinions and are published as presented and without change, in the interest of timely dissemination. Their inclusion in this publication does not necessarily constitute the endorsement by the editors, the Institute of Electrical and Electronics Engineers, Inc.

Copyright and reprint permissions: Abstracting is permitted with credit to the source. Libraries are permitted to photocopy beyond the limits of the U.S. copyright law for private use of patrons those articles in this volume. Instructors are permitted to photocopy isolated articles for noncommercial classroom use without fee. For other copying reprint or republication permission, write to Director, Publishing Services, IEEE, 345 E. 47th St., New York, NY 10017. All rights reserved. Copyright ©1993 by the Institute of Electrical and Electronics Engineers, Inc.

IEEE Catalog Number:	93TH0549-6
ISBN Number: Softbound	0-7803-1284-8
Microfiche Edition:	0-7803-1285-6
Library of Congress Number:	93-77778

## Hybrid Optoelectronic Integration and Packaging Technical Committee

### Co-Chairs

L. Fox  
*Digital Equipment Corp.*

H.F. Lockwood  
*The Lockwood Group*

### Program Committee

P. Anthony  
*AT&T Bell Laboratories*

Ken Jackson  
*IBM Research Division*

D.K. Lewis  
*GE Electronics lab*

C. Armiento  
*GTE Laboratories*

R. Kaneshiro  
*Hewlett Packard*

R. Osgood  
*Columbia University*

R. Frye  
*AT&T Bell Laboratories*

S. Kang  
*University of Illinois*

J. Pazaris  
*Digital Equipment Corp.*

D. Hartman  
*Motorola, Inc.*

M. Kobayashi  
*NTT Optoelectronics  
Laboratories*

J. Schutt-Aine  
*University of Illinois*

R. Higgins  
*Georgia Tech*

P. Krusius  
*Cornell University*

C. Stirk  
*University of Colorado*

Anis Husain  
*Honeywell*

R. Leheny  
*Bellcore*

W.J. Tomlinson  
*Bellcore*

## MONDAY, JULY 26, 1993

### M1: HYBRID INTEGRATION I

M1.1	Solder Bonded Optoelectronic Transceiver Components .....	3
M1.2	Packaging of Liquid Crystal on Silicon Modulators Using Solder .....	5
M1.3	20-channel Optoelectronic Receiver for Free-Space Optical Interconnection .....	8
M1.4	Hybrid Integration of Electrical and Optical Interconnect for MCMs Applications .....	10

### M2: GUIDED WAVES I

M2.1	Waveguide and Diffractive Coupling Elements for Optoelectronic Packaging .....	11
M2.2	Results of OEMCM Packaging Efforts at LLNL .....	13
M2.3	Design and Characterization of a Novel Fiber Optic Coupling Device for Data Communication Applications .....	15
M2.4	A Hybrid Coherent Receiver with a Permanently Pigtailed Semiconductor Waveguide 3-dB Coupler and an Integrated Pin Pair .....	17

### M3: FREE SPACE I

M3.1	Fabrication Issues for Free-Space Optics at the Board Packaging Level .....	19
M3.2	A Three-Dimensional Optical Interconnection Network for Fine-Grain Parallel Architectures .....	21
M3.3	Optical and Package Design Issues for Chip-to-Chip Free-Space Optical Interconnections .....	23

### M4: HYBRID INTEGRATION II

M4.1	Hybrid OEIC Cost Sensitivity .....	25
M4.2	Optoelectronic Integration of Thin Film Devices for Photonic Interconnect .....	27
M4.3	Demonstration of GaAs LEDs on Si Chips Using Epitaxial Liftoff .....	29
M4.4	30% External Quantum Efficiency From Surface Textured, Thin-Film Light-Emitting-Diode Arrays .....	31
M4.5	Liquid Flux Assisted Bump Bonding Process and Thermal Design for Laser Arrays for Optical Interconnection .....	33

## TUESDAY, JULY 27, 1993

### T1: GUIDED WAVES II

T1.1	Rapid Prototyping of Photonic Integrated Circuits .....	37
T1.2	Dispensed Dual-Polymer Waveguides in Silicon V-Grooves .....	39
T1.3	Direct Dispensing of Polymer Waveguides on Silicon Substrates .....	41

### T2: FREE SPACE II

T2.1	Prototype Optically Interconnected Multichip Module with Holographic Optical Interconnects .....	43
T2.2	Simulation Tools for Free-Space Optical Interconnects Based on Computer-Generated Holograms .....	45

# T A B L E   O F   C O N T E N T S

<b>T3.1</b>	<b>Integrated Optical Heads for Optical Data Storage .....</b>	<b>47</b>
<b>T3.2</b>	<b>Thin Film Resonant Cavity Enhanced Photodetectors .....</b>	<b>49</b>
<b>T3.3</b>	<b>Alignment Considerations In the Package Design of Optical Interconnections .....</b>	<b>51</b>
<b>T4:</b>	<b>HYBRID INTEGRATION IV</b>	
<b>T4.1</b>	<b>Hybrid Integration of AlGaAs/GaAs Laser Diode on Si Substrate.....</b>	<b>53</b>
<b>T4.2</b>	<b>GaAs 850nm Surface-normal Modulators Solder-bonded to Silicon .....</b>	<b>55</b>
<b>T4.3</b>	<b>CAD of Solder Joints for Self-Aligned Assemblies .....</b>	<b>57</b>

## WEDNESDAY, JULY 28, 1993

<b>W1:</b>	<b>THE FUTURE OF INDUSTRY, ACADEMIC AND GOVERNMENT COLLABORATIONS</b>	
<b>W1.1</b>	<b>U.S.-Japan Joint Optoelectronics Project.....</b>	<b>63</b>
<b>W1.2</b>	<b>Consortium for Optical and Optoelectronic Technologies for Computing.....</b>	<b>65</b>
<b>W1.3</b>	<b>Direction of Optoelectronics Research at ARPA.....</b>	<b>67</b>
<b>W1.4</b>	<b>Expectations from Optoelectronic Technologies.....</b>	<b>68</b>
<b>Author Index.....</b>		<b>70</b>

Monday, July 26, 1993

**Sessions:**

**M1:** Hybrid Integration I

**M2:** Guided Waves I

**M3:** Free Space I

**M4:** Hybrid Integration II



## **Solder bonded Optoelectronic Transceiver Components**

**A.J. Moseley and M.J. Goodwin**

GEC- Marconi Materials Technology Limited  
Caswell Towcester Northants NN12 8EQ. U.K.

### **Abstract.**

Hybrid solder bonded optical modulator and detector arrays on silicon VLSI circuits, together with solder bonded lasers and micro-fabricated silicon packaging are described. These approaches are being used for integrated components for optical interconnect applications.

### **Introduction.**

Hybrid integration using solder bonding enables optimised optoelectronic and electronic components to be combined for a wide range of applications, particularly in optical interconnect where the technology can impact interchip, board and rack interconnects. In addition sections of the optical pathway may be produced using the self-aligning features of the solder bond technique. In combination with micro-fabricated silicon packaging, more complex functionality transceiver modules can be fabricated. In this paper we will describe solder bonded transceiver components and modules for optical interconnect links. The examples include reflective modulator based systems for low power consumption, and laser based systems for wide temperature operation.

### **Component design and technology.**

The choice of optoelectronic transmitter technology is determined predominantly by power, temperature and reliability constraints [1]. In certain application, for example chip level optical interconnect, low power consumption is a key requirement and the Asymmetric Fabry-Perot modulator (AFFM) [2] device enables this criterion to be met with high reliability. In addition the reflective mode of operation of this device enables fibre based systems to be built with remote optical sources and a simple single fibre interface. The design of such a modulator for operation in the long wavelength fibre optic band is illustrated in figure [1]. This structure is an inverted AFPM which exploits the transparent InP substrate for optical access to the device, whilst enabling the electrical interconnections to the silicon chip to be formed on the opposite side of the device, thus making it ideally suited to flip-chip solder bonding. This solder bond process utilises controlled volumes of solder confined to metallised regions on the chips to be attached to provide both physical attachment and electrical connection. Parasitics are thus minimised, and numerous points of a silicon circuit can be accessed optically; this process is readily extendible to large arrays, (10,000 bonds) [3]. The structure of the device comprises an InGaAs/InP MQW absorbing region in the cavity formed by a highly reflective metal mirror and a low reflectivity ( $\leq 50\%$ ) quarter wavelength stack formed as part of the semiconductor layer structure.

Eight element modulator arrays have been hybridized onto a custom  $1\mu\text{m}$  CMOS driver circuit for digital interconnects in which CMOS logic levels are amplified to provide a 5Volt output to drive the modulator directly. A high degree of uniformity of modulation was obtained across the array with mean modulation of 4.8dB and standard deviation of 0.1dB for standard CMOS input voltages. The hybrid transmitter operated to 140Mb/s with a power consumption of 0.5mW per channel which compares very favourably with the power required for an equivalent electrical interconnect. In addition to free space links these components have been used in a fibre based analogue system. Optical interfacing to the modulators in this case was achieved with a fibre ribbon v-groove assembly and microlens array which enabled a low insertion loss of 3dB to be achieved.

For the optical receivers we use conventional InGaAs/InP planar photodiode technology, again with substrate optical access, solder bonded to silicon ECL receiver circuits fabricated on a  $1\mu\text{m}$  gate array process. Arrays of detectors with up to 64 elements have been fabricated which exhibit dark current values of 46pA for  $100\mu\text{m}$  diameter active areas. The minimum input photocurrent to

switch logical state of the receiver was in the range 8-10 $\mu$ A corresponding to -23dBm. Operation up to 1Gbit/s was demonstrated with a 3dB dynamic range at 800Mbit/s and 6dB at 650Mbit/s.

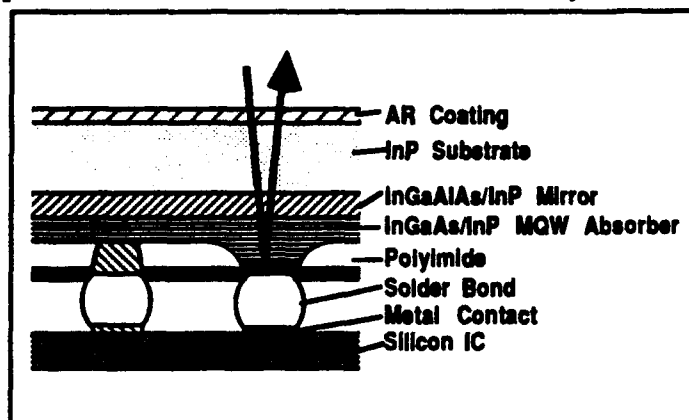


Fig. 1. Cross-section of inverted AFPM.

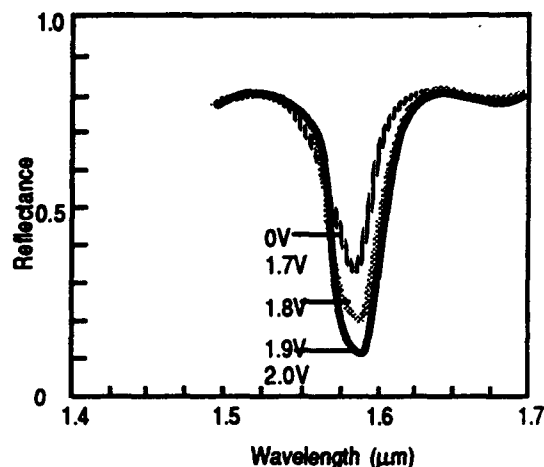


Fig. 2. Reflectivity spectra of CMOS driven modulator

For guided wave applications optical transceiver modules, optoelectronic multi-chip modules, have been fabricated using a combination of micro-fabricated silicon packaging and solder bond chip attachment. The combination of these technologies allows package parts to be fabricated to the lithographic accuracies used in semiconductor device manufacture, efficient optical alignment to be achieved, and complex functionality to be included in a compact low cost package. Figure 3 illustrates the concept of such a module using a laser source solder bonded [3] directly to the silicon package, and pin photodiode detector, together with the required transmitter and receiver integrated circuits. In this application a laser source has been chosen in preference to the modulator for wide temperature range operation. This module has been designed for interfacing to fibre or polymer waveguides for inter board interconnect at data rates up to 625Mb/s, with a low power dissipation and small footprint.

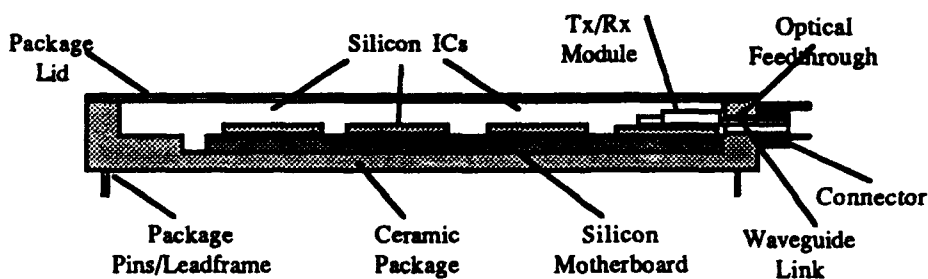


Fig. 3 Schematic cross section of silicon packaged module.

## References.

- [1] Goodwin, M.J., Moseley, A.J., Kearley, M.Q., Morris, R.C., Groves-Kirkby, C.J., Thompson, J., Goodfellow, R.C., and Bennion, I. 'Optoelectronic component arrays for optical interconnection of circuits and sub systems' IEE JLT 9, 12, (1991), 1639-1645.
- [2] Moseley, A.J., Kearley, M.Q., Morris, R.C., Robbins, D.J., Thompson, J., and Goodwin, M.J., 'Uniform 8x8 Array InGaAs/InP Multiple Quantum Well Asymmetric Fabry-Perot Modulators for Flip-Chip Solder Bond Hybrid Optical Interconnect.' Electron. Letts. 1991.
- [3] C. Edge, R.M. Ash, G.G. Jones and M.J. Goodwin, 'Flip-Chip Solder Bond Mounting of Laser Diodes', Electron. Lett. 27, (1991), 499-500
- [4] Wieland, J., Melchior, H., Kearley, M.Q., Morris, C., Moseley, A.J., Goodwin, M.G., Goodfellow, R.C., 'Optical receiver array in silicon bipolar technology with self-aligned, low parasitic III/V detectors for DC-1Gbit/s parallel links' Electron. Letts., 27, (1991) 2211-2212.

This work has been supported by the Commission of the European Community under the ESPRIT programmes 2289 'OLIVES' and 6276 'HOLICS', and the GEC-Marconi businesses.

## **PACKAGING OF LIQUID CRYSTAL ON SILICON MODULATORS USING SOLDER**

Teh-Hua Ju, Wei Lin and Y. C. Lee  
Department of Mechanical Engineering

K. M. Johnson  
Department of Electrical and Computer Engineering  
and  
Center for Optoelectronic Computing Systems  
University of Colorado, Boulder, CO 80309-0427, USA.  
(303)492-3393 (phone, YCL); (303)492-3498 (FAX)  
e-mail address (YCL): leeyc@spot.colorado.edu

### **I. Introduction**

A liquid crystal on metallized silicon modulator is demonstrated by using a self-aligning soldering technology. The technology is critical to package low-cost, high-performance spatial light modulators (SLMs) using ferroelectric liquid crystal (FLC) over a very large scale integrated circuit (VLSI). These SLMs are important components to high-definition displays, pattern correlation, and many other optoelectronic processors.

Figure 1 shows the layout and the cross-section of a demonstration vehicle with two modulators.

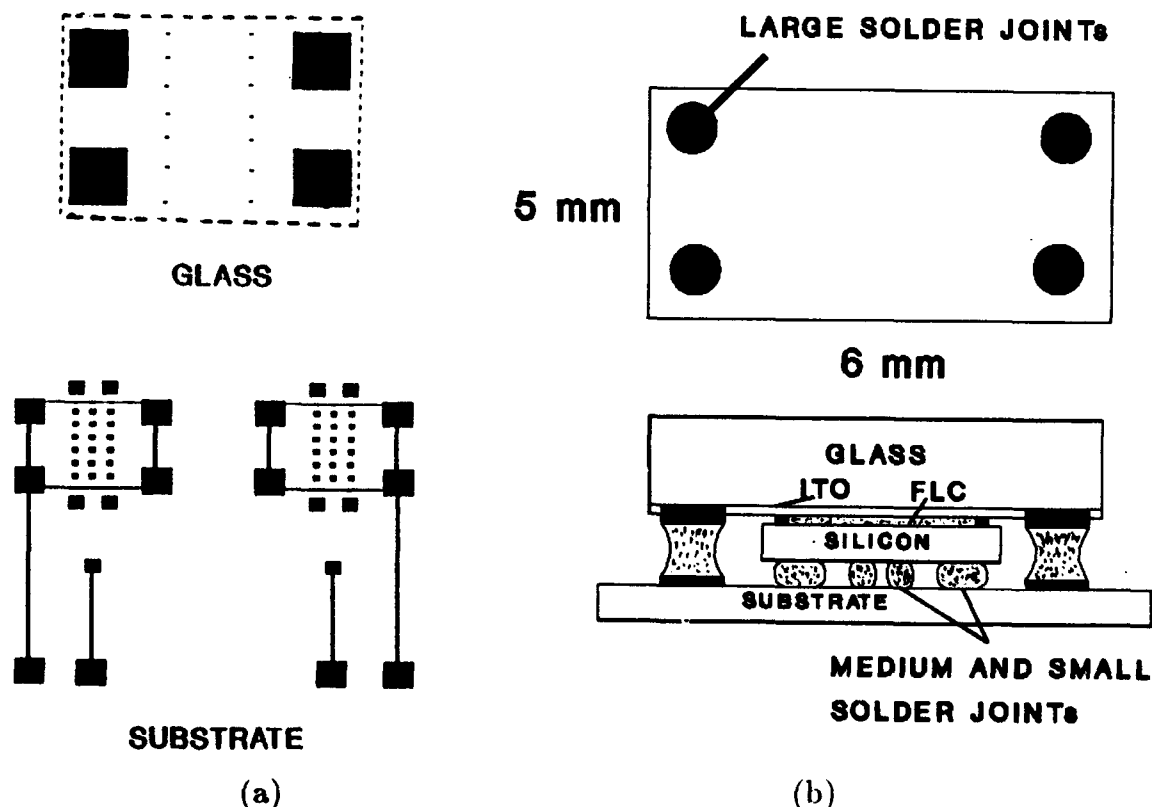


**Fig. 1. (a) Layout and (b) cross-section of the demonstration vehicle**

The major challenge is to achieve a uniform,  $\mu\text{m}$ -level gap between the glass and the metallized silicon. The gap to be filled with FLC should be uniform and in the range from 1 to 2 microns for high-performance modulation. Soldering is identified as the most cost-effective technology for the modulator. Four studies are important to develop the technology. They are 1) the design of the solder joints, 2) the development of a fluxless reflow process, 3) the fabrication of the glass component and the silicon substrate, and 4) the development of a solder bumping technology.

## II. Packaging Studies

The first two studies on the solder design and the fluxless reflow are to be presented in ECTC-43 [1]. These studies specify a right solder volume of the big solder joints that result in the maximum force pulling the glass against the metallized silicon. Also, they identify an optimum set of the temperature ( $280^\circ\text{C}$ ) and the flow rate (2.5 liter/min) for a fluxless soldering process with forming gas. The other two studies develop the fabrication and the solder bumping with the processing steps listed below:

- 1). Get two pieces of optically-flat glass and plate copper solder pads onto each glass.
- 2). Coated with Indium-Tin-Oxide (ITO).
- 3). Coat and pattern a layer of polyimide onto each glass as the spacer (see Figure 1).
- 4). Place solder balls of 63Sn/37Pb with the specified volume onto the pads on each glass.
- 5). Reflow each glass with forming gas to form solder bumps.
- 6). Apply an alignment layer onto each glass.
- 7). Fabricate the silicon substrate with a pattern shown in Figure 1.
- 8). Solder two pieces of metallized silicon onto the substrate.
- 9). Assemble the demonstration vehicle with two modulators.
- 10). Fill FLC into the gap between each metallized silicon and the associated glass.
- 11). Cool the FLC.
- 12). Connect the ITO layer and the metallized silicon to the switch.
- 13). Modulate the assembly using the high-speed switch.

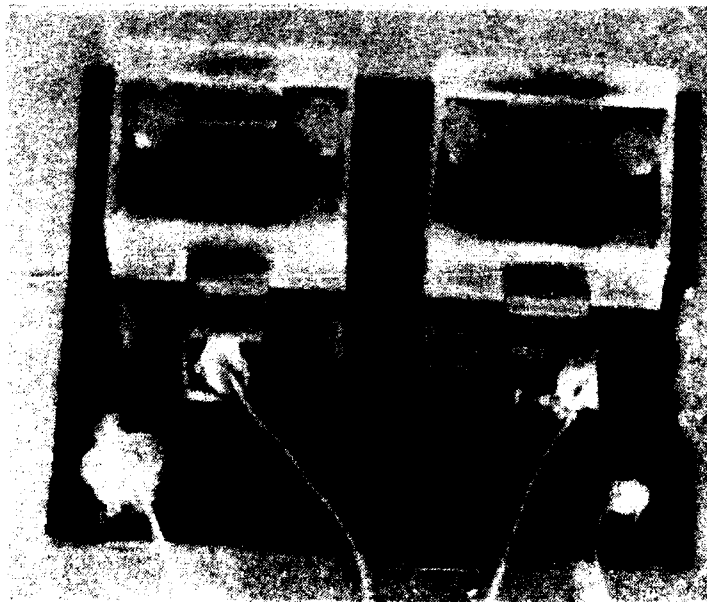


Fig. 2. Photograph of the assembled demonstration vehicle

### III. Summary

The complete demonstration vehicle with two modulators is successfully assembled as shown in Figure 2. The vehicle assembled by the self-aligning solder technology is functionally working as expected. The demonstrated technology significantly improves the existing assembly technology [2], and is being developed for a  $256 \times 256$  SLM with FLC on VLSI.

### IV. Acknowledgment

The authors would like to thank the help of D. Mcknight, D. A. Jared, J. Y. Liu, C. C. Mao, and W. Zhang at the University of Colorado. This work was partially supported by the National Science Foundation Engineering Research Center for Optoelectronic Computing System, ECD-9015128, and EED-9212156.

### V. References

1. W. Lin, Y. C. Lee, and K. M. Johnson, "Study of Soldering for VLSI/FLC Spatial Light Modulators", ECTC, Orlando, Florida, June 2-4, 1993.
2. D. A. Jared, R. Turner, and K. M. Johnson, "Electrically Addressed Spatial Light Modulator That Uses a Dynamic Memory", Optics Letters, Vol. 16, No. 22, pp.1785-1787, 1991.

**20-Channel Optoelectronic Receiver for Free-Space Optical Interconnection**

by

**K.D. Pedrotti, C. W. Seabury, R. L. Pierson**  
Rockwell International Science Center  
1049 Camino Dos Rios  
Thousand Oaks, CA 91360

and

**D. Z. Tsang**  
MIT Lincoln Laboratory  
Lexington, MA 02173

We will report on the construction of a 20-channel optical receiver array for use at 0.9 to 1.55 micron wavelengths for free space communication within computer systems. The receiver array will operate in conjunction with a 980 nm laser array to provide 20 Channels of 1Gbit/sec data transfer. To meet these requirements we have produced GaAs HBT receiver circuits<sup>1</sup> with flip-chip bonded InGaAs PIN detector arrays mounted directly on top.

The main design issues are: latency, power supply rejection, dynamic range, threshold adjustment stability, crosstalk, and thermal stability. These concerns are addressed by the basic circuit design which consists of three stages (see Fig. 1). A transimpedance amplifier, feeds a stage which serves as both a limiting amplifier and decision circuit. This is followed by the output driver stage. The use of a threshold adjust control dispenses with the additional latency and power consumption that would be incurred by the use of an automatic gain control amplifier. This design has moderate sensitivity tailored to the expected range of input optical power and provides transition edge rates slow enough to insure that this part will not interfere with other system parts on the completed circuit board. Limitation of the maximum edge rate to 100 ps by the ultimate end user constrains the maximum bit rate to 2.2 Gbit/sec per channel or an aggregate array capacity of 44 Gbit/sec. The reduced output edge rate increases the latency, or time delay, for this part. The sensitivity of this circuit is defined as the input optical power required to cause full excursion of the output over the ECL high and low voltage output thresholds. This was designed to be -3 dBm with an 8 dB dynamic range. The usual Gaussian noise limited sensitivity is much better, but in this case inappropriate given the application.

Parts have been measured up to their full design speed of 2.2 Gbit/sec. Flip-chip processes, Fig. 2, have been developed to allow the mounting of the InGaAs array detectors using either solder bump or low temperature Indium bump bonding techniques. The detectors were fabricated on N-type substrates using a mesa type process. The detectors have a 50 micron active area. The P and N type regions are both contacted from the top side by array of 50 micron pads used for the flip-chip interconnection. Figure 3 shows the completed receiver sub-assembly consisting of a Si carrier with the receiver mounted and wire bonded to it. The receiver arrays are packaged with micro optic lens arrays to provide the optical interface with a companion 980 nm wavelength laser array.

Careful design techniques were used to minimize optical and electrical crosstalk between receivers in each array. Simulations showed that the majority of the coupling between array elements will be through the shared power busses and not through capacitive or inductive

---

<sup>1</sup>P. M. Asbeck, M. F. Chang, J. A. Higgins, N. H. Sheng, G. J. Sullivan, K.C. Wang, IEEE Trans. Electron. Devices 36 (10), p. 2032, 1989 &

M. F. Chang and P. M. Asbeck, "III-V Heterojunction Bipolar transistors for high-speed applications," Intl. J. of High Speed Electronics, vol. 1, nos. 3 & 4 (1990) 245-301.

coupling at the speeds of concern. The predicted coupling was -46 dB. Crosstalk was measured by driving one channel to full output swing and then observing the peak-to-peak voltage swings on the other output channels. This is shown in Fig. 4. The worst crosstalk is 3 mV which corresponds to a crosstalk of -44.4 dB the average crosstalk is 1.73 mV or -49.2 dB. The above result suggests that for all channels fully loaded with random data the total crosstalk observed on any channel should be 7.74 mV implying a fully loaded crosstalk value of -36 dB.

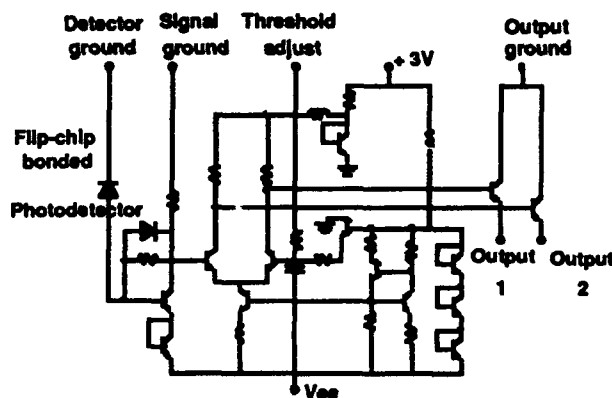


Fig. 1 Schematic Diagram of One Channel of the Receiver Array.

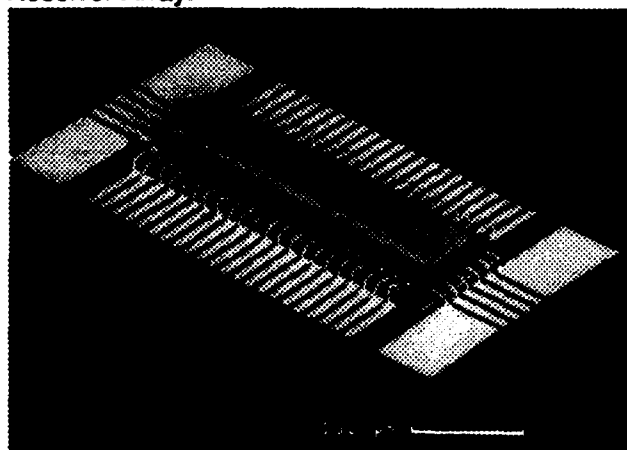


Fig. 3 Completed Receiver Array.

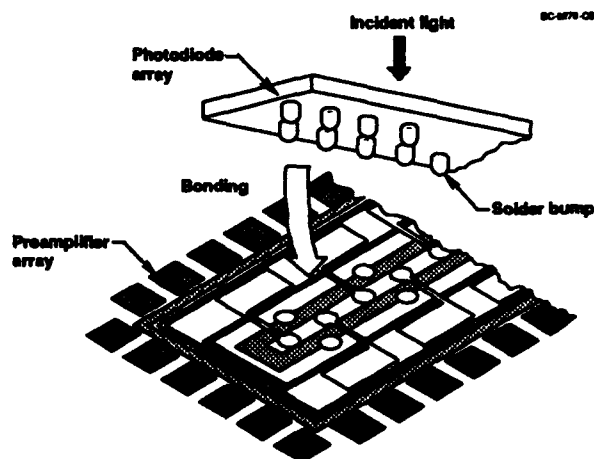


Fig. 2 Flip Chip Array bonding Technique.

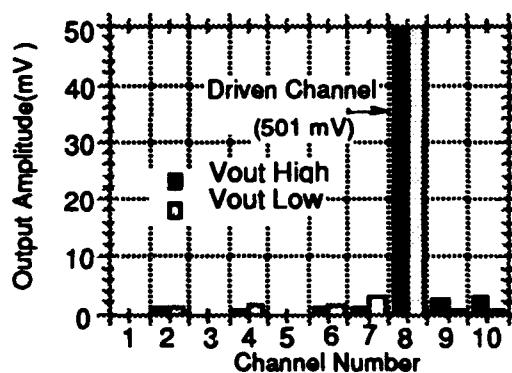


Fig. 4 Array Channel to Channel Crosstalk.

**Hybrid Integration of Electrical and Optical Interconnect for MCMs Applications**

Y.S. Liu  
GE Research and Development Center  
Schenectady, New York 12345  
and  
J. Bristow  
Honeywell System Research Center  
10701 Lyndale Ave., South  
Bloomington, MN 55420

**Summary**

We discuss a recent effort in developing an integrated approach for electrical and optical interconnect for MCMs applications. This approach employs a high-density interconnect (HDI) process which uses thin-film polymeric overlay to hybrid integrate both photonic and electronic devices within a multichip module. The optical waveguide channel can be constructed within the same MCM structure using same planar processes. In addition, a laser lithography technique is applied to pattern optical and electrical interconnects adaptively to eliminate critical steps required for alignment between optical components and waveguide channels.

The HDI process employed here uses a thin-film polymer overlay as the dielectric. Chips are placed first inside the chip wells which were fabricated on a ceramic substrate, followed by dielectric lamination over the chips to form overlay. Micro-vias are drilled using an adaptive UV Argon laser system. The electrical interconnect is fabricated using thin film metallization processes and laser patterning. The latter is an adaptive process so it can compensate chip misalignment. The adaptive laser patterning process not only eliminates the costly and time-consuming mask fabrication, also it reduces the critical requirement for chip alignment. The multi-layer interconnect structure can be fabricated by repeating the process sequence described.

The polymeric overlay structure allows fabrication of optical channels within a MCM using almost identical processing steps. One of key activities in our effort is to develop suitable polymeric waveguiding material with low optical loss and birefringence. Various polymers have been evaluated including polyimide, acrylics, and polyetherimides. Optical loss less than 0.5 db/cm has been measured.

Another main focus of our activity is to define and fabricate optical channels adaptively using the laser lithography system developed for electrical interconnect. This could eliminate the critical alignment required for coupling between a polymer waveguide and an optical transmitter or receiver. In this talk, we will discuss the process and material requirements and report recent experimental results.

## WAVEGUIDE AND DIFFRACTIVE COUPLING ELEMENTS FOR OPTOELECTRONIC PACKAGING

Nile F. Hartman  
Thomas K. Gaylord  
Timothy Drabik

Microelectronic Research Center,  
School of Electrical Engineering  
&  
Electrooptic and Physical Sciences Laboratory  
Georgia Institute of Technology  
Atlanta, Georgia

### INTRODUCTION

Optoelectronics continues to make inroads into computer and signal processing systems requiring high speed interconnection networks. While optical fibers predominate as the interconnect for long path lengths, at lower levels within an electronic system optical waveguides may be used as an interconnect media for signal distribution. Signal distribution using waveguides also implies input/output coupling and the need to redistribute an optical signal within the plane of the waveguide. For the latter, diffractive elements may be used for inplane and out-of-plane signal distribution. Diffractive coupling/signal distribution elements are attractive because of their directional properties and potential manufacturability.

### TECHNICAL DISCUSSION

Optical waveguides containing diffractive elements have been used for input/output coupling elements and for inplane signal deflection[1],[2]. In a multichip module environment this approach may be particularly attractive as through wafer coupling can be utilized by operating at a wavelength to which silicon is transparent. This configuration permits the

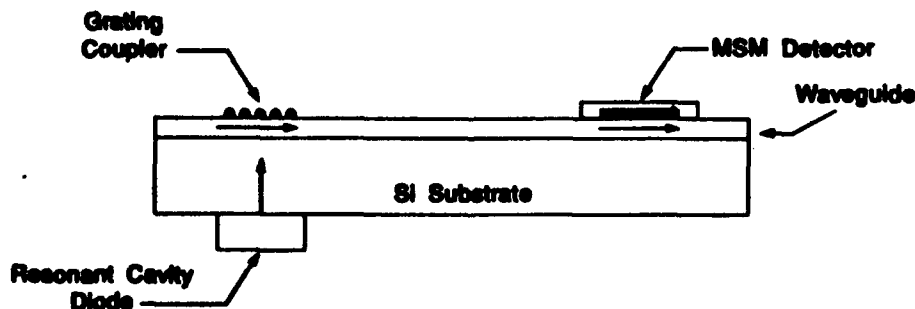


Figure 1. Through Wafer Optical Interconnect.

source and waveguide to be positioned on opposite sides of the wafer and further permits the source to be coupled to the wafer by lift off processes on the waveguide. Simultaneously, waveguide diffractive elements may be utilized to redirect optical signals within the plane of a waveguide. The former approach is illustrated in Figure 1.

The current work at Georgia Tech is directed to using volume or phase gratings to couple source output into optical waveguides deposited on a variety of substrates. The emphasis, however, is silicon substrates. Phase volume and "blazed" grating configurations are being examined analytically and experimentally. Phase volume gratings are attractive due to their potentially very high diffraction efficiencies. Angularly reflective and retroreflective gratings have been generated in optical waveguides with diffraction efficiencies approaching 100%[2]. In a waveguide configuration, high diffraction efficiencies are possible due to the ability to 1) fabricate thick waveguides (tens of micrometers) and 2) achieve reasonable index modulations ( $\Delta n$  in the  $10^{-4}$  to  $10^{-3}$  range). As input coupling elements, that advantage is mitigated somewhat by thickness limitations associated with the optical waveguides. For multimode polymer waveguides, analysis indicates high diffraction efficiencies can be achieved using appropriately shaped optical input beams. The current experimental efforts are directed to demonstrating practical high efficiency coupling elements.

With waveguide coupling and inplane signal distribution elements care must be exercised as degradation of optical pulse intensity profile and temporal shape can occur. Intensity profile distortion occurs with propagation across a grating because the diffracted signal strength (not efficiency) decreases exponentially with increasing propagation length through the gratings. Compensation requires a grating with variable diffraction efficiency over the grating length. For very short optical pulses and thick gratings, pulse length (time) distortions can also occur. The magnitude of representative distortions are of the order of a few femtoseconds per micrometer grating length. Therefore, for most applications involving gigahertz data rates and grating lengths of tens of micrometers, time dependent pulse distortions will be insignificant.

## **SUMMARY**

Optical waveguides incorporating diffractive elements are promising for optical interconnect applications in the multichip module packaging configuration. High efficiency input coupling, inplane signal distribution and through wafer interconnection schemes are possible. Photofabricated waveguides and diffractive elements lend themselves to manufacturable processes.

## **References:**

1. J. M. Hammer, R. A. Bartolini, A. Miller, C. C. Neil, Applied Physics Letters, Vol 28, p. 192, 1976.
2. N. F. Hartman, L. E. Corey, "A New Time Delay Concept Using Integrated Optic Techniques", International IEEE AP-S Symposium, June 24-28, 1991, The University of Western Ontario, London Ontario, Canada.

**Acknowledgments:** The authors gratefully acknowledge the support of the U.S. Army Missile Command, Redstone Arsenal, Alabama, Contract DAAH01-92-D-R005; The Manufacturing Research and the Microelectronic Research Center, Georgia Institute of Technology.

## Results of OEMCM Packaging Efforts at LLNL

O.T. Strand, S.Y.Lu, M.E.Lowry, R.J. Hawkins, D.C. Nelson, M.D. Pocha  
Lawrence Livermore National Laboratory  
Livermore, CA 94550

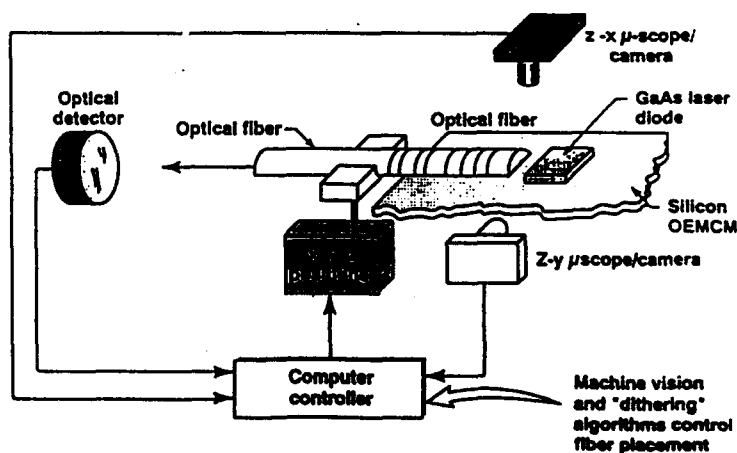
### Introduction

An important problem in realizing mass-produced and cost-effective optoelectronic multi-chip modules (OEMCM) is that of coupling the various photonic devices to the optical fiber. There are two critical issues associated with OEMCM packaging which must be addressed. 1) Single-mode fibers must be aligned with sub-micron tolerances to laser diodes and optical waveguides. At present, the state-of-the-art process involves a human operator viewing through microscopes to visually manipulate the waveguides using sub-micron positioning stages; therefore, a large fraction of the cost associated with photonic packaging is due to the time-consuming job of fiber alignment and attachment. 2) After attachment, back reflections from the end of the fiber into the laser diode cavity may disrupt the single-mode operation of the source. The details of the interface geometry can have a profound effect upon the device performance. This paper presents results of single-mode-fiber packaging technology, including automated packaging concepts, back-reflection diagnostics, and modeling.

### Automated Packaging Concepts

To date, passive alignment techniques have resulted in tolerances greater than 1 micron; we feel that active alignment using operating lasers and silicon microbench techniques will be necessary for sub-micron accuracies. We are developing an active alignment system which relies heavily on automation in order to reduce manufacturing costs. Our approach is to combine 3-dimensional computer vision and robotic techniques coupled with an active feedback system (Figure 1). The computer vision will allow positioning accuracies of a few microns which is sufficient to couple some light between the waveguides. At this point, the final sub-micron positioning is accomplished by maximizing the throughput into the waveguide. Two critical aspects of this project include the computer vision software and the fiber attachment technique. The computer-vision software development is in progress; object recognition algorithms have been developed. A simplified technique for fiber attachment after alignment to a laser diode has been developed; this method may be easily adapted by an assembly line process of fiber-pigtailing using computer-vision and robotic techniques.

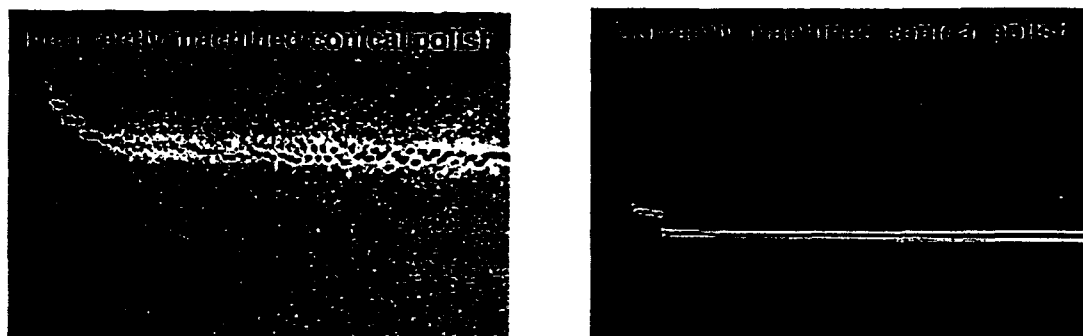
Figure 1.  
Sub-micron alignments are required for single-mode optical waveguide interfaces. Silicon v-grooves and solder bumps may not be sufficient.



## Back-reflection Diagnostics

Instabilities in the operation of a laser diode may be directly related to packaging interface problems. With an incorrectly machined fiber endface, minute amounts of back-reflected optical power create severe instabilities in the packaged laser output. Back-reflections caused by improperly interfaced waveguides located some distance downstream from the source may also disrupt the single-mode operation of the laser. We have developed a streak spectrometer system which allows us to monitor the packaged laser output in real time. The effect of an improperly interfaced junction upon the operation of the laser diode is dramatic (Figure 2). We routinely measure the stability of the source in our optoelectronic packages using these techniques.

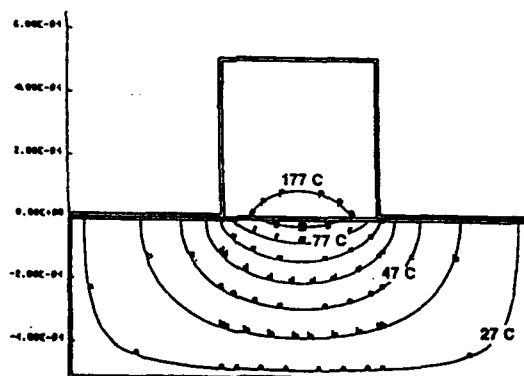
Figure 2. Problems with the fiber endface machining may be diagnosed with a streak spectrometer system. The vertical axis is wavelength and the horizontal axis is time.



## Modeling

Modeling is an important part of our packaging efforts. Thermal modeling allows the identification of potential thermal damage points when using solder-based attachment methods (Figure 3) and identifies insufficient heat sinking of laser diodes. Optical waveguide codes allow package designs to be studied before committing to expensive fabrication and testing cycles. Microwave modeling studies RF losses in various waveguide geometries which will be important for hybrid optoelectronic multi-chip modules.

Figure 3. Modeling allows identification of potential thermal damage points.



## Acknowledgements

We would like to thank the following for technical input: Scott Jordan, Newport-Klinger Corp.; Toshi Uchida, Bandgap Corp.; Gary Bjorklund, IBM-Almaden; Michael Olinger, Smiths Industries; Frederick Leonberger, United Technologies Photonics.

## **Design and Characterization of a Novel Fiber Optic Coupling Device for Data Communication Applications**

A. J. Heiney, C.-L. Jiang, and W. H. Reysen, AMP Incorporated, Lytel Division, Somerville, NJ 08876

### **Abstract:**

Many of the functions necessary for fiber optic coupling in data link applications have been incorporated into one opto-mechanical device called a lens/receptacle. The lens/receptacle enables the assembly of data links with reduced parts count, simplified assembly, lower cost, and streamlined testing with many performance advantages. The packaging consistent with this lens can accommodate data rates in excess of 600 Mb/s.

This paper outlines the design of the lens/receptacle while highlighting the performance benefits of the package as a whole. Performance results presented are on FDDI compliant pre-production prototypes operating at 125 Mb/s at  $\lambda = 1330$  nm.

### **Introduction:**

The availability of inexpensive fiber optic data communication equipment will enable the realization of wide area, shared resource, computer networks. The adoption of the Fiber Distributed Data Interface (FDDI) standard [1], including recent work toward a Low Cost FDDI standard, guides the path to the data communication superhighways of the future. Data link packaging efforts to date [2,3], including so called "low cost" packaging, have concentrated primarily on integrated circuit packaging and consolidation. The trusty "TO" header has been consistently relied upon to house active devices and mate with expensive optical coupling elements such as GRIN lenses and split sleeves. The header has also seen increased integration by housing preamplifier circuits. While this approach is technically sound, it shifts the cost from the drive/receive electronics to the active device mount (ADM).

An approach to manufacturing cost reduction has been taken which involves optical solutions to the ADM problem. The introduction of an integrally molded lens/receptacle element which performs fiber-receiving, light-coupling, and light-bending functions eliminates the need for headers by allowing tight integration of all electronics and active devices on a pre-tested board assembly. The multifunction precision molding further reduces cost by reducing parts count, allowing modular connector assemblies, and improving yield by improving performance. Design and packaging considerations will be described and compared with current data links.

### **Packaging Comparison:**

The construction of the current 16 pin data link follows current industry trends in that an electronic assembly and an optical subassembly are separately built and mated. The electronic assembly consists of integrated circuit(s) and passive components mounted on a cofired ceramic substrate. A Kovar subframe is brazed to the bottom of the ceramic for attachment of the case frame. The optical subassembly consists of a stainless steel fiber receptacle which accepts a "TO" lensed assembly. The optoelectronic device is die bonded to a ceramic submount which is attached to, but electrically isolated from, the header. The device and the top of the submount are then wire bonded to the header leads. A sapphire lens cap provides focusing and is welded to the header, hermetically sealing the opto device. The header assembly is then actively aligned into the receptacle and fixed with epoxy. The tested optical subassembly is then mated to the case frame using a clip and the leads are soldered to the board. Finally a lid is attached for bubble tight sealing. A summary of the assembly operations for both the current and new design data links is given in Table 1.

**TABLE 1: Assembly Operations for Standard and New Design Data Links**

<b>Current Design</b>	<b>New Design</b>
<ul style="list-style-type: none"><li>• Electronics Board Assembly</li><li>• Case Wall Attach</li><li>• Attach Submount to Header</li><li>• Die &amp; Wire Bond Device to Submount</li><li>• Purge Device &amp; Test</li><li>• Cap Weld Lens</li><li>• Active Align to Receptacle &amp; Backfill</li><li>• Cut &amp; Form Leads</li><li>• Attach Receptacle to Case</li><li>• Solder Leads to Board</li><li>• Lid Attach</li><li>• Burn-in &amp; Test</li></ul>	<ul style="list-style-type: none"><li>• Electronics Board Assembly</li><li>• Die &amp; Wire Bond Device to Board</li><li>• Purge/Burn-in Board &amp; Test</li><li>• Attach Fiber Stop to Lens</li><li>• Attach Lens to Case</li><li>• Active Align &amp; Backfill</li></ul>

The construction of the new data link provides the seat for the fiber and the board while conducting the light to/from the optoelectronic device. The 6 layer printed wiring board is assembled with the same circuit and components as the current design using chip-on-board. The PIN/LED is then die & wire bonded onto special low capacitance/high thermal conductivity traces. With this configuration, the opto device can be purged while the populated board can be simultaneously burned in. The advantages of the complete electrical subassembly are: Simpler testing earlier in the integration path; reduced parasitic capacitance leading to higher gain; reduced radiation from long exposed leads; and easier gripping for active alignment compared with headers.

The lens/receptacle is attached to a case and the board is actively aligned in the case. To reduce cost some sacrifices in the specifications had to be made. The fiber receptacle had to be changed from stainless steel to plastic. This turns out to be a relatively small penalty due to the availability of high performance plastics. In moving away from welded metal housings, hermeticity was not feasible. In order to evaluate the elimination of hermeticity of the opto device, extensive 85°C/85% RH testing was performed on bare devices and no degradation was observed.

### Conclusions:

Data links can be built with fewer parts and less labor content while at the same time improving performance in many areas. A comparison of performance in selected areas is provided in Table 2. Preamp input capacitance has been reduced which can be used to improve sensitivity through increased gain or to increase active area for increased lateral optical coupling tolerance. Edge speeds have been improved while staying within the same overshoot guidelines as the standard product. Spectral width has been reduced at room temperature which increases center wavelength tolerance, improving yields for compliance with FDDI standards. More importantly, since the electrical design is temperature compensated, increasing drive current with temperature, the spectral width differential at 70 °C is expected to be approximately 25 nm. There has been a nominal increase in peak LED coupling which may allow decreasing drive current. The only shortfall is PIN coupling efficiency which can be partially recovered by antireflection coating one of the lens surfaces.

### References:

- [1] FDDI Physical Layer Medium Dependent (PMD) standards:
  - US: ANSI Standard X3.166 - 1990
  - International: ISO Standard IEC 9314 - 3; 1990(E)
- [2] M. S. Acarlar, S. L. Moyer, and S. D. Robinson, "Use of Low Cost DIPs and Injection Molded Parts in Packaging of Optical Data Links", ECTC Conference Proceedings, 1992, San Diego, CA, pp.661 - 666.
- [3] D. Chown, R. Musk, D. Manton, C. Sparkes, M. Birch, M. Benton, J. Somerville, R. Hooley, L. Krauss, "Integrated Transceiver for FDDI", ECTC Conference Proceedings, 1989, Houston, TX, pp. 378 - 383.
- [4] C.-L. Jiang, "Ray Tracing Model for Efficient Coupling of LEDs Using a 'TO' Package", AMP Journal of Technology, 1993.

**TABLE 2: Comparison of Data Link Performance**

Performance Property	Units	Device Type	Standard Data Link	New Design Data Link
Effective Capacitance	pf	PIN	1.6	1.1
Rise/Fall Time	ns	LED	1.7/1.8	1.4/1.7
Spectral Width	nm	LED	148	140
Fiber Coupled Power *	dBm	LED	-15.5	-14.8
Coupling Efficiency	%	PIN	90	80 **
Relative Cost	-	Rx & Tx	1.0	.55
- Material	% of total	Rx & Tx	55	75
- Labor	% of total	Rx & Tx	45	25

\* - Ambient reading into 62.5  $\mu$ m core gradient index fiber; less than  $\pm 0.5$  dB variation 0 - 70°C

\*\* - Below Standard due to lack of antireflection coating

**A HYBRID COHERENT RECEIVER WITH A PERMANENTLY PIGTAILED SEMICONDUCTOR WAVEGUIDE 3-dB COUPLER AND AN INTEGRATED PIN PAIR**

F. Delpiano, N. Caponio, G. Destefanis, S. Morasca, M. Puleo, F. Schiattone  
(CSELT S.p.A. - Via G. Reiss Romoli 274, I-10148 Torino, Italy - FAX +39-11-2285695)

E. Legros, M. Billard, L. Giraudet, A. Scavennec  
(CNET - Laboratoire de Bagneux, 196, Av. Henri Ravera, F-92220, France - FAX +33-1-47460417)

**INTRODUCTION** - The monolithic integration of receivers is necessary for a wide diffusion of coherent multi-channel distribution networks. As an intermediate step, the functionality of a hybrid coherent receiver, including semiconductor integrated components, has been experimented, allowing also to assess the permanent twin-fibre coupling to waveguides.

This hybrid receiver (fig. 1) is formed by a waveguide coupler, based on the Two-Mode Interference (TMI) structure [1], butt coupled by micropositioners to a monolithic pair of PIN photodiodes, that are assembled with a two-stage GaAs MESFET preamplifier [2]. The semiconductor TMI coupler provides a compact device with a comparatively low sensitivity to fabrication tolerances and the specially designed Moderately Diluted-MQW (MD-MQW) waveguides structure allows an efficient coupling [3] and a permanent pigtailing to single mode optical fibres.

**3-dB COUPLER** - The TMI 3-dB couplers [4] have been realized on MD-MQW ridge waveguides, including two 160  $\mu\text{m}$  spaced single-mode inputs and outputs, merging with a 20 mm curvature radius in a double-mode region that acts as the coupling section. The device overall length is around 5 mm.

An advanced InGaAsP/InP MD-MQW waveguide structure has been adopted [3] aiming at fibre-guide coupling efficiency. As a relevant feature it has an increased well/barrier ratio, in comparison to the originally proposed diluted MQWs [5], providing improved confinement and curvature performance with a compact cross section (the guiding core thickness is less than 2  $\mu\text{m}$ ). The epitaxial structure, grown on semi-insulating InP by LP-MOCVD is laterally defined using photolithography and reactive ion etching; the facet reflectivity is reduced to  $5 \times 10^{-3}$  by silicon nitride coating. The MD-MQW structure is therefore compatible with integration of optoelectronic and electronic components, while maintaining a good field matching with a standard fibre: the waveguides feature a coupling loss to tapered-lensed fibres as low as 0.5 dB and a 1.5 dB/cm attenuation. A best insertion loss of about 4 dB has been obtained for the couplers.

**COUPLER PIGTAILING** - For the system experiment a coupler balanced at 1543 nm for TE polarisation was selected, with an unbalance sensitivity of 0.05 dB/nm around the 3 dB point (lower sensitivities, 0.03-0.04 dB/nm, are also currently achieved). The insertion loss achieved for this particular device, coupled to a tapered lensed fibre, was 8 dB.

The chip (0.75 mm x 4.8 mm) containing the selected device was cleaved from the wafer and epoxy bonded on a metallic base plate. A 160  $\mu\text{m}$  spaced fibre pair, fixed on a silicon V-groove submount, was aligned to the waveguides, using a miniature vacuum chuck controlled by a micropositioner system having six degrees of freedom with resolutions of about 0.1  $\mu\text{m}$  and 0.003°. After alignment the fibre pair submount was fixed to the base plate by a UV-curable adhesive: a negligible shrinkage misalignment, implying less than 0.4 dB increase in coupling loss, was obtained with a reduced (100  $\mu\text{m}$ ) adhesive thickness and adopting a special curing procedure. After several months the coupling losses, and therefore the alignment, have been verified to remain unchanged, showing the good stability of the fixing procedure.

**HYBRID PHOTORECEIVER** - The hybrid receiver [2], designed for high sensitivity, low noise, high common mode rejection ratio and wide bandwidth, has been purposely adapted for an easy butt coupling to the coupler chip.

A monolithic pair of AlInGaAs/InP PIN photodiodes, with 160  $\mu\text{m}$  spacing, is used for detection, featuring a 0.3 pF total capacitance and a 0.8 A/W responsivity; moreover it shows a better common mode rejection ratio, if compared to a discrete pair, provided that the component and parasitic parameters of the biasing circuits are identical. The receiver is equipped with a hybrid two-stage preamplifier including commercial 0.3  $\mu\text{m}$  GaAs MESFETs. A reduced thermal noise and a flat

frequency response [6] are obtained matching the preamplifier input to the photodiodes by a reactive element, leading to a low pass transimpedance preamplifier. The response is equalized within the preamplifier and is output matched to 50  $\Omega$ . The resulting input noise current is then lower than 7 pA/ $\sqrt{\text{Hz}}$  up to 3 GHz and the frequency response shows a 2.9 GHz bandwidth. With a balanced illumination of both PINs a 35 dB CMRR is obtained. When the semiconductor coupler is faced to the PIN pair a 25 dB CMRR has been measured, with 1 mW power at the photodiodes.

**TRANSMISSION EXPERIMENTS** - The hybrid coherent receiver has been tested in an experimental transmission system at 155 and 622 Mbit/s with On-Off-Keying external modulation. Two manual polarisation controllers have been inserted before the coupler. The total LO power at PINs was about -7 dBm, due to the insertion loss of fibre connectors and 3-dB coupler (about 11.7 and 10.1 dB for the two inputs respectively, in the permanent coupling configuration). The measured BER dependence on the received optical power at fibre ends is reported in fig. 2, showing sensitivities of  $\sim$  -38.0 dBm and -28.8 dBm for  $10^{-9}$  BER at 155 and 622 Mbit/s, that are compatible with the 3-dB coupler losses and the electronic circuit characteristics. Sinusoidal polarisation spreading at the transmitter side [7] was used as well, to overcome the polarisation dependence of heterodyne conversion efficiency. In that case the LO state of polarisation was optimized for the 3-dB coupler operation, while the transmitted signal polarisation was properly modulated: the complete functionality of the semiconductor waveguide 3-dB coupler for an integrated coherent receiver was demonstrated also in this case, by the almost constant level of the demodulated eye-diagram, while the line polarisation was changed. Moreover, no effect of backreflections from the coupler has been observed.

**CONCLUSIONS** - This experiment demonstrates the functionality of a pigtailed MD-MQW semiconductor 3-dB coupler in the receiver of a coherent system. A relatively simple technique for the coupling and fixing of closely spaced twin fibres has been adopted, allowing an easy handling of the component and a good long term stability as required by transmission system experiments.

**ACKNOWLEDGEMENTS** - This work was partially supported by the EEC under Project RACE 1027.

- REFERENCES**
- [1] C. Caldera et al., Proc. ECOC'90, Amsterdam, Sept. 1990, pp. 357-360.
  - [2] E. Legros et al., Proc. EFOC/LAN '92, Paris, 1992, pp. 375-377.
  - [3] S. Morasca et al., SPIE Proc. Vol. 1794, paper N° 18, in press.
  - [4] C. Caldera et al., to be published.
  - [5] R. J. Deri et al., Appl. Phys. Lett., Vol. 55, pp.1495-1497, 1989.
  - [6] G. Jacobsen et al., J. Lightwave Technol, Vol. LT-7, pp 105-114, 1989.
  - [7] N. Caponio et al., Electron. Lett., Vol. 27, pp. 337-338, 1991.

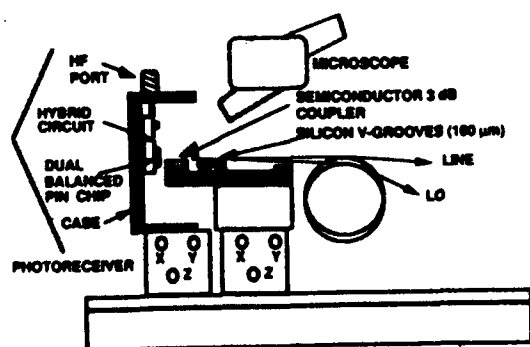


Fig. 1 - Hybrid coherent receiver schematic.

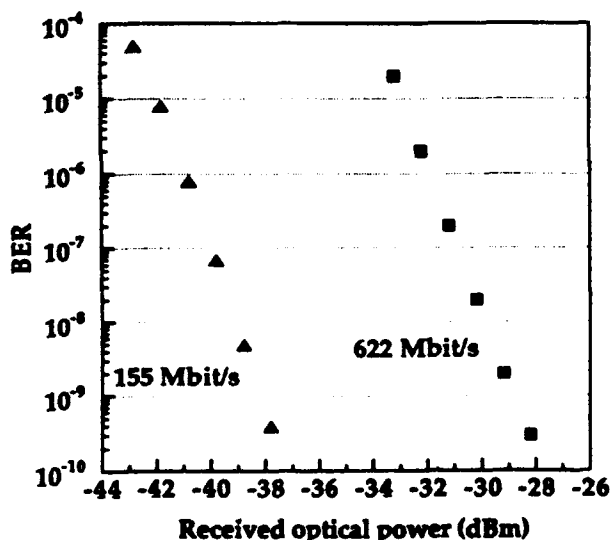


Fig. 2 - Bit error rate vs. power at fibre pigtailed.

**Fabrication Issues for Free-Space Optics**  
**at the Board Packaging Level**

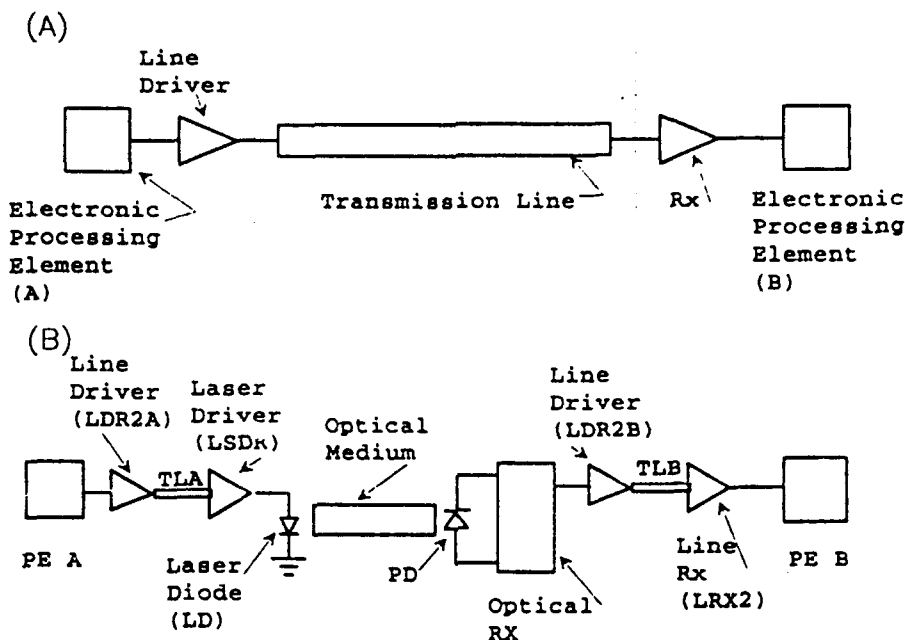
Raymond K. Kostuk

Electrical and Computer Engineering Dept. and  
the Optical Sciences Center  
University of Arizona  
Tucson, AZ 85721

The successful application of optical interconnects to electronic processing systems requires careful consideration of 1) the electronic system in which it will be used, 2) the availability of competitive advanced electrical interconnect methods, 3) the optical system design and fabrication methods, 4) the electro-optic devices and fabrication process, 5) the interface between electro-optic devices and electronic processing elements, 6) the cost of packaging micro-optical components and electro-optic devices with electronic processing elements, and 7) the reliability of optical interconnects relative to comparable performance electrical interconnects. If one or more of these factors are neglected it could result in a design of limited performance, or performance which can easily be superseded by electrical interconnects.

An example of the performance differences between an optical and electrical point-to-point interconnect system is illustrated in Figure 1 between processors A and B. In the electrical system the output from the switching elements of processor A go to a line driver which transmits signals over a transmission line to a receiver which provides input to processor B. Delays occur in the line driver, the transmission line, and receiver. An equivalent optical system is shown in Fig. 1B. In addition to the line driver and receiver delays which occur in the electrical system, delays also take place in the laser driver, laser diode, the optical medium, photodiode, optical receiver, and the receiver end line driver. Therefore in order for the optical interconnect system to offer an advantage in reducing signal propagation delay, the delays caused

FIGURE 1. a) Point-point electrical and b) corresponding optical interconnect<sup>1</sup>.



by these additional circuit components must be less than the transmission line delay in the electrical system. This drastically reduces the competitive advantage of optics for planar interconnect applications. It should be noted that point-to-point interconnects are only one class of connections. When fanout and multiple line interconnects are considered the advantage of electrical methods may diminish, but this determination will require more sophisticated analysis of electrical crosstalk and loading effects.

At the board level of packaging the interconnect problem is three dimensional. Electrical interconnections between on adjacent boards must be routed through a backplane. In this case free-space optical interconnects between adjacent boards can trade off propagation delay for the additional delays produced by the electro-optic interface components.

Therefore optical information transfer between adjacent boards in a processing system is one area where effective optical signal propagation delays can be competitive with electrical interconnects. In this presentation the design and implementation of free-space board-to-board interconnects will be reviewed.

1. R.K. Kostuk, J-H. Yeh, and M. Fink, "Distributed optical data bus for board level interconnects," to be published in Applied Optics 1993.

## A Three-Dimensional Optical Interconnection Network for Fine-Grain Parallel Architectures

D. Scott Wills and Matthias Grossglauser  
School of Electrical Engineering  
Georgia Institute of Technology  
Atlanta, Georgia 30332-0250

Fine-grain, message-passing architectures offer high performance for high-throughput parallel applications such as image processing (e.g., filtering, edge detection, convolution), object recognition, and data compression. Reduced local memory requirements of these applications allow multiple high performance (50 MIPS/node) processing nodes to be integrated on a single chip.

In order to meet the I/O requirements of each node, a high-bandwidth, three-dimensional optical network, is being developed. Using recent advances in epitaxial liftoff and deposition and through-chip transmission, a network is being designed to provide 3.2 Gbits/sec off-chip bandwidth.

Index-guided and free-space techniques for optical interconnects are difficult to incorporate in three-dimensional processing networks. Hybrid integrated optoelectronic devices [2] and through-wafer transmissions [1] offer a three-dimensional optoelectrical interconnection with an *offset cube* topology.

### Physical Architecture

A new technique for combining GaAs and InP-based optoelectrical devices with Si VLSI has been developed in the Microelectronics Research Center at Georgia Tech. Using epitaxial liftoff, small (50 x 50  $\mu\text{m}$ ) GaAs and InP-based light emitting diodes and lasers have successfully been removed from an InGaAsP substrate, aligned, and selectively deposited on a silicon host substrate. This technique has been refined to allow the deposition of arrays of GaAs and InP-based emitters or detectors in parallel.

The GaAs and InP-based devices are deposited on an insulating planarizing layer over the Si substrate, so optoelectronic devices can be placed on top of electronic circuitry. Emission wavelengths for InGaAs and InGaAsP are selected for which Si is transparent, allowing through-wafer transmission.

This network exploits this technology to form a three-dimensional interconnect. Processing elements are designed and fabricated using existing Si VLSI techniques. Bonding pads are provided only for power contacts. (Probe pads are provided for testing.) Holes in the overglass allow GaAs and InP-based emitters or detectors to be attached in a post processing step. Silicon-based driver circuits connect parallel buses from routers on the chip to the faster

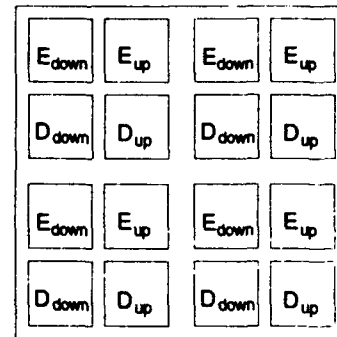


Figure 1: Chip Device Pattern

optical devices (0.1 - 1.0 Gbits/second).

After the Si chips containing the optical devices are fabricated and tested, they are attached to a larger silicon substrate. This provides physical support and also participates in power distribution and cooling. A fully populated substrate forms one plane of the system. Completed substrates are then stacked to create the third dimension. To facilitate manufacturing, all chips and substrates are identical.

Each chip is broken into four quadrants which overlap with eight neighboring chips (four in the plane above, four in the plane below). Although any number of emitter and detectors can be included in each quadrant, the minimum case requires two emitter/detector pairs, shown in Figure 1.

In order for emitter/detector pairs to be correctly aligned, the chips must be offset. To achieve this using identical plane substrates, a spacing equal to one half the chip width plus inter-chip spacing is added to two non-opposing sides of the substrate. Then alternating planes are rotated 180° during assembly providing the correct device alignment.

System I/O is provided by I/O layers which inject data directly into the network on the top and bottom of the stack. Optical clock distribution is also incorporated in this system.

### Topology

Each chip connects to eight neighboring chips: four in the plane above and four in the plane below. There are no inter-chip connections within a substrate plane. This interconnection forms an *offset cube* topology which bears similarities to the well-studied *k*-ary 3-cube. While the physical architecture

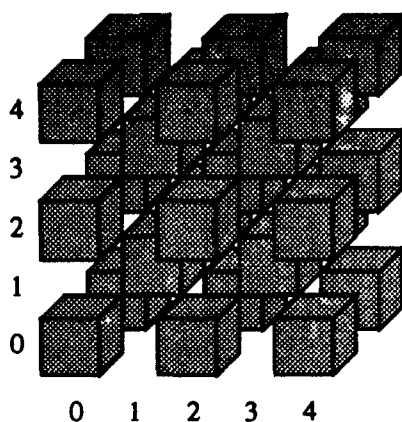


Figure 2: Offset Cube Topology

of the inter-chip network is not symmetric in the vertical and horizontal dimensions, the offset cube topology implemented by this network is isotropic. The topology, shown in Figure 2, is formed by vertices that have all even or all odd coordinates.

In a  $k$ -ary 3-cube, a shortest path routing algorithm uses channel routes to reduce the difference in coordinates of the source and destination nodes. A well-performing deterministic algorithm reduces the coordinate differences one at a time.

A shortest path routing algorithm for an offset cube is more complicated since each channel hop changes all three coordinates. If one coordinate difference reaches zero, it must be increased in the next hop to reduce differences in other dimensions.

#### Network Performance

To compare the  $k$ -ary 3-cube and offset cube topologies, a simulator has been constructed which analyzes network performance under similar conditions and loads [3]. In these experiments, a 16-ary 3-cube (4096 nodes) is compared with a 25-ary offset cube (3925 nodes). A random traffic load is simulated. Wormhole routing is employed with eight virtual channels for each physical channel. Latency is normalized to one for the non-blocking case. All message lengths are 25 flits.

Figure 3 compares the performance of deterministic and adaptive routing algorithms on the two topologies. For the deterministic case, the 16-ary 3-cube routes messages  $x$ - $y$ - $z$ . The offset cube routes along a diagonal shortest path. The offset cube utilizes less than half of the capacity of the 3-cube.

The capacity loss is due to loading in the center of the network. For random traffic, deterministic routing on a 3-cube does a reasonable job of distributing traffic across the entire network. The offset cube's diagonal routing creates much higher traffic in the center of the network. This has been verified by comparing cross-sectional loading profiles for a 3-cube with

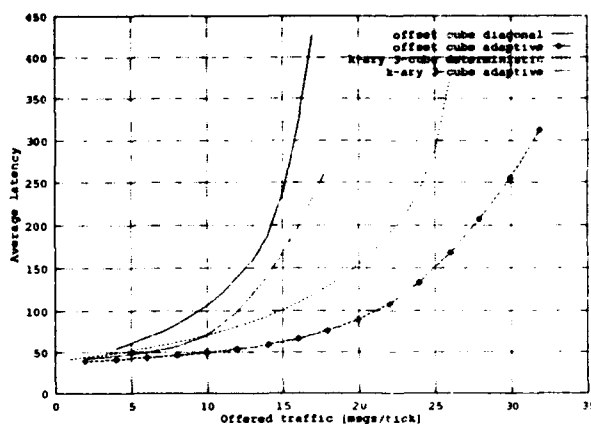


Figure 3: Performance of Offset Cube, 3-Cube

$x$ - $y$ - $z$  and diagonal routing algorithms.

To better utilize the capacity of a offset cube network, a simple adaptive routing algorithm is employed. Local information (the number of virtual channels in use) is used to select between shortest paths at each vertex. Figure 3 compares each topology for both deterministic and adaptive routing strategies. The adaptive offset cube performance exceeds that of the best 3-cube strategy. The adaptive 3-cube performance is lower than the deterministic case because of increased diagonal routing.

#### Status

Currently, a test chip is being built containing parts of the offset cube router and optical channel. A proposed full-scale prototype will contain 32 100 Mbit/sec emitter/detector pairs. Four 50 MIPS processing elements are included on each chip. A processing plane contains 64 chips (256 nodes, 12,800 MIPS) and measures approximately 10 cm by 10 cm. 16 planes contain 1024 chips (4096 nodes, 204,800 MIPS) and fit inside a cube 10 cm on a side. 819.6 Gbits/sec of I/O bandwidth is available from the top and bottom surfaces of the cube. Combining this optoelectronic communication network with new fine-grain machine architectures can lead to extremely dense, high performance parallel systems.

[1] K. H. Calhoun, C. B. Camperi-Ginestet and N. M. Jokerst. Vertical Optical Communication Through Stacked Silicon Wafers Using Hybrid Monolithic Thin Film InGaAsP Emitters and Detectors. *IEEE Photonics Technology Letters*, 5(2):254-257, February 1993.

[2] C. Camperi-Ginestet, M. Hargis, N. Jokerst, and M. Allen. Alignable Epitaxial Liff-off of GaAs Material with Selective Deposition Using Polyimide Diaphragms. *IEEE Transactions Photonics Technology Letters*, 3(12):1123-1126, December 1991.

[3] Matthias Grossglauser and D. Scott Wills. Performance Analysis of an Offset Cube Network using Optical Interconnect. VLSI Architectures Group Technical Report, January 1993.

## Optical and Package Design Issues for Chip-to-Chip Free-Space Optical Interconnections

F. B. McCormick

AT&T Bell Laboratories, 263 Shuman Blvd., Naperville, IL 60566

### 1. Introduction

High-performance digital electronic systems such as high speed switching fabrics or parallel processing engines are pushing the limits of current electronic interconnection technology. To meet the demands of these applications, systems designers are turning to interconnection and packaging solutions that integrate multiple technologies, and this has spurred interest in optical interconnection solutions. By propagating signals as beams of light normal to the plane of the device substrates, the reactive loading effects of 2-D metal interconnections are avoided, potentially offering the benefits of high bandwidth, high density connectivity, low signal skew, and low degradation of signal quality. Additionally, the potential for providing large numbers of high density, high speed interconnections at the chip level can enable novel system partitioning, which can significantly impact architectural designs. Free-space optical interconnections (FSOIs) are currently in a state of technology development, and significant progress is being made in the areas of architecture, device, optics, and packaging. Availability of 2-D optoelectronic device arrays has enabled the fabrication of demonstration systems that require simultaneous optimization and integration of several technologies, and this has begun to focus attention on the practical issues of optical design, alignment, stability, reliability, repairability, and cost.<sup>[1]</sup> The currently embryonic state of this technology requires that the architectures, devices, optics, and packaging be collectively optimized to build viable systems. As our knowledge of the critical system issues and tradeoffs increases, however, standardization of many components and techniques will enable more widespread application of FSOIs.

### 2. FSOI Packaging issues

The 2-D device arrays proposed for use in chip-to-chip FSOI systems have been generically termed "smart-pixels", since each pixel not only incorporates optical I/O, but also may have electronic processing, memory, and I/O. The advent of smart pixels introduces several critical packaging issues. In many smart pixels, the overall optical I/O density is small, having <200 optical I/O per  $\text{mm}^2$ . Thus the most cost effective means of imaging such an array would provide high resolution only at the optical I/O, not across the entire array, and thus use microlenses rather than bulk optics. The diameter of the detectors used in the smart pixels is also important, since it affects the system alignment tolerances, system speed, and electronic power dissipation (due to receiver amplifier dissipation). The addition of large numbers of high-speed transistors significantly raises the electronic power dissipation of these chips, and makes thermal management a critical issue even for modulator-based systems. The use of differential optical signals may be necessitated by low signal contrast, signal non-uniformity across an array, or other noise mechanisms. Variations of transistor or other device characteristics across an array can introduce channel delay variations and signal skew, requiring signal retiming at each chip (e.g. by modulating the modulator optical power supply). Additionally, limited high speed electronic communication off-chip may still be required.<sup>[1]</sup> Flexible configuration of specific device characteristics (detector/source sizes and locations, receiver sensitivities, electrical signal access and processing, etc.) may allow the creation of standardized interfaces not only at the device level, but also within the optics and mechanics.

Three general types of imaging systems have been proposed for FSOIs: "macro" or bulk lenses, microlens arrays, and hybrid macro-microlens systems.<sup>[2]</sup> Macrolens imaging is a well established and understood technology, and several complex macrolens optical free-space system experiments have been demonstrated.<sup>[1]</sup> Macrolens optical system can provide very high SBWP ( $10^4 - 10^6$  object/image points) and low signal transmission skew (< 10 fs). However, the complex lenses used introduce significant latency and cost. In microlens systems the beam spreading due to diffraction is inversely proportional to the transmitter/receiver density, so there is a tradeoff between the connection capacity and the distance between microlens arrays.<sup>[3]</sup> Distances of 2-3 cm may be necessary for the interconnection and fan-in functions, or simply to connect to the next chip, MCM, or board. Time skew between channels will accrue proportionally to the globality of the interconnect. Inexpensive replication of microlens arrays can lower optical system costs, but new alignment and mounting techniques must be developed. Hybrid lenses may offer the best solution for smart pixel imaging. They use macrolenses to control the diffraction of the signal beams and microlens arrays to provide most of the focussing "power" in the system. The macro "front lens" operates at high f-number ( $f/10-30$ ) and provides the geometric image magnification. The microlenses operate at low f-number ( $f/1$  to  $f/5$ ) and provide most of the lens numerical aperture. Hybrid lenses may provide many high resolution channels with low signal skew at relatively low cost.

In addition to laboratory demonstrations constructed on optical benches with discrete optics, electronics, and mechanics, we can define two broad **package integration** levels. The *custom optical bench/frame* (COB) level of integration has been reached by some FSOI demonstrations, and it is used in some commercial products such as optical correlators, free-space optical communication systems, telescopes for tracking or reconnaissance, and supermarket bar-code scanners. These applications demonstrate the high reliability, alignment stability, and commercial viability of COBs. However, manufacturability and the relative costs of these systems suffer from the still low level of integration. *Monolithic optical bench* (MOB) packages integrate the optics, optomechanics, and optoelectronics on a common substrate or substrates. They require more new technology development than COBs, but offer the best chance of achieving low cost and ease of manufacture. Thermal management will be a critical issue in monolithically integrated FSOI packages, because of the high density and lack of accessible surface area. Another important issue may be the lack of test and/or repair capability. Future systems will likely utilize a combination of MOB and COB components within a single package.

### 3. COB packaging in an experimental optical switch

The FSOI switching fabric of Fig. 1 implements a 32-input, 16-output multi-stage switching fabric using 5 stages of FET-SEED "smart pixel" arrays and semiconductor laser diode optical power supplies. The lenses, diffractive optics, retarders, steering prisms, and device arrays are mounted in cylindrical steel cells which are held magnetically in slotted steel base-plate. The modular system mounting scheme kinematically constrains each component's critical degrees of translational or rotation freedom while providing the necessary alignment mechanisms in a compact and simple manner. The system was temperature stabilized by a combination of Peltier coolers and a chilled water heat exchanger. Preliminary experiments have operated the full system at 50Mb/s and a 2-stage portion at 155 Mb/s. The collaboration and support of my colleagues in the Photonic Switching Technologies group is gratefully acknowledged.

### REFERENCES

1. F. B. McCormick, F. A. P. Tooley, J. L. Brubaker, J. M. Sasian, T. J. Cloonan, A. L. Lentine, S. J. Hinterlong, and M. J. Herron, "Optomechanics of a free-space switch: the system", *Optomechanics and Dimensional Stability*, Proc. SPIE 1533, 97-114, (1991).  
and F. B. McCormick, T. J. Cloonan, A. L. Lentine, J. M. Sasian, R. L. Morrison, M. G. Beckman, S. L. Walker, M. J. Wojcik, R. A. Novotny, S. J. Hinterlong, R. J. Crisci, and H. S. Hinton, "A 5-Stage Embedded-Control EGS Network Using FET-SEED Smart Pixel Arrays," in *Photonics in Switching Technical Digest, 1993*, (Optical Society of America, Washington, D.C., 1993), post-deadline paper PD-5. (Submitted to *Applied Optics*, , special issue on Optical Computing, 1993.)
2. A. W. Lohmann, "Scaling Laws for lens systems," *Applied Optics* 28 (23), 4996-4998 (1989).
3. F. B. McCormick, F. A. P. Tooley, T. J. Cloonan, J. M. Sasian, H. S. Hinton, K. O. Mersereau, and A. Y. Feldblum, "Optical Interconnections Using Microlens Arrays," *Optical and Quantum Electronics* 24, S465-S477, (1992).

**Fig. 1.** Prototype smart pixel switching fabric using fiber-bundle input and output (bottom and top), 5 arrays of reflection-mode FET-SEED 2x1 switching nodes with on-board network control memory (right), and modular laser diode optical power supplies (left). Input fiber bundle incorporates a hybrid lens imaging system and the FET-SEED arrays are addressed by a macrolens imaging system. Computer generated phase gratings generate uniform beam arrays for the optical power supply and implement Banyan interconnections between stages.



# Hybrid OEIC Cost Sensitivity

Charles W. Stirk

Center for Optoelectronic Computing Systems  
University of Colorado  
Boulder, CO 80309-0425  
charlie@boulder.colorado.edu

## Abstract

An analytic model is presented that measures the hybrid OEIC manufacturing cost sensitivity to the assembly method, process cost or yield parameter variation, and testing strategy.

## 1 Introduction

Hybrid OEIC manufacturing cost depends on many factors. This paper presents a model that allows analytic expression of the manufacturing cost in terms of the cost and yield parameters of the processing and testing steps. Using the model, we measure the sensitivity of the manufacturing cost to variations in the parameters and processes for common hybrid OEIC's and manufacturing methods.

Some of the questions answerable with this approach include the following.

1. Given a desired monolithic component or a hybrid OEIC and finite set of manufacturing processes, what is the lowest cost manufacturing method?
2. What is the lowest cost partition of a hybrid OEIC onto several chips?
3. In a given manufacturing process sequence, which process is the bottleneck to lowering the overall cost?
4. Given a process sequence, what is the testing strategy that generates the lowest cost?

We will answer these questions for several common hybrid OEIC's and manufacturing methods.

## 2 Monolithic and Hybrids

Let us begin by considering the individual monolithic components in a hybrid OEIC. To a large extent,

monolithic components are made using conventional semiconductor manufacturing equipment whose costs and defect types are well-understood. [1, 2] Given device designs in terms of dimensions and manufacturing steps, we can estimate the yield based on device failure modes, and hence, the cost. [3]

The hybrid component cost can be estimated based on knowledge of the device costs and the cost and yield of assembly. [4] We apply this method to determining the appropriate level of integration for optoelectronic transceivers.

## 3 Process Variation

There are several hybridization methods including wire bonding, flip-chip with solder bumps, and epitaxial liftoff. We show how serial and parallel attachment approaches compare in terms of cost. We also show how alignment structures can reduce the hybrid module cost.

## 4 Parameter Sensitivity

Not only can we measure the cost of different manufacturing methods, we can use the model to find out how best to improve an existing process. By using the technique of experimental design, [5] we can vary the process step costs and defect densities to find where a change in process equipment would most improve the final hybrid cost.

## 5 Testing

Testing is crucial to the overall hybrid cost. For instance, if the components are tested before hybridization rather than after, then the final cost can be much less if the testing cost and component yields are low. In addition, the fault coverage of the test and the pos-

sibility of rework also influence where in the process testing should occur.

## 6 Conclusions

Analytic modeling of the hybrid OEIC manufacturing process allows for consideration of process improvements in terms of their cost. We show under what conditions different assembly methods are advantageous; how to improve a process; and where testing provides the greatest benefit.

## 7 Acknowledgments

I would like to acknowledge support from a Department of Education fellowship and the Center for Optoelectronic Computing Systems. The Center for Optoelectronic Computing Systems is sponsored in part by NSF grant number CDR 8622236 as part of the Engineering Research Centers Program, and the Colorado Advanced Technology Institute (CATI), an agency of the State of Colorado.

## References

- [1] A. R. Alvarez and D. W. Schucker, BiCMOS Technology for Semi-Custom Integrated Circuits, Cust. Int. Cir. Conf, pp. 22.1.1-22.1.5 (1988).
- [2] C. H. Stapper, F. M. Armstrong, and K. Saji, Integrated Circuit Yield Statistics, Proc. IEEE 71(4), pp. 453-470 (1983).
- [3] B. T. Murphy, Cost-Size Optima of Monolithic Integrated Circuits, Proc. IEEE 1537-1545 (1964).
- [4] C. W. Stirk, Cost Models of Components for Free-Space Optically-Interconnected Systems, Proc. SPIE 1773B, paper 7 (1992).
- [5] R. Jain, The Art of Computer Systems Performance Analysis, John Wiley, New York (1991).

*Optoelectronic Integration of Thin Film Devices for Photonic Interconnect*

Nan Marie Jokerst  
School of Electrical Engineering  
Microelectronics Research Center  
Manufacturing Research Center  
Georgia Institute of Technology  
Atlanta, GA 30332-0250

Interconnection in integrated circuits currently limits processing density. Input/output pin limitations also pose a serious packaging problem as integrated circuits increase in size and processing capability. In addition, increased use of parallel processing in computational systems is projected as a primary means of increasing computational throughput in electronic signal processing systems. Photonic interconnections offer a solution to these interconnection and input/output bottlenecks. Additionally, optical interconnections offer particular advantages in parallel interconnection and parallel processing schemes.

One promising method for integrating photonic devices with silicon or gallium arsenide integrated circuits is thin film device integration. Single crystal thin film compound semiconductor devices can be separated from the growth substrate and bonded to foundry silicon circuits using standard microelectronic processes, which is a particularly attractive option for low cost, high performance integrated photonic interconnect. The separation of GaAs and InP-based thin film epitaxial devices from the growth substrate, called epitaxial lift off (ELO) [1], and the subsequent transfer and bonding of these thin film devices to relatively smooth host substrates [2], such as silicon circuits, will be presented.

An important issue in the development of this thin film integration technique is the quality of the thin film materials and devices. A number of studies have demonstrated that the quality of the material is not negatively affected by the processing [3, 4, 5]. Data will be presented which demonstrates that device performance can be degraded by the removal of the growth substrate, but, through passivation of the newly exposed surface, that device performance comparable to that of on-wafer devices can be achieved [6]. Most significantly, device performance can actually be improved with respect to on-wafer performance through careful design of the thin film device [7].

The system performance of these thin film integrated devices is potentially excellent since the circuits and photonic devices are independently optimized. In fact, the thin film devices can be bonded to any relatively smooth host substrate without any crystallinity or lattice matching restrictions, thereby enabling use of optimal materials as determined by the application. High performance is also anticipated through the use of standard deposited metal interconnections between the thin film integrated photonic device and the circuit. This quasi-monolithic approach eliminates the wirebonds used in hybrid packages which may ultimately limit system performance.

This type of thin film integrated system is also low cost through the use of standard foundry circuits and standard microelectronics processing techniques for the formation and integration of the thin film devices. Since the thin film device formation and the integrated circuit fabrication are separated and can be pretested for known good die before integration, yields are also increased, thereby further reducing cost.

The integration of thin film compound semiconductor devices in the InP/InGaAsP system also enables the three dimensional vertical optical interconnection of layers of electronic processing devices, a development which addresses the input/output and interconnection bottlenecks in integrated circuits [8]. A three dimensional integrated circuit hardware scheme which utilizes massively parallel processing will be presented. In this scheme, layers of signal processing circuitry are vertically connected using optical signals which pass through the circuitry wafers. This three dimensional integration vertical optical hardware has been demonstrated using thin film InGaAsP optical emitters and detectors integrated onto silicon. These optical devices emit and detect at wavelengths to which silicon is transparent, enabling through-silicon wafer optical interconnect. This demonstration and the systems performance will be presented.

Applications of the integration of thin film compound semiconductor devices will be presented. These applications include communications receivers, three dimensionally locally interconnected neural networks, and image processing hardware.

- [1] E. Yablonovitch, T. Gmitter, J.P. Harbison, and R. Bhatt, "Extreme Selectivity in the Liftoff of Epitaxial GaAs Films," *Appl. Phys. Lett.*, vol. 51, pp. 2222-2224, 1987.
- [2] C. Camperi-Ginestet, M. Hargis, N.M. Jokerst, and M. Allen, "Alignable Epitaxial Liftoff of GaAs Materials with Selective Deposition Using Polyimide Diaphragms," *IEEE Photon. Techn. Lett.*, vol. 3, pp. 1123-1126, 1991.
- [3] J. F. Klem, E. D. Jones, D. R. Myers, and J. A. Lott, "Characterization of thin AlGaAs/InGaAs/AlGaAs Quantum Well Structures Bonded Directly onto SiO<sub>2</sub>/Si and Glass Substrates," *J. Appl. Phys.*, Vol. 66, pp. 459-462, 1989.
- [4] W. K. Chan, A. Yi-Yan, T. J. Gmitter, "Grafted Semiconductor Optoelectronics," *IEEE J. Quantum Electron.*, Vol 27, pp. 717-725, 1991.
- [5] G. Augustine, N. M. Jokerst, and A. Rohatgi, "Single Crystal Thin Film InP: Fabrication and Absorption Measurements," *Appl. Phys. Lett.*, Vol. 61, pp. 1429-1431, 1992.
- [6] M. C. Hargis, J. S. Brown, and N. M. Jokerst, "Epitaxial Lift-Off Thin Film GaAs Metal-Semiconductor-Metal Photodetectors with Back Passivation," IEEE LEOS Annual Meeting, Baltimore, 1992.
- [7] C. Camperi-Ginestet and N. M. Jokerst, "Thin Film Resonant Cavity Enhanced Photodetectors," IEEE LEOS Summer Topical Meeting on Hybrid Optoelectronic Integration and Packaging, Santa Barbara, 1993.
- [8] K.H. Calhoun, C. Camperi-Ginestet, N.M. Jokerst, "Vertical Optical Communication Through Stacked Silicon Wafers Using Hybrid Monolithic Thin Film InGaAsP Emitters and Detectors," *IEEE Phot. Tech. Lett.*, Feb. 1993.

**DEMONSTRATION of GaAs LEDs on Si CHIPS USING EPITAXIAL LIFTOFF**

**Ali Ersen, Eli Yablonovitch, Itzhak Schnitzer, Vincent Arbet-Engels**  
Electrical Engineering Department, University of California, Los Angeles  
Los Angeles, CA 90024-159410

**Tom Gmitter**  
Bell Communications Research, 331 Newman Springs Road  
Red Bank, New Jersey 07701

**INTRODUCTION**

In this paper we report the integration of GaAs LEDs and Si circuits with very high yields (99.9%). This integration is possible based on a new technique called Epitaxial Lift-off (ELO). This technique relies on the fact that a thin film of GaAs can be detached from its substrate and then attached on the top of a Si chip. Films as large as 5 cm by 1 cm showed no cracks and dislocations after they had been transferred on Si circuits by ELO. LEDs made of these films had no performance degradation compared to those that had not been lifted off. On the contrary, efficiency enhancements up to 36 times have been observed on reflective surfaces [1].

The major advantage of ELO is that Si circuits and GaAs LEDs can be optimized separately and then brought together without effecting the yield and the performance. It is a more reliable method than other monolithic integration techniques such as growth of GaAs on Si by MBE where material defects are still a major consideration. We believe that this integration technique is an important achievement towards the fabrication of reliable optoelectronic integrated circuits (OEICs).

**EXPERIMENTS**

The details of ELO process can be found in Reference 2. The process involves the detachment of a GaAs heterostructure from its substrate by removing a sacrificial layer between the substrate and the heterostructure. This thin film is then transferred on to a different substrate that is covered with Pd. An excellent bond can be obtained as GaAs forms an alloy with Pd ( $\text{Pd}_3\text{GaAs}$ ). Pd is also a good thermal conductor and it makes a good ohmic contact to GaAs.

The most critical issue in achieving a good bond is the surface smoothness on which the film will be bonded. A typical Si chip has up to 3  $\mu\text{m}$  steps with a largely varying spatial frequency. Therefore, it is essential to develop a general planarization technique that is independent of the topography of the underlying layer. Two different techniques have been developed to realize the planarization: plasma etch back (PEB) and chem-mechanical polishing. In PEB, a thick layer of polyimide and photoresist is spun on the sample and then etched back in a plasma system until a planar surface is obtained. The same goal can be achieved by depositing a thick layer of oxide and then removing it by chem-mechanical polishing. At the moment, chem-mechanical polishing seems to be the more promising approach as higher yields have been obtained using this technique. Also, chem-mechanical polishing has become a standard technique in multilevel metal systems of IC production. Polishing process would not be a bottleneck in the fabrication of OEICs as machines with a throughput of 50 wafers/hour have already become commercially available.

After the planarization, Pd is deposited on samples and the lifted-off film is transferred on to the Si substrate. The adhesion of the film is strong enough to go through a five step lithographic process that is necessary to finish the fabrication of GaAs LEDs and to make electrical contact between Si circuits and GaAs LEDs. In a typical experiment, more than 99.9% of LEDs survive this five step fabrication process.

Figure 1 shows the micrograph of a five inch silicon device wafer with two different size GaAs films bonded on to it. The GaAs films contain a heterostructure and can be further processed to make LEDs. We have integrated an 8 by 4 array of GaAs LEDs with silicon driver circuits

using these planarization techniques. Performance results of these LEDs and yield studies will be presented at the conference.

**REFERENCE:**

1. I. Schnitzer, E. Yablonovitch, C. Caneau, A. Ersen, T. J. Gmitter, presented at LEOS Summer Topical Meeting on Integrated Optoelectronics 1992.
2. E. Yablonovitch, T. Sands, D. M. Hwang, I. Schnitzer, T. J. Gmitter, Appl. Phys. Lett., Vol. 59, No. 24, 9 December 1991.

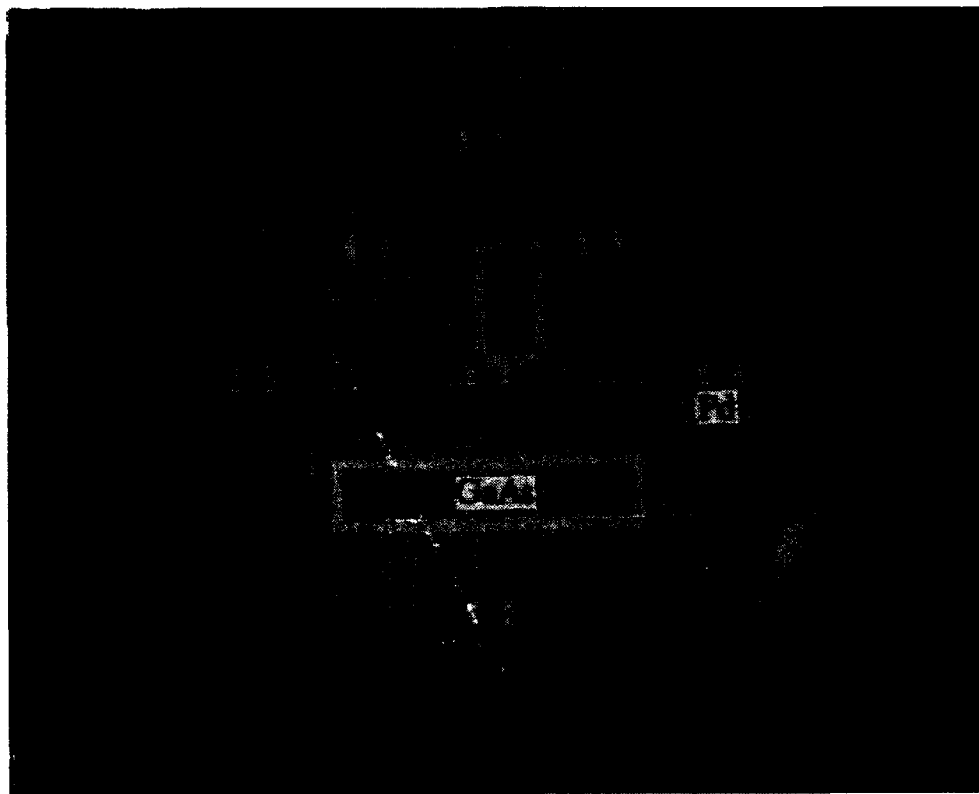


Figure 1. The micrograph of the GaAs films that have been bonded on a silicon wafer that contains electronic circuitry. A thick layer of oxide was deposited on the silicon wafer which was then planarized by chem-mechanical polishing. Each piece of GaAs film is sitting on a Pd pad.

### 30% EXTERNAL QUANTUM EFFICIENCY FROM SURFACE TEXTURED, THIN-FILM LIGHT-EMITTING-DIODE ARRAYS

I. Schnitzer, E. Yablonovitch, A. Ersen, A. Scherer,<sup>†</sup> C. Caneau,<sup>††</sup> and T. J. Gmitter<sup>††</sup>

*The Department of Electrical Engineering, UCLA, 405 Hilgard Ave., Los Angeles, CA 90024-1594*

<sup>†</sup> Caltech, Pasadena, CA 91125, <sup>††</sup> Bellcore, 331 Newman Springs Rd., Red Bank, NJ 07701-7040

High efficiency light-emitting-diodes (LED's) are desired for many applications such as displays, printers, short-haul communication, and opto-electronic computer interconnects. However, there is an enormous gap between the theoretical efficiency of LED's and their actual efficiency. The internal quantum yield,  $\eta$ , of good quality double heterostructures can exceed 99%, as we have demonstrated recently.<sup>1</sup> On the other hand run-of-the-mill commercial LED's are usually only a few percent efficient. The reason for this long-standing shortfall is the difficulty for light to escape from high refractive index semiconductor. A mere 2% of the internally generated light is coupled into free space through the 16° escape cone, the rest suffering total internal reflection and risking re-absorption. The present commercial state-of-the-art, ~20% external efficiency in AlGaAs-based LED's, is achieved by growing a thick transparent semiconductor superstrate, and total substrate removal in a particularly clean, low-loss, optical design which can add greatly to the cost.

The key to increasing the escape probability is to give the photons multiple opportunities to find the escape cone. This requires angular randomization or scrambling of the light rays. One way to do this is by photon high self-absorption, and a very clean, non-dissipative optical design. In ref. 1 (see Fig. 1a) we used the epitaxial liftoff (ELO) technique<sup>2</sup> to mount thin film heterostructures on high reflectivity surfaces. It was found that while the photon re-cycling can yield an ultrahigh external quantum efficiency (72%), it is very susceptible to parasitic loss mechanisms (free carrier absorption in doped layers, for example) or slight degradation in the internal quantum efficiency. A more practical approach, and the one which we propose here is the angular randomization by elastic scattering of the photons from a textured semiconductor surface.

Our approach has two components: i) Separation of thin-film heterojunctions from the growth substrate using the ELO technique, and ii) Nano-texturing of the thin-film semiconductor interface by natural lithography.<sup>3</sup> The implementation of these two components leads to a thin film ( $<1\mu\text{m}$ ) geometry shown in Fig. 1b. This geometry employs the statistical mechanical concept of phase-space filling by angular randomization. We invoke a statistical approach<sup>4</sup> to model the planar and textured film geometries. It is concluded that the textured film geometry can boost the external efficiency to 50% or more, while relieving the demand for the utmost material quality, high self-absorption, and low parasitic losses, as required by the planar film geometry of Ref. 1 (Fig. 1a).

The actual LED structure is a conventional  $n^+$ -AlGaAs/p-GaAs/ $p^+$ -AlGaAs double heterostructure, grown over a  $0.05\mu\text{m}$  thick AlAs release layer by organo-metallic chemical vapor deposition. The LED structure is shown in Fig 2. We have used the concept of current crowding to eliminate parasitic light absorption at the electrodes, a significant problem in all LED's. Edge passivation, another common problem in low injection photonics, is effectively achieved by the diffusion barrier to the exposed step as shown in Fig. 2. Texturing of the light emitting region is the final processing step, following device fabrication, testing, ELO, and Van der Waals bonding by surface tension forces onto dielectric coated Au mirrors. The surface of the LED is coated by a randomly close-packed array of polystyrene spheres,  $0.2\mu\text{m}$  diameter, using the surface forces between the charged spheres and the semiconductor, as shown in Fig. 3. The spheres then act as an etch mask for a  $\text{Cl}_2$  assisted  $\text{Xe}^+$  ion beam etching, about  $0.17\mu\text{m}$  deep.

The light versus current characteristics of these LED's have been measured and modeled (see Fig. 4). We have observed 9% external quantum efficiency from untextured LED's array transforming into 30% external quantum efficiency following the surface texturing treatment. We conclude that by employing the principle of phase-space-filling in an improved device geometry, 56% efficient LED's arrays can be expected. Such LED's are simpler and more reliable than lasers. Unlike lasers they are thresholdless, yet they offer comparable external efficiency. Moreover, the principles and the device geometry that we are proposing can be applied to other semiconductor material systems to obtain very bright visible thin film, top processed, LED's arrays as well. It is clear that the availability of 30%-50% efficient, low-cost, reliable, visible LED's would change dramatically the appearance of our homes, offices, and streets.

1. I. Schnitzer, E. Yablonovitch, C. Caneau, and T. J. Gmitter, *Appl. Phys. Lett.* **62**, 131 (1993).
2. E. Yablonovitch, T. J. Gmitter, J. P. Harbison, and R. Bhat, *Appl. Phys. Lett.* **51**, 2222 (1987).
3. H. W. Deckman and J. H. Dunsmuir, *Appl. Phys. Lett.* **41**, 377 (1982).
4. E. Yablonovitch, *J. Opt. Soc. Am.* **72**, 899 (1982).

Figure 1: Typical photon trajectory in the thin epi-lift-off heterostructure: *a.* In the smooth structure the photons trajectories are randomized by the self-absorption/re-emission events, represented by dots. *b.* In the textured film, angular randomization is achieved by strong surface scattering.

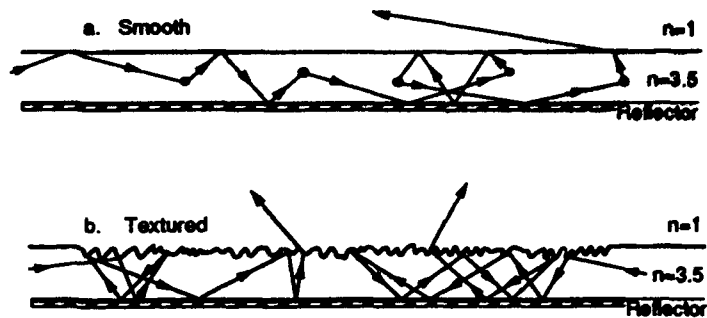


Figure 2: Schematic cross section of an epi-lift-off, textured LED, Van der Waals bonded onto an  $\text{SiO}_2$  coated metallic reflector. The spatial distribution of injection current is represented by the curve on the graph  $j(x)$  versus  $x$ . Current crowding is obtained due to the different conductivity of the  $n^+$  and  $p^+$  contact layers, in order to minimize absorption losses at the metallic electrodes. The width of the textured area is about 50 times the film thickness.

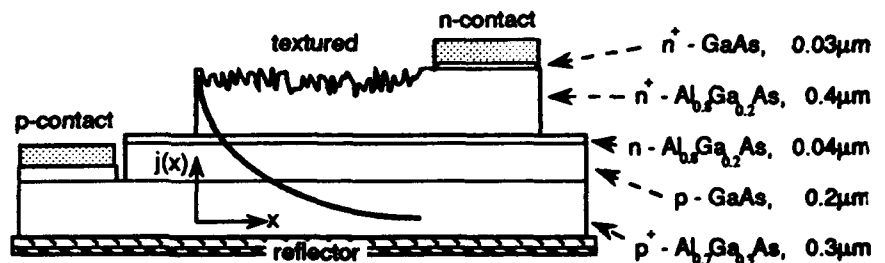


Figure 3: Natural Lithography - Polystyrene spheres, 0.2  $\mu\text{m}$  diameter, coat the surface of the LED in a randomly close-packed array. The spheres then act as an etch mask for a  $\text{Cl}_2$  assisted  $\text{Xe}^+$  ion beam etching, about 0.17  $\mu\text{m}$  deep. The spheres can be easily washed away to leave a clean high refractive index textured surface which enhances the outcoupling of light.

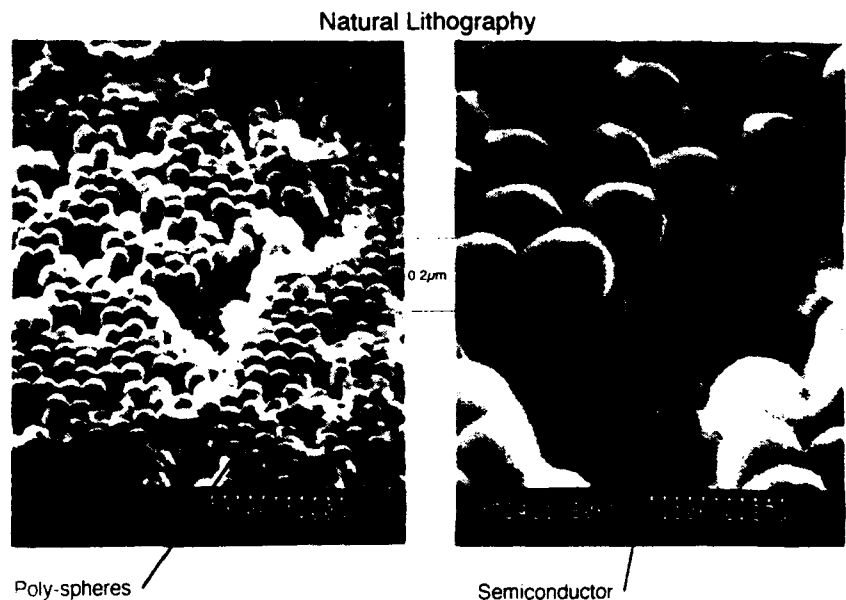
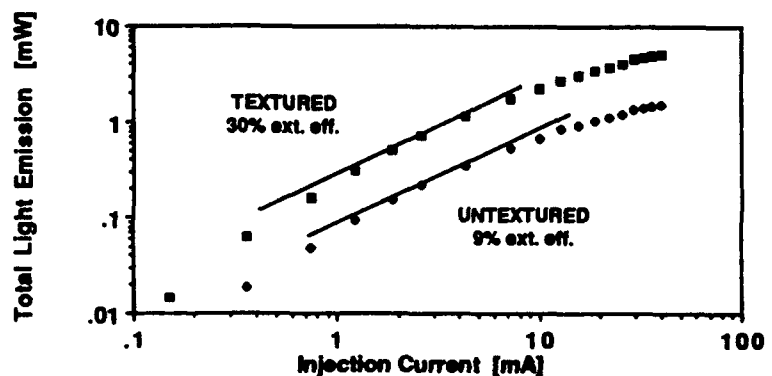


Figure 4: Log-Log plot of the measured total light output versus injection current, for typical textured and untextured (smooth) LED's, as indicated. The linear fits have slopes 1, and their intercepts suggest the indicated external quantum efficiency.



**Liquid Flux Assisted Bump Bonding Process and Thermal Design for Laser Arrays for Optical Interconnection<sup>1</sup>**

**Yiu Man Wong, Howard Chen<sup>+</sup>, Dean Kossives<sup>+</sup>, Fred Warning, C.J. Doherty<sup>+</sup>, T. Mullally, Linda J. Anthony<sup>+</sup>, Maureen Lau<sup>+</sup>, R. Frye<sup>+</sup>**

**AT&T Bell Laboratories, 9999 Hamilton Blvd, Breinigsville, PA 18031**

**<sup>+</sup>AT&T Bell Laboratories, 600 Mountain Ave, P.O. Box, Murray Hill, NJ 07974**

Recently, there have been intense industrial efforts in parallel optical interconnection technology<sup>2</sup> to overcome the well known copper barrier problems in high speed (~ 1 Gb/sec) data communication and processing networks of multi-processor systems. A 18x1 edge-emitting uncooled InP laser array<sup>3</sup> (Figure 1) and a 32x1 surface emitting laser array<sup>4</sup> are bump bonded to silicon optical bench piece with the help of liquid flux solder reflow process. Effects of liquid flux on some device characteristics are presented in Table 1 a and b.

Since the possibility of halide contamination from the use of liquid flux is a major reliability concern in III-V semiconductors, capillary zone electrophoresis measurements were taken. The results reveal that the F, Br, and Cl ions concentration are a few parts per million (when Figure 2 is compared with that from a controlled sample).

Degrees of self-alignment of laser arrays to silicon parts and factors affecting the results will be discussed. Present work indicates that ~ 2  $\mu\text{m}$  perpendicular to the optical beam (lateral) can be achieved. Such low cost passive alignment is thus sufficient for the present system design of laser to multi-mode fiber arrays.

Since InP laser operation and median lifetime are extremely temperature sensitive, a thermal design study is conducted using finite element analysis and robust design methodology. the mean thermal resistances for various design parameters are given (see Table 2). Tradeoffs among solder material, bonding process, physical, and thermal designs will be briefly discussed.

---

<sup>1</sup>Paper submitted to LEOS Summer Topical Meeting on Hybrid Optoelectronic Integration and Packaging, July 26-28, 1993.

<sup>2</sup>John D. Crow, "Optical Interconnects Speed Interprocessor Nets," IEEE Circuits and Devices, 7, 20 (1991); and objectives of Optoelectronic Technology Consortium, (OETC).

<sup>3</sup>R.A. Nordin et. al, "A System Perspective on Digital Interconnection Technology," J. Lightwave Tech. 10, 811 (1992).

<sup>4</sup>R.A. Morgan, "Uniform 64x1 arrays of individually addressed vertical cavity top surface emitting laser." Elect.Lett., 27, 1400 (1991).

Table 1a: Test Results Before/After Liquid Flux Reflow; InP EEL

Run #	Ith(mA)	L(mW) @100 mA	R(W)	Vth(V)
1	26.4	12.03	3.07	1.05
	23.6	13.26	3.44	1.06
2	25.3	12.34	3.11	1.05
	22.1	14.00	3.50	1.05
3	28.1	12.05	4.28	1.10
	25.0	13.17	4.64	1.11
4	31.9	11.36	3.82	1.10
	27.5	13.14	4.22	1.11
5	35.4	11.67	3.63	1.12
	29.6	12.80	3.98	1.12

Table 1b: Test Results Before/After Liquid Flux Reflow; GaAs SEL

Run #	Ith(mA)	Lp(mW)	R( $\Omega$ )	Vth(V)
1	4.02	2.73	400.00	3.61
	3.55	2.73	415.00	3.37
2	3.97	2.77	415.00	3.60
	3.76	2.77	429.50	3.50
3	4.05	2.72	400.50	3.61
	3.98	2.71	415.00	3.57
4	4.20	3.02	405.50	3.62
	3.96	3.06	435.50	3.54
5	4.17	3.01	409.50	3.70
	3.78	3.04	410.00	3.50
6	4.71	1.51	379.50	3.91
	4.53	1.50	370.50	3.77

Table 3b: Sensitivity Table

Parameter	Setting ( $\mu\text{m}$ )	$R_{th}$ (W/cm <sup>2</sup> °K) Mean	% MS
Oxide Thickness: $T_{ox}$	0	113.69*	74.6
	1	160.02	
	2	203.86	
Solder Width: $W_s$	40	182.39	20.1
	60	159.57	
	120	135.62*	
Solder Thickness: $T_s$	3	152.69	5.3
	6	151.76*	
	12	173.12	

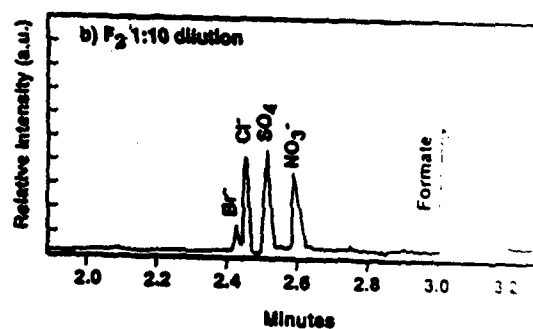
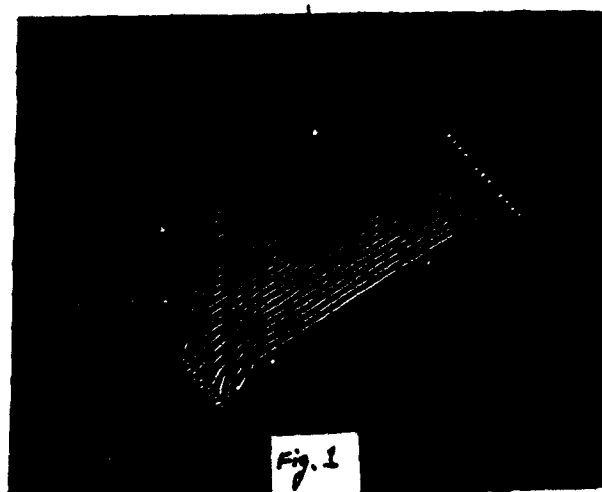


Figure 2

**Tuesday, July 27, 1993**

**Sessions:**

**T1: Guided Waves II**

**T2: Free Space II**

**T3: Hybrid Integration III**

**T4: Hybrid Integration IV**



**T1.1 8:50am - 9:20am  
(Invited)**

## **Rapid Prototyping of Photonic Integrated Circuits**

R. Scarmozzino, L. Eldada, I. Ilic, D.S. Levy, M. Levy, and R.M. Osgood, Jr.

*Microelectronics Sciences Laboratories  
Columbia University  
New York, NY 10027*

Photonic integrated circuits, including those to be used in optical packaging, offer important cost and environmental advantages over circuits composed of discrete components. However, the design and fabrication of complex, large-area optical waveguide circuits is severely limited by the lack of computerized tools for design, production, and testing. In this paper, we will describe our work at Columbia in developing a laser prototyping system, in conjunction with computer simulation, to design, fabricate, and test novel waveguide circuits. The system is also useful for manufacturing small-run circuit designs. A schematic of the main apparatus is shown in Fig. 1.

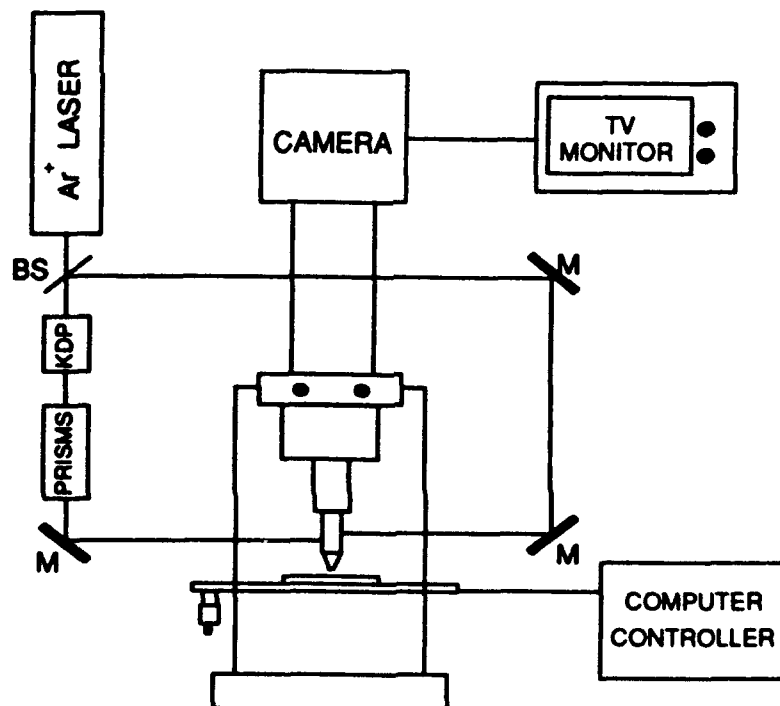


**Figure 1 Schematic of Laser Prototyping System**

The fundamental technique uses a laser-induced photoelectrochemical process for etching GaAs and other III-V compounds.<sup>1</sup> This process uses a focused laser beam to form grooves in GaAs/AlGaAs heterostructures in order to define waveguiding regions.<sup>2</sup> The technique is

maskless and discretionary. The computer-controlled apparatus can be programmed with any desired circuit pattern, and prototype waveguide circuits can be produced within a day. The waveguides and passive components produced with this technique include linear waveguides, tapered waveguides, straight and curved bends, Y-branches, asymmetric splitters, directional couplers, and optical delay lines. These passive devices are single-mode and low-loss (*e.g.*  $\sim 0.5$ - $1.0$  dB/cm for straight waveguides).<sup>2</sup> The suitability of this technique for exploring new device designs has been demonstrated by its use in the development of the first channel dropping filter<sup>3</sup> as proposed by Haus.<sup>4</sup> The technique also has the ability to vary the effective index of refraction along the device by grading the etch depth - something that is not possible using conventional processing technology - and this can be used in novel device structures.<sup>5</sup>

In addition to passive devices, we have recently shown that active switching components can be prototyped by combined passive structures with laser-patterned metal electrodes. These electrodes are produced masklessly using standard metal deposition techniques coupled with laser-patterning of photoresist.<sup>6</sup> In addition, metal can be deposited directly using laser-patterned selective metallorganic CVD.<sup>7</sup> The above techniques have been used to produce and test several optical amplitude modulator designs including polarization modulators with and without on-chip polarizers, and a Mach-Zehnder interferometric amplitude modulator. The novel designs used exhibit unusually low voltage-length products with excellent performance characteristics (*e.g.* extinction ratios up to 17 dB and switching voltages as low as 3-4 V).

In summary, we have developed an advanced technology for rapid prototyping of photonic integrated circuits, and have employed it in the demonstration of several new and novel photonic devices.

This work was supported by the Air Force Office of Scientific Research / Defense Advanced Research Projects Agency and the National Center for Integrated Photonic Technology.

## References

1. M.N. Ruberto, X. Zhang, R. Scarmozzino, A.E. Willner, D.V. Podlesnik, and R.M. Osgood, Jr., *J. Electrochem. Soc.* **138**, 1174 (1991).
2. L. Eldada, M.N. Ruberto, R. Scarmozzino, M. Levy, and R.M. Osgood, Jr., *J. Lightwave Technol.* **10**, 1610 (1992).
3. M. Levy, L. Eldada, R. Scarmozzino, R.M. Osgood, Jr., P.S.D. Lin, and F. Tong, *Photonics Technol. Lett.* **4**, 1378 (1992).
4. H.A. Haus and Y. Lai, *J. Lightwave Technol.* **10**, 57 (1992).
5. M.N. Ruberto, R. Scarmozzino, A.E. Willner, D.V. Podlesnik, and R.M. Osgood, Jr., *SPIE Proc.* **1215**, 538 (1990).
6. L. Eldada, M.N. Ruberto, R. Scarmozzino, M. Levy, G. Scelsi, and R.M. Osgood, Jr., in *Integrated Photonics Research*, Vol. 10, OSA Technical Digest Series, (Optical Society of America, Washington, DC 1992), pp. 336-337.
7. N. Zhu, T. Cacouris, R. Scarmozzino, and R.M. Osgood, Jr., *J. Vac. Sci. Tech. B* **10**, 1167 (1992).

## **DISPENSED DUAL-POLYMER WAVEGUIDES IN SILICON V-GROOVES**

**R. Narendra, J.N. McMullin, B.P. Keyworth and R.I. MacDonald**  
Telecommunications Research Laboratories (TRLabs)  
#800, 10611-98 Ave., Edmonton, Alberta, CANADA, T5K 2P7

### **Abstract**

Waveguides with losses lower than 0.2 dB/cm have been fabricated in silicon v-grooves using a computer-controlled dispensing system. The polymer cladding isolates the waveguide core from any wall roughness which occurs in the etching process.

### **Introduction**

Optical interconnections have been proposed to overcome bandwidth and fanout problems encountered in the development of high speed monolithic and hybrid integrated systems [1]. Polymer waveguides in silicon v-grooves with micromachined reflective taps were previously reported [2] and had losses in the range 0.7-1.0 dB/cm caused primarily by imperfections induced in the fabrication process. We report a simple new method for making polymer waveguides in silicon channels that reduces this loss and which still remains compatible with the micromachining of reflective taps. This procedure should be applicable in channels formed in any substrate by any etching process.

### **Waveguide Fabrication and Loss Measurement**

V-grooves 135  $\mu\text{m}$  in width and 95.5  $\mu\text{m}$  in depth were formed in <100> silicon wafers by anisotropic etching in a solution of ethylene diamine pyracatechol. A cladding layer of Norland-68 optical adhesive ( $n=1.54$ ) was directly dispensed into the v-groove using a hypodermic syringe mounted on computer-controlled xyz micropositioners. The 150  $\mu\text{m}$  stainless steel syringe needle was narrowed to fit inside the groove to aid in self-alignment during movement. The amount of dispensed polymer was controlled so that the walls were wetted but a deep meniscus remained which was smooth due to surface tension. After curing for 10 minutes in UV light, Norland-81 optical adhesive ( $n=1.56$ ), was similarly dispensed into the meniscus and cured for 10 minutes. Fig. 1 shows a microphotograph of the cross-section of the formed dual-polymer waveguide. The outline of the eye-shaped core is clearly visible.

The waveguide loss at 633 nm was measured by capturing the sidescattered light with a large area photodetector. A typical result of the intensity in dB (arbitrary zero) versus distance along the waveguide is shown in Fig. 2. The large peak near 21 mm is due to the reflection of the guided light from the uncoated end-facet of the v-groove. The waveguide loss of approximately 0.2 dB/cm between 1 and 20 mm was determined by linear regression. Neglecting the first few points in the coupling region on the left, the loss is closer to 0.1 dB/cm.

### **Discussion**

The fabrication technique described above is simple, quick, repeatable and amenable to mass production. The measured loss of 0.2 dB/cm at 0.633  $\mu\text{m}$  is comparable to that of glass v-groove waveguides [3] and other reported integrated optical waveguides. Furthermore, this technique should allow bends and splitters to be formed in anisotropically etched waveguides since the wall roughness will be smoothed by the surface tension of the dispensed cladding.

## References

- (1) L.D. Hutchenson and P. Haugen, "Optical interconnections replace hardwire", IEEE Spectrum, March 1987, pp. 30-35.
- (2) S. Kumar, R.I. MacDonald and J.N. McMullin, "Low-loss multimode polymer waveguides with serial out-of-plane taps", Optical Fiber Communication Conference, FA8, San Jose, Calif., February 2-7, 1992.
- (3) R. Narendra and J.N. McMullin, "Single-Mode, Phosphorus-doped silica waveguides in silicon V-grooves", Photonics Technology Letters, Vol. 5, No. 1, January 1993, pp. 43-46.



Fig. 1. Scanning electron microphotograph of the dual-polymer waveguide.  
( $n=1.54$  Norland-68 cladding,  $n=1.56$  Norland-81 core)

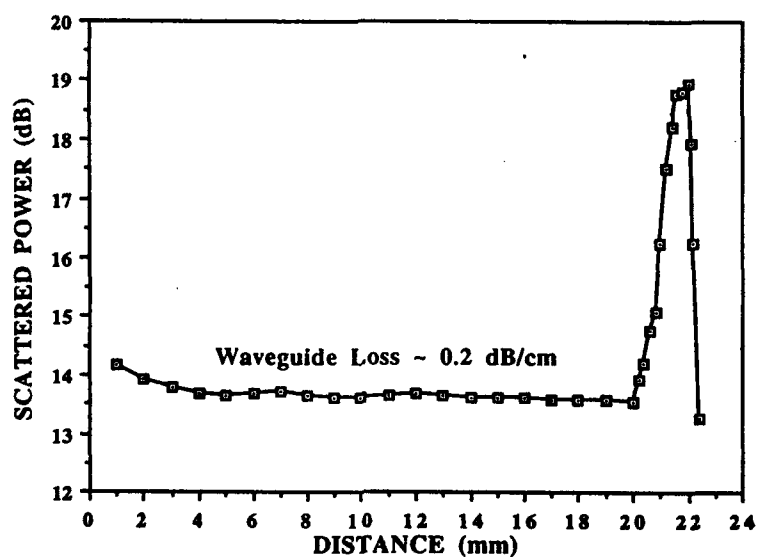


Fig. 2. Sidescattered power from the dual-polymer waveguide

## DIRECT DISPENSING OF POLYMER WAVEGUIDES ON SILICON SUBSTRATES

B.P. Keyworth, R. Narendra, J.N. McMullin, R.I. MacDonald  
Telecommunications Research Laboratories  
Suite 800, 10611 - 98th Ave, Edmonton, Alberta, T5K 2P7

**Abstract:** *An extremely simple, low-cost technique is described for fabrication of multimode optical waveguides for signal distribution in hybrid OEIC's. Results obtained for a 1-to-4 optical splitter are reported.*

**Introduction:** Due to the complexities of monolithic integration of optoelectronic devices, and given the relatively immature state of the technology, hybrid integration is likely to be of interest for some time. Multimode waveguides are suitable for signal routing and distribution in hybrid integrated systems and moderate propagation losses can be tolerated since path lengths are short. Clearly, a simple, inexpensive, and repeatable technique for fabricating these waveguides would have considerable impact.

Previous work has demonstrated both single-mode [1] and multimode [2] waveguides in silicon V-grooves which are formed by anisotropic etching. This technique offers the advantages of micromachined taps for out-of-plane coupling, and alignment grooves for fiber attachment. However, the use of crystallographic planes for definition of the V-grooves imposes a preferred direction. Waveguides formed on planar substrates offer increased flexibility and simplicity. We describe here a process for directly dispensing multimode polymer waveguides onto a planar substrate.

**Results:** The technique uses a computer controlled liquid dispensing system to deposit a UV curable polymer directly onto an oxidized silicon substrate. A 4  $\mu\text{m}$ -thick silicon dioxide layer ( $n=1.46$ ) is first deposited by CVD to act as the lower cladding layer for the waveguides. The polymer used is Norland 68 optical adhesive, which has a refractive index of 1.54 and cures with low shrinkage when exposed to ultraviolet light. The liquid is dispensed through a 160  $\mu\text{m}$ -inner-diameter syringe which has been narrowed to approximately 50  $\mu\text{m}$  width. The substrate is positioned relative to the syringe by an XYZ micropositioning system which is also computer controlled. A variety of waveguide geometries have been programmed, including straight sections, S-bends, and splitters. A schematic layout of a 1-to-2 splitter is shown in Figure 1. A 1-to-8 splitter is implemented by an automated sequence requiring approximately 5 minutes to complete. Allowing 10 minutes for UV curing, this results in a turn-around time of 15 minutes for this type of device (neglecting preparation time of oxidized substrate).

The volume of polymer dispensed, and hence the width of the waveguide, is controlled through a combination of translation speed and pressure in the dispenser. We have achieved waveguide widths of less than 100  $\mu\text{m}$  with excellent uniformity over several centimeters of length. The propagation losses were determined by measuring the light scattered from the surface of the waveguide while illuminated by a HeNe laser source. The beam was first launched into a 50/125  $\mu\text{m}$  step-index fiber which was then coupled to the waveguide. The ends of the waveguide were cleaved to form end facets. A 1mm-diameter plastic pick-up fiber was used to sample the scattered intensity along the length of the straight waveguide section. Results are illustrated in Figure 2.

Three distinct slopes of -2.2 dB/cm, -1 dB/cm, and -0.44 dB/cm can be seen. The steep slope over the first few millimeters is caused by light scattering off the input facet. The slope of -1 dB/cm observed over the next centimeter is believed to be due to light coupled into radiation modes which are quickly stripped off. The waveguide losses then settle down to a low value of -0.44 dB/cm which is in good agreement with that reported by other groups using similar materials [3]. Figure 3 shows the scattered intensity near the first Y-split in a 1-to-4 splitter formed by direct dispensing. The strong radiation observed near the center of the junction (which has been clipped for clarity) is due to light radiating from the split.

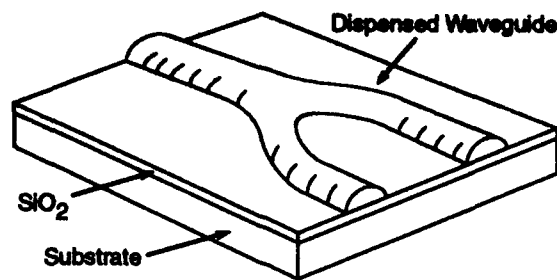


Fig. 1 Layout of a 1-to-2 splitter

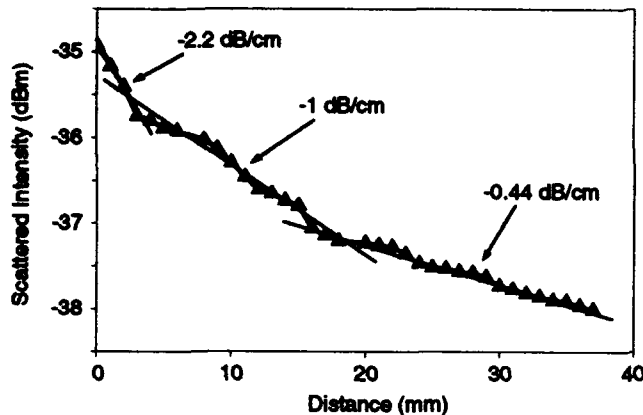


Fig. 2 Propagation losses in various regions along a straight section of waveguide as determined by scattered light intensity.

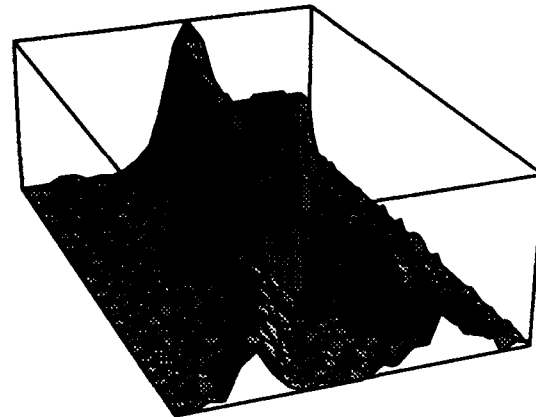


Fig. 3 Scattered intensity near Y-junction. Clipped portion near center of the splitter is due to strong radiation from the junction.

With 2 mW of incident power from the multimode input fiber, the output powers exiting the four waveguides of the 1-to-4 splitter were 47, 50, 35, and 53  $\mu$ W. This corresponds to a total excess loss of approximately 10 dB, of which 2 dB can be attributed to propagation losses in the 4 cm-long structure. Of the remaining 8 dB; 3 dB was found to result from coupling loss, 2 dB was due to the first splitter, and 3 dB was due to the second stage of splitters. The coupling loss was determined by cleaving off the curved input section of the splitter and measuring the throughput of this section only. The excess loss from each splitter was estimated from the scattered intensity before and after the split. The powers measured from the four output ports differ by less than 2 dB, with 3 of the 4 being within 0.5 dB.

**Conclusions:** We have demonstrated the viability of an extremely simple, low-cost fabrication method for optical interconnects. The polymer waveguides are formed directly on the surface of a planar substrate without the use of preforms or etching. Propagation losses were found to be adequate for the lengths available on a standard wafer. Relatively high coupling loss and excess splitting loss was observed. The former could be improved by directly attaching the dispensed waveguide to the input fiber while the latter could be reduced by optimizing the split angle.

**Acknowledgments:** This research was supported by a grant from the Canadian Institute for Telecommunications Research under the NCE program of the Government of Canada. Support from Alberta Microelectronics Center is also acknowledged.

## References

1. S. Kumar, R.I. MacDonald, J.N. McMullin, Dig. of Conf. on Optical Fiber Communications, OSA Tech. Dig., vol. 5, 1992, p.267
2. R. Narendra, J.N. McMullin, *IEEE Phot. Tech. Lett.*, vol. 5 (1), 1993, pp.43-46
3. R.R. Krchnavek, G.R. Lalk, D.H. Hartman, *J. Appl. Phys.*, vol. 66, 1989, pp.5156-5160

**T2.1 10:30am - 11:00am  
(Invited)**

**Prototype Optically Interconnected Multichip Module with Holographic Optical Interconnects**

Michael R. Feldman  
Assistant Professor  
Electrical Engineering Department  
University of North Carolina at Charlotte  
Charlotte, NC 28223

The development of a prototype Optical Interconnected Multichip Module (MCM) is currently underway at UNC-Charlotte. The approach is to use optical interconnects within a digital multichip module for connections that are longer than a certain length (the "break-even line length") [1]. For these connections the optical link will dissipate less power than the corresponding electrical link. One of the main goals of this project is to develop a technology for Optical Interconnects that can be implemented with minimal modification to current devices. We are currently in the process of developing a series of MCM systems. System 1 will be a testbed that will enable testing of hologram encoding techniques, alignment tolerances, optical link efficiency, and thermal properties. System 2 will use the knowledge gained in the development of system 1 to build a small

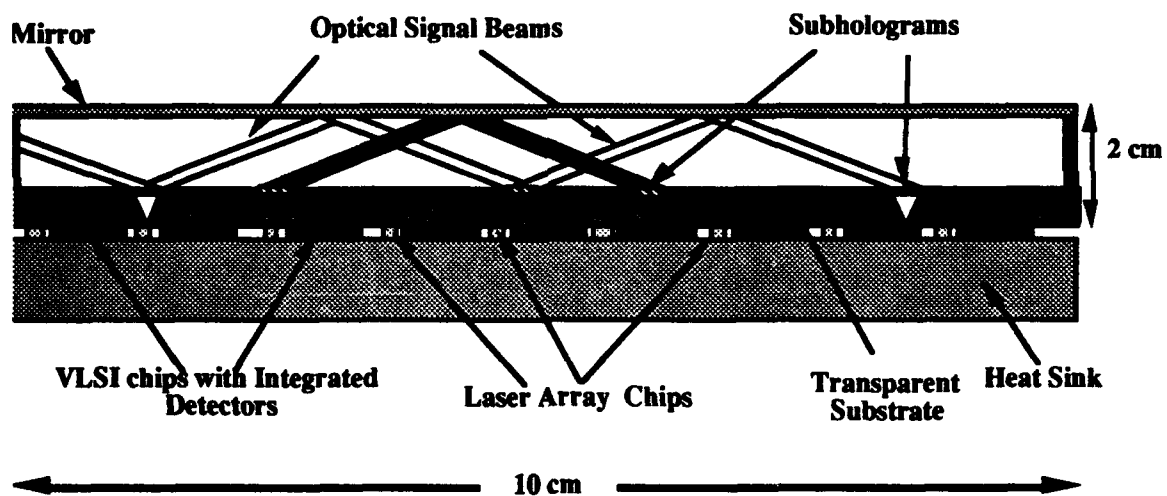


Figure 1. Optical Interconnected MCM Approach.

functional system to demonstrate the technology.

A cross-sectional view of the Optical Interconnected MCM system is shown in figure 1. The MCM is composed of a planar transparent substrate, containing thin film electrical connections. In system 1 this substrate is quartz. All of the devices are flip-chip bonded to one side of the substrate while the holographic optical elements (HOE's) are fabricated on the other side of the substrate. In the ideal system the optical devices (detectors and lasers or modulators) would be integrated directly onto the silicon CMOS chips, in order to reduce the power requirements of the system. If the optical devices are located off-chip then connections to these devices must be made through bonding-pads. At high frequencies the power associated with driving these bonding-pads becomes very significant.

In system 1, detectors are integrated onto the silicon chips. Seperate GaAs laser array chips are bonded near each silicon chip. An optical link is formed between two or more CMOS VLSI chips by activating a laser which propagates a beam of light through the MCM substrate. This beam illuminates a laser sub hologram which directs the beam, through reflection, off of a planar mirror and onto a detector sub hologram. The detector sub hologram focuses the beam through the MCM substrate and onto a photodetector located on the CMOS VLSI chip.

This research has been broken down into four tasks, Photodetectors, Lasers, Computer Generated Holography, and System Integration. The research issues need to be solved in each of these areas and recent progress made toward resolving these issues will be presented.

#### **References**

1. M. R. Feldman, S. C. Esener, C. C. Guest and S. H. Lee, "Comparison between optical and electrical interconnects based on power and speed considerations," Appl. Opt. 27, 1742-1751 (1988).

## Simulation Tools for Free-Space Optical Interconnects Based on Computer-Generated Holograms

J. M. Kahn and J. S. Hoch

Department of Electrical Engineering and Computer Sciences  
University of California, Berkeley, CA 94720

### 1. Introduction

Free-space optical links are a promising, low-latency alternative for chip-to-chip and board-to-board interconnection. Computer-generated holograms (CGHs), acting as specialized lenses, would route and focus light from laser sources to photodetectors. The design of such interconnects will require computer tools to evaluate certain performance metrics. We propose a simulation methodology for free-space systems that makes use of the Rayleigh-Sommerfeld (RS) scalar diffraction formula to model the propagation of light from the CGH to the detector locations. Use of the RS formula allows straightforward computation of diffraction efficiency, spot size, group delay, and crosstalk.

### 2. Simulation Methodology

Due to the large space-bandwidth product of CGHs used for optical interconnection, and in particular those fabricated by electron-beam lithography, it appears impractical to model free-space interconnects through a finite-element solution to Maxwell's equations. A simplification known as scalar diffraction theory is more computationally feasible. Scalar theories ignore the coupling between the electric and magnetic fields, as they only deal with one scalar transverse component of either field; they also reduce to a single integral, where the output field is expressed as a function of the input field within a diffracting aperture.

The Rayleigh-Sommerfeld formula is the most general scalar diffraction theory, and the most valid for modeling of free-space interconnects. It is represented by the following linear time-invariant relationship [1]:

$$U(x_0, y_0) = \frac{1}{j\lambda} \iint_{\Sigma} U(x_1, y_1) \frac{h}{r^2} \exp(jkl) dx_1 dy_1, \quad (1)$$

where  $U(x_0, y_0)$  is the complex value of the field at a point on the observation plane,  $U(x_1, y_1)$  is the value of the field within the aperture,  $h$  is the distance between the observation plane and the aperture,  $l$  is the distance from a point within the aperture to  $(x_0, y_0)$ , and  $k=2\pi/\lambda$ , where  $\lambda$  is the wavelength. The integral is over the entire aperture. The RS formula is valid for  $h \gg \lambda$ , which is not too restrictive for an optical interconnect-

tion. Other scalar diffraction theories, such as the Fresnel and the Fraunhofer formulas, are approximations to (1), and are only valid for larger values of  $h$ . For both of these theories, the minimum required  $h$  may be too large to model a free-space link.

We have constructed a simulation tool that employs the RS formula to investigate the performance of free-space interconnects using single CGHs. No assumptions are made about the environment of the interconnection, whether it be between chips on a multi-chip-module, between boards, or even on a single VLSI. The CGH is assumed to be describable as an array of pixels, where a single complex number denotes the transmittance of each pixel. To date, modeling has focused on surface-relief kinoforms, and no attempt has been made to simulate CGHs encoded with other techniques, such as Arnold's polygon method for tracing fringes [2].

The simulation tool can compute diffraction efficiency to any detector location. The algorithm proceeds by first assuming that the electric field at the input plane of the CGH is an elliptic Gaussian beam from the laser source. The electric field at the output plane of the CGH is the cell-by-cell product of the laser field and the CGH transmittance function. Here the term *cell* refers to a square (no larger than a CGH pixel) within which the spatial variation of the laser electric field is negligible. The RS formula is used to propagate the electric field

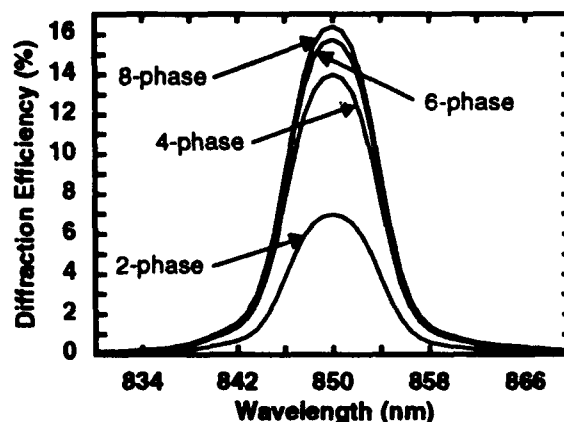


Fig. 1 Diffraction efficiency (to a single detector) versus wavelength for a 2, 4, 6, or 8-phase 4:1 multiplexed kinoform.

from the output plane of the CGH to many points within the detectors. Diffraction efficiency to a single detector is then computed as the ratio of detector power (found by integrating the intensity values over the area of the detector) to laser output power. The computation of spot size is a natural artifact of evaluating the RS formula at many points within the dimensions of the detectors. A measure of crosstalk is achieved during simulation if the diffraction efficiency to undesired locations is computed. The group delay to a single detector is determined by varying the wavelength of the laser radiation, and then noting the change in the phase of the electric field received at the center of the detector.

### 3. Simulation of Four-Way Interconnect

Using the simulation tool previously mentioned, we have performed an extensive study of a hypothetical free-space interconnect that images a single laser to four photodetectors. Considering both faceted and multiplexed CGHs, we evaluated the reduction in diffraction efficiency due to mechanical misalignment, laser wavelength inaccuracies, and errors in kinoform quantization levels, and we quantified variation of group delay with wavelength.

The transmittance function of each section of the four-faceted kinoform, prior to sampling and quantization, was assumed to be similar to a Fresnel zone-plate, with a phase function given by:

$$\left( kz - \eta(z) + \frac{kx^2}{2R_x(z)} + \frac{ky^2}{2R_y(z)} \right) + kr_d(x, y), \quad (2)$$

where the first term in parenthesis corresponds to the elliptic Gaussian beam, and the second term corresponds to a spherical wave converging to one of four detectors. The assumed transmittance function of the 4:1 multiplexed kinoform was similar, except that it was a sum of complex exponentials having phase functions as in (2), with the sum normalized to have unit modulus.

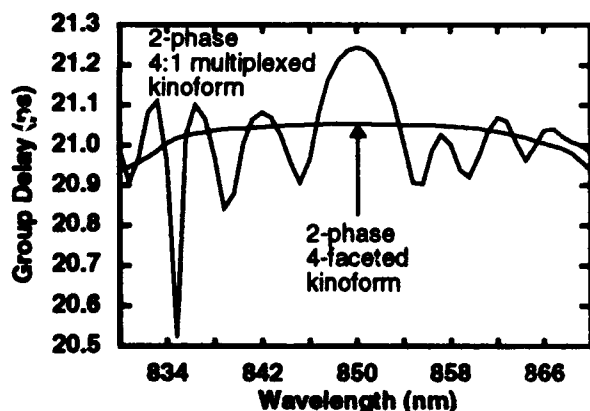


Fig. 2 Group delay (to a single detector) versus wavelength for a 2-phase 4:1 multiplexed kinoform and a 2-phase 4-faceted kinoform.

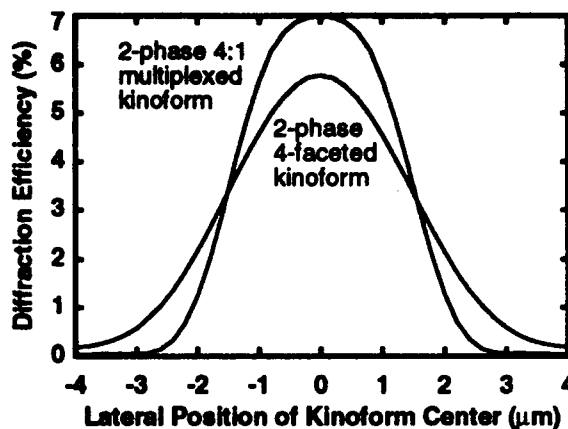


Fig. 3 Diffraction efficiency (to a single detector) versus kinoform lateral position for a 2-phase multiplexed or faceted kinoform.

Figures 1, 2, and 3 are representative results of the study. From Fig. 1, the wavelength stability requirements of the laser source are evident. The free-space interconnect can tolerate wavelength errors of approximately  $\pm 5$  nm with respect to the 850nm design wavelength. Furthermore, the performance improvement obtained by increasing the number of kinoform phase levels is evident. Fig. 2 indicates the dispersion characteristics of an interconnect using binary-phase kinoforms. The faceted kinoform is found to be less dispersive, exhibiting a group-delay variation of about 2.5 fs within a  $\pm 5$  nm separation from the design wavelength. Over this same range, the multiplexed kinoform displays approximately a 350 fs variation of group delay. From Fig. 3, it is evident that the interconnect can tolerate only a couple of wavelengths of horizontal shift of the CGH (at right angles to the CGH normal) before diffraction efficiency to a fixed detector is considerably degraded. A similar result holds for the laser. Other results indicate that the interconnect will tolerate tens of wavelengths of vertical shift (along the CGH normal) of either the laser or kinoform. Simulation of spot size indicates that at the detector plane, multiplexed kinoforms produce smaller spots than do faceted kinoforms of the same overall dimensions, consistent with their larger effective aperture size.

We are currently extending the simulation tool to treat interconnections involving multiple, cascaded CGHs.

### 4. References

1. J.W. Goodman, "Introduction to Fourier Optics," McGraw-Hill, New York, 1968.
2. S.M. Arnold, "Electron beam fabrication of computer-generated holograms," *Optical Engineering*, vol. 24, no. 5, pp. 803-807, September/October 1985.

## Integrated Optical Heads for Optical Data Storage

Bülent N. Kurdi  
IBM Research Division  
Almaden Research Center  
650 Harry Road, K69/803  
San Jose, CA 95120-6099

The growth of the optical data storage market is dependent very much on the storage cost advantage of this storage solution. Thus, a big emphasis is placed on lowering the overall cost of optical data storage. In the area of lowering the head cost, the trend has been toward the simplification of head design, improvement in manufacturability and integration which is exactly where integrated optics technology could play a major role. Since many applications demand a re-writable storage system, we will address only the magneto-optical systems. It should however be noted that the write-once (WORM) or CD-ROM systems (by far the biggest) represent a subset of the MO systems with less demanding system requirements.

In a magneto-optical system, the digital information bits are written on an optical media (typically a layer of an amorphous rare earth-transition metal alloy) as marks of perpendicular magnetic domains. Upon reflection, the incident linearly-polarized light is rotated by a small amount—typically less than  $0.5^\circ$ . Thus, an optical detection system for magneto-optical storage is quite complicated and requires the use of a differential detection scheme. In its most basic form, a magneto-optical head is a sensitive polarization detector which at the same time provides needed servo signals for focusing and tracking. In optical storage, high areal density is accomplished by means of a high numerical aperture objective lens with a diffraction-limited focused spot. Of course, the media removability is provided by the fairly large working distance between the objective lens and the optical disk surface.

These advantageous attributes should be maintained by an integrated optics based solution. Thus, we preclude solutions that are based on the use of flying optical heads as the removability is a must for a successful optical storage solution. In their seminal work in the late 80's, Nishihara *et al.* demonstrated the principles of both differential detection and servo signal generation in their integrated optics disc pickup devices both for read-only<sup>1</sup> and magneto-optical storage systems.<sup>2</sup> However, very high demand was placed on the fabrication tolerances of the grating coupler and this makes it very difficult to obtain high NA, high efficiency, focusing grating couplers. Recently, there has been a trend toward achieving system integration without the integration of a focusing element, i.e. the objective lens. In order to improve the coupling efficiency, even waveguide prism coupling concepts have been used.<sup>3</sup>

Without the use of a bulky prism coupler, one can design an integrated optical head utilizing a simple but crossed linear high efficiency grating coupler.<sup>4</sup> It can be placed in any convenient location for coupling the reflected collimated beam into a waveguide mode for further optical signal processing inside a waveguide. A schematic diagram of such an integrated optical chip is shown in Fig. 1 where the reflected light beam is incident on the crossed-grating coupler region with its plane of polarization oriented  $45^\circ$  with respect to the grating lines. The incident plane polarized light with its plane of polarization at  $45^\circ$  with respect to the grating lines is coupled into the  $TE_0$  modes of the waveguide propagating at orthogonal directions as shown in Fig. 1. These modes are basically identical modes of the planar waveguide and their intensities are balanced by the very nature of the crossed grating coupler which is made up of two identical linear gratings. A single-mode waveguide structure is preferred since the excitation of any TM modes would increase the noise level in the data signal. For that reason and also in order to simplify the waveguide-detector coupling scheme, an anti-resonant reflecting optical waveguide (ARROW), which has advantageous TM and higher-order-mode discrimination properties, is used.<sup>5,6</sup>

In an ARROW waveguide, the waveguiding is made possible due to high reflectivity at one of the interfaces and attenuated total reflection at the other. This high reflectivity can be eliminated by modifying the resonant-layer thickness and causing the mode to "leak" out into the substrate. Thus, one can direct the waveguide mode onto a detector fabricated in the silicon substrate without resorting to complicated coupling tapers, or grating couplers. One important aspect of the ARROW  $TE_0$  mode is the fact that it propagates far from the cut-off regime and is well confined within the thick waveguide layer. Recent analyses indicate that it is possible to fabricate high efficiency ( $\approx 73\%$ ) grating couplers in ARROW structures with reasonable interaction lengths ( $\approx 5\text{mm}$ ).<sup>7,8</sup> Since the crossed grating structure is a superposition of two identical linear

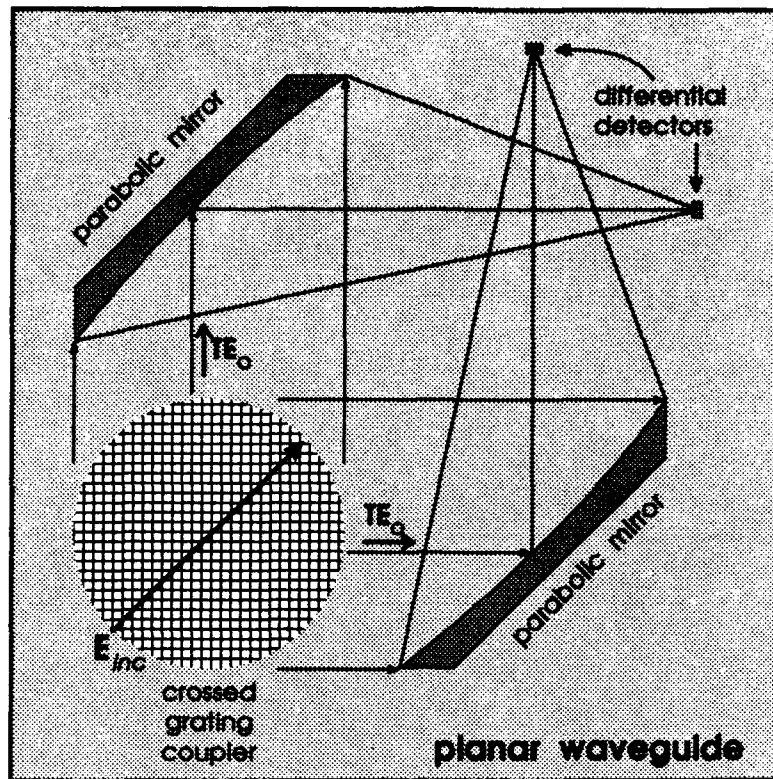


**Figure 1** Schematic drawing of an integrated optical head built on a planar optical waveguide.

gratings, it can be fabricated using double exposure in a holographic interferometric lithography setup. It is easy to fabricate such structures over large areas. As an alternative method, direct e-beam lithography can be used for the fabrication of crossed-grating structures.

The use of reflective components in integrated optical circuits is a well known technique. They can also find applications in waveguide circuits for optical storage heads where a combination of a focusing element and a split-detector arrangement is necessary for the generation of servo signals for tracking and focusing.<sup>3</sup> A parabolic waveguide reflector serves this purpose quite well as shown in Fig. 1.

In summary, we have shown a planar waveguide structure that can be used for magneto-optical signal and servo detection with high sensitivity for optical data storage. For a cost effective implementation, the use of silicon microelectronics compatible materials/processing is emphasized.

<sup>1</sup>S. Ura, T. Suhara, H. Nishihara, and J. Koyama, "An integrated-optics disc pickup device," IEEE J. Lightwave Tech., LT-4, pp. 913-918, (1986).

<sup>2</sup>H. Sunagawa, S. Ura, T. Suhara, and H. Nishihara, "An integrated-optic detection device for magneto-optical disc pickup," Int'l Symp. Optical Memory, Tech. Digest FA-7, Sept. 16-18, 1987 (Tokyo).

<sup>3</sup>K. Yokomori, *et al.*, "Integrated optical disk pickup with highly sensitive servo signal detection," International Symposium on Optical Memory, 1C-5, Sapporo, Oct. 1-4, (1991).

<sup>4</sup>B. N. Kurdi, G. T. Sincerbox, and J. M. Zavislan, U.S. Patent 5,166,989, (1992).

<sup>5</sup>M. A. Duguay, Y. Kokubun, T. L. Koch, and L. Pfeiffer, "Antiresonant reflecting optical waveguides in SiO<sub>2</sub>-Si multilayer structures," App. Phys. Lett. **49**, pp.13-15, (1986).

<sup>6</sup>Y. Kokubun, T. Baba, T. Sakaki, and K. Iga, "Low-loss antiresonant reflecting optical waveguide on Si substrate in visible-wavelength region," Electronic Lett. **22**, pp.892-893, (1986).

<sup>7</sup>R. Emmons, University of Rochester, private communication.

<sup>8</sup>R. Emmons, "Wave Guiding and Grating Coupling Phenomena in Silicon Based Integrated Optics," Ph.D. thesis, University of Rochester, (1992).

## Thin Film Resonant Cavity Enhanced Photodetectors

C. Camperi-Ginestet, and N.M. Jokerst  
 School of Electrical Engineering  
 Microelectronics Research Center  
 Georgia Institute of Technology  
 Atlanta, GA 30332-0269

The separation of single crystal thin film semiconductor devices from the lattice matched growth substrate with subsequent bonding of the thin film device to a host substrate such as silicon circuit, is a promising technique for low cost hybrid optoelectronic integration. To date, researchers have demonstrated that these thin film devices can perform comparably to their on-wafer (as grown) counterparts [1, 2]. This paper presents the first demonstration that these thin film devices may perform *better* than their on-wafer counterparts. When this heightened performance is coupled with the ease of integration of these thin film devices onto silicon circuitry, this epitaxial lift-off process offers a manufacturable, low cost hybrid optoelectronic integration option.

Thin film p-i-n photodetectors separated from the growth substrate can demonstrate higher quantum efficiency at wavelengths to which the optical (Fabry-Perot) cavity formed by the thin film is resonant. These resonant cavity enhanced (RCE) detectors have higher theoretical quantum efficiency than on-wafer p-i-n detectors which absorb only one pass of the incident optical signal. The finesse of the thin film resonant cavity can be increased by coating the back and/or front faces of the RCE detector with a reflective coating such as dielectrics or gold (which also serves as an ohmic contact). The manufacturing simplicity of these thin film RCE detectors is in contrast to on-wafer RCE detectors, which must utilize complex lattice matched semiconductor multilayer mirrors [3].

To demonstrate a thin film RCE detector, a thin film GaAs/AlGaAs p-i-n photodetector was integrated onto a  $\text{Si}_3\text{N}_4$  coated silicon wafer. Using the transfer diaphragm epitaxial lift-off technique [4], it is possible to coat both sides of the thin film device while it is under either growth or host substrate support. The p-i-n structure used for this demonstration has a 200nm AlAs sacrificial layer grown onto a GaAs substrate, a 500 nm thick AlGaAs, p-type ( $p_0 = 5 \cdot 10^{18} \text{ cm}^{-3}$ ) layer, an 1.1  $\mu\text{m}$  thick active region, undoped ( $n_0 = 4 \cdot 10^{14} \text{ cm}^{-3}$ ) and an n-type ( $n_0 = 8 \cdot 10^{17} \text{ cm}^{-3}$ ) AlGaAs layer 500 nm. A broad area p-type AuZn/Au contact which also serves as the back mirror of our cavity ( $R_b = 92\%$ ) was deposited onto the top of the structure. The devices are then mesa etched into 250  $\mu\text{m}$  X 250  $\mu\text{m}$  squares. The top of the devices is then protected with an Apiezon W handling layer and the assembly is placed into the solution which selectively etches the AlAs layer, releasing the devices from the growth substrate. The devices are then bonded to a transparent mylar diaphragm [4]. They are selectively aligned and deposited onto Au pads on the silicon wafer using the transfer mylar diaphragm.

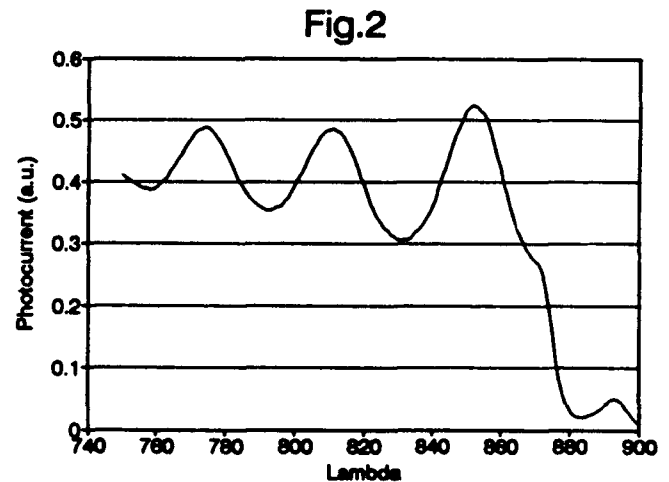
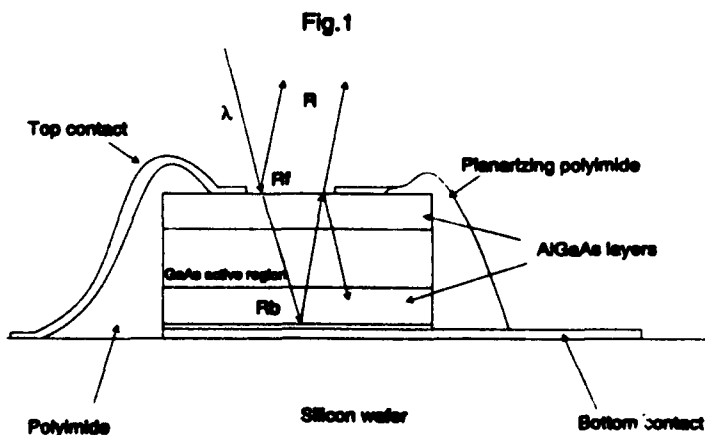
These devices, only microns thick, are planarized using polyimide, and a top ring contact is subsequently deposited, resulting in the device illustrated in Figure 1.

The bottom p-type contact is used as a mirror ( $R_b=92\%$ ), and the front mirror is the semiconductor/air interface ( $R_f=30\%$ ). The resonant cavity thickness can be adjusted through etching to align the resonant peak to the operating wavelength. The thickness of the cavity and the etch rate of the solution are monitored by measuring the photocurrent as a function of wavelength. The measured photocurrent spectra of a device with optimized cavity thickness for 851 nm operation is shown in Figure 2.

For this device the experimental quantum efficiency is 88% (88.5% is the maximum theoretical) which is 1.76 time larger than the quantum efficiency for a conventional on-wafer photodetector (49%) with a 1.1  $\mu\text{m}$  thick active region.

For the first time, we demonstrate an epitaxial lift-off thin film device with performance that is better than the same structure on-wafer. This enhanced performance makes this low cost, manufacturable thin film integration technique a particularly attractive process for hybrid optoelectronic integration.

- [1] E. Yablonovitch, E. Kapon, T.J. Gmitter, C.P. Yun, and R. Bhat, "Double Heterostructure GaAs/AlGaAs Thin Film Diode Lasers on Glass Substrates", *IEEE Phot. Tech. Lett.*, vol.1, pp41-42, 1989.
- [2] M. Hargis, J. Brown, and N.M. Jokerst, "Epitaxial Lift-Off Thin Film GaAs Metal-Semiconductor-Metal Photodetectors with Back Passivation", *IEEE Lasers and Electro-Optic Society 1992, Annual Meeting*, November 1992.
- [3] K. Kishimo, M.S. Unlu, J.-I. Chyi, J. Reed, L. Arsenault, and H. Morkoc, "Resonant Cavity-Enhanced (RCE) Photodetectors", *IEEE J. Quan. Elec.*, vol.27, No 8, August 1991.
- [4] C. Camperi-Ginestet, M. Hargis, N.M. Jokerst, and M. Allen "Alignable Epitaxial Lift-off of GaAs Materials with Selective Deposition Using Polyimide Diaphragms", *Phot. Tech. Lett.*, vol.3, No 12, Dec.1991, pp 1123-1126.



**ALIGNMENT CONSIDERATIONS IN THE PACKAGE DESIGN OF  
OPTICAL INTERCONNECTIONS**

A. K. Ghosh and R. S. Beech  
Department of Electrical and Computer Engineering  
The University of Iowa  
Iowa City, Iowa 52242

**Extended Abstract**

The possibility of using optical interconnects to meet increasingly higher speed and density requirements, which surpass the ability of electrical interconnects, is due to optics' high speed and bandwidth, freedom from capacitive loading effects, and freedom from crosstalk [1]. Because of the need for electrical-to-optical and optical-to-electrical conversion, however, an optical interconnect requires additional components. In addition to substituting a light channel (could be free space or a waveguide) for an electrical channel, replacing a single wire or circuit trace with an optical interconnect requires, at the very minimum, two additional components: an optical source and an optical detector. Usually, more components, such as lenses, holographic elements, mirrors, optical fibers, etc., are also required. Fabrication and assembly of an optical interconnect, with all of these components, requires precise alignment of the light beams and devices. Because of the 3-D, non-contact nature of free space optics, and the increased number of components, achieving the alignment necessary for the interconnect to operate correctly and reliably is a more difficult task than that of simply connecting a wire between two points.

Alignment of an optical interconnect involves angular, longitudinal, and transverse positioning of the optical and electro-optic components. The successful development, fabrication, and deployment of optical interconnects depend on how easily the components of the interconnect can be aligned and/or how tolerant the interconnect is to misalignments. An interconnection system which is difficult or time-consuming to align is costly to develop and fabricate and may be unreliable.

Based upon the realization that proper alignment is critical for practical optical interconnects, the research described in this article was performed to develop a tool for quantitatively specifying the relative difficulty of properly aligning an optical interconnect.

A measure of the ease with which an optical interconnect can be aligned has been developed [2,3]. This measure, called the alignability, uses the efficiency of power transfer in the interconnect as a measure of the quality of the alignment. Because the efficiency varies with changing component sizes, positioning tolerances, etc., the alignability depends upon various parameters of the interconnect and package design. An interconnect or package design which minimizes the alignment offsets, eases the alignment task, or makes the interconnect more tolerant of offsets will increase the alignability.

The link between alignability and the package design is the overall cost measure (OCM). The value of the OCM depends upon various physical parameters of the interconnect, such as spot or device size, the monetary cost of some of the components, and the time required for fabrication and alignment of the interconnect. Intuitively, we expect the alignability to increase or decrease with an increase or decrease in the OCM. For example, if the quality of the positioning devices, used in the interconnect, is increased, then the OCM will increase. And, because of the increased accuracy of higher quality positioners, the alignability should also increase.

To test one part of the OCM model, we performed a simple alignment experiment. In the experiment, a laser beam was aligned with a circular disc. By varying the amount of time allowed for the alignment, we obtained different standard deviations for the transverse offsets; with a decrease in standard deviation for an increase in allowed alignment time. This result supports the conjecture that increased OCM (in this case, longer alignment time) leads to increased alignability. Spot and device sizes also affect the alignability. If the size of the receiving device is increased, for example, then the interconnect will be easier to align and the alignability will increase.

The alignability applies directly to the alignment of a single source with a single receiving device. The alignability of a more complex interconnect is found by considering the interconnect to

be a collection of these simple, single source, single device interconnects. The total alignability is taken to be the product of the alignabilities of the simple interconnects.

A qualitative relationship between alignability, OCM, and device size follows from common sense. However, through the alignability theory, these common sense relationships can be quantified. This may not be useful for researchers; who only want to build one or two prototypes for proof-of-concept or experimentation. But, for someone who wishes to manufacture a large number of interconnects, where low cost, high yield, and high reliability are important, the alignability theory will be an aid in assessing the effects of cost, fabrication, and package design changes on the total yield and reliability.

In this paper, we give the basic definition and a detailed development of alignability. The definition and following development are based on the power transfer efficiency between a single light beam (source) and a single receiving device/aperture. We consider, in detail, the alignability of a uniform source-uniform device interconnect and a Gaussian source-uniform device interconnect. The alignability of a fiber-fiber (i.e. Gaussian source-Gaussian device) interconnect is discussed briefly.

In addition to the alignability, other interconnect performance measures, such as the bandwidth (BW), the signal-to-noise ratio (SNR), and the bit-error-rate (BER), are affected by changes in the device (detector) size of an optical interconnect. Through this mutual dependence, the relationship between an interconnect's alignability and its BW, SNR, and BER have been examined in other publications [4]. The results indicate that a range of device sizes exists for which given threshold values of alignability, BW, and BER (or SNR) are simultaneously met or exceeded.

To understand the application of alignability ideas to a practical interconnect design, we have conducted an alignability case-study. The alignability of a specific optical interconnect technology - integrated planar-optic (IPO) backplanes - is analyzed elsewhere [5]. The resulting data show that the alignability of such a structure can be optimized by varying the thickness of the integrated planar-optic substrate (IPOS) or the angle of reflection used in the IPO backplane design. The case-study analysis also includes a look at the relationship between alignability and channel density. The alignability calculation is extended to include the effects of adjacent channel crosstalk in an IPO backplane with multiple, parallel channels.

## REFERENCES

- [1] J. Goodman, F. Leonberger, S-Y. Kung, and R. Athale, *Proc. IEEE* **72**, 850-866 (1984).
- [2] A. K. Ghosh, *Applied Optics* **29**, 5253-5261 (1990).
- [3] A. K. Ghosh and R. S. Beech, "Analysis of alignment in optical interconnection systems," *Microelectronic Interconnects and Packages: Optical and Electrical Technologies, Proc. SPIE* **1389**, 630-642 (1990).
- [4] R. S. Beech and A. K. Ghosh, "Alignability versus bandwidth and bit-error-rate for optical interconnects," To appear in *Optics Communications* (1993). See also R.S. Beech and A. K. Ghosh, "Alignability versus bandwidth and signal-to-noise ratio for optical interconnects," *Photonics for Computers, Neural Networks, and Memories, SPIE* **1773** (1992).
- [5] R. S. Beech and A. K. Ghosh, "Optimization of alignability in integrated planar-optical interconnect packages," To appear in *Applied Optics* (1993). See also R. S. Beech and A. K. Ghosh, "Alignment analysis of integrated planar-optical interconnects," *Proc. of the 2nd IEEE International Workshop on Photonic Networks, Components, and Applications*, 1.18.1-1.18.10 (1992).

**Hybrid Integration of AlGaAs/GaAs Laser Diode on Si Substrate**

**B. R. Flachsbart, J. I. Malin, and K. C. Hsieh**

**Electrical and Computer Engineering, University of Illinois,  
127 Microelectronics Lab., 208 N. Wright St., Urbana, IL 61801**

Integration of laser diodes to optical waveguides on silicon is a topic of current interest [1-2]. While metal solder has been commonly used for bonding, it can be responsible for 3 dB of loss due to misalignment in the vertical direction [2].

We propose a bonding process which would provide a more controlled and reproducible vertical location of the active region. The process consists of evaporating a thin layer of Pd/Zn/Pd on cleaned GaAs laser material using standard liftoff lithography to pattern the metallization. The laser material is then cleaved and diced into laser diodes, and these diodes are bonded epi-side down on unmetallized p-type Si under pressure in a hydrogen ambient at 250° C for 1 min. The deposition of contact pads and a second anneal (300-500° C) is undertaken prior to electrical characterization. For resistance measurements we use the same process but pattern squares instead of stripes and use (100) GaAs wafers which are Zn doped at  $10^{18} \text{ cm}^{-3}$ . The GaAs epi-layers are standard quantum well structures and are grown by conventional MOCVD. The (100) silicon wafers are Zn doped at mid  $10^{18} \text{ cm}^{-3}$ .

The bonding is accomplished by the Pd metal reacting with the GaAs, forming binary and ternary compounds. This produces Ga vacancies and thus promotes the incorporation and diffusion of Zn into the GaAs to form a heavily doped low resistance region [3]. The mechanism for the Si side of the bond is the formation of low resistance  $\text{Pd}_2\text{Si}$ . Both of these are self-limiting shallow reactions which provide a controlled and reproducible bond.

Figure 1 shows a schematic of a bonded laser diode being probed. A four point probe setup in a similar manner was used to test contact resistance. Figure 2 shows a TEM photograph of the bonded and unbonded regions. The GaAs-Si interface runs horizontally across the middle, with the bonded region on the left and the unbonded region on the right (light line depicts a gap). The photograph also shows the shallow reaction of the metallization. The bonding process achieves very low resistance ohmic contacts as is evident from the I-V curve of Figure 3. Figure 3 shows a 20  $\mu\text{m}$  square bond being probed as in Figure 1, having a resistance of 1.5 Ohms. This low resistance should enable efficient operation and heat removal from the bonded device. Figure 4 shows the L-I curve of a bonded 20 x 500  $\mu\text{m}$  area laser with a threshold current of about 80 mA.

Further characteristics of the hybrid integration will be presented, including TEM analysis of the bonding process, temperature dependence of the I-V curves, and laser diode comparisons and performance under various conditions.

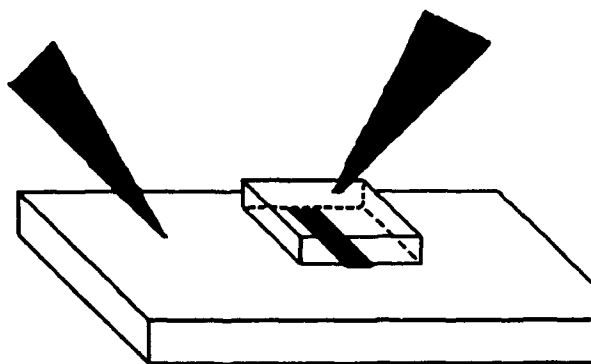


Fig. 1. Schematic diagram of a laser diode bonded to Si.

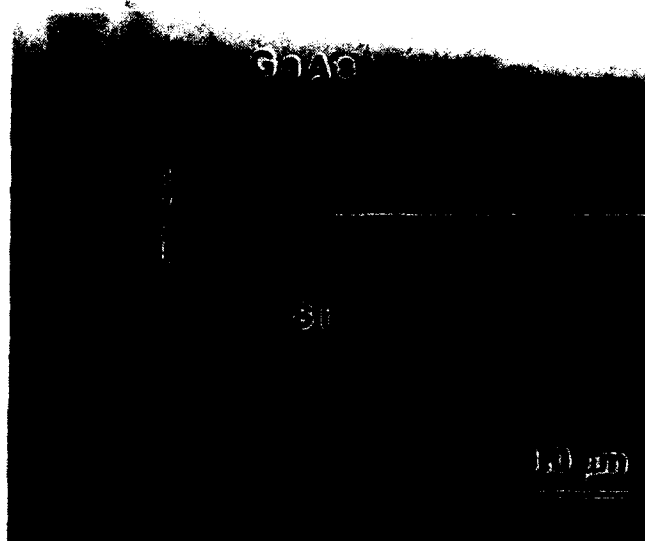


Fig. 2. TEM photograph of bonded and unbonded regions. Unbonded interface on right, bonded on left.

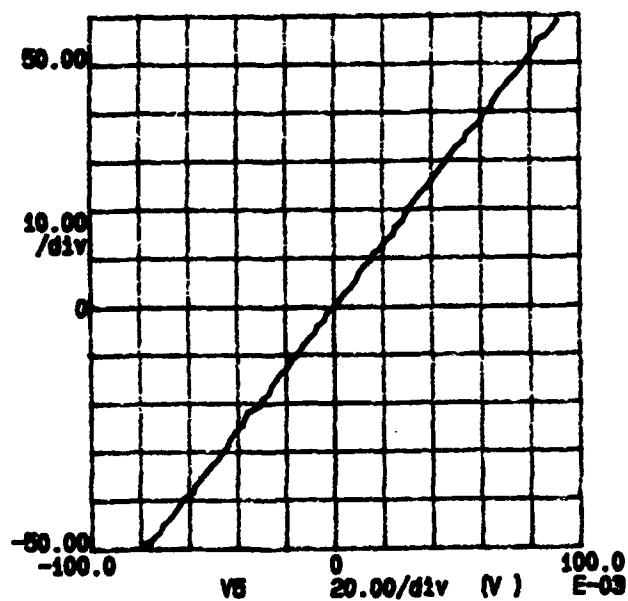


Fig. 3. I-V curve for a 20 x 20 μm bonded pad annealed at 400° C for 1 min. (resistance = 1.5 Ohm)

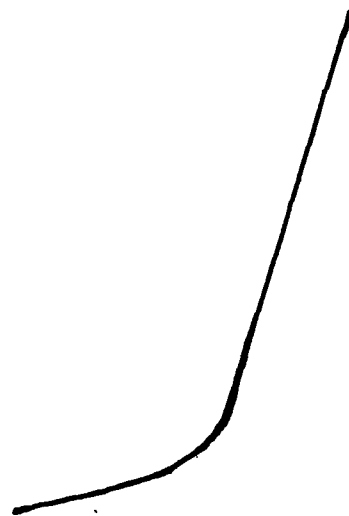


Fig. 4. L-I curve of a 20 x 500 μm bonded area laser with a threshold current of 80 mA.

#### References:

1. C. H. Henry, G. E. Blonder, and R. F. Kazarinov, *J. Lightwave Tech.*, vol. 7., no. 10, pg. 1530 (1989).
2. M. Yanagisawa, et. al., *IEEE Photonics Technology. Letters*, vol. 4, no. 1, pg. 21 (1992).
3. R. Bruce, *J. Electronic Materials*, vol. 19, no. 3, pg. 225 (1990).

**GaAs 850 nm surface-normal modulators solder-bonded to silicon***K.W. Goossen, J.E. Cunningham, and W.Y. Jan**AT&T Bell Laboratories, room 4B-519**Crawfords Corner Road, Holmdel, NJ 07733 (908) 949-6979*

Optical interconnects between electronic integrated circuit chips (IC's) may alleviate their bandwidth and pinout number requirements. This is especially true if surface-normal photonic elements are used since then large two-dimensional arrays of interconnects may be formed. A likely candidate for the photonic elements are multiple quantum well (MQW) modulators. In a system, an off-chip laser would be split into an array of spots focused on the modulators, whose reflectance is modulated by the on-chip electronics. The benefit of increased communication capacity to the chip is most attractive for silicon VLSI IC's. Monolithic integration of these modulators on silicon IC's has been demonstrated by us.<sup>1</sup> However, such integration entails subjecting the IC to temperatures as high as 850 °C during the GaAs growth, causing some degradation of the transistors.

Hybridization offers a possible solution to this problem. InGaAs/InP MQW modulators operating at 1.6  $\mu\text{m}$  have been attached to silicon IC's via solder bonding,<sup>2</sup> but this material system is inferior to the GaAs/AlGaAs system both in modulation performance and since smaller optical spots can be obtained at 850 nm. However, using the GaAs/AlGaAs material system entails removal of the substrate, since it is opaque. This has been performed using an epitaxial lift-off technique,<sup>3</sup> wherein the device layers are removed from the substrate in solution and then deposited with a probe on the silicon IC. This bonding technique would be problematic in a manufacturing environment.

Here for the first time we present the solder-bonding technique for GaAs/AlGaAs 850 nm modulators. A fairly standard p-i(MQW)-n modulator sample was produced by MBE. The MQW consisted of 55 periods of 90 Å GaAs wells and 30 Å  $\text{Al}_{0.3}\text{Ga}_{0.7}\text{As}$  barriers. On a 5 mm square piece of the sample,  $110 \times 110 \mu\text{m}$  gold p contacts (1000 Å thick) were deposited, and around these  $130 \times 130 \mu\text{m}$  inner mesas were etched to within 1500 Å of the buried n layer. Then 7000 Å thick  $50 \times 120 \mu\text{m}$  AuGe/Au n contacts were deposited (to be coplanar with the p contacts). Then 4000 Å of In was deposited above both contacts. Finally  $200 \times 200 \mu\text{m}$  outer mesas were etched down into the substrate, and the contacts were alloyed at 420 °C for 1 minute. A 1 cm square p type Si substrate was patterned with Al/In contacts of the same size and spacing as the p and n contacts on the modulators. The modulator sample was thinned to 200  $\mu\text{m}$  and then aligned upside down on the Si piece and heated to 200 °C for 15 minutes, fusing the In (Fig. 1). Then AZ 4210 photoresist was flowed between the samples, and allowed to dry for 12 hours. The GaAs substrate was then chemically removed using a jet etcher which delivered a  $1 \times 1 \text{ mm}$  jet of  $100:1 \text{ H}_2\text{O}_2:\text{NH}_4\text{OH}$  onto its surface, leaving electrically isolated modulators on the silicon piece (Fig. 2).

A  $\text{SiO}_x$  AR-coating was then deposited. The gold p contact served as an integral reflector. The reflectivity spectra was first measured at low intensity (Fig. 3). Near 850 nm, we obtain a reflectance change ( $\Delta R$ ) from 52 % to 26 % for a 0 to 10 volt bias swing. We then measured  $\Delta R$  with a high power laser (Fig. 4). A saturation intensity (intensity at which modulation decreases by one-half) of  $80 \text{ kW/cm}^2$  was measured (63 mW in a 10  $\mu\text{m}$  diameter spot). This high power shows that we have achieved excellent heat-sinking. We have also cycled the temperature of our hybrid from 30 °C to 100 °C over a hundred times and find no degradation, showing superb robustness.

In conclusion, we have demonstrated a technique for solder-bonding GaAs/AlGaAs 850 nm modulators onto silicon. Using this technique whole arrays of devices may be formed in one step. This technique provides a method for optoelectronic integration of silicon IC's.

**REFERENCES**

- [1] K.W. Goossen, J.A. Walker, J.E. Cunningham, W.Y. Jan, D.A.B. Miller, S.K. Tewksbury, and L.A. Hornak, to be presented at the 1993 Photonics in Switching topical meeting (Optical Society of America), Palm Springs, Calif.
- [2] J. Wieland, H. Melchior, M.Q. Kearley, C. Morris, A.J. Moseley, M.G. Goodwin, and R.C. Goodfellow, *Electron. Lett.*, vol. 27, p. 2211, 1991.
- [3] C. Camperi-Ginestet, M. Hargis, N. Jokerst, and M. Allen, *IEEE Photon. Tech. Lett.*, vol. 3, p. 1123, 1991.

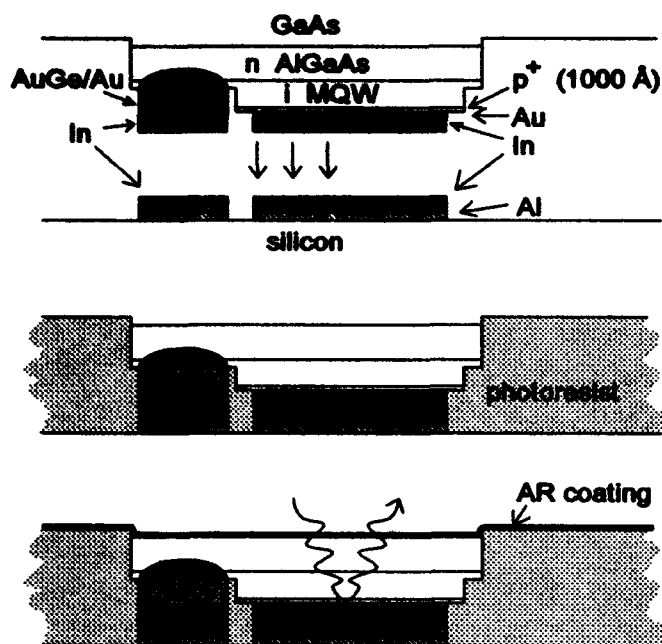


Fig. 1: Three step hybridization process: (1) Fabrication, aligning, and placement of modulator chip on silicon chip. (2) Flowing photoresist between chips. (3) Removal of GaAs substrate and deposition of AR coating.

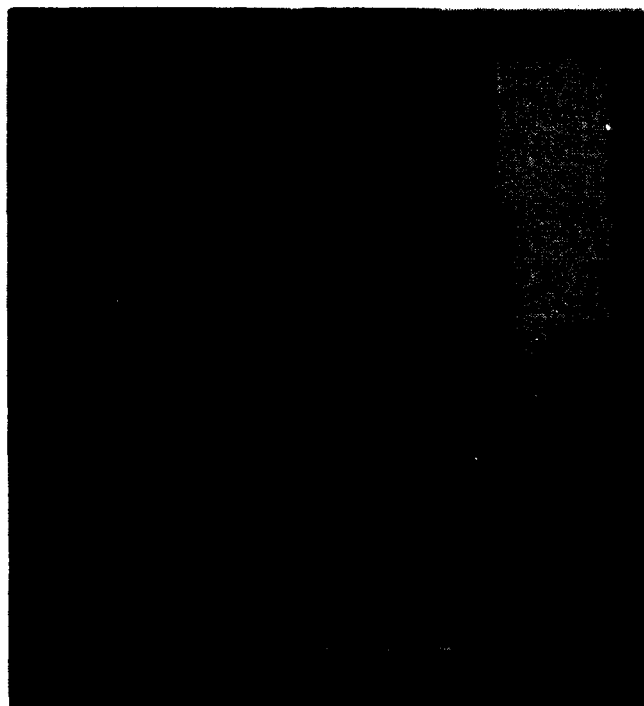


Fig. 2: Photograph of hybrid

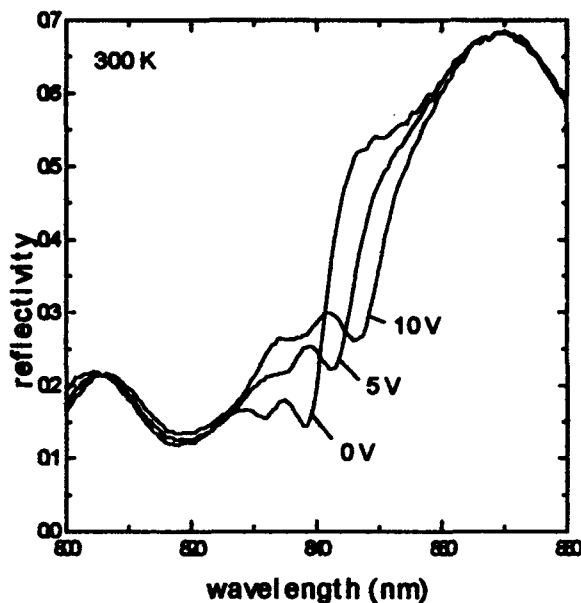


Fig. 3: Reflectivity spectra of our modulator at different reverse biases, at low optical intensity.

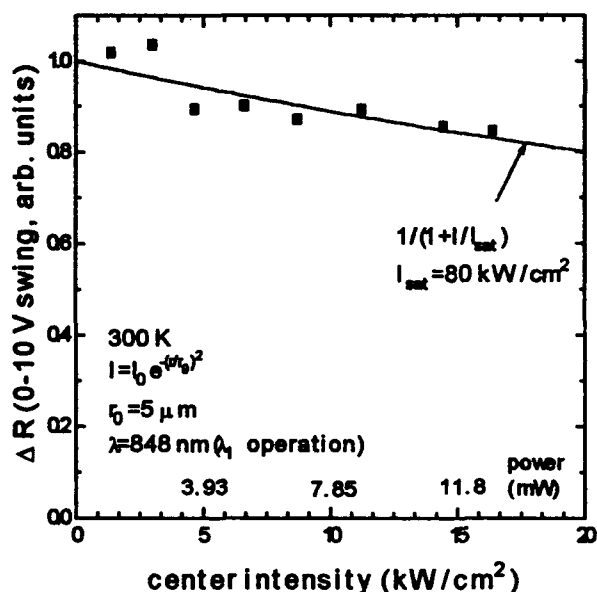


Fig. 4: Measurement of change in reflectivity for a 0-10 volt swing in the applied bias as a function of optical intensity. The optical spot has a gaussian shape with the 1/e point at 5 microns. The device is capable of handling very high power indicating superb heat sinking.

**CAD OF SOLDER JOINTS FOR SELF-ALIGNED ASSEMBLIES**

S. K. Patra, Wei Lin, and Y. C. Lee

Department of Mechanical Engineering

University of Colorado, Boulder, CO 80309, USA

(303)492-3393 (phone, YCL), (303)492-3498 (FAX)

e-mail (YCL): leeyc@spot.colorado.edu

**I. Introduction**

Design of solder joints is critical to precision alignments for optoelectronic components and systems. With an optimum design, we may reach the maximum restoring force for the X-Y alignments, or we may reach the maximum pulling force for the control of uniform,  $\mu\text{m}$ -level gaps [1]. At the University of Colorado - Boulder, three models have been developed to characterize flip-chip soldering's self-alignment mechanism. The models include simple-estimation formulas and differential equations for the solder joints with circular and non-circular pads. A comparison among these three models will help the development of an efficient CAD of solder joints for self-aligned assemblies.

**II. Model of Solder Joints with Non-circular Pads [2]**

The inputs of the model to characterize a single joint are 1) the geometries of the top and the bottom solder pads, 2) the solder volume, 3) the tensile or compressive vertical loading, 4) the misalignment level, and 5) the surface tension coefficient. By numerically solving very complex, non-linear Laplace-Young equations, the model can characterize the self-alignment mechanism with the following outputs: 1) the 3-D profiles including the joint heights during the alignment and 2) the restoring force for the alignment. Sometimes, we would like to know the vertical loading corresponding to a specified height. In this case, the loading becomes the output, and the height becomes the input. Other characteristics can also be switched. These inputs/outputs are also applied to two other models with some limitations.

**III. Model of Solder Joints with Circular Pads [3]**

This model is a much simplified version of the above model. The inputs and the outputs of both models are identical except the pad geometries. The circular model assumes circular pads with any diameters as the inputs. Due to the simplicity, the computation level is reduced by an order of magnitude.

**IV. Simple-Estimation Formulas**

These formulas are further simplified from the circular model. Since the formulas have not been published, they are listed below with the following nomenclatures.

$V$  = solder volume ( $\text{cm}^3$ );  $f_s$  = restoring force (dyne)  $f_n$  = vertical loading per joint (dyne);  $P$  = misalignment (cm);  $r_s$  = substrate pad radius (cm);  $r_c$  = chip pad radius (cm);  $H$  = final joint height (cm); and  $\gamma$  = surface tension coefficient (dyne/cm).

- Height of a spherical joint:

$$H_s = \left[ -A + \sqrt{A^2 + B^3} \right]^{1/3} - \left[ A + \sqrt{A^2 + B^3} \right]^{1/3} \quad (1)$$

$$\text{where } A = -3V/\pi, \quad B = r_c^2 + r_s^2$$

- Solder profile of a spherical joint:

$$r(z) = \left[ r_s^2 + \frac{z}{H_s} (H_s^2 + r_c^2 - r_s^2) - z^2 \right]^{1/2} \quad (2)$$

- Height of a furstrum of a cone:

$$H_c = \frac{3V}{\pi(r_c^2 + r_c r_s + r_s^2)} \quad (3)$$

- Calculation of the joint height by balancing the normal force to the vertical loading:

$$f_n = \frac{F(H - H_s)}{H_c - H_s} \quad (4)$$

$$F = \frac{\gamma\pi}{H_c - H_s} \left[ \left\{ r_s^2 + \frac{H_s^2}{4} + \frac{r_s^2 - r_c^2}{4H_s^2} (r_s^2 - r_c^2 - 2H_s^2) \right\}^{1/2} H_s - (r_s + r_c) \{ H_c^2 + (r_s - r_c)^2 \}^{1/2} \right] \quad (5)$$

- Restoring force as a function of misalignment:

$$f_s(P) = \frac{\pi}{2} \gamma (r_c + r_s) \left[ \frac{P + r_c - r_s}{\{(P + r_c - r_s)^2 + h^2\}^{1/2}} + \frac{P - r_c + r_s}{\{(P - r_c + r_s)^2 + H_c^2\}^{1/2}} \right] \quad (6)$$

The height of the solder joint and the restoring force are calculated by equations (4) and (6). The major limitations of the model are: 1) calculation of joints with circular pads, 2) calculation of the joint heights only at the zero misalignment, and 3) calculation of the restoring forces only with a specified height.

## V. Comparison

Figures 1 and 2 compare the results of the simple-estimation formulas and the circular model. The inputs for both models are: (1) solder volume =  $7.29 \times 10^{-7} \text{ cm}^3$ ; (2) pad radii on the chip and the substrate,  $r_s = r_c = 50 \text{ } \mu\text{m}$ ; (3) surface tension coefficient =  $325 \text{ dyne/cm}$ ; (4) vertical loading per joint =  $0.98 - 4.9 \text{ dynes}$ , and (5) misalignment =  $20 \text{ } \mu\text{m}$ .

Figure 1 shows joint heights versus vertical loadings at the zero misalignment. Figure 2 shows restoring forces versus misalignment levels with a loading of  $4.9 \text{ dynes}$  per joint. As shown in the figures, the simple estimation of a solder joint with no misalignment is very accurate, but the estimation becomes inaccurate when the misalignment level is large.

Figure 3 shows the joint heights, at a zero misalignment and under a constant vertical loading, with respect to different pad geometries. The height is  $18.6 \text{ } \mu\text{m}$  for square pads, but it is  $17.7 \text{ } \mu\text{m}$  for rectangular pads with  $0.5$  aspect ratio. When the pad is not circular, the most comprehensive model should be used in applications demanding  $\mu\text{m}$ -level alignments.

## VI. Acknowledgment

We gratefully acknowledge the supports of National Science Foundation through a Presidential Young Investigator Award. Also, this work was supported by the National Science Foundation Engineering Research Center for Optoelectronic Computing Systems, ECD-9015128.

## VII. References

- 1) Lin, W., Lee, Y. C., and Johnson, K. M., "Study of Soldering for VLSI/FLC Spatial Light Modulators", 43th ECTC, June 1993.
- 2) Patra, S. K., "Self-Aligning Soldering for Electronic and Optoelectronic Packaging", Ph.D. Thesis, University of Colorado at Boulder, 1992.
- 3) Patra, S. K. and Lee, Y. C., "Quasi-Static Modeling of Self-Alignment Mechanism in Flip-Chip Soldering Process, Part I: Single Joint", ASME Journal of Electronic Packaging, Dec. 1991, pp.337-342

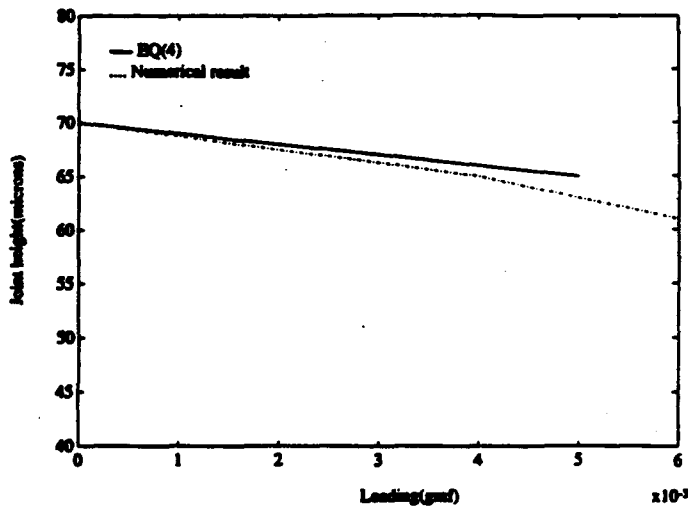


Fig.1 Comparison of Eq(4) with Numerical Result

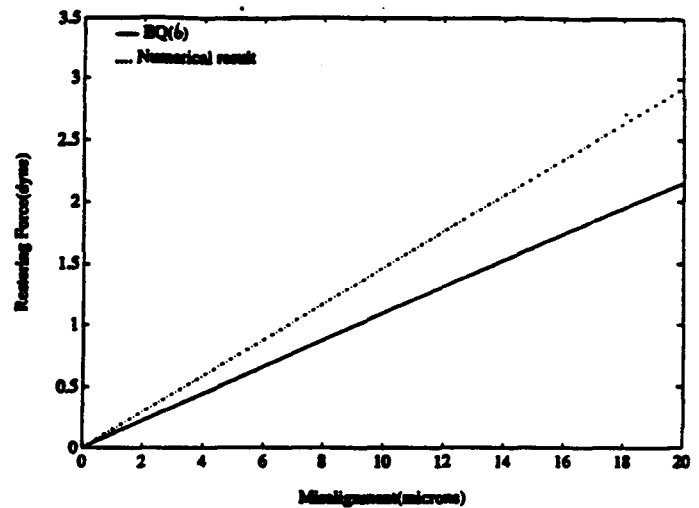


Fig.2 Comparison of Eq(6) with Numerical Result

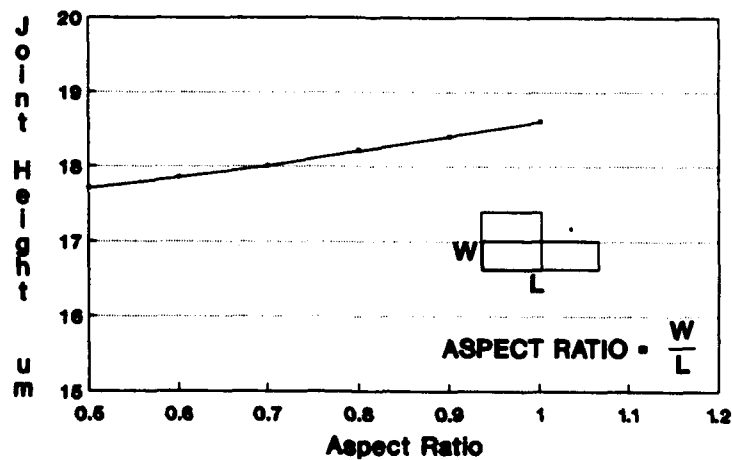


Fig.3 Effect of Different Pad Geometries



**Wednesday, July 28, 1993**

**Sessions:**

**W1: The Future of Industry, Academic and  
Government Collaborations**



**W1.1 8:30am - 9:15am  
(Invited)**

**U.S.-Japan Joint Optoelectronics Project**

**Judson C. French  
Electronics and Electrical Engineering Laboratory  
National Institute of Standards and Technology  
Gaithersburg, Maryland 20899**

The United States and Japanese governments have agreed to undertake a joint prototyping project to further the design and development of advanced computing technologies that combine lightwave and electronic components. The project will be part of Japan's Real World Computing (RWC) program, a ten-year, \$500 million initiative to develop advanced information-processing technologies. It will involve researchers and processing facilities in both nations.

The agreement was worked out over a two-year period beginning in 1990. During this time an interagency group of the Federal Government carried on discussions with Japan's Ministry of International Trade and Industry (MITI) concerning possible U.S. participation in MITI's RWC program with the goal of identifying joint activities that would be mutually beneficial. Following a period of consultation with the research community in the U.S., the U.S. government proposed to MITI the joint optoelectronics prototyping project. This proposal focused on a single project that, in both countries, will stimulate R&D activity in optoelectronics, provide designers with access to leading-edge fabrication facilities, and encourage effective commercialization. If both nations benefit from joint research in an area that is likely to yield commercially important technologies, then other cooperative projects could follow.

Following a feasibility study by the two countries, the general terms of the cooperative agreement were formalized in an exchange of letters between the Associate Director for Industrial Technology of the Office of Science and Technology Policy (OSTP) and the Director General of the Machinery and Information Industries Bureau of MITI.

A 10-member Joint Management Committee, with five members from each nation, will guide the project. In the U.S., the OSTP Director has appointed representatives from the Advanced Research Projects Agency (ARPA), the Departments of Energy and State, the National Institute of Standards and Technology (NIST), and the National Science Foundation (NSF). NIST chairs the U.S. group. MITI has similarly appointed members. This Committee will receive general oversight on policy issues from the Joint High Level Committee (JHLC), co-chaired by the OSTP Director and established by the 1988 U.S.-Japan Agreement on Science and Technology. That agreement calls for coordinating participation in government funded collaborative research projects through diplomatic channels. The JHLC will be kept informed by its Liaison Group on Information Science and Technology of the ongoing activities of the project.

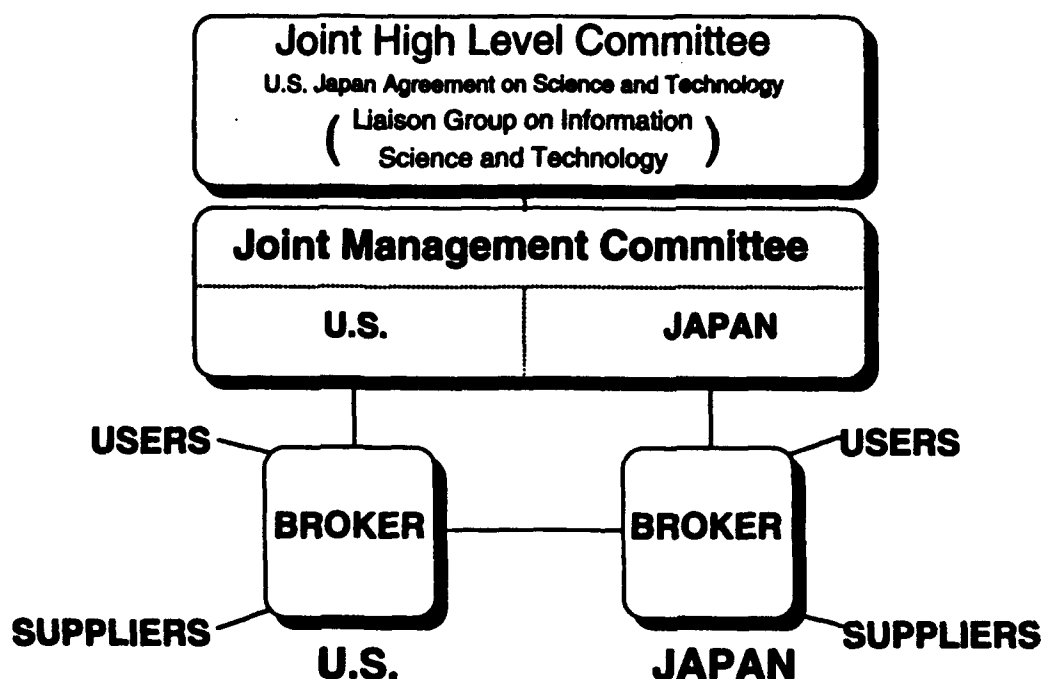
In the proposed project, the hybrid systems to be worked on would serve as a bridge between today's electronic computers and the fully optical machines that are envisioned for the future. Merging optical and electronic technologies offers an evolutionary path to faster, more versatile computers with an expanded range of applications.

Plans call for establishing a service that links designers of optoelectronic devices and modules, the "users", with production facilities, the "suppliers", through a broker. Each country will have its own broker, but suppliers in both nations will be available to Japanese and U.S. users. This mechanism will serve many purposes, including the protection of intellectual property rights, fostering of cross-usage of supplier capabilities, and the collection of data and experiences to establish standards to improve the efficiency of the service. Each country will select its own broker and arrange the funding for its own participants. MITI will finance the broker in both the U.S. and Japan. The Joint Management Committee will develop implementation guidelines for the project and determine an appropriate implementation schedule. At present, draft guidelines proposed by the U.S. members of the Joint Management Committee are under consideration by the Japanese members.

Domestic precedents for broker-facilitated production services exist in the "MOSIS" program for metal-oxide-semiconductor devices operated by the University of Southern California's Information Sciences Institute with joint funding from ARPA and NSF, and the ARPA-supported "CO-OP" program for optoelectronics technology managed by George Mason University.

## **U.S.-Japan Joint Optoelectronics Project**

---



**Consortium for Optical and Optoelectronic Technologies for Computing  
(CO-OP)**

**Ravindra A. Athale**  
**ECE Department**  
**George Mason University**  
**Fairfax, VA. 22030**  
**(703)993-1585, e-mail: rathale@gmu.edu**

Optical and optoelectronic technologies are being intensively investigated for applications in computing systems. These applications range from optical interconnects for electronic systems and optical storage to all-optical optical computers. In spite of this diversity of applications, there does exist a common technological base. These "platform" technology can be divided into two major devices categories: (i) devices that perform a fixed spatial mapping on an optical wave front.

(ii) devices that interact with the incident optical wave fronts in a linear or nonlinear fashion. Examples from the first category include various refractive, reflective and diffractive optical elements (lenses, prisms, beamsplitters, deflectors). Examples from the second category include optical detectors, modulators, sources and nonlinear optical materials. Each application makes different demands on the device performance parameters (e.g., spatial density, speed, power consumption). Since each device technology allows a unique performance trade-off, it is clear that there is a strong coupling between device technology, system design and application requirements. This coupling is particularly crucial for an emerging technology like optoelectronics. Often, researchers working on the device and material technologies and those working on system design and applications come from very different backgrounds and hence are unable to communicate. This communication barrier is even more significant when these researchers come from different institutions.

The Consortium for Optical and Optoelectronic Technologies for Computing (CO-OP) was initiated by the Advanced Projects Research Agency (ARPA) with the aim of overcoming these communication barriers. The main goal of the CO-OP is promote the use of existing technology in novel applications by making them widely accessible and by a cooperative sharing of test data and design methodologies among the Consortium members. The goal in other words is to work **WITH** the existing technologies rather than to work **ON** developing new technologies or improving their performance. In that regard, the purpose of the CO-OP is complementary to the already existing R&D efforts in technology development. The CO-OP is expected to augment

the R&D activities in optical architectures, applications and systems development by making device technologies more readily available to system developers.

The purpose of the Consortium will be achieved through the collaborative efforts of educational institutions, industrial entities and government laboratories. For administrative reasons, the membership is currently limited to US and Canadian institutions only. The membership consists of institutions that have specific technologies to offer and those that are interested in using these technologies. The consortium is currently being managed through an administrative office located at George Mason University. The CO-OP administrative office publishes a catalog annually that details these technologies. The devices can then be purchased by signing a "Terms and Conditions of Sale" document. Furthermore, the CO-OP administrative office is organizing working groups on different technologies (e.g., Smart Pixels, Diffractive Optics). The purpose of these working groups will be to organize user training workshops as well as to develop a consensus within the community on the issue of standards. While the danger of developing standards for device parameters prematurely are well recognized, a complete lack of standards is also equally harmful to a wide spread use of the devices and thereby achieving the economies of scale. The CO-OP, as the name implies, also aims to promote an informal exchange of ideas, views and "tricks-of-the-trade" between its members via newsletter and an e-mail forum. The long-term goal of the CO-OP is to make the optical and optoelectronic technologies easier to use by non-specialists via several foundry services that are supported by standard computer-aided design and simulation tools.

**W1.3 10:30am - 11:15am**  
**(Invited)**

**Direction of Optoelectronics Research at ARPA**  
*A. Yang, ARPA, Arlington, VA*

Objectives of current ARPA programs in Optoelectronics for Information Processing will be described. The programs span research and development of components, process technologies, module integration and packaging, and system demonstrations. From this perspective, some future directions are projected.

Expectations from Optoelectronic Technologies

Arpad A. Bergh  
OIDA

The Optoelectronics Industry Development Association was formed in July of 1991 with the purpose of improving the competitiveness of the North American optoelectronics industry. The voting members of the association include: AMP Inc., AT&T, Bell Northern Research, Bellcore, Corning, Hewlett Packard Co., Hughes/GM, IBM, Motorola Inc., and 3M. Voting members are represented on the Board of Directors, pay a higher membership fee than associate members and contribute to the activities of the association. OIDA is different from the usual industry association in the U.S. in that it includes both suppliers and users of optoelectronics. It also works closely with a number of government agencies, most notably the Commerce Department, in sharing resources and working toward common goals.

The first major undertaking of the Association is a Market Survey and Technology Roadmap activity to generate a high-level worldwide market and technology forecast (Figure 1).

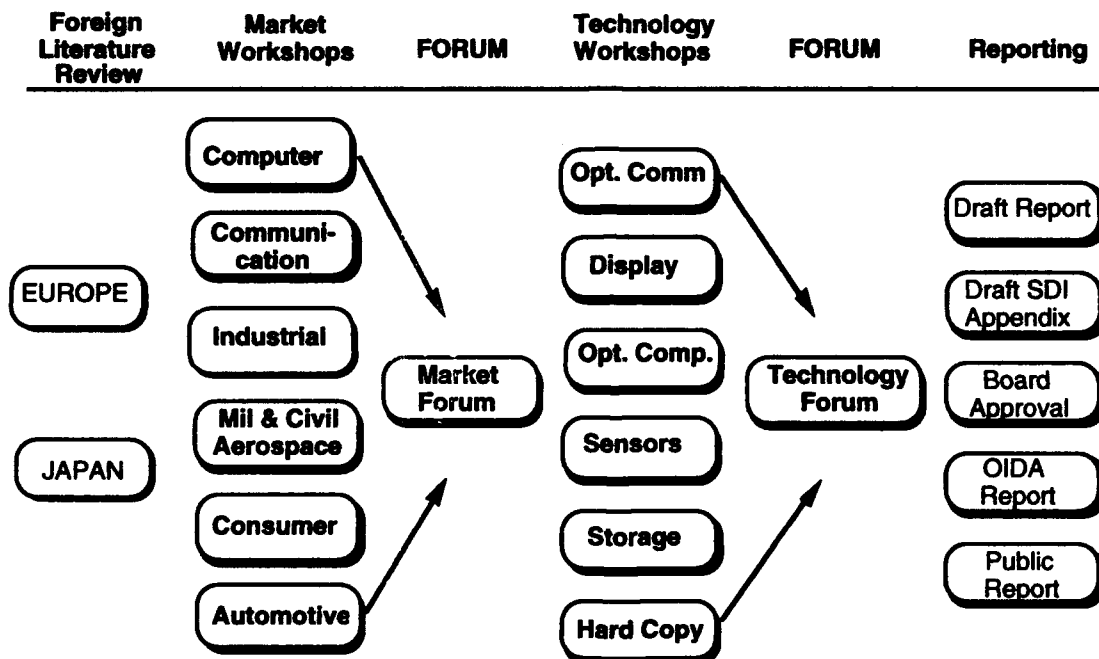


Figure 1

Industry wide Market Sector Working Groups held workshops in 1992, and a comprehensive report will be available for OIDA members in June, 1993. The focus has shifted this year from markets to technology in a set of six workshops as shown in Figure 1. These workshops combine the inputs from industry, government laboratories and academia and will conclude in another Industry Forum by the fall of 1993.

Although substantial growth is expected in all market segments over the next decade the dominant segments will be computers and communications drawing on a rich variety of central and distributed information sources through various peripheral and consumer electronic equipment. The distinction between the two will diminish in time converging into the digital information age technologies.

The increasing demand for these technologies is evident by the rapidly expanding role of information services in the U. S. work force (Figure 2) leading to highly intelligent, photonics-based, digital multimedia information networks of vast capacity. Such networks will be essential to providing voice, data and images in any combination, anywhere, at any time with convenience and economy.

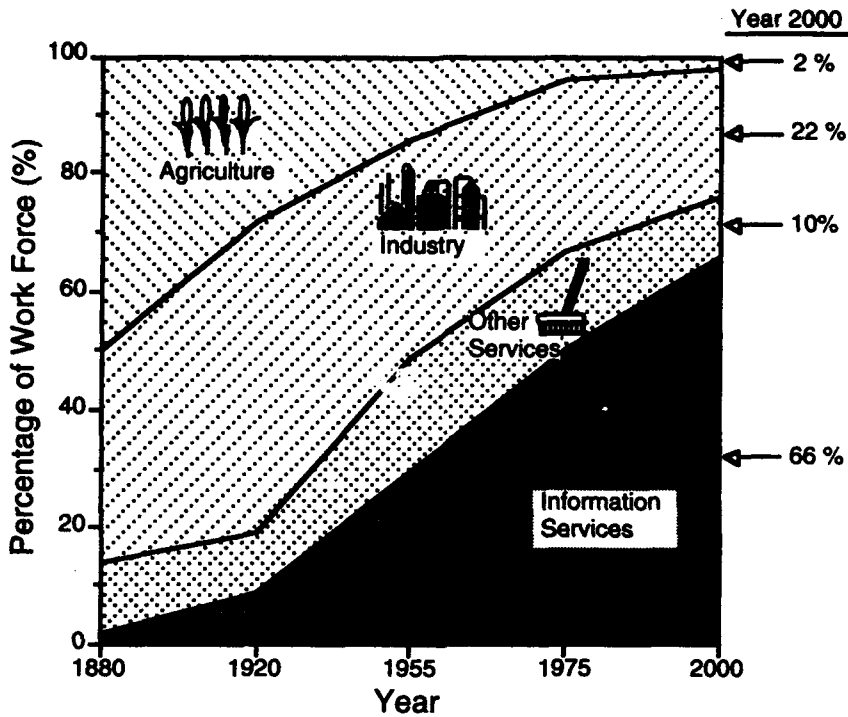


Figure 2

Concerning the immediate market potential of optoelectronics, our studies indicate that the market will be dominated by computers and communications. The third position will go to consumer electronics followed by industry applications including machine vision and medical electronics. The field of applications is similarly wide for optoelectronics in vehicular and military applications.

In terms of technologies the largest markets are expected in flat panel displays, lightwave systems, optical memory, compact discs, video disks, HDTV and machine vision systems. The greatest short term economic impact will probably come from packaging and interconnect technologies. In addition to unforeseen breakthroughs surprise performances might come from blue lasers, integrated optoelectronics (including laser arrays and smart pixels), parallel computing and optical switching.

Although in terms of market share the U.S. currently runs a trade deficit in optoelectronics, it is expected that the trade balance will even out over the next decade through the build up of U.S. production technology and through international partnerships. OIDA's contributions to an equitable international market share are summarized in Figure 3.

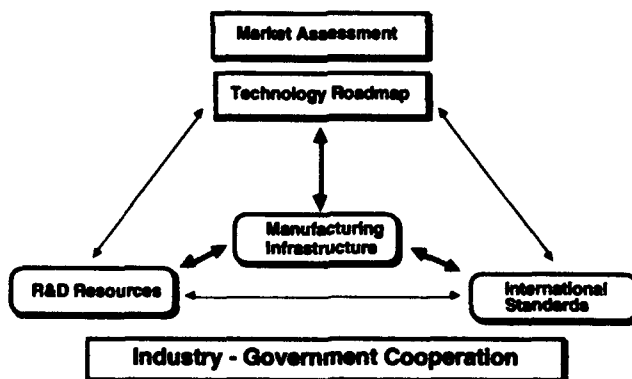


Figure 3

L. Anthony .....	33
V. Arbet-Engels .....	29
R. Athale .....	65
R. Beech .....	51
A. Bergh .....	68
M. Billard .....	17
J. Bristow .....	10
C. Camperi-Ginestet .....	49
C. Caneau .....	31
N. Caponio .....	17
H. Chen .....	33
J. Cunningham .....	55
F. Delpiano .....	17
G. Destefanis .....	17
C. Doherty .....	33
T. Drabik .....	11
L. Eldada .....	37
A. Ersen .....	29, 31
M. Feldman .....	43
B. Flachsbart .....	53
J. French .....	63

R. Frye .....	33
T. Gaylord .....	11
A. Ghosh .....	51
L. Giraudet .....	17
T. Gmitter .....	29, 31
M. Goodwin .....	3
K. Goossen .....	55
M. Grossglauser .....	21
N. Hartman .....	11
R. Hawkins .....	13
A. Heiney .....	15
J. Hoch .....	45
K. Hsieh .....	53
I. Ilic .....	37
W. Jan .....	55
C. Jiang .....	15
N. Jokerst .....	27, 49
K. Johnson .....	5
T. Ju .....	5
J. Kahn .....	45
B. Keyworth .....	39, 41

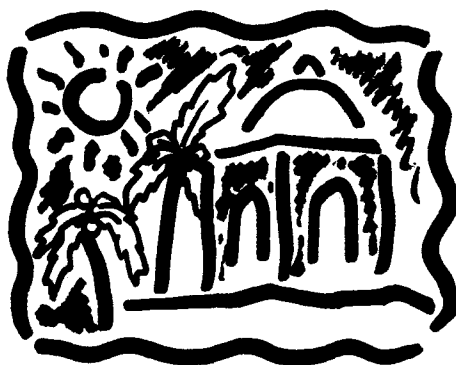
D. Kossives .....	33
R. Kostuk .....	19
B. Kurd .....	47
M. Lau .....	33
Y. Lee .....	5, 57
E. Legros .....	17
D. Levy .....	37
M. Levy .....	37
W. Lin .....	5, 57
Y. Liu .....	10
M. Lowry .....	13
S. Lu .....	13
R. MacDonald .....	39, 41
J. Malin .....	53
F. McCormick .....	23
J. McMullin .....	39, 41
S. Morasca .....	17
A. Moseley .....	3
T. Mullally .....	33
R. Narendra .....	39, 41
D. Nelson .....	13

R. Osgood .....	37
S. Patra .....	57
K. Pedrotti .....	8
R. Pierson .....	8
M. Pocha .....	13
M. Puleo .....	17
W. Reysen .....	15
R. Scarmozzino .....	37
A. Scavennec .....	17
A. Scherer .....	31
F. Schiattone .....	17
I. Schnitzer .....	29, 31
C. Seabury .....	8
C. Stirk .....	25
O. Strand .....	13
D. Tsang .....	8
F. Warning .....	33
D. Wills .....	21
Y. Wong .....	33
E. Yablonovitch .....	29, 31
A. Yang .....	67

# **Gigabit Networks**

**July 26-30, 1993**

**Fess Parker's Red Lion Inn Resort  
Santa Barbara, California**



**Sponsored by  
the IEEE Lasers and Electro-Optics Society  
and IEEE Lasers and Electro-Optics Society**

**IEEE Catalog Number: 93TH0549-6  
Library of Congress Number: 93-77778**

The papers in this book comprise the digest of the meeting mentioned on the cover and title page. They reflect the authors' opinions and are published as presented and without change, in the interest of timely dissemination. Their inclusion in this publication does not necessarily constitute the endorsement by the editors, the Institute of Electrical and Electronics Engineers, Inc.

Copyright and reprint permissions: Abstracting is permitted with credit to the source. Libraries are permitted to photocopy beyond the limits of the U.S. copyright law for private use of patrons those articles in this volume. Instructors are permitted to photocopy isolated articles for noncommercial classroom use without fee. For other copying reprint or republication permission, write to Director, Publishing Services, IEEE, 345 E. 47th St., New York, NY 10017. All rights reserved. Copyright ©1993 by the Institute of Electrical and Electronics Engineers, Inc.

IEEE Catalog Number:	93TH0549-6
ISBN Number: Softbound	0-7803-1284-8
Microfiche Edition:	0-7803-1285-6
Library of Congress Number:	93-77778

## **Gigabit Networks Technical Committee**

### **Co-Chairs**

**N.K. Cheung**  
*Bellcore*

**R.P. Skillen**  
*Northern Telecom*

### **Program Committee**

**R. Binder**  
*Corporation for National  
Research Initiatives*

**S. Wakid**  
*National Institute of  
Standards and Technology*

**K. Eng**  
*AT&T Bell Laboratories*

**S. Wecker**  
*Northeastern University*

**I. Richer**  
*Mitre Corp.*

**K.C. Young, Jr.**  
*Bellcore*

**V. Vinogradov**  
*American Express*

**WEDNESDAY, JULY 28, 1993**

**W1: THE NEW ERA OF GIGABIT NETWORKING**

<b>W1.1</b>	<b>The Coming World Order of Gigabit Networks .....</b>	<b>3</b>
<b>W1.2</b>	<b>What Can Gigabit Networks Learn From the Past?.....</b>	<b>4</b>

**W3: EARLY EXPERIENCE IN GIGABIT TESTBEDS I**

<b>W3.1</b>	<b>Technical Challenges of Turning Up the VISTAnet Gigabit Network .....</b>	<b>6</b>
<b>W3.2</b>	<b>Early Experience from the Casa Gigabit Testbed.....</b>	<b>8</b>
<b>W3.3</b>	<b>The Bellcore Research Network .....</b>	<b>10</b>

**W4: EARLY EXPERIENCE IN GIGABIT TESTBEDS II**

<b>W4.1</b>	<b>Gigabit Networking Research at AT&amp;T Bell Laboratories.....</b>	<b>12</b>
<b>W4.2</b>	<b>Broadband Services and Their Adoption for Research and Development.....</b>	<b>13</b>
<b>W4.3</b>	<b>A HIPPI/ATM/SONET Network Interface for the Nectar Gigabit Testbed.....</b>	<b>14</b>

**THURSDAY, JULY 29, 1993**

**T1: NEW DIRECTIONS IN HIGH SPEED NETWORKING**

<b>T1.1</b>	<b>The Evolution of Broadband Networking.....</b>	<b>19</b>
<b>T1.2</b>	<b>ACT NOW - Advanced Communications Technologies for New Opportunities in the Workplace .....</b>	<b>20</b>
<b>T1.3</b>	<b>High Speed Networking and the Hughes Network Architecture .....</b>	<b>21</b>
<b>T1.4</b>	<b>Who Needs Broadband Services and Why? .....</b>	<b>23</b>

**T2: INTERNETWORKING WITH ASYNCHRONOUS TRANSFER MODE (ATM)**

<b>T2.2</b>	<b>Unshielded and Shielded Twisted Pair Copper Wire Access Technologies for High Performance Local Area Networks .....</b>	<b>24</b>
<b>T2.3</b>	<b>Afterburner: Application-to-Application Networking at Hundreds of Mbit/s .....</b>	<b>26</b>
<b>T2.4</b>	<b>Towards Interoperability of ATM Public and Private Networks.....</b>	<b>28</b>
<b>T2.5</b>	<b>Multidisciplinary Engine Simulations at the NASA Lewis Research Center .....</b>	<b>30</b>

**T3: CONTROL AND MANAGEMENT OF GIGABIT NETWORKS**

<b>T3.1</b>	<b>Performance Barriers to High Speed Networks.....</b>	<b>32</b>
<b>T3.2</b>	<b>Can Shannon Coding Theorem Play a Role In ATM Traffic Management? .....</b>	<b>34</b>
<b>T3.3</b>	<b>On Protective Buffer Policies.....</b>	<b>36</b>
<b>T3.4</b>	<b>A Call Acceptance Algorithm for Gigabit Networks .....</b>	<b>38</b>

# T A B L E O F C O N T E N T S

## **T4: TECHNOLOGIES FOR GIGABIT NETWORKS I**

<b>T4.1</b>	<b>The Impact of 10Gb/s SONET (OC-192) on Gigabit Networks .....</b>	<b>40</b>
<b>T4.2</b>	<b>Gigabit ATM Switching: A Concentrator-Based Growable Switch Architecture and Performance .....</b>	<b>43</b>
<b>T4.3</b>	<b>Probabilities of Undetected Errors Using ATM AAL5 on Real User Data .....</b>	<b>45</b>
<b>T4.4</b>	<b>OC-12 Crossconnect for the VISTAnet Gigabit Network.....</b>	<b>47</b>

**FRIDAY, JULY 30, 1993**

## **F1: RECENT PROGRESS OF THE ALL-OPTICAL NETWORK CONSORTIA**

<b>F1.1</b>	<b>The Optical Network Technology Consortium.....</b>	<b>51</b>
<b>F1.2</b>	<b>The AT&amp;T, Digital, and MIT All Optical Network Consortium .....</b>	<b>52</b>
<b>F1.3</b>	<b>IBM Research Program on All-Optical Networks.....</b>	<b>54</b>

## **F2: TECHNOLOGIES FOR GIGABIT NETWORKS II**

<b>F2.1</b>	<b>Gigabit Network Testbeds with Semiconductor Optical Amplifier based Optical Crossbar Switches .....</b>	<b>56</b>
<b>F2.2</b>	<b>The STARNET Coherent Optical WDM Network: Modulation Format and Computer-to-Optics Interface .....</b>	<b>58</b>
<b>F2.3</b>	<b>Matrix Codes for Ultradense, Gigabit Optical CDMA Networks.....</b>	<b>60</b>
<b>F2.4</b>	<b>A Compact, Directly Modulated, Pulse-Compressed, and Variably-Delayed Time-Division-Multiplexer for Gigabit Multiple-Access Networks.....</b>	<b>62</b>
<b>Author Index.....</b>		<b>64</b>

**Wednesday, July 28, 1993**

**Sessions:**

**W1: The New Era of Gigabit Networking**

**W3: Early Experience in Gigabit Testbeds I**

**W4: Early Experience in Gigabit Testbeds II**



**W1.1 8:45am- 9:30am**

**The Coming World Order of Gigabit Networks**

**R. Snelling, *Georgia Center for Advanced Telecommunications Technology, Atlanta, GA***

**With the current Laboratory Heroic work transpiring in the 10 to 100 gigabit range, it is clear that within this decade a new high capacity, high performance architecture to the "Core Network" will emerge. This presentation will deal with the likely characteristics, timing, and critical issues of this "Core".**

## What Can Gigabit Networks Learn from the Past?

By Amos E. Joel Jr.  
Executive Consultant

Electrical telecommunications commenced with telegraphy. In time improvements brought repeaters to cover longer distances. Higher-speed operation increased capacity but human signal reading capability could no longer be relied upon. Automatic recorders were developed to overcome this deficiency and to improve service generally. Manual switching was added to permit messages to be directed according to addresses.

Early on the demand for service exceeded the capacity of the few network circuits that were available. The great technical search was on for practical ways to increase circuit capacity by "multiplexing". Alexander Graham Bell was seeking such an improvement in the telegraph when he stumbled upon the telephone.

The invention of the telephone and the service it engendered brought a new dimension to telecommunications, the variation of the electrical signals, the analog of the voice sound pressures. New types of repeater, actually amplifiers, eventually extended the range of voice transmission. With the invention of the vacuum tube, frequency multiplexing became practical. Multiplexing was best implemented by separating the two-directions of transmission. Four-wire switching accommodated these circuits.

Only a quarter century ago did it become economical to convert analog voice transmission to digital signals, returning in a sense to the telegraph. More importantly the same telecommunications media, wire or wireless, could now transmit both voice telegraph, now known as "data". Digitizing is resuming with its application to still images and motion pictures.

Digital circuit multiplexing was implemented in the time domain. Interfacing this technique by synchronizing with time multiplexed digital signals has given us time-division digital switching.

As transmission advances have occurred, terminals and switching have changed to optimize synergy with one another. Also with each change in technology there has been an improvement in service functionality and quality. As has been the trend over generations, the quality of telephone transmission today is far superior to that of only 25 years ago. It is endemic that the changes in terminals and switching occur only after the changes in transmission. It took almost 10 years for time division digital switching to catch-up with time division digital transmission.

With the successful development and deployment of optical fiber transmission, photonic switching will become a commercial reality. The next step is the building of all-optical networks, complete with switching and terminal equipment taking advantage of operating at gigabit speeds.

Voice has been the principal telecommunication service. Systems were designed primarily with this in mind. Where telegraph or data service uses this ubiquitous network, data was converted to voice-like signals with modems, or further sub-multiplexing was employed to use the transmission medium with greater efficiency. Video was carried over separate transmission facilities in analog form, and networks were devoted exclusively to this service, essentially carrying the signals as generated by the terminals,

Forecasting future services, a new factor has been added. Users now say they want and are willing to pay for services other than voice such as various video qualities, still image transmission, data at various speeds, for very very short messages to the contents of entire files and tomes. The potential for GIGABIT networks is tremendous capacity and growth. Much speculation is being given on how best to use these facilities.

In the past the capabilities of the transmission improvements, while significant, have not been great enough to lead to a demand for the commingling of different services. Networks have carried services other than those for which they were initially designed and engineered. This includes, for example, the transmission of voice over local area networks, and yes, the transmission of data over the public telephone network. Packet switched networks for data with switches and terminals designed specifically to accommodate the characteristics of these messages have proven to be a much better alternative to the use of circuit switched voice networks.

Generally only the use of common facilities, that is separate channels in media on the same route, is the only mixing of these services. This has popularized and greatly expanded the role of another form of circuit switch, the facilities switch. more specifically for digital facilities the digital cross-connect switch. It not only provides for the switching of facilities but also for channels that may be interchanged, added or dropped at a network node.

For the first time a new issue has arisen, one for which we have had little experience or direction. When the coaxial cable increased by a thousand fold the number of simultaneous channels available for voice messages. the demand for services was great enough to utilize the entire capacity. In an earlier era when telegraphy and the telephone coexisted, where there was a need for additional telegraph channels they were provided using separate channels in same transmission medium. The services were quite apart with one supporting the other only occasionally, such as for long distance communication between test desks.

We see ahead an explosion in both the transmission capabilities and service possibilities. And there is something new and different, the simultaneous use of different services at the terminals. This is being called "multimedia".

The ubiquity of the voice network was the advantage to employ modems for data. Similarly we should be moving more rapidly to ISDN. But we are not. gigabit networks will suffer from the same slow implementation that ISDN has encountered. Let's look at some of the problems of ISDN.

Standards, different switching system implementations, lack of functional station equipment. ISDN will help gigabit networks. It is a technology cannot be skipped. We must have end-to-end digital connectivity before we have gigabit networks. Just as the ISDN picture is clouded by specialized technologies such as HDSL and ADSL, so too multimedia GIGABIT NETWORKS implemented with ATM will have competition with separate broadband services networks.

**Technical Challenges of Turning Up the VISTAnet Gigabit Network**  
**M. Niel Ransom - Director, BellSouth**

The various "gigabit" testbeds (supported in part by DARPA and NSF through the Corporation for National Research Initiatives) have been in development for three years. Achieving network operation at gigabit-per-second rates has proven to be more difficult than anticipated. VISTAnet, a joint project of BellSouth, GTE, MCNC, NC State University and Univ. of North Carolina, was the first of these testbeds to reach operational status and in doing so overcame a number of significant technical challenges.

The primary application research of VISTAnet is the creation of a visualization tool to aid in the planning of radiation treatment for cancer patients. With this tool a radiation oncologist will be able to see on a workstation a 3-dimensional rendering of the patient (created using data from CAT scan or MRI images of the patient), will be able to rotate the image, take slices to see inside the image, and apply radiation sources while viewing (via color shading) the resulting radiation distribution pattern within the patient's anatomy. Our goal is to be able to perform these calculations so rapidly that the oncologist will be able to see the resulting changes to the radiation distribution immediately as he or she varies each of the radiation sources.

The enormous processing capabilities required for this tool is achieved through combining a Cray Y-MP 8/432 at MCNC in Research Triangle Park, a Pixel-Planes 5 raster graphics system under development at the UNC, a MASPAP MP-1 massively parallel computer, and a Silicon Graphics 340 VGX which is used as the Medical Workstation. To demonstrate how a public gigabit network could enable such applications, these computing resources are interconnected via a broadband network consisting of a prototype Fujitsu ATM switch, 2.4 Gb/s SONET facilities, and a prototype broadband cross-connect system designed by GTE.

Very little test equipment exists for debugging gigabit networks. Hence along with designing the network itself, a significant portion of our overall effort was spent in designing the specialized test equipment which would be needed. One of the most valuable tools which was developed by MCNC for the VISTAnet integration effort was the HIPPI Link Data Analyzer (HiLDA). HiLDA is a custom-designed traffic analyzer which can be inserted in a HIPPI connection and provides real-time capture for network traffic statistics and programmable error insertion. HIPPI traffic statistics are displayed on the screen in the form of histograms. The HiLDA user interface is designed to allow remote operations from an X Windows-based workstation. The IOSC HIPPI testing tool by Input Output Systems Corporation was used for stand-alone testing of the terminal and network equipment and was used to generate network traffic prior to availability of the application software. Recently the Hewlett Packard series 90 ATM analyzer was introduced which we are using to test the OC-3c interfaces to the ATM switch.

By far the most difficult network element to test and debug proved to be the Network Terminal Adapter (NTA). In VISTAnet, each of the endpoints connects to the network through an 800 Mb/s HIPPI interface. The NTA receives packets over a HIPPI interface and converts these into ATM cells for transmission through the network. At the destination, the NTA converts cells back into HIPPI packets. A complication to the NTA design was to allow traffic from multiple

sources to be sent simultaneously to the same destination. A further complication was that the design of the NTA was split into a "Core NTA" designed by Fujitsu and a Control and Measurement Subsystem (CMS) designed by BellSouth. Because of the speeds required in the Core NTA, it is implemented primarily in discrete ECL. This required modifications to be made via "white wire" to boards which had to be kept in design synchronization with units in Fujitsu's system lab in Kawasaki, Japan. The CMS, made up of a SUN SPARCEngine and specialized interface hardware, provides the user interface for ATM call establishment and allows collection of various types of traffic measurements. Although not initially intended as a debugging tool, the CMS became a key tool in the system integration effort providing the "eyes and ears" into what was happening inside the network.

The initial plan was for the ATM switch to be operational in the first quarter of 1992. Delivery of the Fujitsu ATM switch was delayed three months due to a problem in a key VLSI device used throughout the system. Final verification of the ATM switch was not complete until July 1991. Further obstacles surfaced in interconnecting the ATM switch and the broadband crossconnect system. SONET specifications allow payload pointers to be updated to allow for clock differences between two locations. When the broadband crossconnect system made pointer adjustments, the ATM switch would lose cell synchronization. The result was that occasional ATM cell losses would occur in the network which was finally traced to pointer adjustments. This was remedied by introducing a clock stabilizing unit in the system suppressing clock jitter and wander thereby reducing SONET pointer updates.

Because of the delays in the availability of the network, a Broadband Communications Products' HIPPI extender was used to interconnect the Pixel Planes 5 to the Cray Y-MP. This allowed software development to proceed in parallel with network debugging although only in a point-to-point configuration.

The VISTAnet architecture provides very little error checking. Given the high data rates in the network, retransmitting packets containing errors would add significant complexity. Fortunately, dose data, where individual bit errors typically should not cause problems, make up the great majority of system traffic. On the other hand, if errors occur in the addressing bytes of a HIPPI packet, the packet will be lost which often results in a system crash. As the debugging of the network progressed, data loss and hence system crashes became less frequent. Nonetheless, our current plan is to add a degree of error recovery to the application software which should eliminate this problem.

By August of 1992, although each network element appeared to be working correctly when tested alone, severe data loss would occur when these elements were interconnected. Occasionally we could get the network to appear to operate correctly with the IOSC testers only to have the network fail when transmission of application data was attempted. A frequent frustration was to painstakingly trace an error condition and discover it to be no more than a loose HIPPI connector. Several difficult months of trying to stabilize the network ensued before a decision was made to introduce a formal acceptance plan. This plan provided, for example, a specific set of point-to-point tests to be completed successfully before 3-point testing would begin. By building a solid base of verified capabilities before adding further complexity, stable network operation was finally achieved in May 1993.

## EARLY EXPERIENCE FROM THE CASA GIGABIT TESTBED

Larry A. Bergman  
 Jet Propulsion Laboratory  
 California Institute of Technology  
 Pasadena, CA 91109

### ABSTRACT

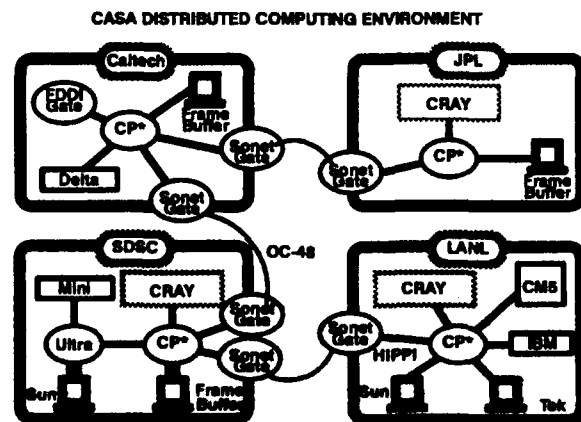
The CASA gigabit testbed will demonstrate the technique of distributed supercomputing over a wide area network. This talk will describe the progress and first results of three key applications that are being developed.

### SUMMARY

High-performance computing has become recognized as a key technology for many scientific and engineering activities. Supercomputers are increasingly used by scientists to study complex phenomena through computer simulation. This use of computers adds an important new method for scientific and engineering research, one that is complementary to theory and experiment; computer models can be used to simulate phenomena that cannot be studied or measured with experiments or simply provide a less costly means for studying phenomena. Examples of application areas include weather prediction, mineral exploration, drug engineering, seismic modeling, global ecosystem change, and chemical reaction analysis. Present supercomputers are powerful enough for computational models to predict complex non-linear phenomena, develop engineering prototypes, explore the physical parameter space prior to doing experiments, and even simulate events occurring in the real world. Some studies can only be carried out through computer simulation.

Networks enter the high-performance computing arena because as scientists study ever more complex phenomena through computer simulation, they often require multi-disciplinary approaches, information stored in varied databases, and computing resources that exceed any single supercomputer. Computer networks can provide the needed connection between the people, the machines, and the data, but current networks are too slow to support most large-scale applications. Supercomputers perform billions of arithmetic operations per second; by the late 1990s, speeds will be a thousand times greater. In contrast, most current wide area networks operate at 1.5 Mb/s, which is equivalent to transmitting the results of only 200,000 arithmetic operations per second. A few of the network backbones operate at 45 Mb/s, but this is still too slow. The mismatch between computer execution rate and network bandwidth precludes effective distribution of work among dispersed supercomputers; the exchange of data among the collaborating computers would be very slow compared to the calculation rate. The computers would spend much of the time waiting for intermediate results to be communicated by their fellow workers so that the next phase of the computation could be tackled.

The CASA testbed [1], one of the original five established by DARPA/NSF, will demonstrate that *distributed supercomputing* using wide-area high-speed networks can provide new levels of computational resources for leading-edge scientific problems. Distributing large computations among several supercomputers provides the opportunity both to bring to bear greater computing power than is available in any single machine and to use the most suitable machine for each step of the task. The testbed consists of five large supercomputers (three Cray, one 1024-node TMC CM-5, and one 512-node Intel Delta) plus several small ones, interconnected by an 800 Mb/s network, at four institutions: the Los Alamos National Laboratory (LANL), the California Institute of Technology (Caltech), the Jet Propulsion Laboratory (JPL), and the San Diego Supercomputer Center (SDSC). The HIPPI crossbar (CP\*) networks at each local institution are interconnected over the wide area by a SONET OC-48 2.4Gb/s network. A special



**HIPPI/SONET Gateway**, designed by LANL, maps HIPPI frames into SONET frames (and vice versa) at the premise/WAN boundaries [2]. **Crossbar Interfaces (CBI)** are also available to provide high-level protocol isolation for the network, translate logical addresses to network physical addresses, request connections of the switching core, and perform security checking enhancements required by more secure computing environments.

The main challenge is to use multiple supercomputers connected by high bandwidth channels to solve important scientific problems, in spite of high communications latency. Two research issues that arise are how to devise algorithms that hide latency and how to write or modify applications software to run in a distributed fashion. These in turn may lead to new programming models, network services and functionality. Additional objectives focus on the design parameters for high bandwidth networks and how to build and operate them.

The approach in CASA has been to use algorithms and software environments that have been developed for parallel computing (Express). These systems provide mechanisms for sending data between processes, for distributing data among several processors, and for overlapping communication with computation. The computations are organized so that (1) communications latency over the wide-area network can be overlapped with computations and (2) algorithms are tailored that minimize the number of messages to be sent by predicting in each processor the values that are being computed by other processors.

The three distributed applications that the CASA testbed are developing are from the areas of chemistry, geophysics, and climate modeling [2]. Chemical reaction dynamics computations are carried out to study the reaction of fluorine and hydrogen, which is relevant to powerful chemical lasers. These computations involve operations on very large matrices and require frequent communication of large blocks of data between the computers that participate in the calculation. The second application, **CALCRUST**, develops an interactive visualization program for geological applications that takes input from Landsat, seismic, and topographic databases. Among the benefits of such analysis will be much clearer identification of fault zones, plate thrusts, surface erosion effects, and an improved ability to predict earthquakes. The global climate modeling (GCM) application will combine ocean and atmospheric models simultaneously running in separate supercomputers and continually exchanging boundary data across the CASA network. The resulting concurrent dynamic model will be much more realistic than existing models that use static data for either the ocean or the atmosphere boundary conditions and will be used to predict global change in long-term climate simulations.

Each of the three CASA applications demonstrates a different parallel programming method and different method of hiding the network latency. The chemical reaction dynamics problem mainly relies on data partitioning to achieve a large enough grain size to render the compute/communicate ratio relatively small. It also matches the algorithms in different portions of the application to achieve non-linear speedup. The **CALCRUST** application employs pipelining on a global scale so that round-trip latencies become less important. However, flow control and dataset synchronization also become issues. Finally, the GCM application employs functional decomposition that allows ocean and atmospheric portions to be run concurrently, with intermediate results exchanged periodically. GCM also employs time domain and data domain partitioning to enhance concurrency as well.

These three methods are expected to exhibit different sensitivities to grain size, and accordingly, different network traffic profiles and load balancing issues. For example, with **CALCRUST**, special attention must be paid to flow control, synchronization, dataset granularity, and decreased apparent capacity when two or more streams in the application overlap in a particular link in transit. With the chemical reaction dynamics applications, more frequent data exchanges of shorter packets between hosts may result in more bursty network traffic and possibly stress not the individual link bandwidth, but rather, the efficiency of the routing layers and switches. The GCM will likely exhibit a mixture of these network characteristics.

In conclusion, a key question therefore is: to what extent can high-speed wide area networks contribute to improving our ability to carry out high-performance computing? This project attempts to answer this question and to identify technical solutions that reduce obstacles and bottlenecks caused by the environment, including network protocols, operating systems facilities, and network hardware.

- References:** (1) Messina, P., *CASA Gigabit Network Testbed*, OFC'92, San Jose, Feb 2-7, 1992.  
(2) Messina, P., *CASA Gigabit Testbed: 1993 Annual Report*, Caltech CCSF-33, May 1993.

## **THE BELLCORE RESEARCH NETWORK**

by  
**Peter Kaiser**

**Bellcore  
331 Newman Springs Road  
Red Bank NJ, 07701  
908-758-2969**

### **Abstract**

The Bellcore Research Network (BRN) is a three-node, multi-wavelength network with optical fiber amplifiers (OFAs) interconnecting three major Bellcore Research Laboratories in Red Bank (NVC, South), Piscataway (RRC) and Morristown (MRE, North), New Jersey. The network is serving as a realistic testbed for advanced optical network technologies, SONET/ATM network control and management concepts, as well as for video and data/multi-media services trials, among others. Experience gained with this testbed is intended to accelerate the introduction of advanced optical network technologies and broadband services into the networks of the Bell Operating Companies. It also should accelerate the creation of a national information network infrastructure, and should aid the generic requirements and standards process.

### **Network Architecture**

The BRN has been built with an existing pair of single-mode fibers (SMFs) provided by New Jersey Bell between the ~60 km spaced locations, resulting in a maximum North-South distance of 123 km (Fig. 1). Operation of the conventional, 1310 nm-optimized SMFs in both the 1310 and 1550nm wavelength regions allows an efficient, multi-functional use of the network. The use of two dispersion compensators with Erbium-doped fiber amplifiers (EDFAs) enabled repeaterless, 1550 nm transmission at 2.5 Gb/s over the 123 km distance. The compensators consist of short fiber sections with large negative dispersion and an EDFA to compensate for the losses of the fibers. An additional EDFA was used as line amplifier at the half-way point at RRC. The available loss budget, including the flexible wavelength-division multiplex (WDM) equipment such as splitters and tunable filters, allows the use of up to 4 wavelengths in the 1530 to 1560 nm band (at 2.5 Gb/s). Aside from the 1310/1550nm WDMs, no compensation/amplifier components were included in the 1310 nm path.

In the current configuration, the BRN is used as a 3-node ring network with commercial 622 Mb/s SONET Add-Drop Multiplexers (OC-12 ADMs), and with the ADMs having either 1310 nm (for the shorter distance, 60 km links) or 1550 nm (for the 123 km link) interfaces. The use of two wavelengths on the same fiber pair permits the creation of a logical ring, thus allowing experimentation with more complex network structures. Utilizing a different set of wavelengths in the 1550nm region, a North-South link was also established with 2.5 Gb/s SONET-rate prototype transceivers, logically bypassing the RRC location. As need arises, the 3-node network can be upgraded with OC-48 (2.5Gb/s) ADMs.

### **SONET/ATM Network Control, Management and Operations**

The OC-12 ring network has SONET/ATM interfaces for the interconnection of ATM subnetworks at the three locations containing different types of ATM switches. One of the more important applications of the BRN is the investigation of network control, management and operations issues related to SONET/ATM networking. Work is in progress on the design of a robust network and software architecture for SONET Switched Networks (SSNs) to provide bandwidth on demand. Other work concentrates on prototyping a SONET sub-network controller which monitors and controls the various network elements, and which will provide integrated operations, provisioning, routing and

network management capabilities, in addition to flexible bandwidth allocation. The BRN also enables the study of operations issues associated with new network elements, such as OFA and WDM components.

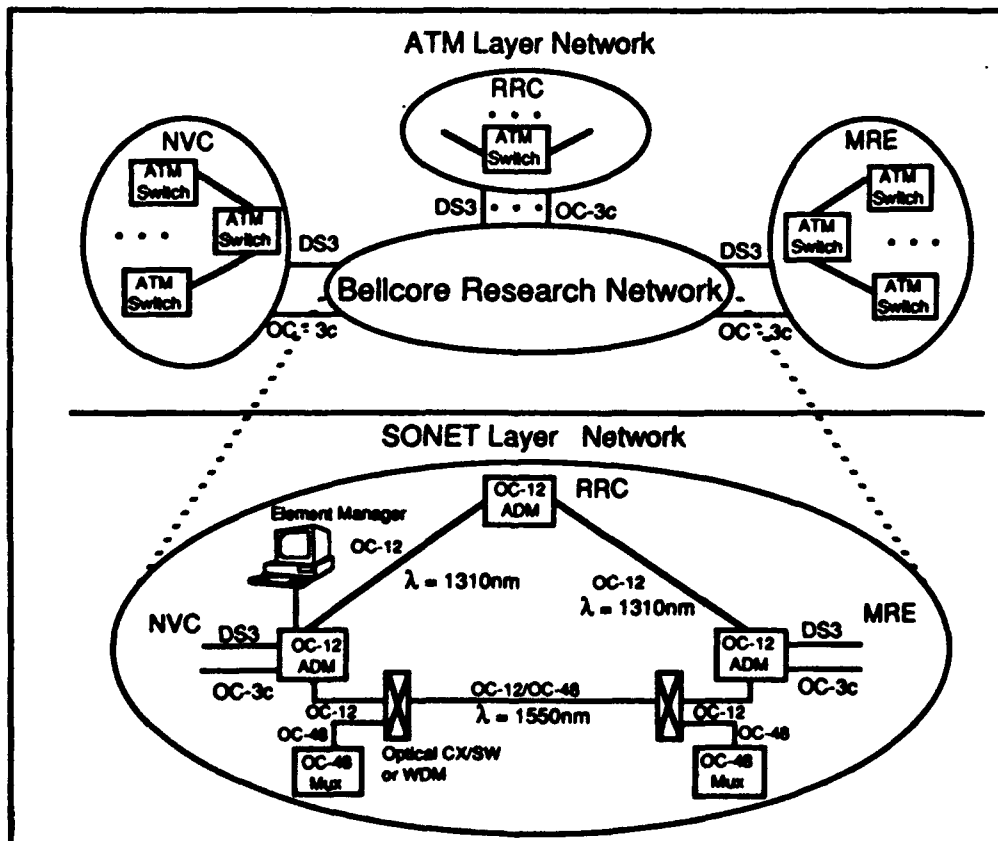
### Service Applications

The BRN is intended for a variety of service trials, including, experimentation with video services (e.g., interactive video services, video-on-demand and distance learning); SMDS applications; remote access to the MRE MASPAR supercomputer and HIPPI LAN; and access to remote databases. The BRN is also intended as a testbed to study the interconnection with different Gigabit Testbeds, including Aurora and Blanca. A variety of interfaces are available to provide connectivity to existing or emerging workstations, supercomputers and CPE equipments. These interfaces include SONET-ATM adaptation layers, SONET-Fiberchannel, HIPPI-on-SONET and HIPPI-ATM-SONET (HAS) interfaces which have been built previously for a variety of applications, including the Carnegie Mellon University Nectar Gigabit Testbed.

In conclusion, the Bellcore Research Network provides a highly flexible platform for research in information network technologies, control & management, and service applications and should help to accelerate the creation of a new national information network infrastructure.

### Acknowledgments

The extensive contributions of many Bellcore researchers to the establishment of the BRN are gratefully acknowledged. Special recognition is due to Chinton Lin, Yukun Tsai and Hossein Izadpanah for coordinating the work associated with the BRN. I would like to thank New Jersey Bell and Bell Atlantic for their cooperation to make specially selected fibers available for research purposes. Finally, I would like to thank Corning, Inc., Alcatel SEL, Fujitsu and AT&T Bell Laboratories for accommodating our special needs for this testbed with equipment prototypes and/or modified commercial equipment.



**W4.1 3:30pm - 4:00pm**

**Gigabit Networking Research at AT&T Bell Laboratories**

*R. Gitlin, AT&T Bell Laboratories, Holmdel, NJ*

We will discuss research in several areas of Broadband ISDN (B-ISDN), with emphasis on the use of the Asynchronous Transfer Mode (ATM) technology to provide a LAN/MAN/WAN infrastructure that supports varied broadband telecommunications services. Specific attention will be given to:

- 1) the design of large gigabit/sec/port/ATM packet switches
- 2) the use of forward error control to improve network performance
- 3) congestion control techniques appropriate for a gigabit/sec WAN

The talk will also describe an AT&T Bell Labs multilocation gigabit research network, LuckyNet, that provides a testbed for research in many aspects of broadband networking (packet switching, network control, protocols, signaling, and applications).

**W4.2 4:00pm - 4:30pm**

**Broadband Services and Their Adoption for Research and Development**

*Y. Lee, Pacific Bell, San Ramon, CA*

In 1993, Pacific Bell announced the implementation of a broadband ATM network in California to serve both the commercial customers and to meet research and education needs. This talk will discuss Pacific Bell's service plans and a program on the data services to encourage innovation in education, medical care and technology development.

## A HIPPI/ATM/SONET Network Interface for the Nectar Gigabit Testbed

K. C. Young, Jr., C. A. Johnston, D. J. Smith, J. W. Mann, J. J. DesMarais,  
M. Z. Iqbal, J. C. Young, K. A. Walsh and W. S. Holden  
Bellcore

445 South Street, Morristown, NJ 07960-6438 USA

### Introduction

This paper describes an experimental prototype of a HIPPI/ATM/SONET (HAS) network interface for the Nectar Gigabit Testbed. The HAS connects High Performance Parallel Interface (HIPPI) local area networks at Carnegie-Mellon University (CMU) and the Pittsburgh Supercomputing Center (PSC) using a high-speed Synchronous Optical Network/Asynchronous Transfer Mode (SONET/ATM) network as shown in Figure 1. [1]

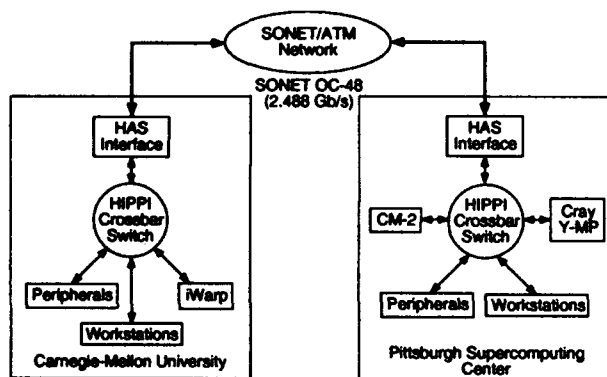


Figure 1 - Nectar Gigabit Testbed

### HAS Description

A block diagram of the HAS showing its four major components is shown in Figure 2. The method

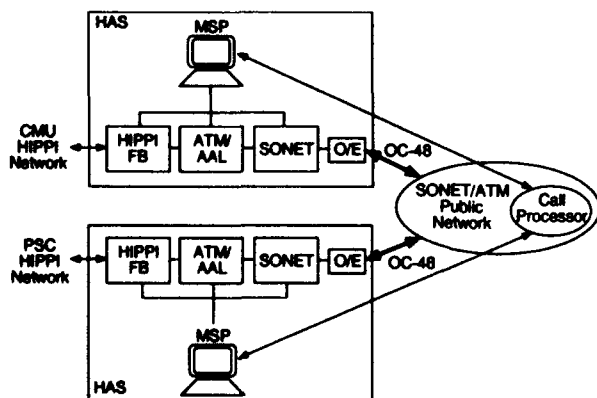


Figure 2 - HAS architecture

selected for carrying HIPPI data over the SONET/ATM network is to terminate the HIPPI protocols

on the transmit HIPPI Fast Buffer (HIPPI FB) module and to reconstruct HIPPI packets on the receive HIPPI FB module. Compared with other approaches, such as encapsulating the HIPPI packets within SONET frames, this approach allows the use of ATM flow and congestion control mechanisms that have been designed for wide-area networks. The approach also allows for sharing of the switched public SONET/ATM network. The function of the HIPPI FB module is to distribute the HIPPI Upper Layer Protocol Data Units (ULPDU) formed by stripping off all HIPPI headers from HIPPI packets, to one STS-3c (155.52 Mb/s) SONET/ATM channel. Up to eight STS-3c channels can be used per HIPPI connection. Both the ATM/AAL and SONET modules are generic, so that they can be used in other applications, such as multimedia.

The ATM/AAL module is responsible for implementing the ATM Adaptation Layer (AAL) and ATM Layer protocols necessary to convert the ULPDUs into ATM cells. [2] The current implementation supports both constant bit rate (CBR - Type 1) and variable bit rate (VBR - Type 3/4) services. Provisions have been made to add the AAL Type 5 protocol in a later version. Protocol processing is performed by separate ATM/AAL transmitter and receiver blocks implemented in field programmable gate array (FPGA) technology. These ATM/AAL transmitter and receiver blocks use separate look-up tables that maintain the mapping between the HIPPI protocol and the ATM/AAL protocols. An embedded processor on the ATM/AAL module creates and updates table entries under control of the Management and Signaling Processor (MSP), whose function is described in more detail below. The ATM/AAL module supports up to 1K virtual circuits.

The ATM/AAL module transfers ATM cells to and from the SONET module. The SONET module consists of separate multiplexing and demultiplexing circuit boards that multiplex sixteen STS-3c channels (eight per 800 Mb/s HIPPI channel) up to the STS-48 rate (2.488 Gb/s) in the transmit direction and demultiplex an STS-48 channel to sixteen STS-3c channels in the receive direction. [3] The SONET module interfaces to an Alcatel OC-48 transmission system that drives the single-mode fi-

ber link connecting the two Nectar sites. [4] The STS-3c framing function on the SONET boards is implemented using FPGAs. The implementation is such that the configuration of the board can be changed from sixteen STS-3c channels to four STS-12c (622.08 Mb/s) channels.

The MSP performs two main functions. It is the agent through which requests for HIPPI connections are used to set up ATM virtual channels between the source and destination HAS. It is also used to monitor the performance of each hardware module of the HAS. The MSP is implemented on a workstation and connects to the HAS hardware, which is contained within a VME card cage. Software running on the MSP was implemented in C++.

The mechanism for setting up connections is as follows. A unique identifier in the ULPGDU transferred from the HIPPI module to the ATM/AAL module indicates a signaling packet. Signaling packets, which contain the source and destination addresses for the requested connection, are directed to the MSP under control of the embedded controller. The format of the information transferred to the MSP allows traffic descriptors and grade-of-service information, as well as other ATM parameters, to be included. Specific VCI/VPI/MID values can also be requested at connection set up time. The MSP then negotiates the connection with a call processor in the network. Connections are negotiated on a per-STS-3c channel basis. Virtual connections can remain open for multiple data packet transfers and provisions have been made to allow data transfer parameters (e. g., VCI/VPI values) to be modified without terminating the call. Either the source or destination HIPPI device can terminate a virtual connection.

The MSP also monitors and reports various error conditions for each of the modules. For example, error signals monitored on the HIPPI module include data parity errors, Length/Longitudinal Redundancy Check (LLRC) word errors and HIPPI sequence number errors. Error signals provided by the ATM/AAL module include cyclical redundancy check (CRC) errors, VCI number rejections, SAR segment type and sequence number errors, and ATM Header Error Check (HEC) errors. The SONET module reports error conditions supported in the SONET overhead bytes including loss of signal and frame, various alarms, and parity errors. Using a graphical interface based on the X-Windows™ system on the MSP allows display of performance data in various forms.

---

™ X-Windows is a trademark of MIT.

## Results

We have successfully demonstrated correct operation of the ATM/AAL and SONET modules and have integrated the two modules to transfer ATM cells across an OC-48 optical link. Logic analyzers were used to inject a variety of ULPGDUs into the transmit side of the ATM/AAL module and to observe incoming ULPGDUs at the receive side of the module in a looped-back configuration. Both signaling and data packets were used during these experiments. Switched virtual circuit set up and tear down operations were also successfully tested.

The ATM/AAL and SONET modules have also been tested individually for performance. Operation of the ATM/AAL module at the required frequency of 19.44 MHz was verified and a maximum frequency of approximately 25 MHz was observed. Correct operation of the SONET module was verified in both STS-3c-to-STS-48 and STS-12c-to-STS-48 modes. The HIPPI transmit and receive circuit boards have been implemented and are currently being tested and integrated with the SONET and ATM/AAL modules.

## Conclusions

We have implemented a HIPPI/ATM/SONET interface that allows HIPPI-based computing resources to communicate over SONET/ATM networks. The HAS experimental prototype serves as a platform to investigate the feasibility of high performance computing using the SONET/ATM public network.

## References

1. N. K. Cheung, "The infrastructure for gigabit computer networks", *IEEE Communications Magazine*, vol. 30, pp. 60-68, April, 1992.
2. C. A. Johnston, K. C. Young, Jr., K. A. Walsh, D. J. Smith and N. K. Cheung, "A programmable ATM/AAL interface for gigabit network applications", *IEEE GLOBECOM '92 Conference Record*, pp. 1191-1195.
3. M. Z. Iqbal, M. Stern, J. Young, H. Izadpanah, R. Standley, O. S. Mia and J. L. Gimlett, "A 2.5 Gb/s SONET datalink with STS-12c inputs and HIPPI interface for gigabit computer networks", *IEEE GLOBECOM '92 Conference Record*, pp. 1106-1200.
4. H. Izadpanah, M. Z. Iqbal, M. Stern, J. L. Gimlett and C. Lin, "An OC-48 SONET optical transmission system for gigabit computer networks", *ICC/Supercomm '92 Conference Record*, pp. 738-742.



## Thursday, July 29, 1993

### **Sessions:**

- T1: New Directions in High Speed  
Networking**
- T2: Internetworking with Asynchronous  
Transfer Mode (ATM)**
- T3: Control and Management of Gigabit  
Networks**
- T4: Technologies for Gigabit Networks I**



**T1.1 8:30am - 9:00am**

**The Evolution of Broadband Networking**

L. Roberts, *NetExpress, Foster City, CA*

Over the past 25 years, packet switching technology has progressed from the original ARPANET to the ATM networks being deployed this year. Over the next decade, there will be a major shift from private to public networks and a major integration of data, voice and video. In examining these trends, the technology issues still remaining will also be addressed.

**T1.2 9:00am - 9:25am**

**ACT NOW – Advanced Communications Technologies for  
New Opportunities in the Workplace**

J. Jacobson, Jet Propulsion Laboratory, Pasadena, CA

ACT NOW is a project to promote the use of advanced communications technologies within the medical, educational, and business arenas. This project could be directed to rebuild the devastated area in Los Angeles after the 1992 civil unrest into a state of the art electronic city that can thrive in the information age.

## **High Speed Networking and the Hughes Network Architecture**

**Robert C. Emmett**

**Hughes Business Communications, Hughes Aircraft Company  
Los Angeles, CA 90009**

Hughes Aircraft Company is a large, decentralized, international high technology manufacturing company in the aerospace, defense and commercial sectors. As the U.S. defense spending began to decline in the later 1980s and early 1990, Hughes began to turn towards more commercial interests. At the same time, the Company's business environment was rapidly refocusing to produce more cost effective products and services and expand more into global markets. This rapid evolution included downsizing, organizational realignment and streamlining and a thorough re-engineering of business, engineering and manufacturing processes.

Early on, information technology was recognized as a key factor in accomplishing the Company's goals. Over the past three years, Hughes has progressively defined formal, enterprise-wide architectures for networking, client-server applications and information systems. In a 1991 survey, the data communications infrastructure of the Company was identified as a bottleneck in the successful deployment of these information architectures.

To avoid this condition, Hughes developed the Hughes Enterprise Network Architecture (ENA). The ENA converges the Company's diverse networks around strategic technologies and standards-based transport protocols, applications programming interfaces and management systems. The ENA was adopted as policy in 1992 and is in the process of being deployed, on an as-needed basis, throughout the Company.

The ENA focuses on three, broad elements of networking:

- Physical
- Logical
- Management

The ENA's physical architecture defines wiring standards, network topology, the use of routers and cell switches and the target end system interfaces of Ethernet, dedicated Ethernet and STS-3/TAXI.

The general plan is to reduce a very complex hierarchy of routed Ethernet segments to a two layer hierarchy of: 1) primarily Ethernet interfaces connected to multiprotocol routing hubs, and 2) campus and wide area backbones of asynchronous transfer mode (ATM) cell switches.

The logical architecture extends those ISO layers usually thought of as "network" to include from layer 1 into layer 6 (Presentation). The core of the logical architecture is the convergence on two transport protocol suites: DARPA's TCP/IP and OSI. All other transport protocols are being decommissioned or converted to TCP/IP or OSI. At higher layers, company standard applications programming interfaces and technologies are identified, including POSIX 1003.2, MOTIF X/11, OSF DCE RPC, X.500, and OMG CORBA.

The company's vision of the future includes an environment where information flows freely to all employees and is shared, as appropriate, with suppliers, customers and external organizations. A person's geographic location should not affect their access to information. The network must enable interoperability among applications and must be ubiquitous, fast, scalable, reliable and cost-effective. The aggregate capacity of Hughes' networks must increase by an order of magnitude, not just because of increases in processor power, but also because that power makes vastly more useful applications possible. In effect, the network becomes the backplane of a massively parallel computer.

The way Hughes will achieve this is through broadband, backbone technologies such as ATM that can support all types of digital traffic and can operate seamlessly across public and private networks. The bursty, connectionless nature of the most important types of data traffic requires a public, high performance infrastructure so that aggregated peak traffic can be transported at high speed without having to reserve peak bandwidth around the clock.

**T1.4 9:50am - 10:15am**

**Who Needs Broadband Services and Why?**

*S. Klux, Lawrence Livermore Laboratory, Livermore, CA*

The decade of the 1990s will see the beginning of deployment of broadband services to millions of customers around the world using some of the networking techniques developed in the 1980s. This paper contemplates potential broadband applications, likely beneficiaries of these services and related issues.

## **Unshielded and Shielded Twisted Pair Copper Wire Access Technologies for High Performance Local Area Networks**

**W. E. Stephens  
Bellcore  
445 South Street  
Morristown, N. J. 07960-6438**

There is a growing demand for transmission of digital data over distances of 10 to 400 meters at rates up to 194 Mbit/sec in high performance local area networks and in future subscriber loops. Although optical fiber is the preferred medium because of its greater bandwidth and noise immunity, a low-cost and reliable transmission link using unshielded or even shielded twisted pair could be more desirable in many local area networks and subscriber loop applications due to the large embedded base of copper and the cost that would have to be incurred to replace that medium. According to a study by Forrester Research, Inc.,<sup>[1]</sup> the present installed base in intra-building wiring consists primarily of unshielded twisted pair (63 percent), shielded twisted pair (25 percent) and coaxial cable (8 percent) supporting telephony and low-to-medium speed data networking applications. Presently, the installed base of optical fiber for LANs (primarily FDDI) is approximately 4 percent and is not expected to grow quickly.<sup>[1]</sup>

Voice grade unshielded twisted pair (UTP) such as Distributed Internal Wiring (DWI) and TIA/EIA Category 3 are the most popular of the wiring types and are used to support both data and voice using standard building practice.<sup>[2][3][4]</sup> For some high speed data networks, data-grade wiring (TIA/EIA Category 5<sup>[2][3]</sup>) is being installed but at present the installed base is small due to the newness of the standard defining Category 5. Coaxial cable and shielded twisted pair has been installed to support Systems Network Architecture (SNA), Token Ring and Ethernet Local Area Networks (LANs). For high performance LANs to see widespread use, it is necessary to make use of the existing copper plant.

High-speed transmission over the intra-building copper plant is a challenge due to conflicting requirements of achieving a low bit-error-rate ( $10^{-11}$  or better) and meeting emissions and susceptibility requirements specified by FCC Part 15 Subpart J.<sup>[5]</sup> This challenge is further aggravated by the fact that the present installed base of building wiring systems uses cable bundles (4 wire pairs and 25 wire pairs) and the data signals traverse punch-down blocks, jacks, connectors, wire gauge changes and numerous splices. These systems have problems with Near-End and Far-End Cross Talk (NEXT, FEXT) from other pairs in the cable and electromagnetic emissions that come from common-mode signal conversion at discontinuities in that signal path.

Several approaches for using the various grades of copper wiring have been proposed as contributions for standards at the ATM Forum, ANSI X3T9.5, EIA/TIA and elsewhere. These proposals incorporate different techniques (analog and/or digital signal processing) to shape the data signal transmit power spectrum, and to equalize the received signal to compensate for variable cable attenuation and cross talk impairments.<sup>[6]</sup> The major proposals are summarized in Table 1.

This paper will review the current status of a series of draft standards and proposals for high-speed data transmission over the intra-building copper plant and discuss some of the recent experimental results.

## REFERENCES

- [1] P. D. Callahan, M. A. Modahl, "The Right Wire," The Network Strategy Report, Forrester Research Inc., Vol. 6., No. 4, March, 1992, pp. 2-13.
- [2] ANSI/EIA/TIA-568-1991, "Commercial Building Telecommunications Wiring Standard", July 1991.
- [3] EIA/TIA Technical Systems Bulletin #36, "Additional Cable Specifications for Unshielded Twisted Pair Cables", November 1991.
- [4] About 30 percent of the new drop cable is comparable to Category 3 wiring.
- [5] *Federal Communication Commission Rules (FCC)*, Part 15, Subpart J.
- [6] W. E. Stephens, T. C. Banwell, G. R. Lalk, T. J. Robe, and K. C. Young, "Transmission of STS-3c (155 Mbit/sec) SONET/ATM Signals over Unshielded and Shielded Twisted Pair Copper Wire," IEEE GLOBECOM'92, December 6-9, 1992, vol. 1, pp. 170-174.

**Table 1: Some Approaches to High Speed Transmission of Data over Copper**

Line Code	Complexity	Data Rate	Wiring Type	EMC/I (to date)	Comments
NRZI	Low	25.6 to 194 Mb/s	Category 5, Also Shielded TP	Under test	UTP proposal, in ATM Forum Document for STP
MLT-3	Medium	125 to 155 Mb/s	Category 5	Under test	2 dB penalty compared to NRZI
PR-4	Medium	125 to 155 Mb/s	Category 5	Under test	2 dB penalty compared to NRZI
2B1Q	Medium	155 Mb/s	Category 5		
QPR IV	High	125 to 155 Mb/s	Category 3		Uses Digital Signal Processing
16-CAP	High	51 Mb/s	Category 3	Cutoff below FCC Requirements	Uses Digital Signal Processing
32-CAP	High	125 Mb/s	Category 5	Cutoff below FCC Requirements	Uses Digital Signal Processing
64-CAP	High	155 Mb/s	Category 5	Cutoff below FCC Requirements	Uses Digital Signal Processing
DMT	High	6 Mb/s	Telco Loop Plant	Cutoff below FCC Requirements	Uses Digital Signal Processing

**T2.3 11:20am - 11:40am**

**Afterburner: Application-to-Application Networking at Hundreds of Mbit/s**

**Greg Watson**

**Hewlett-Packard Laboratories,  
Filton Rd, Stoke Gifford,  
Bristol BS12 6QZ, U.K.  
gcaw@hplb.hpl.hp.com**

Many researchers have observed that while the link level rates of some networks are now in the Gbit/s range, the effective throughput between remote applications is usually an order of magnitude less. Although a number of components within computing systems have been postulated as the cause of this imbalance, it is now widely recognised that network protocols are not to blame, although poor implementations of protocols such as TCP/IP may limit performance.

One reason many implementations fail to achieve high throughput is that they access user data several times between the instant the data are generated and the instant the data are transmitted on the network. A widely-used protocol stack consists of the Socket protocol, TCP, and IP, together with a low-level driver that manages the network hardware. When an application makes a call to send some data the Socket protocol first copies the data from the application buffer into a new buffer in memory. This copy is made so that the application can continue immediately without waiting until the data is actually sent. The TCP protocol then reads every word of data again in order to calculate a checksum value. When a complete packet has been assembled the driver is called which copies the packet from main memory to a buffer in the network card. Consequently every byte of user data is read three times and written twice.

In 1990 Van Jacobson described how a very simple network card could support a single-copy protocol stack [1]. The main requirement is that the network card contains enough buffer memory to store the outbound and inbound packets while they are processed by the various protocols. The network buffer appears to the processor as main memory and so the protocols are executed on the workstation; the network card does not have its own processor.

In 1991/92 a group at HP Labs, UK, built the Medusa FDDI network card which was based on many of Jacobson's ideas [2]. The Medusa card, together with a single-copy implementation of the protocols, enabled an HP 720 workstation to use the entire 100 Mbit/s bandwidth of FDDI.

In 1992 we decided to exploit what we learned from Medusa to develop an experimental network card which would support link rates up to 1 Gbit/s. While FDDI was the obvious choice for a 100 Mbit/s LAN, there was no obvious candidate for a 1 Gbit/s LAN. Consequently our 1 Gbit/s card, called Afterburner, provides a very simple and generic physical interface which consists of two high speed FIFOs. A 'link adapter' card is then plugged into this interface to provide the physical and MAC layers of any specific network such as ATM or FibreChannel. Figure 1 shows how Afterburner is combined with a link adapter.

The operation of Afterburner is very simple. On transmit, the Socket protocol acquires a buffer on the Afterburner card and copies the application data from the application's buffer to the buffer on Afterburner. During the copy the TCP checksum is calculated by hardware on the card.

The Socket protocol then calls TCP which builds a protocol header in a separate Afterburner buffer, and inserts the TCP checksum into the header. IP adds its own header to the TCP header and calls the driver. The driver then writes the address of each buffer to the buffer controller hardware on the card, and this in turn transmits the buffers.

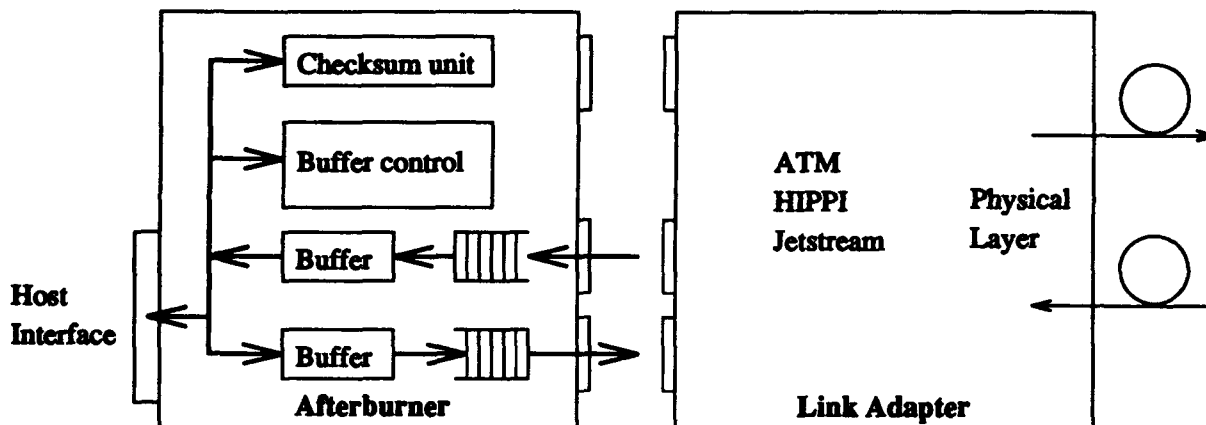


Figure 1. Afterburner is used in conjunction with a Link Adapter card.

On the receive side the link adapter passes incoming packets to Afterburner, which stores the packets in empty buffers. When the link adapter signals that a complete packet has been received, the Afterburner card then interrupts the host. The IP and TCP protocols check the newly arrived packet, and the Socket protocol then copies the packet data from the Afterburner buffers to the application's buffers.

A number of modifications must be made to the protocols in order to achieve a single copy. Details of the Afterburner card and its associated software can be found in [3].

We have measured the performance of two Afterburners connected back-to-back via ribbon cables. A source application repeatedly sends the same data to a destination application which consumes the data without looking at it. The experiment uses HP 730 workstations with the HP-UX 8.07 operating system. Our single-copy implementation of TCP uses RFC 1323 window scaling and the Socket protocol has 192 KByte buffers. The source repeatedly sends 4 KByte units and Afterburner uses 16 KByte buffers. The peak measured throughput is 25MByte/s (210 Mbit/s).

- [1] Van Jacobson, "Efficient Protocol Implementation", ACM SIGCOMM '90 Tutorial, September 1990.
- [2] D. Banks, M. Prudence, "A High Performance Network Architecture for a PA-RISC Workstation", *IEEE Jnl. Sel. Areas in Comms*, Vol. 11, No. 2, Feb 1993.
- [3] C. Dalton, *et al*, "Afterburner: Architectural Support for High Performance Protocols", *IEEE Network magazine*, July 1993.

## Towards Interoperability of ATM Public and Private Networks

S. Bajaj, C. Brazdziunas, T. Robe, W. Stephens, F. Vakil  
Bellcore, 445 South Street, New Jersey 07960-6438

Asynchronous transfer mode (ATM) is expected to be the global standard for data multiplexing and switching. It is hoped that connectivity between private ATM LANs and an ubiquitous public ATM network can be accomplished without the need for internetworking units that perform bridging and protocol conversion. Presently, this is not achievable due to physical and data layer incompatibilities. In this paper, we present the first step towards achieving the goal of seamless connectivity. We discuss an experimental network which supports MPEG-1 video and IP-traffic over a heterogeneous transport platform consisting of 4B/5B block encoded transport (similar to that used in FDDI) and SONET. We believe that this is the first demonstration of interoperability between a SONET public network element and a private ATM LAN.

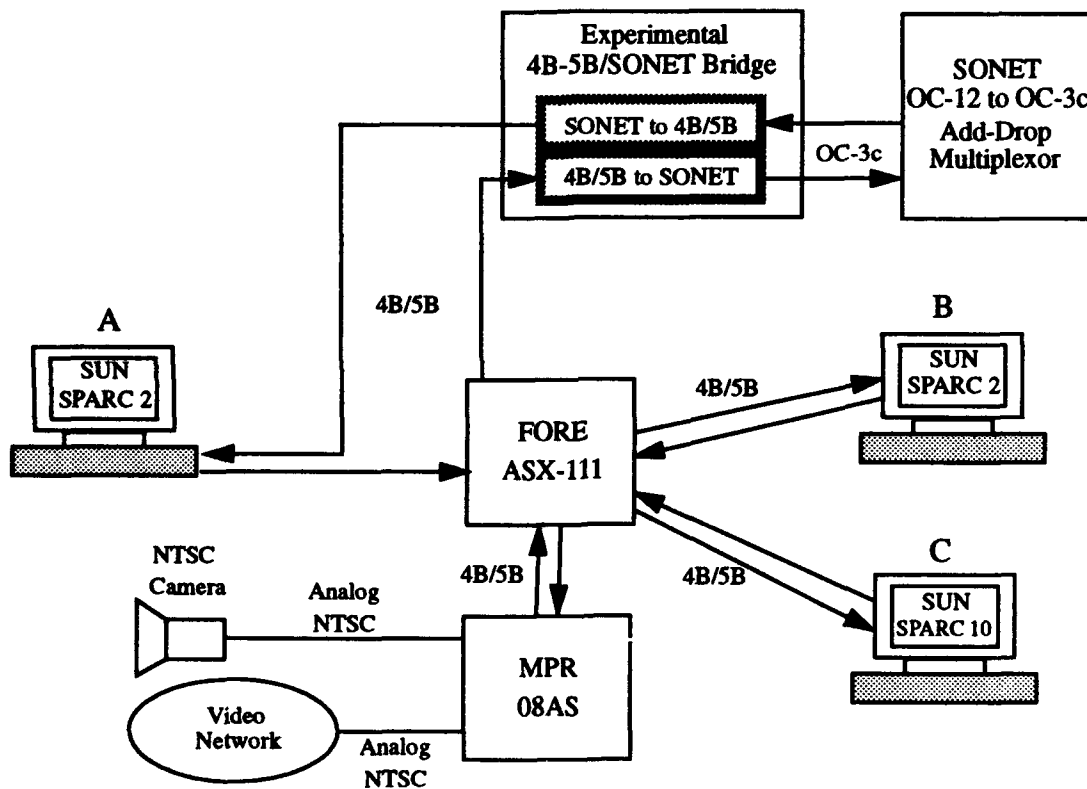


**Figure 1: Interoperability Testbed**

The topology of the ATM network is shown in Figure 1. Three Sun workstations are connected to a FORE Systems ASX-111 ATM switch via FORE Systems SBA-100 network interface cards [2]. The FORE switch can support up to 16 I/O ports via a 2.4 Gbps parallel bus. The physical layer interface used is 175 Mbps 4B/5B transmission. A commercial SONET OC-12 to OC-3c add-drop multiplexor is connected to workstation A and the FORE switch via a prototype 4B-5B/SONET bridge built by Bellcore [1]. This bridge performs the necessary physical layer conversion from 4B/5B block encoding to SONET OC-3c (155 Mbps) and vice-versa. As shown in the figure, all traffic received by workstation A passes through the bridge and multiplexor. Therefore,

this data undergoes numerous conversions: from 4B/5B to SONET OC-3c, from OC-3c to OC-12 and back to OC-3c within the multiplexor, and finally back to 4B/5B from OC-3c. Of the three attached workstations in the network, workstation C performs multiple roles. It acts as the controller for the ATM switch, a network file server for the other two workstations, and finally as a router from this ATM network to our internal corporate network.

The above network topology can be segmented into public and private network components. The workstations with the switch represent a private LAN while the multiplexor (together with bridge) represent the public network component. Not only are the framing protocols being converted but also the physical media itself. The workstation adapters and the switch use FDDI-compatible 1300-nanometer multimode fiber while the connections to the multiplexor require 1300-nanometer single mode fiber. Thus, the bridge is required to support multiple physical media. This is an important consideration because most public ATM equipment supports single-mode optics. To further simulate a public-private network division, optical attenuators are placed between the connections to the multiplexor to simulate the potential effect of having long physical lines between the two networks.

This ATM LAN provides a functional working environment. The Internet Protocol (IP) is used so such network applications as NFS and NIS are supported unaltered. Furthermore, we have demonstrated the transmission of MPEG-1 video using the X-protocol across the network. TCP/IP application throughputs of 20 to 25 Mbps have been achieved with the bottleneck residing primarily in the TCP implementation on the workstations. No transmission errors have been witnessed which would result in TCP retransmissions and lower measured throughput. Using a commercial ATM/SONET analyzer, we have loaded the network to the maximum block encoded data rate of 134.91 Mbps and witnessed no errors over a 12 hour period.

In a separate experiment, we also demonstrated a "circuit emulation" capability on the testbed with the transport of 85 Mbps NTSC video. An MPR Teltech 08A5 ATM switch with an NTSC line card was connected to our network [3]. An NTSC video camera is connected to this switch and digitized video was routed from the MPR switch, through our network, back into the MPR switch and into a Bellcore experimental video conferencing network. For synchronization and cell loss recovery, an AAL-1 like adaption layer is used by MPR. In this configuration, no cell loss was detected.

This prototype network is an initial demonstration of public-private network interworking. The focus is directed primarily on the physical layer. Once the issues of physical interconnectivity are resolved, a great deal of work remains to be done to ensure interoperability. The issues of network and traffic management, addressing, and routing will then assume a heightened importance.

The reference to any company or product name is for illustrative purposes only and is not intended as a recommendation by Bellcore of that company or product.

## References

- 1) T. Robe, T. Banwell, J. Hodge, J. Mann, and W. Stephens, "A 4B/5B Block Code to SONET OC-3 (155Mb/s) Interface for ATM Local Area Networks," OFC/IOOC' 93 Technical Digest, Vol 4, paper WJ3, p. 148.
- 2) FORE Systems, Inc., *ATM ASX Switch Documentation / SBA-100 SBus ATM Computer Interface Release 2.1.0*, 1993.
- 3) MPR Teltech Ltd., *ATMNET User's Manual*, 1992.

## Multidisciplinary Engine Simulations at the NASA Lewis Research Center

Gregory J. Follen  
NASA Lewis Research Center  
Interdisciplinary Technology Office  
M.S. 142-5  
Cleveland, Ohio 44135

The Numerical Propulsion System Simulation is a program focused on reducing the cost and time in developing aeropropulsion engines by addressing the multidisciplinary nature of this problem early on and by applying new computer hardware and software techniques into this process. Together with NPSS's Industrial partners and Universities, the program has established short term milestones designed to guide the progress of integrating the disciplines, components, high performance computing and advanced networks into a dynamic and flexible simulation environment.

Simulations and in particular a Simulation Environment for the development of engines prior to the building of the actual hardware is the means by which the NPSS project intends to reduce the time and cost of building new engines. The environment allows flexible simulations of varying levels of complexity that the engineer chooses in real time. NPSS calls this function "Zooming". Figure 1 describes the various levels of model fidelity within NPSS.

Lewis's NPSS project is building a simulation environment that provides a generic 1D component view of an aeropropulsion engine. The environment allows the engineer to Zoom to finer levels of fidelity on a component specific basis while operating at the 1D view of the engine. Currently Lewis is using AVS as the visual simulation environment along with object oriented techniques to numerically assemble component codes into a complete engine simulation. Figure 2 illustrates a component 1D view of the F100 engine. The component codes can be assembled independent of computer architecture and location into a numerical engine. Up to this point, flexibility of the NPSS environment has been described. The natural follow on is to tune the simulation for speed.

By today's standards, the limitations the NPSS project is faced with is that "real time" simulations can not be achieved. Only really "realistic time" simulations are possible. In particular, if and when "real time" can be achieved, the simulation is limited to one physical location. Although, NPSS has allowed industry to do simulations that could not be done before. The next step in numerical engine simulations is to bring the solution time down into the "real time" domain and not constrain these simulations to one location. For this to occur, engine codes need porting to massively parallel machines, Object Oriented design needs to be employed for data and code management and Gigabit networks need to be introduced to connect this architecture together. In the NPSS design, simulations are comprised of codes that execute on different architectures in different parts of the United States. The NPSS environment provides the proper structure for the engine companies to maintain their competitive advantages while accessing machines or codes that the government can provide. However, the real time constraint still exists for these simulations.

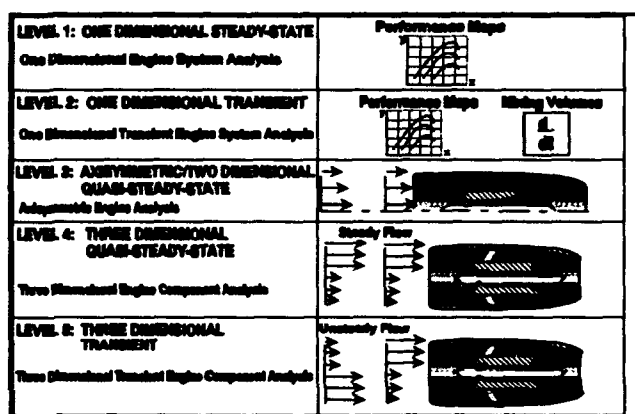
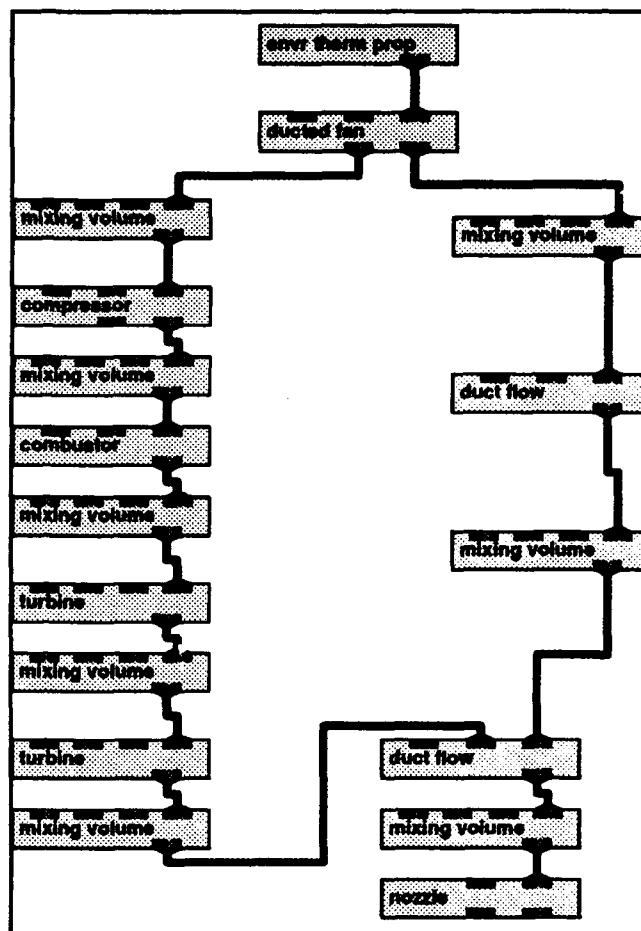


Figure 1 NPSS Levels

The NPSS project will initiate an effort in the summer of FY 93 that involves the use of ATM switches on UNIX workstations to see if this technology can be used for real time 1D engine simulations using the AVS model of the F100 engine defined in Figure 2. Although the 1D model does not involve moving large amounts data throughout the component codes, the real issue here is Zooming to a level IV analysis of the Fan or the Compressor code. The Fan or Compressor codes could be executing on local or remote machines. The Level IV analysis codes create megabytes of data that will need to be visualized and at the same time reduced back to a 1D view for integration into the 1D engine model.

In conclusion, the NPSS project will build an engine simulation environment that provides the engineer the ability to assemble flexible and dynamic real time simulations by accessing Massively Parallel architectures, following Object Oriented Design principles and employing Gigabit networks.



**Figure 2** AVS Network of F100 Engine

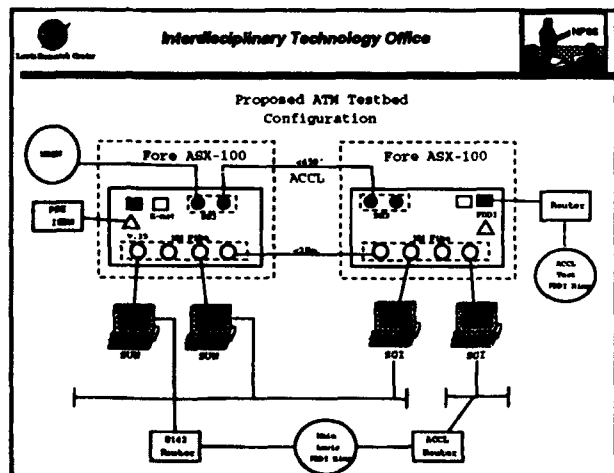


**Figure 3** ATM Configuration

## Performance Barriers to High Speed Networks

By

A. Mink, Y. Fouquet, S. Wakid

Advanced Systems Division

National Institute of Standards and Technology

Data transfer via TCP/IP over both an Ethernet (10 Mbit/sec) and a HIPPI (800 Mbit/sec) LAN is analyzed with the help of the NIST MultiKron\*\* [1] low perturbation data collection hardware. These accurate measurements provide a good understanding of the protocol bottlenecks which limit the realization of the underlying channel bandwidth. For the purpose of these experiments, a UNIX\* operating system was chosen with a typical implementation of TCP/IP in its kernel. The only modification done to this commercially available kernel was to add the measurement probe code necessary to interface to the memory mapped MultiKron. Each measurement probe consists of only a single assignment statement.

Our traffic model is a large amount of data transmitted in one direction over a high speed channel, with only acknowledgements returning. We simulated this environment using the program outlined in Figure 1 to transfer 85 files of image data totalling about 15 Mbytes. Figure 2 shows the measured communication throughput delivered to the application over both Ethernet and HIPPI networks. We then measured the execution time of the TCP/IP protocol in the operating system kernel, to determine why no significant increase in throughput was obtained over the faster HIPPI network. These measurements are presented in Table 1 and indicate that protocol processing on our workstations is substantially slower than the 10 Mbits/s Ethernet and thus cannot obtain any benefit from a faster network such as HIPPI. When communicating between a supercomputer, running a similar version of UNIX and TCP/IP, and a workstation, the slight increase in throughput obtained is due solely to the increase in instruction execution rates of the supercomputer. These measurements clearly show that the majority of the processing time for this implementation of the protocol is concerned with checksumming and data management. This substantiates the TCP/IP analysis performed by Clark, et. al. [2] stating that the processing bottleneck in TCP/IP is due to the overhead of the implementation, not the protocol itself. Recently Jacobson [3] reported a new implementation of TCP/IP that is extremely efficient and whose performance is only limited by the processor-memory bandwidth.

## REFERENCES

- [1] Mink, A., and Carpenter, R., "Operating Principles of MultiKron Performance Instrumentation for MIMD Computers", National Institute of Standards and Technology, NISTIR 4737, Mar. 1992.
- [2] Clark, D., Jacobson, V., Romkey, J., and Salwen, H. "An Analysis of TCP Processing Overhead", IEEE Communications Magazine, Vol. 27, No. 6, June 1989, pp. 23-29.
- [3] Jacobson, V., "A High Performance TCP/IP Implementation", presentation at NRI Gigabit TCP Workshop, Reston, Va., Mar. 1993.

---

\* UNIX is a trademark of AT&T.

\*\*MultiKron is a trademark of NIST.

This National Institute of Standards and Technology contribution is not subject to copyright in the United States. Certain commercial equipment, instruments, or materials may be identified in this paper to adequately specify experimental procedures. Such identification does not imply recommendation or endorsement by the National Institute of Standards and Technology, nor does it imply that materials or equipment identified are necessarily the best available for the purpose.

This work was partially sponsored by the Advanced Research Projects Agency.

	Sending			Receiving		
	Time (us)	Data % of layer	Ack Time (us) % of layer	Time (us)	Data % of layer	Ack Time (us) % of layer
Kernel Supervisory call/rtn overhead	68.9	100%		68.9	100%	
Socket Layer	158	100%		97.8	100%	
-socket processing	8.8		5.6			
-data handling buffer mgt	136	86.4		93.3	95.4	
-enqueue/dequeue socket queue	12.8	8.0		4.5	4.6	
TCP Layer:	176	100%	40.5	117.9	100%	85.0
-TCP processing	1.4	0.8	19.9	34.6	29.4	63.0
-checksumming	72.5	41.2	5.8	14.3	68.4	7.2
-allocate & link in data header	87.2	49.6				
-fill in & process header	14.8	8.4	14.8	36.6	14.9	12.6
IP Layer	20.4	100%	20.7	100%	100%	15.6
-IP processing	7.7	37.7	9.9	47.8	16.2	81
-checksumming	4.3	21.1	4.1	19.8	1.8	9
-routing	8.4	41.2	6.7	32.4	2.0	10
Device Driver Layer	87.1	100%	68.6	100%	100%	84.8
-processing	8.8	10.1	10.8	15.8	20.0	23.2
-queuing dequeuing	16.7	19.2	16.6	24.2	18.6	21.5
-data handling	58.6	67.3	38.7	56.4	35.7	41.5
-device handling	3.0	3.4	2.5	3.6	11.9	13.8
Layer Totals	510.4		129.8	390.8		185.4

Table 1. Execution time measurements of the TCP/IP protocol layers. All measurements are averages with approximately a 10 % variation.

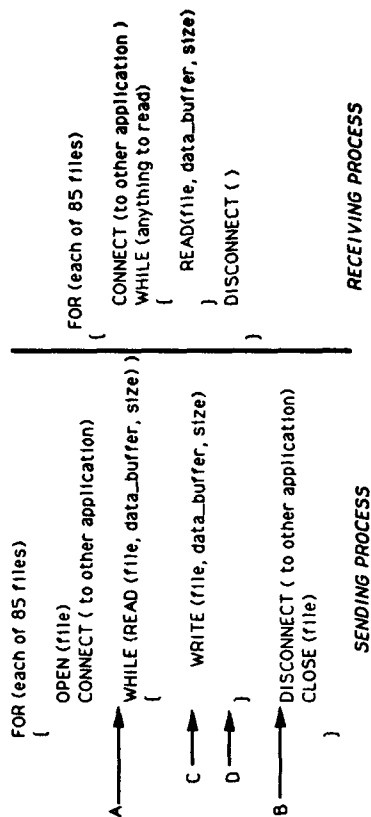


Fig 1. Measured Application

Application	Buffer Size (bytes)	Interval [A-B]	Interval [C-D]	Interval [A-B]	Interval [C-D]
Ethernet Workstation to Workstation	1460	3.87	4.19	4.09	3.87
HIPPI Workstation to Workstation	462	4.66	4.97	4.39	4.34
HIPPI Supercomputer to Workstation	15.4	6.42	6.01	5.25	5.28
	17.3	15.2	15.5	14.9	16.1
					16.5

Fig 2. Effective Data Rate (Mbits/s) to the Application

## Can Shannon Coding Theorem Play a Role in ATM Traffic Management?

Faramak Vakil  
 Bellcore  
 Room 2M-187  
 Morristown, NJ 07960-6438

ATM networks are expected to support applications that have widely diverse statistical behaviors and quality of service requirements. Such diversity of applications could significantly complicate the resource allocation and traffic management tasks of an ATM network. A key challenge in the ultimate success of ATM in a gigabit environment is to define and implement a resource allocation and traffic control strategy that provides for an efficient sharing of network resources among different services. The challenge stems from the fact that different services and applications of an ATM network have widely diverse statistical behaviors and quality of service (QOS) requirements. A fundamental issue is how an ATM network estimates the amount of capacity required for a virtual channel (VC) that supports an application whose traffic descriptor<sup>1</sup> and quality of service (QOS) requirements are given. This is a key issue in the implementation of ATM networks because the capacity allocation rule of a network affects its tariff structures, service provisioning, admission control, routing, and flow control strategies.

We pursue a fundamentally different approach for deriving a traffic management scheme for ATM networks. Unlike the conventional approaches which are primarily based on queueing theory, the theoretical underpinning of this approach is based on information theory. It views an ATM network as a digital transport system which transmits cells instead of bits and models traffic management of ATM networks as a "coding" problem where resource allocation is analogous to source coding and congestion/error control is analogous to the channel coding. The strength of this approach is that it uses the basic results of information theory to derive a set of fundamental requirements for ATM traffic management. It uses the Shannon noiseless coding theorem to derive a resource allocation rule, and uses the converse to the coding theorem to propose a congestion control scheme for ATM networks. The resulting traffic management strategy enables an ATM network to achieve statistical multiplexing gain and provide "guaranteed" QOS for its applications.

An essential element of a traffic management scheme is its capacity allocation rule which uses the traffic descriptor of an application to determine its equivalent capacity. The equivalent capacity of an application is the cell rate which should be transmitted over an ATM virtual channel so that the receiver is able to recover the source cell stream within a predetermined QOS requirements. Apart from the fact that the basic unit of information is a cell instead of a bit, the estimation of the equivalent capacity of an ATM application is similar to the source coding problem in digital communications. We model the output cell stream of an ATM application as a point process source, and use the Shannon noiseless coding theorem and entropy rate of point processes to show that the equivalent capacity of an application,  $C$ , is given by:

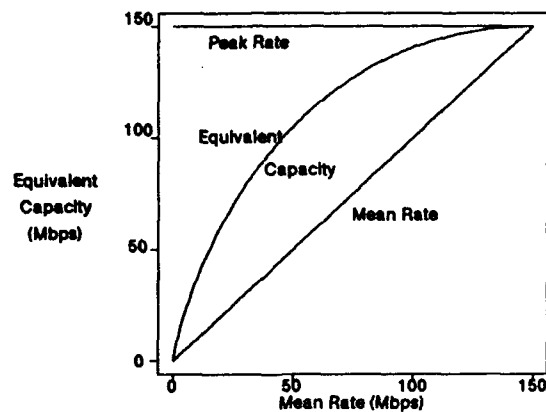
$$C = R_a(1 - \text{Log}(R_a/R_p)) \quad , \quad (1)$$

where  $R_p$  is the peak rate of the application and  $R_a$  is its mean rate. It is worth noting that  $R_a \leq C \leq R_p$ , and  $C$  is an increasing function of  $R_p$  and  $R_a$  because

$$\frac{\partial C}{\partial R_p} = \frac{R_a}{R_p} \geq 0, \quad \text{and} \quad \frac{\partial C}{\partial R_a} = \text{Log}(R_p/R_a) \geq 0 \quad . \quad (2)$$

1. The traffic descriptor of an application refers to a set of parameters that characterize its traffic. Such parameters may include the peak and average bit rates, ..., etc.

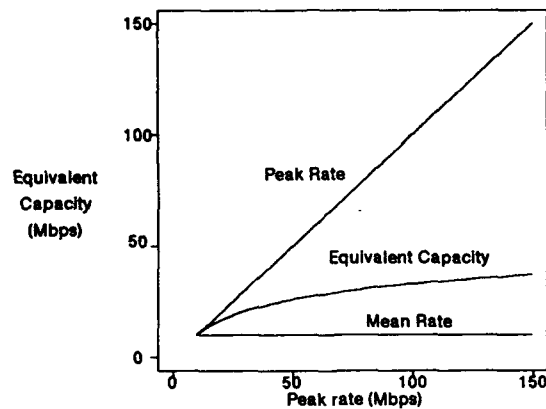
For instance, **Figure 1** illustrates the equivalent capacity of an application whose peak rate is 150 Mbps, and its mean rate varies in the range of 0 to 150 Mbps.



Peak rate = 150 Mbps

**Figure 1.** Impact of mean rate on equivalent capacity

While **Figure 2** shows the equivalent capacity of a source whose mean rate is 10 Mbps, and its peak rate varies in the range of 10 to 150 Mbps.



Mean rate = 10 Mbps

**Figure 2.** Impact of peak rate on equivalent capacity

The rule shows that the equivalent capacity of an application only depends on its mean rate and peak rate. Interesting observations about the rule are that i): the equivalent capacity is linearly dependent on the logarithm of the burstiness<sup>2</sup> of the application, and ii): the rule favors multiplexing of multimedia applications at the higher layers. The performance analysis of a network node that operates according to the capacity allocation rule and supports identical bursty sources indicates that the node satisfies the QOS requirements of stringent bursty applications. we will describe in the talk an admission control scheme for ATM networks to illustrate the simplicity of the multi-rate "circuit switched" approach and the role of equivalent capacity in it.

2. Burstiness of an application is defined as the ratio of its peak rate to its mean rate.

## On Protective Buffer Policies

Israel Cidon\*

Department of Electrical Engineering  
Technion, Haifa 32000, Israel

Roch Guérin

IBM T.J. Watson Research Center  
Yorktown Heights, NY 10598

Asad Khamisy†

Department of Electrical Engineering  
Technion, Haifa 32000, Israel

### EXTENDED ABSTRACT:

This paper (see [1] for details) is concerned with the study of buffering policies that arise in the context of fast packet-switched networks carrying different classes of traffic. These networks are faced with the difficult task of satisfying the needs of connections requiring different Qualities Of Service (QOS), but sharing the same physical resources, e.g., bandwidth and buffers. Here, we focus on space priority disciplines, which provide different loss priorities to packets as a function of their service class.

Specifically, the system under consideration is that of a buffer shared by high and low priority packets, and where the task of the buffering policy is to ensure an acceptable performance to the high priority packets with no change in packet delivery ordering. The main issue being investigated is the performance degradation experienced by high priority packets, in case of excessive low priority traffic. That is, we are interested in buffering policies that can guarantee performance, i.e., loss probability, to high priority packets, *irrespective* of the traffic intensity and arrival patterns of low priority packets, while preserving the original ordering among packets. The goals are to identify and evaluate such policies, while assessing the *cost* of this protection to low priority packets, i.e., what is the associated increase in loss probability. Such policies are motivated by the possible presence within the same connection of packets with different loss probability guarantees/requirements. Therefore, the selective discarding (in case of congestion) of lower priority packets must be done while maintaining in sequence delivery.

In particular, it is desirable to identify buffer admission policies, which can guarantee the loss probability of high priority packets with minimal or no assumptions on the arrival patterns of low priority ones. We term

such policies *protective*. The need for such policies is motivated by the difficulty to characterize or even size low priority traffic, which is often subject to large and unpredictable variations. For example, a change to a high motion scene may significantly increase the output rate of a video coder over an extended period of time, or a rate-controlled data user may suddenly send a large amount of tagged packets because of the transfer of a large file.

The goal is, therefore, first to define the performance guarantees that protective policies provide to high priority packets, and then identify policies which meet these requirements. In particular, it is of interest to determine which, if any, of the previously proposed buffer admission policies can provide such guarantees. In addition, it is desirable to achieve protection of high priority traffic, while dropping the fewest low priority packets. For this purpose, it is useful to evaluate for each policy the impact of protection on low priority traffic, and use this information to devise better policies that for a given level of protection maximize the low priority throughput.

First, we examine three well known policies which were all proposed for the tasks of discrimination and protection, and we demonstrate that even though all of them are intuitively quite reasonable they do not always provide the level of protection required. For purposes of notation, we denote high-priority packets as green and low priority ones as red.

The first policy we investigate is the pushout policy [2]. It attempts to protect the green cells by discarding first the red ones in case of congestion, i.e., a full buffer. The pushout policy always accommodates a cell irrespective of its color, if an empty buffer is available. If no buffer is available and the arriving cell is red, it is discarded. If it is green and red cells are currently buffered, then one of them is dropped from the system (pushed out of the buffer) and the green cell is accommodated at the end of the queue. Otherwise, the arriving green cell is discarded. Traditionally, this policy has been considered as complex to implement, but as the best choice from a performance point of view

\* and IBM T.J. Watson Research Center, P.O. Box 704, Yorktown Heights, NY 10598

†Part of the work of this author was done while visiting the IBM T.J. Watson Research Center.

[2]. The intuition behind this is that the pushout policy exploits the available buffers as much as possible, and refrains from discarding red cells as long as no congestion is present. However, we prove that it is quite limited in providing the necessary protection to green cells.

The next policy we consider is the limited red policy, which was suggested in [3] as another potential policy for protecting the green traffic against the red while allowing an acceptable level of service to the red cells. This policy enables the buffering of up to  $L$  red cells at the same time in the system. Green cells are always accommodated if there is a free buffer, but an arriving red cell is accepted if and only if there is a free buffer available and less than  $L$  red cells are present in the queue. We also show that the limited red policy is quite limited in providing the necessary protection to green cells.

Finally, we examine a threshold-based policy. The admission criterion used by a threshold policy is to accommodate red cells in the system, if and only if the number of occupied buffers (containing red or green cells) is less than some value  $T$ . We show that by properly selecting the threshold value, the threshold policy does its work faithfully when it comes to providing protection to green cells. We also quantify the impact of this property on the service provided to red cells.

Figure (1), provides a numerical example illustrating the above results. It shows the evolution of the loss probability of green cells as a function of the average arrival rate of red cells  $\lambda_r$  for the threshold policy (which is protective), and for the two non-protective policies discussed above, i.e., the limited red policy and the pushout policy. For the pushout policy we use two replacement strategies (see [2]); FIFO-pushout in which the earliest red cell in the buffer is pushed out upon congestion, and LIFO-pushout in which the latest red cell is pushed out. In all cases, the arrival rate of green cells was set to  $\lambda_g = 0.9$ . For comparison purposes, we give the loss probability for a reference system with only green cells present, where it was equal to 0.0147. A total of  $M = 10$  buffers were available in this reference system, while  $N = 15$  buffers were provided in the system where both green and red cells were present.

Figure (1) shows that under the threshold policy the green loss probability remains smaller than or equal to that in the reference system for all values of the red load, while under all the non-protective policies the green loss probability eventually becomes larger than that of the reference system as the red load gets higher. This illustrates the fact that non-protective policies are not capable of guaranteeing performance (i.e., the loss probability of the reference system) to the high priority traffic, while protective policies do.

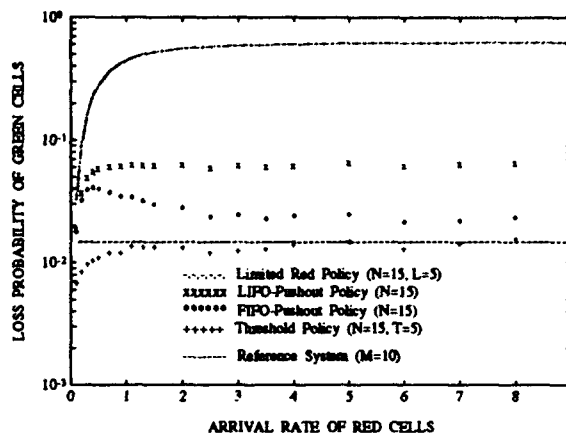


Figure 1: Loss probability of green cells as a function of  $\lambda_r$  for  $N = 15$ ,  $M = 10$  and  $\lambda_g = 0.9$ .

In [1], we then apply the understanding gained from the investigations of the three above policies, to propose new policies which are not only protective but also improve on the threshold policy in terms of the performance offered to low priority (red) traffic. Two of these new policies are simple extensions of the threshold policy, and two are based on simulating another system called the reference system. Numerical examples showed approximately of factor of four improvement in the red cell loss probability for the best such policies, i.e., the simulated policies, while preserving the protective property.

## References

- [1] I. Cidon, R. Guérin, and A. Khamisy. Protective buffer management policies. In *In Proc. INFOCOM'93*, pages 1051–1058, San Francisco, CA, March 1993. (See also IBM Research Report RC 18113).
- [2] H. Kröner, G. Hébuterne, P. Boyer, and A. Gravey. Priority management in ATM switching nodes. *IEEE Trans. Commun.*, COM-9(3):418–427, April 1991. (See also *Proc. INFOCOM'90*).
- [3] K. Bala, I. Cidon, and K. Sohraby. Congestion control for high-speed packet switched networks. In *Proc. INFOCOM'90*, San Francisco, 1990.

# A CALL ACCEPTANCE ALGORITHM FOR GIGABIT NETWORKS

Saragur M. Srinidhi  
Sterling Federal Systems, Inc.  
NASA Lewis Research Center  
Cleveland, OH 44135

Vijaya K. Konangi  
Department of Electrical Engineering  
Cleveland State University  
Cleveland, OH 44115

This paper presents a real time front-end admission control scheme for gigabit networks which dynamically shapes the traffic. In this model the calls, characterized by their mean and variance *a priori*, arrive with a Poisson distribution and have an exponential duration. The state of the transmission link is completely described by the net mean and variance which increases linearly with the number of calls. It can be reasonably assumed that the traffic on the link tends towards a Gaussian distribution as the number of users increase. Figure 1 shows the effect of the burstiness on the distribution of the statistically multiplexed traffic on the link. The distribution tends to shift and widen as traffic on the link grows. The traffic is correlated and is akin to white noise passed through a low pass filter. When the demand on the link exceeds the capacity of the link, cells (53 Byte cell) are lost and we can compute the Cell Loss Probability (CLP) analytically by using the Gaussian approximation. Figure 2 shows the CLP as a function of the number of users on a 1 Gbps link. Three classes of calls are depicted: Class A relates to the set of calls with a 10 Mbps peak rate at 10% duty cycle (DC), Class B represents non-bursty calls with a 4 Mbps peak with 25% DC, and Class C signifies very bursty traffic with a peak of 25 Mbps at 4% DC (notice that the average data rate is 1 Mbps in all three classes).

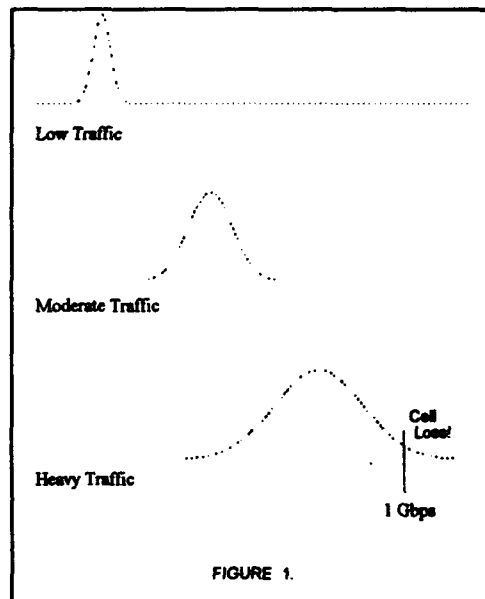


FIGURE 1.

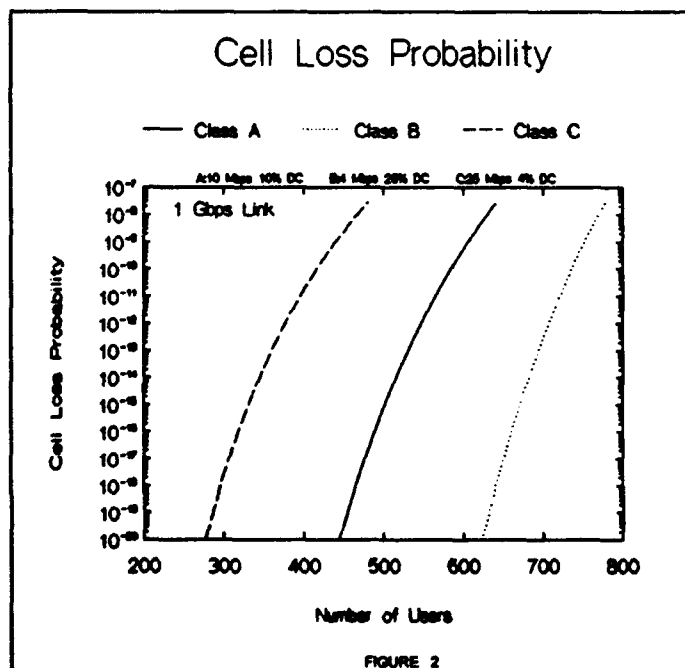
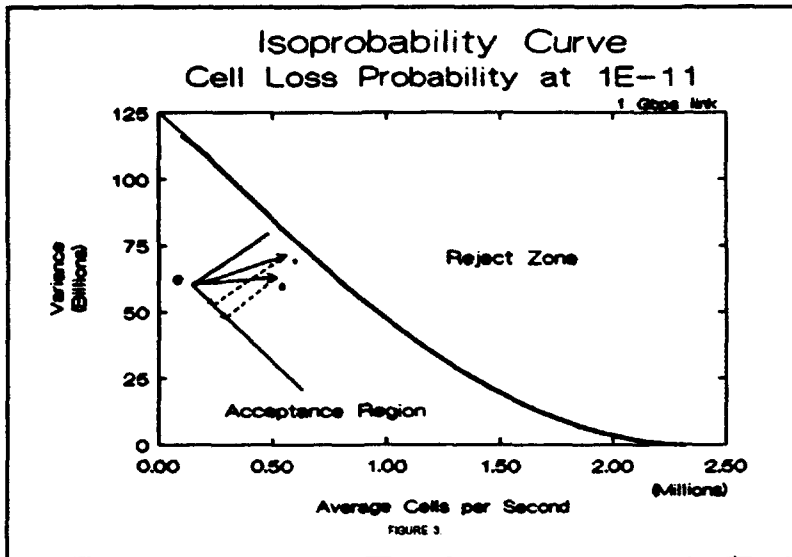
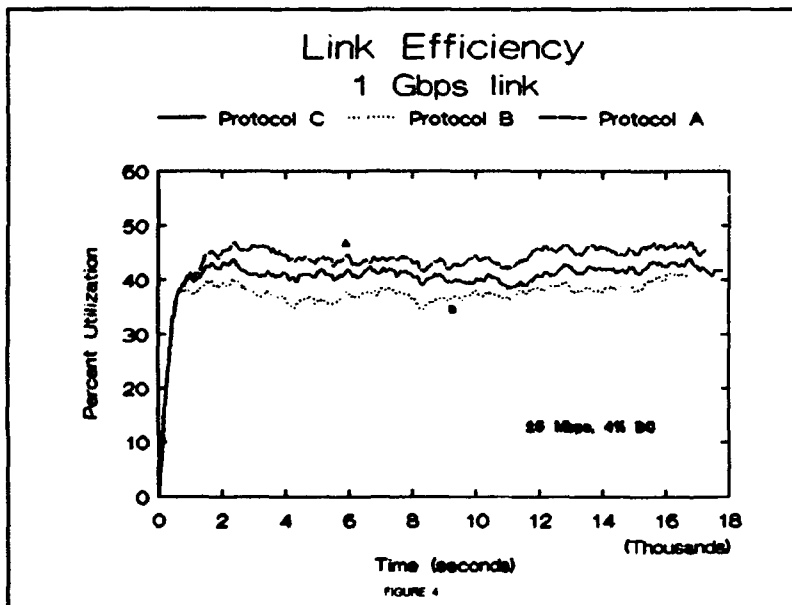


FIGURE 2

The burstiness of the traffic limits the number of calls that can be multiplexed on the link. If we were to arbitrarily choose to operate the link at a CLP of, say,  $10^{-11}$  we can expect a statistical gain of 3 for a Class B call, and 10 for a Class C (bursty) call. The inherent statistics of the traffic on the link are best exploited by calls that are more bursty. For any state of the link there exists a specific CLP and we can extract the constant loss probability (Isoprobability) curve corresponding to the CLP. Figure 3 defines the desired operating region and blocks (rejects) all calls that would take the state of the link above the threshold set by the Isoprobability curve. An algorithm is needed to make the decision on admitting a call into the system, or to keep it in the queue for reconsideration. The approaches considered in this paper exploit the statistics associated with the calls to maximize the link utilization. At this point we have a set of calls contending for admission



operating point determines the metric used to allow calls into the system. We admit that call which has the highest correlation in the direction we want (higher means and lower variance) if and only if that call does not drive the state of the link beyond the Iso curve. All remaining calls, and newly arriving calls will continue to contend for the link. If a call remains in the waiting queue for a period greater than, say, 20 seconds it will be blocked (dropped from the queue). A penalty is assessed for calls that have been waiting in the queue as a linear function of time.



longer than the other two since it had a waiting factor built in and tended not to drop as many calls but at the expense of link utilization. It is to be noted here that calls, generated by a random process, do not have the same mean, variance and holding times but statistically follow exponential distributions. While Protocol A shows a 47% link utilization, Protocol C yields about 43 % demonstrating that there exists a tradeoff between link utilization and call blockage. Protocol B is the least sophisticated with 38% efficiency and is consistent with the analytically derived curves shown in Figure 2. Protocol B does not dynamically shape the traffic. It is necessary to note here that the link efficiency is a strong function of the number of calls contending for admission. In this simulation, the inter arrival times and the call holding times were chosen to keep the average queue length to be 20.

In conclusion, this acceptance algorithm is an analytically simple call admission procedure for connection oriented transport used in high speed networks.

into the system. When the link is heavily loaded we want calls with low variances and high means. The optimal direction for the system to move would be down and along the Isoprobability curve. Given this constraint, the task of choosing the best of the contending calls (that would propel the state of the link closer to the Iso curve) can be accomplished by taking the difference of the dot product of each of those calls. The scheme is illustrated in Figure 3. The current state of the system is denoted by the point C and the arrival of calls 1 and 2 moves the state of the system to points 1 and 2, respectively. The dot product of each call's mean and variance with a unit vector tangent to the Isoprobability curve near the current

An example of the simulation results for a 1 Gbps link capacity are presented here. Figure 4 shows the results of the simulation for a bursty (4% DC) traffic source with the desired CLP at  $10^{-11}$ . Three variations of the algorithm are shown; Protocol A computes the metric without consideration to the amount of time spent waiting in the queue, Protocol B allows calls into the system if bandwidth is available and no metric is computed, while Protocol C enhances the computed metric by adding a factor which increases linearly with the time spent in the queue. In all these cases the requested demand on the link is approximately twice its capacity. In this simulation, data was collected until 5000 cells were dropped. Protocol C took

## **The Impact of 10 Gb/s SONET (OC-192) on Gigabit Networks**

**N. K. Cheung  
Bellcore  
445 South Street  
Morristown, NJ 07960-6438**

The Synchronous Optical Network (SONET) provides a key enabling technology in the recent development of gigabit networks because of its flexibility and standardized interfaces. The majority of the gigabit testbeds deployed to-date employ SONET OC-48 transmission systems as their physical layer. With the rapid advances in optical and electronic technologies, it is anticipated that SONET OC-192 (9.953 Gb/s) will be commonly available by the end of the decade. OC-192 offers an attractive alternative to OC-48 (2.488 Gb/s) in the implementation of the proposed National Information Infrastructure. In this paper we examine the rationale for the introduction of the 10 Gb/s SONET and examine some of the potential impacts in the evolution of the gigabit networks.

The demand for SONET OC-192 transport facilities in the next decade will likely be driven by the two interrelated factors of service growth and switch consolidation. The service growth occurs as a result of the emerging gigabit networks, broadband ISDN, ISDN, and residential video services. Switch consolidation occurs as the cost of transmission decreases rapidly compared to switching [1]. Such cost tradeoffs led to a trend to replace the mesh network by a network of interconnecting rings. Some of the switches in the mesh network can be replaced by add-drop multiplexers on the ring backbone for routing to a smaller number of larger switches where the traffic can be processed more efficiently and maintenance can be handled in a more centralized manner [2]. The reduction of switches and the backhauling of traffic to larger switches in turn increases the traffic demand. A high traffic demand limits the present SONET OC-48 ring to a small size of about 5 to 6 nodes. With the availability of OC-192 systems, one can replace the relatively small OC-48 rings by a larger and more efficient OC-192 ring.

Consolidation of the traffic into large OC-192 rings could greatly simplify the network architecture and increase the network reliability. The larger rings require less interconnection between the rings with back-to-back add-drop multiplexer or wideband digital cross-connect systems at hub buildings. This in turn simplifies the operations and planning.

The most important advantage in deploying SONET OC-192 systems is perhaps in the significant reduction in the network implementation cost. An increase in system line rate has historically resulted in substantial savings in point-to-point systems. Thus one single OC-192 point-to-point system is expected to be less expensive than four OC-48 point-to-point systems. Such savings also apply to the SONET self-healing ring networks [3]. A recent study showed that a SONET OC-192 self-healing ring results in a cost saving of 27% for single homing configurations and 23% for dual homing configurations compared to an equivalent number of OC-48 rings. The study was based on a metropolitan LATA network with 53 central offices and 84 links, taking into account the costs of SONET regenerators and add-drop multiplexers, fiber, cable and system installation [3].

Additional cost savings and simplifications in network operations and maintenance could be achieved if we extend the concept of SONET OC-192 STM self-healing ring into an OC-192 virtual path SONET/ATM self-healing ring[4]. The virtual path SONET/ATM self-healing ring combines the best features of SONET and ATM: the simplicity and hierarchical multiplexing of SONET and the bandwidth flexibility and nonhierarchical multiplexing of ATM. In this scheme, the relatively complex SONET STM add-drop multiplexer is replaced by the simpler, and thus less expensive, ATM add-drop multiplexer. The analysis of the virtual path ATM self-healing ring in Ref. [4] is based on the STS-3c terminations for ATM cells because of the straight forward evolution of present

SONET systems. With the advent of gigabit networks and the future availability of STS-12c, STS-48c, or even STS-192c interfaces, the OC-192 virtual path SONET/ATM self-healing ring could provide a natural and efficient transport facility for gigabit networking applications.

One such application is the transport of multiple HIPPI (High Performance Parallel Interface) channels over the public network [5]. The line rates for single and double HIPPI channels are 800 Mb/s and 1600 Mb/s, respectively. An early attempt at the transmission of HIPPI channels over the SONET public network is to map the HIPPI directly over the SONET payload [6,7]. For example, the CASA Gigabit Testbed uses 7 OC-3 channels to carry a HIPPI channel, and the 8th channel can be used for control [6]. Another approach is to map the entire HIPPI channel into a STS-12c payload [7]. These approaches can only accommodate 2 to 4 single HIPPIs over a SONET OC-48 link. A more flexible approach is to carry the HIPPI packets over ATM cells mapped into the SONET payload [8,9]. The VISTAnet Gigabit Testbed employs a HIPPI Network Terminal Adaptor (NTA) which converts the HIPPI packets to and from B-ISDN ATM cells at 622 Mb/s rates [8], while the Nectar Gigabit Testbed employs a HIPPI-ATM-SONET (HAS) adaptor to convert each HIPPI packet into ATM cells in an STS-3c channel [9]. Each HIPPI channel is carried by up to 8 STS-3c channels in an OC-48 link. In these approaches, the entire OC-48 link is more or less dedicated to a small number of single HIPPI channels and the SONET bandwidth may not be used efficiently for all applications. It is even more inefficient to carry a double HIPPI over an OC-48 link.

The high speed SONET OC-192 system permits a more efficient and flexible way of utilizing the transmission facilities than, say, a group of 4 OC-48 systems. The entire useful payload of the OC-192 can be allocated for different applications without requiring cross-connects at each network node. If we assume peak rate allocation, one may carry 12 single HIPPIs and 6 double HIPPIs over a SONET OC-192 link. One may also take advantage of the burstiness of the HIPPI traffic, and employ resource allocation at call setup to statistically allocate the equivalent capacity of each HIPPI channel as an ATM virtual circuit. As an example, if we use the multirate circuit switching model of resource allocation [10], and assuming a utilization rate  $\alpha$  = average rate / peak rate, the number of HIPPI channels that can be supported varies from 37 for  $\alpha = 0.1$  to 12 for  $\alpha = 1$  (i.e. peak rate). Alternatively, for situations where only a fraction of the total traffic is HIPPI, one can allocate the appropriate fraction of the bandwidth for HIPPI, and the balance of the capacity for other lower speed ATM traffics.

To summarize, SONET OC-192 (10 Gb/s) systems are expected to offer significant cost savings in the implementation of the new National Information Infrastructure. They can also be employed to accommodate statistically a large number of HIPPI channels as well as a wide variety of lower speed applications in the emerging gigabit networks.

## REFERENCE

- [1] S. L. Moondra, "Impact of emerging switching-transmission cost tradeoffs on future telecommunications network architectures", *IEEE Journal on Selected Areas in Communications*, Vol. 7, pp.1207-1218, October 1989.
- [2] P. E. White, "Broadband networking: A new paradigm for communications", Columbia University Workshop on Telecommunications, 'Broadband Networking: The State of the Art and Beyond', Conference Digest, New York, NY, September 21-22, 1992.
- [3] O. J. Wasem, T. H. Wu, and R. H. Cardwell, "OC-96/OC-192 technology impact on SONET self-healing rings", *OFC'92*, Paper ThL4, San Jose, CA, 1992.

- [4] T. H. Wu, D. T. Kong, and R. C. Lau, "An economic feasibility study for a broadband virtual path SONET/ATM self-healing ring architecture", IEEE Journal on Selected Areas in Communications, Vol. 10, pp.1459-1473, December 1992.
- [5] N. K. Cheung, "The Infrastructure for Gigabit Computer Networks", IEEE Communications Magazine, Vol. 30, pp.60-68, April 1992.
- [6] D. E. Tolmie, "Gigabit Networking", IEEE Lightwave Telecommunications Systems Magazine, Vol. 3, pp.28 - 36, May 1992.
- [7] M. Z. Iqbal, M. Stern, J. Young, H. Izadpanah, R. Standley, O. S. Mia, and J. L. Gimlett, "A 2.5 Gb/s SONET datalink with STS-12c inputs and HIPPI interface for gigabit computer networks", Proceedings of GLOBECOM'93, pp. 1196 -1200, Orlando, FL, December 1992.
- [8] M. N. Ransom and K. Bischoff Talman, "ATM traffic measurement in the VISTAnet network", Proceedings of GLOBECOM'93, pp. 1184 - 1190, Orlando, FL, December 1992.
- [9] K. C. Young, Jr., C. A. Johnston, D. J. Smith, J. W. Mann, J. J. DesMarais, M. Z. Iqbal, J. Young, K. Walsh, and W. Holden, "A HIPPI/ATM/SONET network interface for the Nectar Gigabit Testbed", Proceedings of IEEE LEOS Summer Topical Meeting on Gigabit Networks, Santa Barbara, CA, July 28-30, 1993.
- [10] F. Vakil, "Can Shannon Coding Theorem Play a Role in ATM Traffic Management?", Proceedings of IEEE LEOS Summer Topical Meeting on Gigabit Networks, Santa Barbara, CA, July 28-30, 1993.

## **Gigabit ATM Switching: A Concentrator-Based Growable Switch Architecture and Performance\***

*Kai Y. Eng and Mark J. Karol*

AT&T Bell Laboratories

Room 4F525

101 Crawfords Corner Road

Holmdel, NJ 07733-3030

Phone: (908) 949-2201 Email: kye@boole.att.com

### **SUMMARY**

We have an on-going focused research effort in establishing an architecture and associated technologies for achieving a Gigabit ATM switch of a Terabit throughput capacity. Our goal is to advance our technological capability from feasibility demonstration to technology transfer, and prototyping for field trials is thus part of our research cycle. Our prototyping activities have been guided by a long-term architectural plan based on the theory of the Growable Switch Architecture [1]. Although the architecture is fundamentally independent of its implementation speed and technology, a particular concentrator-based arrangement ( $32 \times 32$  example in Fig. 1) is found to be near-optimal in delay-throughput performance (Fig. 2) and practical for development. Note that this arrangement of Fig. 1 is growable from  $8 \times 8$  to  $32 \times 32$ . As a first step, we have successfully prototyped a shared-memory  $8 \times 8$  switch at 2.5 Gb/s per port, and with this, also a stand-alone switch system supporting Universal Line Card Slots for 2.4 Gb/s OC-48, 622 Mb/s OC-12 and 155 Mb/s OC-3 [2,3]. As our prototyping efforts are progressing towards the  $32 \times 32$  version, we show here how the architecture can be extended to much larger sizes, e.g.  $256 \times 256$  and  $512 \times 512$  at 2.5 Gb/s per port. Essential characteristics such as modular growth, priority, multicast and cell sequence maintenance are all guaranteed.

As shown in Fig. 1, a  $32 \times 32$  switch requires the use of  $32:8$  Concentrators. We show in the extended arrangement that only  $64:8$  Concentrators are needed for switch sizes up to  $512 \times 512$ . As a first step, we demonstrate with extensive computer simulations that the delay-throughput performance under various traffic patterns remains near-optimal. We also show the buffer sizing for these concentrators to be reasonable for practical implementation even for cell loss rates as low as  $10^{-10}$ . The next steps are to identify the key technological bottlenecks in realizing the switch, and pursue technical approaches that will overcome the obstacles. This latter work is still in progress, and a brief discussion of its status will be provided.

### **References:**

- [1] K. Y. Eng, M. J. Karol and Y. S. Yeh, "A Growable Packet (ATM) Switch Architecture: Design Principles and Applications," *IEEE Trans. Comm.*, February 1992.
- [2] K. Y. Eng, M. A. Pashan, R. A. Spanke, M. J. Karol and G. D. Martin, "A High-Performance Prototype 2.5 Gb/s ATM Switch For Broadband Applications," *IEEE Globecom '92*.
- [3] K. Y. Eng, M. A. Pashan, G. D. Martin and C. R. Crue, "An ATM Cross-Connect System For Broadband Trials and Applications," submitted to *IEEE Globecom '93*.

---

\* Part of this work was supported under DARPA contract N00174-93-C-0050.

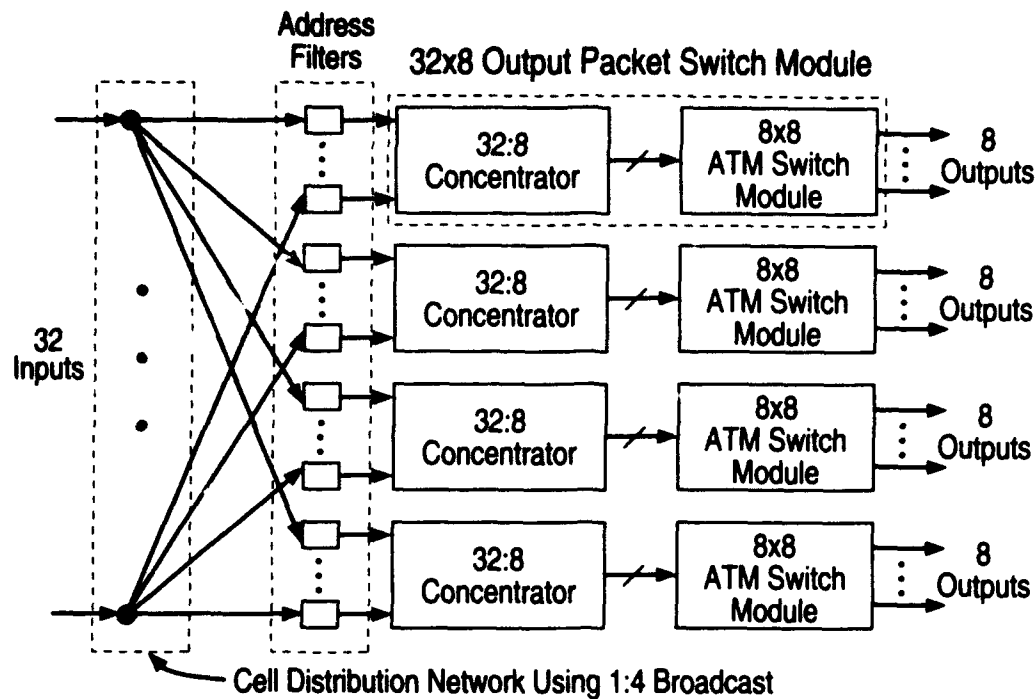


**Fig. 1 A 32x32 Switch Using The Concentrator-Based Growable Switch Architecture**

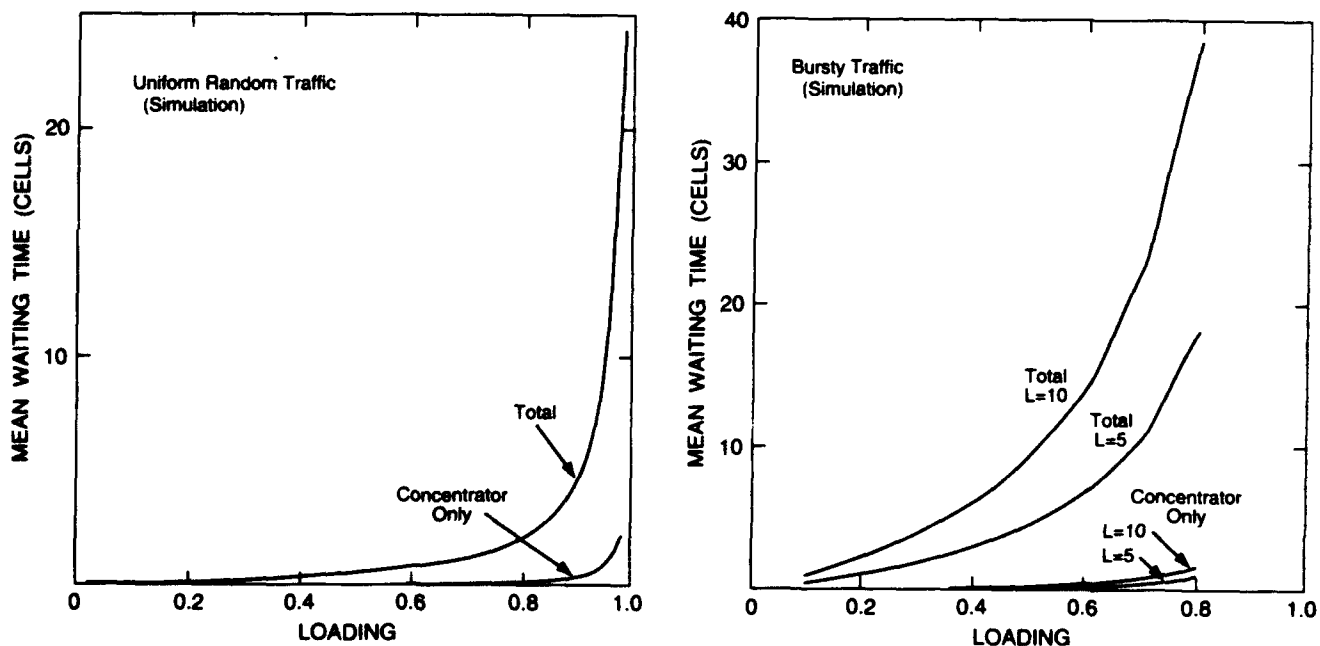


**Fig. 2 Delay-Throughput Performance Of The 32x32 Output Packet Switch Module in Uniform and Bursty Traffics**

## Probabilities of Undetected Errors using ATM AAL5 on Real User Data

James P. Hughes  
Network Systems Corporation

### 1 Introduction

ATM AAL5 is a simple protocol with certain failure modes. This paper concentrates on one of these modes which is called a "packet splice". A packet splice can occur during periods of high cell loss when the packet delimiter cell of the first packet is lost along with enough other cells between the 2 packets so that the length check on the new combined packet will be correct.

The probability of this kind of event is not discussed in this paper because actual information regarding the actual distribution within a burst cell loss event has not been tested and is implementation dependent.

What this paper describes is what happens once a packet splice occurs with a correct length field. Valid packet splice must be detected by the remaining check mechanisms. These mechanisms include the AAL5 CRC and the TCP or UDP checksum (if one exists). Theory based on random data states that the probability of an undetected error within a packet splice situation is  $2^{-32}$ . The question remains, what is the actual coverage of CRC and checksum if real (not random) data is to be protected.

At Network Systems we have a large NFS file server with approximately 20GB of user data. The assumption of this paper is that if the data is stored on the file server is representative of data which could be moved over a future AAL5 ATM network<sup>1</sup>.

We also have 100+ personal Sun and HP workstations networked, which, on evenings and weekends, can be used for embarrassingly simple and effective parallel processing. This processing power was used to examine a portion of this data, segmenting this data into typical TCP packets, creating packet splices and determining if the remaining checks would hold. The statistics of these determinations are gathered and presented in this paper.

### 2 Packet Splices

To form a packet splice, two packets are segmented into cells and a certain portion of these cells can be lost to form a composite packet. The AAL5 length field is used as a first level attack against all cell loss events, but it can be fooled. In the case where there are 2 consecutive packets of length (in cells)  $L_1$  and  $L_2$ , to fool the length field exactly  $L_1$  cells must be lost and the end cell of the first packet must also be lost and the last cell of the second packet must be included. The exact sequence of cell lossage is not necessarily uniform. The cells can be lost in a single group or the cells can be lost over both packets. (It is assumed that the cells arrive in order according to the ATM specification.)

For TCP packets, there are integrity checks of the header (which vary by implementation) and will through out inconsistent packets. This paper assumes that for packets to be processed by TCP, packet splices would include the first cell of the first packet (the entire typical TCP header).

---

1. A point of fact is that, since this is a NFS repository, portions of this data is moved across our internal network every day. The processing that this data discusses did read the data across the network.

Typical in TCP processing, a file will be sent as consecutive group of packets forming a packet train. Each packet in the train will have a given length equal to the MTU. This analysis has taken this assumption and used a 512 byte MTU for all packets except the last packet in a file. A 512 byte block of data with a typical TCP header would be contained in 12 ATM cells. A two packet train would be further cellified into a 24 cell train. To form a valid packet splice, the first cell of the first packet and last cell of the last packet must arrive, and the last cell of the first packet must be lost and exactly 11 cells out of the remaining 21 must also be lost. The number of possible valid splices within 24 cell train is 21 pick 11 or approximately 700,000 combinations per packet pair (which is processed every 512 bytes of user data).

The program also checks the TCP checksum for the packet splice. An interesting side note is that if there are 2 packets containing the identical repetitive user data (i.e. all 0s) then the splice will have a valid TCP and UDP checksum, but will also be a correct packet. This happens because the TCP checksum is in a header and that the data is correct. In the case of the CRC, the header is for the first packet and the trailer containing the CRC is for the second packet and since the two packets have differing TCP offsets, packets with equal data will not splice. It is (remotely) possible for 2 packets with different user data to splice to form a packet identical to the first while still passing the length, CRC and checksum tests.

Finally the program keeps statistics which describes the integrity features which catch errors and the combinations in which these errors occur.

Given all these possibilities for catching errors, it was proven by XXX that there are files, that when sent, will contain a splice that will pass the length, CRC, and TCP checksum and contain incorrect data. This file was created from a C program that uses arguments within a printf statement to "tune" the resulting load module so that it would splice without a detected error.

### 3 Results

The results of a 60 hour run was that 30 billion packet splices were tested and 7 valid CRC events were found. The results for random data should have been around 7.5 valid splices. These events were all from files containing different data. Some of the valid CRC events occurred in binary files and some in ASCII files. The results were repeatable and were shown as a part of the presentation.

When the splice did not create a packet identical to the first, there were TCP checksum events at a rate of  $2^{-16}$ . Again this correlates with the expected results of the TCP checksum with random data.

Of the 7 valid CRC events, none had a valid TCP checksum.

If the CRC32 and the TCP checksum is indeed unrelated<sup>2</sup>, the resulting probabilities of failure of both to detect a packet should be  $2^{-48}$ . At the time of this writing, this result has not been verified.

### 4 Conclusion

This paper describes empirical data in support of the supposition that real user data can be considered to be similar to random data when ATM AAL5 packet splices occur. The data also supports the argument that the TCP checksum does increase the probability of a packet splice being detected beyond the CRC's  $2^{-32}$ .

---

2. considering that the 2 techniques are so different in terms of feedback, they may well be unrelated especially considering large burst errors.

## OC-12 Crossconnect for the VISTAnet Gigabit Network

B. Basch, R. Moolenbeek, V. Samalam, M. Procanik

GTE Laboratories Incorporated  
40 Sylvan Road, Waltham, MA 02254

The design, construction, and installation of an OC-12c crossconnect switch for the VISTAnet network <sup>1,2</sup> has been completed. The crossconnect switch has been designed as SONET-compliant line terminating equipment and provides switching for up to 16 OC-12c signals. The system consists of up to eight trunk interface cards with two bidirectional OC-12 ports, a synchronous switch card, and a control module with craft interface to provide service monitoring, provisioning, and maintenance functions.

Several novel concepts such as distributed power systems and integrated electro-optical backplane connectors were incorporated in the design of the crossconnect. The operating speed stresses the limit of available CMOS technology. Particular attention was given to equipping the crossconnect with extensive diagnostic capability to facilitate network performance monitoring. Graphic user-interface technology provides an easy interface for either operator or maintenance personnel. A block-diagram of the crossconnect architecture is shown in Figure 1.

The trunk interface card provides electro-optical conversion, clock extraction, and framing. It also processes the SONET section and line overhead. Full access is provided to the section and line data communication channels, the user channel, and the orderwire channels. The trunk interface card accepts OC-12/12c signals which, after detection and amplification, are routed to a clock recovery/data regeneration module. The regenerated data and recovered clock are processed by a SONET framer/demultiplexer circuit that converts the serial input stream to an 8-bit parallel output (byte) format. All SONET overhead processing and subsequent switching on the synchronous switch card is performed in this byte format. An on-board controller, consisting of a microprocessor with associated memory, is used to customize and monitor the operation of the trunk interface card.

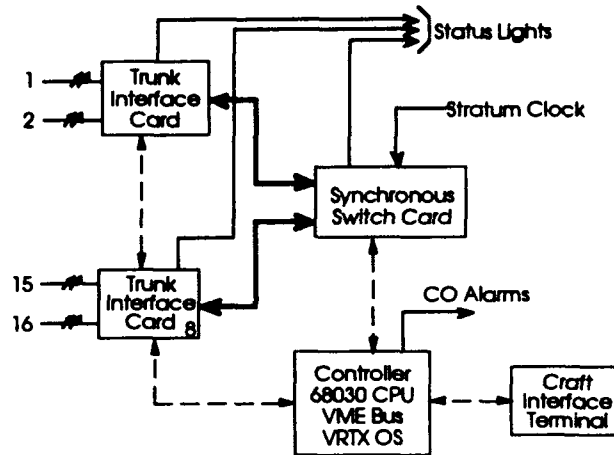


Figure 1. Crossconnect configuration.

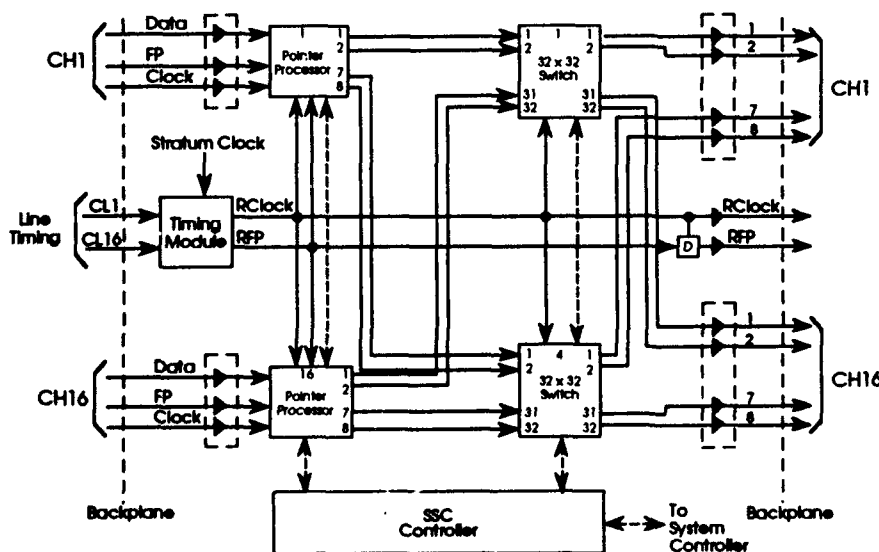


Figure 2. Synchronous switch card.

The synchronous switch card, shown in Figure 2, contains the crossconnect's switch fabric, consisting of four synchronous CMOS  $32 \times 32$  switch chips, and retimes all incoming signals using pointer-processing chips. The synchronization provided by the pointer processors removes accumulated jitter from the incoming signals and phase aligns all channels to allow synchronous switching in the switch matrix. Control of the switch matrix and monitoring of the incoming and outgoing pointer adjustments is performed by three on-board controllers. These controllers communicate with and receive commands from the system control module. The synchronous switch card uses a highly stable internal clock

which is slaved to an external timing reference from either a Stratum clock or one of the incoming OC-12 signals. The internal clock also can be used for self-timing when the external reference fails.

The control module consists of one to three 68030 microprocessor-based single-board computers on a common VME bus, all running the VRTX real-time operating system; a SUN workstation, functioning as the craft interface, connects to one of the system processors via Ethernet. The control module uses a VME sub-bus to communicate with the controllers on the trunk interface card and synchronous switch card. The main functions of the control module are to configure the system, provide monitoring of the system status, and generate central office alarms when required. The SUN craft interface displays alarms and status conditions in a form that allows the operator to configure and monitor the crossconnect easily. All major functions required for normal operation have been preprogrammed, with the interface consisting of windows and icons that can be activated or deactivated by means of a mouse. In addition, all control and status registers in the system can be accessed via their system addresses.

The windows and associated information are of two types. The first set of windows consists of alarm indicators and provides the status information of the system as a whole. The alarm indicators, which are both visual and aural, report on any SONET-related alarms as well as bit error rates that exceed major or minor thresholds. A second set of windows provides more detailed information on the performance of the system. These windows are mainly of interest to the skilled technician. As an example, Figure 3 shows the status for one of the SONET overhead processing circuits in the trunk interface card. The connection panel, shown in Figure 4, eases provisioning by allowing connections to be set up or torn down by pointing and dragging. Other windows displays provide information on the stuffing rates of the pointer processors as well as information on the status of various clocks in the system. Because the crossconnect's hardware and software both were designed in modular fashion, additional functionality, like automatic protection switching, can be implemented by adding appropriate software modules without a major redesign of the system. The detailed design of the crossconnect and early interworking experience in the VISTAnet Gigabit Network will be presented.

Figure 3. SONET overhead control panel.

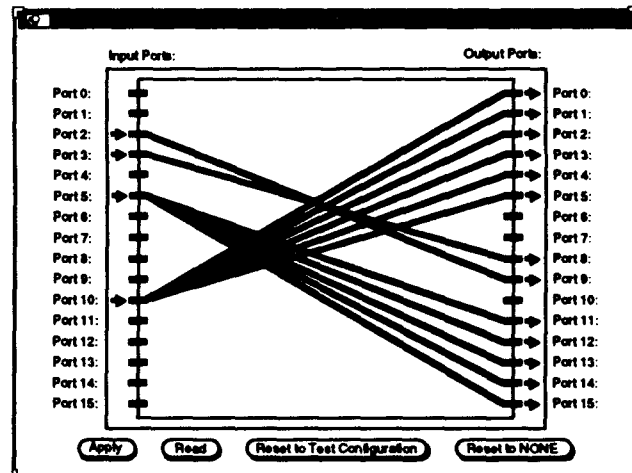


Figure 4. Switch connections panel.

## References

1. Niel Ransom, "Technical challenges of turning up the VISTAnet Gigabit Network," invited paper.
2. B. Basch, et al., "VISTAnet: A B-ISDN Field Trial," IEEE LTS 2,3, August 1991.

**Friday, July 30, 1993**

**Sessions:**

**F1: Recent Progress of the  
All-Optical Network Consortia**

**F2: Technologies for Gigabit Networks II**



**F1.1 8:30am - 9:00am**

**The Optical Network Technology Consortium**  
C. Brackett, *Belcore, Morristown, NJ*

*Paper not available at time of print.*

## **The AT&T, Digital, and MIT All Optical Network Consortium**

**V. W. S. Chan (MIT), A. J. Kirby (Digital), A. A. M. Saleh (AT&T)**

The American Telephone and Telegraph Company (AT&T), Digital Equipment Corporation (Digital), and Massachusetts Institute of Technology (MIT) are forming a pre-competitive consortium to address the challenges of utilizing the evolving terahertz bandwidth capability of optical fiber technology to develop a national information infrastructure capable of providing flexible transport, common conventions and common servers.

Our long term goal is to pursue the research and development of the technology, architecture, and applications necessary for the realization of a scalable, universal, wideband optical network. Our more immediate goal is to determine how these challenges can best be met and to demonstrate that capability in a manner that can be further developed, engineered and produced by the communications and computer industries of the United States. Our research vehicle to reach these goals is an extensive test-bed utilizing state-of-the-art components. Research and development on technology, architecture, and applications will revolve around this activity.

Our network architecture is all optical. Optical signals flow between users across the network without being converted to electronic signals within the network. Thus, the network is unimpeded by optical-to-electronic transformations. This is made possible by the introduction of optical amplifiers and other unique optical components, such as frequency routers and frequency converters. Some of the components are commercially available, but a significant fraction will be unique research devices.

The baseline architecture will potentially allow frequency-division multiplexing to access the 25 THz (200 nm) of fiber bandwidth. The architecture will support three basic services: 1) point-to-point or point-to-multipoint high-speed circuit-switched multi-Gbps digital or analog sessions, 2) time-division multiplexed (TDM) circuit-switched sessions the range of a few Mbps to the full channel rate of multi-Gbps, and 3) a service used for control, scheduling and network management that can also be used for datagram service. All three services have all-optical paths but typically will use electronics for set-up and control.

We have in mind the creation of an architecture that is scalable in the dimensions of geographic span, number of users and data rates. Thus, we have developed a hierarchical architecture that includes local area networks (LANs), metropolitan area networks (MANs) and wide area networks (WANs). Since it is designed to scale gracefully to hundreds of thousands of all-optical end-nodes, it provides a framework for a national or global high-speed communications infrastructure. The modular nature of the design allows the incorporation of future technological advances and serves as a guide to such

advances. In addition, the flexible high-rate services provided by this architecture will serve as a stimulus to new application areas.

In addition to the more mature technology used in the test-bed, we intend to pursue research in a few technology areas of great potential impact to network architecture and performance, e.g. an all-optical packet switch. These modest research efforts have higher risks, though higher pay-offs, and will not be part of the baseline architecture of the test-bed.

A key theme of our effort is in the construction of an extensive test-bed system. It will form a proof-of-concept demonstration of a universal, scalable, optical network and will provide a common forum in which the interactions of applications, architectures, and technologies may be investigated. This extensive test-bed will be geographically distributed and will be connected via dark fiber whenever possible.

**IBM Research Program on All-Optical Networks**

**Paul E. Green, Jr.**

**IBM T. J. Watson Research Center, Hawthorne, NY 10532**

**pgreen@watson.ibm.com / 914-784-7337**

**Introduction** - Our experience, during the five-year existence of our program, has shown us that the value of these networks is not just in the great carrying capacity of optical fiber, but in the ability of FDM/WDM architectures to carry different protocols on different wavelengths, thus avoiding the usual translations to a common protocol and bit rate basis. This "protocol transparency" has proved of paramount interest to those users with which we have been dealing.

Our focus has been on local and metropolitan area networks, partly because dark fiber is most readily available in those environments, partly because commercialized erbium doped fiber amplifiers arrived late on our scene, and partly because we see the earliest applications to lie in the 1 to 100 kilometer range of interconnection. As mentioned below, we have recently begun looking at extending these experiences to highly scalable ("million node") nationwide networks.

**Rainbow-I** - Rainbow-I is a network of up to 32 nodes, each implemented on a single printed circuit card that plugs into the industry standard Microchannel system bus. Thus a single PS/2 desktop computer, or equivalent, that can accomodate double-height cards, can house one or more Rainbow-I nodes. It uses the Micron Optics FP-100 piezo-tunable fiber Fabry-Perot filter.

The Rainbow-I network was first field tested in Westchester County in late 1990, in the Geneva-CERN area (10 km. distances) in October, 1991, in Tokyo in 1992, and now operates between three IBM Research sites in Westchester County, NY, over a distance of 25 kilometers. Various wavelengths handle 270 Mb/s serial digital video, 100 Mb/s FDDI and 3 Mb/s. digital (CD format) audio. A "circular search" protocol, implemented partly on the Rainbow card and partly in CPU cycles, sets up bidirectional links 50 msec. after the single keyboard character is input designating the desired target node. The 50 msec. setup time implies a circuit-switch mode of operation.

**Rainbow-II** - Rainbow-II, a joint project of IBM and Los Alamos National Lab (LANL) is a direct circuit-switched extension of Rainbow-I for circuit-switched interconnection of up to 32 supercomputers and their peripherals at 1 Gb/s rates over several kilometers. Initially, Rainbow-II uses the industry standard HIPPI (High Performance Parallel Interface) connection to each machine, but this will evolve to Serial HIPPI or Fiber Channel Standard as the chipsets become available. LANL serves as our environment for beta tests that are expected to begin in early 1994.

Each machine connects into the Rainbow-II network by means of an ONA (optical network adaptor) box, which can be thought of as a sort of external modem. At the attached node side there is a 100-pin HIPPI socket (rather than a 25-pin RS-232 socket), at the other end is a pair of single mode fibers (rather than a copper wire pair), and the logical effect of a connection request is a wavelength connection (rather than a telephone call).

The upper-level communication protocol stack to be used is TCP. Packets are transferred between ONA boxes by means of our very slim protocol called OTP (Optical Transport Protocol), and there are several alternatives for splicing the path between TCP's transport interface (Berkeley socket interface) and OTP. In order to offload as many execution cycles as possible from the host to the RISC microprocessors in the ONA, IBM, LANL and Intel have jointly developed SHIP (Simple Host Intersocket Protocol) which runs in the attached machine, in ONA, and in other LANL environments. This protocol consumes very few CPU cycles in transferring data between host and ONA at 1 Gb/s, while preserving the socket appearance that the application code was written against. Thus, no changes are necessary in existing application code and the required system code changes can be implemented by accessing the SHIP code library.

**Tunability technology** Our target of achieving packet switch of 1 Gb/s traffic calls for sub-microsecond tuning time. Early in the program we sponsored work by Coldren at UCSB on tunable semiconductor laser diodes. They have recently achieved many tens of nm. of tuning range with a phase-matching approach and even better results with a sampled-grating four-section structure. Eventually, such components should become commercially available. In addition we have sponsored work by Johnson at University of Colorado on fast tunability using liquid-crystal index tuning, and have made some investigations on our own.

The acoustooptically tuned double wedge filter uses two crossed wedge etalons (one thin one for coarse wavelength resolution and a thicker one for fine resolution) to form an X-Y plane so that acoustooptically deflecting a light beam to a given X-Y position results in narrow filtering that resolves one of 600 wavelengths. This can be accomplished in several tens of microseconds. While functionally successful, the prototype proved to be too large physically for printed circuit board use, so we turned to other structures.

One of these involved an EOTF/AOTF cascade, the EOTF for fine resolution and the AOTF for coarse resolution. The EOTF was a simple Fabry-Perot cavity of GaAs at 1.5 microns and the AOTF was of the polarization diversity type pioneered by Smith at Bellcore. This was a joint project with Bellcore.

The most promising approach we have found has been a grating followed by a photodetector array followed by an electrical selection and amplification network. We are currently working toward a 128-channel such component.

**Photonic amplification** - We are convinced that low-cost EDFAs are a particularly important technology for further development of all fiber communications, and so we have built on a single 1" x 7" x 5" "daughter board" a tunable receiver, consisting of several meters of doped fiber, a 980 nm. pump laser diode developed at IBM Zurich, a FFP-100 following the erbium fiber, then a PIN/FET unit and then electrical postamplification stages. The usual dichroic coupler and two isolators are included. In our view, this form of packaged receiver (for which the filter is necessary anyhow to remove most of the amplified stimulated emission) is the preferred embodiment of all future high-sensitivity receivers, and should be redone in planar technology for cost reduction.

**MuxMaster** - We are studying the development of a simple multiwavelength bidirectional link using a grating at each end of the link, some wavelengths going in one direction and some in the other. While providing only multiplex rather than multiaccess capability (flexible addressing), such technology offers considerable cost reduction, compared to renting an equivalent number of dark fiber strands.

**Multiaccess protocols** - Realizing that fast-tuning receiver and transmitter technology will eventually become commercially available, we have developed a number of packet switch protocols, several of which can deliver a packet to a destination in only slightly more than a single one-way propagation time.

**Scalable network protocols** - We are using ARPA funding not only to develop the protocol offloading mentioned earlier in connection with Rainbow-II, but to support Brackett at Bellcore by the analysis and design of algorithms for call setup in highly scalable all-optical networks using wavelength routing. Early results include bounds on number of wavelengths required (for fixed-routing nodes, switchable-routing nodes, and wavelength-shifting nodes), and several heuristic wavelength assignment algorithms.

**Gigabit Network Testbeds with Semiconductor Optical Amplifier based Optical Crossbar Switches**

*L. R. McAdams, A. M. Gerrish*  
Optivision Inc. 4009 Miranda Ave, Palo Alto, CA 94304

Optivision has recently designed and built several high performance optical crossbar switches. These switches are complete turnkey systems and represent an important step forward for photonic switching from the laboratory to demonstration testbeds. The goal of the work presented here is to apply Optivision's optical switching expertise to create a scalable, high bandwidth, all-optical switched network for interconnecting high performance computers, workstations and peripherals. Two 8x8 optical crossbar switches have been deployed to form two separate single-switch testbeds. One testbed supports gigabit/sec computer networking experiments. The other testbed is exploring the transport of mixed analog and digital data within a common network. In both testbeds the information is transported in optical form with electro-optic conversion performed only at the end points of the networks.

The heart of the testbeds is the optical crossbar switch. Figure 1 shows a schematic diagram of the switch's optics module. The optics module supports eight fiber optic inputs and eight fiber optic outputs (at present, only four inputs and outputs have been interconnected for the purposes of demonstration). It is based on the matrix-vector-multiplier (MVM) architecture and provides fully non-blocking point-to-point and multicast connectivity between the inputs and the outputs. The optics module is constructed using 1x8 single mode fiber optic splitters and semiconductor optical amplifiers (SOAs). The inputs are fanned-out along the columns of the crosspoint array and the outputs are fanned-in across the rows. The SOAs used in the crosspoint array provide both high speed switching and optical gain to compensate for the fan-out loss. The optics module also has a second stage of SOAs after the 8x1 single mode combiners. These SOAs are not switched, but simply provide optical gain to compensate for fan-in loss.

The transmission properties of the optics module have been well characterized. The average center wavelength of the channels is 1312 nm with variation of  $\pm 2$  nm. The average 3 dB optical bandwidth of the channels is 35 nm. For low power input signals (-9 dBm) the average loss through the optics module is 0 dB with a variation of  $\pm 1.5$  dB. For higher power input signals (-3 dBm) the SOAs saturate and the optical gain is reduced -2 dB on the average. The fidelity of the channels has been measured with a bit error rate (BER) test set. Under laboratory conditions, all channels operate with a BER of  $<1 \times 10^{-12}$  at 1.1 Gb/s for input signals  $>-10$  dBm.

The optical crossbar switch contains a number of electronic modules that work in conjunction with the optics module to form a useful network switch, as shown in Figure 2. The analog module contains low noise constant current sources, one for each SOA in the optical crossbar switch. The current levels from these sources determine the optical gains achieved in the SOAs. The digital module consists of an array of multiplexers. Its function is to decode commands into ECL signals that are used to directly switch the individual SOAs. The TEC controller module contains the control electronics needed to drive the thermoelectric coolers used to temperature stabilize the optics module. The AT computer module provides several functions. It monitors the switch circuitry for error conditions, collects switch usage information, and supports a graphical interface for administration and maintenance functions and manual control.

Two methods have been developed to control the optical crossbar switch through the network. The initial approach is based upon out-of-band control. Using this approach, a SCSI interface is added to the AT computer module to allow the nodes in the network to communicate connection requests to the optical crossbar switch. This initial control scheme allows us to demonstrate the *format and protocol independent* nature of the channels through the optical crossbar switch. The

second control approach is based on in-band control and is shown in Figure 2. Here a polling receiver and an optical network interface unit (ONIU) have been added to the optical crossbar switch. The ONIU is connected to the optical crossbar switch optically through an input and an output and electrically through the polling receiver. The ONIU provides an electro-optic interface between the serial optical signals in the network and the High Performance Parallel Interface (HIPPI) signals used by the polling receiver and the nodes in the network. The polling receiver contains call processing software that causes the digital module to connect the ONIU's optical receiver to the switch inputs in a round robin fashion. If a connection request is present at an input, the polling receiver decodes the destination address and forms the connection (assuming no contention). If a connection is in progress when an input is polled, connection disconnects can be detected with no loss of information due to the multicast ability of the optical crossbar switch.

Quantitative evaluation of the in-band control approach is underway using a number of different ONIUs which are all compatible with HIPPI but differ in the serial optical protocols they implement. A test setup consisting of an optical crossbar switch equipped for in-band control connected to a remote ONIU and a HIPPI protocol tester has been established. This configuration allows the functionality and performance of the in-band control approach to be investigated. Connection setup times and link efficiency are being examined as functions of ONIU synchronization times and polling receiver call processing times.

Several efforts are ongoing to more fully exploit SOA-based optical crossbar switches in gigabit networks. These efforts include implementing real-time multicast functions and multiswitch networks. The authors wish to acknowledge DARPA support for this work through NCCOSC contract # N66001-86-C-0382.

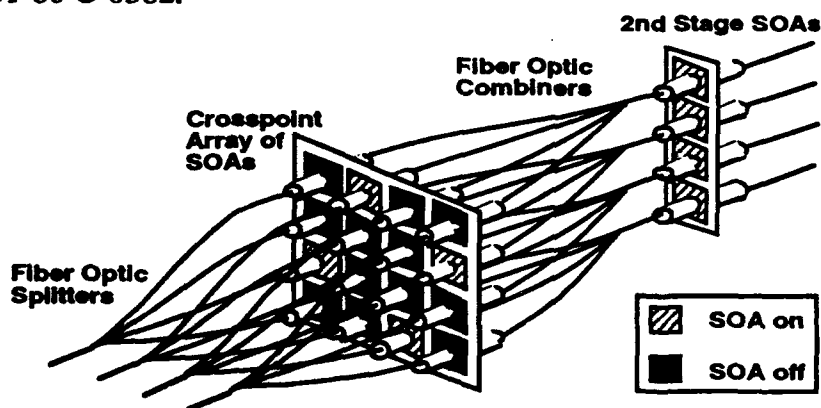


Figure 1: Schematic diagram of the optics module.

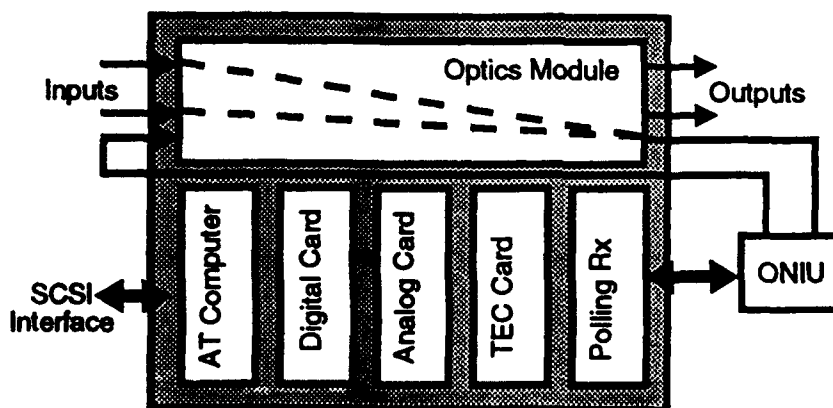


Figure 2: Block diagram of the optical crossbar switch.

## The STARNET Coherent Optical WDM Network: Modulation Format and Computer-to-Optics Interface

Michael Hickey, Charles Barry, Ciro Noronha, and Leonid Kazovsky

Stanford University, Department of Electrical Engineering  
Durand 202, Stanford, CA 94305-4055

### I. Introduction

STARNET is a novel experimental coherent optical WDM network being investigated at Stanford University. STARNET supports both circuit-switched traffic and packet-switched traffic by creating two logical sub-networks, a 2.488 Gb/s per node tunable circuit-switched sub-network and a 100 Mb/s FDDI-compatible, fixed-tuned, packet-switched, ring sub-network, on a single physical star topology [1]. Fig. 1 shows a diagram of the STARNET logical topology.

The two logical sub-networks are implemented with only one transmitter laser per node by multiplexing packet-switched data using amplitude-shift keyed (ASK) modulation and circuit-switched data using phase-shift keyed (PSK) modulation on the same optical carrier. Each node is equipped with two receivers to recover the ASK and PSK data separately. Thus, STARNET addresses two fundamental problems with WDM networks: (1) the need to support both packet-switched and circuit-switched services, and (2) the need to control high-speed circuit connections before virtual circuits are set up [2-3]. Both of these problems are solved using the virtual-ring, packet-switched sub-network.

### II. Combined PSK and ASK Modulation

To investigate simultaneous transmission and reception of ASK packet-switched and PSK circuit-switched data using the same optical carrier, we analyzed the impact of the amplitude modulation depth on the sensitivity of ASK and PSK receivers. An example of our results is shown in Figs. 2 and 3. For

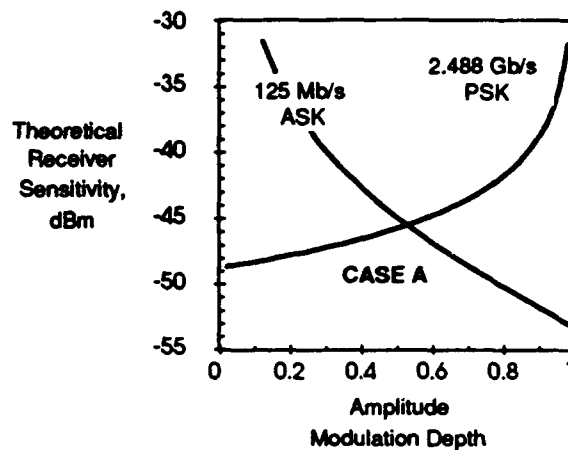


Fig. 2. Theoretical ASK and PSK receiver sensitivity versus amplitude modulation depth.

case A (Fig. 2), high-speed data are transferred via PSK modulation while low-speed data are transferred via ASK modulation. The sensitivity of the ASK receiver improves as the modulation depth is increased while the sensitivity of the PSK receiver deteriorates due to the reduced signal power at the PSK receiver when an ASK '0' is transmitted. For a modulation depth around 0.5, the ASK and PSK receivers operate with equal sensitivities. This point represents the optimum modulation depth for a node transceiver.

Fig. 3 illustrates case B; the high-speed data are transferred via ASK modulation and the low-speed data are transferred via PSK modulation. This

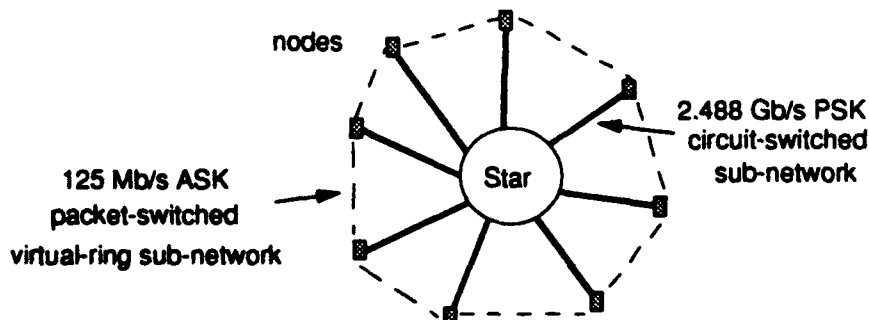


Fig. 1. STARNET logical topology.

analysis predicts that both cases A and B have sensitivities around -45 dBm. However, when the AM modulation depth approaches 1, our experimental results have shown that the PSK receiver does not function properly. Therefore, the proper combination is case A, PSK for the high-speed data and ASK for the low-speed data.

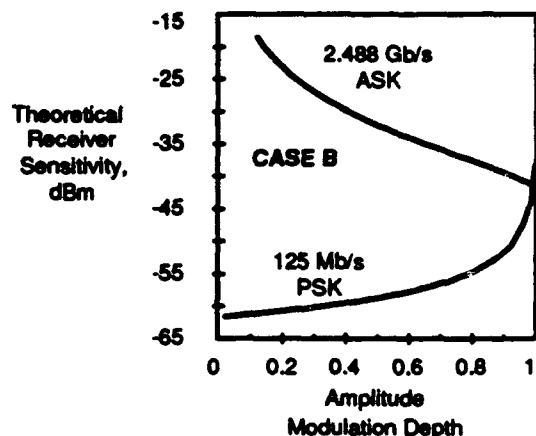


Fig. 3. Theoretical ASK and PSK receiver sensitivity versus amplitude modulation depth.

To verify our theory experimentally, we constructed an experimental node transceiver [4]. The transmitter has an output power of 5 dBm at 1.32  $\mu\text{m}$ . The sensitivity of the 2.488 Gb/s PSK receiver is -33.3 dBm with no ASK modulation. The sensitivity of the 125 Mb/s ASK receiver is -45 dBm with no PSK modulation. With both amplitude and phase modulation on the same lightwave, the ASK and PSK receivers operate with equal sensitivities when the amplitude modulation depth is 0.6.

### III. Computer-to-Optics Interface

We have investigated the issue of WDM network-to-computer interfacing and designed a 1.244 Gb/s computer-to-optics interface for a RISC workstation. The workstation connects to a STARNET transceiver via electronic hardware modules that are installed in the DECstation's TURBOchannel™ I/O bus.

Fig. 4 shows the functionality of the interface. The experimental STARNET transceiver provides full-duplex communication at a sustained rate of 1.244 Gb/s. A conservative estimate of the average TURBOchannel I/O bandwidth available to the high-speed sub-network is 200-250 Mb/s (800 Mb/s peak). Therefore, the STARNET transceiver is capable of sending and receiving at a rate 5 times greater than the current workstation bus can sustain. To take advantage of the remaining bandwidth of the STARNET transceiver, the high speed circuit switched sub-net-

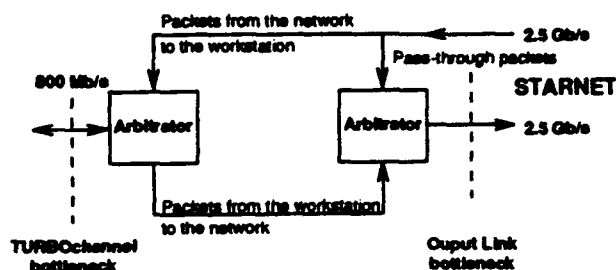


Fig. 4. High-speed network bottlenecks.

work interface is designed for multihop packet switching. Routing of incoming packets on the circuit-switched sub-network is done on-the-fly on a packet by packet basis. The headers of incoming packets are checked. If they are destined for the receiving node, they are placed in a receive arbiter. Packets not destined for the workstation are forwarded to the node's output arbiter without being seen by the node's local bus. The result is a high-speed 2x2 multihop packet switch architecture over the circuit-switched sub-network.

### IV. Conclusions

Both packet-switched and circuit-switched data can be transmitted on a single lightwave using combined amplitude and phase modulation. Our theoretical and experimental results indicate that the proper combination is transmitting high-speed data using PSK modulation and low-speed data using ASK modulation. Our experimental STARNET computer-to-optics interface allows us to transmit data directly from a workstation over the WDM network at a bit rate of 1.244 Gb/s and is one of the first of its kind.

### V. References

- [1] P. Poggiolini and L. Kazovsky, "STARNET: A Multi-Gbit/s Optical LAN Utilizing A Passive WDM Star," *IEEE/OSA J. of Lightwave Tech.*, May 1993.
- [2] N. R. Dono, P. E. Green, K. Liu, R. Ramaswami, and F. F. Tong, "A wavelength division multiple access network for computer communication," *IEEE J. Select. Areas Comm.*, vol. 8, no. 6, pp. 983-994, August 1990.
- [3] M. W. Maeda, A. E. Willner, J. R. Wullert II, J. Patel, and M. Allersma, "Wavelength-division multiple-access network based on centralized common-wavelength control," *IEEE Photonics Tech. Letters*, vol. 5, no. 1, pp. 83-85, Jan. 1993.
- [4] M. Hickey, C. Barry, C. Noronha, and L. Kazovsky, "Experimental PSK/ASK transceiver for the STARNET WDM computer communication network," *IEEE Photonics Tech. Letters*, May 1993.

MATRIX CODES FOR ULTRADENSE, GIGABIT  
OPTICAL CDMA NETWORKS

by

Antonio J. Mendez  
MENDEZ R&D ASSOCIATES  
P.O.Box 2756  
El Segundo, CA 90245  
(310)640-0497

and

Robert M. Gagliardi  
University of Southern California  
Communication Sciences Institute  
Los Angeles, CA 90089

SUMMARY

Several seminal research efforts have shown that pseudo-orthogonal (0,1) pulse sequences can be readily translated into optical code division multiple access (optical CDMA) waveforms and associated optical correlators. These (0,1) pulse sequences are derivable by combinatoric methods (Ref.1,2). While these (0,1) pulse sequences are extremely convenient for synthesis, analysis, and simulation, they are inefficient from the viewpoint of physical implementation in the sense that they require a "time penalty" (ratio of bit time to chip time) given by

$$N * w * (w - 1) / 2$$

where N is the number of pseudo-orthogonal codes (i.e., users or nodes in the network) and w is the weight of the code. This "time penalty" is excessive when large networks (more than ten) or fast networks (i.e., Gb/s) are involved. This inefficiency of the (0,1) linear codes has driven us to develop matrix coding (Ref.3) as a more efficient alternative which is scalable to ultradense, Gigabit networks. Matrix coding is a particular implementation of multi-attribute coding (Ref. 4). The particular matrix codes which we have studied are based on folding the (0,1) pulse sequences into matrices and interpreting the resulting (0,1) two dimensional arrays as temporal/spatial waveforms. We have shown by analysis, design, and measurement that temporal/spatial optical CDMA is demonstrably more efficient and dense than temporal coding alone (Ref. 5).

Temporal/spatial coding is also modular. The design methodology proceeds by dividing the system into subassemblies which are functions of the (1) number of network users (N) and the spatial degree (f); (2) the spatial degree and the code weight (w); and (3) the network point to point data rate (D). Note that this modular

approach separates the distribution and the transceiver requirements of the problem. Figure 1 shows a typical partitioning of the problem into these kinds of sub-assemblies. Figure 2 shows the front panel of a 4x4 breadboard designed by these rules.

This talk will discuss analysis, design, and measurements of the 4x4 optical CDMA breadboard and correct techniques for predicting the multiple access performance of this class of Gigabit networks.

#### REFERENCES

- (1) F. Khansefid, H. Taylor, and R. Gagliardi, "Design of (0,1) Sequence Sets for Pulsed Coded Systems", USC-CSI-88-03-03 (1988).
- (2) A.J. Mendez, S. Kuroda, R. Gagliardi, and E. Garmire, "Generalized Temporal Code Division Multiple Access (CDMA) for Optical Communication", SPIE Proc., Vol.1125, p.208 (1989).
- (3) R.M. Gagliardi and A.J. Mendez, "Pulse Combining and Time-Space Coding for Multiple Accessing with Fiber Arrays", 1990 IEEE/LEOS Summer Topical Meeting on Opt.Mult.Access Networks, paper OMth14.
- (4) J.Y. Hui, "Pattern Code Modulation and Optical Decoding-A Novel Code-Division Multiplexing for Multifiber Networks", IEEE J.Select.Areas Commun., SAC-3, p. 916 (1985).
- (5) E. Park, A.J. Mendez, and E. Garmire, "Temporal/spatial optical CDMA networks-design, demonstration, and comparison with temporal networks", IEEE Photonics Technology Letters, Vol.4, p.1160, (1992).

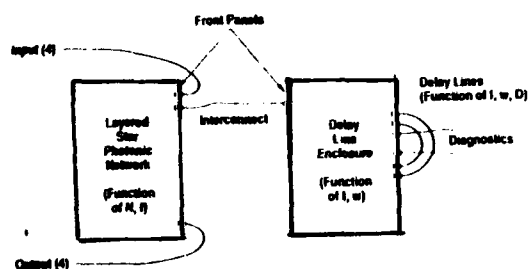


Figure 1. Partitioning of optical CDMA into functional subassemblies.

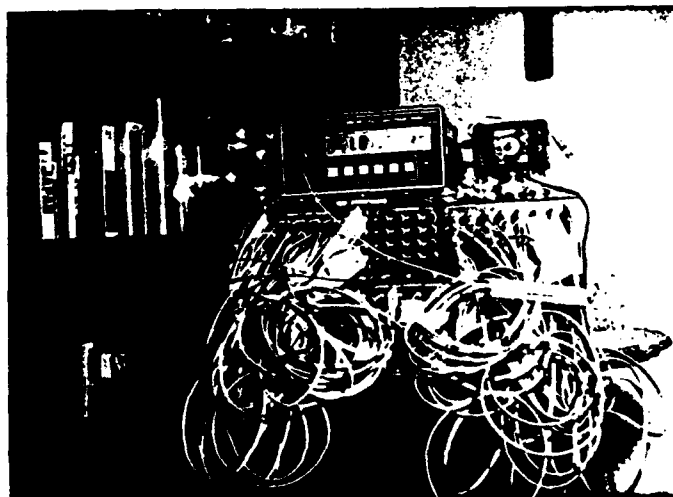


Figure 2. Front panel of 4x4 breadboard based on design rules.

**A Compact, Directly Modulated, Pulse-Compressed, and Variably-Delayed Time-Division-Multiplexer for Gigabit Multiple-Access Networks**

Yin-Chen Lu, Julian Cheng

University of New Mexico, Center for High Technology Materials, Albuquerque, NM 87131

Broadband-ISDN multiple access networks with individual subscriber nodes operating at a data rate in excess of 1 GB/s can transmit a total data capacity of many tens of Gb/s over a single optical fiber. Electronic data multiplexing is difficult at these rates, and the direct or external modulation of an optical source at several tens of Gb/s is not yet feasible. One solution is to optically time-division-multiplex (OTDM) and/or wavelength-division-multiplex (WDM) a large number of synchronous optical sources that are individually modulated at a 1 Gb/s rate.<sup>1</sup> We describe below a novel, compact OTDM multiplexing scheme which can achieve a potential multiplexed data-capacity of several tens of Gb/s without the use of ultra high-speed sources, modulators or drive electronics. The functions of a TDM multiplexer - data modulation, pulse compression, relative time-delay, variable time-slot-interchange (TSI) for switching operations, and the bit-interleaving of multiple data streams - are all combined in a single operation.

The experimental set-up and operating principles of the TDMA multiplexing scheme are shown in Figures 1 and 2, respectively. At each subscriber node, a laser is modulated by a composite drive current containing a dc pre-bias, a modulation current pulse and a clock pulse ( $\approx 1$  ns). The prebias and modulation current levels are chosen to bias the laser below threshold, while clock pulses ( $\approx 100$  ps wide) from a comb generator are added to the data pulses to trigger laser emission. The laser is gain-switched only when a data pulse (logic 1) and a clock pulse are both present, following a turn-on delay that may be varied by either electronically altering the time delay between the clock and data pulses, or by controlling the total prebias and data levels. The gain-switched laser output provides a pulse-compressed and variably-delayed optical replica of the input modulation signal. Multiple sources are independently modulated and compressed, and delayed by different intervals to be subsequently time-interleaved using a passive Nx1 fiber multiplexer. The important functions of the multiplexer are schematically depicted in Fig. 2.

Vertical-cavity surface-emitting lasers (VCSELs) are used in the experimental demonstration, although this multiplexing scheme does not require any special laser. Input data consisting of sub-threshold, 500 Mb/s pseudorandom pulses (RZ) with a 3.6 mA dc prebias are applied to the VCSEL, which remains turned off. This is combined with 500 MHz clock pulses (100 ps wide) from a comb generator (Fig. 3a, top trace) to selectively drive the VCSEL above threshold, producing gain-switched, modulated, and compressed optical output pulses (50 ps width) that replicate the input data (Fig. 3a, lower trace), with a peak optical power of 2.5 mW. The shortest gain-switched and modulated pulses have a full-width at half-maximum (FWHM) of less than 27 ps.

To time-interleave the data from multiple sources and to effect TSI for switching operations, the pulses from different VCSELs need to be variably and differentially time-delayed. While longer time delays can be achieved for packet-interleaved TDMA systems using directional coupler switches and fixed fiber delay lines,<sup>2</sup> the shorter delays for bit-interleaved TDMA can be directly implemented without any additional hardware. Since all the compressed and interleaved pulses reside within a single clock period, the maximum time delay required is less than 1 ns. The turn-on delay of the gain-switched pulses can be varied by changing the pre-bias and the phase(or amplitude) of the clock pulses. Linearly variable time delays with a range of  $>500$  ps has been achieved using an electronically adjustable time delay between the data and clock pulses, with amplitude variations of less than 20%. Alternatively, an adjustable time delay of  $>300$  ps can also be achieved by adjusting the data and prebias levels. The interleaving of independently-modulated and relatively time-delayed pulses from two neighboring VCSELs in a monolithic array is shown in Fig. 4, with channel 2 differentially delayed from reference channel 1 by  $\Delta T$ ,  $2\Delta T$ ,  $3\Delta T$ , and  $4\Delta T$ , respectively (superimposed).

Since the width of the gain-switched optical pulses limits the time interval between neighboring TDM channels, the total channel capacity is determined by the pulse compression ratio (PCR), which can be improved by using better optimized VCSELs or by driving them harder. For a PCR of 20:1, twenty 1Gb/s channels may be multiplexed, producing a total data throughput of 20 Gb/s. Several different TDMA modules, each containing a number of time-multiplexed channels and each characterized by a different laser emission wavelength, can be further multiplexed in the WDM regime to provide a very large aggregate network capacity.

## REFERENCES:

- [1] H. S. Hinton, "Photonic time-division switching systems", IEEE Circuits & Devices Mag., Vol. 5, No. 4, pp. 39-43, 1989.
- [2] P. R. Prucnal, P. A. Perrier, "Optically-processed routing for fast packet switching", IEEE Lightwave Commun. Sys. Mag., LCS Vol. 1, No. 2, pp. 54-67, 1990.

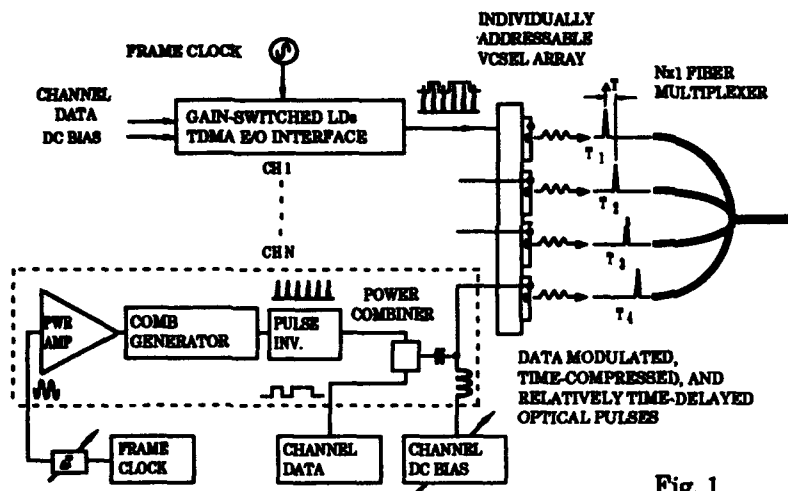


Fig. 1. A time-division multiple-access (TDMA) module consisting of an array of lasers, each of which is individually modulated by the combination of a data pulse, a clock pulse, and a dc bias to produce gain-switched, time-compressed and relatively delayed optical output pulses that are interleaved by an Nx1 fiber multiplexer.

Fig. 1

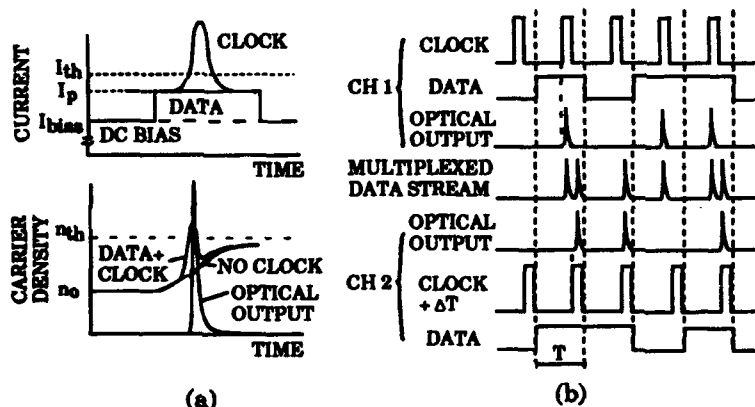


Fig. 2. (a) The operating principles of the TDMA multiplexer, showing the roles of the dc pre-bias, clock and data pulses in producing a gain-switched and directly modulated optical pulse. (b) Illustrates the time compression, relative delay, and bit-interleaving of two independently modulated channels.

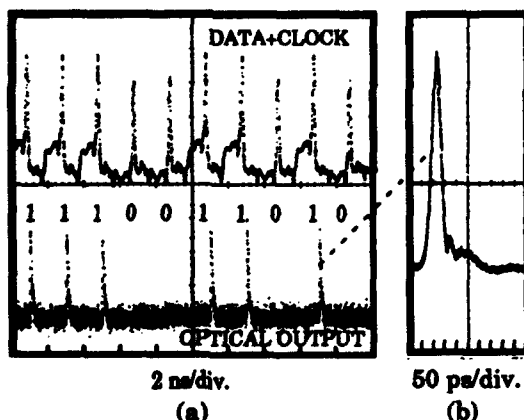


Fig. 3. (a) The composite drive current (upper trace) with clock and data pulses, and the optical pulsed output of the VCSEL (lower trace) with (b) an enlarged view.

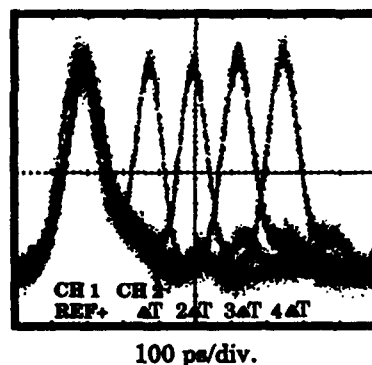


Fig. 4. Superimposed view of two time-multiplexed and independently modulated pulsed data channels with four different values of relative time delay. The pulse broadening and apparent inter-symbol interference are photodetector-limited, and are absent when a time-resolved detector is used.

S. Bajaj.....	28
C. Barry.....	58
B. Basch.....	47
L. Bergman.....	8
C. Brackett.....	51
C. Brazdziunas.....	28
V. Chan.....	52
J. Cheng.....	62
N. Cheung.....	40
I. Cidon.....	36
J. DesMarais.....	14
R. Emmett.....	21
K. Eng.....	43
G. Follen.....	30
Y. Fouquet.....	32

R. Gagliardi.....	60
A. Gerrish.....	56
R. Gitlin.....	12
P. Green.....	54
R. Guerin.....	36
M. Hicky.....	58
W. Holden.....	14
J. Hughes.....	45
M. Iqbal.....	14
J. Jacobson.....	20
A. Joel.....	4
C. Johnston.....	14
P. Kaiser.....	10
M. Karol.....	43
L. Kazovsky.....	58

A. Khamisy.....	36
A. Kirby.....	52
S. Klux.....	23
V. Konangi.....	38
Y. Lee.....	13
Y. Lu.....	62
J. Mann.....	14
L. McAdams.....	56
A. Mendez.....	60
A. Mink.....	32
R. Moolenbeek.....	47
C. Noronha.....	58
M. Procanik.....	47
N. Ransom.....	6
T. Robe.....	28

L. Roberts.....	19
A. Saleh.....	52
V. Samalam.....	47
D. Smith.....	14
R. Snelling.....	3
S. Srinidhi.....	38
W. Stephens.....	24, 28
F. Vakil.....	28, 34
S. Wakid.....	32
K. Walsh.....	14
G. Watson.....	26
J. Young.....	14
K. Young.....	14